



UNIVERSITY OF  
LIVERPOOL

# Laser Induced Plasmas: A Light Source For Biological Spectroscopy

Thesis submitted in accordance with the requirements of the University  
of Liverpool for the degree of Doctor in Philosophy.

By

Joseph Holman

March 2016

## Abstract

The work presented in this thesis investigates the viability using a laser induced plasmas as a high intensity, UV/VIS/IR benchtop light source for biological spectroscopic applications. It is well known that plasmas make excellent light sources due to their broadband emission throughout the UV/VIS/IR. A detailed account is given of the construction and testing of a prototype benchtop spectrometer that utilised a laser induced plasma as its light source. The parts to build this spectrometer had a total cost of £6480.49, a competitive price for an instrument capable of measuring absorbance/turbidity spectra in the wavelength range of 380 to 700 nm at a rate of up to 5 times a second and to a wavelength resolution of approximately 0.2 nm. The production of shorter wavelength is very possible using this technology but would require a much more expensive, higher repetition rate laser, which was beyond the scope of this project.

A review of the physical factors influencing the emission of light from a plasma is first presented. Several noble gases were tested to optimise the intensity and short wavelength output of the plasma. The results showed that argon had the highest emission intensity light for reasonable cost. The prototype instrument can be run in two different modes, static mode and dynamic mode. In static mode, the spectrometer can determine the absorbance spectrum of samples that do not change over time such as coloured dyes. In dynamic mode that monitors the absorbance of samples whose absorbance/turbidity varies with time. The accuracy of the prototype plasma spectrometer was tested by determining the absorption spectrum of holmium oxide in perchloric acid, a standard solution often employed for spectrometer calibration and testing. The prototype spectrometer was then successfully employed to investigate the effect of heparin, in the presence of the cations  $\text{Fe}^{2+}$ ,  $\text{Zn}^{2+}$  and  $\text{Cu}^{2+}$ , on the aggregation rate of the protein human lysozyme, over a range of pHs. The aggregation of lysozyme was an interesting system to monitor, as it has been proposed as a model for the formation of the fibrils found in amyloid plaques.

## Table of Contents

Abstract	I
Contents	II
List of Abbreviations	V
List of Figures	VI
List of Tables	XV
List of Equations	XVIII

### **CHAPTER 1 - Introduction**

1.1 Background	1
1.2 Biological spectroscopy: A review of light source requirements	3
1.2.1 Molecular excitation processes	4
1.2.2 Molecular relaxation processes	22
1.3 The spectroscopy of heparin and heparan sulphate	30
1.4 Signal to noise ratios in absorbance spectroscopy	44
1.5 Plasma as a high intensity light source	61
1.6 Laser induced plasmas and plasma fundamentals	69
1.6.1. Physical processes in laser induced plasmas	73
1.6.2 Plasma heating processes - multiphoton ionisation	78
1.6.3 Plasma heating processes - collisional ionisation	82
1.6.4 Cooling processes - bremsstrahlung	83
1.7 Chapter summary	101
List of materials	103
Breakdown of materials and costs for the construction of the prototype instrument	104

### **CHAPTER 2 - Instrument design, build and commissioning**

2.1 MI Engineering's initial light source design	107
2.2 Proposed plasma light source: concept and design	113
2.3 Choice of laser for plasma generation	114

2.4	Focusing optics for the generation of laser induced plasma	125
2.5	Optics for the capture and collimation of laser induced plasma light	131
2.6	Sealed chamber design and construction	141
2.7	Spectrometer timing electronics and control programs	149
2.8	Determination of sample absorbance using the plasma light source instrument.	157
2.9	Instrument testing using a holmium oxide standard	166
2.10	Instrument testing using coloured dyes	170
2.11	Time resolved absorbance: spectral determination	174
<b>CHAPTER 3 - Improving instrument performance and reliability</b>		
3.1	Investigation of the factors influencing the performance and reliability of the prototype instrument	177
3.2	Testing of focusing lenses	195
3.3	Noble gases as the plasma medium	228
3.4	The pressure dependency of laser induced breakdown	234
3.5	Gas testing and results	241
<b>CHAPTER 4 - Instrument measurements</b>		
4.1	The effect of heparin on protein aggregation	251
4.2	Monitoring protein aggregation using the plasma spectrometer	258
4.3.	Commercial UV/vis scanning spectrophotometer comparison	282
4.4	Analysis of lysozyme/fibrinogen turbidity data	294
<b>CHAPTER 5 - Discussion</b>		
5.1	Costs of prototype instrument	303
5.2	Instrument performance	304
5.3	Conclusions relating to the protein aggregation experiments	306
5.4	Improvements to plasma spectrometer	308

<b>Chapter 6 - Conclusions</b>	<b>315</b>
References	319
Appendix A: Derivation of the thermal brehmsstrahlung emission from plasma.	343
Appendix B: C++ code control code for the plasma spectrometer.	352
Appendix C: Visual basic for applications (VBA) code used in this project.	362

## List of Abbreviations

LIP	Laser Induced Plasma
EM	Electromagnetic
VCD	Vibrational Circular Dichroism
IR	Infrared
SNR	Signal to Noise Ratio
RMS	Root Mean Squared
VUV	Vacuum Ultraviolet
MI	MI Engineering LTD
EUV	Extreme Ultraviolet
LIBS	Laser Induced Breakdown Spectroscopy
DLS	Dynamic Light Scattering
CD	Circular Dichroism
UVCD	Ultraviolet Circular Dichroism
REMPI	Resonance Enhanced Multiphoton Ionisation
FWHM	Full Width Half Maximum
KDP	Potassium Dihydrogen Phosphate
LTE	Local Thermal Equilibrium
LIH	Linear, Isotropic and Homogeneous
CCD	Charged-Coupled Device
VBA	Visual Basic for Applications
GAGs	Glycosaminoglycans
HS	Heparan Sulphate
HSPG	Heparan Sulphate Proteoglycans
PMH	Porcine Mucosal Heparin
ECM	Extracellular Matrix
GPI	Glycosylphosphatidylinositol
LMWH	Low Molecular Weight Heparins
FTIR	Fourier Transform Infrared
NMR	Nuclear Magnetic Resonance
VBA	Visual Basic for Applications
DFT	Density Functional Theory

## List of Figures

<b>Figure 1.</b> The relative levels of the electronic, vibrational and rotational energy states of a molecule.	5
<b>Figure 2.</b> Schematic of the excitation and emission processes described in this chapter.	6
<b>Figure 3.</b> The relative energies of the molecular transitions.	9
<b>Figure 4.</b> Electronic CD spectra of some of the secondary structures present in proteins.	18
<b>Figure 5.</b> Diagram of the Raleigh scattering process from a single spherical particle.	24
<b>Figure 6.</b> The Raleigh and Raman scattering spectral peaks observed with excitation by at a monochromatic light source.	28
<b>Figure 7.</b> The monosaccharide building blocks of heparin and HS.	31
<b>Figure 8.</b> The minimal pentasaccharide antithrombin binding site.	40
<b>Figure 9.</b> The VCD (left) and IR transmission (right) spectra of heparin, HS and chondroitin sulphate B at 25 mg/ml.	43
<b>Figure 10.</b> VCD spectra of concanavalin A, heparin and concanavalin A bound to heparin.	44
<b>Figure 11.</b> The spectral responsivity of the Thorlabs FDS100 silicon photodiode as measured by NIST.	46
<b>Figure 12.</b> A graph of signal to noise ratio against the sample absorbance for a simple absorbance measurement.	52
<b>Figure 13.</b> A graph of signal to noise ratio against the sample absorbance for a simple absorbance measurement where the time taken for the baseline measurement is unity.	53
<b>Figure 14.</b> A graph of signal to noise ratio against sample absorbance for a simple absorbance measurement where the light source is of a constant known intensity.	55
<b>Figure 15.</b> A schematic of the optical arrangement for the determination of sample absorbance with a varying light source intensity.	56

<b>Figure 16.</b> A contour plot of the SNR of measurements conducted using the experimental arrangement shown in Figure 15.	60
<b>Figure 17.</b> The intensity of the HPX-2000 Xenon light source as a function of wavelength.	64
<b>Figure 18.</b> Blackbody spectral radiance emission curves plotted against wavelength for three different temperatures.	66
<b>Figure 19.</b> A logarithmic graph showing the radiance of a blackbody over a wide range of wavelengths.	67
<b>Figure 20.</b> LIB spectral emission of argon showing line emission peaks from bound transitions and background continuum emission from free transitions.	74
<b>Figure 21.</b> The electron transitions occurring in plasma.	77
<b>Figure 22.</b> The potential energy diagram of a three photon REMPI event.	81
<b>Figure 23.</b> The multiphoton resonance effect of neon with a ruby laser.	81
<b>Figure 24.</b> A schematic diagram of the collisional ionisation process.	83
<b>Figure 25.</b> A schematic diagram of the bremsstrahlung and inverse bremsstrahlung processes.	84
<b>Figure 26.</b> Numerical values of the Gaunt factor.	89
<b>Figure 27.</b> The frequency averaged Gaunt factor ( $Z=1$ )	90
<b>Figure 28.</b> The measured electron density in a laser induced plasma.	92
<b>Figure 29.</b> Gaunt factors for various laser wavelengths and charges in an argon plasma.	93
<b>Figure 30.</b> Brehmsstralung emission plotted against wavelength for the region 0-20 $\mu$ m.	94
<b>Figure 31.</b> Brehmsstralung emission plotted against wavelength for the region 0-1 $\mu$ m.	95
<b>Figure 32.</b> Log graph showing the dependence of absorption coefficient against frequency.	98
<b>Figure 33.</b> Bremsstrahlung spectral shape including self-absorbance.	99



<b>Figures 34 and 35.</b> MI's proposed light source design.	108
<b>Figure 36.</b> A schematic of the proposed plasma spectrometer	114
<b>Figure 37.</b> A diagram of the main components within a Q-switched laser.	116
<b>Figure 38.</b> The tattoo removal machine showing the housing for the electronics and water pump.	119
<b>Figure 39.</b> The handheld laser "gun" and its internal components.	120
<b>Figure 40.</b> The energy level diagram of neodymium atoms in an Nd:YAG laser.	121
<b>Figure 41.</b> Peak effective stimulated emission cross section at 1064nm of 1% Nd:YAG as a function of temperature.	122
<b>Figure 42.</b> Electron temperature and density dependency on laser pulse energy.	125
<b>Figure 43.</b> The transmission properties of UV fused silica, N-BK7 and N-SF11.	129
<b>Figure 44.</b> Galilean and Kaplerian beam expanders.	130
<b>Figure 45.</b> The two types of common optical collimator.	131
<b>Figure 46.</b> The effect of attempting to collimate a non-point light source.	132
<b>Figure 47.</b> Possible optical arrangements for the capture and collimation of light emitted from a plasma.	133
<b>Figure 48.</b> A diagram of the angle subtended by the Thorlabs CM254-019-F01 parabolic lens.	134
<b>Figure 49.</b> The reflective characteristics of the CM254-019-F01 parabolic lens.	135
<b>Figure 50.</b> A laser induced plasma at the focal points of the focusing lens and the parabolic capture mirror.	135
<b>Figure 51.</b> A schematic diagram of the optical apparatus for the capture, collimation and analysis of plasma light.	137
<b>Figure 52.</b> The spectrum of a laser induced plasma in air at atmospheric pressure fitted with an approximate blackbody curve.	139
<b>Figure 53.</b> A diagram of the spectrometer for measuring the absorbance/turbidity of time varying samples.	140

<b>Figure 54.</b> The complete optics showing the collimation optics, the beam splitter and optical fibre ports with beam focusing optics.	141
<b>Figure 55.</b> The Autocad drawing of the plasma chamber.	144
<b>Figure 56.</b> The Autocad drawing of the lid of the plasma chamber.	145
<b>Figure 57.</b> Pictures of the pressure chamber showing the main components.	147
<b>Figure 58.</b> The electrically isolated mount for the laser housing.	148
<b>Figure 59.</b> The plasma spectrometer showing the laser, pressure chamber and optics.	149
<b>Figure 60.</b> A picture of an Arduino Uno microcontroller showing the location of digital and analogue connectors, power and USB cables.	152
<b>Figure 61.</b> The TSL257 light to voltage converter, pin diagram and functional block diagram of the. $V_{DD}$ is the +5 V power pin for the converter.	153
<b>Figure 62.</b> A wiring diagram of the connections between the light to voltage converter, Arduino Uno, PC and spectrometers.	154
<b>Figure 63.</b> A schematic of the light beams in the spectrometer.	158
<b>Figure 64.</b> The mean transmittance and standard deviation error of transmittance obtained for the Thorlabs BSW26 50/50 beam splitter.	164
<b>Figure 65.</b> The mean and standard deviation of $C_{\lambda}$ obtained for the Thorlabs BSW26 50/50 beam splitter.	164
<b>Figure 66.</b> A bar chart showing how the standard deviation of the transmittance of the beam splitter varied with wavelength.	165
<b>Figure 67.</b> A bar chart showing how the standard deviation of $C_{\lambda}$ varied with wavelength.	166
<b>Figure 68.</b> The absorbance spectra of holmium (III) oxide (4%) in perchloric acid (10%) obtained using the plasma spectrometer and a Thermo Scientific spectrophotometer.	169
<b>Figure 69.</b> The NIST SRM 2034 (lot95) standard spectrum of holmium (III) oxide (4%) in perchloric acid (10%) measured using a HP 8453 spectrophotometer.	169
<b>Figures 70 &amp; 71.</b> The absorbance spectra of AzureA at several different concentrations.	171

<b>Figures 72 &amp; 73.</b> The absorbance spectra of Bromocresol Green at several concentrations.	172
<b>Figures 74 &amp; 75.</b> The absorbance spectra of Phenol Red at several concentrations.	173
<b>Figure 76.</b> The time resolved spectrum obtained from a one hour blank run of the plasma spectrometer.	176
<b>Figure 77.</b> Energy absorption study of laser induced breakdown of air.	183
<b>Figure 78.</b> Dielectric breakdown curves for dry air with and without the presence of ionising radiation.	186
<b>Figure 79.</b> Intensity distributions in the vicinity of the focal point of the lens.	187
<b>Figure 80.</b> Collinear plasmas formed in air at 1 atm produced by a 30 ns ruby laser at $\lambda=0.69 \mu\text{m}$ .	188
<b>Figure 81.</b> Typical temporal profile of an Nd:YAG laser showing that the pulse is actually far from Gaussian in shape.	190
<b>Figure 82.</b> Breakdown voltage characteristics for air, CO <sub>2</sub> and hydrogen.	192
<b>Figure 83.</b> Frame 1787 from a 5 min video capture, showing the laser induced plasma obtained using 5 cm focal length lens.	197
<b>Figure 84.</b> Frame 5342 from a 5 minute video capture showing the cross image phenomenon.	198
<b>Figure 85.</b> A sequence of images showing how the position of the cross-like objects changes over time.	198
<b>Figure 86.</b> Scatter plot of the dependant and independent variables in the lens testing experiments.	207
<b>Figure 87.</b> A graph of the plasma probability against x.	208
<b>Figure 88.</b> The diagnostic plots for the logarithmic regression of the dependent binary variable 'Plasma in frame Y/N'.	214
<b>Figure 89.</b> A graph of the plasma probability per pulse against the focal length from the logarithmic regression modelling.	215
<b>Figure 90.</b> Box plot of the plasma size against the focal length	216

<b>Figure 91.</b> Box plot of the reciprocal of focal length and the reciprocal of the square of focal length.	217
<b>Figures 92.</b> Box plot of the plasma size against the reciprocal of the square of focal length.	217
<b>Figure 93.</b> A graph of plasma size against focal length from the best fit multiple regression model.	220
<b>Figure 94.</b> The diagnostic plots for the multiple linear regression of the dependent binary variable “Plasma Size”.	222
<b>Figure 95.</b> The diagnostic plots for the linear model that predicts the distance of the plasma from the focal lens.	225
<b>Figure 96.</b> The plasma spectrometer cooling system.	227
<b>Figure 97.</b> A graph of first ionisation energy against atomic number for the first six periods of elements in the periodic table.	230
<b>Figure 98.</b> The number of multiphoton ions created as a function of laser intensity at the focal point.	232
<b>Figure 99.</b> Breakdown threshold intensities against pressure for Argon and Xenon at 4 different wavelengths.	236
<b>Figure 100.</b> The relationship of breakdown intensity against pressure for several gases at the second harmonic of ruby laser ( $\lambda=3472 \text{ \AA}$ ) with 7cm focal length lens.	237
<b>Figure 101.</b> Experimental and theoretical laser-induced breakdown thresholds for argon at $\lambda=532 \text{ nm}$ .	238
<b>Figure 102.</b> The mean spectra of light emitted from a laser induced plasma in helium at pressures of up to 2.2 bar.	241
<b>Figure 103.</b> The mean spectra of light emitted from a laser induced plasma in helium at pressures of up to 2.2 bar. The laser is frequency doubled to 532 nm.	242
<b>Figure 104.</b> The mean spectra of light emitted from a laser induced plasma in neon at pressures of up to 2.2 bar.	242
<b>Figure 105.</b> The mean spectra of light emitted from a laser induced plasma in neon at pressures of up to 2.2 bar. The laser is frequency doubled to 532 nm.	243

<b>Figure 106.</b> The mean spectra of light emitted from a laser induced plasma in argon at pressures of up to 2.2 bar.	243
<b>Figure 107.</b> The mean spectra of light emitted from a laser induced plasma in argon at pressures of up to 2.2 bar. The laser is frequency doubled to 532 nm.	244
<b>Figure 108.</b> The mean spectra of light emitted from a laser induced plasma in krypton at pressures of up to 1.8 bar.	244
<b>Figure 109.</b> The mean spectra of light emitted from a laser induced plasma in krypton at pressures of up to 1.8 bar. The laser is frequency doubled to 532 nm.	245
<b>Figure 110.</b> The total spectral power for each of the gases tested, showing the effect of pressure and frequency doubling.	246
<b>Figure 111.</b> The time resolved turbidity spectrum of the pH 10 solution of 0.5 mg/ml lysozyme with 20 µg heparin.	260
<b>Figure 112.</b> The time resolved turbidity spectrum of the pH 10 solution of 1 mg/ml lysozyme with 20 µg heparin.	260
<b>Figure 113.</b> The time resolved turbidity spectrum of the pH 10 solution of 1.5 mg/mL lysozyme with 20 µg heparin.	261
<b>Figure 114.</b> The time resolved turbidity spectrum of the pH 10 solution of 2 mg/mL lysozyme with 20 µg heparin.	261
<b>Figure 115.</b> The time resolved turbidity spectrum of the pH 10 solution of 2.5 mg/mL lysozyme with 20 µg heparin.	262
<b>Figure 116.</b> The time resolved turbidity spectrum of the pH 10 solution of 3 mg/mL lysozyme with 20 µg heparin.	262
<b>Figure 117.</b> The turbidity spectra of lysozyme, aggregating in the presence of copper heparin at pH 8.5 and sodium heparin at pH 10, recorded at 702 seconds.	272
<b>Figure 118.</b> The turbidity spectra of fibrinogen, aggregating in the presence of copper heparin at pH 8.5 and sodium heparin at pH 3.5, recorded at 202 seconds.	281
<b>Figure 119.</b> The calculated rate of change of turbidity of 2mg/ml lysozyme against pH for each heparin, obtained using the plasma spectrometer at 550 nm.	297

<b>Figure 120.</b> The calculated rate of change of turbidity of 2mg/ml lysozyme against pH for each heparin, obtained using the plate reader at 550 nm.	297
<b>Figure 121.</b> The calculated rate of change of turbidity of 2mg/ml lysozyme against pH for each heparin, obtained using the plasma spectrometer at 600 nm.	298
<b>Figure 122.</b> The calculated rate of change of turbidity of 2mg/ml lysozyme against pH for each heparin, obtained using the plate reader at 600 nm.	298
<b>Figure 123.</b> The calculated rate of change of turbidity of 2mg/ml fibrinogen against pH for each heparin, obtained using the plasma spectrometer at 550 nm.	299
<b>Figure 124.</b> The calculated rate of change of turbidity of 2mg/ml fibrinogen against pH for each heparin, obtained using the plate reader at 550 nm.	299
<b>Figure 125.</b> The calculated rate of change of turbidity of 2mg/ml fibrinogen against pH for each heparin, obtained using the plasma spectrometer at 600 nm.	300
<b>Figure 126.</b> The calculated rate of change of turbidity of 2mg/ml fibrinogen against pH for each heparin, obtained using the plate reader at 600 nm.	300
<b>Figure 127.</b> The focused images of the pinhole formed at each of the fibre optic ports.	305
<b>Figure 128.</b> A schematic of the optical arrangement for the simultaneous determination of sample absorbance minus the background absorbance due to buffer absorbance.	310
<b>Figure 129.</b> The spectrum of the flashlamp inside the ML-LASER-YB5 Nd:YAG laser.	312
<b>Figure 130.</b> The transmission properties of various flashlamp envelope materials.	313
<b>Figure 131.</b> An electron moving past a positive ion of charge $+Ze$ at time= $t$ .	344

- Figure 132.** A cloud of plasma with ion density  $N_i$  and electron density  $N_e$ . 346
- Figure 133.** A plot of the function  $f(x) = e^{-x}/x$ . 348

## List of Tables

<b>Table 1.</b> Important biological chromophores	11
<b>Table 2.</b> The band assignments of the main IR chromophores in biomolecules.	13
<b>Table 3.</b> The GAG family of carbohydrates	35
<b>Table 4.</b> Commonly used light sources for spectroscopy.	63
<b>Table 5.</b> Some common elements by atomic number and the number of photons each must absorb to undergo ionisation with an Nd:YAG laser at $\lambda=1064$ nm.	80
<b>Table 6.</b> A breakdown of the triggering code and communication between the PC and the Arduino Uno.	155
<b>Table 7.</b> Typical .csv output of the CCS200 spectrometer.	157
<b>Table 8.</b> The recorded intensities of the transmitted beam	160
<b>Table 9.</b> The recorded intensities of the reflected beam.	160
<b>Table 10.</b> The format of the final worksheet in the Excel file after running the VBA code.	163
<b>Table 11.</b> The experimental parameters and the results from the published investigations into the breakdown threshold of air or nitrogen using an Nd:YAG laser.	181
<b>Table 12.</b> Number of photons required in multiphoton ionisation to produce a positively ionised molecule and free electron.	191
<b>Table 13.</b> A summary of the results of the lens testing experiments.	203
<b>Table 14.</b> The correlation matrix of the dependant and independent variables in the lens testing experiments.	205
<b>Table 15.</b> Results of threshold breakdown intensity measurements for LIPs formed in noble gases at different Nd:YAG laser harmonics.	233
<b>Table 16.</b> A summary of the experimentally derived pressure dependence of laser induced breakdown in argon and xenon	240
<b>Table 17.</b> A summary of the total spectral power (arbitrary units) for each noble gas at different pressures, with or without frequency doubling	246



<b>Table 18.</b> The mean and standard deviation intensity of the plasma at 600 nm for each gas over a range of pressures from 0 to 2.2 bar.	249
<b>Table 19.</b> Plots of the turbidity of lysozyme in the presence of different heparins at pH 3.5-4.5 monitored using the plasma spectrometer.	265
<b>Table 20.</b> Plots of the turbidity of lysozyme in the presence of different heparins at pH 5-6 monitored using the plasma spectrometer.	266
<b>Table 21.</b> Plots of the turbidity of lysozyme in the presence of different heparins at pH 6.5-7.5 monitored using the plasma spectrometer.	267
<b>Table 22.</b> Plots of the turbidity of lysozyme in the presence of different heparins at pH 8-9 monitored using the plasma spectrometer.	268
<b>Table 23.</b> Plots of the turbidity of lysozyme in the presence of different heparins at pH 9.5-10.5 monitored using the plasma spectrometer.	269
<b>Table 24.</b> Plots of the turbidity of fibrinogen in the presence of different heparins at pH 3.5-4.5 monitored using the plasma spectrometer.	275
<b>Table 25.</b> Plots of the turbidity of fibrinogen in the presence of different heparins at pH 5-6 monitored using the plasma spectrometer.	276
<b>Table 26.</b> Plots of the turbidity of fibrinogen in the presence of different heparins at pH 6.5-7.5 monitored using the plasma spectrometer.	277
<b>Table 27.</b> Plots of the turbidity of fibrinogen in the presence of different heparins at pH 8-9 monitored using the plasma spectrometer.	278
<b>Table 28.</b> Plots of the turbidity of fibrinogen in the presence of different heparins at pH 9.5-10.5 monitored using the plasma spectrometer.	279

<b>Table 29.</b> Plots of the turbidity of lysozyme in the presence of different heparins at pH 3.5-4.5 monitored using the Tecan Infinite plate reader.	284
<b>Table 30.</b> Plots of the turbidity of lysozyme in the presence of different heparins at pH 5-6 monitored using the Tecan Infinite plate reader.	285
<b>Table 31.</b> Plots of the turbidity of lysozyme in the presence of different heparins at pH 6.5-7.5 monitored using the Tecan Infinite plate reader.	286
<b>Table 32.</b> Plots of the turbidity of lysozyme in the presence of different heparins at pH 8-9 monitored using the Tecan Infinite plate reader.	287
<b>Table 33.</b> Plots of the turbidity of lysozyme in the presence of different heparins at pH 5-6 monitored using the Tecan Infinite plate reader.	288
<b>Table 34.</b> Plots of the turbidity of fibrinogen in the presence of different heparins at pH 3.5-4.5 monitored using the Tecan Infinite plate reader.	289
<b>Table 35.</b> Plots of the turbidity of fibrinogen in the presence of different heparins at pH 5-6 monitored using the Tecan Infinite plate reader.	290
<b>Table 36.</b> Plots of the turbidity of fibrinogen in the presence of different heparins at pH 6.5-7.5 monitored using the Tecan Infinite plate reader.	291
<b>Table 37.</b> Plots of the turbidity of fibrinogen in the presence of different heparins at pH 8-9 monitored using the Tecan Infinite plate reader.	292
<b>Table 38.</b> Plots of the turbidity of fibrinogen in the presence of different heparins at pH 9.5-10.5 monitored using the Tecan Infinite plate reader.	293

## List of Equations

<b>Equation 1.</b> The Planck relation	4
<b>Equation 2.</b> The intensity of Raleigh scattered light from a spherical particle	24
<b>Equation 3.</b> The signal to noise ratio of a photon counting detector	48
<b>Equation 4.</b> The signal to noise ratio of a simple absorbance measurement	51
<b>Equation 5.</b> The signal to noise ratio of a simple absorbance measurement with a constant light source.	54
<b>Equation 6.</b> The signal to noise ratio of a simple absorbance measurement with a variable light source.	59
<b>Equation 7.</b> Planck's law of thermal radiative emission from a blackbody	65
<b>Equation 8.</b> The brehmsstrahlung emission from a gas of electrons and ions	85
<b>Equation 9.</b> The refractive index of an electrically neutral plasma	86
<b>Equation 10.</b> The brehmsstrahlung emission from a gas of electrons and ions at a specific frequency	88
<b>Equation 11.</b> The brehmsstrahlung emission coefficient	88
<b>Equation 12.</b> The brehmsstrahlung emission from a gas of electrons and ions at a specific wavelength	91
<b>Equation 13.</b> The solution to the radiative transfer equation of an electrically neutral plasma	98
<b>Equation 14.</b> The complete solution for the spectrum of thermal brehmsstrahlung	100
<b>Equation 15.</b> The peak power of a pulsed laser	123
<b>Equation 16:</b> The resolving power of a diffraction limited lens	127
<b>Equation 17.</b> The intensity of a pulsed laser at the focal point of a plano-convex lens	128
<b>Equation 18.</b> The absorbance of a sample as measured by the plasma spectrometer	158

<b>Equation 19.</b> The error in the absorbance of a sample measured by the plasma spectrometer.	159
<b>Equation 20.</b> Paschen's law.	191
<b>Equation 21.</b> The pressure dependence of gas breakdown.	234
<b>Equation 22.</b> The Beer-Lambert law for turbidity.	252
<b>Equation 23.</b> The power emitted from a plasma by brehmsstrahlung per Hz per unit volume.	350

# One

---

## Introduction

---

### 1.1 Background

Interest in laser induced plasmas (LIPs), as high intensity broadband light sources for biological spectroscopy, originally arose in the glycosaminoglycan (GAG) research group of Dr E.A. Yates at Liverpool University during vibrational circular dichroism (VCD: circular dichroism in the infrared region) experiments to investigate changes occurring in protein structure when proteins bind to heparin polysaccharides. The Yates group has an interest in different spectroscopies over a wide range of wavelengths including the UV and visible regions but VCD is a particularly useful technique for the examination of protein:GAG interactions because the VCD absorption of GAGs is very weak compared to protein VCD absorption. This enables the direct interpretation of VCD spectra in terms of protein structure without the prior need to deconvolute spectra into separate protein and GAG components. However, the weakness of the protein VCD signal ( $10^{-4}$  –  $10^{-5}$  by Kuhn's

dissymmetry factor, see below) made it difficult to obtain spectra that had good signal to noise ratios (SNRs).

SNRs in spectroscopic experiments can be increased by using more protein but this is not always possible due to the increased cost and associated difficulties with obtaining biologically important proteins in greater quantities. It was hypothesised that it would be possible to obtain increased SNRs and/or shorter measurement times by increasing the intensity of the light source. It was known that a hot plasma light source would be able to generate intense broadband light throughout the IR (infrared) range needed for VCD and also that a plasma light source would also be a good UV and visible emitter (Borghese and Di Palma, 2007, Hanafi et al., 2000). It was realised that such a light source, capable of emitting light at other wavelengths, would also provide a wide-range of other experimental possibilities, which are explored later.

One simple method to generate a hot plasma is to focus a pulsed laser through a convex lens. A hot plasma is formed at the focal point of the lens. It was the purpose of this project to investigate the viability of using a laser induced plasma as a UV/Vis/IR spectroscopic light source. It was hoped that laser induced plasmas would provide intense, broadband light for use in a spectroscopic instruments and that the light source would be inexpensive and compact enough for a bench top instrument.

To test the viability of such a source in biological spectroscopy, a prototype plasma light source needed be developed. A collaboration with MI Engineering Ltd (herein referred to as MI) was sought in order to acquire the necessary engineering expertise to development a prototype instrument. An agreement was reached in which the prototype would be designed, developed and built at MI. The prototype would then be tested, with further modifications designed, installed and tested in the Liverpool laboratory of Dr Yates. The work presented in this thesis is a record of research into the scientific and commercial viability of laser induced plasmas (LIP) as light sources for biological spectroscopy.

The Yates laboratory would use the prototype instrument to spectroscopically probe biologically important glycosaminoglycan (GAG):protein interactions. This class of polysaccharides (to which heparin belongs) are of increasing interest as drug candidates due to their ability to bind, often in a specific manner, to several hundred proteins (Ori et al., 2011, Jackson et al., 1991). GAG binding often significantly alters ligand binding affinities and can alter enzymatic activity by several orders of magnitude (Li et al., 2000, Desai et al., 1998, Butler et al., 1999). Research to determine how GAGs can regulate the structure, function and activity of proteins is ongoing in the laboratory of Dr Yates and in many other research establishments throughout the world. It is hoped that this research will lead to the engineering of new GAG based therapeutics capable of binding specifically to selective drug targets. To this end, one of the most powerful tools available to the scientist in the field of therapeutic research, and in many other areas of scientific research, is spectroscopy.

## 1.2 Biological Spectroscopy: A Review of Light Source Requirements

In order to provide an overview of the scientific background to this project and to demonstrate the need for high intensity broadband plasma light sources for biological spectroscopy, a short review of the spectroscopy of important biomolecules is necessary. The particulars of GAG spectroscopy will be discussed in further detail.

Spectroscopy is the study of the interaction of matter with electromagnetic (EM) radiation. These interactions give rise to three different phenomenon: absorbance, emission and scattering. Spectroscopic techniques involve the irradiation of a sample by EM radiation, followed by measurement of the absorption, emission or scattering of the sample as a function of some experimental parameters. These measurements may be for example, the absorption coefficient at a particular wavelength, the emission lifetime of a fluorophore or the scattered intensity as a function of angle. The results of

spectroscopic experiments can then be analysed, using prior knowledge of the physical basis of the interaction of radiation with matter, to yield useful information concerning molecular structure, dynamics and energetics.

The emission of biological molecules following their excitation, possibly by an external light source, are of interest when designing spectroscopic detectors but are of lesser importance for light source design. It is the absorbance and scattering processes that are of primary consideration. Molecules must absorb or scatter within the working wavelength range of the impinging light source. The dependency of the absorption and scattering of biological molecules on the wavelength and intensity of the impinging radiation must therefore be examined.

### 1.2.1 Molecular Excitation Processes

Three major types of molecular excitation are observed upon absorbance of light. As well as excitation between electronic states, the internal energy of a molecule is partitioned into energies that correspond to the internal degrees of freedom of the molecule. These degrees of freedom are the rotations of the molecule around its centre of mass, the oscillations/vibrations of its atoms about their equilibrium positions. The internal energy of a molecule does not include translational kinetic energy or potential energies imparted by external fields. Nuclear energies are also ignored in this definition. Each molecule therefore exists in a number of possible rotational, vibrational and electronic energy states. These states are quantised, meaning that only specific discrete energy states are allowed. Transitions between energy states generally require the absorption/emission of a photon with a wavelength given by the Planck relation:

$$E_2 - E_1 = h\nu = \frac{hc}{\lambda} \quad \textbf{Equation 1}$$

$E_1$  is the energy of the initial state,  $E_2$  is the energy of the final state,  $h$  is Planck's constant,  $\nu$  is the photon frequency,  $c$  is the speed of light and  $\lambda$  is



the photon wavelength. Transitions between rotational, vibrational and electronic states generally occur in the microwave, IR and UV-Vis regions respectively. The difference between energy levels is therefore greatest for electronic transitions, less for vibrational transitions and least for rotational transitions. Figure 1 shows the relative size of electronic, rotational and vibrational energy levels.

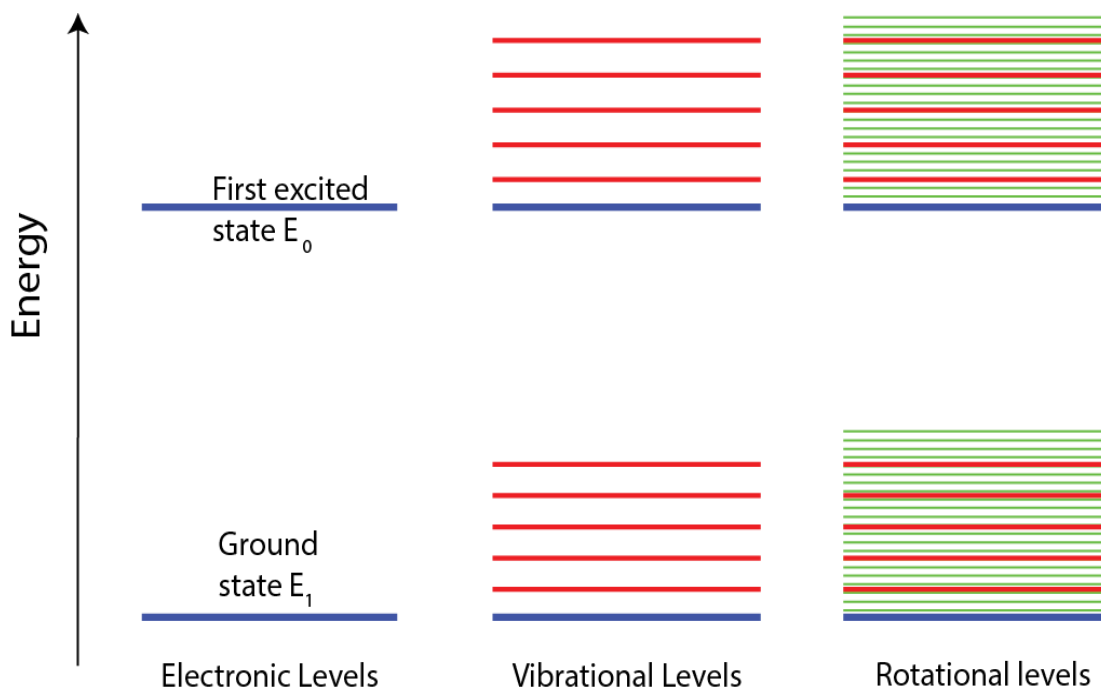


**Figure 1.** The relative levels of the electronic, vibrational and rotational energy states of a molecule. Electronic states are shown in blue, vibrational states in red and rotational states in green. EM radiation absorbed by a molecule may produce transitions between these states.

One of the fundamental interactions between light and matter is that an impinging photon transfers all of its energy to an atom or molecule. The energy transferred raises a molecule to higher electronic, vibrational or rotational energy states. This is absorption. The two most useful absorption techniques in biological spectroscopy are UV-Visible (electronic transitions) and infrared-IR (vibrational transitions) spectroscopy. Figure 2 shows the excitation and relaxation processes discussed in this chapter.

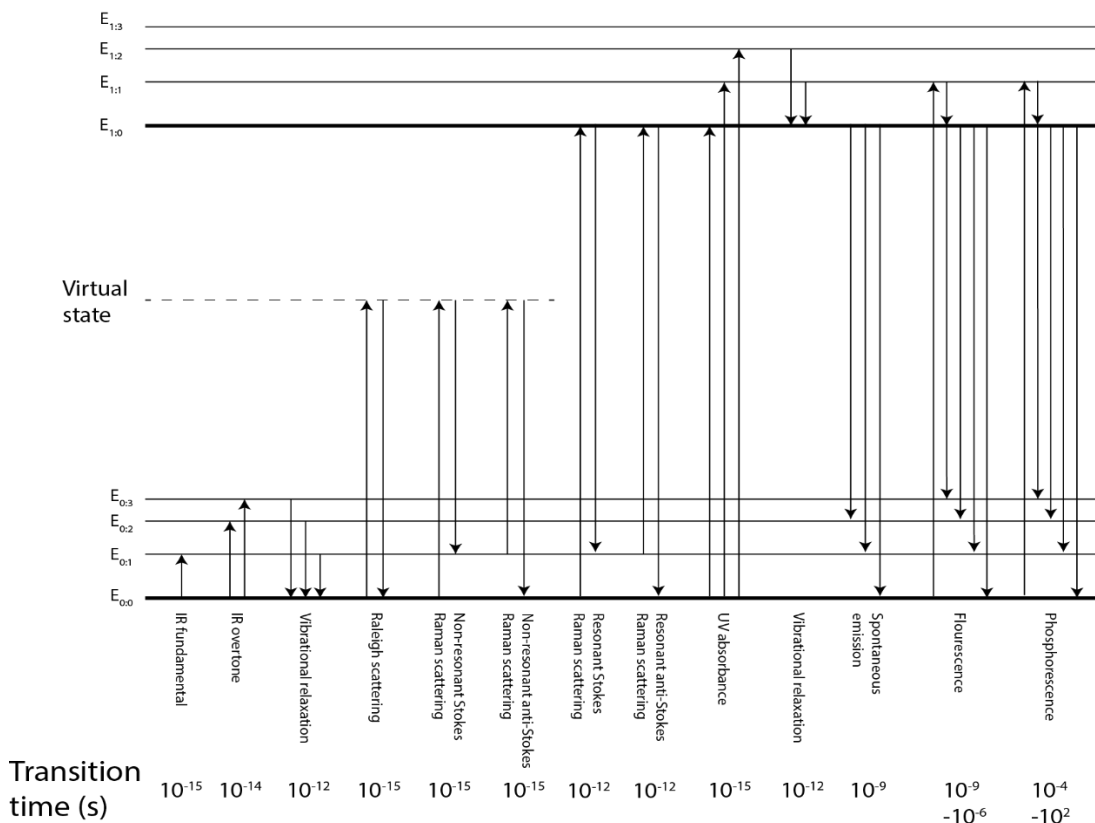


**Figure 2.** Schematic of the excitation and emission processes described in this chapter. The distance between electronic states has been compressed by a factor of at least ten compared to the distance between vibrational states. Adapted from Handbook of Spectroscopy (Hof and Machan, 2014)

Microwave spectroscopy (rotational transitions) is seldom employed on biological samples because of the low transmission of microwaves through water. Water is highly absorbent of microwave radiation because its rotational transitions occur at the energies of microwave photons. These rotational transitions do not occur at sharply defined frequencies due to heterogeneous hydrogen bonding between water molecules as well as the spreading of transition energies due to Heisenberg's uncertainty principle. This spreading of transition energies causes broad absorbance throughout the microwave region.

The probability that an impinging photon is absorbed by an atom or molecule is governed by several rules. The first rule is that a transition is most probable when the energy of the photon matches (or resonates with) the difference

between the transition energy levels as given by Equation 1. The absorption band is generally Lorentzian (following a Lorentz distribution) in shape and is not infinitely narrow for a number of reasons including the accuracy of the measuring instrument, molecular velocities and the environment of the absorbing material. In biological spectroscopy, molecular collisions and many different solvent environments cause the broadening of the absorption band. Ideally, excitation of molecules is achieved using a laser but lasers are not always available at the required wavelength so broadband sources must be used.

The second rule is that absorption depends upon difference between the populations of the initial and final energy levels. At thermal equilibrium the populations of molecules in the ground and excited state are given by the Boltzmann law:

$$\frac{n_i}{n_0} = g_i \exp\left(\frac{E_i}{kT}\right)$$

Where  $n_i$  is the population of the state  $i$ ,  $n_0$  is the population of the ground state,  $g_i$  is the degeneracy and  $E_i$  is the energy of state  $i$  relative to the ground state. The application of electromagnetic radiation perturbs the Boltzmann distribution, raising molecules to the higher energy state. Electromagnetic waves also cause transitions from a higher energy state to a lower one through the processes of stimulated emission. Through absorption and stimulated emission, electromagnetic radiation can equalise the populations of the excited and ground state. At this point the sample is saturated and no more absorption occurs.

The third rule is that there must be a displacement of charge in going from one energy state to another. There are two fundamental types of charge displacement: a linear displacement or an electric transition dipole, and a rotational displacement or a magnetic transition dipole. The electric transition dipole interacts with the oscillating electric field of the impinging radiation and the magnetic transition dipole interacts with the oscillating magnetic field.

Magnetic transition dipoles are generally much smaller than electric transition dipoles as rotations of charge within a molecule are usually much smaller than the separations of charge induced by electric fields. Combine this with the fact that in an EM wave the magnetic component is much smaller than the electric component as  $\vec{E} = c\vec{B}$ , electric transition probabilities are much greater than magnetic transition probabilities. The electric transition probabilities are proportional to the absolute square of the electric transition dipole moment:

$$P_{I \rightarrow F} \propto \left| -e \int \Psi_F^*(\vec{r}) \vec{r} \Psi_I(\vec{r}) \right|^2$$

Where  $e$  is the charge of the electron,  $\vec{r}$  is the position vector of the electron and  $\Psi_I$  and  $\Psi_R$  are the wavefunctions of the initial and final states. The transition dipole moment is a vector that corresponds to the movement of charge within the molecule. The absorption coefficient is proportional to the transition probability. The above equation is used to derive selection rules that predict the probability of a transition. These rules are not strictly obeyed due to the many possible distortions of molecular wavefunctions that can occur.

The probability of a transition occurring also depends on the orientation of the transition dipole moment with respect to the direction of oscillation of the electric field vector of the EM wave. If the angle between the direction of the electric field in an EM wave and the transition moment is  $\theta$ , then the effective transition moment is proportional to  $\cos \theta$  and the transition probability is proportional to  $\cos^2 \theta$ . In unpolarised light, the electric field is orientated in all possible directions normal to the direction of travel of the wave. Therefore, the electric field always has a component that is parallel to the transition moment and so the effective transition moment is non-zero. The transition moments of molecules in solution take up all possible directions and so there is also a component of the electric field that is parallel to a transition vector and the effective transition moment is again non-zero. If the EM wave is polarised and the molecules are orientated in a specific direction, such as in a crystal, then there will be a direction for which effective transition moment is zero. The effective transition moment will be at a maximum normal to this direction. This

gives rise to the phenomenon of dichroism or the differential absorption of light that is polarised in different directions. The differential absorption of plane polarised light is known as linear dichroism and the differential absorption of circularly polarised light is known as circular dichroism (CD). Ultraviolet CD (UVCD) and infrared CD (VCD) is of particular interest for probing the structure of biomacromolecules and will be discussed shortly.

In general, the energy provided to molecules by photons promotes electrons from their electronic ground state orbitals to electronic excited state orbitals or antibonding orbits. Three types of ground state orbitals may be involved. These are the  $\sigma$ ,  $\pi$  and  $n$  orbits and correspond to single and double bonds and non-bonding electrons respectively. Electrons may be promoted to two different types of antibonding orbitals: the  $\sigma^*$  and  $\pi^*$  orbitals. There are no  $n^*$  orbitals as the  $n$  orbital electrons do not form bonds. The following four transitions can occur:  $\sigma \rightarrow \sigma^*$ ,  $n \rightarrow \sigma^*$ ,  $n \rightarrow \pi^*$  and  $\pi \rightarrow \pi^*$ . The general pattern of energy levels is shown in Figure 3.

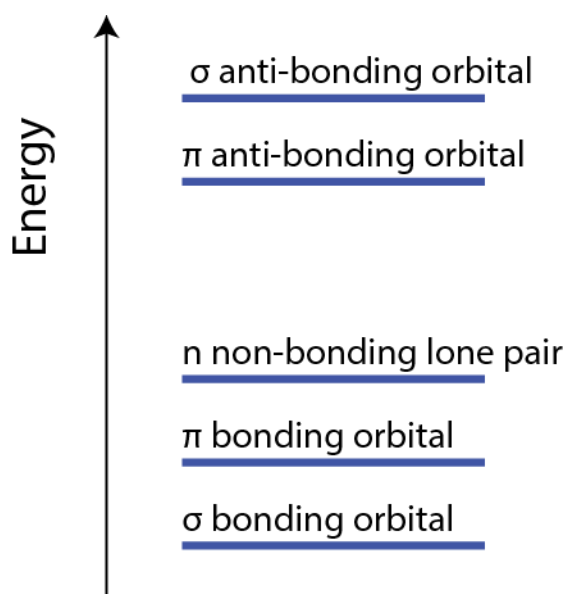


**Figure 3.** The relative energies of the molecular transitions.

Both  $\sigma \rightarrow \sigma^*$  and  $n \rightarrow \sigma^*$  transitions require a large amount of energy and therefore occur in the far UV region. The transitions  $n \rightarrow \pi^*$  and  $\pi \rightarrow \pi^*$ , occurring in molecules with unsaturated bonds, require less energy and therefore occur at longer wavelengths. For example, the  $\sigma \rightarrow \sigma^*$  transition that

occurs in ethane has a  $\lambda_{\max}$  of 135 nm but the  $\pi \rightarrow \pi^*$  transition in ethylene occurs at a  $\lambda_{\max}$  of 175 nm.

Although the initial interest in laser induced plasmas came about through the need for a brighter IR light source for VCD, a bright broadband light source would also be extremely useful at other wavelengths. In particular, many chromophores present in biological molecules are absorbent in the mid-UV region between 200-300 nm. Table 1 lists the maximal absorption band of important biological chromophores in water at pH 7. The wavelength absorbance maxima and molar extinction coefficients are highly dependent on environmental factors such as the secondary structure of macromolecule, temperature, pH and the presence of conjugated groups. All the absorbance bands of the major chromophores in biomacromolecules occur in the mid-UV region of the electromagnetic spectrum apart from the  $\pi \rightarrow \pi^*$  transition of the peptide bond which occurs around 190 nm. Owing to the strong absorption of molecular oxygen at 190 nm, peptide bond spectroscopy is often carried out at 205 nm, where the absorbance is about half that at 190 nm, and/or in a nitrogen atmosphere (Scopes, 1974, Rosenheck and Doty, 1961, Woods and O'Bar, 1970). Both water and D<sub>2</sub>O are strongly absorbent below 170 nm, hampering biological spectroscopy below this wavelength (Mota et al., 2005, Ikehata et al., 2008). In the mid-UV region between 250-300nm, the aromatic amino acids and disulphide bonds exhibit characteristic spectral features that are sensitive to conformation. For example, tyrosine exhibits absorption maxima at 275nm and 282nm. Spectral effects due to these aromatic groups may be used to estimate tertiary or quaternary structure.

Chromophore	$\lambda_{\max}$ (nm)	$\epsilon$ at $\lambda_{\max}$ ( $\text{cm}^2\text{mol}^{-1}$ )	Reference
Peptide $\pi \rightarrow \pi^*$	~190	~7000	(Engelhardt et al., 1990, Tsai, 2006)
Peptide $n \rightarrow \pi^*$ (forbidden)	~220	~100	(Tsai, 2006)
Tyrosine	274	1405	(Mihalyi, 1968)
Tryptophan	280	5560	(Mihalyi, 1968)
Phenylalanine	257	195	(Mihalyi, 1968)
Cystine (disulphide bond)	250	300	(Tsai, 2006)
Histidine	211	5900	(Tsai, 2006)
Adenosine	259	15400	(Bock et al., 1956)
Guanosine	252	13700	(Bock et al., 1956)
Cytidine	271	8900	(Bock et al., 1956)
Thymidine	265	7890	(Shugar and Fox, 1952)
Uridine	262	10000	(Bock et al., 1956)
DNA	258	6600	(Tsai, 2006)
RNA	258	7400	(Tsai, 2006)
Heparin/Heparan Sulphate following cleavage by heparitinases	232	5000-6600	(Kariya et al., 1992, Rice and Linhardt, 1989)

**Table 1.** Important biological chromophores listing the absorbance wavelength and extinction coefficient. The absorption wavelength of the double bond in heparin/HS following enzymatic cleavage is included because of its relevance to this project.

In the visible range (400-700 nm), many transition metals are strongly absorbent. This absorbance is due to ligands complexing with transition metal ions. Repulsion between electrons in the ligands and electrons in the metal ion causes a shifting and splitting of the energy levels of the *d* orbitals in the metal ion. The absorbance of a photon, generally with a wavelength in the visible region, can promote an electron from the lower level to the higher level *d* orbital. The energy of the transition is highly depend on oxidation state, ligand identity, anion presence and solvation. Transition metal complexes can be optically active, differentially absorbing circularly polarised visible light due to the chiral arrangement of their ligands. Metal ions and their complexes are of great interest to biological science. Eight transition metals - vanadium,

manganese, iron, cobalt, nickel, copper, zinc, and molybdenum considered essential for control of various metabolic and signalling pathways (Šoltés and Kogan, 2009) and the homeostasis of these metals is a vital part of the cellular function (Bleackley and MacGillivray, 2011). Metalloproteins, or metal binding proteins also account for over a third of all structurally characterised proteins (Finney and O'Halloran, 2003, Andreini et al., 2006). In blood plasma and in synovial fluid, the concentrations of transition metals are typically in the order of micrograms per gram wet weight (2005) but high concentrations in the millimolar range have been observed, for the more common elements, in tissues and organelles (Somlyo et al., 1985, Beilby et al., 1999, Frederickson et al., 2000). At these concentrations, spectroscopy such as atomic absorption spectroscopy (AAS) and inductively coupled plasma emission spectroscopy can be used to accurately quantify levels of metal ions, but these methods require purification of samples and are destructive of the sample and any information concerning the nature of metal ligands present.

Bright broadband light sources are used in atomic absorption spectroscopy where a continuous source, most often a xenon arc lamp or deuterium lamp, is used to illuminate the ionised sample. It is important however that the source has minimal flicker to give acceptable SNR ratios and to allow for the correction of background absorbance and radiation scattering. Using a continuous light source of constant intensity combined with a high resolution monochromator allows for very high sensitivity and SNRs using this technique (Dietz and Rubinstein, 1973, Abdelhalim et al., 2010).

In the infrared (IR) region, bright broadband light sources are of immense interest. Sources that are currently used in FTIR and VCD machines are glowbars heated to around 800°C. This is a low temperature compared to plasma light sources that can easily achieve several thousand degrees. As has been discussed in the previous section, both glowbar and plasma are approximately blackbody emitters. Heating a blackbody radiator increases the intensity of emitted light across the entire wavelength range, with the total intensity proportional to the fourth power of the temperature according to Stefan's Law. The dramatic increase in temperature offered by plasma light



sources therefore makes them strong candidates for intense IR sources. Table 2 lists some of the characteristic IR absorption bands of biomolecules.

Wavenumber (cm <sup>-1</sup> )	Assignment
3250-3300	Amide A, protein backbone N-H stretching in resonance with Amide II overtones
3080-3100	Amide B, protein backbone N-H stretching
3010	=C-H stretching of alkenes
3000-3100	C-H stretching in aromatics
2957	Asymmetric CH <sub>3</sub> stretching
2920	Asymmetric CH <sub>2</sub> stretching
2872	Symmetric CH <sub>3</sub> stretching
2851	Symmetric CH <sub>2</sub> stretching
1738	C=O Stretching
1600-1700	Amide I, protein backbone C=O stretching
1480-1575	Amide II, protein backbone N-H bend in plane and C-N stretch
1468	CH <sub>2</sub> scissoring
1430-1650	C=C skeletal vibrations of aromatic rings
1395	C=O stretching of COO <sup>-</sup>
1378	CH <sub>3</sub> symmetric bending
1343	CH <sub>2</sub> wagging
1230-1330	Amide III, protein backbone N-H bend in plane and C-N stretch
1240	Asymmetric PO <sub>2</sub> <sup>-</sup> stretching
1170	Ester C-O asymmetric stretching
1080	Symmetric PO <sub>2</sub> <sup>-</sup> stretching
1000-1275	C-H in plane bending in aromatics
720	CH <sub>2</sub> rocking
625-770	Amide IV, protein backbone mainly O=C-N bending
640-800	Amide V, protein backbone out of plane N-H bending
537-606	Amide VI, protein backbone out of plane C-H bending
390-900	C-H out of plane bending in aromatics

**Table 2.** The band assignments of the main IR chromophores in biomolecules. As is the convention in IR spectroscopy wavenumbers are quoted. Data from (Rehman et al., 2012, Krimm and Bandekar, 1986, Bandekar, 1992, Elliott and Ambrose, 1950, Miyazawa et al., 1956)

Of all the vibrational absorbance bands, the most important in biological spectroscopy are the amide I and amide II bands because they both originate from the absorption of the peptide backbone of proteins. The absorption of the amide I band (1600-1700  $\text{cm}^{-1}$ ) is the most intense protein absorption band and is mainly associated with C=O stretching. The amide II band (1480-1575  $\text{cm}^{-1}$ ) originates mainly from N-H bending and stretching of the C-N bond. The absorption of both bands is sensitive to conformation due to hydrogen bonding between the electropositive oxygen of the amide group and an electronegative hydrogen, bound to the nitrogen atom in the amide group, causing shifts in the vibrational energy levels of the C=O and N-H. Through the comparison of the vibrational spectra of proteins with model peptides, such as poly-L-lysine that possess a single known secondary structure, the relative proportions of secondary structures present in a protein can be estimated (Nevskaya and Chirgadze, 1976). The deconvolution of the amide I and II bands into contributions from different secondary structures is complicated by vibrational contributions from C=O and N-H groups present in amino acid side chains. Contributions from side chains must be removed prior to deconvolution.

FTIR gives accurate predictions of the proportions of secondary structures. This can be seen by comparing the relative amounts of secondary structures predicted by FTIR with the solved protein structure determined by crystallography (Kong and Yu, 2007). X-ray crystallography gives very precise positions for the atoms in protein crystals but provides only a static picture and limited insight into the dynamics, which is often crucial for an understanding of function *in vivo*. The structures of many proteins, carbohydrates and other interesting biomolecules have not been solved by x-ray diffraction methods due to the difficulties of growing high purity crystals, a process which can take several weeks if not months. Crystallography may also reveal little of biological relevance as crystals of biomolecules may not contain biologically important conformations. By dehydrating biomolecules to create crystals suitable for diffraction studies, we may be altering the biologically important conformations whose existence requires the hydrogen bonding of.

Water absorbance is a problem in the infrared region as it is absorbent throughout the IR region. This is compounded by the fact that the concentration of water is 55M but sample concentrations are often millimolar or less. The problem of water absorbance can be mitigated by using heavy water D<sub>2</sub>O. The change in the reduced mass of the oscillating bonds in D<sub>2</sub>O shifts the absorbance bands away regions of biological interest, in particular the Amide I and II bands. The utility of IR spectroscopy is still limited using D<sub>2</sub>O as the solvent, because its absorbance is still significant across much of the IR range. Mathematical approaches can be used to subtract the omnipresent water/D<sub>2</sub>O absorbance but water is too absorbent at certain wavelengths to obtain precise and accurate results. It may be advantageous in some cases to determine the vibrational energy levels of molecules using Raman scattering, rather than direct IR absorption, even though the Raman scattering effect is itself very weak. Raman scattering will be discussed in further detail below.

Although IR spectroscopy is unable to determine the complete structure of macromolecules due the presence of multiple overlapping bands and water or D<sub>2</sub>O absorption, IR spectroscopy can yield a wealth of information concerning changes in bond length (as bond length and bond strength are directly related) (Tonge and Carey, 1990, Andersson and Barth, 2006), bond angles (Klähn et al., 2005, Cheng et al., 2001) and conformational freedom (protein IR absorption bands often narrow upon protein:ligand binding as a result of conformational restriction (Wharton, 2000)) (Barth and Mäntele, 1998, Deng and Callender, 1999, Hellwig et al., 1999). IR absorption is highly sensitive to changes in molecular structure caused by changes in bond strengths. The coupling of the vibrational modes of adjacent parts of molecules reveals information concerning the local environment of the vibrating bond. IR spectroscopy is also one of the few methods that directly reports the strength of hydrogen bonding. Hydrogen bonding generally lowers the frequency of stretching vibrations since it reduces the restoring force, and increases the frequency of bending vibrations since an additional restoring force is produced (Badger, 1940, Tonge et al., 1996). Because of its sensitivity, IR spectroscopy finds many uses in the biological sciences such as the determination of protonation states of specific amino acids in proteins (Hienerwadel et al., 1997,

Noguchi et al., 1999), detection of protein phosphorylation (Barth and Mäntele, 1998), the monitoring of enzyme catalysed reactions (Thoenges and Barth, 2002, Barth et al., 1991, Pacheco et al., 2003) and the monitoring of protein folding, unfolding and misfolding (Fabian et al., 1999, Dyer et al., 1998, Dioumaev, 2001).

As well as the straightforward absorption of non-polarised light, optically active molecules exhibit circular dichroism or differentially absorb left and right circularly polarised light. CD can be expressed in terms of molar absorbance in units of  $\text{cm}^{-1} \text{mol}^{-1}$ :

$$\Delta\varepsilon = \varepsilon_l - \varepsilon_r$$

$\varepsilon_l$  is the molar absorbance in left circularly polarised light and  $\varepsilon_r$  is the molar absorbance in right circularly polarised light. The observed circular dichroism of a sample is often quoted as the ellipticity:

$$\theta(\lambda) = \frac{2.303[OD_l(\lambda) - OD_r(\lambda)] \cdot 180}{4\pi}$$

Here  $OD_l$  and  $OD_r$  are the optical densities observed using left or right circular polarised light. The molar ellipticity is also used because it is a function of the properties of the optically active biomolecules only:

$$[\theta](\lambda) = \frac{100 \cdot \theta(\lambda)}{c \cdot l}$$

$C$  is the concentration of the biomolecules in  $\text{mol L}^{-1}$  and  $l$  is the path length in cm. The units of molar ellipticity are usually  $\text{deg.cm}^{-2}.\text{dmol}^{-1}$

Nearly all molecules synthesised by living organisms are optically active. A molecule that exhibits CD will also possess different refractive indices for each of its circularly polarised components, an effect known as circular birefringence and the difference in refractive index as a function of wavelength is called optical rotary dispersion. These two effects are related (CD is related to ORD

via the Kronig-Kramers transforms) but CD is generally preferred as a spectroscopic probe because CD only occurs at the frequency of absorbance bands.

Optical activity ultimately depends upon the asymmetry/chirality of the molecule under examination. The rotational strength (proportional to the area under an absorbance band in CD) of a transition is given by:

$$R_{0a} = \text{imag}(\langle \Psi_0 | \mu | \Psi_a \rangle \cdot \langle \Psi_a | e | \Psi_0 \rangle)$$

where  $\mu$  and  $e$  are the magnetic and electric dipole operators. The quantities  $\langle \Psi_0 | \mu | \Psi_a \rangle$  and  $\langle \Psi_a | e | \Psi_0 \rangle$  are the magnetic and electric transition moments. These moments take the form of vectors in complex space. In a molecule with a plane of symmetry the real component of the rotational strength will always be zero, so the molecule will show no optical activity. Chiral molecules, that possess levorotary (*L*) and dextrorotary (*D*) enantiomers, do not possess a plane of symmetry and are asymmetric about their chiral centre(s). Therefore chiral molecules possess a rotational strength in circularly polarised light or so called optical activity.

Optical activity arises in amino acids from the asymmetry of the groups surrounding the central chiral carbon atom. In nearly all naturally occurring proteins, for as yet unknown reasons, amino acids are always present in the *L* configuration. *D* amino acids are found in peptidoglycans that form the cell walls of most bacteria, making bacteria resistance to proteases and other enzymes. The optical activity of a protein is usually much greater than the sum of the optical activity of its constituent amino acids due to the regular arrangement and orientation of chiral centres that occur in secondary structures. If a number of chromophores of the same type are in close proximity, they can behave as if they are one single absorbing unit or exciton, giving rise to spectral features in the CD spectra that are characteristic of the type of secondary structure present. UVCD is also known as electronic CD because the electron transitions occur at energies in the UV region. In this region, spectral features are broadened, due to the distribution of molecular

vibrational and rotational states within a single electronic state. In the far-UV (170-250nm), protein absorption occurs mainly due to  $\pi \rightarrow \pi^*$  peptide bond transitions around 200nm. Protein far-UVCD exhibits characteristic CD spectral features for  $\alpha$ -helices,  $\beta$ -sheets and random coils (Figure 4). By comparison of the far-UVCD spectra of a protein with a library of proteins of known structure (structures in the Protein Data Bank obtained by X-ray crystallography) or homopolypeptides known to contain only one type of secondary structure, the proportions of structures can be estimated. As an approximation, one can consider the UVCD spectra as a simple linear combination of the absorbance of  $\alpha$ -helices,  $\beta$ -sheets and random coils:

$$\theta(\lambda) = A[\theta_{\alpha}] + B[\theta_{\beta}] + C[\theta_r]$$

where A,B and C are the relative proportions of secondary structures present.

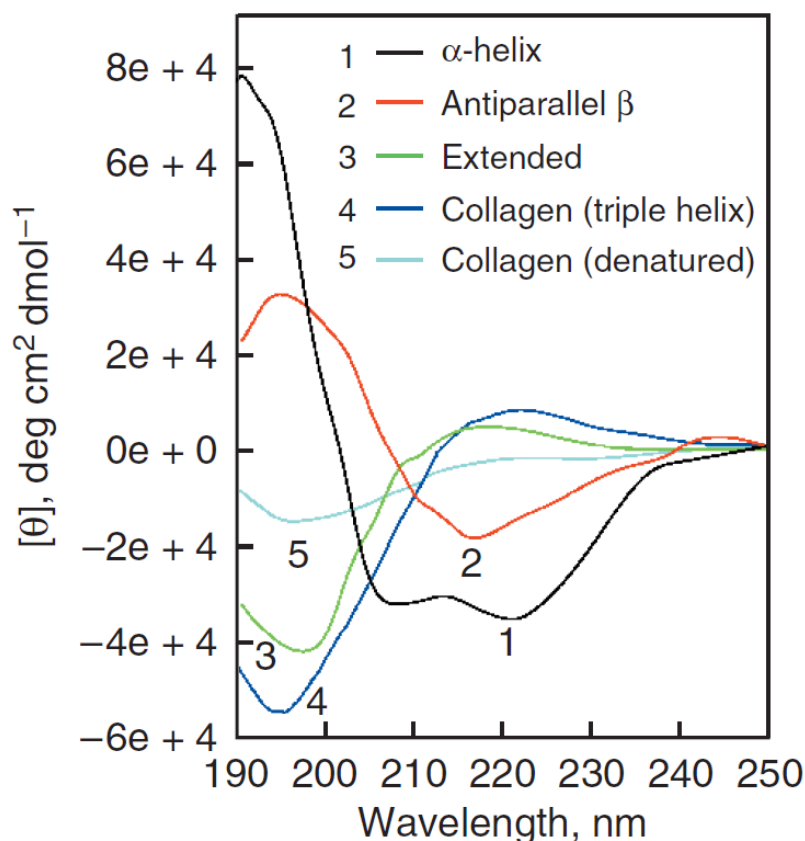


**Figure 4.** Electronic CD spectra of some of the secondary structures present in proteins. (Greenfield, 2006).

The spatial relationships of specific structural motifs cannot be obtained by UVCD but UVCD does possess some advantages over other structural methods. UVCD can be used over a range of conditions such as pH and temperature, is able to examine protein structure in solution and in quasi-natural conditions (unlike X-ray crystallography). With UVCD spectroscopy, smaller amounts of sample are needed as the intensity of the UV light increases. Typically 100 µg of protein is enough to determine a protein UVCD spectrum using a modern synchrotron radiation source. UVCD is also a relatively rapid technique requiring relatively little sample preparation and greatly reduced scanning times when compared to NMR or crystallography. UVCD is also non-destructive so the sample can be recovered and reused if necessary. UVCD can be used to monitor dynamic processes such as stability, intermediate structures, folding, aggregation and binding. This makes UVCD an invaluable technique, particularly for the investigation of protein conformational changes in proteins upon binding of drug candidates.

VCD is infrared analogue of UVCD and is the differential response to left and right circularly polarised infrared radiation during a vibrational transition. VCD combines the sensitivity of optical activity with the rich structural information obtained with vibrational spectroscopy. VCD can relatively easily determine the absolute configuration (*S* or *R*) of enantiomeric molecules, determine the racemic purity of a sample and probe the conformational properties of molecules in solution (Figadere et al., 2008, Polavarapu and Zhao, Kott et al., 2014, Freedman et al., 2002). VCD distinguishes between *S* and *R* enantiomers because their VCD spectra are reflections of each other about the *x* or zero axis. The ability to determine the absolute configuration and racemic purity of samples is of particular importance to the pharmaceutical industry because the physiological effects of different drug enantiomers are often very different. For example, the *R* enantiomer of the analgesic drug Naproxen is known to be highly toxic to the liver. The drive to improve drug efficacy has made the search for single enantiomer drugs an important area of therapeutic research, with VCD an indispensable tool for the measurement of the enantiomeric properties of samples.

VCD has proven a useful technique for the analysis of protein structure. The vibrational transactions of the Amide I and II bands are well resolved in VCD (Gupta and Keiderling, 1992) and it is known from the analysis of the VCD spectra of polypeptides that it is mainly secondary structure, that determines the shape of these bands (Singh and Keiderling, 1981, Freedman et al., 1995, Keiderling and Xu, 2002, Tanaka et al., 2001). The amide I band is most easily studied because it lies in a spectral window of D<sub>2</sub>O and has a high VCD intensity. The amide I VCD spectra of the  $\alpha$ -helix, antiparallel  $\beta$  sheet, random coil,  $\beta$  hairpin and  $\beta$  turn structures have now been characterised in polypeptides and are distinctly different (Keiderling, 1986, Paterlini et al., 1986). Because IR transitions involve the oscillations of the atomic nuclei within molecules, isotopic substitution and labelling has been used to shift the vibrational frequencies of particular residues and groups to spectroscopically unique positions and yield site specific conformational information (Torres et al., 2001, Silva et al., 2000). The dependence of VCD band shape on secondary structure has led to the development of factor analysis methods to separate spectral contributions and quantify the ratios of each type of secondary structure present (Pancoska et al., 1995). These methods are similar to the methods of principal component analysis often applied to UVCD but because VCD is a relatively new technique, few protein spectral standards currently exist for analytical comparison.

In some respects, VCD offers some advantages over UVC, although both methods yield information concerning secondary structure which should be compared in a proper structural analysis. There are relatively few electronic transitions accessible that show conformational sensitivity, limiting the information that can be obtained by UVCD. Aromatic modes, which overlap the amide bands in UVCD, are much more resolved in VCD spectra and can be used to study secondary structure near aromatic residues (Yasui and Keiderling, 1986, Tanaka et al., 2006). UVCD spectra are inherently low resolution and show much more overlap than VCD spectra. Vibrational coupling tends to be shorter range, generally sensitive to the next residue or hydrogen bonded residue (Keiderling, 2002). Because of this local nature, VCD spectra are closer to being proportional to the number of secondary



structural elements present. This is unlike UVCD, where the spectra tend to be dominated by  $\alpha$ -helices.

*Ab initio* approaches, using quantum mechanical methods such as density functional theory (DFT), have been able to accurately predict the VCD spectra of simple molecules allowing for the direct comparison of theoretical structures with measured spectra (Stephens et al., 2008, Freedman et al., 2002). The use of density functional theory for predicting the molecular structure has had a significant impact on the study of small chiral molecules. For larger biomolecules, predictive models of structure and conformation become inaccurate and unreliable but progress is being made with the modelling of small peptides (Kubelka et al., 2002, Kubelka and Keiderling, 2001b, Bour et al., 2000). The effect of solvent on the structure of peptides is also beginning to be addressed in structural models (Knapp-Mohammady et al., 1999, Han et al., 2000, Kubelka and Keiderling, 2001a).

The results of a VCD measurement are two vibrational absorption spectra for right and left polarised light. The unpolarised IR absorbance is the sum of the left and the right absorption spectra. The magnitude of VCD is commonly expressed as Kuhn's dissymmetry factor (Kuhn, 1930):

$$\frac{\Delta\varepsilon}{\varepsilon} = \frac{2(\varepsilon_L - \varepsilon_R)}{\varepsilon_L + \varepsilon_R} = \frac{Ad}{\lambda}$$

The quantity  $\Delta\varepsilon/\varepsilon$  is the anisotropy ratio, the ratio between the VCD absorbance and the IR absorbance.  $\varepsilon_L$  and  $\varepsilon_R$  are the molar absorption coefficients of left and right circularly polarised light. Kuhn's dissymmetry factor is dimensionless and proportional to  $d/\lambda$ , where  $A$  is the constant of proportionality,  $d$  is the typical internuclear distance and  $\lambda$  is the wavelength of the light (Gibbs, 1882). The inverse proportionality of Kuhn's dissymmetry factor with wavelength explains why the VCD effect is weaker than UVCD. Typical values of Kuhn's dissymmetry factor are  $10^{-4}$ - $10^{-5}$  in the IR and  $10^{-3}$  in the near-UV (Buckingham, 1994), often resulting in VCD scan times of several hours to acquire data with good SNRs, even with modern VCD spectrometers.

The VCD effect can be seen more easily by increasing path lengths and/or sample concentrations but with many important biological molecules, the acquisition of larger sample quantities may not be possible.

### 1.2.2 Molecular Relaxation Processes

Following excitation and absorption, molecules return to thermal equilibrium and achieve a Boltzmann distribution through relaxation processes. Molecules may relax back to the ground state through several stages including through non-radiative transitions, vibrational transitions between different vibrational states and electronic transitions between different electronic states. There are three types of transition through which an atom/molecule may relax back to the ground state.

The first mechanism through which molecules lose energy and relax back to their ground states is through non-radiative transitions. Non-radiative transitions do not involve the emission of a photon and occur through the collision of an excited molecule with another molecule, transferring its energy to that molecule in the form of kinetic energy. This increase in kinetic energy causes heating of the absorbing material.

The second mechanism through which energy is released is through the spontaneous emission of a photon, occurring over a timescale of nanoseconds. A photon is emitted from the atom/molecule in a different, random direction to the original exciting photon. This process is termed spontaneous emission. Two other important related mechanisms are fluorescence and phosphorescence. In these processes, energy is released as photons in a similar manner to spontaneous emission but over a longer period of time ranging from a nanoseconds to hours. The emitted photon is usually at a longer wavelength to the exciting photon as relaxation often occurs through several stages. This is exploited in the labelling of biomolecules with fluorescent molecules or fluorophores, usually polyaromatics or heterocyclic molecules, which enables selective detection of particular components of

biomolecular assemblies such as in live cells. Broadband light sources are often required to excite fluorophores as lasers may not be available at the fluorophore's excitation wavelength.

The third mechanism through which molecules/atoms may lose energy is stimulated emission. Stimulated emission occurs when an incoming photon close to the energy to the relaxation transition energy, stimulates the excited atom/molecule to emit a photon. The emitted photon travels in the same direction as the incoming photon. The two photons are the same wavelength and are in phase with each other. Stimulated emission amplifies the incoming radiation and is the basis for laser amplification.

The combination of absorption followed by instantaneous or near instantaneous emission of photons is the basis for two important processes: Rayleigh (or Mie) scattering and Raman scattering. Rayleigh scattering occurs when the wavelength of light impinging upon a sample does not match any energy difference between two electronic states of the molecules in the sample. In this situation, the incident electromagnetic wave causes an oscillation of the electron cloud surrounding the molecules. Classically, oscillating electron clouds form an oscillating electric dipole that radiates electromagnetic waves at the same frequency of the inducing oscillation. An electron can be said to transit to a virtual state following the absorption of a photon, then transit back to the ground state emitting a photon of identical energy. The emitted photon has a different propagation vector from the incident photon. Rayleigh scattering is an elastic process, that is, the wavelengths of the scattered photons are the same as the wavelengths of the incident photons.

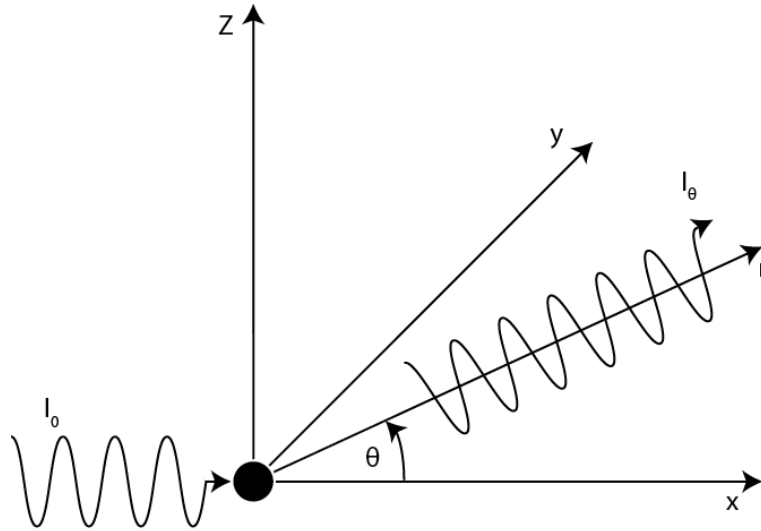


**Figure 5.** An incident EM wave of intensity  $I_0$  travelling in the  $x$  direction is incident on a spherical particle. The intensity of the emitted EM wave is measured at a distance  $r$ , at an angle  $\theta$  from the  $x$  axis in the  $x$ - $y$  plane.

Raleigh scattering occurs when the size of the molecule is much smaller than the wavelength of the incident light. This ensures that all parts of the electron cloud receive EM waves that are of the same phase. For Raleigh scattering of unpolarised light from a single spherical particle (Figure 5), the intensity of the scattered light  $I_\theta$  at a distance  $r$  as a function of angle from the direction of propagation of the incident light is given by:

$$I_\theta = I_0 \frac{8\pi^4 \alpha^2}{r^2 \lambda^4} (1 + \cos^2 \theta) \quad \text{Equation 2}$$

$I_0$  is the intensity of the incident light,  $\alpha$  is the molecular polarisability,  $\lambda$  is the wavelength of the incident light and  $\theta$  is the angle from the direction of propagation of the incident light measured in the  $x$ - $y$  plane. The molecular polarisability  $\alpha$  describes the ease with which the electron cloud is distorted by an external electric field. The electric dipole  $\vec{\mu}$  induced in the molecule is:

$$\vec{\mu} = \alpha \vec{E}_0 \cos \frac{2\pi ct}{\lambda}$$

$\vec{E}_0$  is the maximum amplitude of the electric field vector in an EM wave and  $c$  is the speed of light. Equation 2 demonstrates that the intensity of the incident light determines the sensitivity of Raleigh scattering experiments. Incident light is scattered in all directions, thus the intensity of light arriving at a detector is greatly reduced compared to the incident intensity. In order to increase SNRs or deduce the measurement time of Raleigh scattering experiments, the incident light must be as intense as possible. This is of even greater importance in time variant scattering experiments such as the measurement of protein aggregation over time, where the intervals of time over which scattering is recorded may be short and SNRs consequently low.

A useful expression of Equation 2 is the Raleigh ratio, which expresses the amount of scattering but is independent of  $r$ ,  $\theta$  and the incident light intensity:

$$R_\theta = \frac{I_\theta}{I_0} \frac{r^2}{(1 + \cos^2 \theta)} = \frac{8\pi^4 \alpha^2}{\lambda^4}$$

For a monodisperse solution, the Raleigh ratio can also be determined by replacing the molecular polarizability with a term containing the refractive indexes of the solvent and the solution:

$$\alpha = \frac{M}{CN_A} \frac{(n_0^2 - n_s^2)}{4\pi}$$

$M$  is the molecular weight of the solute,  $C$  is the concentration of the solution,  $N_A$  is Avogadro's number,  $n_0$  is the refractive index of the solvent and  $n_s$  is the refractive index of the solution. For a monodisperse solution, the Raleigh ratio becomes:

$$R_\theta = \frac{I_\theta}{I_0} \frac{r^2}{V(1 + \cos^2 \theta)} = \frac{2\pi^2 n_s^2 CM}{\lambda^4 N_A} \left( \frac{dn}{dC} \right)^2 = KCM$$

The constant terms in the above equation are usually grouped as the constant  $K$  so that the amount of scattering only depends upon the molecular mass and the concentration. If the solution is polydisperse, the above equation is

modified by replacing  $M$  by  $\bar{M}$ , the weight average molecular weight. Strictly this equation is only valid at infinite dilution but at higher concentrations, deviations from linear behaviour are modelled by inclusion of the second and third virial coefficients such that:

$$\frac{KC}{R_\theta} = \frac{1}{\bar{M}} + 2A_2C + 3A_3C^2$$

If the particle size is comparable to the wavelength of the incident light, the result is Mie scattering and a more complicated angular distribution of the scattered light is observed. In Mie theory, larger particles are treated as being composed of an infinite number of scattering centres. Integration over these scattering centres, results in interference due to path length differences from scattering centres to the observer. No interference is observed at  $\theta=0$  as the path difference from scattering centres to the observer is zero. The angular dependence of the scattered light intensity from large particles depends upon the radius of gyration of the scattering particle. The radius of gyration  $R_G$  and the average molecular weight  $\bar{M}$  of the scattering particle can be determined by measuring the angular dependence of scattered light for different concentrations of solution using the Debye-Zimm relationship:

$$\lim_{\theta \rightarrow 0} \frac{KC}{R_\theta} = \left( \frac{1}{\bar{M}} + 2A_2C \right) \left( 1 + \frac{q^2 R_G^2}{3} \right)$$

The parameter  $q$  contains the angular and wavelength dependence of the scattering:

$$q = \frac{4\pi}{\lambda} \sin \frac{\theta}{2}$$

Plotting  $KC/R_\theta$  against  $q + KC$  (a so called Zimm plot) and extrapolating for  $q=0$  and  $c=0$ , yields values for the radius of gyration and the average molecular weight (Zimm, 1948). The determination of the radius of gyration may also yield

information concerning the shape of biomolecules as for a sphere  $R_G = \sqrt{\frac{3}{5}} r_{sphere}$  and for a rod of length,  $R_G = \sqrt{12} l$ .

If the scattering volume is very small, it is possible to record fluctuations in the scattered intensity caused by the diffusion of particles in and out of the scattering volume. This is the basis of the technique of dynamic light scattering. By recording fluctuations in the scattered light, it is possible to derive diffusion coefficients, radii of gyration, the distribution of molecular masses and the shape of molecules. Both static light scattering and dynamic light scattering can be used to monitor changes in average molecular mass and radii of gyration, for example in protein aggregation.

The second type of scattering that is of importance in biological spectroscopy is Raman scattering. When light is scattered by a molecule, most of the photons are scattered elastically (Rayleigh scattering) and the wavelength of the scattered photon is identical to wavelength of the exciting photon. A small fraction of the scattered light is scattered inelastically, with the result that the molecule either losses or gains vibrational energy. Raman scattered photons therefore have a different wavelength to the incident photons. If the molecule losses vibrational energy the scattering is known as Stokes-Raman scattering and if the molecule gains vibrational energy the scattering is anti-Stokes-Raman scattering. The smaller Stokes peaks are observed either side of the main Rayleigh scattering peak in the spectrum of the scattered light (Figure 6). The Stokes peak is much larger than the anti-Stokes peak due to the greater population of molecules in the vibrational ground state. For this reason, the Stokes peak is usually measured in Raman spectroscopy. The fraction of molecules initially in the vibrational excited state is given by the factor  $\exp(-E/kT)$  where  $E$  is the energy difference between the ground and the excited state,  $k$  is Boltzmann's constant and  $T$  is the temperature. At room temperature this is a small fraction of the molecules in the ground state.

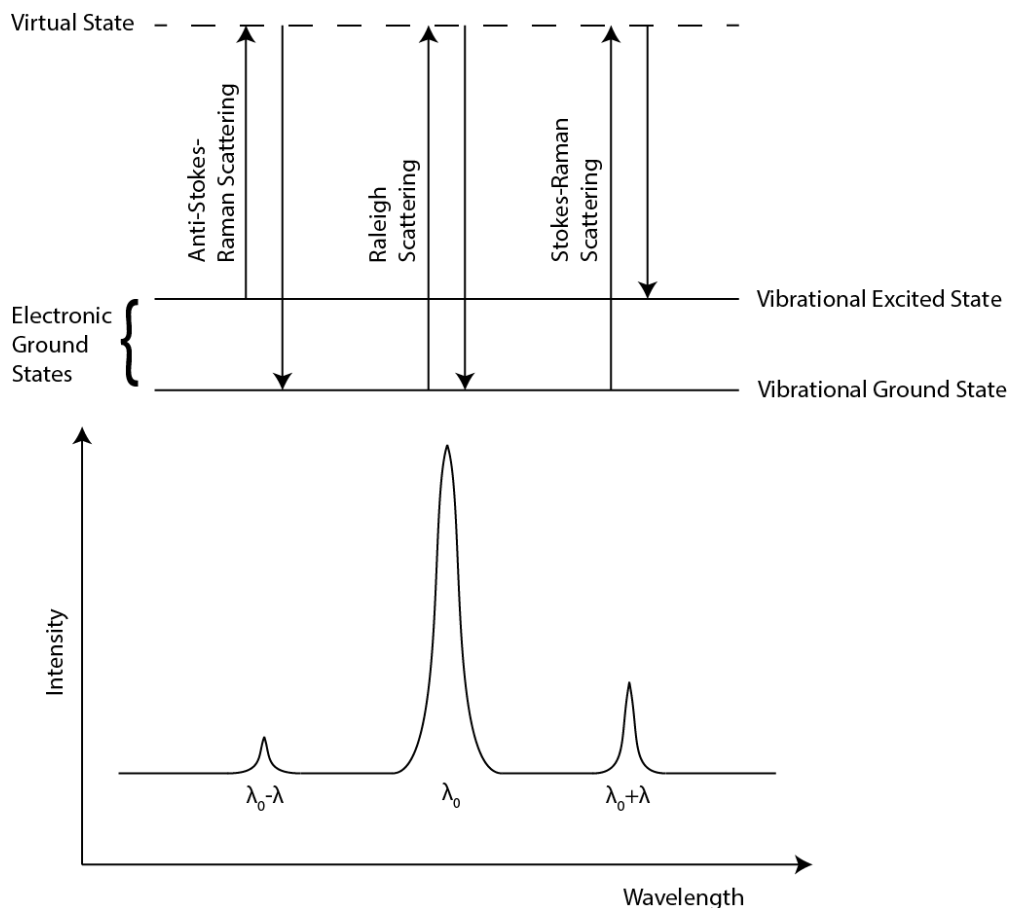


**Figure 6.** The Raleigh and Raman scattering spectral peaks observed with excitation by at a monochromatic light source. Raman scattering peaks are observed at either side of the Raleigh scattering peak. The wavelength difference between the Raman peaks and the Raleigh peak is equal to the energy difference between the vibrational states. The Stokes peak is of greater intensity than the anti-Stokes peak because of the greater population of molecules in the vibrational ground state.

In conventional Raman spectroscopy, the energy of the incident photons does not match the energy difference between electronic states. Molecules are excited to a virtual state before relaxing back to the electronic ground state via different vibrational states. Resonant Raman scattering occurs if the energy of the incident photons matches that of the transition between the electronic ground state and an excited electronic state. The selection rule for a molecule to be Raman active is that a change in the polarisation of the electron cloud must occur during the interaction with the incident radiation. The absorbance of a photon and the transition of an electron to a higher electronic state, for some molecules results in a large change in the polarisation of the electron



cloud and a large increase in the likelihood of a Raman transition of up to  $10^6$  times. Such transitions are said to be resonance enhanced

Conventional Raman scattering is very weak compared to Raleigh scattering and as a result, very high intensity light sources, high sensitivity detectors and/or very high solution concentrations are required to detect Raman transitions. The intensity of a Stokes-Raman scattering peak is given by:

$$I = \frac{CI_0\alpha^2}{\lambda^4}$$

$C$  is a constant that depends upon several factors including sample concentration and temperature,  $I_0$  is the intensity of the incident light,  $\alpha$  is the molecular polarisability and  $\lambda$  is the wavelength of the incident light. In resonance enhanced Raman spectroscopy, it is a large increase in the molecular polarisability that leads to a very large increases in the intensity of the Stokes peaks.

Raman scattering is of particular interest in biological spectroscopy because it allows for determination of vibrational energy levels of molecules in water. The excitation frequency for Raman scattering is in the UV/Visible region where water is a weak absorber/scatterer. This allows for the determination of the vibrational levels of specific groups throughout the region  $200-2000\text{cm}^{-1}$ , where IR spectroscopy would be inhibited by the absorbance of water or  $\text{D}_2\text{O}$ . An example of this is the Amide III band, occurring at  $1230-1295\text{cm}^{-1}$ , which can only be studied by Raman scattering. The applications of Raman are generally the same as IR spectroscopy where the vibrational energy levels of molecular bonds are sensitive to factors such as conformation, ionisation state and ligand binding.

The research undertaken here relates to the spectroscopic studies of glycosaminoglycan-protein interactions. It is to GAG spectroscopy that attention is now focused.

### 1.3 The Spectroscopy of Heparin and Heparan Sulphate

The GAG family of carbohydrates (Table 3), particularly polysaccharides based on heparan sulphate (HS) and closely related heparin, are of increasing interest to medicinal science due to their ability to bind to and regulate the function of a few hundred different proteins (Ori et al., 2011, Jackson et al., 1991). This ability is imparted by the extremely high negative charge density and structural complexity of heparin and HS. Protein structure, and consequently function and activity, are often significantly altered upon binding to heparin/HS.

Heparin and HS are both linear polysaccharides consisting composed of alternate units of  $\alpha$ -D-glucosamine (GlcN) and uronic acid, either  $\beta$ -D-glucuronic acid (GlcA) or  $\alpha$ -L-iduronic acid (IdoA). An oxygen atom covalently bonds monosaccharides at the first and fourth carbon atoms in the saccharide ring. This linkage is known as a 1 $\rightarrow$ 4 O-glycosidic bond and can rotate through a variety of angles. These rotations are defined by the angles formed by H1-C1-O-C4 and C1-O-C4-H4 and have been energy mapped using NMR and DFT for the ATIII binding pentasaccharide (Ragazzi et al., 1990, Hricovíni, 2015) and some chemically modified heparins (Mulloy and Forster, 2000). Variable patterns of the disaccharide subunits with epimerisation, N-sulphate, O-sulphate and N-acetyl groups give rise to a large number of complex sequences (Figure 7).

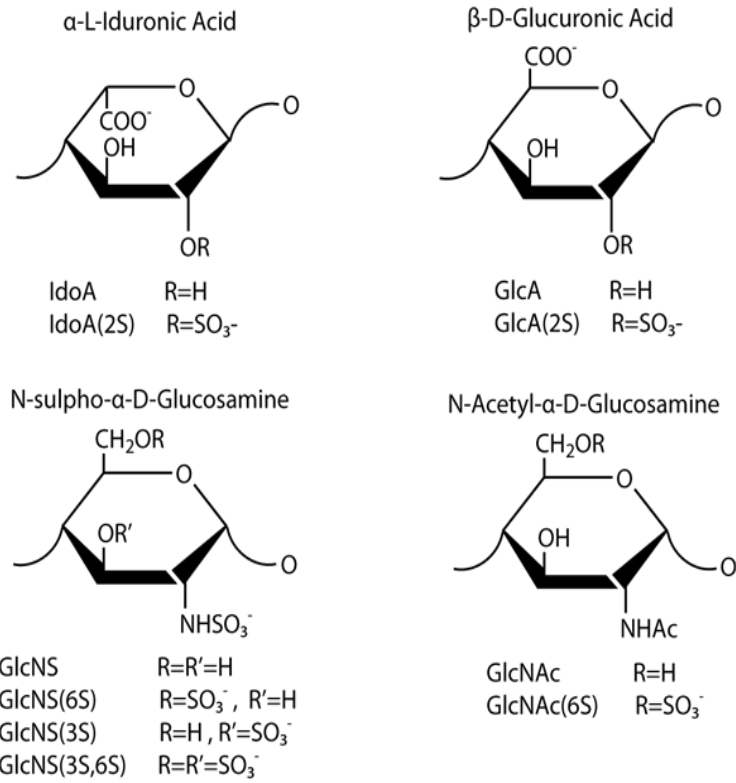


**Figure 7.** Monosaccharide building blocks of heparin and HS.

Disaccharide Repeating Unit			Notes
Name	Hexuronic Acid Monosaccharide	Hexosamine Monosaccharide	
Hyaluronic acid			<p>The only unsulphated GAG and the only GAG not found attached to a core protein.</p> <p>Can be very high molecular weight, up to 1 million Daltons.</p>
	GlcA	GlcNAc	<p>Found in synovial fluid, cartilage, skin and the ECM of connective tissue.</p>
Keratan sulphate			<p>Found in the cornea, bone, the central nervous system and localised with chondroitin sulfate in cartilage.</p>
	Gal or Gal(6S)	R <sub>1</sub> =H R <sub>1</sub> =SO <sub>3</sub> H	

Disaccharide Repeating Unit			Notes
Name	Hexuronic Acid Monosaccharide	Hexosamine Monosaccharide	
<b>Chondroitin sulphate</b>			<p>Is the most abundant GAG in the human body.</p> <p>Found in cartilage, bone, heart valves and is a major component of the ECM.</p> <p>The loss of chondroitin sulphate from cartilage is a major cause of osteoarthritis.</p>
	<p>GlcA R<sub>1</sub>=H or GlcA(2S) R<sub>1</sub>=SO<sub>3</sub>H</p>	<p>GalNAc R<sub>2</sub>=H R<sub>3</sub>=H or GalNAc(4S) R<sub>2</sub>=H R<sub>3</sub>=SO<sub>3</sub>H or GalNAc(6S) R<sub>2</sub>=SO<sub>3</sub>H R<sub>3</sub>=H or GalNAc(4S,6S) R<sub>2</sub>=SO<sub>3</sub>H R<sub>3</sub>=SO<sub>3</sub>H</p>	
<b>Dermatan sulphate</b>			<p>Originally known as chondroitin sulphate B.</p> <p>Found in skin, endothelium cells, heart valves, muscle tendons and the lungs.</p>
	<p>GlcA R<sub>1</sub>=H or IdoA R<sub>1</sub>=H or IdoA(2S) R<sub>1</sub>=SO<sub>3</sub>H</p>	<p>GalNAc R<sub>2</sub>=H R<sub>3</sub>=H or GalNAc(4S) R<sub>2</sub>=H R<sub>3</sub>=SO<sub>3</sub>H or GalNAc(6S) R<sub>2</sub>=SO<sub>3</sub>H R<sub>3</sub>=H or GalNAc(4S,6S) R<sub>2</sub>=SO<sub>3</sub>H R<sub>3</sub>=SO<sub>3</sub>H</p>	

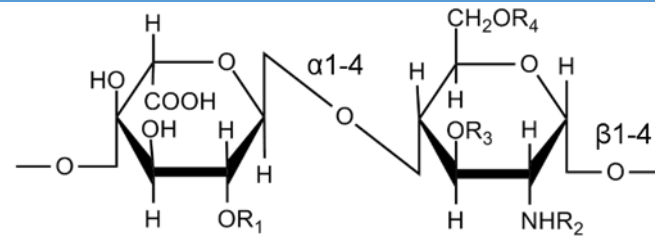
Disaccharide Repeating Unit

Name

Notes

Hexuronic Acid Monosaccharide

Hexosamine Monosaccharide



Heparin

GlcA R<sub>1</sub>=H  
 or IdoA R<sub>1</sub>=H  
 or IdoA(2S) R<sub>1</sub>=SO<sub>3</sub>H

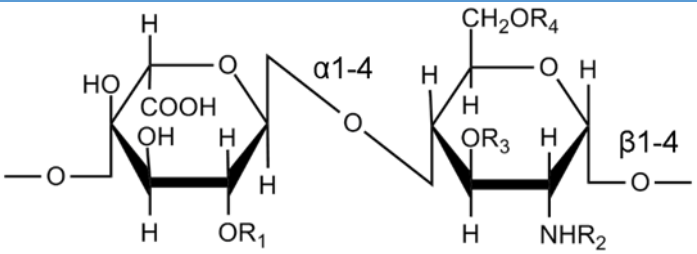
GlcNAc R<sub>2</sub>=COCH<sub>3</sub> R<sub>3</sub>=H R<sub>4</sub>=H  
 or GlcNAc(6S) R<sub>2</sub>=COCH<sub>3</sub> R<sub>3</sub>=H R<sub>4</sub>=SO<sub>3</sub>H  
 or GlcNS R<sub>2</sub>=SO<sub>3</sub>H R<sub>3</sub>=H R<sub>4</sub>=H  
 or GlcNS(6S) R<sub>2</sub>=SO<sub>3</sub>H R<sub>3</sub>=SO<sub>3</sub>H R<sub>4</sub>=SO<sub>3</sub>H  
 or GlcNS(3S) R<sub>2</sub>=SO<sub>3</sub>H R<sub>3</sub>=SO<sub>3</sub>H R<sub>4</sub>=H  
 or GlcNS(3S,6S) R<sub>2</sub>=SO<sub>3</sub>H R<sub>3</sub>=SO<sub>3</sub>H R<sub>4</sub>=SO<sub>3</sub>H

Highest negative charge density of any known biological molecule.

Most common disaccharide is IdoA(2S)-GlcNS(6S) between 70-90%

Found inside intercellular granules in mast cells.

Wildly used as an intravenous anticoagulant

Disaccharide Repeating Unit			Notes
Name	Hexuronic Acid Monosaccharide	Hexosamine Monosaccharide	
Heparan sulphate		<p>GlcA    R<sub>1</sub>=H  or IdoA    R<sub>1</sub>=H  or IdoA(2S) R<sub>1</sub>=SO<sub>3</sub>H</p> <p>GlcNAc    R<sub>2</sub>=COCH<sub>3</sub> R<sub>3</sub>=H    R<sub>4</sub>=H  or GlcNAc(6S) R<sub>2</sub>=COCH<sub>3</sub> R<sub>3</sub>=H    R<sub>4</sub>=SO<sub>3</sub>H  or GlcNS    R<sub>2</sub>=SO<sub>3</sub>H    R<sub>3</sub>=H    R<sub>4</sub>=H  or GlcNS(6S) R<sub>2</sub>=SO<sub>3</sub>H    R<sub>3</sub>=SO<sub>3</sub>H R<sub>4</sub>=SO<sub>3</sub>H  or GlcNS(3S,6S) R<sub>2</sub>=SO<sub>3</sub>H R<sub>3</sub>=SO<sub>3</sub>H R<sub>4</sub>=SO<sub>3</sub>H</p>	

**Table 3.** The GAG family of carbohydrates showing the disaccharide repeating unit and the possible substituent groups.

Although there are 24 possible disaccharide subunits, not all are commonly found in HS/heparin. HS possesses a domain structure (unlike heparin) consisting of blocks of repeating GlcAc-(1→4)-GlcNAc disaccharides, the most common disaccharide in HS (Lyon and Gallagher, 1998) (NA domains) and blocks of highly sulphated heparin-like IdoA-(1→4)-GlcNS disaccharides (NS domains) (Rabenstein, 2002a). The NA and NS domains are separated by a mix of both GlcNAc and GlcNS containing disaccharides known as the NA/NS domain. The disaccharide makeup of HS is known to depend on the type and the age of the cell (Feyzi et al., 1998). The most common disaccharide in heparin is IdoA(2S)-GlcNS(6S) and is found throughout the heparin chain (Patey et al., 2006). This means that heparin has mainly  $\alpha$  1→4 glycosidic linkages. The structure of heparin is comparable to the NS domains of HS.

These biologically important molecules are already used medicinally, most notably heparin, which is used intravenously to prevent blood coagulation. The global heparin market is very large, estimated at £8.2 bn in 2014 and growing at a rate of 6.3% *per annum* (2015). Heparin binds to and activates the serine protease inhibitor anti-thrombin III (ATIII) which in turn de-activates several proteins in the coagulation cascade. Heparin is synthesised as a proteoglycan in the Golgi apparatus of mast cells, where it consists of a serglycin core protein to which is attached multiple heparin chains (Carlsson et al., 2008). Following synthesis, the heparin proteoglycan is transported to the cytoplasmic secretory granules of mast cells. Pharmaceutical heparin is produced by the extraction of the heparin proteoglycan from large amounts of mast cell containing tissue (usually bovine lung or porcine intestinal mucosa), followed by cleavage of the heparin chains by a number of methods including alkaline beta elimination, nitrous acid digestion and cleavage by endo- $\beta$ -D-glucuronidase to form a polydisperse mixture of heparin molecules.

Heparan sulphate is a major component of the extra-cellular medium (ECM) and is found attached to the surface of many different cell types in metazoan organisms via membrane spanning proteins as a heparan sulphate proteoglycan (HSPG). HSPGs are a group of complex macromolecules that are found extensively in the extracellular matrix (ECM) of all mammalian cells.



They consist of a core protein that is covalently bound to one or more highly anionic HS chains. These molecules fall into three groups according to their locality. These groups are: membrane bound HSPGs such as glycosylphosphatidylinositol (GPI) anchored proteoglycans (glypican core protein) and syndecans, the secreted ECM HSPGs agrin, perlecan and type XVIII collagen and the secretory vesicle proteoglycan (PG) serglycin, onto which mast cell heparin is biosynthesised (Sarrazin et al., 2011).

HS appears to have different functions, notably the regulation of many different forms of ligand-receptor binding by its requirement as a cofactor for the binding of cytokines and growth factors to their receptors. Many ligands require binding to HS before being in a suitable conformation for binding to and activation of receptors. Many of these HS binding proteins regulate important cellular activities, including growth (Forsten-Williams et al., 2008) and differentiation factors (Dombrowski et al., 2008), morphogens (Colombres et al., 2008), proteases and protease inhibitors (Griffith, 1983), chemokines (Lortat-Jacob et al., 2002, Bao et al., 2010), cytokines (Webb et al., 1993, Murphy et al., 2007), adhesion molecules (Kallapur and Akeson, 1992, Peter et al., 1999) and components of the extracellular matrix (Trindade et al., 2008). Through their ability to change protein function and activity, GAGs regulate or are important in numerous physiological processes, including cell differentiation (Holley et al., 2011, Castellot et al., 1985), proliferation (Flint et al., 1994, Aviezer et al., 1994) and migration (Higashiyama et al., 1993), embryonic development (Lin et al., 1999, Morio et al., 2003), blood coagulation (Marcum et al., 1986), angiogenesis (van Wijk and van Kuppevelt, 2014, Aviezer et al., 1994), inflammation (Parish, 2006, Zhang et al., 2014), axon guidance (Bülow et al., Irie et al., 2002), amyloidogenesis (Magnus et al., 1992, Snow and Wight, 1989) and tumorigenesis (Nagarajan et al., 2015), viral invasion (Summerford and Samulski, 1998, Marchetti et al., 2004) and metastasis (Sanderson et al., 2004, Sanderson, 2001, Hulett et al., 1999, Yin et al., 2010, Vlodaysky et al., 1999). It is because of this regulatory role that both native and engineered/synthetic GAGS and carbohydrates in general are of interest as drug candidates.

The ability of GAGs to modify the function and activity of proteins has led to much research into the possibility of engineering GAGs for selectively regulating specific protein structures and functions, whilst attempting to minimise binding to other non-target proteins to reduce side effects. Heparin has often been used in bioassays as a proxy for HS, as heparin is much more easily obtained in large quantities and can be easily chemically modified to examine the effect of specific groups and sequences on the binding affinity and activity of proteins (Chung et al., 2015, Lapierre et al., 1996). Heparin is also used for economic reasons, because of the difficulties of acquiring large amounts of HS. Although the anticoagulant properties of heparin are of great importance to healthcare, when attempting to create heparin/HS based therapeutics for bind to proteins other than ATIII, the anticoagulant properties of these molecules must be minimised. Research has shown that heparin/HS is capable of inhibiting cellular invasion by HIV, H5N1, herpes simplex and dengue viruses (Howell et al., 1996, Skidmore et al., 2015, Chen et al., 1997, Nahmias and Kibrick, 1964, Copeland et al., 2008), preventing erythrocyte invasion and rosetting in *plasmodium falciparum* malaria (Skidmore et al., 2008, Boyle et al., 2010), attenuating the activity of Alzheimer's  $\beta$ -secretase BACE-1 (Patey et al., 2006) and inhibiting cell proliferation (Silber et al., 1993, Benitz et al., 1986). Heparin can both promote and inhibit protein aggregation, the understanding and control of which is of particular relevance to the food industry as well as the medical industry (Raffaele and Peter, 2013). Pathological protein aggregation occurs in the amyloid diseases of prion disease (Vieira et al., 2014), Parkinson's (Cohlberg et al., 2002) and Alzheimer's disease. HSPGs have been found in nearly all amyloid plaques investigated to date (Snow et al., 1989, Stenstad et al., 1991, Magnus et al., 1992, Brandt et al., 1974, Snow et al., 1988b, Snow et al., 1987). These HSPGs are known to be deposited during amyloid fibrillogenesis (Snow and Kisilevsky, 1985) and for this reason are thought to play a key role in fibril formation (Snow and Wight, 1989). To date however, the exact mechanism of fibril formation and the involvement of HS has not been discerned.

Progress has been made in identifying specific structural requirements and some of the minimum saccharide sequences required for protein binding have

now been developed. The minimum fragment requirement varies from a tetrasaccharide for annexin V (Ishitsuka et al., 1998, Capila et al., 2001, Capila et al., 1999) (calcium ions are also a requirement for HS:Annexin binding) to a dodecasaccharide for binding and activation of FGFR2 (Walker et al., 1994). Minimal saccharide sequences and the presence of specific groups have been elucidated for binding to some proteins, including the pentasaccharide sequence that is required for binding to the protein ATIII that imparts heparin with its anticoagulant properties (Figure 8) (Lindahl et al., 1980, Rosenberg and Lam, 1979, Lindahl et al., 1984, Desai et al., 1998). This has led to the development of low molecular weight heparins, notably the pentasaccharide drug Arixtra, as a treatment for heparin induced thrombocytopenia, a condition in which the binding of heparin to blood platelets via platelet factor 4 forms an immunogenic complex. The minimal saccharide sequences required binding to apolipoprotein E (Bazin et al., 2002), lipoprotein lipase (Parthasarathy et al., 1994), HIV-1 tat protein (Rusnati et al., 1997, Rusnati et al., 1998, Rusnati et al., 1999), CCL2 protein (Sweeney et al., 2006), platelet derived growth factor A (PDGF-A) (Feyzi et al., 1997), basic fibroblast growth factor (FGF2) (Turnbull et al., 1992, Habuchi et al., 1992, Maccarana et al., 1993, Walker et al., 1994, Guimond et al., 1993), fibroblast growth factor receptor 2 (FGFR-2) (Walker et al., 1994), fibroblast growth factor receptor 4 (FGFR-4) (Loo et al., 2001) and hepatocyte growth factor (HGF) (Ashikari et al., 1995, Lyon et al., 1994) have also been identified. We are however, very far from a complete heparin/HS interactome and how specific protein binding sites are created is not fully understood. Although the enzymes that are involved in heparin/HS biosynthesis of GAGs are thought to have all been identified, how exactly they act to create the required sequences and conformations is yet to be elucidated.

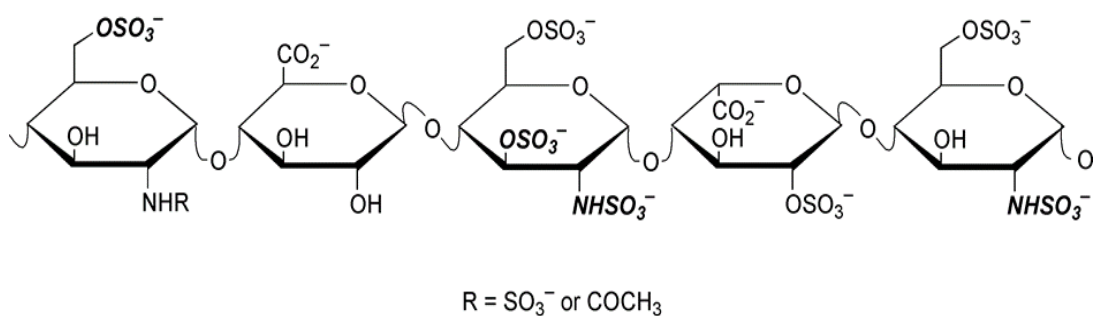


**Figure 8.** Minimal pentasaccharide antithrombin binding site. From (Rabenstein, 2002b)

The lack of knowledge concerning binding sequences and/or conformations is mainly due to the extremely high information content, encoded in HS/heparin. There may be an amount of conformational redundancy and degeneracy present in heparin/HS sequences (Meneghetti et al., 2015) but from a combinatorial perspective, a small oligosaccharide such as a DP12 (Degree of Polymerisation of 12 monosaccharides) can potentially contain just over a billion possible separate structures, many of which will be isomeric. Combined with the knowledge that heparin/HS can be hundreds of monosaccharides long, the possible variety of these molecules makes them very difficult to fractionate to pure molecular structures. Obtaining pure heparin structures in reasonable amounts for assay or spectroscopy (~nM) is extremely time and labour intensive and in practice is currently an impossible task for all but the shortest of oligosaccharides. Even using modern separation techniques such as HPLC, fractions may still contain many different molecular isomers and samples are obtainable only in very small amounts after multiple fractionations. The difficulties of obtaining pure samples in reasonable amounts, limits the use of analytical techniques that are routinely used for sequencing and structural determination of proteins: Nuclear Magnetic Resonance (NMR), Mass Spectrometry (MS) and X-ray crystallography.

The structural determination of GAGs using NMR suffers from the fact that NMR spectra show only an average of the structural features present in the sample molecules. NMR spectra of heparin are further complicated by dynamic conformational flexibility of the iduronate pyranose ring. This ring can be found in the <sup>1</sup>C<sub>4</sub> and <sup>4</sup>C<sub>1</sub> chair and <sup>2</sup>S<sub>0</sub> skew boat conformations if the ring is found at the reducing end (the C1 carbon not involved in a glycosidic bond)

and in the  ${}^1C_4$  and  ${}^2S_0$  throughout the chain. The glucuronic acid (GlcA) and glucosamine residues have been found to be in the  ${}^4C_1$  conformation. These conformations were originally identified from NMR spectra (Mulloy et al., 1993, Sanderson et al., 1987, Ferro et al., 1990) but complicate any further structural analysis by NMR. Line broadening also occurs in NMR spectra of polysaccharides as the length of the polysaccharide chain increases in the sample. This is due to decreasing mobility of the molecules leading to heterogeneities and anisotropy in the applied magnetic field. In practice this means that it becomes difficult to assign all the peaks in the spectra of samples containing oligosaccharides of length greater than DP12 because of poorly resolved spectra.

Mass spectrometry can determine sulphation patterns and the identity of the amino groups in oligosaccharides below around a DP12. Combined with affinity and size exclusion chromatography, MS can determine sequences that possess binding affinities for proteins. In order to facilitate sequence determination, MS requires that samples be of homogenous sulphation and amino group pattern, so the difficulties of saccharide separation are then encountered. MS is unable to determine however, the identity of the anomeric iduronate ring and with oligosaccharides above DP12, the number of ion fragments seen in MS data makes sequence determination very complex. MS also reveals no direct information concerning the conformation of polysaccharides.

X-ray diffraction crystallography although an extremely successful technique for determining the structure of proteins and protein complexes, has severely limited applications when it comes to the structural determination of heparin/HS, not least due to the difficulties of crystallising pure polysaccharide structures. To date this has not been done with heparin or HS.

To further our study of GAG-protein interactions, we need to look for other spectroscopic techniques that may provide understanding as to the structural and conformational requirements for binding. We must also seek insight into the dynamics and conformational changes that occur in upon binding. One

such phenomenon that we can exploit to probe polysaccharide-protein binding is that of optical activity. However, problems are encountered when applying electronic CD (UVCD) to GAG-protein interactions due to the difficulty of deconvoluting spectra into separate contributions from GAG or protein. This is mainly due to the overlap of spectral features around 190nm because of UV chromophores present in the GAG, predominantly from carboxyl groups, present in the uronic acid residues ( $n-\pi^*$  transitions) and N-acetyl groups in the glucosamine residues ( $\pi-\pi^*$  transitions). The dependence of heparin conformation on the presence of cations and substitution pattern, gives unique far-UVCD spectra (Morris et al., 1975, Rudd et al., 2007), which further complicates attempts to attribute spectral components to either GAG or protein.

IR spectroscopy offers a potential solution to the problems encountered with UVCD analysis of GAG-protein interactions. The FTIR spectra of GAGs has peaks in both the regions of the amide I and amide II bands, arising from the C=O bond in the N-Acetyl groups. This presents the same problems with separation of protein and polysaccharide components that are seen in UV spectroscopy. It is therefore impossible to assign changes in spectral features to conformational changes in either GAG or protein that occur upon binding. However, looking at GAGs using infra-red CD or VCD, the amide I band is featureless (Figure 9) and so changes in spectral features upon GAG:protein binding can be directly attributed to conformational changes occurring in proteins.

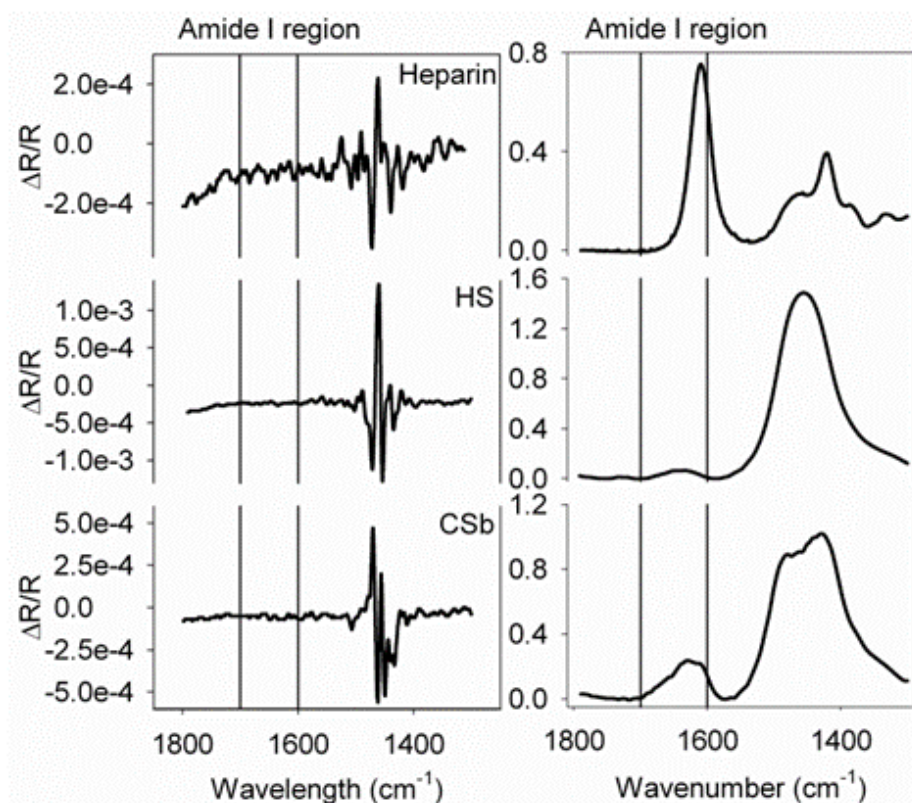


**Figure 9.** The VCD (left) and IR transmission (right) spectra of heparin, HS and Chondroitin Sulphate B at 25 mg/ml. The amide I region is essentially featureless in VCD. From (Rudd et al., 2008a).

The lack of a GAG VCD signal in the amide I is thought to be due to the irregular arrangement of N-acetyl groups. This prevents the formation of a regular geometric arrangement of hydrogen bonds and leads to a lack of chirality. This is strong evidence that GAGs do not form a regular repeating structure such as an  $\alpha$  helix. There is no longer a need to subtract or deconvolute spectra as only the protein components can be seen in the amide I region. We can exploit this lack of a GAG peak in the amide I band to selectively observe conformational changes occurring in a protein upon binding to a GAG (Figure 10).

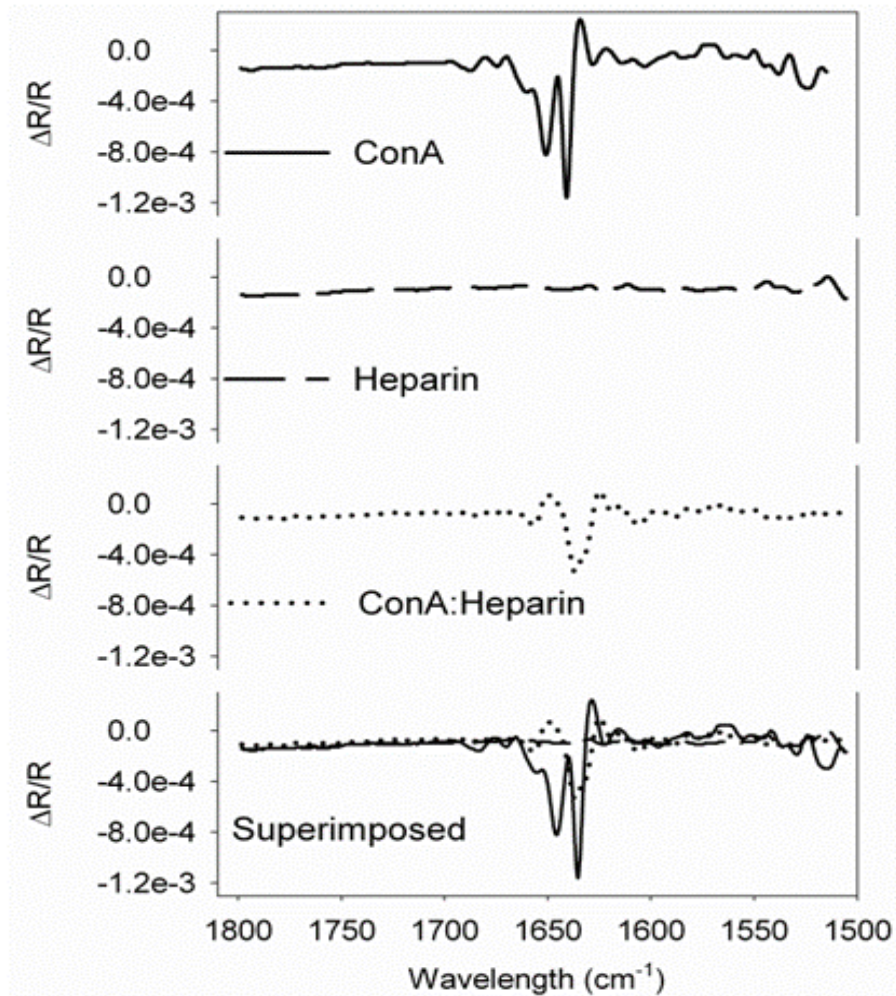


**Figure 10.** VCD spectra of concanavalin A, heparin and concanavalin A bound to heparin. concanavalin A is at 100 mg/ml and heparin is present at a molar equivalent. Concanavalin A is a tetrameric lectin that is mitogenic in plants. The conformational change in concanavalin A upon binding to heparin can easily be seen. From (Rudd et al., 2008a).

#### 1.4 SNRs in Spectroscopy

Although VCD presents a unique way of examining structural and conformation changes occurring in a protein upon binding to a GAG, the weakness of the VCD signal meant that experiments were run for a long time in order to obtain results with good SNRs. The low VCD absorbance of proteins also precluded time resolved experiments on GAG:protein binding because these interactions occurring occur over a time scale of seconds and minutes. This also hampers the utility of VCD in many other interesting, time varying biological systems. It was therefore of practical scientific interest to the



Yates laboratory to determine methods to increase SNRs so that VCD and other spectroscopic techniques could be utilised for GAG spectroscopy. It was hypothesised that improved SNRs might be obtained by increasing the intensity of the infrared (IR) light source. To test this hypothesis further, a quantitative analysis of the dependency of SNRs in absorbance spectroscopy was necessary to determine the effect on SNRs of increasing the light source intensity.

Spectral noise has two effects on absorbance measurements. Firstly, baseline noise limits ability of the experimenter to discern small signal peaks and secondly, noise limits the precision of larger peaks. In protein VCD spectroscopy, where the absorbance of circularly polarised infra-red light by the protein is very low, it is the former effect that leads to low SNRs. Spectral noise comes from the inherent imprecision of the photon detector to determine the exact physical intensity of impinging light  $I_p$ . During this analysis, the symbol  $i$  will denote current and capital  $I$  to denote light intensity. The subscript  $I_p$  will denote the actual physical light intensity and  $I_m$  will denote the measured light intensity. Photon detectors convert some proportion of the power of the impinging photons, in a wavelength dependant manner, into an electromotive force or voltage  $V$ . This voltage generates a signal current  $i$  that is directly proportional (through Ohm's Law) to the resistance/impedance of the detector. The current  $i$  is measured and then converted into a light intensity  $I_m$ . Within the operating intensity of the detector i.e. below the saturation intensity and above the minimum detectable intensity (also known as noise-equivalent power),  $i$  is directly proportional to  $I_m$ . The coefficient relating  $i$  to  $I_m$  is a function of wavelength that depends on detector type:

$$I_m = f(\lambda)i$$

The proportionality factor  $f(\lambda)$  is known as the *spectral responsivity* and is usually determined by the manufacturer of the detector by measuring the current generated at a known intensity  $I_p$  over the operating wavelength range of the detector. Figure 11 shows the spectral responsivity of a typical photodiode. In commercially available spectrophotometers the current  $i$  is

converted to  $I_m$  by the supplied hardware/software using the predetermined responsivity.

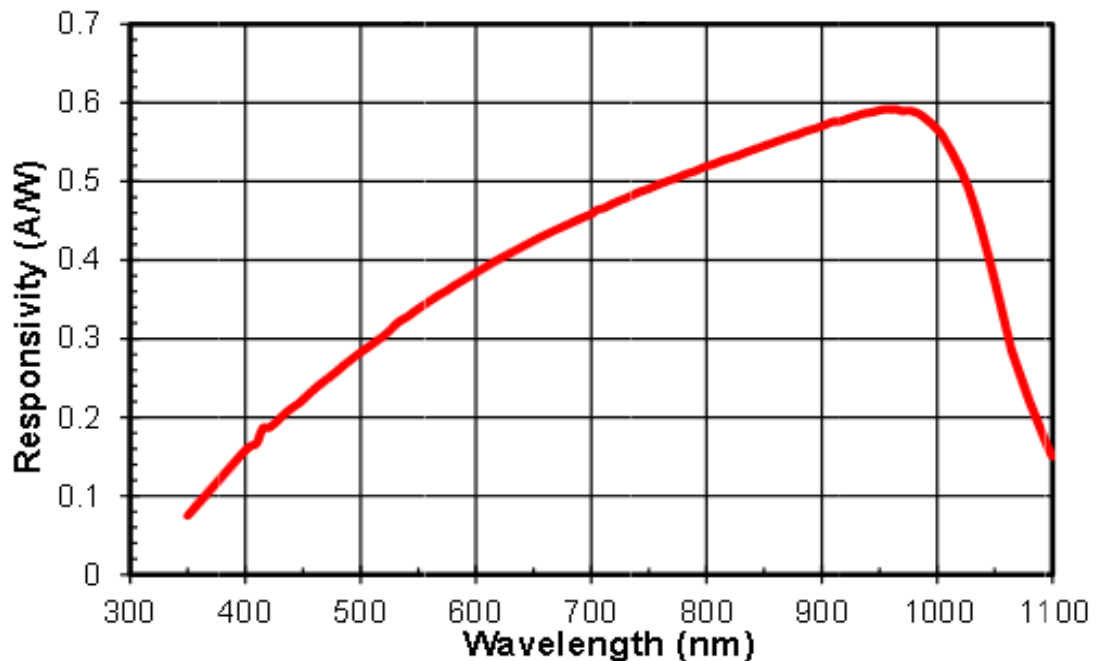


**Figure 11.** The spectral responsivity of the Thorlabs FDS100 silicon photodiode as measured by NIST. The units of the responsivity are A/W which is current in Amps over light intensity in Watts. Source: <http://www.thorlabs.de/thorcat/0600/FDS100-CAL-SpecSheet.pdf>

In a noiseless system and below the saturation intensity of the detector, the current  $i$  is directly proportional to the physical impinging intensity  $I_p$ . Deviations in this relationship are caused by spectral noise. These fluctuations lead to differences between the actual intensity  $I_p$  and the measured intensity  $I_m$  and arise from three distinct sources. These sources are termed thermal, proportional noise and shot noise.

Thermal noise, also known as Johnson noise or fixed noise, is generated by the detector electronics and is temperature dependant and independent of the magnitude of the light intensity  $I_p$ . Thermal noise dominates at low  $I_p$  and is observed as baseline fluctuations as  $I_p$  approaches zero. The amount of thermal noise in a detector can be measured by recording the dark current: the intensity  $I_m$  that the detector measures at  $I_p = 0$ . In the low intensity regime, the SNR of the detector is therefore proportional to the signal current  $i$  (or  $I_p$ ), because the amount of noise is fixed.

Proportional or technical noise originates from fluctuations in the light source intensity  $I_p$ . This noise is known as proportional noise because it is directly proportional to the light intensity  $I_p$ . In most absorbance techniques, the light source intensity can be corrected for by some method of measuring  $I_p$  (such as beam sampling). The contribution of proportional noise to the SNR is independent of the absorbance signal magnitude.

Shot or Poisson noise originates from the quantised nature of photon detection. Photon detection obeys Poisson statistics because detection events are independent, counted in positive integers and follow a random temporal distribution. If  $N$  is the actual number of photons detected by the detector in a time  $t$  and it is assumed that the light source intensity is constant over time, then the probability distribution of detected photons is:

$$P(N) = \frac{e^{-pt}(pt)^N}{N!}$$

Where  $p$  is the mean number of photons detected in unit time. For large  $N$ , the Poisson distribution approaches a normal distribution centred at the mean. Poisson distributions have the property that the mean number of events occurring in a time  $t$  is equal to the variance, therefore:

$$\langle N \rangle = \sigma^2 N = pt$$

The standard deviation is:

$$\sigma(N) = \langle N \rangle^{1/2} = (pt)^{1/2}$$

The contributions of each type of noise to the variation in the signal current are statistically independent and depend upon the experimental conditions. The total RMS noise current can therefore be written as:

$$i_n = (i_T^2 + i_p^2 + i_S^2)^{1/2}$$

$i_T$  denotes thermal,  $i_p$  denotes proportional and  $i_s$  is shot current. In order to obtain the maximum SNR ratio to be obtained it is necessary for  $i_p, i_T \ll i_s$ . Even under ideal experimental conditions, where thermal and proportional noise have been eliminated, shot noise due to intrinsic variations in the number of detected photons is always present. The amount of shot noise thus provides a lower bound for the uncertainty in the signal. The SNR under ideal conditions is therefore given by:

$$\frac{\text{Signal}}{\text{Noise}} = \frac{\langle N \rangle}{\sigma(N)} = \frac{pt}{(pt)^{1/2}} = (pt)^{1/2}$$

This is the upper bound for the SNR with photon counting detection. The mean number of photons detected in unit time,  $p$  is:

$$p = Q_\lambda I$$

Where  $Q$  is the wavelength dependant quantum efficiency of the detector and  $I$  is the intensity impinging upon the detector. The quantum efficiency of a detector is a measure of the sensitivity of the detector and is a ratio of the number of photons detected to the number of photons impinging upon the detector. An ideal detector has a quantum efficiency of one. The SNR of a measurement conducted over a time  $t$  is therefore:

$$\frac{\text{Signal}}{\text{Noise}} = (Q_\lambda I t)^{1/2} \quad \text{Equation 3}$$

The SNR of a measurement can therefore be increased by increasing the detection time or increasing the light intensity. To double the SNR either the detector quantum efficiency, light intensity or the count time must be increased by a factor of four. Spectral averaging can also be used to increase the SNR and has an identical effect to increasing the run time  $t$ . Spectral averaging increases SNRs proportionally to the square root of the number of measurements that are averaged.

It is a more complex problem to determine the maximum obtainable SNR for absorbance measurements. Increasing the intensity of the source or the detection time may not necessarily lead to increased SNR for absorbance measurements. This is because absorbance is the logarithm of the ratio of the light intensity  $I_1$  passed through the sample to the intensity of light  $I_0$  impinging upon the sample. The Beer-Lambert law further relates the absorbance to the absorption coefficient  $\epsilon$  of a sample:

$$\text{Absorbance} = \log_{10} \left( \frac{I_0}{I_1} \right) = lc\epsilon$$

$l$  is the path length of the light through the sample and  $c$  is the sample concentration. I will use subscript zero or one to denote measurement variables in the presence (<sub>1</sub>) or absence (<sub>0</sub>) of the sample.

The simplest method to determine  $I_1$  and  $I_0$  is to conduct two measurements, with and without the sample in place, counting the number of photons arriving at the detector in each case. In practical biological spectroscopy, the measurement conducted without the sample in place is a control measurement, usually a cuvette containing only the relevant biological buffer. This method works as long as the intensity of the light source  $I_0$ , does not change between measurements. If  $I_0$  varies between measurements, incorrect absorbance values will be calculated. This method can therefore be used with light sources of constant spectral intensity such as lasers and bulbs. Due to the probabilistic nature of detection, the absolute intensities  $I_0$  and  $I_1$  are unknown and must be inferred from the  $N_{0/1}$ , the number of photons detected in measurement times  $t_{0/1}$ .

$$\text{Measured intensity } I_{0/1} = \frac{N_{0/1}}{Qt_{0/1}}$$

As  $N$  becomes larger, the measured intensities  $I_0$  and  $I_1$  approach Normal distributions with means given by:

$$\langle I_{0/1} \rangle = \frac{\langle N_{0/1} \rangle}{Qt_{0/1}}$$

If the number of detection events  $N$  is very low, approaching single photon detection, the measured intensity can be very different from the mean intensity, leading to a much greater random error in the calculated absorbance. This can occur in extreme situations where the sample is of very high absorbance, the detector is of very low  $Q$ , the light intensity is very low or the measurement times are very short. In these situations, the assumption that the measured  $I_{0/1} = \langle I_{0/1} \rangle$  cannot be used. When  $N$  is large, the absorbance calculated from the two measurements is:

$$Absorbance = \log_{10} \left( \frac{I_0}{I_1} \right) = \log_{10} \left( \frac{t_1 N_0}{t_0 N_1} \right) = l c \epsilon$$

$N_{0/1}$  is the number of photons detected in each measurement. The mean absorbance over a large number of detected photons is simply:

$$\langle Abs \rangle = \log_{10} \left( \frac{\langle I_0 \rangle}{\langle I_1 \rangle} \right) = l c \epsilon$$

The standard deviation of the absorbance can be determined using the formula for the propagation of errors:

$$\sigma^2(Abs) = \left( \frac{\partial Abs}{\delta N_0} \right)^2 \sigma^2(N_0) + \left( \frac{\partial Abs}{\delta N_1} \right)^2 \sigma^2(N_1)$$

The partial derivatives are easy to solve by a change of base to the natural logarithm:

$$Absorbance = \frac{1}{\ln 10} \ln \left( \frac{I_0}{I_1} \right) = \frac{1}{\ln 10} \ln \left( \frac{t_1 N_0}{t_0 N_1} \right)$$

Putting this into the propagation of errors formula:

$$\begin{aligned}
\sigma^2(Abs) &= \left(\frac{1}{\ln 10}\right)^2 \left( \left(\frac{\partial}{\partial N_0} \ln \left(\frac{t_1 N_0}{t_0 N_1}\right)\right)^2 \sigma^2(N_0) + \left(\frac{\partial}{\partial N_1} \ln \left(\frac{t_1 N_0}{t_0 N_1}\right)\right)^2 \sigma^2(N_1) \right) \\
&= \left(\frac{1}{\ln 10}\right)^2 \left( \left(\frac{1}{N_0}\right)^2 Q I_0 t_0 + \left(\frac{-1}{N_1}\right)^2 Q I_1 t_1 \right) \\
&= \left(\frac{1}{\ln 10}\right)^2 \left( \left(\frac{1}{Q I_0 t_0}\right)^2 Q I_0 t_0 + \left(\frac{-1}{Q I_1 t_1}\right)^2 Q I_1 t_1 \right) \\
&= \left(\frac{1}{\ln 10}\right)^2 \frac{1}{Q} \left( \frac{1}{I_0 t_0} + \frac{1}{I_1 t_1} \right)
\end{aligned}$$

Using  $I_1 = I_0 10^{-Abs}$  the variance can be formed as:

$$\sigma^2(Abs) = \left(\frac{1}{\ln 10}\right)^2 \frac{1}{Q} \left( \frac{1}{I_0 t_0} + \frac{10^{Abs}}{I_0 t_1} \right)$$

The maximum obtainable SNR for absorbance measurements is therefore:

$$\begin{aligned}
\frac{Signal}{Noise} &= \frac{\langle Abs \rangle}{\sigma(Abs)} = Abs / \left( \left(\frac{1}{\ln 10}\right)^2 \frac{1}{Q} \left( \frac{1}{I_0 t_0} + \frac{10^{Abs}}{I_0 t_1} \right) \right)^{1/2} \\
&= Abs / \left( \frac{1}{\ln 10} Q^{-1/2} \left( \frac{1}{I_0 t_0} + \frac{10^{Abs}}{I_0 t_1} \right)^{1/2} \right) \\
&= \ln 10 Q^{\frac{1}{2}} I_0^{\frac{1}{2}} Abs \left( \frac{1}{t_0} + \frac{10^{Abs}}{t_1} \right)^{-1/2} \\
&= \ln 10 Q^{\frac{1}{2}} I_0^{\frac{1}{2}} Abs \left( \frac{t_1 t_0}{t_1 + t_0 10^{Abs}} \right)^{1/2} \\
&= \ln 10 (Q I_0 t_0 t_1)^{\frac{1}{2}} Abs (t_1 + t_0 10^{Abs})^{-1/2} \quad \text{Equation 4}
\end{aligned}$$

Equation 4 is the maximum possible SNR for an absorbance measurement with perfect noise reduction. Equation 4 is of similar form to Equation 3, depending linearly upon the square roots of the source intensity and detector quantum efficiency. The equation for the SNR is parameterised in  $t_1$  and  $t_0$ , containing a more complex time factor  $\left( \frac{t_1 t_0}{t_1 + t_0 10^{Abs}} \right)^{1/2}$  that contains the

absorbance term. Note that *Equation 4* does not hold as  $t_0$  or  $t_1 \rightarrow 0$  or as the absorbance becomes very large as the small number of photons detected leads to deviations in the measured intensity  $I_{0/1}$  from the mean intensity  $\langle I_{0/1} \rangle$ .

To determine how the SNR behaves as the sample absorbance varies, the constant  $\ln 10 I_0^{1/2} Q^{1/2}$  is set to unity. The times  $t_0$  and  $t_1$  are allowed to take any real positive values. The resultant functions of setting  $t_0 = t_1$  for a variety of times and absorbance values in the range  $0 < Abs < 5$  are plotted in Figure 12.

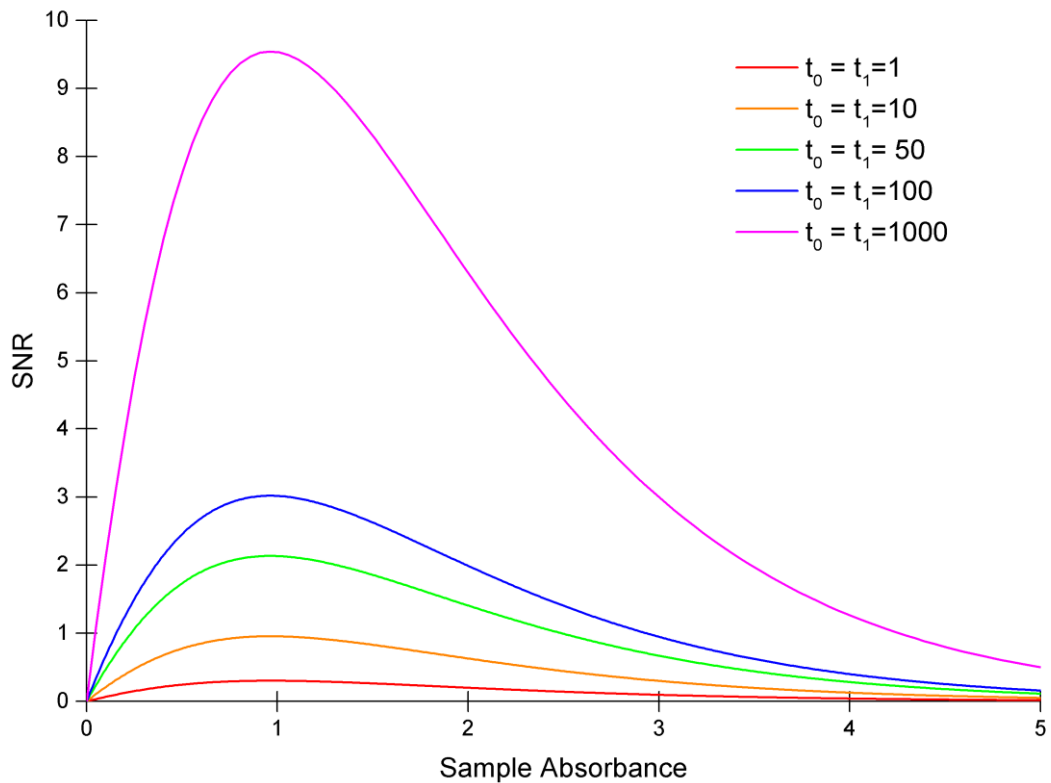


**Figure 12.** A graph of the function  $SNR = Abs \left( \frac{t_1 t_0}{t_1 + t_0 10^{Abs}} \right)^{1/2}$ . SNR and absorbance are both dimensionless quantities.

Figure 12 shows that if  $t_0 = t_1$  the maximum SNR is achieved when a sample has an absorbance of approximately 1. To further explore the consequences of varying the measurement times, the resultant functions of setting  $t_0 = 1$  and allowing  $t_1$  to vary are plotted in Figure 13.



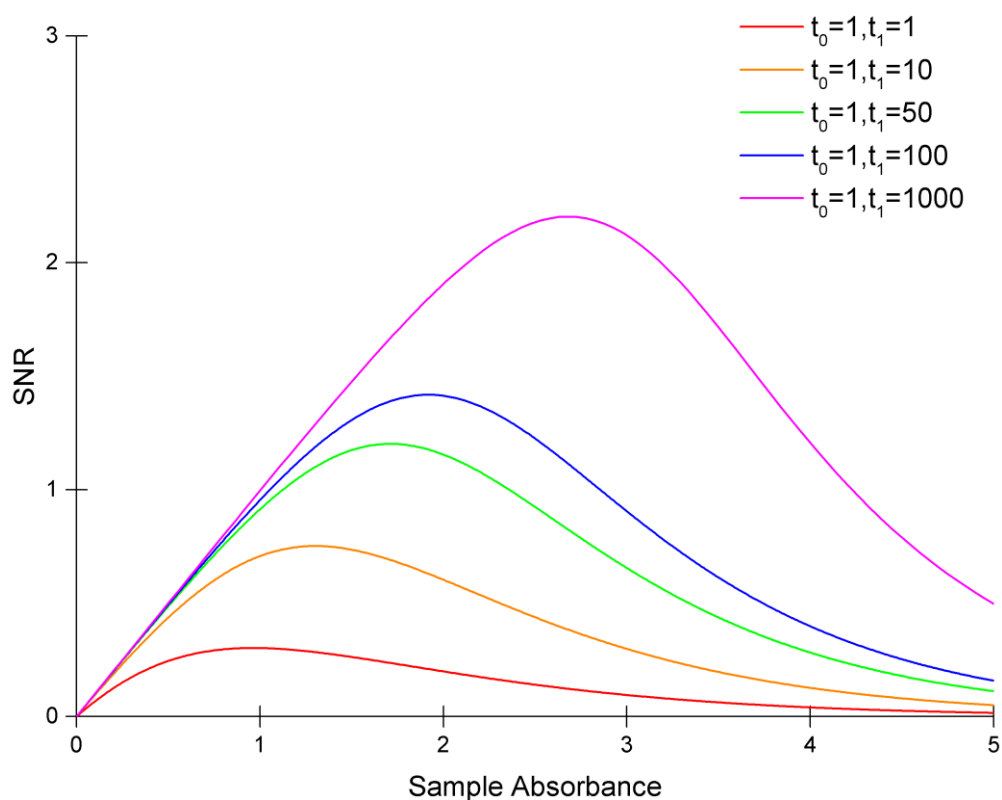


**Figure 13.** A graph of the function  $SNR = Abs \left( \frac{t_1 t_0}{t_1 + t_0 10^{Abs}} \right)^{\frac{1}{2}}$  where  $t_0=1$  and  $t_1$  takes a range of values from 1 to 1000. S/N and absorbance are both dimensionless quantities.

Figure 13 shows that if  $t_1$  increases while  $t_0$  is held constant, SNR ratios increase in a non-linear manner with absorbance. A comparison of Figures 12 and 13 shows that, in this simple case, that by increasing the time of the blank measurement  $t_0$  as well as increasing the sample measurement  $t_1$ , substantial increases in SNRs can be obtained. For example,  $t_0=t_1=1000$  gives a maximal SNR of approximately 9.5 whereas  $t_0=1, t_1=1000$  gives an approximate SNR of 2.25, an increase in the SNR ratio by a factor of 4.2 for a doubling of the total measurement time. Maximal SNRs can be also achieved by optimising the sample absorbance. Figures 12 and 13 clearly show that samples of low (<0.5) or high (>4) absorbance will necessarily produce low spectral SNRs. It is therefore advantageous to prepare the absorbance of a sample so that the greatest improvement in SNR can be achieved for increased measurement times. This can be achieved by varying the path length or the concentration of

the sample. The differentiation of Equation 4 reveals the exact absorbance at which the SNR is maximal or minimal for any  $t_0$  and  $t_1$ :

$$\frac{dSNR}{dAbs} = \ln 10 (QI_0 t_0 t_1)^{\frac{1}{2}} \frac{d}{dAbs} Abs (t_1 + t_0 10^{Abs})^{-1/2}$$

Setting this differential to zero to obtain maxima and minima the following equation is obtained:

$$\frac{t_1}{t_0} = 10^{Abs} \left( \frac{\ln 10}{2} Abs - 1 \right)$$

Equations of this form are unsolvable for the absorbance using analytical methods but it is obvious that  $t_0, t_1 > 0$  and that there are no solutions where the absorbance is less than  $\ln 10 / 2 = 0.87$  or  $t_0, t_1 = 0$ .

In many practical situations the intensity of the light source  $I_0$  and its variance  $\sigma^2(I_0)$  may be known prior to the experiment. The experimenter may therefore not need to measure and determine these parameters in advance. In this case, the variance of the absorbance is:

$$\sigma^2(Abs) = \left( \frac{1}{\ln 10} \right)^2 \frac{1}{QI_1 t_1}$$

Using  $I_1 = I_0 10^{-Abs}$  the variance can be formed as:

$$\sigma^2(Abs) = \left( \frac{1}{\ln 10} \right)^2 \frac{10^{Abs}}{Qt_1 I_0}$$

The maximum obtainable SNR for absorbance measurements is therefore:

$$\begin{aligned} \frac{Signal}{Noise} &= \frac{\langle Abs \rangle}{\sigma(Abs)} = Abs / \frac{1}{\ln 10} \left( \frac{10^{Abs}}{Qt_1 I_0} \right)^{1/2} \\ &= \ln 10 Abs \left( \frac{Qt_1 I_0}{10^{Abs}} \right)^{1/2} \end{aligned} \quad \textbf{Equation 5}$$

This is the maximal possible obtainable SNR for this experiment arrangement. The graph of this function for a variety of values of  $t_0$  is plotted in Figure 14. For simplicity the constant  $\ln 10(QI_0)^{\frac{1}{2}}$  is set to unity.

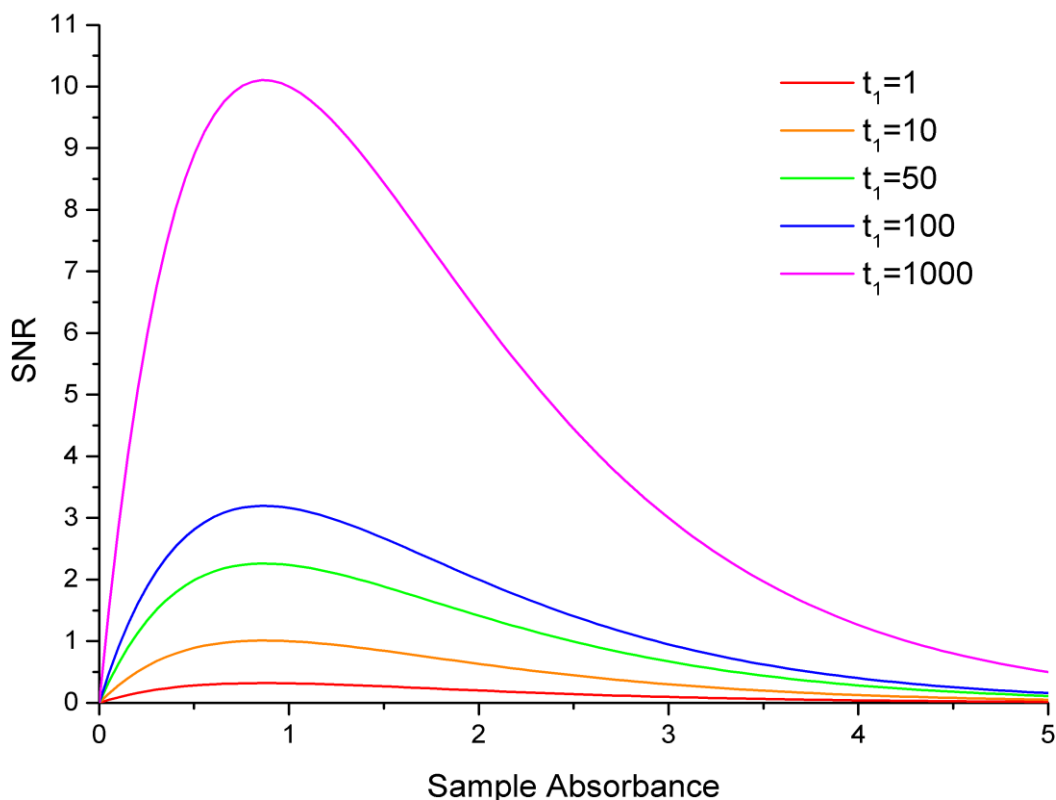


**Figure 14.** A graph of the function  $SNR = t_1^{\frac{1}{2}} Abs 10^{-Abs/2}$ .  $t_1$  takes a range of values from 1 to 1000. S/N and absorbance are both dimensionless quantities.

Again, the maxima are found by derivatisation of Equation 5 and setting to zero:

$$Abs = \frac{2}{\ln 10} = 0.87$$

This is the sample absorbance that gives the maximum SNR when the variance of the impinging light intensity is a small fraction of the intensity. It is therefore advantageous to prepare samples with an absorbance of 0.87 (or as close to this value as possible).

These methods can also be used to determine time varying absorbance. Firstly, the intensity of the beam  $I_0$  and its variation  $\sigma^2(I_0)$  due to Poisson noise

are determined by recording the signal current  $i_0$  over a time interval  $t_0$  without a sample in the beam. Secondly, with a sample in the beam, intensities  $I_1$  are recorded for consecutive time intervals of length  $t_1$ . Consecutive absorbance spectra can now be determined for each time interval. Each spectra will have a different SNR, given by Equation 5, because of the changing absorbance properties of the sample.

These crude but simple and effective methods of absorbance determination assume that the light source intensity  $I_0$  and its variance  $\sigma^2(I_0)$  does not change over time. If a pulsed light source such as a flashlamp or a laser induced plasma is used, the intensity varies between pulses and also varies over the lifetime of a pulse. In order to determine the absorbance of a sample, the total number of photons detected for all pulses must be used. The total number of photons impinging upon the sample and transmitted through the sample must be determined. This can be done by placing a beam sampler in the beam before it impinges upon the sample and counting the number of photons reflected from the beam sampler and transmitted through the sample. A schematic of this arrangement is shown in Figure 15. If the transmission/reflection of the beam sampler is known as a function of wavelength, the total integrated intensity  $I_0$  for all pulses can be determined.

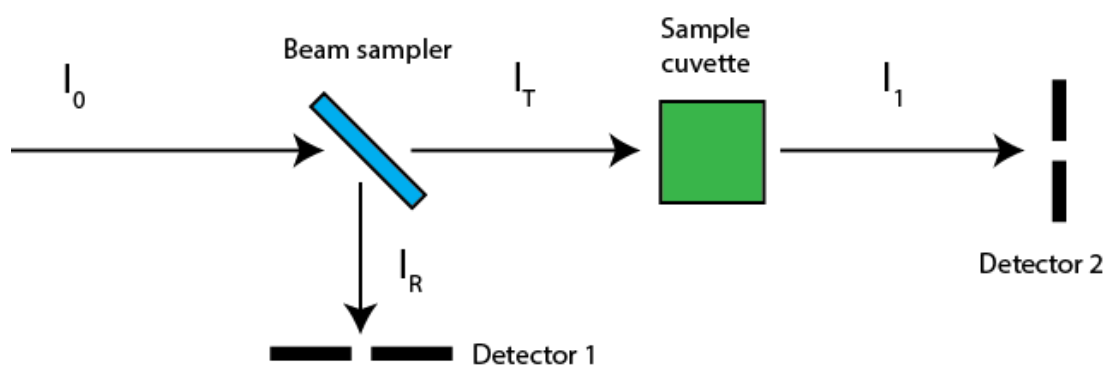


**Figure 15.** A schematic of the optical arrangement for the determination of sample absorbance with a varying light source intensity.

To determine the minimal possible SNR due to Poisson noise of such an arrangement, the previous equations must be modified. The probability distribution of detected photons for one detector becomes:

$$P(N) = \frac{e^{-p} p^N}{N!}$$

$p$  is now the mean number of photons detected for all pulses.  $N$  is the actual number of photons detected for all pulses. This probability distribution is still Poissonian and so the variance is equal to the mean  $p$ :

$$\langle N \rangle = \sigma^2 N = p = QI$$

$I$  is the intensity integrated over all pulses. The standard deviation is:

$$\sigma(N) = \langle N \rangle^{1/2} = p^{1/2} = (QI)^{1/2}$$

For a single detector the SNR is therefore:

$$\frac{\text{Signal}}{\text{Noise}} = \frac{\langle N \rangle}{\sigma(N)} = \frac{p}{p^{1/2}} = p^{1/2} = (QI)^{1/2}$$

To determine the SNR for absorbance measurements obtained using the optical arrangement shown in Figure 15, the mean and variance in the integrated intensity  $I_T$  must be constructed from the mean and variance in the integrated intensity  $I_R$ . This can be done if the transmittance of the beam splitter as a function of wavelength is known. It is assumed that the beam sampler has an absorbance of zero at all wavelengths:

$$\text{Transmittance of beamsplitter } T_\lambda = \frac{I_T}{I_0}$$

$$I_T = \frac{T_\lambda}{1 - T_\lambda} I_R$$

$$\langle N_T \rangle = \frac{T_\lambda}{1 - T_\lambda} \langle N_R \rangle$$

It is assumed that Detectors 1 and 2 have the same quantum efficiency  $Q$ . The mean number of photons detected in the beam  $I_R$  by Detector 1 is:

$$\langle N_R \rangle = \sigma^2 N_R = p_R = QI_R$$

The variance in the number of photons in the beam  $I_T$  can now be found using the propagation of errors formula:

$$\begin{aligned}\sigma^2(N_T) &= \left(\frac{\partial N_T}{\partial N_R}\right)^2 \sigma^2(N_R) = \left(\frac{T_\lambda}{1-T_\lambda}\right)^2 \sigma^2 N_R = \left(\frac{T_\lambda}{1-T_\lambda}\right)^2 Q I_R \\ &= \left(\frac{T_\lambda}{1-T_\lambda}\right)^2 Q(1-T)I_0 = \left(\frac{T^2}{1-T}\right) Q I_0\end{aligned}$$

The mean number of photons detected in the beam  $I_1$  is:

$$\langle N_1 \rangle = \sigma^2 N_1 = p_1 = Q I_1$$

The absorbance over a large number of detected photons is simply:

$$\text{Absorbance} = \frac{1}{\ln 10} \ln\left(\frac{I_T}{I_1}\right) = \frac{1}{\ln 10} \ln\left(\frac{N_T}{N_1}\right)$$

Again, applying the propagation of errors formula to obtain the variance in the absorbance:

$$\begin{aligned}\sigma^2(\text{Abs}) &= \left(\frac{\partial \text{Abs}}{\partial N_T}\right)^2 \sigma^2(N_T) + \left(\frac{\partial \text{Abs}}{\partial N_1}\right)^2 \sigma^2(N_1) \\ &= \left(\frac{1}{\ln 10}\right)^2 \left( \left(\frac{\partial}{\partial N_T} \ln\left(\frac{N_T}{N_1}\right)\right)^2 \sigma^2(N_T) + \left(\frac{\partial}{\partial N_1} \ln\left(\frac{N_T}{N_1}\right)\right)^2 \sigma^2(N_1) \right) \\ &= \left(\frac{1}{\ln 10}\right)^2 \left( \left(\frac{1}{N_T}\right)^2 \left(\frac{T^2}{1-T}\right) N_T + \left(\frac{-1}{N_1}\right)^2 N_1 \right) \\ &= \left(\frac{1}{\ln 10}\right)^2 \left( \left(\frac{T^2}{1-T}\right) \frac{1}{N_0} + \frac{1}{N_1} \right) = \left(\frac{1}{\ln 10}\right)^2 \left( \left(\frac{T^2}{1-T}\right) \frac{1}{Q I_0} + \frac{1}{Q I_1} \right) \\ &= \left(\frac{1}{\ln 10}\right)^2 \frac{1}{Q} \left( \left(\frac{T^2}{1-T}\right) \frac{1}{I_0} + \frac{1}{I_1} \right)\end{aligned}$$

Using  $I_1 = I_T 10^{-Abs}$  the variance of the absorbance becomes:

$$\sigma^2(Abs) = \left(\frac{1}{\ln 10}\right)^2 \frac{1}{Q} \left( \left(\frac{T^2}{1-T}\right) \frac{1}{I_0} + \frac{10^{Abs}}{I_T} \right)$$

$I_T$  is substituted using  $T = \frac{I_T}{I_0}$  or  $I_T = T I_0$ :

$$\sigma^2(Abs) = \left(\frac{1}{\ln 10}\right)^2 \frac{1}{Q} \left( \left(\frac{T^2}{1-T}\right) \frac{1}{I_0} + \frac{10^{Abs}}{T I_0} \right) = \left(\frac{1}{\ln 10}\right)^2 \frac{1}{Q I_0} \left( \frac{T^2}{1-T} + \frac{10^{Abs}}{T} \right)$$

The SNR for this experimental arrangement can now be determined:

$$\begin{aligned} SNR &= Abs / \left( \left(\frac{1}{\ln 10}\right)^2 \frac{1}{Q I_0} \left( \frac{T^2}{1-T} + \frac{10^{Abs}}{T} \right) \right)^{\frac{1}{2}} = \ln 10 (Q I_0)^{\frac{1}{2}} Abs \left( \frac{T^2}{1-T} + \frac{10^{Abs}}{T} \right)^{-\frac{1}{2}} \\ &= \ln 10 (Q I_0)^{\frac{1}{2}} Abs \left( \frac{T(1-T)}{T^3 + (1-T)10^{Abs}} \right)^{\frac{1}{2}} \end{aligned} \quad \text{Equation 6}$$

The SNR depends strongly upon the transmission of the beam sampler as well as the sample absorbance. The SNR, as in the other experimental arrangements previously discussed, also depends upon the square root of the source intensity  $I_0$  and the quantum efficiency of the detector. A contour plot of the SNR against beam sampler transmission and sample absorbance is shown in Figure 16 with the quantity  $\ln 10 (Q I_0)^{\frac{1}{2}}$  set to unity. The figure shows that the greatest SNR can be achieved in this case with a sample absorbance of approximately 1 and a beam sampler transmission of approximately 0.75.

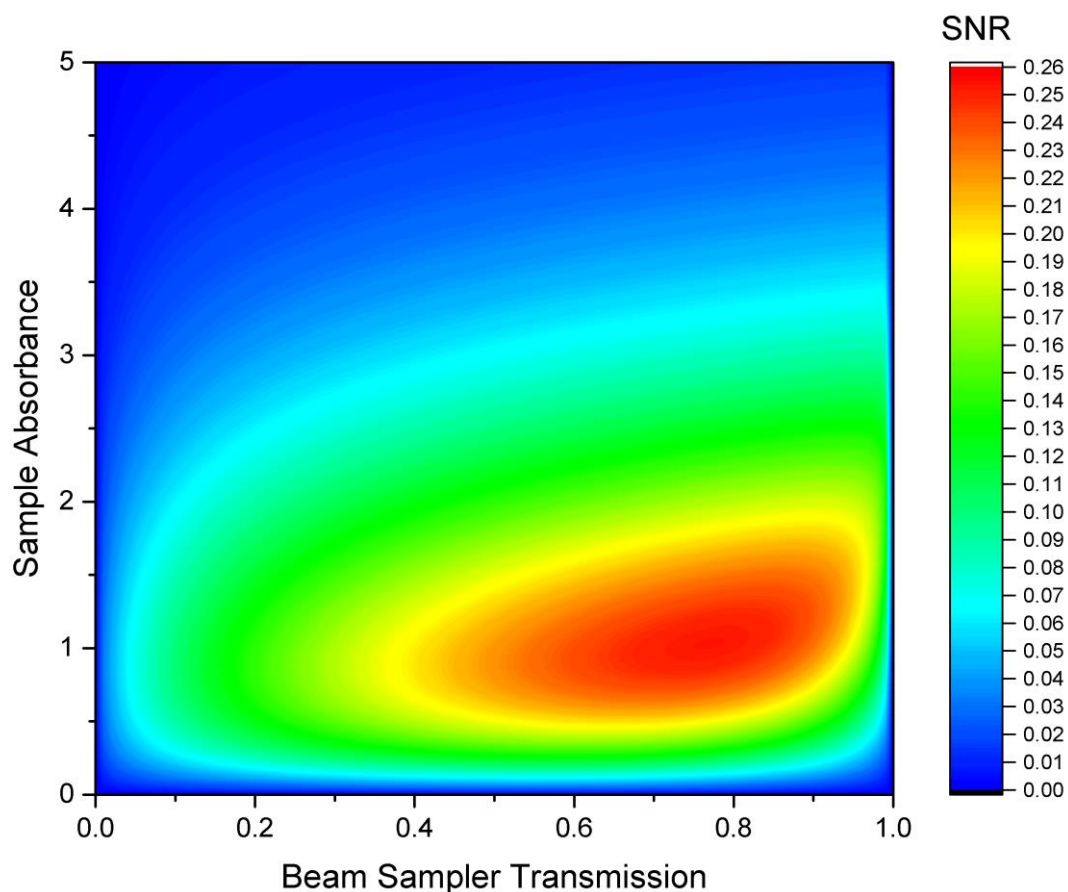


**Figure 16.** A contour plot of the SNR of measurements conducted using the experimental arrangement shown in Figure 15. The plot is derived from Equation 6 with the quantity

$$\ln_{10}(QI_0)^{\frac{1}{2}} \text{ set to unity.}$$

The analysis presented above has examined the nature of SNR ratios in absorbance spectroscopy using light sources that are both constant and varying and has demonstrated that:

- SNRs are proportional to the square root of light source intensity, thereby justifying the need for high intensity light sources in absorbance spectroscopy. Increasing the light source intensity is therefore of particular interest for the spectroscopy of low absorbance samples i.e. in GAG:Protein VCD spectroscopy where the absorbance signals (and consequently SNRs) are very small.
- SNRs are proportional to the square root of detector quantum efficiency. The quantum efficiency of a detector is defined as the ratio of the squared



SNR of the input signal to the square SNR of the output. It is a measure of the efficiency of a detector in converting incident light into a spectral signal. A perfect detector has an efficiency of 1.

- If a beam sampler is used to determine the intensity of light impinging upon a sample, the maximum SNR is obtainable when the beam sampler has a transmission of approximately 0.75. This value ensures that optimal amount of light is impinging upon the sample so that its intensity (and consequently the sample absorbance) can be determined with a minimal amount of variance due to Poisson noise.

## 1.5 Plasma as a High Intensity Light Source

Although VCD presents a unique way of examining structural and conformation changes occurring in a protein upon binding to a GAG, the weakness of the VCD signal means that these experiments needed to be run for a several hours to obtain measurements that had good SNRs. To overcome this, several methods were identified that could improve SNRs and therefore improve the scanning time and sensitivity of modern spectrometers. These were:

- To increase the concentration of the sample. This increases the absorbance/scattering of the sample according to the Beer-Lambert Law ( $A = \epsilon cl$ ). This may not be possible in many situations, in particular when only small amounts of sample are available due to the expense/practicalities of obtaining biologically interesting (and high purity) GAGs and proteins.
- Increase the path length of the light through the sample (as  $A = \epsilon cl$ ). Again, this may not be possible as increased quantities of sample are required to achieve longer path lengths.
- Increase the quantum efficiency of the detector. Modern detectors are usually semiconductor based, employing charged coupled devices and avalanche photodiode arrays. Very high sensitivity can be obtained (single photon counting is possible with short wavelength radiation) using

photomultiplier devices. It was not within the resources of this project in time, money or expertise, to attempt to improve on modern detectors.

- Increase the intensity of the light source. In absorption spectroscopy, SNRs increase as the square root of the light intensity (see Section 1.1). For samples that are of very low concentration and/or possess very low cross sections of interaction, increasing the intensity of the light source offers the best opportunity for increasing SNRs.

The most viable way to improve SNRs in absorbance spectroscopy, specifically in GAG:Protein VCD, and consequently improve measurement times and sensitivity was to try to increase the intensity of the light source. Modern VCD spectrometers are essentially FTIR instruments adapted for VCD by the inclusion of a photoelastic modulator (PEM) to circularly polarise the IR light coming from the source. In most FTIR or VCD instruments the IR light is provided by a heated element or glowbar. Glowbars are silicon carbide rods, electrically heated up to temperatures of around 1500 K and emit IR light in a wavelength range of approximately 1 to 25  $\mu\text{m}$ .

Light generation in the UV/visible range is commonly achieved in benchtop laboratory spectrometers use a combination of a UV producing source such as a deuterium or xenon bulb and a visible/NIR (near infrared) source, which is usually a tungsten halogen bulb. A number of different light sources are commercially available that can be used to generate broadband light across the UV, visible and IR spectral range. Broadband light sources commonly used in absorption spectrometry are listed in Table 4. If higher intensity short wavelength light is required then the current alternatives are to use synchrotron light sources (Yarwood et al., 1984) that can generate very high intensity light down to 180nm, and other similarly expensive (and therefore not widely available) technologies. Spectroscopy on certain samples may be impossible without the high intensity light provided by a synchrotron. There is therefore a need to produce an inexpensive, high intensity, compact UV/Vis/IR light source for certain applications where the absorbance of the sample may be minimal, leading to very long scanning times.

Lamp Type	Wavelength Range	Colour Temperature	Approximate cost of Light source	Notes
Xenon arc lamps	200 to 2500 nm	Up to 6000K	£5200 £300 – 1000 per lamp	<ul style="list-style-type: none"> <li>• Very high irradiance</li> <li>• Produces small high irradiance arc</li> <li>• Intense UV spectrum</li> <li>• Can simulate solar light</li> </ul>
Mercury vapour lamps	200 to 2500 nm	Up to 6800K	£5200 £30 – 100 per lamp	<ul style="list-style-type: none"> <li>• Long lamp lifetimes</li> <li>• Good output in UV</li> <li>• 10 min warmup time.</li> <li>• Inexpensive</li> <li>• Often used as calibration lamps</li> </ul>
Deuterium lamps	180 to 800nm		£3000 £400 per lamp	<ul style="list-style-type: none"> <li>• Intense continuous UV spectrum</li> <li>• Not a blackbody spectral emitter</li> <li>• Preferred source for UV spectroscopy</li> <li>• High stability</li> <li>• Negligible UV/Vis output</li> </ul>
Xenon flash lamp	160 to 2000nm	Up to 15000K	£4000 £300 per lamp	<ul style="list-style-type: none"> <li>• Pulsed light source up to 100Hz</li> <li>• Very high intensity</li> <li>• Intense UV output</li> <li>• Pulse length ~ 100ms</li> <li>• May require water cooling at higher repetition rates</li> <li>• Short lifetimes due to electrode decay.</li> </ul>
Tungsten Halogen lamps	250 to 2500nm	2800 to 3400 K	£3800 £20 - 100 per lamp	<ul style="list-style-type: none"> <li>• High efficiency and relatively inexpensive</li> <li>• Almost no line emission</li> <li>• Excellent stability</li> <li>• High total visible output</li> <li>• Very little UV spectrum</li> </ul>
IR ceramic sources (glowbars)	1- 25 $\mu$ m	Approximately 1500 K	£200 per lamp	<ul style="list-style-type: none"> <li>• High emissivity.</li> <li>• Good for IR spectroscopy</li> <li>• Relatively low temperature</li> <li>• Relatively inexpensive</li> <li>• Long lifetime</li> </ul>

**Table 4.** Commonly used light sources for spectroscopy. The approximate cost includes both the cost of a standalone light source for research use and the cost of a replacement lamp.

Approximate prices are from Newport Corporation.

All of the above light sources produce both line emission and continuum emission. By heating a lamp up to thousands of degrees, electrons transit to higher energy states. These may be discrete bound states or, if the temperature is high enough, unbound (or free) states that are no longer bound in molecular or atomic orbitals. If an electron transits to an unbound state, a plasma is generated. These unbound states form a continuum of energies above the discrete bound states. Over time, electrons relax back to equilibrium and move to lower energy states, releasing a photon in the process. When an electron transits from an upper bound to a lower bound discrete energy state, line emission is produced and when the unbound electrons lose energy and move to a lower energy bound or unbound state, continuum emission is produced. Continuous emission is broadband because of the continuous nature of the free electron energy states. In Figure 17, the spectrum of light emitted from the HPX-2000 Xenon Light Source from Ocean Optics Ltd, line emission spectrum can be seen as humps or spikes above the continuum emission. The continuum emission has a maximum intensity just below 600 nm.

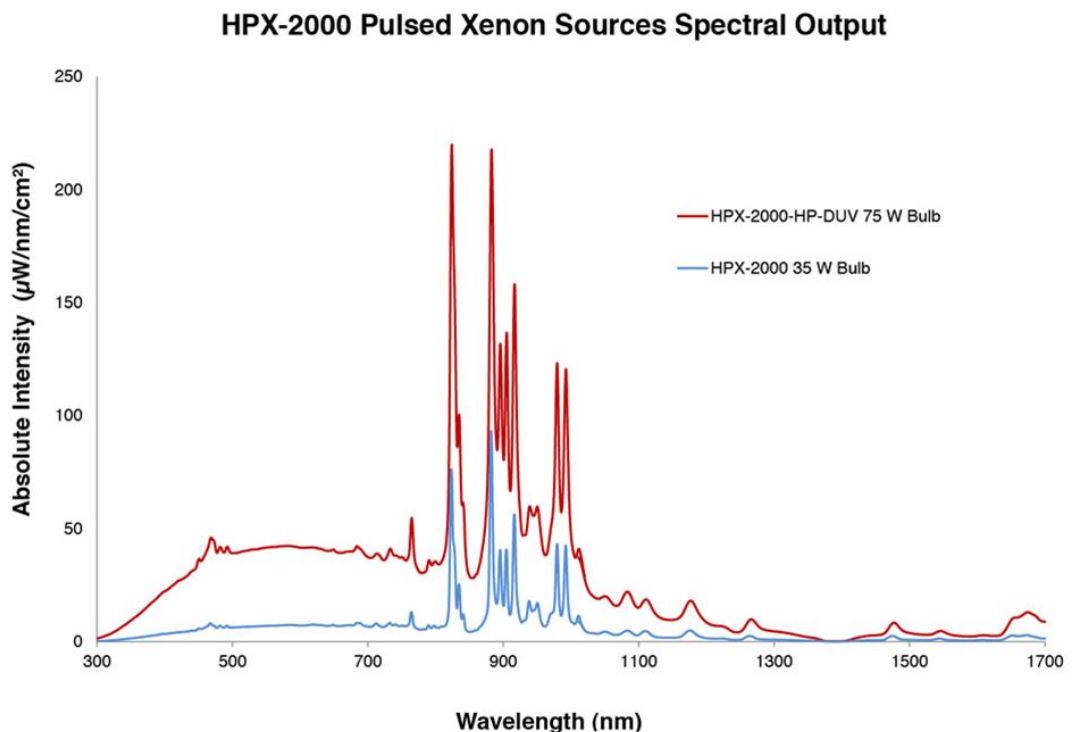


**Figure 17.** The intensity of the HPX-2000 Xenon Light Source as a function of wavelength. This light source retails for around £7000 and has an emission output of 35 W (or 75 W for the more powerful version) in the wavelength range 185 nm to 2200 nm. Source: [www.oceanoptics.com](http://www.oceanoptics.com).

The intensity and wavelength of both line and continuum emission depend upon the identity and temperature of the heated substance. At low temperatures during the warming phase of lamp, the electrons only occupy discrete bound states and only line emission will initially be radiated. As the lamp heats up, a plasma is formed and further heating increases the amount of continuum relative to the line radiation. Continuum radiation reaches a maximum at the operating temperature of the lamp.

All of the lamps listed in Table 4, apart from the deuterium lamp, radiate the vast majority of their light through thermal radiation. The deuterium lamp has the narrowest thermal continuum, radiating from 180 to 370 nm, but does not produce most of its UV radiation through thermal radiation processes. The strong UV emission of a deuterium lamp is produced by the relaxation of the excited vibrational and rotational states of molecular deuterium. Although the vibrational and rotational energy levels of molecular deuterium are discrete, their multitude and overlap creates an effective continuous distribution of photon energies. This enables the deuterium lamp to run at a much lower operating temperature than other bulbs e.g. the xenon lamp, which generate UV by thermal processes.

Thermal radiation, generated by the thermal motion of electrons in the heated element, is approximately blackbody in nature. A blackbody is a perfect emitter and absorber of radiation (it has an emissivity of unity) and the spectrum of light emitted from a blackbody is given by Planks law:

$$B_{\lambda}(\lambda, T) = \frac{2hc^2}{\lambda^5} \frac{1}{e^{\frac{hc}{\lambda k_B T}} - 1} \quad \text{Equation 7}$$

where  $h$  is the Planck constant,  $K_B$  is the Boltzmann constant and  $c$  is the speed of light in a vacuum. The units are  $W.Sr^{-1}m^{-3}$ . This equation describes the spectral radiance of a blackbody  $B_{\lambda}(\lambda, T)$  or the power emitted per unit solid angle as a function of wavelength. The colour temperature of a lamp is the temperature of a blackbody radiating with the same spectral radiance as the

lamp. The spectral radiance  $B_\lambda(\lambda, T)$  of light emitted from blackbodies of three different temperatures is plotted against wavelength in Figure 18. The logarithmic graph of spectral radiance against wavelength is shown in Figure 19.

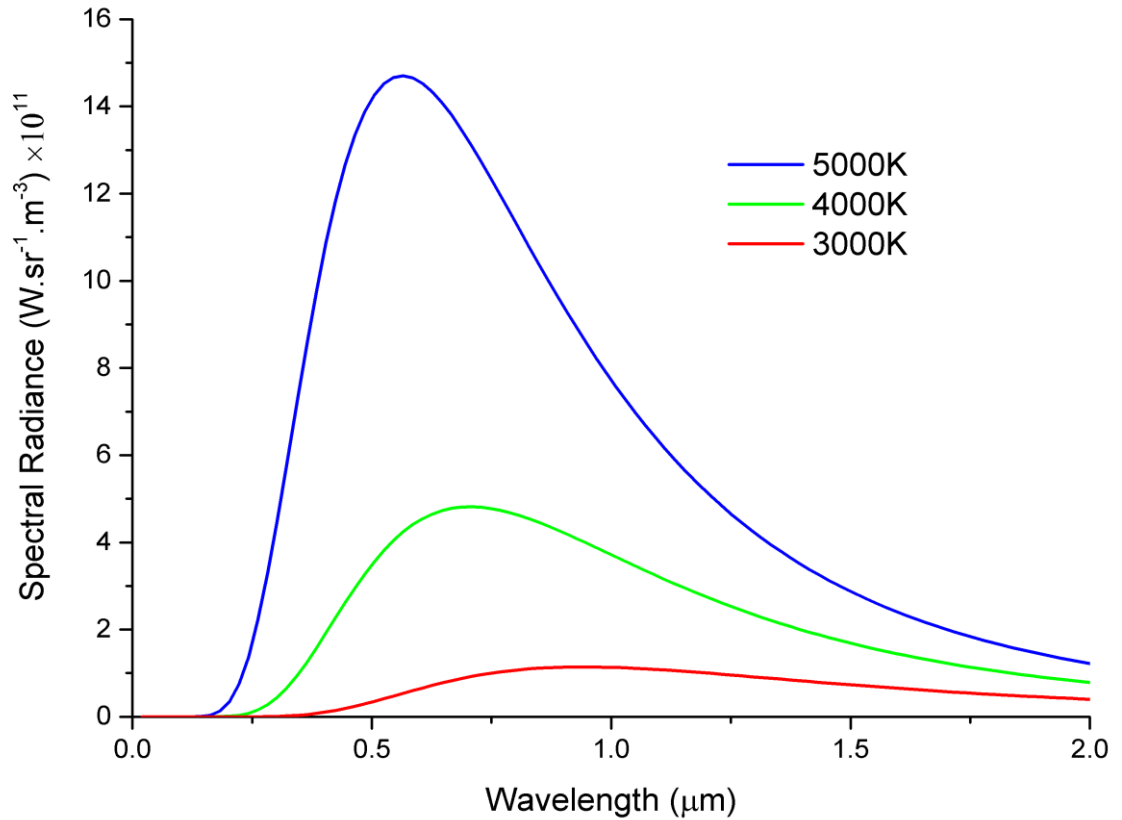


**Figure 18.** Blackbody spectral radiance emission curves plotted against wavelength for three different temperatures.

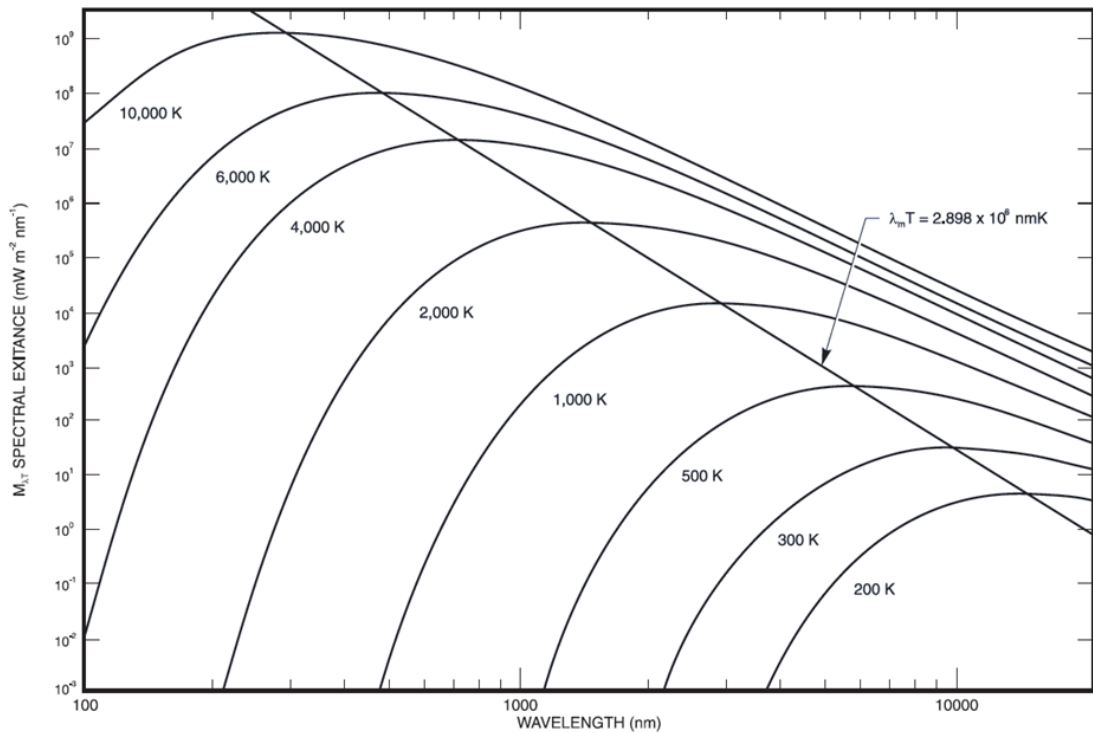


**Figure 19.** A logarithmic graph showing the radiance of a blackbody over a wide range of wavelengths. The straight line shows the Wein's Law relationship for the most intense wavelength emitted (Oriel, 2012).

Planck's law represents the upper limit of the amount of radiation that a substance may emit at a given temperature. The ratio of the actual emitted radiation  $R_\lambda$  to that emitted by a blackbody  $B_\lambda$  at any given wavelength is known as the emissivity  $\epsilon_\lambda$ :

$$\epsilon_\lambda = R_\lambda / B_\lambda$$

Plasmas are approximately blackbodies, meaning that their emissivity is almost unity. This makes them extremely good light sources as any absorbed energy is almost entirely reemitted as electromagnetic (EM) radiation. The radiation emitted from a blackbody obeys two well-known laws. The first is Wein's displacement law:

$$\lambda_{max} = \frac{b}{T}$$

T is the absolute temperature in Kelvin and b is the constant of proportionality equal to  $2.9 \times 10^{-3}$  mK. This law describes how the radiance of a blackbody peaks at a wavelength that is inversely proportional to the temperature. The second law is the Stefan-Boltzmann Law:

$$j = \sigma T^4$$

This law describes that the emissive power  $j$  or the power radiated per unit surface area across all wavelengths, increases as the fourth power of the absolute temperature  $T$  of the surface. In Figures 18 and 19,  $j$  is the area under a blackbody emission curve with temperature  $T$ . It can also be seen from Figures 18 and 19 that an increase in intensity occurs across all wavelengths as a result of increased temperature.

High temperature sources are necessarily plasma sources, because all substances form ionised plasmas at high temperatures. The subsequent increase in intensity from replacing the glowbar with a plasma light source can be found by evaluating, or integrating Equation 7. Fortunately, a website exists at [http://www.spectralcalc.com/blackbody\\_calculator/blackbody.php](http://www.spectralcalc.com/blackbody_calculator/blackbody.php) that evaluates these integrals to determine the radiance at a particular wavelength or within a wavelength range. The glowbar was assumed to be at a temperature of 1000 K and the plasma was assumed to be at a temperature of 10000K. Both emitters were assumed to have an emissivity of unity. The calculated radiances at the amide I absorption band at  $6\mu\text{m}$  are:

$T_{\text{glowbar}} = 1000\text{K}$	Radiance = 1.53 kW/m <sup>2</sup> /sr/ $\mu\text{m}$
$T_{\text{plasma}} = 10000\text{K}$	Radiance = 56.5 kW/m <sup>2</sup> /sr/ $\mu\text{m}$

This is an increase in radiance of 36.9 times, or a corresponding increase in SNRs of 6 times. In the UV/Visible range, plasma sources offer even greater increases in radiant intensity as temperature increases.



## 1.6 Laser Induced Plasmas and Plasma Fundamentals

Heating a substance to the high temperatures required for plasma formation requires a great amount of energy and can be extremely inefficient due to constant heat loss through diffusion, conduction, convection and radiation processes. One of the best ways to minimise entropic energy losses and achieve high temperatures is to input energy over as short a time period as possible. In this way, cooling does not have time to occur and maximum temperatures can be achieved. This principle is key to achieving the highest possible temperatures per input energy. The application of a focused laser pulse is an effective way to very quickly raise the temperature of a substance high enough to induce plasma formation. The idea for the prototype light source was to harness the IR and also the UV/Visible light emitted from a laser induced plasma (LIP) and investigate the viability of such a light source for biological spectroscopy.

The discovery that pulsed lasers can breakdown air and other substances was reported soon after the invention of the q-switched laser in the early nineteen sixties (International Quantum Electronics, 1964, Damon and Tomlinson, 1963, Meyerand and Haught, 1963). A rapid and concentrated delivery of energy, via a short, very intense pulse of coherent photons, can heat electrons to the ionisation energies. Any molecular bonds present before heating are endothermically destroyed during the heating process. It is a relatively simple process to produce a plasma (even in air) by directing a pulsed laser (usually a Q-switched laser) with the requisite peak energy through a convex lens. A pulsed laser generates a much higher intensity at the pulse peak maximum a pulse than a continuous wave laser can generate. The electric field strength of a pulse at the focal point becomes very high due to the interference of coherent plane waves. When the electric field strength produced by the focused pulse exceeds the dielectric strength of the media, material that is normally electrically neutral and transparent becomes ionised, resulting in a plasma. This phenomenon has since been extensively studied in a variety of gases at different pressures and using lasers of different wavelengths and pulse durations (Ireland and Morgan, 1974, Daiber and Winans, 1968, Rosen and

Weyl, 1987). A commonly used pulse laser in these experiments was the Q-switched Nd:YAGv with a fundamental mode at 1064nm. The breakdown threshold at 1064nm for air at atmospheric pressure is approximately  $10^{12}$  Wcm<sup>-2</sup> (Lencioni, 1974). This intensity must be obtained at the focal point of the lens in order for plasma formation in air to occur.

Instruments that utilise the emission from a plasma as an IR spectroscopic light source have already been built and tested with some degree of success, most notably in a paper by Adamson and Cimolino (Adamson and Cimolino, 1984b). In this paper the authors generate laser induced plasmas in both air and argon and utilise the IR emission to successfully measure the absorbance of tungsten hexacarboxyl in the carbonyl stretching region ( $\sim 2000$  cm<sup>-1</sup>). Intensity measurements over a 2 ms sample time are compared to a glowbar source (data shown were only for air plasma). Peak intensity from the plasma was found to be 25 times higher than the glowbar source in this timeframe showing that a LIP is indeed a promising high intensity light source in the IR region. Adamson and Cimolino are referenced by Musselman (Musselman, 1987) in which an optical setup for the capture of the IR emission from a LIP is described.

Focused laser pulses have been used to generate radiation at much shorter wavelengths. In Borghese *et al* (Borghese and Di Palma, 2007), a 250 mJ Q-switched Nd:YAG laser was focused onto a pulsed 250  $\mu$ s jet of Xenon gas emitted from a high pressure nozzle . The authors were able to generate and characterise the VUV spectral output of the generated plasma between 110-210 nm. Photons with even shorter wavelengths may have been emitted, but the MgF<sub>2</sub> coated aluminium grating that was used to disperse the spectral output was vanishingly reflective below 110 nm. Such short wavelengths were obtainable due to high electron temperatures generated within the plasma.

The generation of high temperatures using focused laser pulses is used in several important areas of ongoing scientific research. The most powerful pulsed lasers in the world are used to generate the millions of degrees Kelvin needed for a sustained inertial containment fusion reaction to occur. Using this

technology, the required temperatures have been reached, but as of 2015, the problem of how to harness the released energy in a manner commensurate with power generation has not yet been overcome (Craxton et al., 2015).

LIP technologies are of particular interest to the computer hardware industry where research is underway to develop an extreme UV (EUV) light source, capable of emitting as low as 13.5nm, for the nanometre scale lithography of CPUs (Fomenkov et al., 2004, Bakshi, 2006, Hassanein et al., Igor V. Fomenkov et al., 2007). The sources are based on high pulse rate, high energy lasers focused onto a stream or jet of tin particles or xenon gas. The plasma must be formed in a vacuum as VUV/EUV radiation is highly absorbent by most matter due to a multitude of atomic resonances in the VUV/EUV region. In particular, air is strongly absorbent below 200 nm due to absorption by molecular oxygen and absorbent below 150 nm due to molecular nitrogen. If the light source is to be used for the generation of wavelengths shorter than 150 nm, as with the device constructed by Borghese and colleagues (Borghese and Di Palma, 2007), the plasma must be generated in a vacuum to prevent reabsorption of the emitted radiation (hence the term vacuum UV). This is why supersonic nozzles are employed to inject a pulse of gas at high pressure into a vacuum chamber. The gas must be injected into the chamber and ionised by the laser before it can expand beyond the point at which attenuating reabsorption can occur. The vacuum must be restored after each pulse of gas.

The commercial viability of EUV light sources using laser induced plasmas is still in doubt, even though substantial amounts of time and money have been invested. The main obstacle is the manufacture of suitable optics. The absorbance of materials at short wavelengths (<150 nm) prevents the use of refractive optics, so reflectors must be used to collect and collimate the emitted light. Mirrors become increasingly difficult to manufacture at short wavelengths because in order to obtain a high degree of reflectivity, the surface of the mirror must be smooth to within the wavelength of the incident light. This poses a serious engineering challenge. Currently, silicon and molybdenum based multi-layered mirrors can be cut to an average roughness of 0.2 nm RMS

(Lowisch et al., 2010) and offer up to 70% reflectivity at 13.5nm (Muharrem et al., 2012). This is further complicated by the fact that the mirrors are directly exposed to the plasma and are therefore subject to damage from the impact of high energy ions, debris and stresses due to expansive shock (Harilal et al., 2005a, Hassanein et al., 2004, Hansson et al., 2002, Srivastava et al., 2007). EUV plasmas can be generated by laser heating of particulate matter, (Harilal et al., 2005a, Harilal et al., 2005b, Srivastava et al., 2007), usually tin vapour, as much more of the energy of the laser pulse is deposited in the plasma. One of the main problems with these sources is the removal of the vapour and debris from the vacuum chamber. The high energy heavy ions formed in these sources can be very damaging to expensive optics and other components. Damage can be mitigated by guiding the vapour plume away from sensitive components with strong external magnetic fields generated by superconducting magnets.

The spectral emission from LIPs is commonly utilised in the area of Laser Induced Breakdown Spectroscopy (LIBS) where it is used to identify the elemental composition of solids, liquids, gases and aerosols. There exists considerable literature concerning the optimisation of LIPs for LIBS. A summary of some of the most useful equations and definitions used in LIBS can be found in Hahn and Omenetto (Hahn and Omenetto, 2010). In LIBS, a focused laser beam is directed at the surface of a solid or liquid, or onto a streaming gas or aerosol. For the purpose of elemental analysis, high sensitivity requires reducing the intensity of continuum emission and increasing the intensity of line emission (Hanafi et al., 2000, Friedland, 1975). This is achieved by using the minimal laser power required to heat the sample so that its atomic spectral lines are visible and continuum emission is at a minimum. Continuum emission dominates the spectra during the early lifetime of the plasma <100ns, with line emission becoming prevalent as the plasma expands and cools. The life time of the plasma, the time it takes to cool to ambient temperature, is in the order of microseconds and depends upon several factors including the nature of the material being ionised (in LIBS), the composition and pressure of the ambient gas, laser wavelength, laser peak energy and peak lifetime (Hanafi et al., 2000).

To design, build and optimise a spectrometer that uses a laser induced plasma as its light source, it is necessary to understand some of the physical processes that underlie the emission of light from plasma. In particular, it is useful to understand these processes in terms of energy states and their transitions. Presented here is a summary of the physics of energy states and the state transitions that occur in laser induced plasmas. An understanding of these processes has been useful during the design, build and testing of the spectrometer and has helped improve both the suitability of plasma as a light source and instrument's reliability.

### **1.6.1 Physical Processes in Laser Induced Plasmas**

Owing to the destruction of the molecular bonds (atomisation) that occurs during the laser heating process, vibrational and rotational energy states and their transitions do not occur in plasmas. A description of the radiative processes that occur in plasmas can therefore be described solely in terms of electronic energy states and their associated radiative transitions. In the presence of external electric and magnetic fields, the energy levels of atomic electrons are split and shifted. This is known as the Stark Effect for electric fields and the Zeeman Effect for magnetic fields. The magnitude of this splitting/shifting depends on the magnitude and direction of the external fields. In laser induced plasmas, the source of external electric and magnetic fields comes initially from the laser light and then from the free electrons and positive ions that are generated. The magnitude and direction of an EM field at any point in space is the vector sum total of the contributions from each source of charge. The total field "felt" by any one bound electron within a plasma can therefore vary significantly. Thus the allowed atomic energy levels of any one atom in a plasma (and therefore the transition energies) can be significantly different from another. Over the many atoms emitting within the plasma, this leads to a broadening and overlapping of the line emission, often forming a continuum of broad peaks rather than narrow lines. Determination of the electron density and electron temperature in plasma is most often achieved by measuring the Stark broadening of line emission peaks (Griem, 1964). In LIP

spectra, these peaks are visible over the top of the much wider blackbody radiation curve generated by the bremsstrahlung radiation of free electrons (see Figure 20).

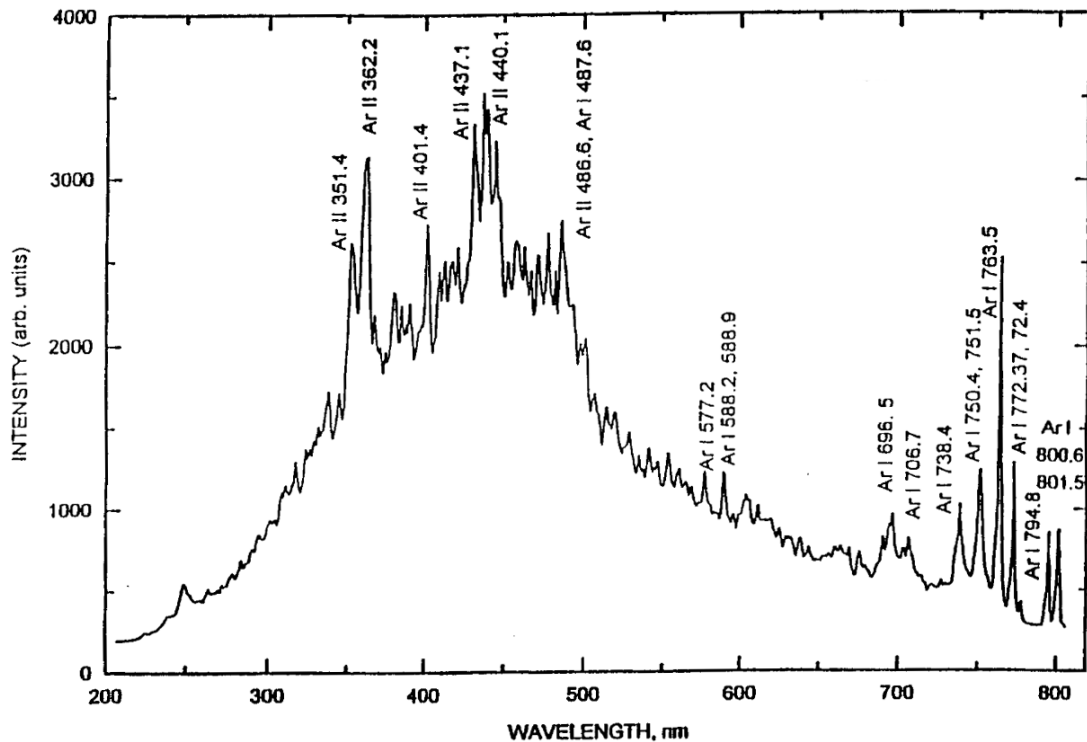


**Figure 20.** LIB spectral emission of Argon showing line emission peaks from bound transitions and background continuum emission from free transitions. The continuum emission approximates a blackbody radiator or Planck distribution. The plasma is created using a ruby laser with a pulse energy of 1.5 J at 694.3 nm, with a pulse width of 40 ns. The argon pressure is 0.78 atm. Reproduced from Hanafi, M., *Study of Laser-Induced Breakdown Spectroscopy of Gases*, 1999 (Hanafi et al., 2000)

The important energy exchange processes occurring during the formation, existence and decay of the plasma are inelastic collision processes. These are the processes of excitation, ionisation, bremsstrahlung and recombination, which are described in turn:

**Excitation:** An atom absorbs energy by collision with either a free electron or a photon, exciting one of its orbital electrons into a higher energy orbital. These interactions are bound-bound transitions.

For free electron-atom collisions:



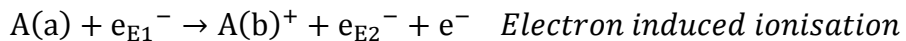
In electron induced excitation, the free electron loses some kinetic energy, exciting the atom from state a, to a higher energy state b. The reverse process, collisional de-excitation, is known as quenching. In this process the free electron gains kinetic energy rather than losing it.

For atom-photon collisions:



Absorbance of photons excites electrons in the atom to higher energy orbitals. The reverse process produces the line emission peaks seen in the emission spectrum of the plasma and are used to identify elemental composition of materials in LIBS. Line emission is generally in the UV/Vis region of the spectrum due to the energy spacing of the electronic states of atoms.

**Ionization:** If an orbital electron absorbs enough energy through collision with electrons/photons, it may possess more energy than the most energetic orbital in the atom. When this occurs, the electron makes the transition to a free state and is no longer bound within an orbital of the atom. These are bound-free transitions and result in the ionisation of the atom:

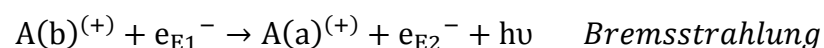


Under high intensity photon flux such as is found in LIPs, multiphoton excitation and ionisation occurs, in which an atom simultaneously absorbs multiple photons, exciting bound electrons to higher energy orbitals or into free states. Multiphoton absorption is the initial process through which seed electrons are

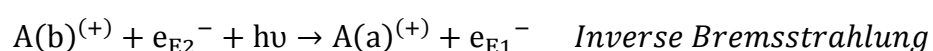
generated. It is multiphoton absorption that enables long wavelength lasers (~20 μm) to induce plasma formation in gases where single laser photons do not possess enough energy for photoionisation to occur.

The production of seed electrons leads to a cascade ionisation effect in which free electrons create one or more free electrons via electron induced ionisation. This cascading effect rapidly increases the electron density in the plasma. In a low pressure gas (<0.1 atm), the dominant mechanism of free electron production is photon induced ionisation, whereas at higher pressures the dominant mechanism is electron induced ionisation. This is because the shorter mean free path for electrons at high pressures increases the rate of collision ionisation (Gamal and Harith, 1983). Cascade ionisation is the main process through which free electrons are generated for lasers of moderate intensity and photon energy, such as the Nd:YAG laser at a wavelength of 1064 nm.

**Bremsstrahlung (braking radiation):** Bremsstrahlung radiation is the main source of the continuum of blackbody-like radiation from plasmas. Energetic free electrons that move close to ions or neutral atoms, are deflected/accelerated by the local electric field. Bremsstrahlung converts the electron kinetic energy into synchrotron radiation.



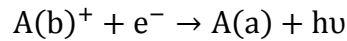
Inverse bremsstrahlung can also occur in which free electrons absorb laser energy in the vicinity of ions or neutral atoms. This is the mechanism by which free electrons can absorb laser energy increasing free electron temperatures. It is the inverse bremsstrahlung process that causes broadband absorbance and opacity of plasma.



The bremsstrahlung processes allow free electrons to occupy and move through a continuum of energy states:



**Recombination:** Recombination is the reverse process to ionisation. Recombination can occur either by the emission of a photon, called radiative recombination, or capture of a free electron as a result of its collision with an atom, called collisional recombination:



These are free-bound transitions and contribute significantly to the continuum spectra. The recombination of electrons to discrete bound states takes place from free electron states that have a continuous distribution of energy states. Recombination produces blackbody like emission spectra.

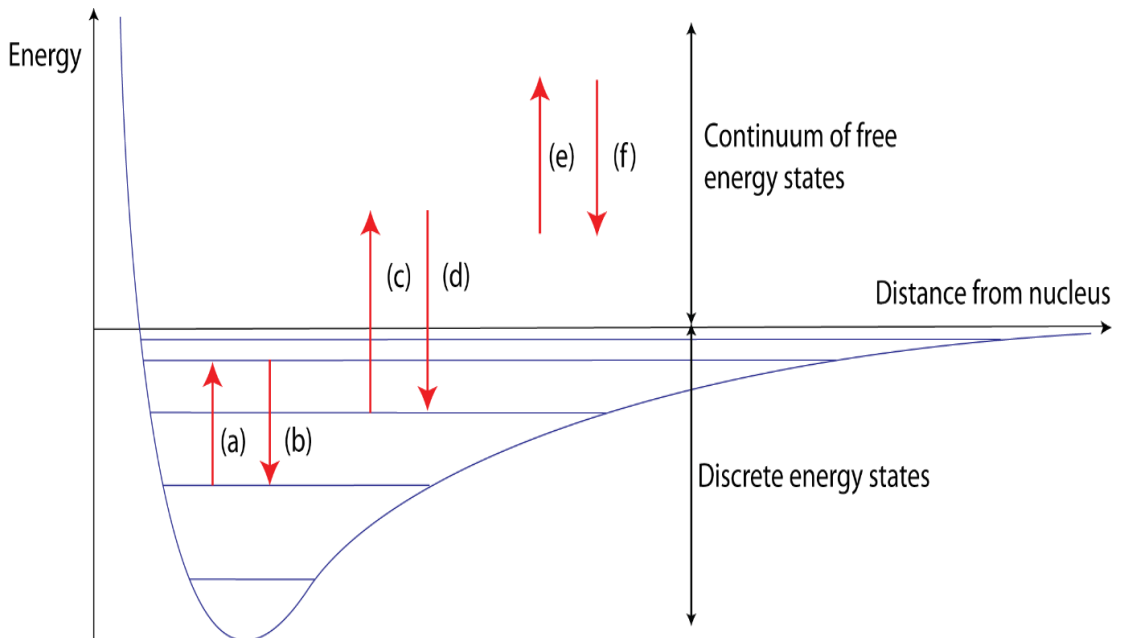


**Figure 21.** The electron transitions occurring in plasma. The blue lines denote the Coulomb potential energy as a function of distance from the nucleus and the associated allowed discrete energy states. Above zero potential energy, the electron states are continuous and are the ionisation states. The radiative transitions between states are (a) excitation: bound-bound absorbance (b) de-excitation: bound-bound spontaneous emission (line emission) (c) ionisation: bound-free absorbance (photoionisation, collisional ionisation) (d) free-bound emission (recombination radiation) (e) free-free absorbance (inverse brehmsstrahlung) (f) free-free emission (brehmsstrahlung).

Electron energy state transitions in plasma can be divided into the heating and cooling processes shown in Figure 21. The cooling processes are all emission processes, generating either line or continuum emission:

Electron heating (absorption processes):

Bound-bound transitions: Photo-absorption

Bound-free transitions: Multiphoton ionisation, Collisional ionisation

Free-free transitions: Inverse Bremsstrahlung

Electron cooling (emission processes):

Bound-bound transitions: Spontaneous emission – Line emission.

Free-free transitions: Bremsstrahlung radiation – Continuous emission

Free-bound transitions: Recombination radiation – Continuous emission

The spectral emission of a plasma is interpreted in terms of the spectral sum of each of the electron cooling processes. An understanding of these processes facilitate the optimisation of broadband emission from a plasma light source. Accurate determination of theoretical plasma spectra by summation the contributions from each of these processes is highly complex, requiring the quantum mechanical consideration of the populations of both bound and free electron energy states and the associated transition rates between states. The problem is further complicated by the fact that the parameters of a pulsed plasma are constantly changing in time and space. No attempt will be made here to construct a suitable model of the determination of theoretical spectra but the most important processes and their contributions to the overall spectrum are discussed separately in the following sections.

### **1.6.2 Plasma Heating Processes - Multiphoton Ionisation**

At very high light intensities, multiphoton absorption can occur between energy states. Multiple photons are simultaneously absorbed, ionising an electron from its bound orbital states. Two photon ionisation was predicted by Maria Göppert-Mayer in 1931 (Göppert-Mayer, 1931) but due to the lack of a sufficiently intense light source was not demonstrated experimentally until the

invention of the pulsed laser in the early 1960s. High intensity light sources are required for multiphoton ionisation to occur due to the very small cross sections of interaction of multiphoton absorption. These cross sections become vanishingly small for multiphoton ionisation events in which large numbers of photons are absorbed. Quantum mechanically, the probability of a multiphoton ionisation event occurring in unit time tends to zero as increasing numbers of photons are absorbed during the event. Although this probability vanishes for large numbers of photons, it never reaches zero and so with a high enough light intensity, an atom can be ionised through multiphoton ionisation regardless of the photon energies or number of photons absorbed.

The number of photons that are required for ionisation is a very good indicator of the ease with which an atom becomes ionised under intense light. The more photons that are required for ionisation, the higher the intensity of light that must be applied. The number of photons required for ionisation,  $N$ , is dependent upon the wavelength of the light source used,  $\lambda$ , and the first molar ionisation energies of the atoms  $I$ . The first molar ionisation energy is the energy required to ionise one mole of neutral atoms. Therefore:

*No. of photons absorbed during ionisation  $N$*

$$= \frac{\text{Ionisation energy of one atom}}{\text{Energy of each photon}} = \frac{I/A}{hc/\lambda} = \frac{I\lambda}{hcA}$$

$A$  is Avagadro's constant. Fractions of a photon are always rounded up. Table 5 lists some common elements, their molar ionisation energies and the number of photons required for multiphoton ionisation by an Nd:YAG laser at  $\lambda=1064$  nm.

Element	Atomic Number	First Molar Ionisation Energy (eV)	Number of Photons at 1064nm for Ionisation
H	1	13.59	12
He	2	24.59	22
C	6	11.26	10
N	7	14.53	13
O	8	13.62	12
Ne	10	21.56	19
Na	11	5.14	5
Ar	18	15.76	14
Ca	20	6.11	6
Cu	29	7.73	7
Kr	36	14	13
Xe	54	12.13	11

**Table 5.** Some common elements by atomic number and the number of photons each must absorb to undergo ionisation with an Nd:YAG laser at  $\lambda=1064$  nm.

The likelihood of an ionisation event is substantially increased if resonant absorption occurs between electron bound states at the laser wavelength. This process is known as resonance-enhanced multiphoton ionisation (REMPI) and is shown in Figure 22. Resonant absorption occurs if an allowed transition energy between bound states is an integer multiple of the photon energy. The energy difference of 21.43 eV between the ground state and the  $11p[3/2]_2$  excited state of Neon, allows for “near resonance”, with multiphoton absorbance of 12 photons simultaneously at the wavelength of a ruby laser (photon energy  $h\nu=1.785$  eV) (Figure 23) (Baravian et al., 1976).

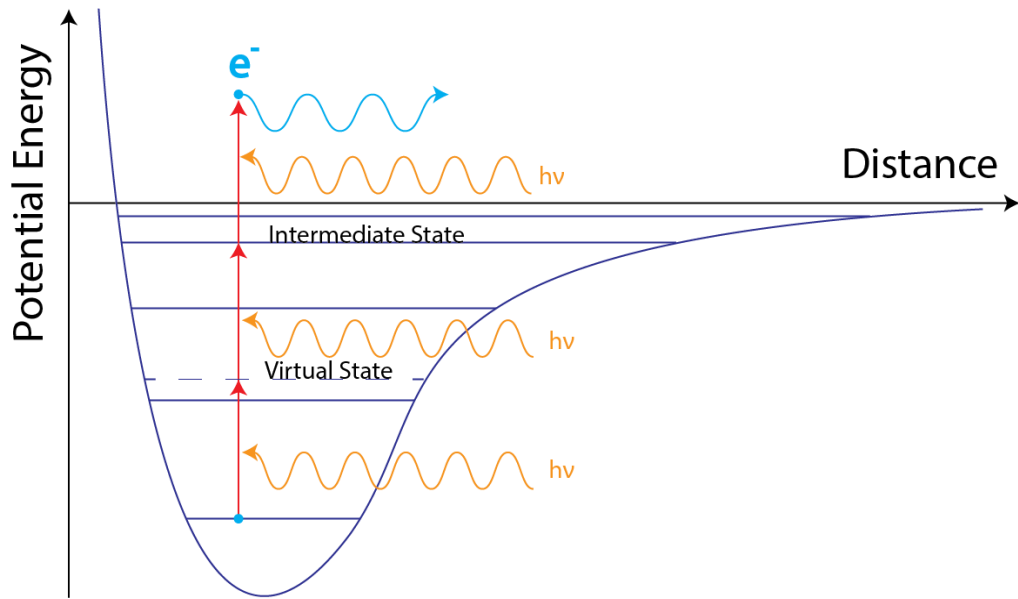


**Figure 22.** A three photon REMPI event. The electron passes through two other transient states prior to ionisation, a virtual state and an intermediate bound state. This REMPI event is actually two photon absorption to the intermediate state, followed by single photon absorption to the ionised state. The rate limiting step is the two photon absorption process, because single photon absorption is much more probable than two photon absorption for the same light intensity. Therefore, the light intensity required for this process is greatly reduced when compared to a single, three photon ionisation event.

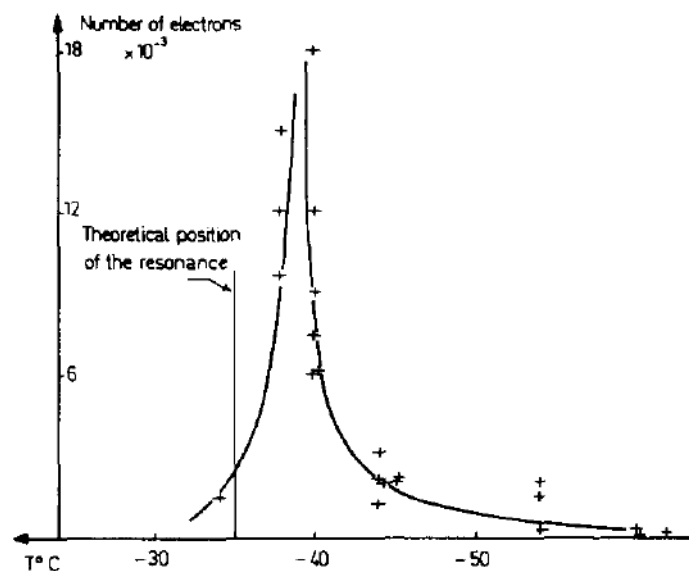


**Figure 23.** The multiphoton resonance effect of Neon with a ruby laser. The authors attribute the difference in the theoretical position to the experimentally determined position of resonance to errors in the laser temperature rather than to Stark effects. Reproduced from Baravian et al, Multiphoton ionisation of Neon: Experimental study of a resonance, 1969 (Baravian et al., 1976).

Resonant absorption between bound states followed by ionisation from the excited intermediate state is much more likely than a single multiphoton ionisation transition. For this reason, much lower intensity light is needed to induce a plasma in a medium that can undergo resonant absorption at the photon wavelength. The Stark effect (see below) can also split and shift energy levels in and out of resonance depending upon the power of the laser. However, owing to wavelength gaps in the availability of lasers, it may be very expensive or impossible to obtain a laser for use at the resonant absorption wavelength. These wavelength gaps exist because of a lack of lasing mediums that can undergo stimulated emission at the required wavelength.

### 1.6.3 Plasma Heating Processes - Collisional Ionisation

Following photoionisation, the free electron and positively charged ion are accelerated and gain kinetic energy from the electric field of the impinging EM wave (they are also accelerated by the magnetic component of the wave but, this is much smaller because, for an EM wave,  $|B| = |E|/c$ ). The Lorentz force acting upon the ion and electron in the electric field of the laser light are equal in magnitude but opposite in direction. Owing to the large difference in mass between the ion and the electron, the electron gains much more kinetic energy than the ion. This is easily seen from the consideration that, if both the ion and electron are acted on by the same force for the same time, they gain the same momentum. Kinetic energy is  $p^2/2m$ , so the kinetic energy gained by each particle in the electric field is inversely proportional to its mass. The kinetic energy of particles in an ideal gas is related to temperature via  $\frac{1}{2}m\overline{v^2} = \frac{3}{2}kT$ . This means that the acceleration due to the Lorentz force creates a large temperature difference between the ions and the electrons and is the reason why laser induced plasmas are initially non-thermal plasmas i.e. not in thermal equilibrium. This complicates the physics somewhat as the assumption of thermal equilibrium is often a prerequisite of many ideal physical systems.

If free electrons gain enough kinetic energy from the external electric field to reach a fraction of the ionisation energy of the atoms/ions in the plasma, bound

electrons can be ionised by the impact of free electrons. This is the second mechanism through which free electrons are generated and is termed collisional ionisation. Multiphoton ionisation is the main process through which the initial seed electrons are generated (seed electrons can also be generated via other means such as ionising radiation), but the vast majority of free electrons in a high pressure plasma (>100 torr) are generated via collisional ionisation. This is because the free electrons that are generated via collisional ionisation are also accelerated in the EM field and so can go on to generate more free electrons through further collisions. Collisional ionisation is thus a cascading effect, causing the avalanche breakdown of a medium in an intense EM field (Figure 24).

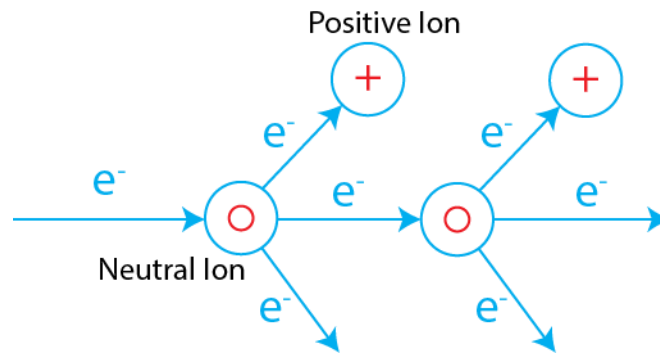


**Figure 24.** A schematic diagram of the collisional ionisation process. Each electron ionised during the process can go on to ionise other atoms or, if they possess enough energy, further ionise positive ions.

Following ionisation, the potential energy of a free electron is approximately zero. Energy (from the laser photons) that was not needed to raise the electron potential energy to zero can increase the kinetic energy of free electron through inverse bremsstrahlung.

#### 1.6.4 Cooling Processes - Bremsstrahlung

As well as accelerations arising from interactions with external EM fields i.e. the laser, free electrons also undergo accelerations (and decelerations) due to the internal Coulomb fields of charged particles i.e. the positive ions in the plasma. Owing to energy conservation, these processes result in the production of a photon in the case of deceleration and the absorption of a

photon (from an external source of EM radiation) in the case of acceleration. The radiation emitted during decelerations is bremsstrahlung radiation or free-free emission. The free-free absorption of radiation is inverse bremsstrahlung. Figure 25 shows a schematic representation of these processes.

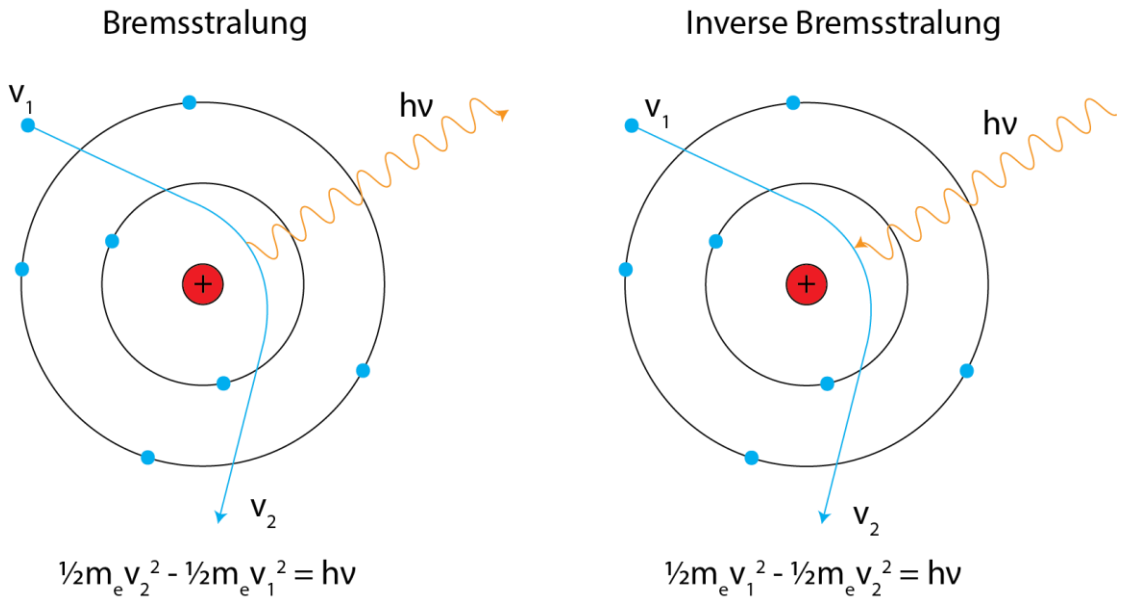


**Figure 25.** A schematic diagram of the bremsstrahlung and inverse bremsstrahlung processes. The change in the kinetic energy of the electron is equal to the energy of the emitted/absorbed photon in both processes.

Immediately following ionisation, the electron kinetic energies take specific discrete values that are determined by the ionisation potentials of the target atoms and the laser photon energy  $hc/\lambda$ . The bremsstrahlung processes then provide the energy exchange mechanism through which free electrons, after some time has passed, obtain thermal equilibrium and a continuous distribution of kinetic energies (velocities). If thermal equilibrium is achieved, the electron velocities relax into a Maxwell-Boltzmann distribution:

$$f(v) = \sqrt{\left(\frac{m}{2\pi kT}\right)^3} 4\pi v^2 e^{-\frac{mv^2}{2kT}}$$

This distribution is a probability density function that gives the probability of finding that a randomly selected electron has a velocity near  $v$ . Bremsstrahlung



radiation from electrons with a Maxwellian distribution of velocities is termed thermal bremsstrahlung.

The intensity of bremsstrahlung and thermal bremsstrahlung radiation, as a function of frequency, emitted from a laser induced plasma in thermal equilibrium at temperature  $T$ , can be derived by treating the plasma as a thermally equilibrated gas of electrons and positive ions. An exact treatment requires a knowledge of quantum electrodynamics, but an accurate equation can be derived using simpler approximation methods. A derivation in cgs units can be found in Rybicki and Lightman (Rybicki and Lightman, 2004). The equations for bremsstrahlung emissions are often derived using cgs units due to their use in describing the emission from astrophysical plasmas. A derivation of the bremsstrahlung radiation spectrum in SI units is presented in the appendix for the purposes of understanding the origin and nature of bremsstrahlung radiation. The result is stated here for the emission from a gas of electrons and ions in Joules per Hertz per second per kilogram:

$$\frac{dW}{dfdt dV} = \frac{Z^2 e^6 N_i N_e}{96 \pi^4 \epsilon_0^3 c^3 m_e^2} \frac{n_r \pi}{v \sqrt{3}} g(v, f) \quad \text{Equation 8}$$

$Z$  is the charge of the positive ions

$N_i$  is the number density of positive ions

$N_e$  is the number density of electrons

$n_r$  is the refractive index of plasma

$V$  is the electron velocity

$m_e$  is the electron mass

$g(v, f)$  is the Gaunt factor and is of order unity. The Gaunt factor is, to an approximation, used to combine various temperature and frequency effects. This equation is applicable to hydrogenic (hydrogen-like) ions that possess no other bound electrons following ionisation. The nuclear charge of the ion is therefore unshielded. For non-hydrogenic ions, where the shielding effect is taken into account, the Gaunt factor is replaced by the Biberman factor  $\xi$ . There are many different experimental and theoretical determinations of the

Gaunt factor and Biberman factor in the literature for a variety of different plasmas (Griem, 1964, Hughes, 1975, Stallcop and Billman, 1974, Brussaard and van de Hulst, 1962, Molinari et al., 2004, Karzas and Latter, 1961). A more precise derivation of Brehmsstrahlung emission takes into account the exact trajectory of the electron, dispersion (the refractive index of plasma), as well as quantum mechanical and relativistic effects. A complete quantum mechanical description of bremsstrahlung radiation can be found in Bethe and Heitler, 1934 (Bethe and Heitler, 1934).

The real part of the refractive index  $n_r$  is included in Equation 8 to account for dispersion effects within the plasma. In a low density plasma, such as those formed in gases at atmospheric pressure (the so called collisionless regime), the refractive index of a plasma is given by:

$$\tilde{n} = \sqrt{1 - \frac{\omega_p^2}{\omega^2}} = \sqrt{1 - \frac{f_p^2}{f^2}} \quad \text{Equation 9}$$

The accent above the n indicates that the refractive index can be a complex quantity with real and imaginary parts given by  $\tilde{n} = n_r + in_i$ .  $\omega$  is the angular frequency of the incident wave, related to the frequency of the wave by  $\omega = 2\pi f$ .  $f_p$  is the plasma frequency and is the natural frequency of the simple harmonic motion of electrons within a plasma about their equilibrium position following a small perturbation. It can be seen that if  $f > f_p$  then the refractive index of the plasma is real and lies between zero and unity. The wave propagates with a wavenumber given by:

$$k = \frac{n\omega}{c}$$

Substituting for the refractive index in Equation 9, we find the dispersion relation for EM waves in plasma:

$$\omega^2 = \omega_p^2 + k^2c^2$$

In Equation 9, if  $f < f_p$  then both the refractive index and the wavenumber are imaginary. The physical interpretation of this is that the wave is evanescent. The wave is unable to propagate through the plasma and is reflected back. This means that radiation below the plasma frequency is not emitted from the plasma. The real part of the refractive index and therefore the emission, falls-off close to, and becomes zero at, the plasma frequency.

To obtain the spectrum of bremsstrahlung emission (the intensity as a function of frequency) from Equation 8, the distribution of electron velocities (Temperatures) and densities in space and time as well as appropriate Gaunt factors must be known. Consideration of these parameters in practical LIPs, with the intention of deriving the intensity of the continuum emission spectrum as a function of wavelength, is a complex task which will not be attempted here (see (T.L, 1985, Regt et al., 1995, D'Yachkov et al.) for how this can be done). However, it is possible to solve for these parameters (often computationally) to determine the bremsstrahlung emission. If these are known, the emission is found by integrating the expression for a single velocity (Equation 8) over the velocity distribution. If  $P(v)$  is the probability of a random electron in a plasma having a velocity between  $v$  and  $dv$ , then for a normalised probability density function ( $\int P(v)dv = 1$ ), the emission is:

$$\varepsilon(f, v) = \int_{v_{min}}^{\infty} \frac{dW}{df dt dV} P(v) dv$$

The minimum allowable velocity  $v_{min}$  occurs in the lower limit because, for an electron to emit a photon of frequency  $f$ , it must have a kinetic energy greater than the emitted photon:  $\frac{1}{2}mv^2 \geq hf$ . This is a photon discreteness effect arising from quantisation. Rearranging, we get:

$$v \geq \sqrt{\frac{2hf}{m}} \text{ or } v_{min} = \sqrt{\frac{2hf}{m}}.$$

The distribution of electron velocities  $P(v,t)$  can be very difficult to determine for many plasmas and for this reason the assumption of thermal equilibrium is often made. If the plasma is in thermal equilibrium, the emission is termed

thermal bremsstrahlung and  $P(v)$  is given by the Maxwell-Boltzmann distribution. Strictly, the Fermi-Dirac distribution should be used rather than the Boltzmann, but this adds a third parameter, the Helmholtz free energy, to the dependency of the Gaunt factor and so for simplicity the Maxwell-Boltzmann distribution is used. The Maxwell Boltzmann distribution is:

$$P(v)dv = \left(\frac{m}{2\pi kT}\right)^{\frac{3}{2}} 4\pi v^2 e^{-\frac{mv^2}{2kT}} dv$$

The bremsstrahlung emission (in  $J^{-1}s^{-1}m^{-3}Hz^{-1}$ ) at a frequency  $f$  is therefore:

$$\begin{aligned} \varepsilon(T, f) &= \frac{Z^2 e^6 N_i N_e n_r}{96\pi^4 \varepsilon_0^3 c^3 m_e^2} \left(\frac{m_e}{2\pi kT}\right)^{\frac{3}{2}} 4\pi \frac{\pi}{\sqrt{3}} \int_{\sqrt{\frac{2hf}{m}}}^{\infty} v e^{-\frac{mv^2}{2kT}} g(v, f) dv \\ &= \frac{Z^2 e^6 N_i N_e}{24\pi^3 \varepsilon_0^3 c^3 m_e^2} \left(\frac{1}{2\pi}\right)^{\frac{3}{2}} \left(\frac{m_e}{k}\right)^{\frac{1}{2}} T^{-\frac{1}{2}} e^{-\frac{hf}{kT}} \frac{\pi}{\sqrt{3}} \bar{g}(T, f) \quad \text{Equation 10} \\ &= 2.38 \times 10^{-53} Z^2 N_p N_e T^{-\frac{1}{2}} e^{-\frac{hf}{kT}} \frac{\pi}{\sqrt{3}} \bar{g}(T, f) \end{aligned}$$

The **emission co-efficient**  $J(T, f)$  is defined as the emission per unit volume per unit frequency per unit solid angle ( $Js^{-1}m^{-3}Hz^{-1}sr^{-1}$ ):

$$\begin{aligned} J(T, f) &= \frac{\varepsilon(T, f)}{4\pi} \\ &= \frac{Z^2 e^6 N_i N_e n_r}{96\pi^4 \varepsilon_0^3 c^3 m_e^2} \left(\frac{1}{2\pi}\right)^{\frac{3}{2}} \left(\frac{m_e}{k}\right)^{\frac{1}{2}} T^{-\frac{1}{2}} e^{-\frac{hf}{kT}} \frac{\pi}{\sqrt{3}} \bar{g}(T, f) \quad \text{Equation 11} \end{aligned}$$

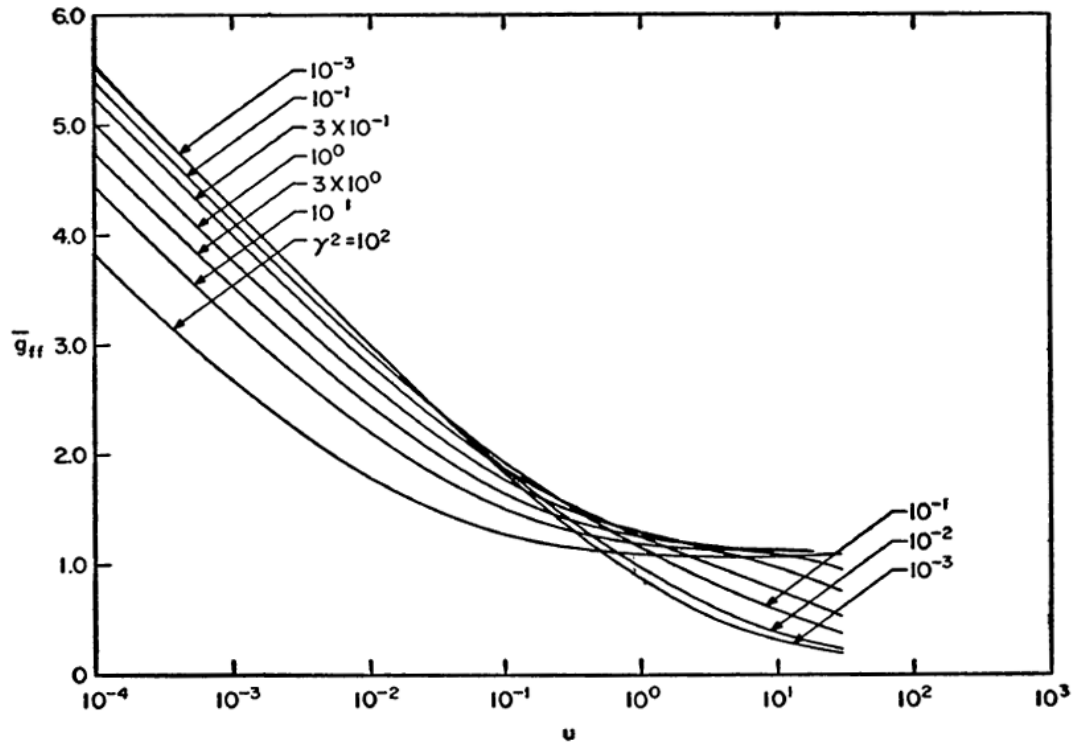


**Figure 26.** Numerical values of the Gaunt factor  $\bar{g}(T, f)$ .  $u$  is the frequency variable  $hf/kT$  and the lines trace different temperatures for which  $\gamma^2 = Z^2 Ry/kT$ , where  $Ry$  is the Rydberg energy  $me^4/2\hbar^2$ . Reproduced from Karzas and Latter 1960 (Karzas and Latter, 1961).

$\bar{g}(T, f)$  is the velocity averaged Gaunt factor. Numerical approximations of the velocity averaged Gaunt factor can be found in Karzas and Latter (Karzas and Latter, 1961). This Gaunt factor is plotted against  $hf/kT$  in Figure 26. The values of the Gaunt factor for  $hf > kT$  are unimportant as the emission decreases exponentially in this range. For  $hf \approx kT$  the Gaunt factor is approximately unity. For  $hf < kT$  the Gaunt factor is in the range 1-5. It can be seen from Figure 26 that good order of magnitude results can be obtained by approximating the Gaunt factor as unity.

The total power emitted per unit volume ( $\text{Wm}^{-3}$ ) is found by integrating the emission over the frequency:

$$\int \varepsilon(T, f) df = \frac{Z^2 e^6 N_i N_e n_r}{24 \pi^3 \varepsilon_0^3 c^3 m_e^2} \left( \frac{1}{2\pi} \right)^{\frac{3}{2}} \left( \frac{m_e}{k} \right)^{\frac{1}{2}} \frac{\pi}{\sqrt{3}} T^{-\frac{1}{2}} \int_0^\infty e^{-\frac{hf}{kT}} \bar{g}(T, f) df$$

$$= \frac{Z^2 e^6 N_i N_e n_r}{24 \pi^3 \varepsilon_0^3 c^3 m_e h} \left( \frac{1}{2\pi} \right)^{\frac{3}{2}} (k m_e)^{\frac{1}{2}} \frac{\pi}{\sqrt{3}} T^{\frac{1}{2}} \bar{g}(T)$$

$\bar{g}(T)$  is the frequency average of the velocity average Gaunt factor. Note that the total power emitted is proportional to  $T^{\frac{1}{2}} \propto v \propto E^{\frac{1}{2}}$  where E is the kinetic energy of the electron. The Gaunt factor  $\bar{g}(T)$  is almost constant over a broad range of temperatures as can be seen in Figure 27.

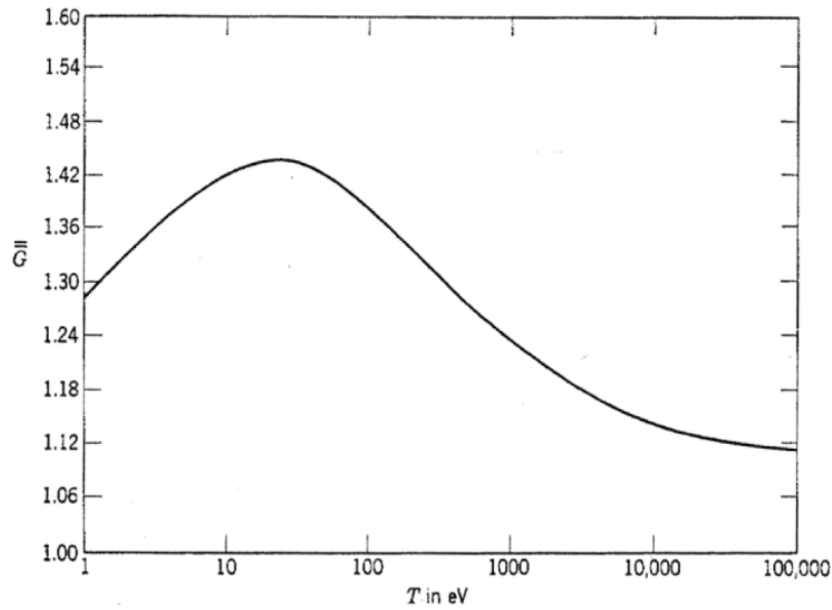


**Figure 27.** The frequency averaged Gaunt factor ( $Z=1$ ) from Bekefi, G., *Radiation Processes in Plasmas* (Bekefi, 1966). The curve is obtained from a numerical integration of a formula obtained by Sommerfeld (Sommerfeld, 1953).

The emission intensity determination given here assumes that the plasma is in thermal equilibrium but this may not be the case in a laser induced plasma. Immediately following laser ionisation, the electron kinetic energies take discrete values due to the discrete nature of the bound orbitals and the monochromatic (single photon energy) nature of the ionising laser light. Over a short period of time, the electron kinetic energies relax into a continuum and eventually thermal equilibrium is obtained via the bremsstrahlung processes, but the time required to achieve equilibrium may be longer than the lifetime of the plasma spark. More rigorous modelling of the spark requires a

consideration of electron partition functions and the differential rate equations to determine the distribution of electron velocities in time and space. A more in-depth analysis of this can be found in Griem (Griem, 1964), but for the purpose of deriving approximate emission spectra it is reasonable to assume LTE. To obtain the spectrum of the emitted radiation, Equation 10 is converted to a function of wavelength using  $f = c/\lambda$ :

$$\varepsilon(T, \lambda) = \frac{Z^2 e^6 N_i N_e n_r}{24 \pi^3 \varepsilon_0^3 c^3 m_e^2} \left( \frac{1}{2\pi} \right)^{\frac{3}{2}} \left( \frac{m_e}{k} \right)^{\frac{1}{2}} T^{-\frac{1}{2}} e^{-\frac{hc}{\lambda k T}} \frac{\pi}{\sqrt{3}} \bar{g}(T, \lambda) \quad \text{Equation 12}$$

The above equation for the bremsstrahlung emission from a plasma can now be applied to typical laser induced plasmas to determine theoretical spectra and assist with light source design. Approximate values for each of the variables in Equation 12 can be found in the past literature concerning laser induced plasmas. These variables are:

- $N_i$  and  $N_e$ , the number density of ions and electrons.
- $n_r$ , the real part of the refractive index of the plasma.
- $\bar{g}(T, \lambda)$  the velocity averaged Gaunt factor.
- $T$ , the electron temperature of the plasma.

In a low temperature, weakly ionised, electrically neutral laboratory plasma and for the purposes of determining theoretical spectra, it is acceptable to assume that the number densities of ions and electrons are equivalent  $N_i = N_e$ , but the electron number density in a plasma can be determined experimentally using the Stark effect. By measuring the Stark broadening of the emission peaks of singly charged ions, the number density of electrons in a laser induced plasma spark can be determined (see Griem, *The Principles of Plasma Spectroscopy* (Griem, 1964)). In *Bhindu et al*, the electron density for both air and argon sparks with laser powers of 50-200mJ (Figure 28) were determined by Stark broadening to be approximately  $2 \times 10^{24} \text{ m}^{-3}$ .

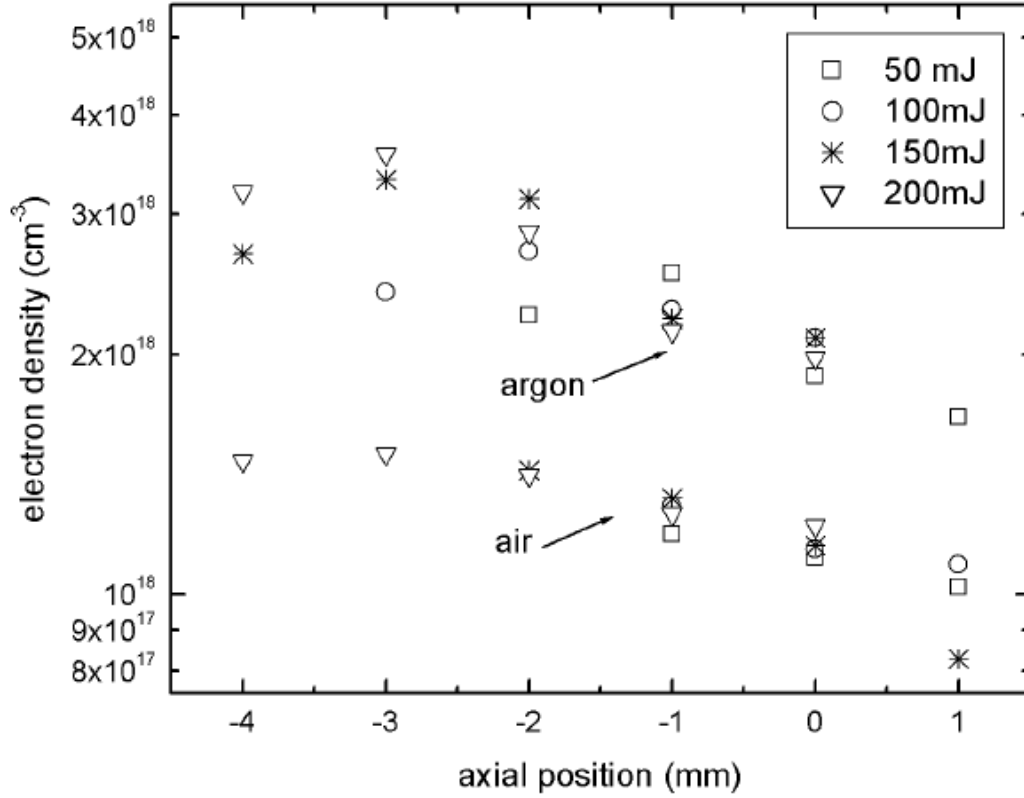


**Figure 28.** The measured electron density in a laser induced plasma. The focal point of the laser is at zero with the positive direction away from the direction of the impinging laser pulse. The laser is a frequency doubled Nd:YAG at 532nm with a pulse width of 8ns at FWHM. The focal length of the focusing lens is 75mm. Reproduced from (Bindhu et al., 2004).

The real part of the plasma refractive index can be approximated by a step function which is zero above the plasma frequency and unity below. In a linear, isotropic, homogenous (LIH), singly ionised plasma, the plasma frequency is given by:

$$\omega_p = \sqrt{\frac{N_e e^2}{m_e \epsilon_0}} \quad \text{or} \quad f_p = \sqrt{\frac{N_e e^2}{4\pi^2 m_e \epsilon_0}}$$

Using the experimentally determined value for the electron density of  $2 \times 10^{24} \text{ m}^{-3}$  from Bindhu *et al*, the plasma frequency is  $f_p = 1.27 \times 10^{13} \text{ Hz}$ . The wavelength of light in air (for refractive index  $n \approx 1$ ) that this frequency corresponds to is:



$$\lambda = \frac{c}{f_p} = 2.36 \times 10^{-5} \text{ m or } 23.6 \mu\text{m}$$

Waves above this wavelength do not propagate through the plasma and are reflected back. This wavelength corresponds to the mid infrared region of the EM spectrum. It is for this reason that infrared light have been used to probe laser induced plasma structure (Kroesen et al., 1996). For the purposes of utilising a laser induced plasma as an UV/Vis/IR source, the effects of dispersion can be ignored, as the production of light above this wavelength is not needed for spectroscopy of biomolecules. The real part of the refractive index  $n_r$  in Equation 12 can therefore be assumed to be unity.

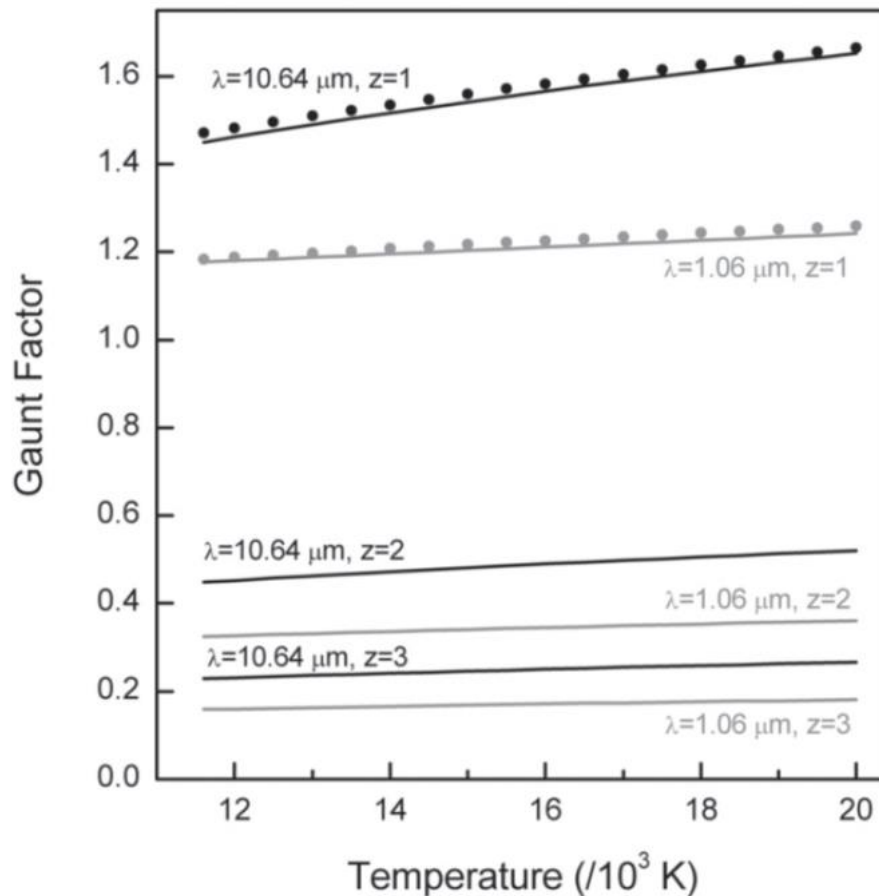


**Figure 29.** Gaunt factors for various laser wavelengths and charges in an argon plasma. The points are plotted from a numerical approximation found in (Paulini and Simon, 1993) and lines from (Stallcop and Billman, 1974).

Numerical approximations of the velocity averaged Gaunt factor have been calculated for laser induced plasmas. These approximations are used for the accurate determination of elemental composition in LIBS. Figure 28 shows the numerical approximations for velocity average Gaunt factors for an argon plasma induced by the focused pulse of an Nd:YAG or CO<sub>2</sub> laser. The Gaunt factor varies slowly with temperature for laser induced plasmas. For a singly ionised plasma, induced by the pulse from a fundamental mode ND:YAG laser at 1064nm, the Gaunt factor is approximately 1.2. In further calculations, it will be assumed that the velocity averaged Gaunt factor is 1.2. By assuming a singly ionised plasma and approximate values for the electron number density  $N_e=2 \times 10^{24} \text{ m}^{-1}$  and the velocity averaged Gaunt factor=1.2, the plasma emission  $\varepsilon(T, \lambda)$  (Equation 12) becomes a pure function of wavelength and temperature:

$$\varepsilon(T, \lambda) = 2.072 \times 10^{-4} T^{-\frac{1}{2}} e^{-hc/\lambda kT}$$

This equation is plotted in Figures 30 and 31.

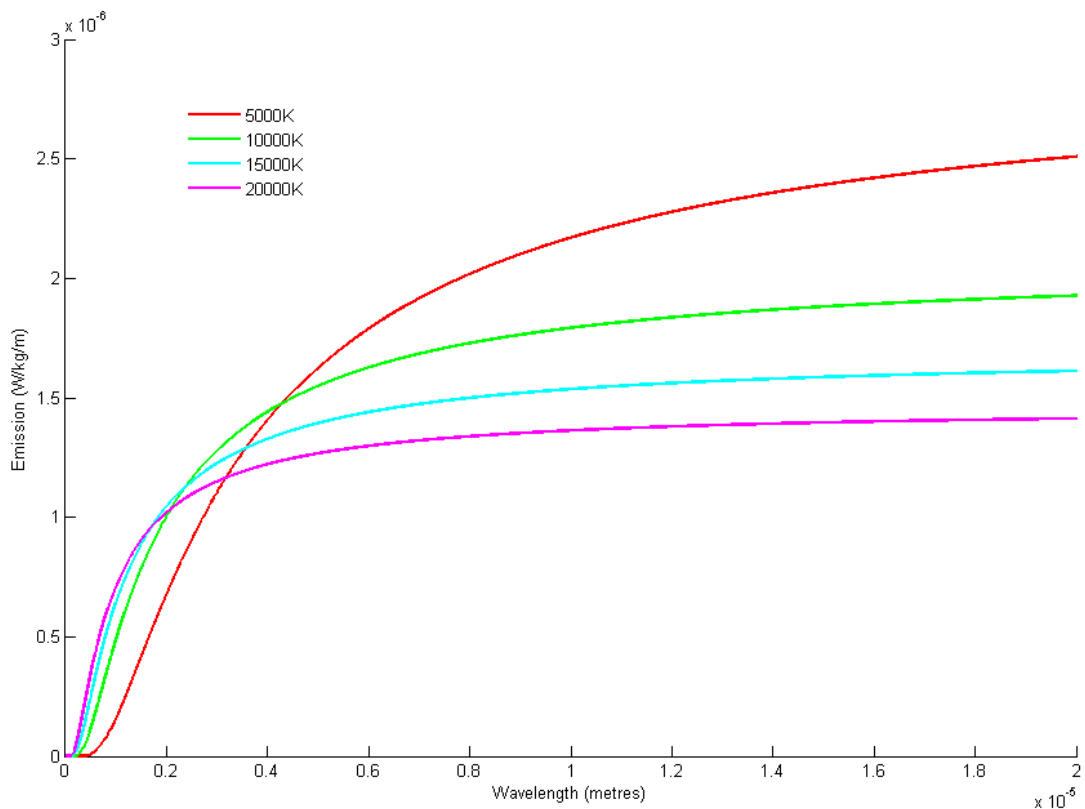


**Figure 30.** Brehmsstrahlung emission plotted against wavelength for the region 0-20  $\mu\text{m}$ .

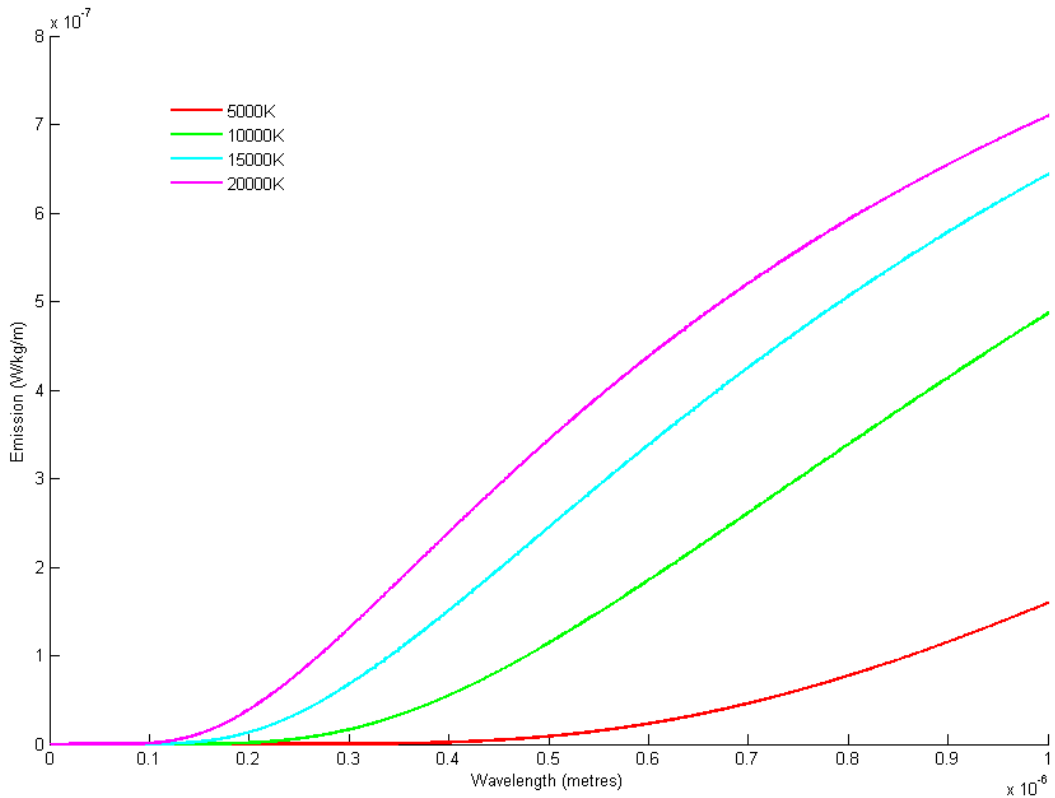


**Figure 31.** Bremsstrahlung emission plotted against wavelength for the region 0-1  $\mu\text{m}$ . Note that very little emission occurs below 300 nm for electron temperatures below 10000°K.

Figures 30 and 31 appear to violate the second law of thermodynamics by emitting increasing intensities of radiation as the wavelength becomes longer. However, the amount of radiation emitted from a plasma  $\varepsilon(T, \lambda)$ , is not equal to the amount of radiation that an observer receives, due to the reabsorption of radiation via the free-free (inverse bremsstrahlung) and bound-free absorption processes. The absorption coefficient  $\alpha_f$  of a medium is defined as the fractional loss of energy  $dI_f$  (in  $\text{Js}^{-1}\text{m}^{-3}\text{sr}^{-1}$ ) at a particular wavelength, when moving through a small distance  $dL$ :

$$\frac{dI_f}{dL} = -\alpha_f I_f$$

The absorption coefficient has units of  $\text{m}^{-1}$ . The solution to this equation is simply:

$$I_f = I_{f0} e^{-\alpha_f L}$$

Where  $L$  is the depth of the plasma. The quantity  $\alpha_f L$  is the optical depth or the negative logarithm of the fraction of light that is not absorbed along the path  $0 \rightarrow L$ . The absorption coefficient  $\alpha_f$  can also be related to a cross-section of interaction  $\sigma_f$  via  $\alpha_f = n\sigma_f = \rho\sigma_f/m$ .

In order to determine the bremsstrahlung spectrum obtained from combined emission and absorption effects the total radiation field is defined by summing the emission and absorbance (assuming no back illumination) in a radiative transfer equation:

$$\frac{dI_f}{dL} = j_f - \alpha_f I_f$$

This first order differential equation is relatively simple to solve if the assumption of thermal equilibrium is made. For a body in thermal equilibrium, where the underlying particle distribution is Maxwellian, Kirchhoff's thermal radiation law can be used to find the absorption coefficient  $\alpha_f$ . Kirchhoff's law states that the emission is equal to the absorbance so that  $\frac{dI_f}{dL} = 0$ . From the radiative transfer equation it follows that:

$$j_f = \alpha_f I_f$$

or

$$I_f = \frac{j_f}{\alpha_f}$$

Furthermore, Planck's Law states that for a blackbody the emission of the thermal radiation is given by:

$$I_f = B(T, f) = \frac{2hf^3}{c^2(\exp(hf/kT) - 1)}$$

$B(T, f)$  is the Planck function and is the emitted intensity of a blackbody at a temperature  $T$  and frequency  $f$ . Taking  $j_f$  from Equation 11 and rearranging for  $\alpha_f$ :

$$\alpha_f = \frac{j_f}{B(T, f)} = \frac{Z^2 e^6 N_i N_e}{192 \pi^4 \epsilon_0^3 m_e^2 c h f^3} \left(\frac{1}{2\pi}\right)^{\frac{3}{2}} \left(\frac{m_e}{k}\right)^{\frac{1}{2}} T^{-\frac{1}{2}} (1 - \exp(-hf/kT)) \frac{\pi}{\sqrt{3}} \bar{g}(T, f)$$

The absorption coefficient,  $\alpha_f$  depends strongly on frequency. At high frequencies (the Wien region) the absorption is negligible due to the limits of  $f^{-3}$  and  $\exp(-hf/kT)$ . At low frequencies  $hf \ll kT$  (the Rayleigh-Jeans regime), using the series expansion of  $e^x$ , the absorption coefficient reduces to:

$$\alpha_f = \frac{Z^2 e^6 N_i N_e}{192 \pi^4 \epsilon_0^3 m_e^2 c h f^3} \left(\frac{1}{2\pi}\right)^{\frac{3}{2}} \left(\frac{m_e}{k}\right)^{\frac{1}{2}} T^{-\frac{1}{2}} \frac{hf}{kT} \frac{\pi}{\sqrt{3}} \bar{g}(T, f)$$

At low frequencies, the absorption coefficient is a function of  $f^2$ . By increasing the number density of electrons and ions, self-absorbance occurs at higher frequencies. If the entire spectrum is self-absorbed, the observed spectrum is that of a blackbody. The absorption as a function of frequency for both the low and the high frequency regimes is plotted in Figure 32.

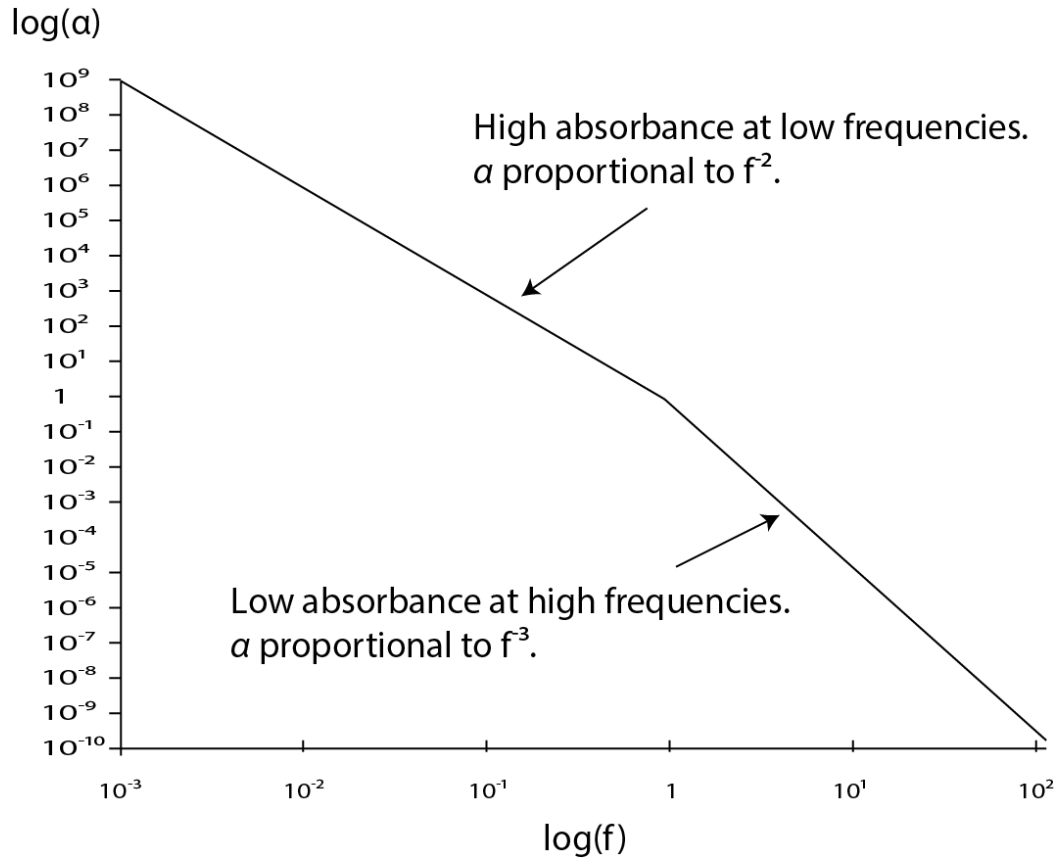


**Figure 32.** Log graph showing the dependence of absorption coefficient against frequency.

The radiative transfer equation is solved for the general case by a separation of variables:

$$\int_0^{I_f} \frac{dI_f}{j_f - \alpha_f I_f} = \int_0^L dL = L(\text{Depth of plasma})$$

$$L = \frac{1}{\alpha_f} \ln \left( \frac{j_f}{j_f - \alpha_f I_f} \right)$$

$$I_f = \frac{j_f}{\alpha_f} (1 - e^{-\alpha_f L}) = B(T, f)(1 - e^{-\alpha_f L}) = \frac{2hf^3(1 - e^{-\alpha_f L})}{c^2(e^{hf/kT} - 1)} \quad \text{Equation 13}$$

The solution to the radiative transfer equation gives the classical bremsstrahlung spectra as plotted in Figure 33.

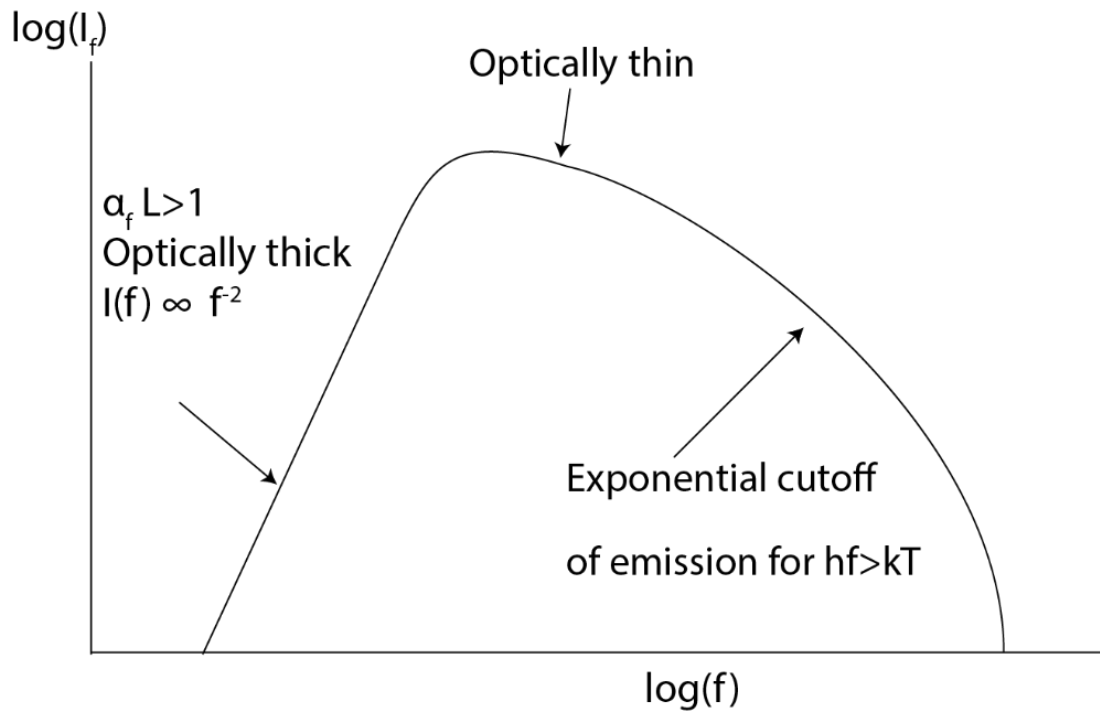


**Figure 33.** Bremsstrahlung spectral shape showing areas of self-absorbance.

The bremsstrahlung emission (including self-absorption) from a plasma has three characteristic frequency regimes depending upon the value of the optical depth  $\alpha_f L$ :

- The Wein region ( $\alpha_f L \ll 1$ ) occurs at high frequencies. In this frequency range, plasma is said to be optically thin. The self-absorption is negligible due to the  $f^3$  dependence of  $\alpha_f$ . The radiation seen by the observer is simply the emission contribution from each volume element along the line of sight,  $I_f = \int j_f dL$ .
- The Raleigh-Jeans regime ( $\alpha_f L \gg 1$ ) occurs at low frequencies. In this frequency range, plasma is said to be optically thick. Owing to self-absorption, plasma is opaque to the propagation of radiation with a dependency of  $f^2$  on the absorption coefficient  $\alpha_f$ . The observed spectrum is that of a blackbody.
- When the optical depth is approximately unity, plasma is semi-transparent.

By converting frequency in Equation 13 to wavelength and simplifying, the **full solution for the spectrum of thermal bremsstrahlung** is obtained:

$$I_\lambda = \frac{2hc^2(1 - e^{-\alpha L})}{\lambda^5 \left( e^{hc/\lambda kT} - 1 \right)} \quad \text{Equation 14}$$

where

$$\alpha_f = \frac{Z^2 e^6 N_i N_e \lambda^3}{192 \pi^4 \epsilon_0^3 m_e^2 hc^4} \left( \frac{1}{2\pi} \right)^{\frac{3}{2}} \left( \frac{m_e}{k} \right)^{\frac{1}{2}} T^{-\frac{1}{2}} (1 - \exp(-hc/\lambda kT)) \frac{\pi}{\sqrt{3}} \bar{g}(T, f)$$

The units of  $I_\lambda$  are  $\text{W} \cdot \text{Sr}^{-1} \cdot \text{m}^{-3}$ . This equation describes the spectral radiance of a blackbody or the power emitted per unit solid angle as a function of wavelength.

In an electrically neutral plasma, such as a laser induced plasma, the free electron number density  $N_e$  is approximately equal to the ion number density  $N_i$  and the ion charge  $Z$  via the relationship:

$$N_e \approx ZN_i$$

This simple equation shows that an increase in the electron number density is accompanied by either an increase in average ion charge or an increase in ion number density or both. Replacing  $ZN_i$  with the electron density  $N_e$  in Equation 14 gives an absorption co-efficient of:

$$\alpha_f = \frac{e^6 Z N_e^2 \lambda^3}{192 \pi^4 \epsilon_0^3 m_e^2 hc^4} \left( \frac{1}{2\pi} \right)^{\frac{3}{2}} \left( \frac{m_e}{k} \right)^{\frac{1}{2}} T^{-\frac{1}{2}} (1 - \exp(-hc/\lambda kT)) \frac{\pi}{\sqrt{3}} \bar{g}(T, f)$$

As the electron density  $N_e$  increases, the absorption coefficient becomes very large. In laboratory laser induced plasmas, measured electron densities are high enough ( $N_e = 2 \times 10^{24} \text{ m}^{-3}$  (Bastiaans and Mangold, 1985)) so that the absorption coefficient is large and the plasma has the emission spectrum of a blackbody.

If the plasma is a blackbody, then the most important physical property of the plasma for the generation of short wavelength, high intensity light are high



electron temperatures as the emission from a blackbody is proportion to  $e^{-hc/\lambda kT}$ . The electron temperatures are directly related to their velocities via the relation  $\frac{1}{2}mv^2 = \frac{3}{2}kT$  from kinetic theory of gases. An increase in the electron temperatures results in both an increase in the spectral power output across all wavelengths and a shifts the emission towards shorter wavelengths.

## 1.7 Chapter Summary

Preliminary investigations into ways of increasing SNRs in VCD, and many other forms of absorbance spectroscopy, concluded that:

$$SNRs \propto (QIt)^{\frac{1}{2}}$$

$Q$  is the detector quantum efficiency,  $I$  is the light source intensity and  $t$  is time or some function of time. Replacing the glowbar inside the VCD spectrometer with a higher intensity emitter would therefore lead to improved SNRs in VCD. The glowbar inside the spectrometer is emitting approximately blackbody radiation at a temperature of 1500K. Plasma based light sources, such as xenon lamps, are commonly used in the laboratory as a spectroscopic source of UV and visible light. These lamps radiate approximately blackbody, continuous radiation that is many thousands of degrees Kelvin in temperature. Both the IR glowbar and plasma light sources are approximately radiators that obey the Stefan-Boltzmann law that states that the total radiative emission from a blackbody is proportional to the forth power of temperature. High temperature plasmas should be able to emit high intensity light throughout the IR, visible and into the UV and potential offer substantial improvements in source intensity and spectroscopic SNRs.

A simple way to generate a high temperature plasma is to focus a pulsed laser through a convex lens. A plasma is formed at the focal point of the lens. This technology is capable of reaching very high temperatures and is used to generate high temperature in several areas of cutting edge of research such

as the generation of EUV light. LIP based technologies should be able to generation light that is useful for biological spectroscopy. As well as a broadband light source in the IR, a broadband light source emitting in the region 200-300nm would be extremely useful as many biological chromophores absorb in this region. As well as absorption spectroscopy, a bright broadband light source would be of considerable use in other forms of spectroscopy such as Rayleigh scattering and turbidity experiments.

An analysis of the emission spectrum of a laser induced plasma is composed of line and continuum emission. It is the continuum emission that is useful as a broadband light source. An examination of the physical processes involved reveals that **it is the brehmsstrahlung and recombination processes that generate the continuum emission from a plasma. The power output of these processes is an important consideration and should be maximised in a plasma light source.** The brehmsstrahlung emission from the plasma follows the equation:

$$I_{\lambda} = \frac{2hc^2(1 - e^{-\alpha L})}{\lambda^5 (e^{hc/\lambda kT} - 1)}$$

If the absorption coefficient  $\alpha$  is large, the continuum emission is maximal and is that of a blackbody. In most laboratory plasmas, the absorption coefficient is large due to high electron densities. The design of a plasma spectrometer must seek to maximise the electron temperature in order to maximise the blackbody-like, bremsstrahlung spectral power output.

## List of Materials

L1667 SIGMA Lysozyme human

LONZ17-517Q VWR PBS buffer solution 10x concentrate - Calcium & magnesium free

10467010 ACROS Iron(III) chloride, 98%, pure, anhydrous

10563951 ACROS Copper(II) chloride, anhydrous, 99%, extra pure

10062590 ACROS Zinc chloride, 98+%, extra pure

11904191 ACROS Iron(II) chloride, 99%, anhydrous

114359 SIGMA Bromocresol Green ACS reagent, Dye content 95 %

32661 SIGMA Phenol Red ACS reagent

A3004 Applichem Heparin sodium salt 208 IU/mg

10910.03 Alfa Aesar Holmium (III) oxide REacton®

77233 SIGMA-ALDRICH Perchloric acid, puriss. p.a., 20%

428760 SIGMA Dowex Marathon ion exchange resin

101720-L BOC N4.6 Helium 99.996%

112008-BC BOC N5.0 Neon 99.999%

112034-BOC Grade A Argon 99.9% N5.0

112005-BOC Krypton 99.999% N5.0

Thermo Scientific GENESYS 10S UV/Visible Scanning Spectrophotometer

Tecan Infinite® M200 PRO series

## Breakdown of Materials and Costs for the Construction of the Prototype Instrument

Number of Items	Supplier	Item Code	Item Description	Cost Each	Total Cost
2	Thorlabs	CCS200/M	Compact Spectrometer	£1980	£3960
1	WeiFang MingLiang Electronics Company Ltd	ML-LASER-YB5	Nd:YAG Laser Treatment System	\$1150 (£736)	£736
2	Thorlabs	MB2020/M	Aluminum Breadboard, 200 mm x 200 mm x 12.7 mm, M6 Taps	£54	£108
1	Thorlabs	MB1560/M	Aluminum Breadboard, 150 mm x 600 mm x 12.7 mm, M6 Taps	£111.60	£111.60
12	Thorlabs	PH50/M	Ø12.7 mm Post Holder, Spring-Loaded Hex-Locking Thumbscrew, L=50 mm	£5.54	£66.48
12	Thorlabs	BA1S/M	Mounting Base, 25 mm x 58 mm x 10 mm	£3.74	£44.88
12	Thorlabs	TR50/M	Ø12.7 mm Optical Post, SS, M4 Setscrew, M6 Tap, L = 50 mm	£3.74	£44.88
3	Thorlabs	LMR05	Lens Mount For 0.5" Optics, M4 Tap	£10.81	£32.43
6	Thorlabs	LMR1/M	Lens Mount For 1" Optics, M4 Tap	£10.96	£65.76
1	Thorlabs	SM05L05	Lens Tube, Ø1/2", 0.50" Thread Depth	£9.90	£9.90
1	Thorlabs	SM1L05	SM1 Lens Tube, 0.5" Thread Depth,	£9.06	£9.06

1	Thorlabs	83373	English (Imperial) Tap: 0.535"-40 Thread (SM05 Standard)	£62.06	£62.06
1	Thorlabs	97355	English (Imperial) Tap: 1.035"-40 Thread (SM1 Standard)	£62.06	£62.06
2	Thorlabs	SM1SMA	SMA Fiber Adapter Plate with External SM1 (1.035"-40) Thread	£20.41	£40.82
1	Thorlabs	BSW26	Ø1" 50:50 UVFS Plate Beamsplitter, Coating: 350 - 1100 nm, t = 5 mm	£195.84	£195.84
3	Thorlabs	LA4647	f = 20.1 mm, Ø1/2" UV Fused Silica Plano- Convex Lens, Uncoated	£59.11	£177.33
2	Thorlabs	LA4052	f = 35.1 mm, Ø1" UV Fused Silica Plano- Convex Lens, Uncoated	£67.54	£135.08
1	Thorlabs	CM254-019- F01	Ø1" UV Enhanced Al- Coated Concave Mirror, f=19.0 mm	£37.44	£37.44
1	Thorlabs	WG40530	Ø1/2" UVFS Broadband Precision Window, Uncoated	£45.72	£45.72
1	Thorlabs	WG41010	Ø1" UVFS Broadband Precision Window, Uncoated, 1 mm Thick	£60.77	£60.77
1	Thorlabs	KM200B/M	77 mm x 77 mm Kinematic Platform Mount	£65.73	£65.73
1	Thorlab	KM05	Kinematic Mount for Ø1/2" Optics	£28.08	£28.08
1	Thorlabs	ID8	Standard Iris, Ø8.0 mm max. Aperture	£32.31	£32.31

1	Wescol		Single Stage Argon Regulator	£40	£40
1	RS-Online	715-4081	Arduino Uno ATmega328 MCU Board Rev 3	£17.33	£17.33
1	RS-Online	774-7068	Clear 30m PUR Air Hose	£50.85	£50.85
1	Mi Engineering		Bespoke Pressure Chamber	Approx Cost £200	£200
1	Farnell	1226886	TSL257-LF SENSOR, LIGHT-VOLTAGE CONVERTER	£1.21	£1.21
1	Gas Equipment LTD		4 bar Safety Valve	£6.50	£6.50
2	Gas Equipment LTD		3/4 BSP Male Hose Adapter	£4.49	£8.98
1	RS-Online	812-5273	RS Process Ball Valve	£6.21	£6.21
1	RS-Online	506-3090	Black Natural Rubber Sheet, 1000mm x 600mm x 3mm	£17.32	£17.32
				<b>Total</b>	<b>£6480.49</b>

# Two

---

## Instrument Design, Build and Commissioning

---

### 2.1 MI Engineering's Initial Light Source Design

Prior to the start of the project and meetings between engineers at MI, the PI and myself, MI Engineering had drafted a preliminary design for a plasma light source. The Autocad drawings for MI's light source are shown in Figures 34 & 35. Prior to the start of the project and meetings between engineers at MI, the PI and myself, MI Engineering had drafted a preliminary design for a plasma light source. The Autocad drawings for MI's light source are shown in Figures 33 & 34. This design was based on publications by Borghese *et al* (Borghese and Di Palma, 2007) and Adamson and Cimolino (Adamson and Cimolino, 1984a) and discussions that took place between MI and the PI.







The concept behind MI's design is similar to plasma light sources that employ high pressure supersonic nozzles and vacuum chambers to generate VUV and EUV radiation (Bielesch et al., 1998, Bartnik et al., 2013, Hansson et al., 2001). Some of the problems of this technology were discussed previously in connection with the generation of EUV for CPU lithography. The main obstacles to the commercial viability of EUV technologies are:

- The manufacture of suitable optics. As noted previously, very expensive precision mirrors are required for the optics to capture the EUV light but optics for use in the biologically interesting mid-UV range (200-300 nm) are cheap and widely available through use of aluminium coating to enhance reflectivity in the UV. The availability and low cost of these mirrors mitigates the problem of damage occurring over time through the heating of particular matter and the impact of high energy particles. Mirrors can simply be replaced if reflectivity falls.
- The cost of the ionising laser. In EUV lithography, very high laser powers (>10 kW) are needed to generate the required intensities at the focal point ( $\sim 10^{11}$  W/cm<sup>2</sup>) (Hansson et al., 2002). A laser able to do this with 10 % efficiency consumes an electrical power of 100 kW. This leads to further difficulties with the engineering of lenses capable of transmitting such high intensity light without thermal damage/deformation arising from absorption. Lasers for the production of very short wavelength light need to have a very high repetition rate. This is because the plasma needs to be excited multiple times in order to generate the ultra-high speed electrons needed to radiate in the EUV. The lifespan of a laser induced plasma is in the order of 1ms (Bindhu et al., 2004, Bindhu et al., 2003, Chen et al., 2000). This means that a laser must have a repetition rate of MHz in order to excite a plasma more than once. These high repetition rates are only available from very expensive mode-locked lasers that employ methods such as cavity dumping and electro-optic q-switching to obtain short high power pulses at high repetition rates. Lasers with kHz repetition rates have been proposed as VUV sources (Bielesch et al., 1998) as the laser ignites the hot gas that is left over from the preceding pulse. If the repetition rate of a laser is high enough, the electron density

in the focal volume can remain at a high level. The presence of residual free electrons in the focal volume dramatically reduces the breakdown threshold and results in a much greater proportion of the pulse energy absorbed by the plasma.

Following an examination of the drawings, it was apparent that there were several issues with MI's design:

- Which wavelength region was the light source intended to generate? Plasmas can generate both UV, visible and IR radiation simultaneously, due to their close approximation to a blackbody radiator. However, the choice of light capture optics depends upon the wavelength region of interest. The drawings are marked for use with an IR lens but are based on a design used by Borghese *et al* to generate VUV radiation. To generate IR radiation, Adamson and Cimolino did not need to employ a high pressure nozzle or a vacuum chamber because the IR radiation was not absorbed by the medium (air or argon) in which the plasma was formed. It may be possible to employ more than one set of optics to simultaneously use the plasma as a light source for more than one wavelength region. This would require significant changes to MI's original design.
- How would the gas jet and laser pulse be timed to coincide? The timing of the laser pulse to the emission of the gas from the nozzle is critical to obtain the optimal radiative emission from the generated plasma. If the laser pulse impinges on the gas too early, then a sufficient quantity of gas will not be in the target volume (or worse, no gas at all) to absorb a substantial fraction of the laser energy. If the laser impinges on the gas too late, reabsorption of short wavelength radiation will occur. In Borghese *et al*, a 7 ns laser was focused onto a 250  $\mu$ s pulsed jet of Xenon gas. With these pulsed gas jet light sources, it is necessary to employ complex equipment to adjust the timing of both/either the laser and/or the injection of the gas.
- Would MI's design be suitable for the generation of a high vacuum inside the chamber? Vacuums for the generation of EUV/VUV are often in the

order of  $10^{-6}$  Torr (Hansson et al., 2002). A good quality vacuum pump would need to be used to obtain this very low pressure. In addition, the design may need to be strengthened to accommodate such a vacuum, especially around windows and seals.

- Xenon is very expensive (~£1000 per litre at atmospheric pressure). For testing and initial experiments it would make sense to use a much cheaper noble gas such as argon.
- Would the optical elements (mirror and lens) be damaged by the aerodynamic shock of a laser heated, rapidly expanding gas?
- Solarisation of the optical fibre. In MI's design the emitted light from the plasma is focused onto an optical fibre port and into an optical fibre, which then transmits the light for use in spectrometers. High energy UV radiation below 260 nm causes defects in the fused silica that is often used for short wavelength optical fibres. This effect is known as solarisation. Over time, solarisation causes significant transmission losses and eventually leads to the fibre becoming unusable. Solarisation can be reduced by the infusion of hydrogen into the fibre's silica core. However, the hydrogen will slowly diffuse out of the cable, eventually resulting in solarisation. It would be better if this light source did not employ a fibre optic cable for these reasons.

Although it would be interesting to explore the sub-200 nm region on many different molecules with a broadband spectrometer, the difficulties presented by the construction of a device employing a high pressure nozzle and vacuum chamber were beyond the scope of this project. Such a design is not needed for the generation of light in the interesting biological range of 200-300 nm. Removal of the need for a plasma light source to generate light below 200 nm allows for a simplification of the original design and substantially reduces the costs involved in the construction of a prototype. The plasma no longer needs to be generated in a vacuum because light with wavelengths above 200 nm is not reabsorbed by the medium in which the plasma is formed. This removes the need to pulse the gas into a vacuum through a high pressure nozzle and with it the need for a vacuum pump and complex jet/laser pulse timing equipment.

## 2.2 Proposed Plasma Light Source: Concept and Design

If the requirement to generate light below 200 nm is removed, then there is no need to pulse the gaseous medium into a vacuum through a high pressure nozzle. Instead, the plasma can be formed by focusing the laser pulse into a sealed chamber that is filled with a gaseous medium. Light emitted from the plasma would gain egress through a window perpendicular to the laser beam. It would be possible hypothetically for the chamber to have multiple windows, which are transparent to light of different wavelengths. In this way, the light source may be useful across a broad range of wavelengths from the Mid-UV to the IR.

Based on a sealed chamber design, a plasma light source spectrometer for the generation of light above 200 nm would consist of 5 main components:

1. A pulsed laser.
2. Focusing optics.
3. A sealed chamber containing the gaseous medium in which the plasma is formed.
4. Optics for the capture and collimation of emitted light.
5. A suitable detector(s) system for the measurement of a sample's transmission or scattering properties.

Ideally, the instrument should be able to record the absorbance and/or scattering characteristics of a sample as they evolve over time. Key features of the instrument are:

1. The ability to repeatedly measure the absorbance/scattering characteristics of a sample over a time scale of seconds to hours. The repetition rate of the laser dictates the number of times a second that a measurement can be taken.
2. The ability to record measurements simultaneously across a broad range of wavelengths. This allows for time and wavelength resolved correlation

spectroscopy to be used to identify patterns and relationships within sets of samples.

The schematic diagram of the proposed plasma spectrometer is shown in Figure 36. The following section examines the design considerations and choices made for each of the components.

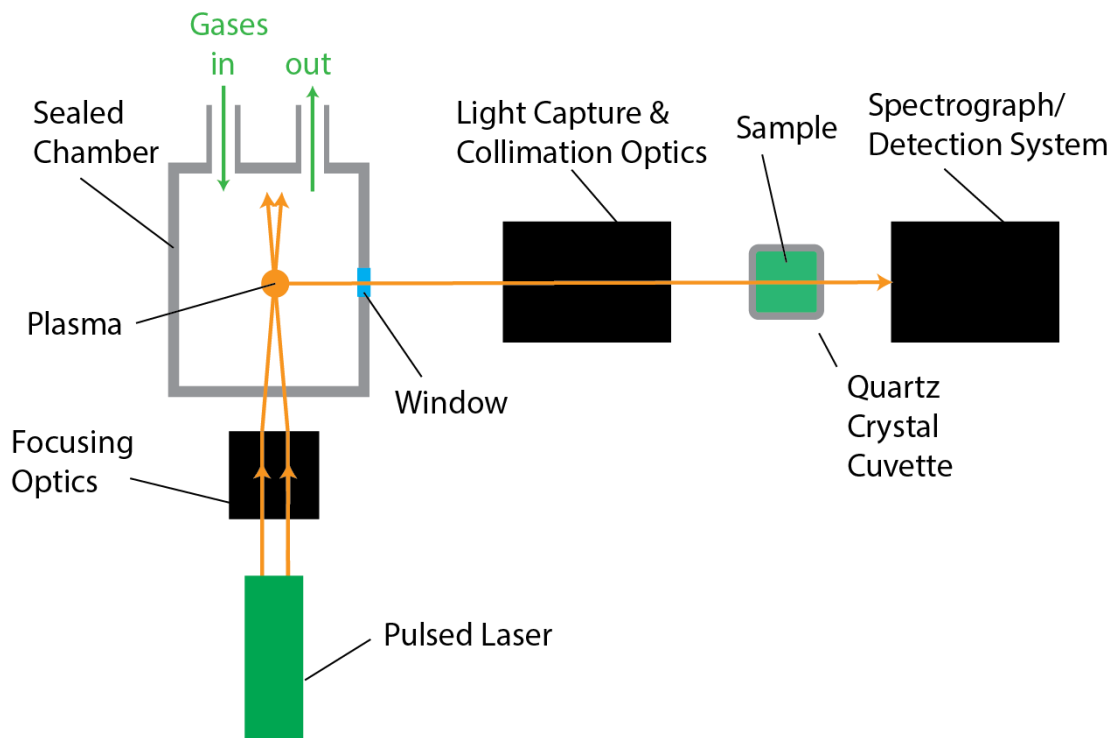


**Figure 36.** A schematic of the proposed plasma spectrometer design showing the five main component parts.

### 2.3 Choice of Laser for Plasma Generation

For a laser to ionise a gaseous medium it must be capable of producing, when focused, a very high output power ( $>10^{10}$  Wcm<sup>-2</sup> for air). Only pulsed lasers, rather than continuous wave lasers, are able to generate focused powers of this magnitude. In pulsed laser operation, the energy stored in the laser cavity is released in a very short (in the order of nanoseconds or less), very intense pulse, sufficient to ionise air and other gases.

Pulsed laser operation is achieved by a variety of methods. The most common types are mode locked and Q-switched lasers. Mode-locking is the act of fixing the phase relationships between the resonating modes in the laser cavity. Very bright pulses of light can be obtained by fixing the phase between modes in such a way as to cause them to constructively interfere in a periodic manner. Mode locked lasers are capable of producing femtosecond or even picosecond pulses. Mode-locked lasers are often expensive due to the non-trivial task of fixing the phase of the cavity modes, at repetition rates often in the MHz range, with pulse energies in the mJ range. It is especially difficult to combine high repetition rate with high pulse energy. Higher pulse energies from mode locked lasers can be obtained by amplifying pulses at a lower repetition rate using a regenerative amplifier but this introduces added complexity and expense.

The phenomenon of laser induced breakdown of gases was first reported using a Q-switched laser (Maker et al., 1964). Q-switched lasers can be obtained much more cheaply than mode locked lasers and allow for much higher pulse energies ( $\sim 1\text{J}$ ), although at the expense of longer pulse durations ( $\sim \text{ns}$ ) and lower repetition rates ( $\sim \text{Hz}$ ). For the manufacture of a prototype plasma spectrometer it was not necessary to use a mode-locked laser with a very short pulse duration and high repetition rate. A Q-switched laser with a repetition rate of a few Hz, but with high pulse energies could be used to keep down the costs of a prototype. However, due to the low pulse rate, a LIP generated by the Q-switched laser will not be excited multiple times by the laser. This will lead to reduced plasma temperatures with the consequence that the emission will not be as intense or short in wavelength. A more expensive laser mode locked laser can be acquired at a later stage to upgrade the light source to provide higher intensity, shorter wavelength light. For a proof of concept prototype design a Q-switch laser will be used to keep within the budget of this project.

Q-switched lasers are pumped by very intense but low repetition rate pulsed sources such as flashlamps but, pulsed photodiodes are becoming more common for pumping Q-switched lasers with advances in technology and cost of these semiconductor devices. Q-switching a laser is achieved by placing an

attenuator inside the laser cavity. This is equivalent to heavily damping an oscillator so that it has a low quality or Q factor. The attenuator prevents light that leaves the gain medium from returning, thereby preventing feedback and subsequent resonant lasing action via stimulated emission. This allows the energy stored in the gain medium, in the form of electrons in high states, to build up as the medium is pumped. At the point of maximum energy storage, known as *gain saturation*, the attenuator is switched off. This is equivalent to removing the damping force from an oscillator so that it now has a high Q factor, hence the term Q-switching. Light emitted from the medium via spontaneous emission can now be reflected back from the high reflector and through the lasing medium, allowing feedback and resonant amplification via stimulated emission to occur. The components of a Q-switched Nd:YAG laser are shown in Figure 37.

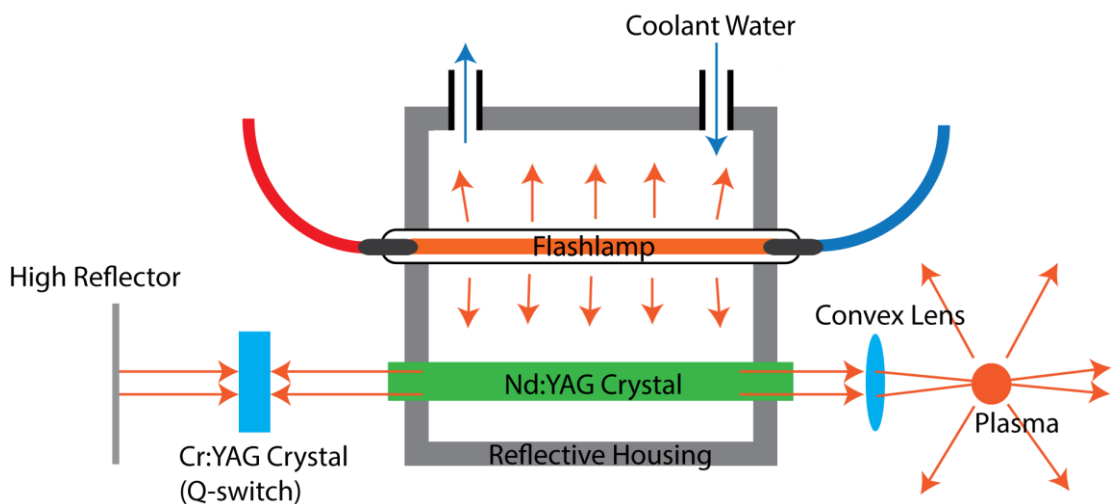


**Figure 37.** The main components within a Q-switched laser. The flashlamp excites the Nd:YAG crystal causing spontaneous emission to occur. At the point of population inversion, the Q-switch is saturated and transparent. This allows light to reflect back through the Nd:YAG crystal from the high reflector causing stimulated emission and lasing to occur.

Q-switching ensures that lasing only takes place when the electrons in the lasing medium are at maximum population inversion. By using a medium such as solid state ND:YAG whose lasing atoms (in this case Neodymium atoms) have a large stimulated emission cross section of interaction (in other words a



high *gain* medium), the sudden change in Q-factor of the cavity produces a very intense pulse of coherent light.

Q-switching can be done both “actively” and “passively”. Active Q switches are externally controllable mechanical devices such as a chopper wheel, or electronic devices, such as a Pockle’s cell. Electronically controlled active Q-switches generally allow for better control and faster switching from low to high Q, but are often much more expensive than mechanical devices or passive Q-switches. A Passive Q-switch is usually a material that is a saturable absorber of light at the lasing wavelength. A saturable absorber is absorbent until the light intensity reaches some threshold value, usually proportional to the width of the absorbent material, at which point the absorber is saturated and becomes transmissive. Suitable saturable absorbers can be dyes, semiconductor materials or ion doped crystals. The doped crystal Cr:YAG is commonly used as the passive Q-switch in Nd:YAG lasers as it is a saturable absorber at the lasing wavelength: 1064 nm. It has a recovery time of 8 ns from fully transmissive to fully absorbent after an impinging light beam has been turned off.

Solid state Q-switched lasers such as the Nd:YAG are routinely employed to generate plasmas in the technique of LIBS, used to determine the elemental composition of a compound. In LIBS, a sample (often in the solid state but can also be liquid or gaseous) is heated to a plasma state by a focused pulse of laser energy. The light emitted from the plasma is then analysed by a spectrograph. The spectrum obtained is the sum of two components: the continuous bremsstrahlung emission from the thermal unbound electrons within the plasma and line emission obtained from the transitions of electrons between bound states. The line emission spectrum is characteristic of the elemental composition of the sample and can be deconvoluted to determine the relative proportions of each element present in the sample

In LIBS, the laser and optics are optimised to reduce the amount of continuous background emission, as this masks the line emission spectrum. The intensity of the background spectrum is temperature dependant via the Stefan-

Boltzmann law and is independent of sample composition. By applying the minimum amount of energy to a sample that is required to achieve a plasma state, the amount of energy is available for bremsstrahlung absorption (and subsequent blackbody radiation) by free thermal electrons is also minimised. Applying the minimum laser power required to ionise to a sample maximises the line emission to continuum emission ratio. For a plasma to be used as a broadband light source it is the continuum emission that needs to be maximised and the line emission that needs to be attenuated. One simple way to achieve this is to apply the maximum possible amount of energy during plasma generation. In this way, more energy is available for thermally heating the free electrons that are present in the plasma. This leads to an increase in plasma temperature and more intense continuum emission. The line emission spectra of the medium in which the plasma is generated will always be present but, as the temperature of the plasma increases, the line emission to continuum emission ratio becomes smaller.

Q-switched lasers are routinely used for tattoo removal. Tattoos consist of pigment particles embedded in the dermis of the skin. These particles are too large to be removed by the body's normal regeneration processes. By applying short but powerful pulses of light at the absorption wavelengths of the pigment, the particles rapidly heat up and fragment, allowing them to be removed from the body. The most commonly used laser for the removal of tattoos is also the Q-switched Nd:YAG laser emitting at 1064 nm. At this wavelength, melanin and haemoglobin are poor absorbers and so this laser is often the laser of choice for tattoo removal. Nd:YAG lasers are also one of the most commonly used lasers in many publications concerning laser induced plasmas (Davis et al., 1991, Harilal, 2004, Sircar et al., 1996). Owing to its use in tattoo removal, Q-switched Nd:YAG laser machines are widely available and relatively cheap. The manufacturers state that these lasers are able to output a 6 mm wide beam of up to 1 J in 9 ns. These lasers are economical but are powerful enough to generate laser induced plasmas in air. They also come supplied with a frequency doubling crystal to convert a fraction of the beam to 532 nm. This is useful for visualisation of the beam. As of 2013/14, tattoo removal machines manufactured in China are available for around £1000. Quotations obtained

from manufacturers of Q-switched Nd:YAG lasers for use in scientific research were much more expensive. For the manufacture of a prototype device it was decided to purchase and modify a tattoo removal machine. The tattoo removal machine that was purchased was the ML-LASER-YB5 Nd:YAG Laser Treatment System from Wei Fang Ming Liang Electronics Company Ltd. (Figure 38).



**Figure 38.** The tattoo removal machine showing the housing for the electronics and water pump. The foot pedal and laser gun are on the right.

The manufacturer states that the specifications of the laser are:

Laser Type: Q-switched Nd:YAG  
Laser Wavelength:  $\lambda=1064$  and  $532$  nm  
Max Energy:  $800$  mJ  
Pulse Width:  $<10$  ns  
Pulse Repetition Frequency:  $1-6$  Hz  
Laser Spot diameter:  $3$  mm  
Power Supply:  $220$  V,  $50$  Hz,  $6$  A  
Environment Temperature:  $5-40$  °C  
Relative Humidity:  $\leq 70$  %

Cooling System: Water cooled with airflow cooling

The machine consists of a large plastic housing that is connected via a tube to a hand held “gun” that contains the laser cavity (Figure 39). The large plastic housing contains the laser pumping electronics, as well as a water pump for the cooling system. A digital control panel on the front of the housing allows adjustment of the pulse energy and the repetition rate, and also displays a readout of the water temperature as well as the number of pulses administered during the session. The tube joining the gun to the main housing contains the live and ground wires to trigger the laser pumping flash lamp inside the gun and also inlet and outlet tubes to circulate the water. The machine is switched on by a key and fired by the depression of the foot pedal switch.

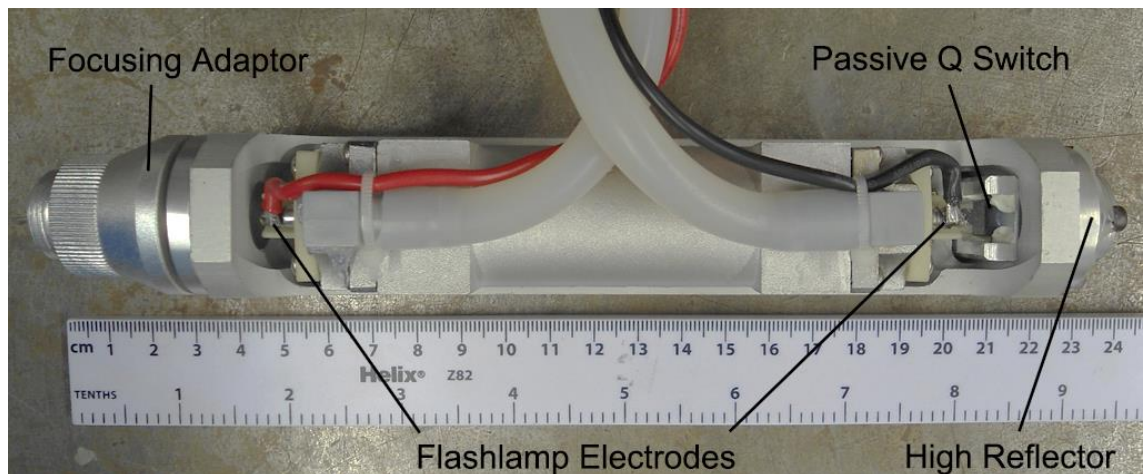


**Figure 39.** The handheld laser “gun” and its internal components.

Inside the handheld “gun” are the main components of the laser (Figure 39). This instrument utilises a passive Q-switch in the form of a small crystal of Cr:YAG cut to the right length to allow lasing at the point of maximum population inversion. The lasing medium is 10 cm, 6 mm diameter rod of Nd:YAG crystal. This is a crystal of Yttrium Aluminium Garnet doped with around 1 % trivalent Neodymium or  $\text{Nd}^{3+}$ . It is the Neodymium atoms that are excited by the pumping flashlamp and provide the lasing activity of the crystal. The excitation of the Neodymium atoms by the flash lamp and their subsequent de-excitation is a four level system (Figure 40).

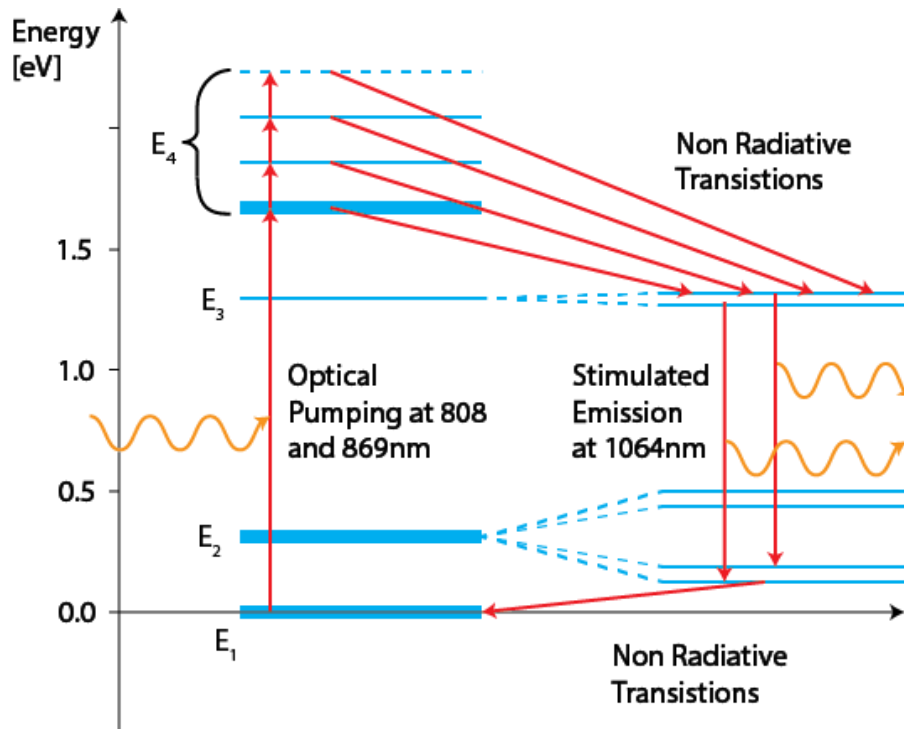


**Figure 40.** The energy level diagram of Neodymium atoms in an Nd:YAG laser. Optical pumping from  $E_1$  to  $E_4$  is achieved through the absorption of photons emitted from the flashlamp. Non-radiative transitions lose energy through the thermal heating of the Nd:YAG crystal.

Pumping the crystal via the flashlamp excites electrons in the  $E_1$  orbital to the  $E_4$  orbitals. Stimulated emission occurs at 1064 nm and is the fundamental mode of the laser. In  $\text{Nd}^{3+}$  other emission lines occur 946, 1123, 1319, 1338, 1415 and 1444 nm but these are very weak compared to the fundamental transition at 1064 nm and can be ignored. The non-radiative transitions from  $E_4$  to  $E_3$  and from  $E_2$  to  $E_1$ , lose energy via thermal heating of the laser rod. For this reason, the Nd:YAG crystal heats up during laser operation. Excessive heating results in warping, possible damage to the crystal and thermal lensing of the laser light (Koechner, 1970). To cool the lasing crystal, the instrument must be filled to the required level with deionised water that circulates around the crystal and flash lamp. Water flowing around the flash lamp prolongs its lifetime. To prevent damage to the laser, the machine automatically shuts off if the water temperature exceeds  $50^\circ\text{C}$ .

The efficiency, more specifically the gain (amplification by stimulated emission per unit length) of the laser, is sensitive to temperature. This is because the rate of non-radiative transitions is temperature dependant. Stimulated emission from  $E_3$  to  $E_2$  can occur only if there is an orbital available to receive the electron. The population of the energy level  $E_2$  must therefore be maintained at a low level in order for a high rate of stimulated emission from  $E_3$  to  $E_2$  to occur. If the temperature of the lasing crystal increases, the rate of non-radiative transitions from  $E_2$  to  $E_1$  decreases, leading to an increase in the population of  $E_2$  and a subsequent reduction in the rate of stimulated emission from  $E_3$  to  $E_2$ . This decrease in the likelihood of stimulated emission can be modelled as a decrease in the stimulated emission cross section of the Neodymium atoms (Figure 41). At high temperatures ( $>40^\circ\text{C}$ ), when using a frequency doubler and concave lens to visualise the beam, it was noticed that the centre of the beam darkens, indicating a loss of lasing activity along the central axis of the crystal. It is thought that this is due to the lack of adequate cooling within the crystal and the subsequent overpopulation of the  $E_2$  energy level, preventing emission from the  $E_3$  level. It is therefore important to ensure that the cooling water is not overheating and is circulating sufficiently to maintain a high laser output and prevent damage to the crystal.

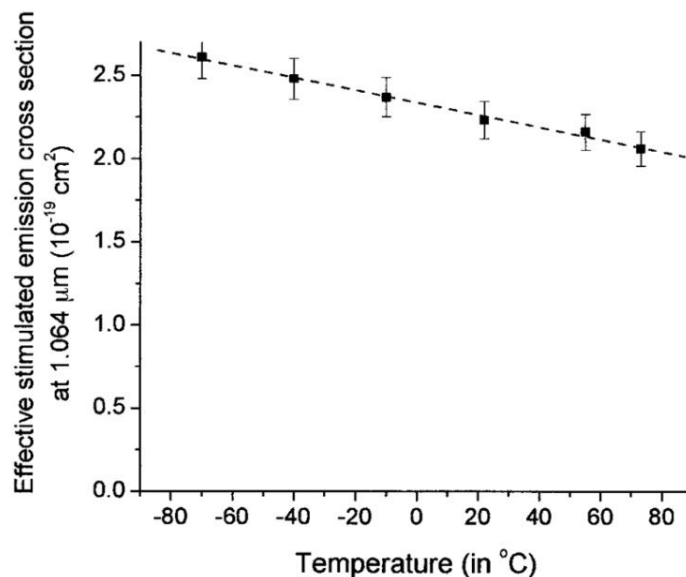


**Figure 41.** Peak effective stimulated emission cross section at  $\lambda=1064\text{nm}$  of 1% Nd:YAG as a function of temperature. The dashed line is a linear fit that gives  $\sigma_{\text{eff}} = (2.35 - 3.7 \times 10^{-3}T) \times 10^{-19} \text{ cm}^2$  where  $T$  is in  $^\circ\text{C}$ . Reproduced from (Rapaport et al., 2002).

It is interesting to note that, unlike most conventional lasers, this laser does not possess an optical coupler. An optical coupler is a semi-reflective mirror which allows some of the lasing light to exit the cavity as the beam, but also reflects light back through the crystal. In most lasers, an optical coupler increases the path length of light passing through the gain medium by providing feedback in the form of an optical cavity. The absence of an optical coupler prevents standing wave formation in the optical cavity between the high reflector and the optical coupler. In this Nd:YAG laser, an increase in path length is not required due to the large cross section of interaction of Neodymium atoms and the resultant high gain. Light at 1064nm only requires one pass through the Nd:YAG crystal in order for stimulated emission of the vast majority of Neodymium atoms and for high intensity lasing to occur. In fact, the addition of an optical coupler probably leads to a reduction in the peak emitted power, due to a broadening of the pulse length, reabsorption of laser light due to excitation from the E<sub>2</sub> to E<sub>3</sub> energy levels and thermal losses due to imperfections in the mirrors. The absence of an optical coupler also prevents higher modes from forming in the optical cavity with the result that, unless a frequency multiplier is used, only the fundamental mode at 1064 nm is emitted from the laser.

The most important parameter of the laser for the generation of plasmas is the pulse peak power. The pulse peak power must be large enough to obtain the required threshold intensity for breakdown. The peak power P of a pulsed laser can be calculated from pulse duration  $\tau$  and the total energy in the pulse E. The pulse duration is defined as the FWHM time of one pulse. If a Gaussian shaped pulse is assumed:

$$Peak\ power \approx 0.94 \frac{E}{\tau} \quad \text{Equation 15}$$

If the pulse is not Gaussian, the factor of 0.94 needs to be adjusted. The greater the pulse peak power the greater the intensity obtained at the focal point of the focusing lens. The peak pulse power in combination with the focal

length of the lens and the laser beam diameter can be used to calculate the intensity at the focal point (see next section).

To determine pulse peak power of the Chinese tattoo removal laser, the pulse energy and the pulse width were both measured. The pulse width was measured with a Thorlabs DET10A silicon photodiode, rise time 1 ns, and a Tektronix TDS3032 digital oscilloscope with 300 MHz bandwidth (yielding a rise time of ~1 ns). The measured pulse width was 11.5 ns. The laser pulse energy was measured with a Molectron EM400 digital joulemeter equipped with a J25 probe. The measured pulse energy was 280 mj. This gives a peak power of  $2.289 \times 10^7$  W.

It is obvious that using the laser at its maximum power, maximises the peak power and improves the likelihood of breakdown occurring. The effect of increasing the laser power also increases the resulting plasma's electron temperatures and densities as can be seen in Figure 42. The position of the plasma also shifts towards the direction of the incoming beam as laser power is increased. It follows from Figure 42 that the location along the optical axis of highest plasma emission is likely to be slightly closer to the focusing lens than exactly at the focal point.



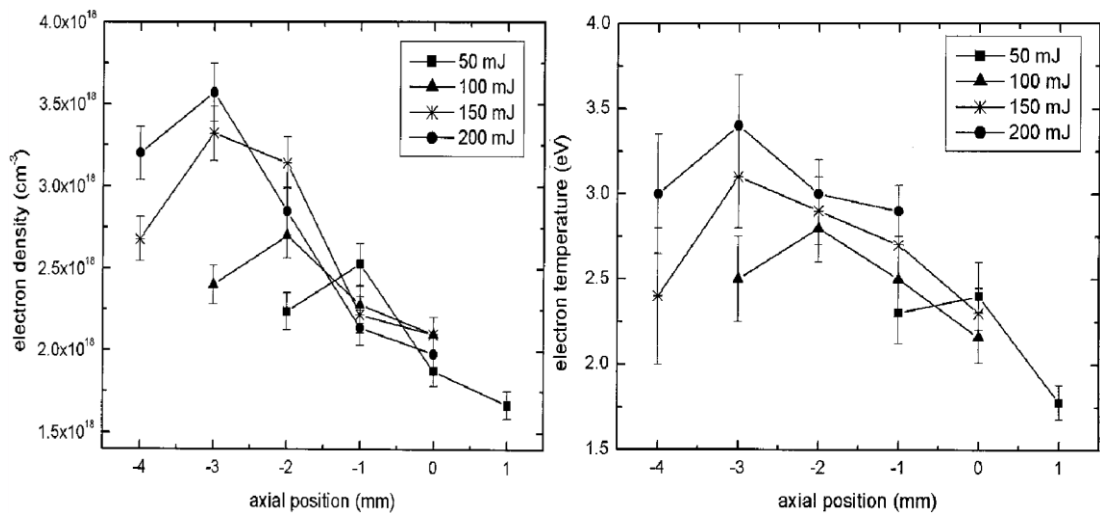


**Figure 42.** Electron temperature and density dependence on laser pulse energy. The plasma is created with a frequency doubled Nd:YAG laser at 532 nm with a pulse width of 8 ns in argon at 1 atm. The lens has a focal length of 75 mm. The zero position on the x axis corresponds to the focal length with the negative positions closer to the focusing lens.

Reproduced from (Harilal, 2004).

## 2.4 Focusing Optics for the Generation of Laser Induced Plasma

The tattoo removal machine is supplied with two different adaptors, intended for the removal of different coloured inks from skin. The first consists of a 10 cm focal length plano-convex lens with an anti-reflective coating at 1064 nm. The second consists of a frequency doubling crystal followed by a 10 cm focal length plano-convex lens with an anti-reflective at 532 nm. The frequency doubler (a crystal of Lithium triborate ( $\text{LiB}_3\text{O}_5$ ), converts some of the emitted 1064nm laser light to 532 nm, enabling it to be seen by the naked eye. Using these adaptors in air, plasmas were not formed at the focal point, although erratic plasmas were observed at various points along the beam. These erratic plasmas were likely to have been caused by the laser light impinging upon dust present in the air, causing local heating and ionisation. It was therefore necessary to identify optics better suited to the reliable production of plasmas.

To be of practical use as a spectroscopic light source, a laser induced plasma must possess the following properties. From these, practical considerations can also be derived:

1. Reliable plasma formation per laser pulse. Because laser induced plasmas are pulsed light sources, spectra can only be recorded during the interval of the pulse. Over a period of time, many spectra will be recorded which can then be analysed to yield useful physical information such as how the transmission/absorbance changes over time. If during a pulse the laser fires but does not induce a plasma in the medium, a blank spectrum will be recorded which will contain only noise and no useful information. During the analysis, the presence of blank spectra may cause problems. It is possible to remove blank spectra using a checking algorithm or for the user to do it manually, but this complicates the analysis and leads to incomplete data sets. It would be much better if blank frames were not generated by choosing the best possible setup for reliable plasma production.
2. The plasma emission needs to be above a certain minimum intensity. If the light emitted from the plasma is to be collimated, split using a beam splitter, passed through a sample and recorded across a broad range of wavelengths, the light intensity should not be too low so that a good SNRs can be maintained. If the emission intensity is too high, the light can always be attenuated by adjusting the collection and collimation optics. It is therefore necessary to try to generate as bright a plasma as possible.
3. The plasma should be induced at the same location during each pulse. During the initial testing of laser focusing optics, it was noticed that at low laser power and/or longer focal length lenses, plasmas were being produced along the beam with high positional variance. It was thought that this is due to the fact that the intensity at the focal point is too low to induce plasmas in clean air but high enough to induce plasmas by heating dust particles that are present in the beam. Other investigators have noticed a reduction in the required intensity to induce plasmas if dust particles are present in the beam (Lencioni, 1974, Lencioni, 1973). This mechanism of plasma production is not useful for a light source because it is impossible to collimate light from sources that are continually changing location between pulses. By reliably inducing plasmas at the same location for each pulse, the collimation of emitted light is not only greatly simplified but, the attainable intensity of the collimated beam should be maximised because light from the hottest part of the plasma can be captured.

The plasma that forms upon reaching the breakdown threshold is opaque to laser light, due to inverse bremsstrahlung absorbance by free electrons. In a laser pulse that is intense enough to induce breakdown, approximately 90% of the energy in the pulse is absorbed by the plasma with around 10% being transmitted straight through (Chen et al., 2000). The opacity of the plasma to the impinging laser produces localised heating at the surface of the plasma, resulting in the expansion of the plasma in the direction of the incoming laser beam (Hanafi et al., 2000). As was noted from Figure 42, as the laser power increases, breakdown occurs at a distance along the optical axis closer to the focusing lens than the focal length. The growth of the plasma spark may be an important factor to take into account when designing an optical setup for the capture of the emitted light because the plasma may not necessarily be spherical and the most intense emission may not necessarily be at the focal point.

In order to meet the above criterion for a laser induced plasma spectrometer, it is necessary to reliably generate a minimum intensity of light at the focal point of the lens. This minimum intensity is known as the breakdown threshold intensity. The value of the breakdown threshold (in SI units of  $\text{Js}^{-1}\text{m}^{-2}$ ), in different media and under various conditions, depends on several factors. Some of these factors are identified and discussed in the next chapter.

Breakdown thresholds are determined experimentally, using the peak pulse power found using Equation 15, and from the diameter of the beam at the focal point, using the Raleigh criterion for the resolving power of a diffraction limited lens:

$$D_1 \approx 1.22\lambda \frac{f}{D_2} \quad \text{Equation 16}$$

$D_1$  is the diameter of the beam at the focal point,  $f$  is the focal length,  $\lambda$  is the laser wavelength and  $D_2$  is the diameter of the laser beam before focusing (Singh and Khakur, 2007). The beam is assumed to have a Gaussian profile with  $D_2$  measured at the point of  $1/e^2$  of the peak intensity. Equation 16 shows

that it is impossible to focus a beam to an infinite point and also that shorter focal length lenses and wider initial beam diameters produce smaller diameters at the focal point. Therefore, by employing short focal length lenses and lasers with wide beams (and/or beam expanding optics), greater light intensities can be produced at the focal point.

The intensity obtained at the focal point is calculated from:

$$\begin{aligned} \text{Intensity at focal point } I &= \frac{\text{Peak Pulse Power at Breakdown}}{\text{Area of Beam at Focal Point}} = \frac{P}{\pi \left(\frac{D_1}{2}\right)^2} \\ &= \frac{2.527E}{\pi\tau} \left(\frac{D_2}{\lambda f}\right)^2 \quad \text{Equation 17} \end{aligned}$$

The above equation shows that the maximum intensity is inversely proportional to the square of the focusing lens focal length and is proportional to the square of the beam diameter before focusing. It is somewhat counter intuitively that a wider beam can be focused through a smaller area at the focal point. Therefore, the intensity obtained at the focal point can be maximised by using a short a focal length lens and by expanding the beam if possible, using a beam expander, before focusing.

If the breakdown threshold is known, as well as the pulse energy, pulse width and beam diameter, the above equation can be rearranged to calculate the longest focal length lens that is needed to obtain the required intensity. The breakdown threshold at 1064 nm for air at atmospheric pressure is approximately  $10^{12} \text{ Wcm}^{-2}$  (Lencioni, 1974). The tattoo removal laser has a pulse energy of 280 mJ, a pulse width of 11.5 ns of  $2.289 \times 10^7 \text{ W}$  and a beam width of 3 mm:

$$f = \frac{D_2}{\lambda} \sqrt{\frac{2.527E}{I\pi\tau}} = \frac{0.003}{1064 \times 10^{-9}} \sqrt{\frac{2.527 \times 0.28}{\pi \times 10^{16} \times 11.5 \times 10^{-9}}} = 12.5 \text{ cm}$$

Therefore, by employing lenses with focal lengths of a few centimetres, the required intensity at the focal point should be obtained. However, the 10 cm

lenses supplied with the machine for the purpose of tattoo removal do not reliably induce plasma in air at the focal point. Small intermittent plasmas are observed at various points along the beam. It is probable that other factors, such as the practicalities of lens alignment and other factors that are discussed in the next chapter, reduce the irradiance at the focal point.

Lenses for use with pulsed Nd:YAG lasers need to be made of a material that has a high transmission at 1064nm. Optics for pulsed laser focusing also need to have a high damage threshold. At very high intensities, lens material can undergo dielectric breakdown. Two materials that are relatively cheap and have a high transmission at 1064nm are N-SF11 and N-BK7. If a more durable lens that has a higher breakdown intensity is required, UV fused silica can be used. UV fused silica is a more expensive but a more durable lens material. The transmission properties of these lens materials is shown in Figure 43.

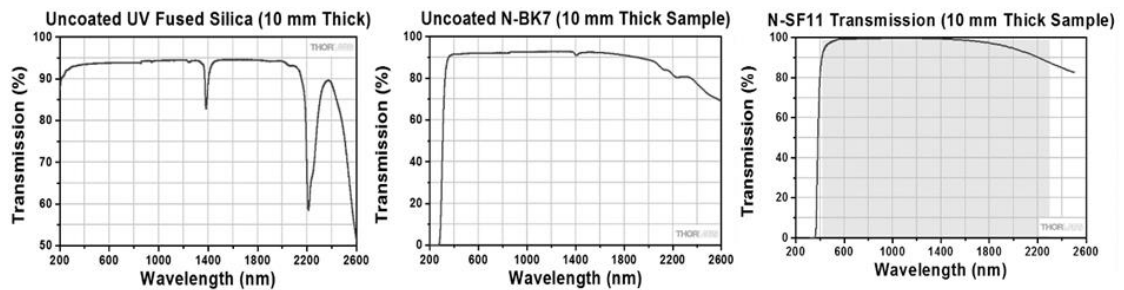


**Figure 43.** The transmission properties of UV fused silica, N-BK7 and N-SF11. Source: [www.Thorlabs.com](http://www.Thorlabs.com)

From Equation 17, it can also be seen that expanding the beam before focusing (increasing  $D_2$  in the above equations) will reduce the cross sectional area at the waist of the beam, therefore increasing the irradiance at the focal point. If beam expanding optics were used, they would need to take the form of a Galilean beam expander (shown in Figure 44). In a Galilean expander, the light beam is expanded by passing it through concave lens, before collimation and focusing by two larger convex lenses. A Kaplerian beam expander cannot be used as the laser light is focused to a point before it is expanded, causing premature plasma generation in the expander. Beam expanding optics offer the possibility of one or two orders of magnitude higher focal intensities but add expense and complexity to the prototype. If plasmas can be reliably

induced using a single lens, beam expanding optics will not be required. In practice, the theoretically intensities obtainable using beam expanders are extremely difficult to produce. Lenses are not perfectly transmissive and may be imperfectly aligned or suffer from aberrations, leading to losses in intensity that become significant as more lenses are employed.

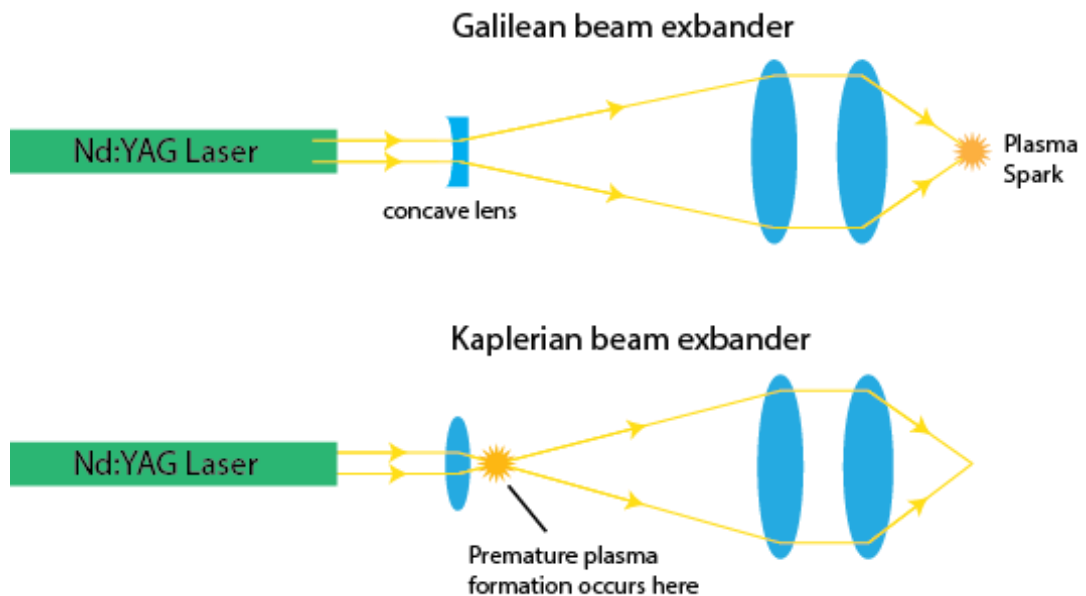


**Figure 44.** Galilean and Keplerian beam expanders. The Galilean design uses a concave lens to expand the beam. The Keplerian design uses a convex lens to expand the beam but is unsuitable for use with pulsed lasers.

It was clear from Equation 17 that the simplest way to achieve a high irradiance at the focal point was to use as short a focal length lens as possible. A 2 cm focal length lens (Thorlabs LA4647, UV Fused silica plano-convex lens, diameter 12.5mm) was finally chosen to focus the laser. This lens was found to be the most reliable at generating plasmas compared to lenses of longer focal lengths. The results of lens testing and can be found in the next chapter.

## 2.5 Optics for the Capture and Collimation of Laser Induced Plasma Light

Light emitted from a spectroscopic light source must be captured and collimated into a beam before it is passed through a sample. A collimated beam is much easier to manipulate with, beam expanding/contracting optics and other optical components. Ideally, the beam must be perfectly collimated (perfectly parallel rays with no divergence) so that the rays in the beam all pass through a sample at the same angle. Beam collimation can be achieved with a variety of different optical arrangements but generally consist of a parabolic mirror or plano-convex lens with the light source or an image of the light source at its focus (Figure 45). Plano-convex lenses are designed to focus parallel rays to a point and visa-versa. Light from the point source (image or real) is bent by the mirror or lens to create a parallel beam which replicates the light emitted from a source at infinity with no parallax.

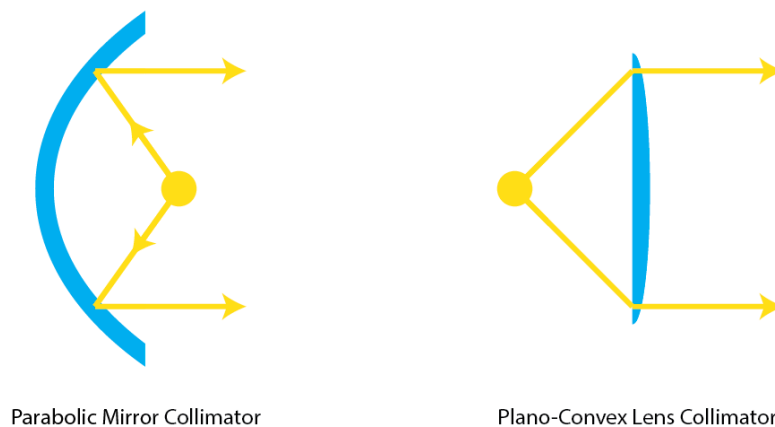


**Figure 45.** *The two types of common optical collimator.*

The simple reflector or lens collimators in Figure 45 work well as long as the light is emitted from a point source. It is actually only possible to perfectly collimate light from a point source but in practice, no light source is a point source, as all sources emit from a surface that have some dimension(s) of size. For a laser induced plasma in air this size is in the millimetre range. Assuming the plasma to be approximately spherical, light from the top of the source will take a different route to light from the bottom of the source with the effect that

these rays will not be parallel as they emerge from the collimating lens or mirror (Figure 46).

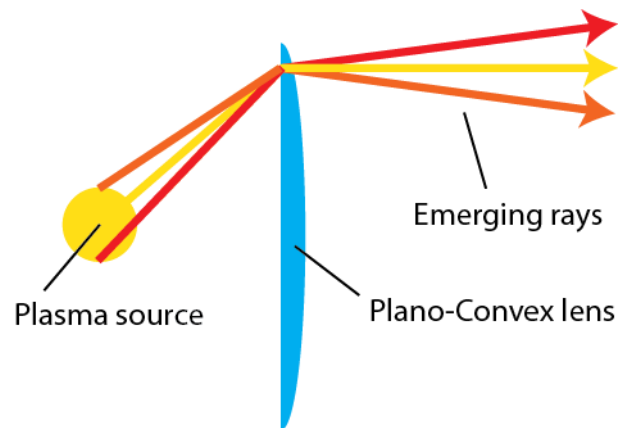


**Figure 46.** The effect of attempting to collimate a non-point light source. The rays from the top of the source travel along a different path to rays from the bottom of the source. The result is that non parallel rays emerge from the collimating lens.

The solution (compromise) is to focus the light emitted from the plasma through a small pinhole size aperture. This simulates a point source, the light emitted from which can easily be collimated. Passing the light through a pinhole is achieved by focusing the (roughly) parallel rays onto a pinhole placed at the focal point of the focusing lens. A real, inverted and smaller image of the plasma is formed at the pinhole. The position of the pinhole is then adjusted in the directions perpendicular to the optical axis so that brightest part of the image of the plasma passes through the hole. Possible arrangements for pinhole collimators are shown in Figure 47.



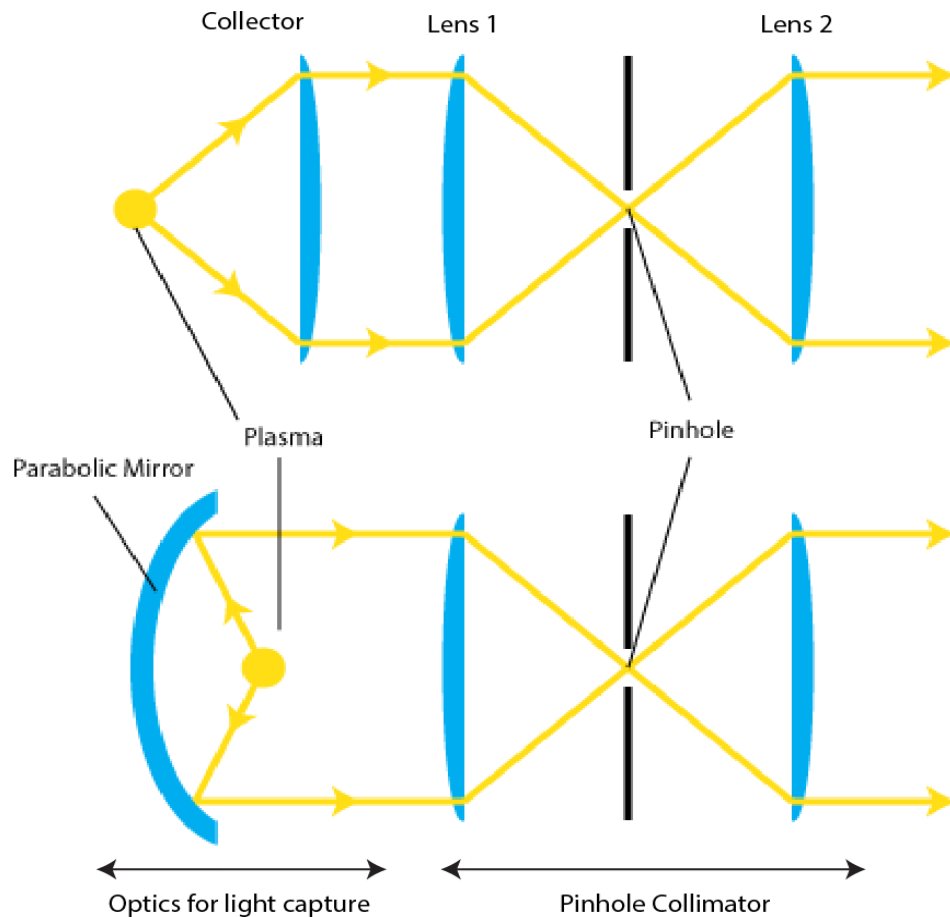


**Figure 47.** Possible optical arrangements for the capture and collimation of light emitted from a plasma. Both arrangements contain either a collector mirror or lens for light capture and a pinhole collimator. An image of the plasma is formed at the position of the pinhole. By adjusting the position of the pinhole so that the brightest part of the image falls on the hole, the maximum amount of light can be collimated.

Following collection, the light rays entering Lens 1 in Figure 47 are parallel, replicating the rays emitted from an object at infinity. These parallel rays, when focused through a convex lens, form a real inverted image of the object at the focal point of the lens. By positioning a pinhole at the brightest part of the image, the greatest amount of light passes through. Rays that are not parallel to the optical axis before entering Lens 1 are not focused onto the pinhole and so are blocked. A larger diameter pinhole allows more light to pass through but also allows more un-collimated light to pass. The size of the pinhole is therefore a compromise between beam collimation and intensity. The pinhole that is used in the collimator is a Thorlabs ID8/M aperture with an adjustable hole size of between 1-8 mm. The testing of optical arrangements used

commercially available optical elements that were mounted on an anodised aluminium optical breadboard with a grid of M6 threaded holes every 2.5cm

Initial testing with both types of collector in Figure 47 found that it was much easier to adjust a parabolic mirror, so that the plasma was at the focal point, rather than a plano-convex lens. A circle of reflected light from the mirror can be seen by placing a piece of paper in front of Lens 1. The circle of light should be the same diameter as the mirror (25.4 mm) if the plasma is at the focal point of the mirror. The mirror can be relatively easily adjusted so that reflected light was roughly parallel before passing through the Lens 1 and focusing at the pinhole. The relative ease with which a parabolic mirror collector could be adjusted was the major reason why a parabolic collector was preferred over lens collection.

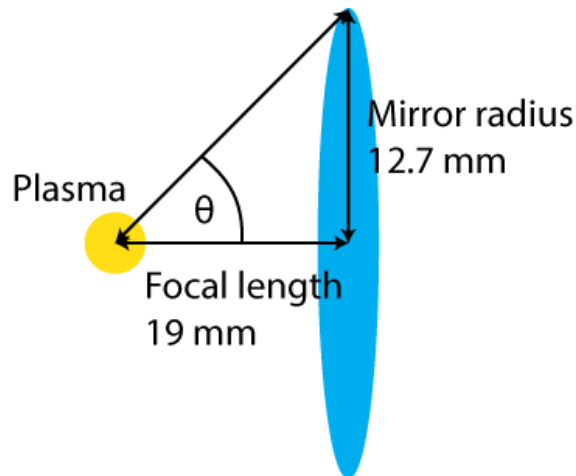


**Figure 48.** A diagram of the angle subtended by the Thorlabs CM254-019-F01 parabolic mirror. The angle  $\theta$  is  $\arctan \frac{12.7}{19} = 0.59$  radians.

To capture the maximum amount of light possible, the parabolic mirror needed to subtend the maximum solid angle possible from the centre of the plasma, when the plasma is at the focal point of the mirror (Figure 48). The subtended angle of several mirrors were investigated and the most suitable one with the largest subtended angle (of 0.59 radians) was identified as the Thorlabs CM254-019-F01, which is a 1 inch diameter parabolic aluminium mirror with a focal length of 19 mm. This mirror is coated to enhance its reflectivity below 450 nm (Figure 49). Figure 50 shows the plasma at the focal points of the laser focusing plano-convex lens and the parabolic collimating mirror.

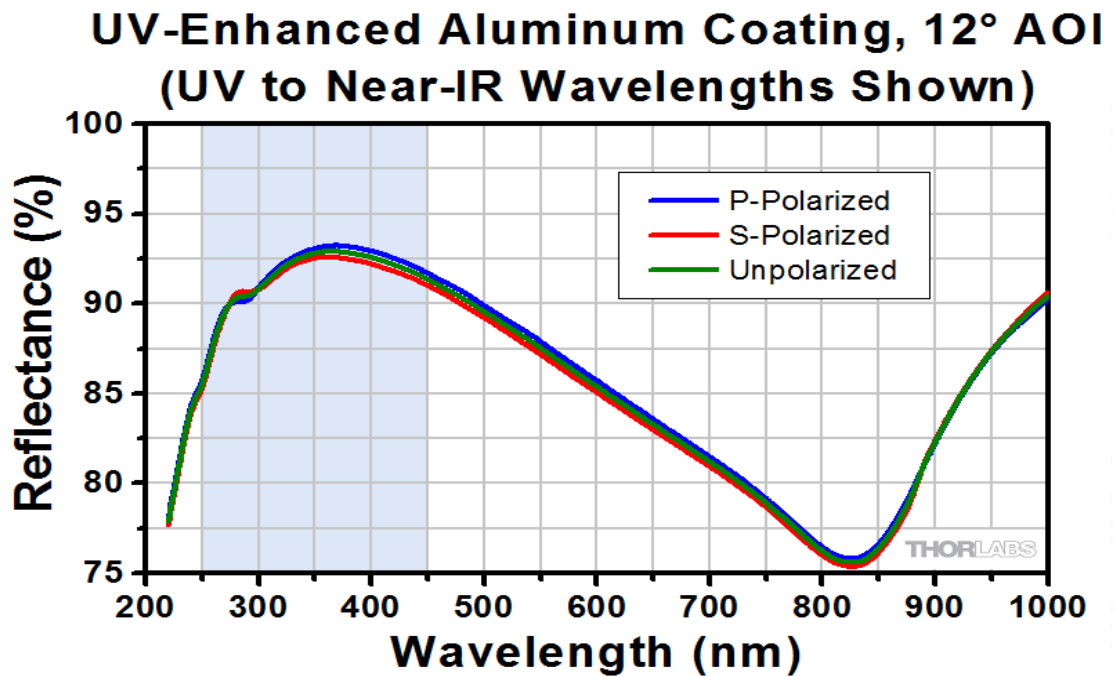


Figure 49. The reflective characteristics of the CM254-019-F01 parabolic lens. Reproduced from [www.Thorlabs.com](http://www.Thorlabs.com).

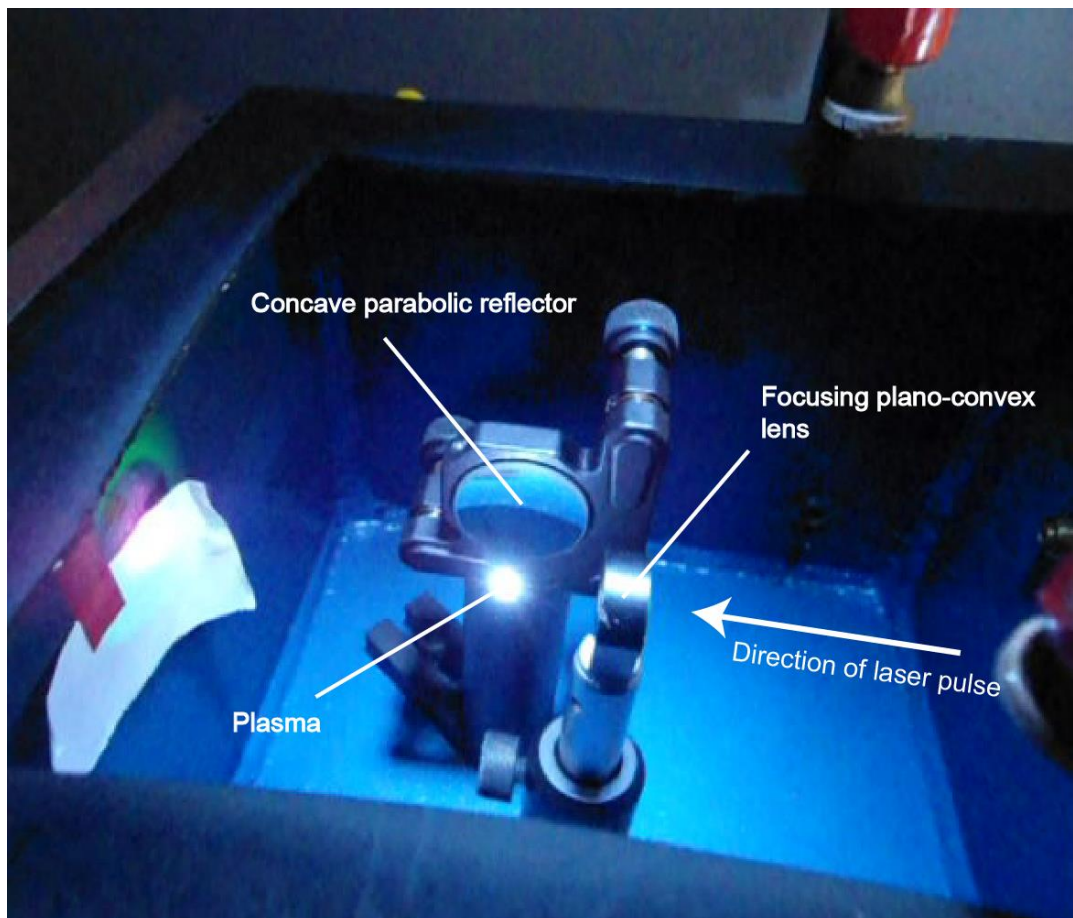


Figure 50. A laser induced plasma at the focal points of the focusing lens and the parabolic capture mirror.

The plano-convex lenses in the collimator needed to be the same diameter as the parabolic mirror (25.4 mm). The lenses also needed to be of the shortest possible focal length so that the smallest possible image could be focused at the position of the pinhole. By forming a very small image of the plasma at the pinhole, the maximum amount of light emitted from the plasma can be collimated. The size of an image formed at the focal point by an object at infinity is proportional to the focal length of the lens. The shortest focal length lens available with a 25.4 mm diameter is the Thorlabs LA4052 UV fused silica plano-convex lens with a focal length of 35 mm. Two of these lenses facing in opposite directions were used in the pinhole collimator.

For light detection and analysis, a Thorlabs CCS200 spectrometer was used. This spectrometer, by far the most expensive piece of equipment used in this project (cost £2000, August 2012), was able to measure and record the intensity of light, as a function of wavelength, between 200 and 1000 nm. The spectrometer records (integrates) the intensity of light, at a particular wavelength, within a time interval set by the experimenter. The intensity at any wavelength is then output as a value between zero and one. The intensities are output to the screen to show spectra in real time and/or output as a .csv file. The absolute intensities (in  $\text{Wm}^{-2}$  per unit wavelength) measured by the spectrometer are difficult to determine but for absorbance measurements it is not necessary to determine the absolute spectral intensities. To determine the absorbance of a sample, only the relative intensities before and after the sample need to be known.

In normal operating mode, the spectrometer records the intensities of consecutive time intervals or triggered time intervals. The trigger is provided by a 5V input pulse through a BNC cable and connector. The ability to trigger the spectrometer is essential for the recording of intensities from pulsed light sources. The specifications of the spectrometer are:

Wavelength Range: 200-1000 nm

Spectral Resolution: <2 nm FWHM at  $\lambda=633$  nm

Slit Size: 20 $\mu\text{m}$   $\times$  2 mm

Grating: 600 lines/mm, 800 mm Blaze  
CCD Pixel Number: 3648  
CCD Resolution: 6 px/nm  
Integration Time: 10  $\mu$ s – 10 s  
Max Scan Rate: 200 Scans/s  
S/N Ratio:  $\leq$ 2000:1  
External Trigger Connector: SMA 905  
Trigger Input: SMB  
Trigger Signal: TTL  
Trigger Max Frequency: 100 Hz  
Minimum Trigger Pulse Length: 0.5  $\mu$ s  
Trigger Delay: 8.125  $\mu$ s  $\pm$  125 ns

The light input to the spectrometer was via an optic fibre (Thorlabs BFH22-200-030-SMA-1M 1 m SMA MMF Patch cable, 200  $\mu$ m/0.22 NA). The other end of the fibre is coupled to a fibre port on an optical post that is positioned in-line with the collimated beam. The collimated beam was much wider than the width of the optical fibre port and so a short focal length plano-convex lens (Thorlabs LA4936 UV fused silica plano-convex lens, diameter 12.6 mm, focal length 30 mm) was used to focus the beam onto the port. These optics are shown in Figure 51.

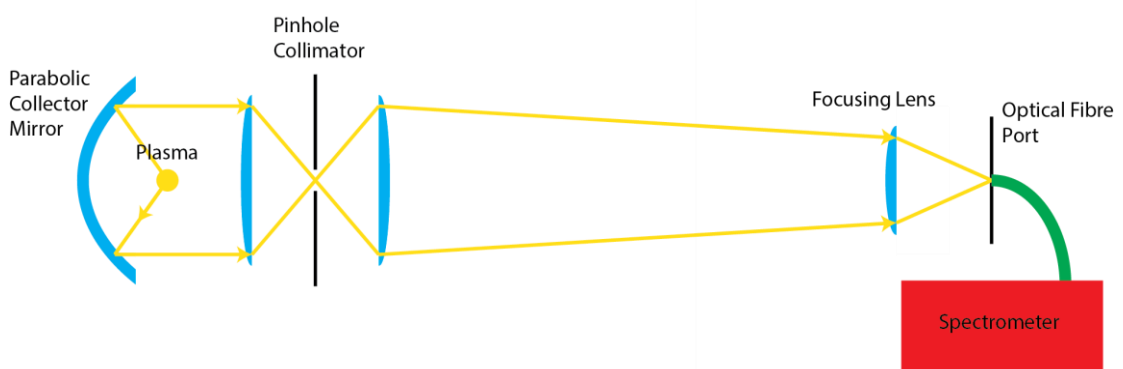


**Figure 51.** A schematic diagram of the optical apparatus for the capture, collimation and analysis of plasma light.

The intensity of light entering the spectrometer can be intensified or attenuated by adjusting the distance of the fibre port from its focusing lens. Adjusting the

position of the optical port relative to the focusing lens was the main method by which the intensity was adjusted to within the working range of the spectrometer. Modern broadband detectors (often a grating with a CCD array detector) have a maximum intensity that can be read by a pixel in the CCD. If the intensity at a particular wavelength is too high for the detector (too many photons hitting the pixel within the integration time set by the user), the spectrometer records the intensity as the maximum value of one. If the true value of the intensity is greater than 1, any measurements and calculations at this wavelength will be incorrect. This loss of correct intensity values leads to large errors in later calculations of sample absorbance. Too little light and the signal to noise ratio of the data is affected. Therefore, the position of the fibre optic port must be set so that the intensity is not too high or low. The aim of adjusting the position of the fibre port was to maximise the total spectral power without overloading the CCD. This can be difficult if strong line emission is present.

The focusing lens must be positioned first before the location of the optical port is set. The distance from the second collimator lens to the fibre port focusing lens must be maximised for the beam to be as parallel as possible between these components. In practice, this distance was dictated by the length of the optical breadboard, as all of the optical components in Figure 51 must fit on the breadboard. Once all of the components were positioned approximately, the second collimator lens was adjusted so that an image of the pinhole was formed at the fibre port focusing lens. This image was observed by placing a piece of white paper over the lens. When focused, the image of the pinhole was slightly smaller than the diameter of the focusing lens (~6 mm). The position of the optical fibre port was then adjusted so that the intensity of light entering the port was within the working range of the spectrometer.

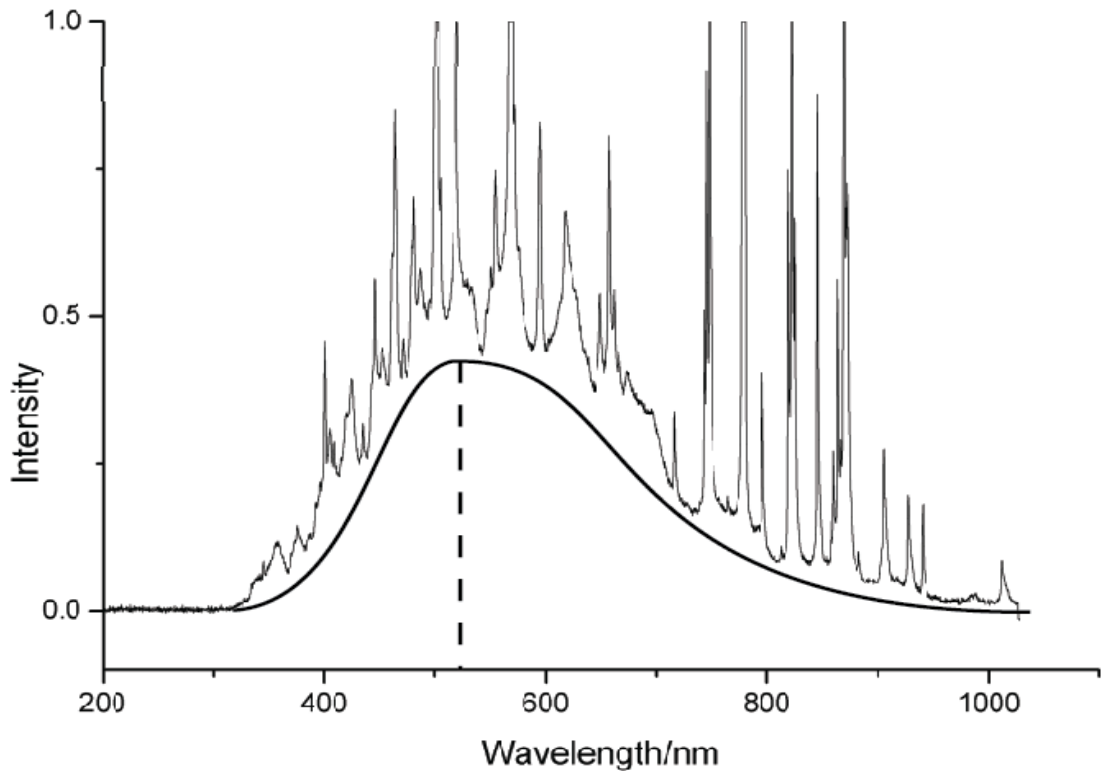


**Figure 52.** The spectrum of a laser induced plasma in air at atmospheric pressure fitted with an approximate blackbody curve. The wavelength of maximum intensity is approximately 520 nm.

Using the optical arrangement shown in Figure 51, the spectrum of a laser induced plasma in air at atmospheric pressure was recorded (Figure 52). An approximate blackbody emission curve is drawn under the spectrum. Using Wien's law, the approximate temperature of the plasma can be deduced from the wavelength of the maximum intensity:

$$Temperature = \frac{b}{\lambda_{max}} = \frac{2.897 \times 10^{-3}}{520 \times 10^{-9}} = 5571 K$$

In order to determine the absorbance of a sample using the collimated broadband light it was necessary to use sample the beam using a broadband beam splitter. Two spectrometers are necessary to determine absorbance with a light source that is changing in intensity. One spectrometer was used to sample the intensity of the beam as a function of wavelength, the other spectrometer was used to record the intensity of the beam after it has passed through the sample. From this data, the intensities of the beam, as a function

of wavelength, before and after the sample can be determined and from these intensities, the absorbance/turbidity of the sample, as a function of wavelength, can be calculated. Exactly how this is done is discussed in the next section.

The beam was sampled using a broadband non-polarising beam splitter (Thorlabs BSW26 50/50 beam splitter, 25.4 mm diameter, 350-1100 nm). A diagram of the instrument for measuring the absorbance of a sample is shown in Figure 53.

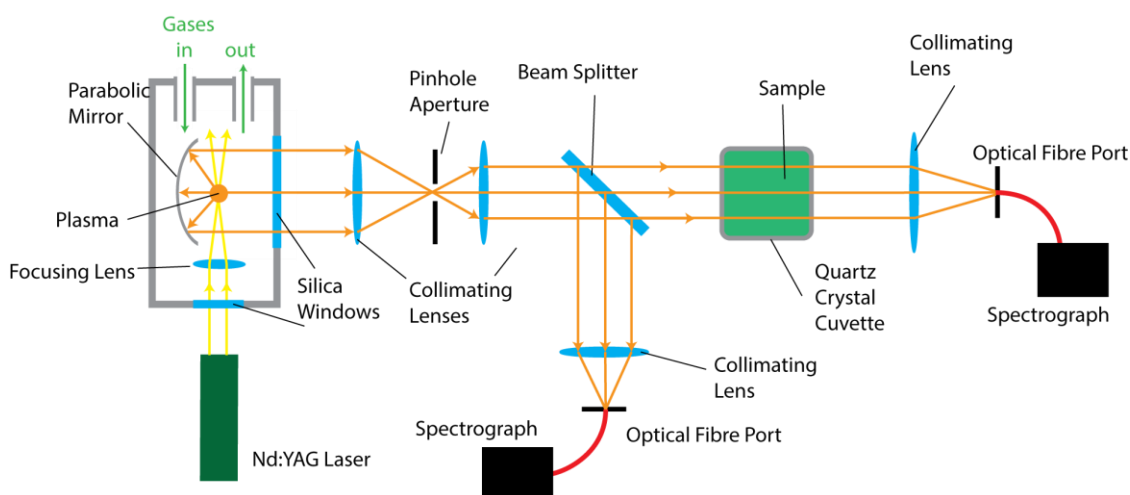


**Figure 53.** A diagram of the spectrometer for measuring the absorbance/turbidity of time varying samples.

A sample to be measured is loaded into a 10×10 mm, 50 µL volume quartz crystal cuvette. Light enters the cuvette through a 2.2 × 2.2 mm window and has a path length through the sample of 10 mm. Although the sample cuvette has a sample volume of 50 µL in the path volume of the light, a minimum sample volume of 150 µL was required for the beam to pass cleanly along the path without encountering bubbles.



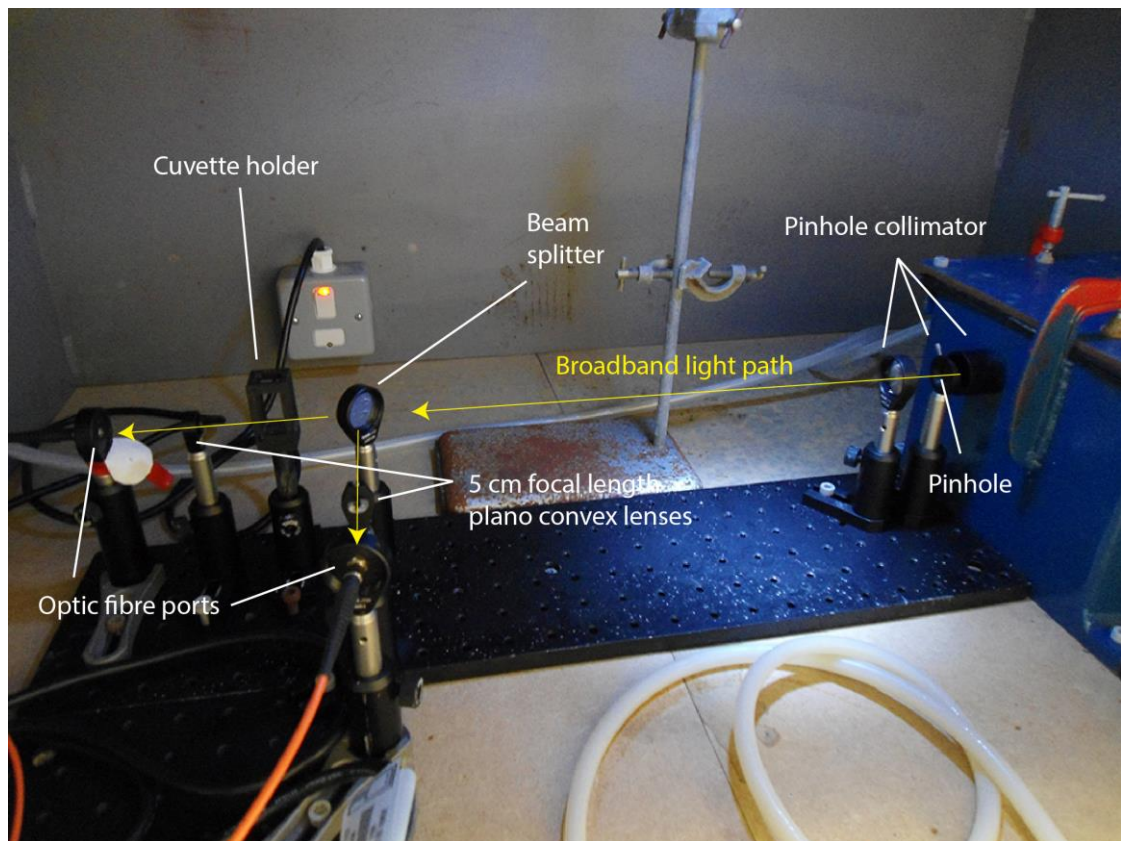


**Figure 54.** The complete optics showing the collimation optics (right), the beam splitter and optical fibre ports with beam focusing optics (left).

## 2.6 Sealed Chamber Design and Construction

By changing the gaseous medium in which the plasma is formed, the emission may be more intense and shifted to shorter wavelengths. This occurs due to an increase in electron temperatures within the plasma. For the generation of laser induced plasmas in different gases over a range of pressures, a sealed chamber was designed and constructed. The sealed plasma chamber needed to fulfil the following requirements:

- The chamber must be large enough to house the focusing and capture optics.
- It must be possible to drill M6 holes in the bottom of the chamber for mounting optical posts.

- The chamber must be fitted with a gas inlet and outlet. The gas inlet was a ¼ BSP screwed adapter attached to the hose with a hose clamp. The gas outlet was a manually operated ¼ BSP ball valve.
- The chamber needed to be fitted with a safety valve so that the pressure is released should it become too high for any reason.
- The chamber must have a removable lid for adjustment of the internal optics.
- The chamber must be fitted with a window that is transparent at 1064 nm for the laser pulse to enter. This window must have a minimum diameter of 12.7 mm which is the same diameter as the focusing lens.
- The chamber needed to be fitted with a window to allow light reflected from the parabolic capture mirror. This window needed to be the same size as the mirror since the reflected rays are parallel when exiting the chamber.
- The chamber needed to be fitted with a pressure gauge for reading the chamber pressure.
- It must be possible to securely seal the lid to the chamber.
- All the fittings for the chamber (windows, valves, lid etc.) must be sealed to prevent loss of pressure.
- The top of the chamber needs to be as flat as possible to make a good seal with the lid.

With these requirements in mind, a design for the chamber was drawn in the Autocad computer aided design package. The drawings for the chamber are shown in Figures 55 and 56. Points to note from the drawing are:

- The windows for light to enter and exit the chamber are mounted in lens tubes. The lens tubes are: Thorlabs SM05L10 12.7 mm diameter and Thorlabs SM1L10 25.4 mm diameter. These are externally threaded tubes, threaded with bespoke Thorlabs SM05 and SM1 threads. To cut the threads it was necessary to buy the taps from Thorlabs. The taps are: Thorlabs 83373 - Imperial Tap 0.535"-40 Thread (SM05 Standard) and Thorlabs 97355 - English Imperial Tap 1.035"-40 Thread (SM1 Standard).

These taps were the most expensive items that were purchased to make the chamber.

- The lid was secured by four M6 nuts and bolts, one through each corner of the lid.
- The base of the chamber was a 10mm thick steel plate. The rest of the chamber was constructed from 5mm steel plate. M6 holes were drilled and tapped in the bottom of the chamber for the securing of the focusing lens and collection mirror.

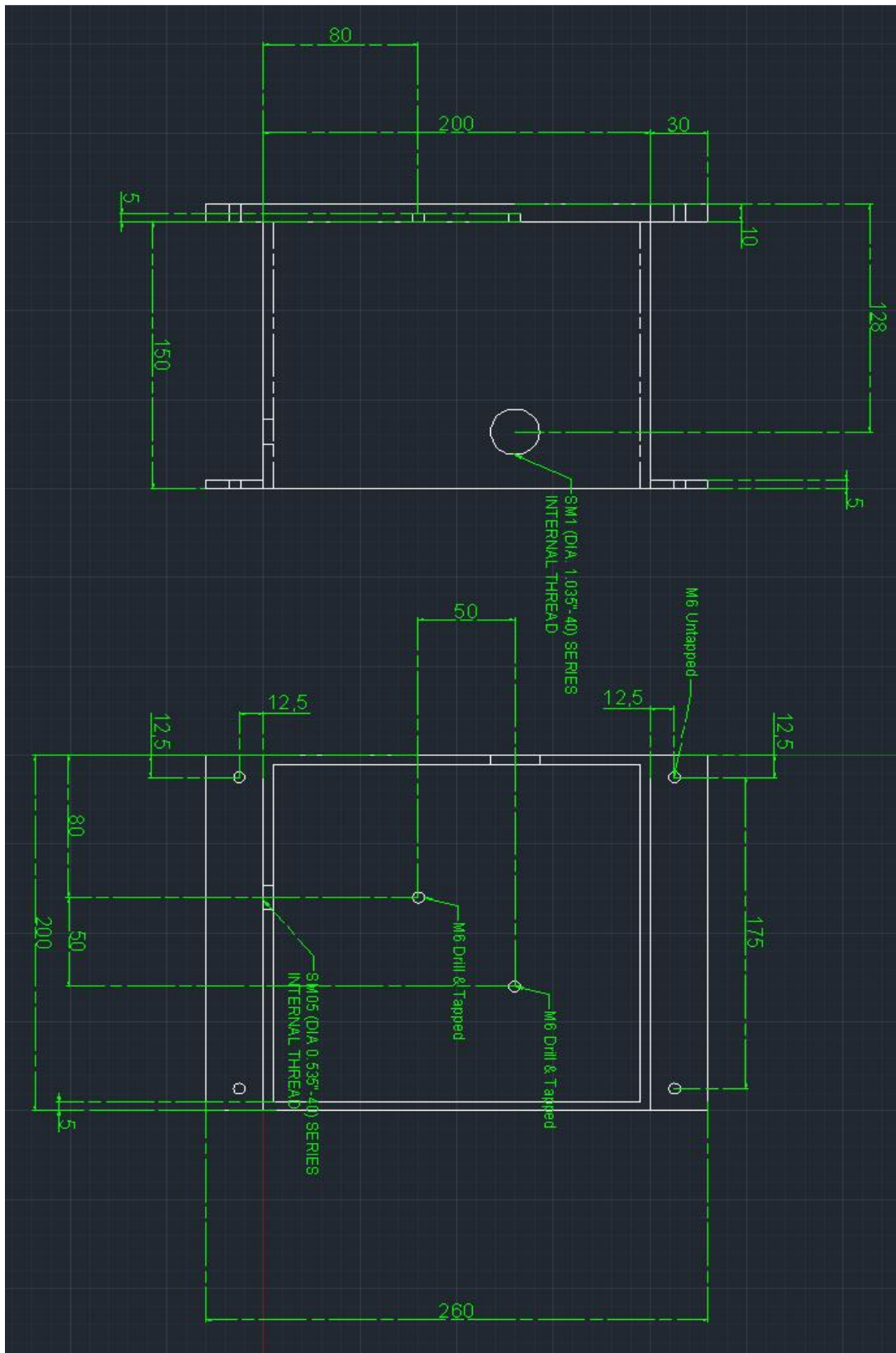


**Figure 55.** The Autocad drawing of the plasma chamber. All of the dimensions are in mm.

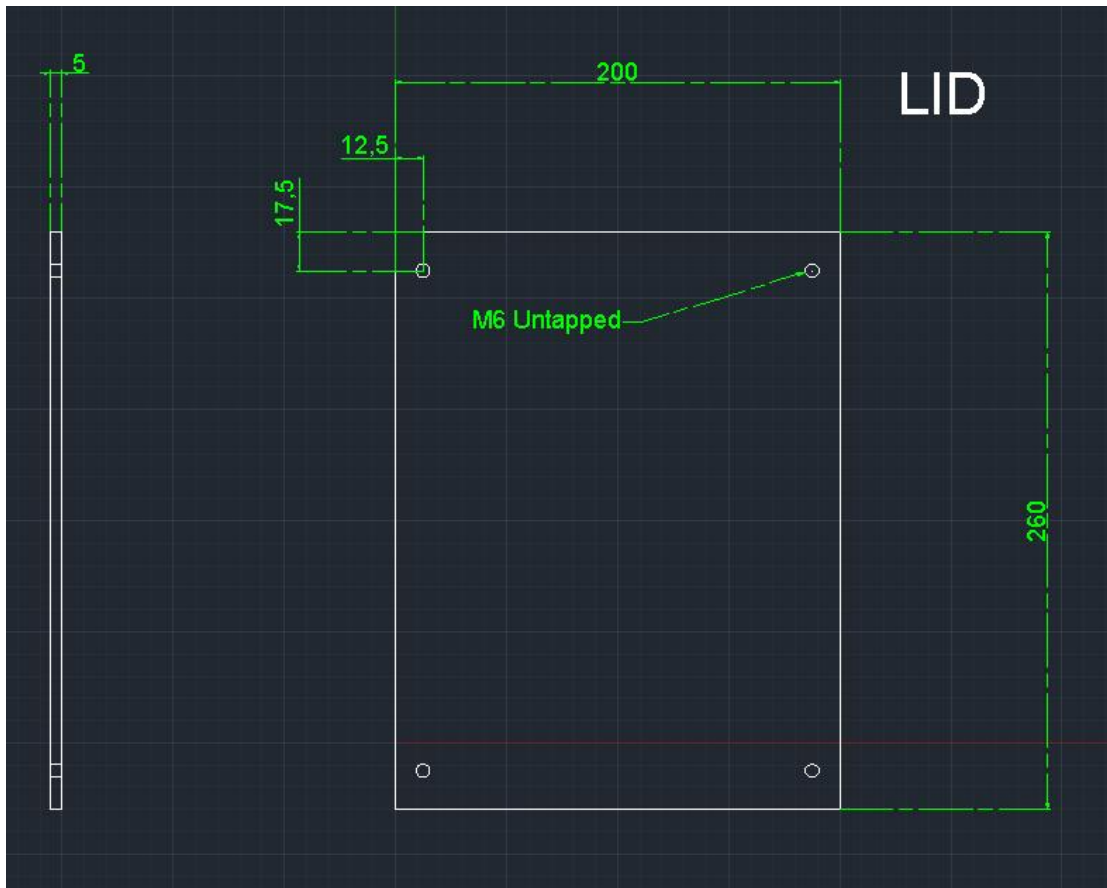


**Figure 56.** The Autocad drawing of the lid of the plasma chamber. All dimensions are in mm.

- Some of the fittings such as the gas inlet/outlet valves and the pressure release valve do not appear on the drawing. This is because the locations of these fittings do not require precise positioning and can be positioned and fitted after the main chamber has been made.

The top of the chamber was ground down on a milling machine to make a level surface so that the lid would be have an airtight fit. Following the fabrication of the chamber at MI Engineering, a number of components were purchased:

- Thorlabs SM05L10 12.7 mm diameter and Thorlabs SM1L10 25.4 mm diameter lens tubes.
- Thorlabs WG40530 - Ø1/2" Uncoated UVFS broadband precision window, Thorlabs WG41050 - Ø1" Uncoated UVFS broadband precision window.
- Niezgodka Type 66 Open Discharge Safety Relief Valve 4 bar.
- 2 × 1/4" BSP Male screwed adapter.

- 1/4" BSP Ball valve (RS Online).
- Black natural rubber sheet for a rubber gasket, 1000 mm x 600 mm x 3 mm (RS Online).
- 1/4" BSP 0-10 bar pressure gauge.
- 1/4 BSP 10 m Reinforced pneumatic hose.

Each of these components was fitted to the chamber and sealed so that the chamber would be airtight. The UV fused silica windows were fitted into the lens tubes with 2 rubber O-rings and glued in place. The lens tubes were then glued in place with thread sealant. The lid was sealed with a gasket made from 3 mm thick natural rubber sheet. Holes were drilled and tapped in suitable locations for the safety valve, pressure gauge and gas inlet and outlet. These components were screwed in place and sealed with thread sealant. The completed chamber is shown in Figure 57.

The pressure gauge reads the pressure relative to atmospheric pressure and so a reading on the gauge of one bar is an absolute pressure of two bar. The highest pressure that the chamber has been tested with is an absolute pressure of 2.8 bar. The likeliest places for the chamber to fail due to excessive pressure are the two windows contained in lens tubes that allow light in and out of the chamber. The failure pressure of the chamber is currently unknown.

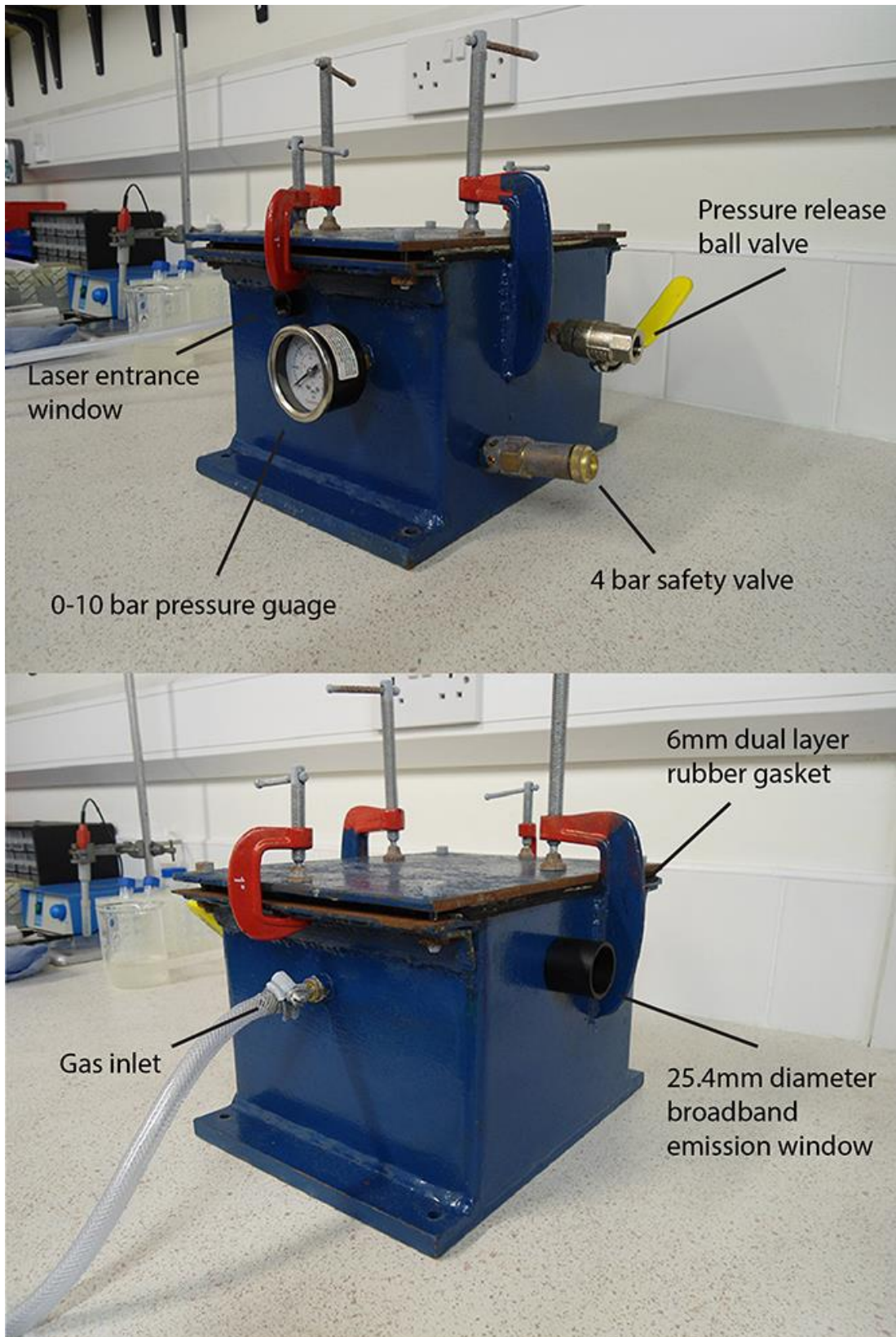


**Figure 57.** Pictures of the pressure chamber showing the main components.

In the drawings of the chamber it can be seen that the height of the centre of the laser window is 128 mm above the base of the chamber. To make the laser

pulse enter the chamber at this height, the laser was mounted on a Thorlabs 77 mm x 77 mm KM200B/M kinematic mount which was attached to the breadboard via an adjustable Thorlabs ½ inch optical post. Owing to the high operating voltages of the laser, the laser needed to be electrically isolated from the mount. Isolating the laser prevents damage to the laser occurring due to shorting or electrical arcing. A 6 mm wide piece of Perspex was cut and attached to the bottom of the laser with M3 nylon screws before screwing the laser to the mount with M6 and M2 nylon screws. The laser mount is shown in Figure 58.

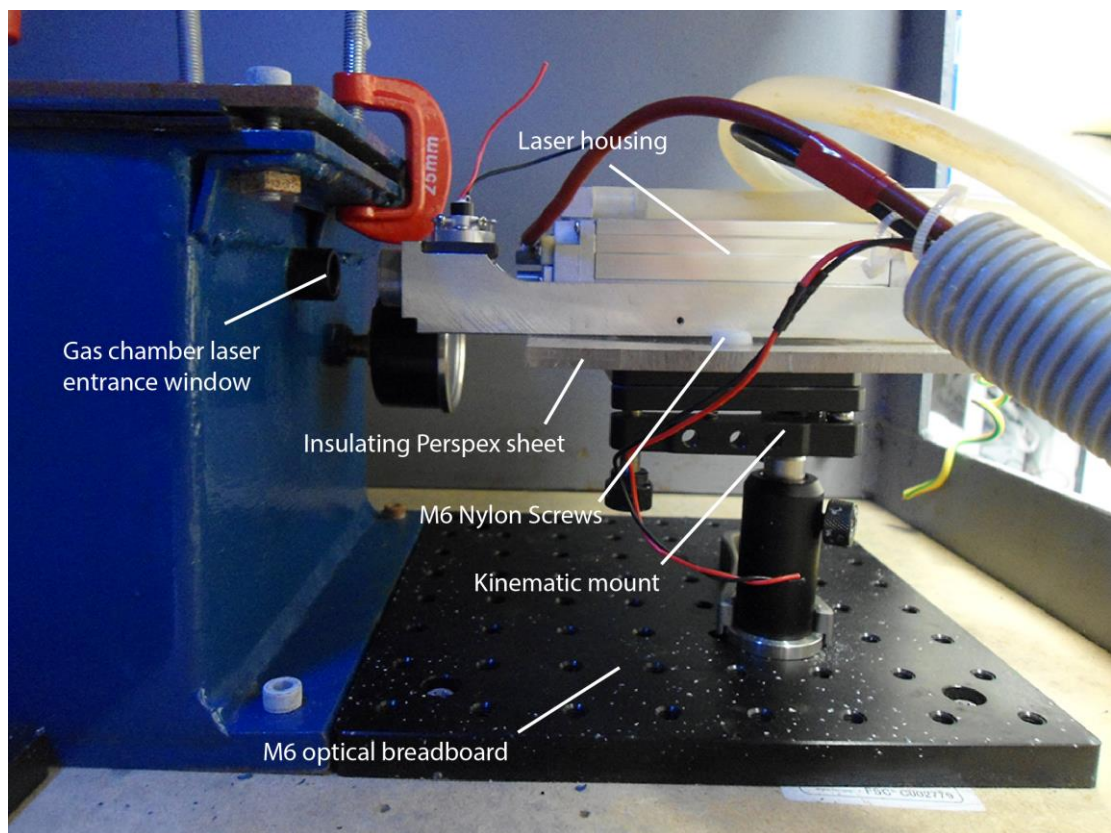


**Figure 58.** The electrically isolated mount for the laser housing. The Perspex prevents the accidental conduction of current through the mount and optical breadboard.

The laser focusing lens and parabolic collector mirror were attached to the inside of the chamber using Thorlab's lens and mirror mounts that were screwed down using M6 bolts. These optics were adjusted so that the plasma was formed at the correct location for light to be captured by the mirror. The mirror was then adjusted so that parallel rays of light reflected from the mirror were able to exit the chamber via the 25.4 mm window. The rest of the optics



for the collimation and analysis of the broadband light were adjusted and aligned to the correct positions. The complete plasma spectrometer is shown in Figure 59.

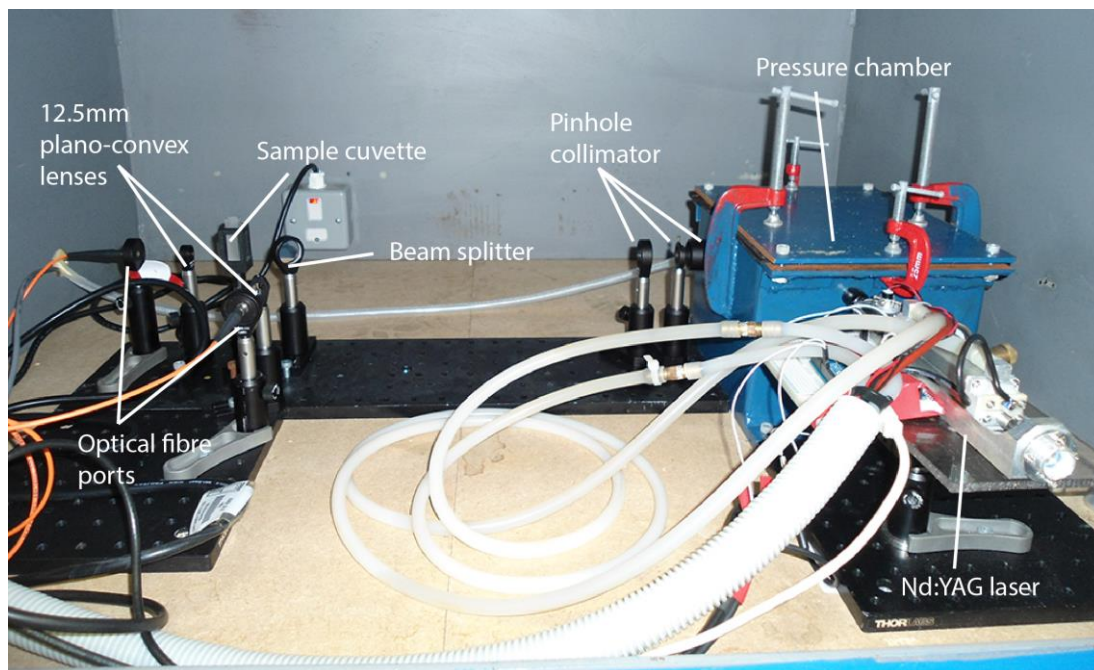


**Figure 59.** The plasma spectrometer showing the laser, pressure chamber and optics.

## 2.7 Spectrometer Timing Electronics and Control Programs

In normal operating mode, the Thorlab's CCS200 spectrometer integrates the total amount of light received over a range of wavelengths in a set time period. This time period is set by the operator (10 $\mu$ s-10s). For each of these consecutive time periods, the spectrometer outputs the integrated intensity at a particular wavelength in the form of a number between zero and one. This mode of operation is good for recording the spectra of continuously emitting sources but if used to record the spectra of individual, regularly repeating, pulsed light sources there is a problem. If the laser pulses at, for example, 1 pulse/sec and the spectrometer is set to record in consecutive 1 second periods, the spectrometer and the laser, even if started at the same time, will eventually become desynchronised. This happens because one second for the laser is not exactly the same as one second as timed by the spectrometer. As the laser and spectrometer fall out of synch, the light from a single plasma can

be split over two integrated time periods or the laser may not pulse during the integration time.

The analysis of the data from a spectrometer operating in normal mode could be done but would be complex and probably involve a visual inspection of the recorded spectra to find blank frames and other timing issues. What was needed was a way to record for a set time interval, but only when the laser was pulsing. When in triggered fast sequential scanning mode, the spectrometer can be triggered to start recording by either an internal timer or an external +5 V pulse through a BNC cable. The trigger is a pulsed signal that switches between 0 V to +5 V and then back to 0 V. To trigger the spectrometer, the +5 V must be held for a minimum of 0.5  $\mu$ s. The pulse is therefore approximately square (the cable has some inductance and capacitance). After the spectrometer has been triggered it records the light intensity for the integration time set by the operator. It then resets and listens for the next trigger. The spectrometer exits the run after a specific number of spectra have been acquired. In sequential recording mode the spectrometer can be triggered using a microcontroller to record the spectra of consecutive laser pulses. The microcontroller outputs a 0 to 5 volt pulse to the BNC cable which triggers the spectrometer. The microcontroller can trigger multiple spectrometers simultaneously simply by using a BNC splitter as long as the current draw on the microcontrollers output pin does not exceed the recommended maximum (40 mA for Arduino Uno).

The problem now was to co-ordinate the triggering pulse from the microcontroller with the laser pulse. This was solved by programming the microcontroller to listen for input from a photodiode before sending out a pulse to the external trigger. The photodiode is placed next to the flashlamp of the laser. If the lamp flashes, the signal from the photodiode rapidly increases to near maximum. The microcontroller reads this increase in voltage and waits a set time period before sending out a triggering pulse. For example, if the laser pulses approximately once per second, the microcontroller waits 975 ms before sending out a triggering pulse to the spectrometer. The time to wait depends upon the repetition rate of the laser as entered by the user in the PC

software. The spectrometer then starts a 50 ms integration window that captures the spectrum of the plasma that occurs approximately 1000 ms after the flashlamp. This process is looped so that each flash of the lamp triggers a 50 ms integration. In this way, the timing issues were resolved and each 50 ms interval contained a single plasma flash. The only problem was that the very first pulse was not recorded, as it was not triggered by a previous flash, but this was a minor problem that only meant that the first plasma following the start of the experiment is not recorded. The first spectra recorded would therefore correspond to the second plasma from the start of the experiment.

An Arduino Uno microcontroller was suitable to be programmed to read the analogue output of a photodiode and output a triggering signal to the spectrometers. The Arduino Uno is shown in Figure 60. The Arduino Uno has 14 digital I/O pins and 6 analogue inputs and is connected to a PC via USB 2.0. Programs to be run on the Arduino are uploaded from the PC via the serial port. This microcontroller is controlled and programmed using a bespoke scripting language that is included as a C++ library. Standard C++ commands can also be used. The microcontroller can be programmed using a manufacturer supplied programming interface and compiler but instead it was decided to install the Arduino plugin for Microsoft Visual Studio as MVS is a much more powerful programming environment.

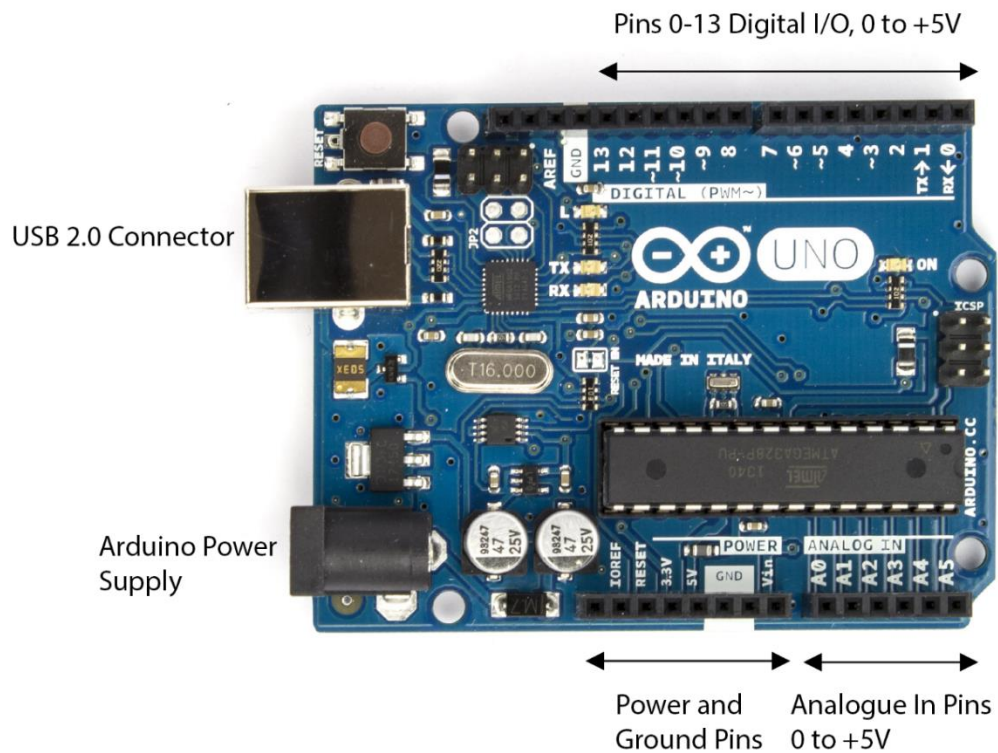


**Figure 60.** A picture of an Arduino Uno microcontroller showing the location of digital and analogue connectors, power and USB cables.

The digital pins of the Arduino all operate at either 0 or +5 volts. The analogue pins output a voltage between 0 and +5 V. The photodiode must output a voltage in this range for correct reading by the analogue input pin. A suitable photodiode that outputs a 0 to 5 V analogue voltage is the TSL257 Light to Voltage Converter (Figure 61). This component is actually a combined photodiode and transimpedance amplifier. The amplifier reads the signal from the photodiode and converts it into a 0 to 5 V output.

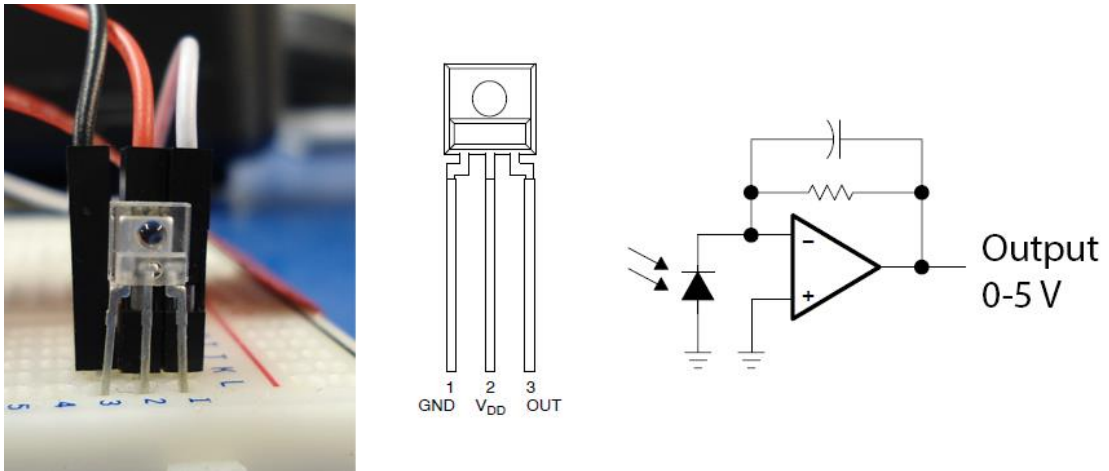


**Figure 61.** The TSL257 Light to Voltage Converter, pin diagram and functional block diagram.  $V_{DD}$  is the +5V power pin for the converter.

The wiring diagram for the triggering circuit is shown in Figure 62. The Arduino continuously reads the analogue voltage from the light to voltage converter and converts it into a number between 0 and 1024 (10 bit). This number is normally around 20 in a dark room but increases to above 1000 for a few milliseconds when the flashlamp fires. Any output greater than 400 was chosen as the triggering output. If an output greater than 400 is registered, the Arduino waits a set amount of time. This time depends upon the user entered repetition rate of the laser (975 ms for 1 second laser pulses). After this time period is over, the Arduino sets the voltage of digital pin 10 to +5V for 10 ms. This pin is connected to the spectrometer trigger. The increase in voltage triggers the spectrometer to record for an amount of time specified by the integration time set in the manufacturer's spectrometer software.

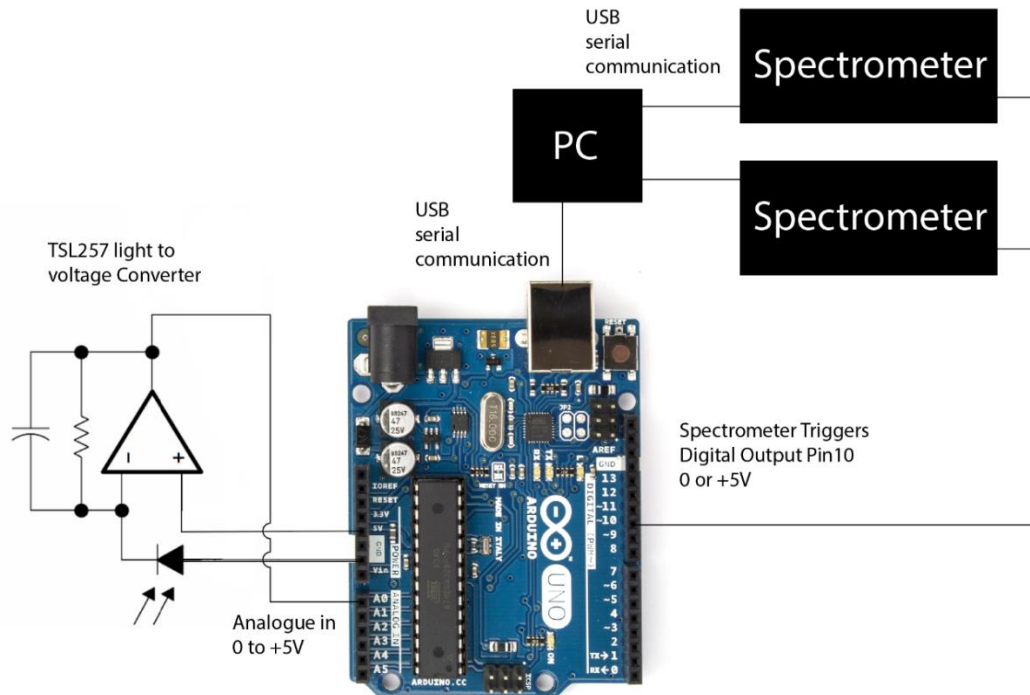


**Figure 62.** A wiring diagram of the connections between the light to voltage converter, Arduino Uno, PC and spectrometers. These connections are required for timed spectrometer triggering. The voltage to light converter is connected to the ground, +5 V and A0 pins of the Arduino.

Including the integration time, there are several pieces of information that need to be entered into the spectrometer's software when using triggered fast sequential scanning mode. These are:

- Integration time. This is the time window during which the spectrometer records the light intensity after triggering. Normally this is set to 50 ms.
- Name and location of CVS file in which to save data.
- Number of triggered scans to record. The spectrometer will record until this number of scans is completed.
- The spectrometer needs to have the external trigger box ticked.

As well as a program running on the Arduino, a command line program running on the PC asks the user to choose from a number of options and passes to the Arduino the information required to complete these requests. The PC also

tells the Arduino when to execute certain parts of the code such as when to start and stop a scan. The information that user must supply the PC is:

- The pulse rate of the laser.
- When to start a run.
- How long a run will last.

Once the user has inputted the required parameters the scan can be started. The basic structure of the main code to run a scan is shown in Table 6.

PC	Arduino Uno
Send pulse rate and start code to Arduino and then wait a set time specified by the user →	Receive start code. ↓
After waiting for a user defined amount of time, send stop code to the Arduino. →	Check for stop code. If stop code is received go to next code block (“End”). Otherwise continue to next command. ↓ Read output from photodiode. ↓ If photodiode output is >400. Wait a set time that depends upon the repetition rate (975 ms for 1 Hz). Set Pin 10 to +5 V. Wait 10 ms. Set Pin 10 to 0 V. ↓ Loop back to start of block (“Check for stop code”).
	End

**Table 6.** A breakdown of the triggering code and communication between the PC and the Arduino Uno. The middle row loops continuously once started until a stop code is sent from the PC.

Upon running the program, it attempts to communicate with the Arduino microcontroller through the serial port and generates an error if communication is not established. The C++ code for the PC command line program uses a standard Microsoft Windows API: windows.h for serial port communication. The full C++ code for the PC command line program and the program for the Arduino microcontroller can both be found in Appendix I. The PC program has 4 different options that the user can select from the initial menu:

1. Read the output from the light to voltage converter and output to a CSV file if required. This is included for checking the operation of the photodiode.
2. Run a scan specifying the repetition rate of the laser from 1-6 and the number of scans to run. The number of scans specified here should be more (at least 20 more) than the number of scans specified in the manufacturer's spectrometer control software. This is to make sure that the full number of scans are recorded by the spectrometers
3. Run a scan once every 4 seconds for an hour. The spectrometer has a maximum of 1000 scans that can be run before it runs out of memory. One scan every 4 seconds for an hour is 900 scans. The repetition rate of the laser is 1Hz so the spectrometer will record 1 in 4 scans.
4. Purge the input and output buffers. This is sometimes necessary if an error occurs or a program exits prematurely as characters can still be stored in the buffer.

After selecting an option, the user is prompted to enter a number of relevant parameters such as the laser repetition rate and how long they would like the run to last. The Thorlabs spectrometer can record a maximum of one thousand individual spectra which, at 1 Hz pulse rate, is a run time of 16.6 minutes. In order to increase the maximum run time, the Arduino code was altered so that the spectrometer was not triggered every pulse. The third user option in the list sets a run time of one hour with the spectrometer triggering every 4<sup>th</sup> pulse. The program waits for the user to hit 'Enter' before running the scan. This gives the user time to prepare and load the sample before starting the run. After the



run finishes, the program asks the user whether they would like to do another run, in which case both programs loop back to the start, or exit.

## 2.8 Determination of Broadband Sample Absorbance Using the Plasma Light Source Instrument.

Following a run, each spectrometer outputs a csv (comma separated values) file containing the beam intensity, as a value between zero and one, recorded over the spectrometer's 50 ms integration time. The format of these csv files is shown in Table 7.

13h_35m_33s _973ms	0ms	996ms	1989ms	2985ms
199.7095149	0.00040423	0.0005036	0.00140727	0.00133888
199.9117787	-0.00098486	0.00023894	0.00034906	0.00094217
200.1140596	-0.00087461	-0.00033451	0.00083407	0.00100829
200.3163575	-0.00116125	-0.00059918	-0.00134848	-0.00053445
200.5186725	0.00066882	0.00048155	0.00076793	-0.00104135
200.7210045	-0.00180068	-0.0006874	0.0007018	-0.00126174
200.9233536	-0.00047773	-0.00053301	0.00052543	0.00092014

**Table 7.** The typical .csv output of the CCS200 spectrometer. Wavelength in nm is listed in the first column. The column headers list the start time of each measurement. The intensity is recorded as a value between zero and one but the dark noise of the spectrometer produces very small negative values. In this test, the laser was set to pulse once per second. The variation in the difference of measurement times demonstrates the necessity for timing hardware and software to synchronise the laser and spectrometer.

The csv files contain intensities of both the transmitted or reflected beam, labelled as  $I_T$  ( $I_A$  if a sample is in place) and  $I_R$  in Figure 63. From this data the absorbance of a sample can be determined.

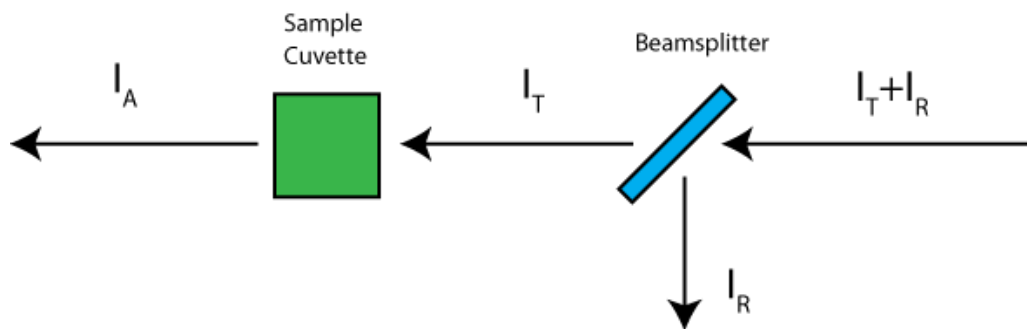


**Figure 63.** A schematic of the light beams in the spectrometer with abbreviations for light intensity at different locations.  $I_A$  and  $I_R$  are the intensities recorded by the spectrometers. Losses from the beam splitter are assumed to be negligible.

The absorbance of a sample is normally calculated as:

$$\text{Absorbance} = \log_{10} \left( \frac{I_T}{I_A} \right)$$

However,  $I_T$  was not known but could be determined from  $I_R$  and the wavelength dependant transmittance of the beam splitter. The transmittance of the beam splitter as a function of wavelength can be determined by recording  $I_R$  and  $I_T$  in the absence of a sample:

$$\text{Transmittance of beamsplitter } T_\lambda = \frac{I_T}{I_T + I_R}$$

$$I_T = \frac{T_\lambda}{1 - T_\lambda} I_R = C_\lambda I_R$$

$$C_\lambda = \frac{T_\lambda}{1 - T_\lambda} = \frac{I_T}{I_R}$$

The absorbance of a sample is calculated by measuring the intensities  $I_A$  and  $I_T$ :

$$\text{Absorbance of sample } \text{Abs}_\lambda = \log_{10} \left( \frac{I_T}{I_A} \right) = \log_{10} \left( \frac{C_\lambda I_R}{I_A} \right) \quad \text{Equation 18}$$

Using CCS200 spectrometers as the detectors meant that the maximum absorbance that could possibly be measured is an absorbance of 2 (%1 Transmittance). This is because the dark noise of the spectrometer was 0.01

and the maximum value that can be measured was 1. The dark noise of the spectrometer was determined by recording the dark noise of three hundred consecutive 50 millisecond integration time intervals. None of the dark noise values that was recorded was over 0.009 for any wavelength. Values below 0.01 were therefore assumed to be zero signal.

The error in the absorbance is calculated from the error in  $C_\lambda$ :

$$\text{Error in absorbance of sample } \Delta Abs = \left( \frac{\partial Abs_\lambda}{\partial C_\lambda} \right) \Delta C_\lambda$$

$$\text{Let } u = \frac{C_\lambda I_R}{I_A}$$

$$\frac{\partial u}{\partial C_\lambda} = \frac{I_R}{I_A} \quad \frac{\partial Abs_\lambda}{\partial u} = \frac{1}{\ln 10} \frac{I_A}{C_\lambda I_R}$$

From chain rule:

$$\frac{\partial Abs_\lambda}{\partial C_\lambda} = \frac{\partial Abs_\lambda}{\partial u} \frac{\partial u}{\partial C_\lambda} = \frac{1}{\ln 10 \cdot C_\lambda}$$

Therefore:

$$\Delta Abs = \frac{\Delta C_\lambda}{\ln 10 \cdot C_\lambda} \quad \text{Equation 19}$$

To determine the values of the transmittance  $T_\lambda$  and  $C_\lambda$  as a function of wavelength,  $I_R$  and  $I_T$  are recorded for each laser pulse at a rate of 2 per second for 5 minutes with a sample absent. The spectrometers output two .csv files. An examination of the output revealed that one of the spectrometers was not triggering correctly. Occasionally, one of the CCS200 spectrometers would miss a measurement (see Tables 8&9), resulting in a csv file that had less than 300 columns. Missing columns caused the times of the columns to not match up, presenting problems with further analysis. Several attempts were made to fix this, including switching the triggering pins on the Arduino and increasing the duration of the triggering pulse. It was not thought that the inductance and capacitance of the BNC trigger cable was high enough to prevent the voltage at the spectrometer from reaching the required +5V but increasing the voltage to the spectrometer trigger by using a transistor with a +5V gate (Model ZVNL120A) connected to Arduino and the transistor source connected to the

+5V output of an ATX power supply, did not solve the problem. The missing measurements only seem to occur with one of the CCS200 spectrometers, so this may be an internal problem with the spectrometer.

16937ms	17933ms	18930ms	20922ms	21919ms	22915ms
0.000971	0.001335	0.003226	-0.00025	-0.00132	0.001399
0.000391	0.001091	0.003196	0.000455	-0.00126	5.59E-05
0.002069	0.003625	0.001092	0.00073	-0.00117	0.000941
0.00274	0.001	0.001824	0.00073	-0.00135	0.003077
0.002374	0.002312	0.000269	0.002104	0.000664	0.002833
-0.00251	-0.00196	-0.00025	-0.00031	-0.00089	8.65E-05
-0.00107	-0.00016	-0.00052	-0.00052	0.002008	0.0003

16937ms	17933ms	18930ms	19925ms	20922ms	21919ms
0.000839	0.000923	-0.00014	0.000165	-0.00052	0.000289
0.000157	0.000527	0.000317	0.001527	0.000143	-0.00052
-0.00011	0.000264	-0.00146	-0.00096	-0.00069	0.000179
-0.00125	-0.00211	-0.00076	-0.00021	-0.0014	-0.00099
0.000685	-0.00024	-0.00065	0.000472	-0.00016	-0.0009
-0.00081	-0.0007	-0.00201	-0.00052	-0.00107	-0.00138
0.000619	0.000571	0.0008	0.000428	-0.00089	-0.00103

**Tables 8 & 9.** Table 8 lists the recorded intensities of the transmitted beam and Table 9 lists the intensities of the reflected beam. The spectrometer recording the transmitted beam has missed a measurement at around 19925ms preventing the columns from matching up.

The problem of the missing columns was resolved by importing the raw .csv files from the spectrometer into Excel (.xlsm) and manipulating the data using a visual basic for applications (VBA) script. Altogether, three VBA scripts were used for different purposes to manipulate large datasets using Excel. These scripts are labelled Scripts 1-3 for reference. The VBA scripts each operate on the Excel files, identifying missing measurements and inserting blank columns so that the times of each of the columns match up. Once a complete dataset has been created, the scripts manipulate the data and calculate transmittance,  $C_{\lambda}$ , absorbance and other values. The scripts also allow for subtraction of

buffer or solvent absorbance. These three scripts can be found in Appendix II. The scripts used in this thesis are:

Script 1: Calculates the transmittance and  $C_{\lambda}$  of the beam splitter for each pulse from the values of  $I_T$  and  $I_R$  recorded by the spectrometers and then averages. Outputs the results to the last worksheet created.

Script 2: Calculates the absorbance of a sample from  $I_R$ ,  $I_A$  and  $C_{\lambda}$ . Calculates the absorbance for each pulse and averages the results. Allows for buffer/solvent absorbance subtraction and batch Excel file processing. Outputs the results to the last worksheet created. Used to determine the absorbance of non-time varying samples.

Script 3: Calculates the absorbance of a sample from  $I_R$ ,  $I_A$  and  $C_{\lambda}$ . Allows for buffer/solvent absorbance subtraction and batch Excel file processing. Calculates the absorbance for each pulse and exports the results to a csv file containing three columns: Wavelength, Time and Absorbance. This csv can be easily imported into graphing or statistical software for analysis. Used to determine the time varying absorbance of samples.

The raw .csvs are imported into Excel as separate worksheets labelled "Trans" and "Refl" after the beams transmitted and reflected by the beam splitter. The .csv files from each CCS200 spectrometer are copy/pasted into the respective worksheet. The Excel file also contains two other worksheets labelled "Splitter" and "Buffer" which are required by Scripts 2 and 3. "Splitter" contains the wavelength dependant values for  $C_{\lambda}$  which must be entered by the user.  $C_{\lambda}$  is used rather than the transmittance as the absorbance calculation is simpler. "Buffer" contains the background absorbance values of the buffer or solvent as previously determined by the plasma spectrometer. This background absorbance is subtracted from the sample absorbance before outputting the results. Leave blank if not required.

To determine the transmittance and  $C_{\lambda}$  of the beam splitter the .csv files from each of the CCS200 spectrometers were copied in Excel and Script 1 was run.

As well as fix missing measurements, Script 1 calculates the values of the wavelength dependent  $T_\lambda$  and  $C_\lambda$  for each pulse and averages the results to determine the mean value and standard deviation of  $T_\lambda$  and  $C_\lambda$  at each wavelength. This is only done if a measurement returns a valid value of  $T_\lambda$  and  $C_\lambda$ . Valid values of  $T_\lambda$  and  $C_\lambda$  are not returned if:

- A cell in either the “Trans” or “Refl” worksheet was blank. This is caused by the VBA code inserting a blank column for missing measurements.
- A cell in the “Refl” worksheet was less than the noise value of 0.01. This indicates that the light source was not intense enough at that wavelength to give a signal. Including smaller values than this can have a large effect on the calculated absorbance as  $I_R$  is in the denominator in Equation 18.
- A cell in either the “Trans” or “Refl” worksheet was equal to 1. This indicates that the true intensity value was larger than 1 but the maximum intensity the CCD in the spectrometer can read was reached. Using a value of 1 gives incorrect values for the transmittance and  $C_\lambda$ .

If any of these criterion were met, rather than calculate incorrect values, Script 1 inserts a blank value for  $T_\lambda$  and  $C_\lambda$  for the measurement. These blank cells are ignored in mean and standard deviation calculations. During the execution of the Script 1 on the Excel file, the script adds several worksheets to the .xlsm file. The last worksheet created contains the output of the mean and standard deviation of the transmittance as well as the mean and standard deviation of  $C_\lambda$ . The format of this worksheet is shown in Table 10.

Wavelength (nm)	Mean Transmittance	Standard Deviation of Transmittance	Mean $C_\lambda$	Standard Deviation $C_\lambda$	Number of Data Points
354.0772585					0
354.2912933					0
354.505344	0.194605451	0.004191873	0.241661111	0.006462529	2
354.7194105	0.200736362	0.038159105	0.254080948	0.061416933	27
354.933493	0.185286252	0.038081409	0.230216355	0.059807549	40
355.1475913	0.203810821	0.038231971	0.258975093	0.062460796	95
355.3617056	0.165195994	0.031382645	0.199660018	0.047253868	68

**Table 10.** The format of the final worksheet in the Excel file after running the VBA code. The data shown is the output of the VBA for several wavelengths around 355nm. Blank cells have occurred because one/both spectrometers recorded an intensity less than 0.01 at that wavelength.

From the final worksheet in the Excel file, the mean transmittance  $T_\lambda$  and  $C_\lambda$  of the beam splitter as well as the standard deviations are plotted against wavelength in Figures 64-67.

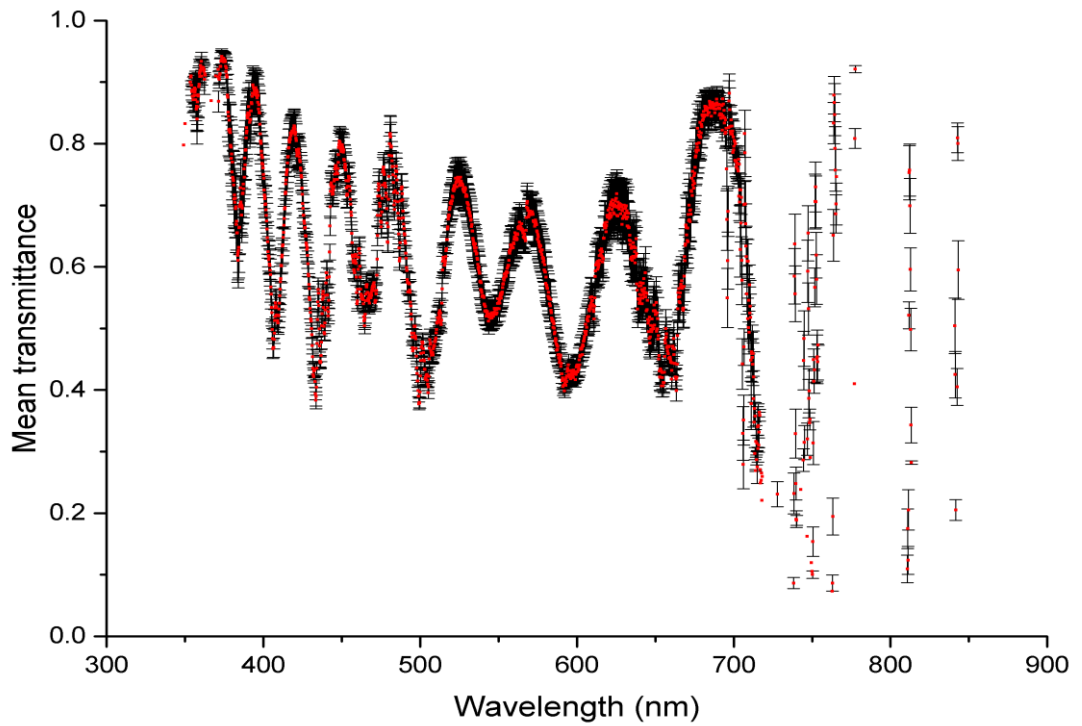


**Figure 64.** The mean transmittance (red) and standard deviation error (blue) of transmittance obtained for the Thorlabs BSW26 50/50 beam splitter. The results are averaged over 300 laser pulses.

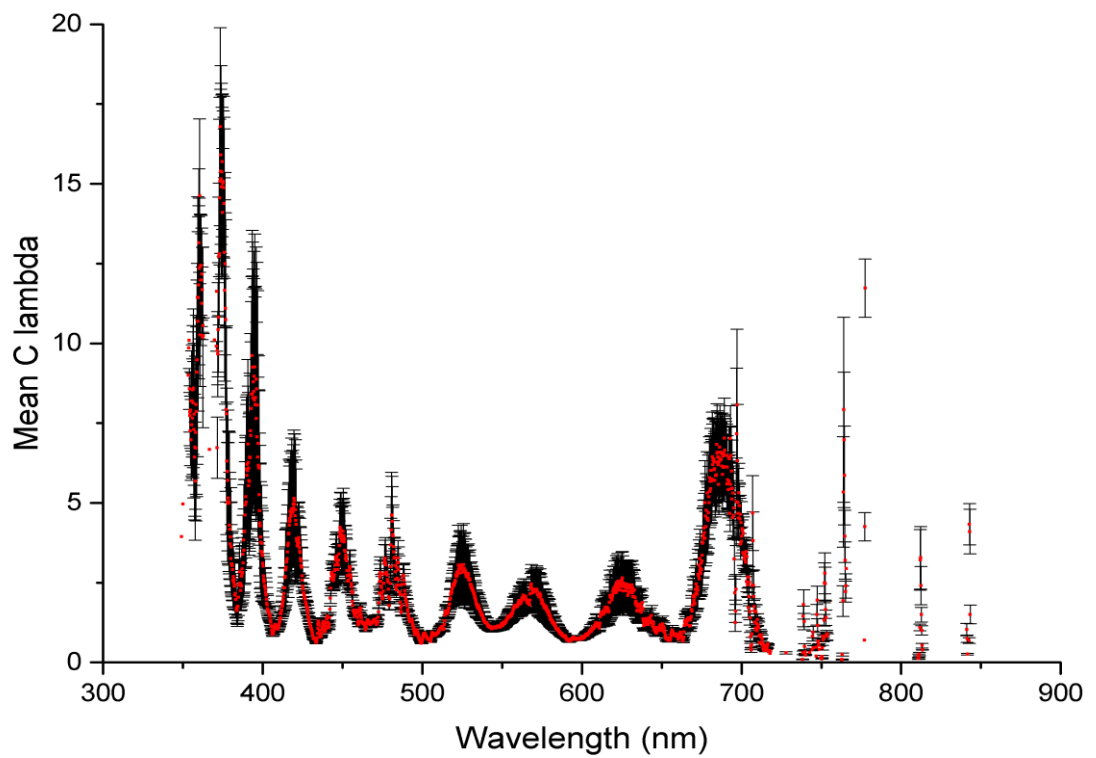


**Figure 65.** The mean (red) and standard deviation (blue) of  $C_\lambda$  obtained for the Thorlabs BSW26 50/50 beam splitter. The results are averaged over 300 laser pulses.



To see more clearly how the standard deviation of  $T_\lambda$  and  $C_\lambda$  varied with wavelength, the magnitude of the standard deviation is plotted against wavelength in Figures 88 & 89.

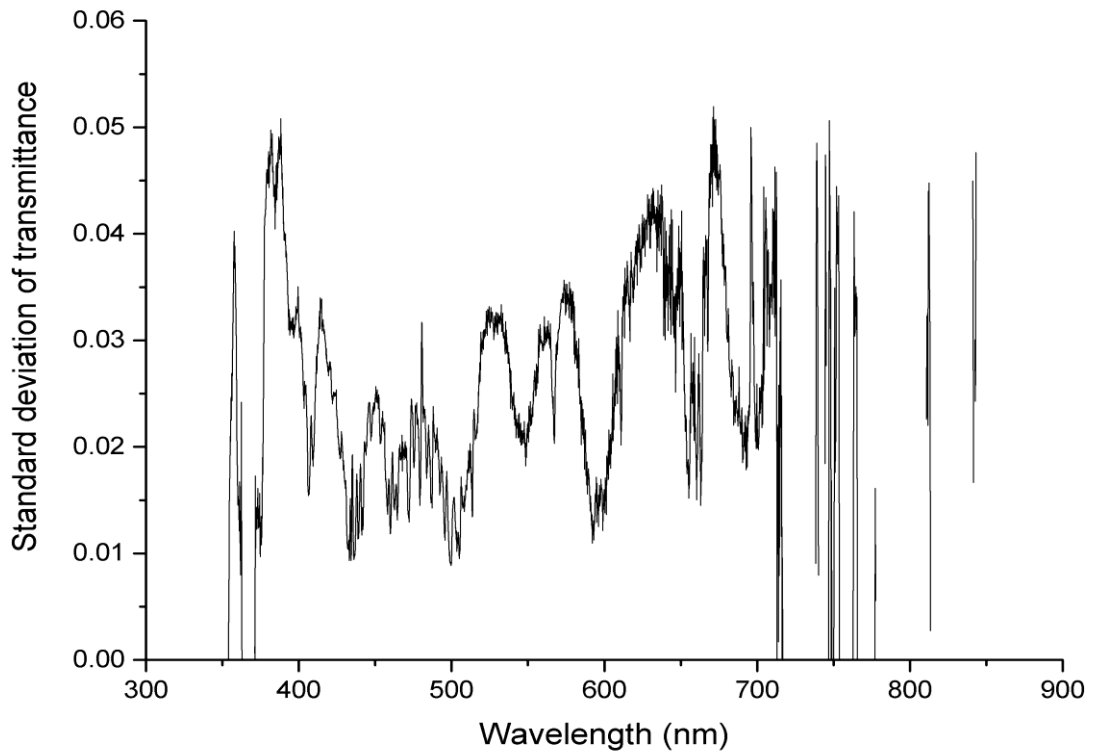


**Figure 66.** A bar chart showing how the standard deviation of the transmittance of the beam splitter varied with wavelength. The results are averaged over 300 laser pulses. There are missing data points below 380nm and 700nm due to the low intensity of the plasma emission at these wavelengths.

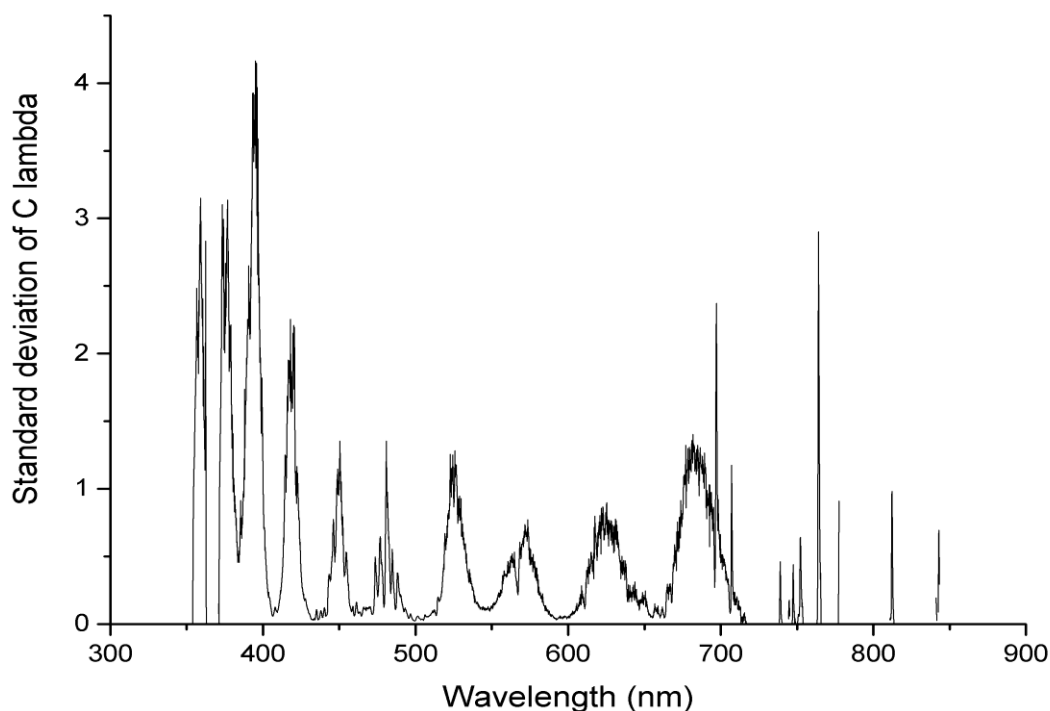


**Figure 67.** A bar chart showing how the standard deviation of  $C_\lambda$  varied with wavelength. The results are averaged over 300 laser pulses. There are missing data points below 380nm and 700nm due to the low intensity of the plasma emission at these wavelengths.

Outside of the wavelength range 380 to 700 nm, data points are missing due to low light intensities. Missing values for the transmittance and  $C_\lambda$  of the beam splitter prevent the determination of sample absorbance at the wavelengths of the missing values. The missing data points in Figures 66 and 67 show that the spectrometer is only effective in the wavelength range of approximately 380 to 700nm. It is highly recommended that the transmittance and  $C_\lambda$  of the beam splitter should be redetermined if any adjustment to the optics occurs.

## 2.9 Instrument Testing Using a Holmium Oxide Standard

The transmission or  $C_\lambda$  of the beam splitter as a function of wavelength can now be used to determine the absorbance a sample between 380 and 700 nm. The absorbance spectrum of the sample can be calculated from a single laser pulse using Equation 18 but the results are more accurate if the absorbance is calculated for multiple pulses and then averaged. Averaging can only be done

with samples that do not change in absorbance over time. The intensity of the transmitted and reflected beams are recorded for each laser pulse, for example at a rate of 1 pulse per second for 5 minutes. The spectrometer outputs two .csv files containing the intensities  $I_A$  and  $I_T$ . These csv files are copied into an Excel (.xslm) file for manipulation by Script 2. The script requires three input in the form of worksheets named "Trans", "Refl" and "Splitter". "Trans" and "Refl" contain the raw output of from each of the CCS200 spectrometers and "Splitter" contains the wavelength dependant values for  $C_\lambda$ .  $C_\lambda$  is used rather than the transmittance as the absorbance calculation is simpler.

Script 2 fixes missing columns and bad data as before but has one additional fix. If the "Trans" value is less than 0.01 and the "Refl" value is between 0.01 and 1, this indicates that the sample is highly absorbent at that wavelength, but an exact value for the absorbance cannot be ascertained. If this is the case, the absorbance is assigned the maximum possible value of 2. The script allows for batch processing to determine the absorbance of multiple samples. Following execution on the .xslm file, Script 2 outputs the results in four columns in the final worksheet of the file. These columns are: wavelength, mean absorbance, standard deviation absorbance and number of good data points used to determine the absorbance. These calculated values can be directly exported for plotting in graphing software.

To confirm the accuracy of the absorbance spectra produced by the plasma spectrometer, a standard, holmium (III) oxide (4%) in perchloric acid (10%) was scanned in the spectrometer for 5 minutes at 1 pulse/sec. The path length of the broadband beam through the sample was 10 mm. This solution is used as a laboratory standard to calibrate and verify the wavelength scale of UV/Vis spectrometers as it has fourteen traceable peaks in the wavelength range 240 to 650 nm. The absorbance peaks in the usable range of the plasma spectrometer (380-700 nm) are 385.4, 416.1, 451.1, 467.8, 485.2, 536.5 and 640.6 nm. For comparison, the absorbance spectra of the calibration solution was also determined in a Thermo Scientific GENESYS 10S UV/Visible

Scanning Spectrophotometer in the range 380 to 700 nm in wavelength increments of 0.5 nm.

Both the plasma spectrometer and the Thermo Scientific spectrophotometer require baselining with a cuvette containing pure water. This is so the absorbance of the quartz crystal cuvette and the water solvent can be subtracted from the absorbance of the holmium oxide and perchloric acid. The baseline absorbance of the water sample is measured using the plasma spectrometer by recording  $I_A$  and  $I_T$  for each pulse. The output cvs are pasted into Excel along with the values of  $C_\lambda$  and the absorbance as a function of wavelength is calculated using Script 2.  $I_A$  and  $I_T$  of the sample are then measured, and the data are pasted as worksheets into a .xlsm file along with  $C_\lambda$  as before. The baseline absorbance data is added as a new worksheet with the label "buffer". Script 2 is now run on the worksheet. The script fixes missing entries and calculates the absorbance as before, but now subtracts the background absorbance. Figure 68 shows the spectrum of holmium (III) oxide (4%) in perchloric acid (10%) obtained using the plasma spectrometer. The results of these experiments as well as the NIST standard calibration spectrum are shown in Figures 68-69.

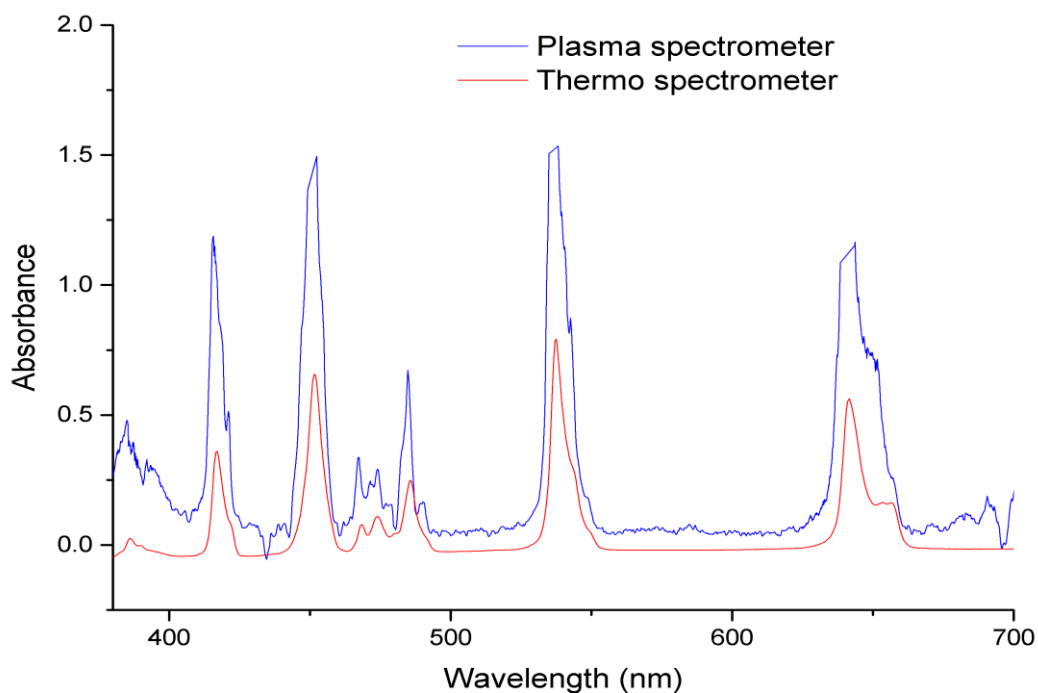


**Figure 68.** The absorbance spectra of holmium (III) oxide (4%) in perchloric acid (10%) obtained using the plasma spectrometer and a Thermo Scientific spectrophotometer. The path length is 10 mm. In the spectrum obtained using the plasma spectrometer, some of the data points are missing at high absorbance because the intensity of light at that wavelength, after passing through the sample, gave a smaller signal than the dark noise of the spectrometer (intensity less than 0.01).

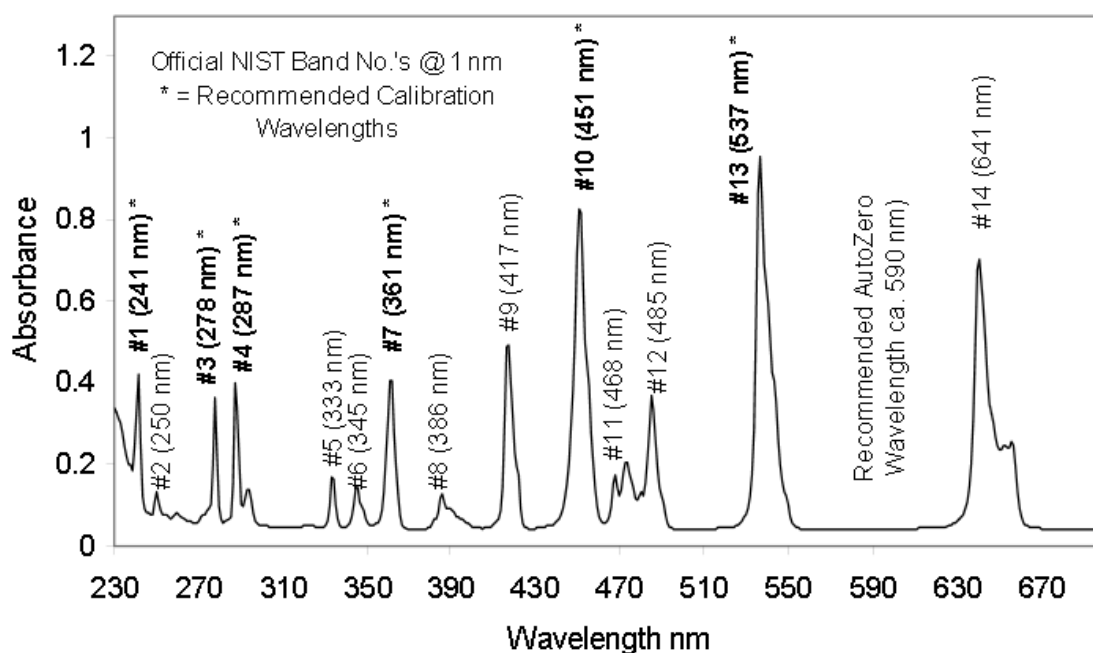
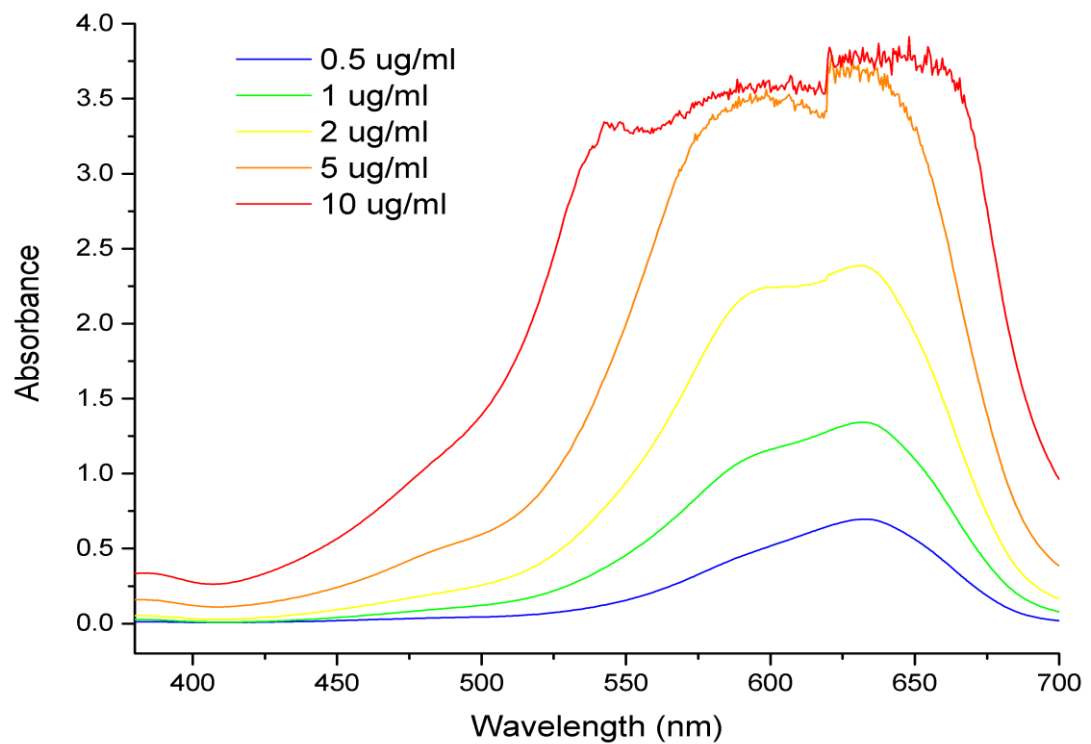
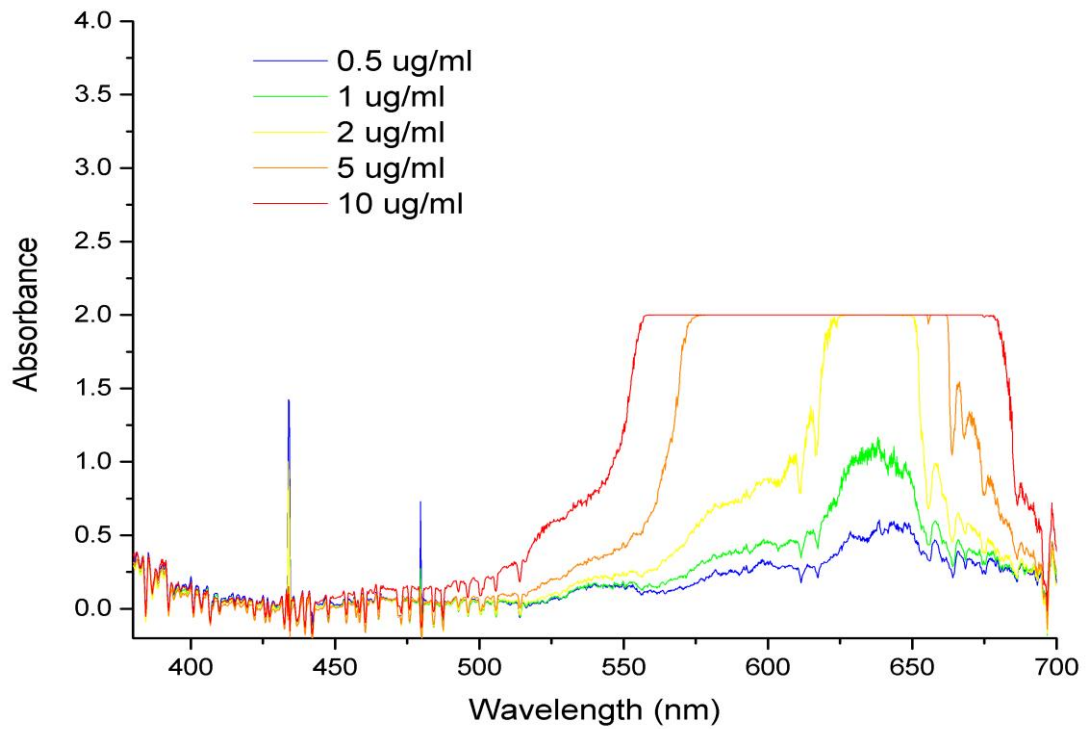


**Figure 69.** The NIST SRM 2034 (lot95) standard spectrum of holmium (III) oxide (4%) in perchloric acid (10%) measured using a HP 8453 spectrophotometer.

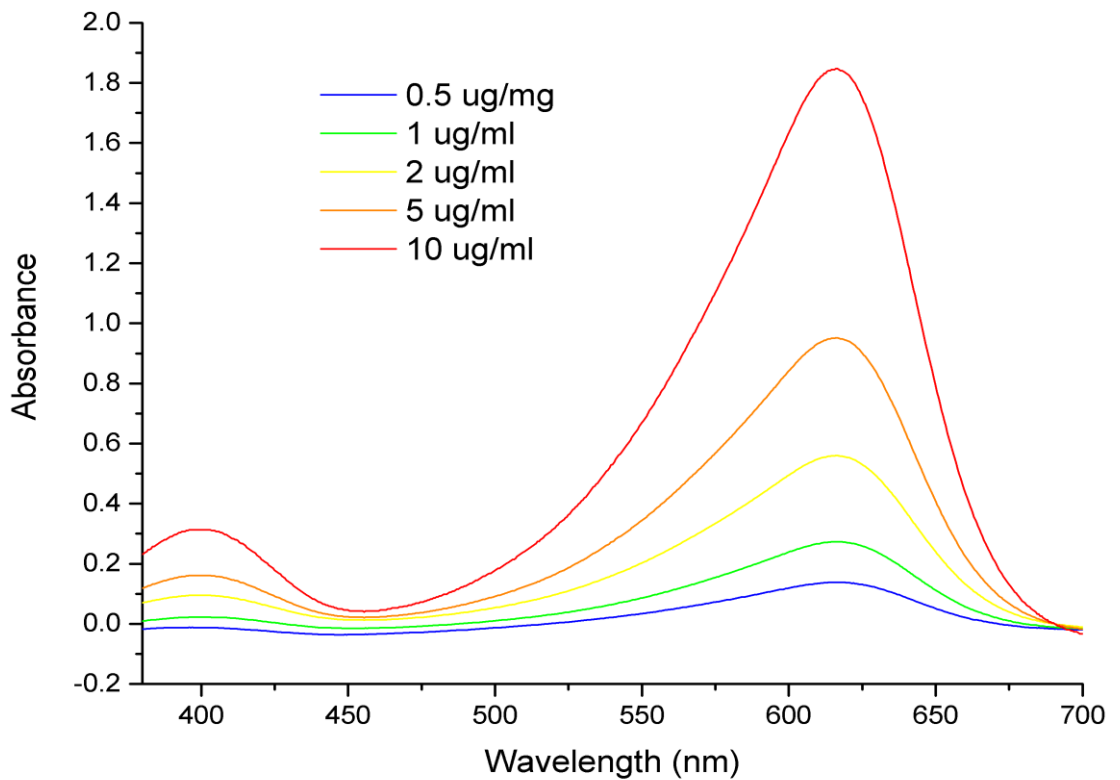
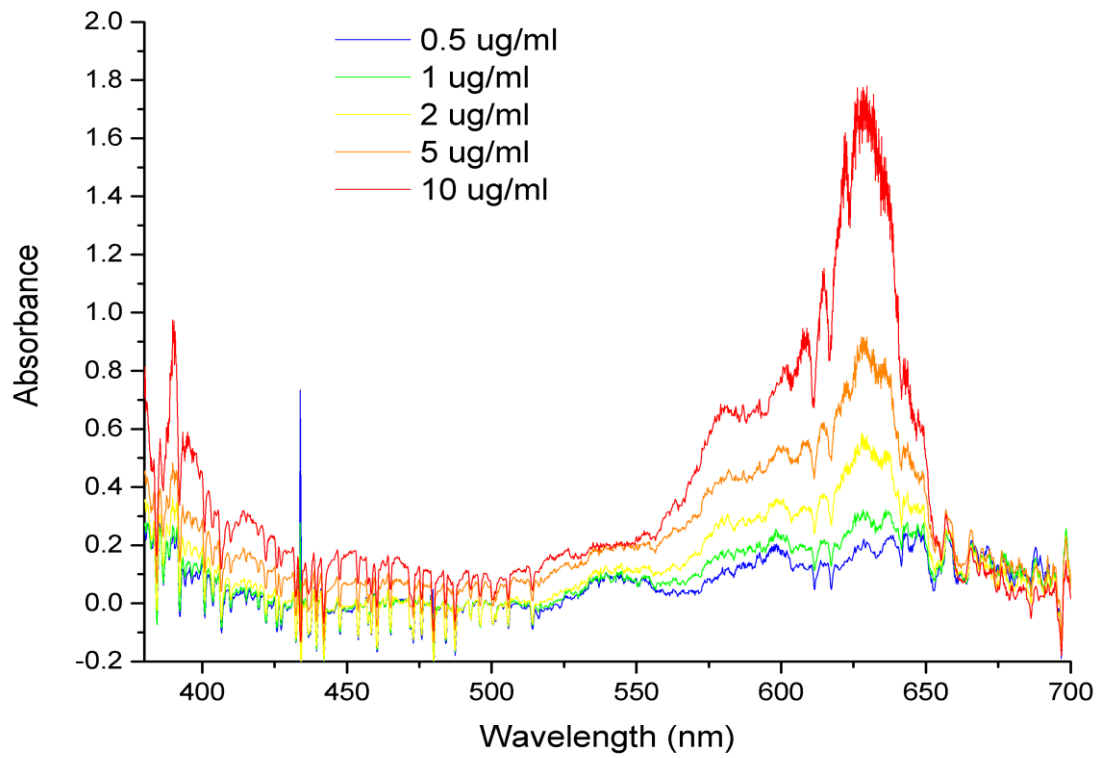
A comparison of the holmium oxide spectra in Figures 68 & 69 shows that within the operating of the spectrometer the wavelengths of the peaks match up almost exactly, confirming the ability of the instrument to measure absorbance to a high degree of wavelength accuracy. However, the absorbance values obtained using the plasma spectrometer are approximately twice that of the NIST standard. This is not so much of a problem as it is the relative rather than the absolute absorbance values which are important. The absolute absorbance values can always be obtained, if necessary, by multiplication of a factor (~0.5 in this case) determined from an absorbance standard.

## 2.10 Instrument Testing Using Coloured Dyes

To further test the viability of the plasma spectrometer for absorption spectroscopy, the coloured compounds bromocresol green, azure A and phenol red were tested at concentrations from 0.5 to 20 mg/mL. These compounds are chromophores in the visible range are used as dyes and pH indicators. The samples were run for 5 minutes at 1 pulse per second (300 scans). For comparison, the absorbance spectra of these compounds, at a concentration of 0.5 mg/ml, were also determined in a Thermo Scientific GENESYS 10S UV/Visible Scanning Spectrophotometer in wavelength increments of 0.5 nm. The results of these experiments as well as comparison spectra are shown in Figures 70-75.

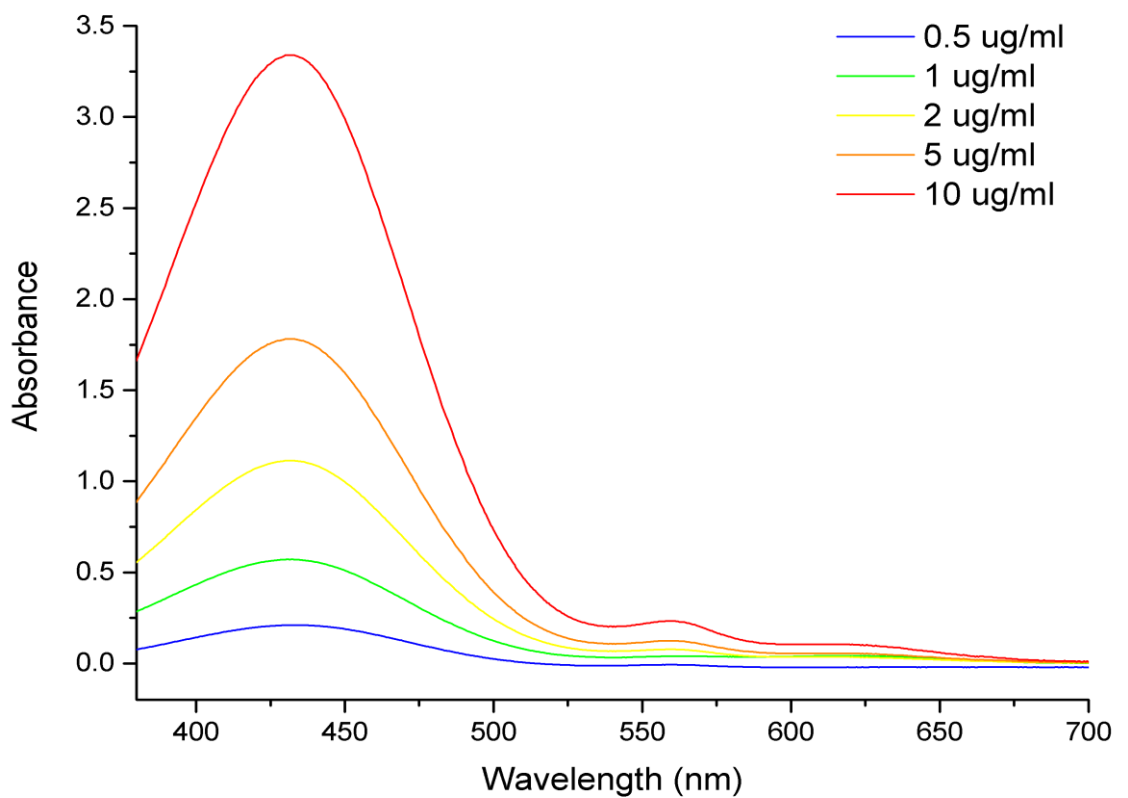
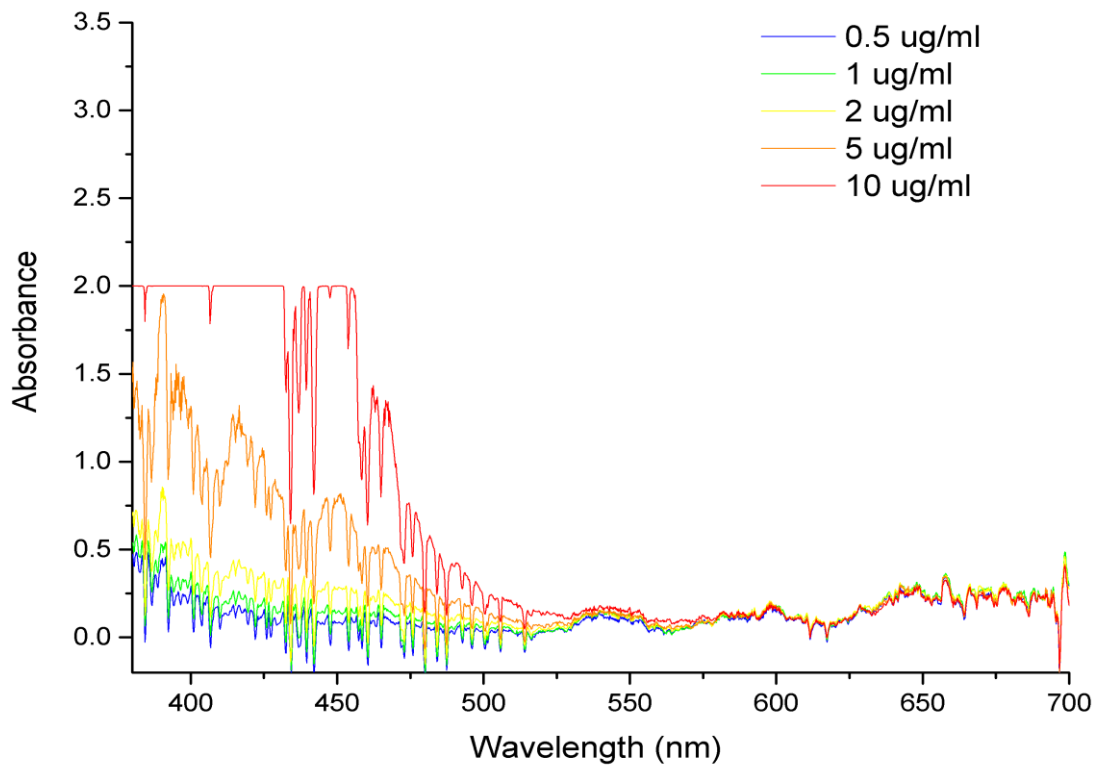


**Figures 70 & 71.** The absorbance spectra of AzureA at several different concentrations. The top spectra was determined using the plasma spectrometer. The bottom spectra was determined by the Thermo Scientific spectrometer



**Figures 72 & 73.** The absorbance spectra of Bromocresol Green at several concentrations. The top spectra was determined using the plasma spectrometer. The bottom spectra was determined by the Thermo Scientific spectrometer





**Figures 74 & 75.** The absorbance spectra of Phenol Red at several concentrations. The top spectra was determined using the plasma spectrometer. The bottom spectra was determined by the Thermo Scientific spectrometer

Figures 70 to 75 showed good correlation between the spectra determined using the plasma spectrometer and spectra determined using the UV/Visible Spectrophotometer. The peaks that occurred at longer wavelengths, the peak at 635 nm with AzureA and the peak at 620 nm with Bromocresol Green, matched up well between instruments. At shorter wavelengths, similar absorbance peaks were observed, the peak at 400 nm in Bromocresol Green and the peak at 430 nm in Phenol Red, but in both spectra the plasma spectrometer showed absorbance increasing as the wavelength became shorter, with the absorbance appearing to still increasing below 380 nm. This may have been caused by an increase in the error of the absorbance, due to the low intensity of light emitted from the plasma source at short wavelengths.

The spectra produced on the plasma spectrometer were much more structured than those produced on the UV/Visible Spectrophotometer. This is most likely due to the higher resolution of the CCS200 spectrometer. The output of the CCS200 spectrometer lists the intensity measured by each pixel on the CCD. The manufacturer's manual states that this spectrometer is accurate to a wavelength 2 nm but in the .csv file output each pixel has a wavelength resolution of approximately 0.2 nm. The comparison UV/Vis spectra are scanned at a resolution of 0.5 nm. The CCS200 may therefore be resolving smaller spectral structures and features than the UV/Visible Spectrophotometer is able to.

## 2.11 Time Resolved Absorbance: Spectral Determination

The real power of the plasma spectrometer lies in its ability to determine time resolved spectra across a broad range of wavelengths. In its current form, the spectrometer is able to determine broadband absorbance spectra up to six times per second. The rate of measurement is limited by the pulse rate of the laser (6 Hz) but the CCS spectrometer can record spectra at up to 200 times a second.

The determination of time resolved absorbance spectra used Script 3 constructed time stamped absorbance spectra in an identical way to Script 2 but these spectra were not averaged to determine a mean absorbance spectra. Instead, Script 3 constructs and outputs a list a list of data points with each data point contained time, wavelength and absorbance information. The script exports the list of data points to a .csv file for visualisation in graphing software.

Script 3 operates on an .xmls file contained four worksheets called “Trans”, “Refl”, “Splitter” and “Buffer”. These worksheets contained the recorded the raw intensity data of transmitted beam, the raw intensity data of the reflected beam, the previously determined values of  $C_\lambda$  and the absorbance spectrum of the buffer/solvent, respectively.

The early versions of the script took a long time to run and outputted datasets that were very large, each generally contained over one million data points. Each time stamped spectra contained 3649 separate wavelength recordings with the spectrometer recording up to 1000 spectra (laser pulses). Datasets this large are very demanding for computer hardware and graphing software, required large amounts of memory and were extremely difficult to edit due to very slow screen updating. Several improvements to Script 3 were added to reduce the number of data points. In order of execution these were:

- The deletion of any data points that were outside the wavelength range 380 – 700 nm.
- Three rows (wavelengths) were merged into one by calculating the average of the three rows. Blank cells are ignored in the averaging function.
- Two columns were merged into one by calculating the average of the two columns. Blank cells are ignored in the averaging function.
- The deletion of any remaining blank rows or columns.
- Following the creation of the list of data points, any data points containing a blank value are deleted.

If the “Trans” value was less than 0.01 and the “Refl” value was between 0.01 and 1, it meant that the sample was too absorbent at that wavelength for the CCS 200 spectrometer to register an intensity signal. In this case, rather than calculate an incorrect value, the intensity was assigned the maximum value of 2. This also allowed for better visual comparison of the final data, as the range of the absorbance values was the same for each spectra.

The first test of the plasma spectrometer was to run it at a pulse rate of 1Hz for 1 hour with no sample. The time resolved absorbance spectra obtained is shown in Figure 76. The Figure shows that the absorbance is approximately zero and does not vary over the course of 1 hour.

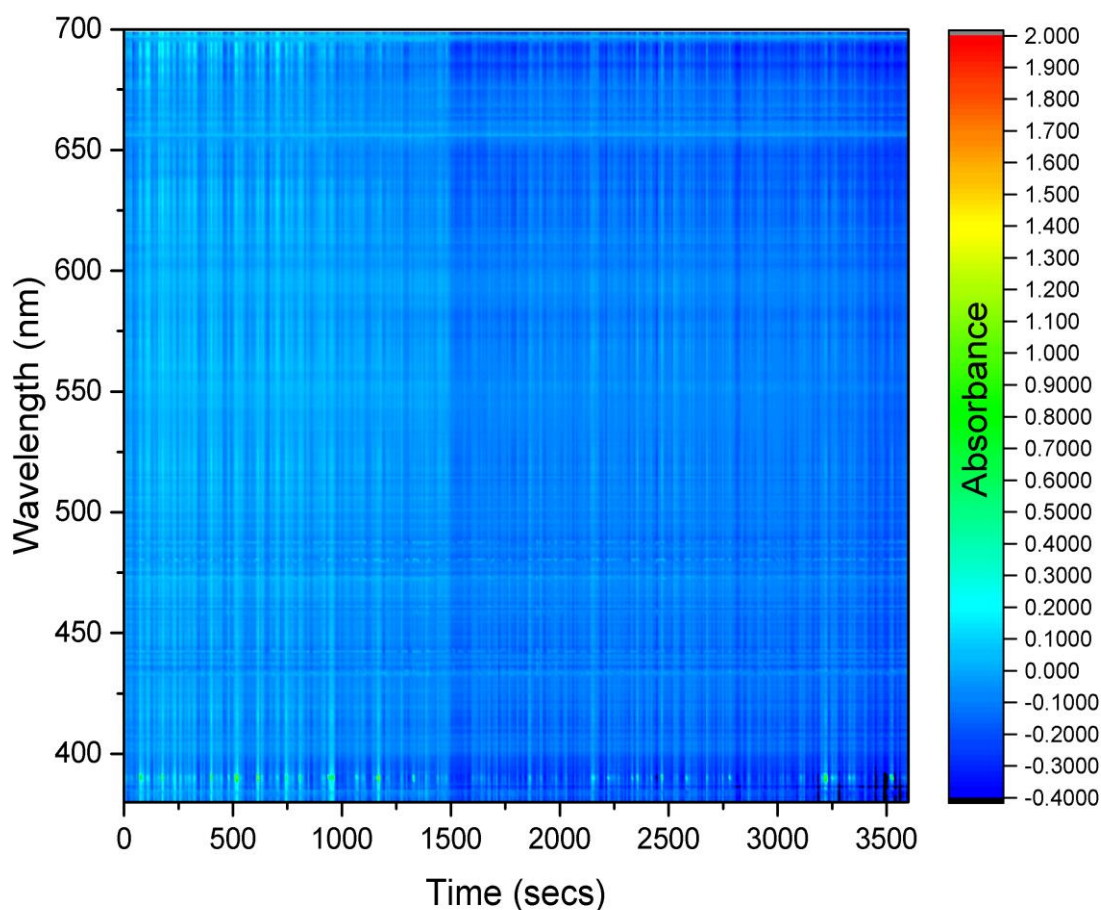


**Figure 76.** The time resolved spectrum obtained from a one hour blank run of the plasma spectrometer.

## Three

---

### Improving Instrument Performance and Reliability

---

#### 3.1 Investigation of the Factors Influencing the Performance and Reliability of the Prototype Instrument

A review of the past scientific literature concerning breakdown thresholds is useful for the comparison of theory with experiment. Table 11 lists relevant examples of the experimentally derived breakdown thresholds in air or nitrogen using an Nd:YAG laser under different conditions.

Ref.	Gas	Pressure	Wavelength 1064nm				Wavelength 512nm			
			Pulse Duration (ns)	Lens Focal Length (cm)	Beam Waist Diameter ( $\mu\text{m}$ )	Breakdown Threshold Irradiance ( $\text{TWcm}^{-2}$ )	Pulse Duration (ns)	Lens Focal Length (cm)	Beam Waist Diameter ( $\mu\text{m}$ )	Breakdown Threshold Irradiance ( $\text{TWcm}^{-2}$ )
(Stricker and Parker, 1982)	Air	1 atm	10	17.8	180	0.082				
(Simeonsson and Miziolek, 1994)	Air	1 atm	8	10	?	0.02	7	10	?	0.015
(Lencioni, 1974)	Air	1 atm	100	51	30	1				
(Smith and Tomlinson, 1967)	Air	1 atm	40	2.69	?	0.1				
(Tambay and Thareja, 1991)	Air	1 atm	8	10	60	0.3	1.8	10	60	0.35
(De Michelis, 1970)	Air	1 atm	0.01	25	?	53 *				

(Meyer and Timm, 1972)	Air	1 atm	0.2	2	?	3				
(Ireland and Morgan, 1974)	N <sub>2</sub>	700 Torr	0.02	5	?	60				
(Davis et al., 1991)	N <sub>2</sub>	700 Torr	8.5	10	90	0.1	7.5	10	90	0.04
(Dewhurst, 1978)	N <sub>2</sub>	700 Torr	0.007	4.2	?	1000	0.025	6.6	?	40
(Armstrong et al., 1983a)	N <sub>2</sub>	760 Torr	<10ns	5.8	29	0.25				
(Alcock et al., 1968)	Air	1 atm	0.01	2	?	100				
(Alcock and Richardson, 1968)	Air	1 atm	0.01	2	?	300				
(Orlov et al., 1972)	Air	1 atm	0.003	5	?	23	0.003	5	?	40
(Phuoc, 2000)	Air	760 Torr	5.5	7.5	17	2.2	5.5	7.5	8.5	3.3
(Bindhu et al., 2004)	Air	1 atm					8	7.5	6	2.5

(Williams et al., 1983)	Air	1 atm					0.02	3.7	3.4	72
							0.033			38
							0.08			18
							0.1			13
							0.14			10.07
							0.032	7.5	7.2	44
							0.089			17
							0.11			11.5
(Van Stryland et al., 1981)	Air	1 atm	0.191	8	19.3	929 *				
			0.104			1062 *				
			0.04			1460 *				
			31		10.3	265 *				
			0.183			1195 *				
			0.117			133 *				
			0.047			1728 *				
			31		5	6.1				584 *
			0.125	1566 *						
			0.1	1620 *						
			0.043	2124 *						
			31	5		797 *				
			0.134			2124 *				
			0.1			2655 *				
			0.044			3584 *				



(Rosen and Weyl, 1987)	N <sub>2</sub>	1 atm					15	?	6.5	4
(Akhmanov et al., 1965)	Air	1 atm	40	200	40	0.033				
(Chylek et al., 1990a)	Air	700 Torr					6.5	10	33	0.17
(Pinnick et al., 1988)	Air	1 atm	8-9	10	30	320	6-7	10	38	150
				30	80	550		10	40	170
								25	62	220
								30	100	350

**Table 11.** The experimental parameters and the results from the published investigations into the breakdown threshold of air or nitrogen using an Nd:YAG laser. The asterisk denotes a conversion to breakdown threshold irradiance from the experimentally determined electric field using  $|I| = \frac{n^2 \epsilon_0}{2} |E|^2$ .

The values for the breakdown threshold in Table 11 vary considerably and are difficult to compare due to variations in the extent and type of investigations undertaken. The data suggest that Equation 17 is not a good model for the breakdown threshold intensity and that the physical reality is more complex. There are a number of parameters that are not taken into account when using Equation 17 to experimentally derive the breakdown intensity. These parameters include:

- The method used to determine whether a breakdown had occurred. As other experimenters have observed (Tomlinson et al., 1966) and as was observed during the present testing, plasma formation is probabilistic at intensities close to the breakdown threshold (Figure 77). Some pulses induce plasma formation while others do not. The reasons for this probabilistic nature have not been thoroughly investigated and no single accepted explanation(s) exists for this behaviour. One possible explanation is the probabilistic nature of multiphoton ionisation. For a single molecule, the production of a seed electron is highly unlikely due to the large number of photons that must be simultaneously absorbed (Table 5). For a large number of molecules the number of seed electrons generated  $X$ , is a discrete random variable taking values  $x_1, x_2, \dots$  with probabilities  $p_1, p_2, \dots$ . These probabilities are some function of laser intensity  $p_i = f(I)$ . If  $N$  is the number of initial seed electrons that are required for plasma formation to proceed through cascade ionisation in a particular case, there will be a laser intensity  $I_t$  at which the expectation value for the number of electrons generated by multiphoton ionisation is  $N$ . This laser intensity  $I_t$  is the breakdown threshold intensity. At laser intensities close to  $I_t$ , the number of seed electrons produced will have high pulse to pulse variation and may be more or less than  $N$ , the required number to induce a plasma. This would give highly erratic and probabilistic plasma production. To ensure the reliability of a plasma being formed for each laser pulse, it is best to design an instrument that minimises the breakdown threshold of the gas and maximises the laser intensity at the focal point of the lens.

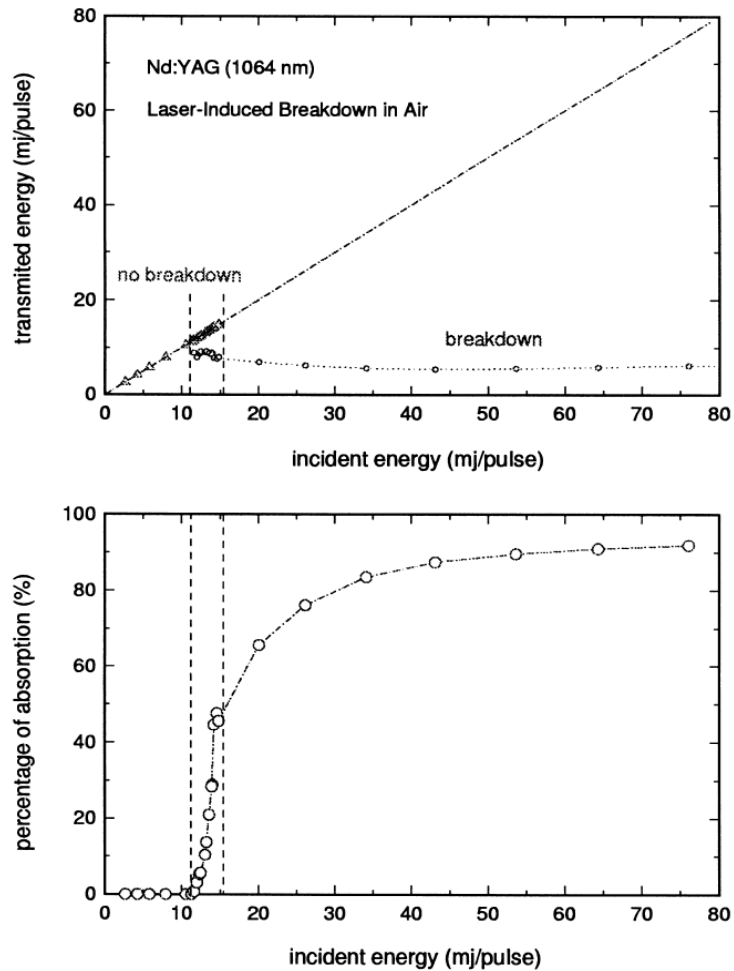


**Figure 77.** Energy absorption study of laser induced breakdown of air. Note the probabilistic occurrence of the plasma in the region between no breakdown and complete breakdown in the top figure. Reproduced from (Chen et al., 2000).

Owing to this probabilistic behaviour and the lack of knowledge concerning its causes, it is a matter for the experimenter to define the point at which breakdown is occurring. Stricker and Parker (Stricker and Parker, 1982) define the breakdown threshold as the lowest laser intensity at which a visible spark is observed for a particular experimental arrangement. Simeonsson and Miziolek (Simeonsson and Miziolek, 1994) choose the threshold as the point at which a spark is visually observed in 90% of pulses. Lencioni (Lencioni, 1974) defines the threshold as the point at which a spark is generated 50% of the time. This variability in the experimental definition of breakdown threshold between authors, combined with a lack of knowledge concerning the probability of plasma occurrence, hampers comparison of the experimental data.

It is important to note from Figure 77 that the breakdown of air is certain to occur above a specific intensity. Therefore, all that is needed for reliable plasma generation is to engineer this specific intensity at the focal point every time the laser pulses.

- The presence of laboratory dust in the air. It can be seen in Figure 77 that for clean air around the breakdown threshold intensity only around 50% of the pulse energy is actually absorbed. This percentage can be greatly increased by the inclusion of dust particles in the focal volume. Dust reduces the breakdown threshold of air as it is highly absorbent of laser radiation. Clean air is only absorbent at very high intensities which initiate the production and seeding of free electrons. Absorption of the laser pulse by particulate matter causes rapid localised heating on the surface of the particulates, generating the initial seed electrons required for further plasma growth by cascade ionisation. Increasing the energy efficiency of plasma generation (and subsequently the electron temperature and density) by the inclusion of particulates in the focal volume is utilised in recent EUV technologies where the heating of tin vapour using a pulsed laser is currently the most viable method for the production of EUV at 13.5 nm.

Two publications by Lencioni (Lencioni, 1974, Lencioni, 1973) study the effect of dust particles, specifically a carbon aerosol, on the breakdown threshold of air. In both publications, the presence of dust particles was found to reduce the breakdown threshold by up to  $10^2$  times. The breakdown threshold was also found to be strongly dependent on the size of the dust particles with larger particles more substantially reducing the breakdown threshold. The presence or absence of dust in the focal volume may explain the probabilistic nature of plasma formation close to the breakdown threshold. If a dust particle happens to be present in the focal volume during the laser pulse, the breakdown threshold may be reduced below the pulse intensity and plasma formation then occurs. Otherwise the breakdown threshold may be too high and a plasma is not formed. This being the case, experiments to accurately determine breakdown thresholds should be carried out in clean gases. These experiments may allow better determination of breakdown thresholds for reliable plasma formation by narrowing (or altogether removing) the range of intensities in which probability based plasma formation occurs. Clean air is

often stated as being used where the pressure dependence of breakdown thresholds is investigated. However some of the publications in Table 11 do not specifically mention using cleaned air and as a result, it is possible that breakdown thresholds could have been greatly reduced by the presence of laboratory dust.

- The presence of ionising radiation in the focal volume is another possible explanation for the erratic nature of plasma formation close to the breakdown threshold. Ionising radiation generates free electrons in air which, if generated in the focal volume, can be subsequently accelerated in the electric field of the laser light leading to plasma growth by cascade ionisation. However, experiments on the radiation enhanced dielectric breakdown of air using static and oscillating electric fields suggest this to be a very small effect at the levels of background radiation. Lewis (Lewis, 1939) found that the breakdown voltage in a 2 cm spark gap was reduced by only 2.5% by the presence of ionising radiation (see Figure 78). Much higher levels of radiation in the order of 1 Gy/s (background radiation is roughly  $9.5 \times 10^{-11}$  Gy/s) are required to significantly reduce breakdown voltages (Hodgson and Morono, 2001). Background radiation can therefore be disregarded as an important factor influencing plasma formation.



amounts of aberration (Zernike and Nijboer, 1946, Evans and Morgan, 1968), but must be solved numerically for aberrations greater than one wavelength (Li and Yu, 1989). Figure 79 shows the resulting intensity distributions for a variety of aberration quantities. Even a lens that completely lacks spherical aberration produces complex patterns of intensity around the focal point (Figure 79 (a)).

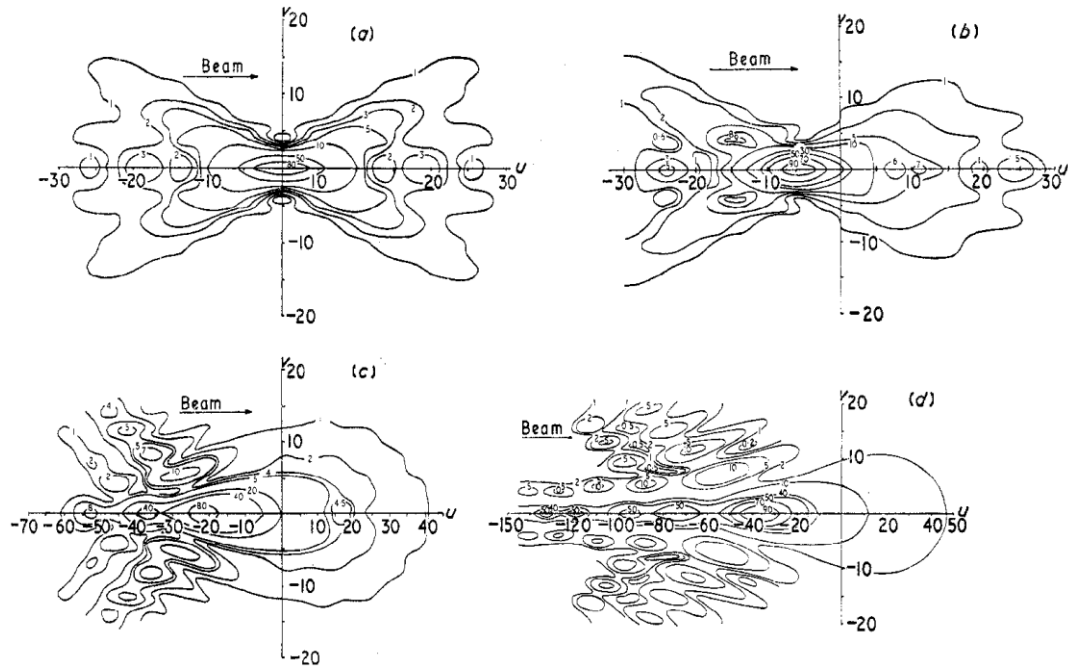


**Figure 79.** Intensity distributions in the vicinity of the focal point of the lens for aberration functions  $\phi_{Max}$  (a) zero aberration (b)  $0.5\lambda$  (c)  $1.8\lambda$  and (d)  $6\lambda$ .  $U$  and  $V$  are dimensionless parameters dependent upon  $f, a$  and  $\lambda$ . The lines are isophotes and trace areas of constant intensity. Reproduced from (Evans and Morgan, 1969).

As can be seen in Figure 79, the effect of wave interference is to produce high intensities at multiple locations around the focal point. This can lead to the breakdown of gas at multiple locations along the beam, generating collinear plasmas (Figure 80). The intensities obtained around the focal point vary depending on the degree of spherical aberration present. As spherical aberration increases, regions of high intensity are formed more towards the direction of the incoming beam. Increasing the power of the laser increases the size and number of regions where the intensity is greater than the breakdown intensity, resulting in the formation of multiple plasmas. These plasmas coalesce as they expand giving the impression that increasing the

laser peak power also increases the size of the plasma. The effect of wave interference introduces complex variation which is difficult to control when attempting to determine the breakdown intensity of a gas. Aspheric lenses can be used, which have minimal spherical aberration but, most experimental determinations of breakdown intensity state that a plano-convex lens is used. A correction for spherical aberration is given in Ireland, Aaron and Morgan (Ireland et al., 1974) but, many authors do not apply this. Unless experiments are designed with lenses of identical type, size, refractive index and focal length, the effect of spherical aberration makes it hard to compare experimentally derived breakdown thresholds.

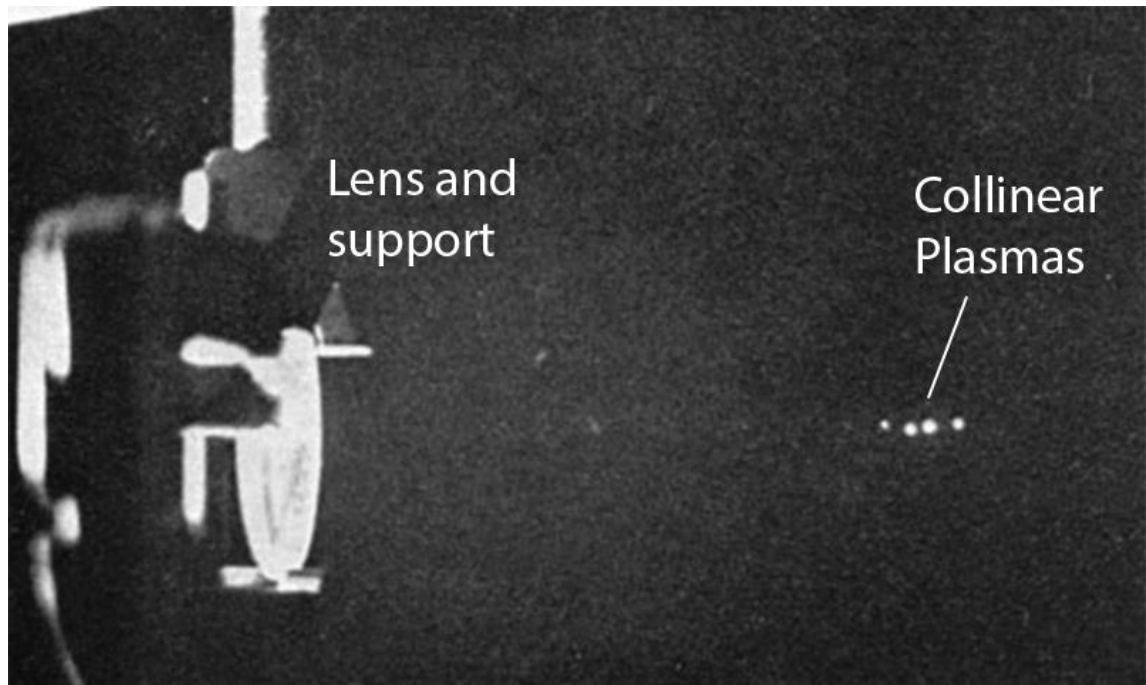


**Figure 80.** Collinear plasmas formed in air at 1 atm produced by a 30 ns ruby laser at  $\lambda=0.69 \mu\text{m}$ . Reproduced from (Morgan, 1975).

The complex intensity distributions in time and space around the focal point are very sensitive to small variations in the experimental parameters. Any subtle variation, such as a small change in the refractive index of air, can produce drastic changes in these intensities. This limits the predictability of the system and may explain the erratic generation of plasmas close to the breakdown intensity threshold.



- The ratio of the first to second laser harmonics. Frequency doubling an Nd:YAG laser using a crystal such as Potassium Dihydrogen Phosphate (KDP) converts some of the radiation at 1064 nm to its second harmonic at 532 nm. Unless it is specifically measured, the ratio of 1064 nm to 532 nm radiation that frequency doubling generates is unknown. Therefore, experiments using a frequency doubler that are designed to investigate the effect of short wavelengths upon the breakdown intensity, should block the fundamental wavelength. In many of the experiments that use a frequency doubling, no mention is made of any method to filter out the fundamental wavelength and so an unknown quantity of the fundamental is still present. This is a source of systematic variation, which complicates the comparison of experiments that investigate breakdown intensities at 532 nm.
- Rate of diffusion of free electrons out of the focal volume. If free electrons are able to diffuse out of the focal volume during the pulse, they are no longer available for plasma growth via cascade breakdown. Thus, the breakdown intensity is influenced by the rate of free electron diffusion out of the focal volume. This rate depends upon the size of the focal volume, the duration of the laser pulse and the gas pressure (Van Stryland et al., 1981). The duration of the laser pulse and the gas pressure determine the characteristic diffusion length that an electron will travel during the laser pulse. If the diffusion length is of comparable size to the diameter of the focal volume, diffusion losses become significant, subsequently increasing the breakdown intensity. This is often the case with nanosecond lasers, resulting in significant losses of free electrons from the focal volume and higher breakdown intensities (Bunkin et al., 1971). For laser pulses in the picosecond range, the laser pulse is short enough for electron diffusion losses in air at atmospheric pressure to be neglected (De Michelis, 1970). Bunkin *et al* note that the measured breakdown threshold can be as much as two orders of magnitude different between long and short focal length lenses. This is explained by the fact that short focal length lenses have smaller focal volumes according to Equation 16. The size of the focal volume also depends on the beam diameter before focusing as well as the focal length of the lens.
- Beam temporal and spatial shape. When determining breakdown intensities it is assumed that laser pulse is perfectly Gaussian in both time and space.

The factor of 0.94 in Equation 15 comes from the assumption that the pulse energy is Gaussian in time. In reality, this may not be the case (Figure 81) with the result that errors are introduced into the breakdown threshold calculations. Deviations away from a perfect Gaussian spatial beam profile add further complexity to the already complex interference patterns around the focal point that are seen in Figure 79.

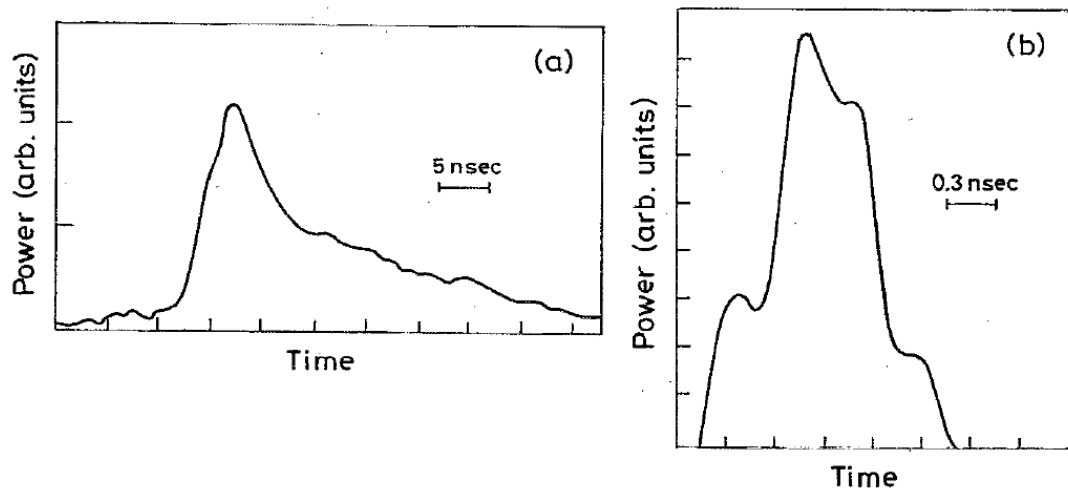


**Figure 81.** Typical temporal profile of an Nd:YAG laser showing that the pulse is actually far from Gaussian in shape. (a) 1064 nm, 8 ns (FWHM); (b) 532 nm, 1.8 ns (FWHM).  
Reproduced from (Tambay and Thareja, 1991).

- The effect of ambient air conditions such as humidity, pressure and temperature. It is known that the ambient air conditions affect the breakdown threshold in both static and varying electric fields. Experiments that have investigated the electrical breakdown of air by static electric fields have found that water vapour in the air can increase the breakdown voltage of air by a few percent (Allen and Phillips, 1959, Lewis, 1939). In laser breakdown experiments, the presence of micron sized water droplets lowers the breakdown threshold of air by up to 2-3 orders of magnitude (Pinnick et al., 1988). These droplets are too large to be normally present in laboratory air and must be induced artificially by an aerosol. Molecular water is not absorbent at the first or second harmonic of Nd:YAG but Table 12 shows the number of photons required to ionise a water molecule is less than that of either nitrogen or oxygen. The generation of seed electrons via the multiphoton ionisation process, and breakdown, would therefore occur at a lower intensity.

Wavelength (nm)	Photon Energy (ev)	Number of Photons		
		Nitrogen	Oxygen	Water
1064	1.17	14	11	6
532	2.34	7	6	3

**Table 12.** Number of photons required in multiphoton ionisation to produce a positively ionised molecule and free electron. Reproduced from (Pinnick et al., 1988).

Data that show the effect of humidity on laser induced plasma breakdown threshold intensities is scarce. Yalcin *et al*, using laser sparks induced in nitrogen, have shown that varying the humidity has very little effect on the electron temperature and density of the plasma (Yalçin et al., 1999). If electron temperature and density are largely unaffected by the ambient humidity, it is strong evidence that breakdown thresholds are also unaffected. Electron temperature and density in a laser induced plasma are directly related to breakdown thresholds. If the breakdown threshold is high compared to the intensity at the focal point, fewer free electrons are generated and these electrons have lower mean kinetic energies i.e. lower electron density and temperature. It is also interesting to note that Yalcin *et al* observe an increase in electron density but no increase in temperature as the laser pulse energy is increased. The photon flux has increased but the photon energies remain unchanged, corresponding to an increase in the spectral power output but with no shift in emitted wavelengths. Conversely, this implies that by using a shorter wavelength laser, the temperature of the plasma can be increased, shifting the black body emission maximum to shorter wavelengths.

Breakdown thresholds for gases in both laser induced and static electric fields are known to depend on the gas pressure. In the presence of static electrical fields the breakdown voltage of a gas follows Paschen's law:

$$\text{Breakdown Voltage} = \frac{apd}{\ln(pd) + b} \quad \text{Equation 19}$$

Where  $p$  is the pressure in atmospheres,  $d$  is the distance between the electrodes and the constants  $a$  and  $b$  depend upon the gas composition. This equation holds for gaps larger than about  $10\ \mu\text{m}$ . The graphs of this equation for different gases are known as Paschen curves (Figure 82).

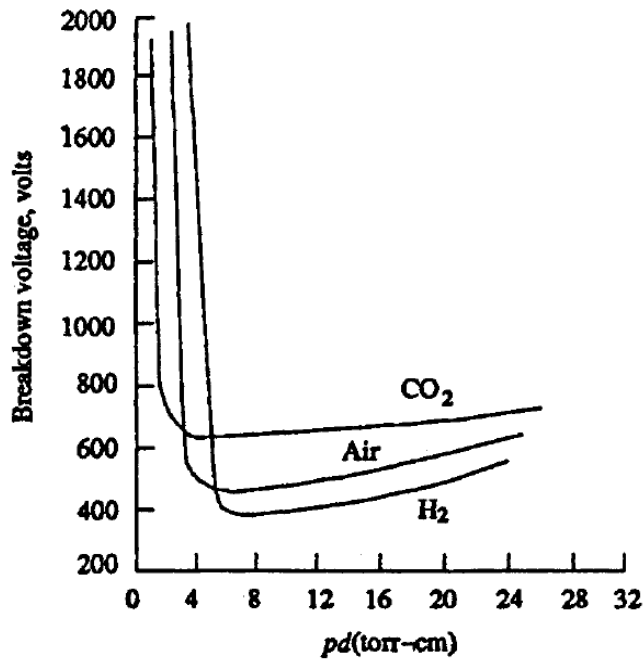


**Figure 82.** Breakdown voltage characteristics for air, CO<sub>2</sub> and hydrogen. Reproduced from (Naidu and Kamaraju, 1996).

The physical mechanism behind this law is similar to the cascade ionisation process occurring in laser induced plasmas. Free electrons are generated by and acquire energy from the external electric field. These electrons then collide with neutral atoms and if they are able to gain more energy from the electric field than the first atomic ionisation potential (for nitrogen this is 15 eV) an electron is freed and the atom becomes ionised. This freed electron is now accelerated in the external electric field and can free more electrons through collisional ionisation leading to cascading and avalanche breakdown. Whether an electron can acquire more energy than the ionisation potential depends upon the magnitude of its mean free path in the gas. The mean free path is inversely proportional to pressure. Thus, if the pressure is low enough the mean free path is long and electrons can acquire enough energy on

average to ionise neutral atoms. However, if the pressure is too low, insufficient collisions occur to start avalanche breakdown and a plasma is not generated. Thus there must exist an optimal pressure at which to perform the laser induced breakdown of gas. Experiments on the effects on emission intensity and plasma reliability in different gases at different pressures follow in the next chapter. The experiments were unable to determine the optimal pressure but showed that plasma emission and reliability both increases as pressure increased from 1 to 2.2 bar.

At low pressures, less than 100 Torr, a weaker dependence of breakdown intensities on pressure is observed. This is due to the long mean free path of electrons and associated lack of collision events. Experiments investigating the multi-photon ionisation process use very low pressure gases ( $10^{-3}$  Torr) to prevent the occurrence of collisional ionisation. At pressures greater than 100 Torr the dominant mechanism of free electron production is cascade ionisation (Agostini et al., 1970b). For laser induced plasmas, a strong dependence on pressure for breakdown intensities is thought to be due to the dominance of cascade ionisation over multi-photon ionisation processes. The air pressure at sea level varies between 980-1050 mbar which is a pressure of 0.967-1.036 atm. At this pressure, the dominant mechanism of breakdown is cascade ionisation. The variation of atmospheric pressure is not great enough to be able to significantly vary the breakdown threshold of air.

- Variations in the refractive index of air. The refractive index of air is also known to depend upon the ambient humidity, temperature and pressure. The effect of the variations in the refractive index of air on breakdown thresholds is likely to be of a two-fold nature. Firstly, changes in the refractive index of air will change the intensity at the focal point by modifying the focusing of the laser pulse. This can be easily seen from Snell's law of refraction at a dielectric boundary:

$$\frac{\sin \theta_1}{\sin \theta_2} = \frac{n_2}{n_1}$$

$n_1$  is the refractive index of air,  $n_2$  is the refractive index of air,  $\theta_1$  is the angle of incidence and  $\theta_2$  is the angle of propagation . The refractive index of air  $n_1$  is often assumed to be unity but slight variations change the angle of propagation. Owing to wave superposition, these small changes in the angle of propagation can cause significant changes in the intensity at the focal point as seen in Figure 79.

Secondly, at very high intensities the refractive index of a medium is modified non-linearly, resulting in self-focusing of the propagating beam. There are two important processes that cause self-focusing: the Kerr effect and plasma self-focusing. At high intensities, the refractive index of a dielectric is modified non-linearly due to the optical Kerr Effect. The refractive index is changed according to:

$$n = n_0 + n_2 I$$

Where  $I$  is the intensity of the light. The non-linear index  $n_2$  for air depends upon the ambient conditions. With a laser beam that has a Gaussian profile, the non-linear refractive index is maximal along the optical axis because the intensity is the highest along this line and decreases away from the central optical axis. This variation of refractive index along the beam profile acts like a lens or waveguide causing the beam to be focused to a point. This process is known as self-focusing. This effect can also amplify the noise across the beam profile, causing the beam to split up into separate self-focusing elements.

The ambient air conditions have a direct effect upon the breakdown threshold of air by changing the rate of the multi-photon and cascade ionisation processes. However, the effect of ambient air conditions on breakdown thresholds is likely to be small when inducing plasmas in laboratory air, due to the relatively small variations of air humidity, temperature and pressure. Much larger variations in laboratory air would be required to explain the several orders of magnitude variations seen in Table 11.

- Investigators of laser induced plasma phenomenon have noted that once breakdown had occurred in a sealed virgin gas, the threshold irradiance was reduced by 20-25% (Chan et al., 1973, Stricker and Parker, 1982). No explanation exists for this behaviour, but a more rigorous time resolved analysis may confirm the existence of such an effect.

Owing to the fact that the original 10 cm focal length lenses, supplied by Wei Fang Ming Liang Electronics Company Ltd, did not produce plasmas in air, it was necessary to conduct testing with focusing optics including several lenses of differing focal lengths and also to test a set of beam expanding optics.

### **3.2 Testing of Focusing Lenses**

The next stage was to test a number of lenses that could be used in a simple, single plano-convex focusing lens arrangement without beam expansion. The lenses that were tested were as follows:

1. Chinese tattoo removal manufacturer's lens, focal length 10 cm
2. Thorlabs LA4600, UV fused silica plano-convex lens, diameter 12.5mm, focal length 10 cm.
3. Thorlabs LA4764, UV Fused silica plano-convex lens, diameter 12.5mm, focal length 5 cm.
4. Thorlabs LA4647, UV Fused silica plano-convex lens, diameter 12.5mm, focal length 2 cm.

Each of these was tested with or without frequency doubling to 532 nm and at 1, 3 and 5 Hz repetition rates. For each set of values of the experimental parameters, the plasmas were recorded in a 5 minute video on a Fujifilm Finepix S5800 Digital Camera. This camera captures at a frame rate of 30 frames per second, making a total of 9000 frames per experiment. The temperature of the laser was also recorded every 30 seconds by reading off the digital panel on the laser housing.

Each video was broken down into individual frames and the frames during which the laser was pulsing were separated from the other frames. To avoid timing issues arising from starting and stopping the camera, only frames 50-8950 were analysed. The frames which did not feature a laser pulse were discarded. Each frame remaining was examined to see whether it contained a plasma. The size and location of each observed plasma was measured to the nearest 0.5 mm. For each frame, a number of variables were recorded. The dependent variables were:

- Plasma in frame: Yes/No stored as a Boolean variable, 0 or 1.
- Plasma diameter in mm. The size of a laser induced plasma was a few millimetres (Chen et al., 2000) but appeared larger due to absorption of UV light, and subsequent re-radiation, by air molecules of photons in the visible region of the spectrum. The size of the plasma therefore gave a good indication of spectral power output radiated by the plasma.
- Plasma distance from lens in mm. The variance in this parameter needed to be minimal if the light emitted from the plasma were to be captured and collimated.

The independent variables were:

- Focal length in metres.
- Reciprocal of the square of focal length in  $\text{m}^{-2}$ . This was included in the data because from Equation 17 the intensity at the focal point is proportional to the reciprocal of the square of the focal length. Using these data, generalised linear modelling was used to test how varying the intensity at the focal point affects the dependant variables. Either the focal length or the reciprocal square of focal length can enter into statistical modelling as a predictor variable but not both.
- Reciprocal of focal length in  $\text{m}^{-1}$ . It may be useful when looking for relationships to examine the dependencies of this variable.
- Whether the laser is frequency doubled. Stored as a Boolean value.
- The repetition rate of the laser. This variable has a value of 1, 3 or 5.
- Frame number from 50 to 8950.
- Laser coolant water temperature in degrees Kelvin.



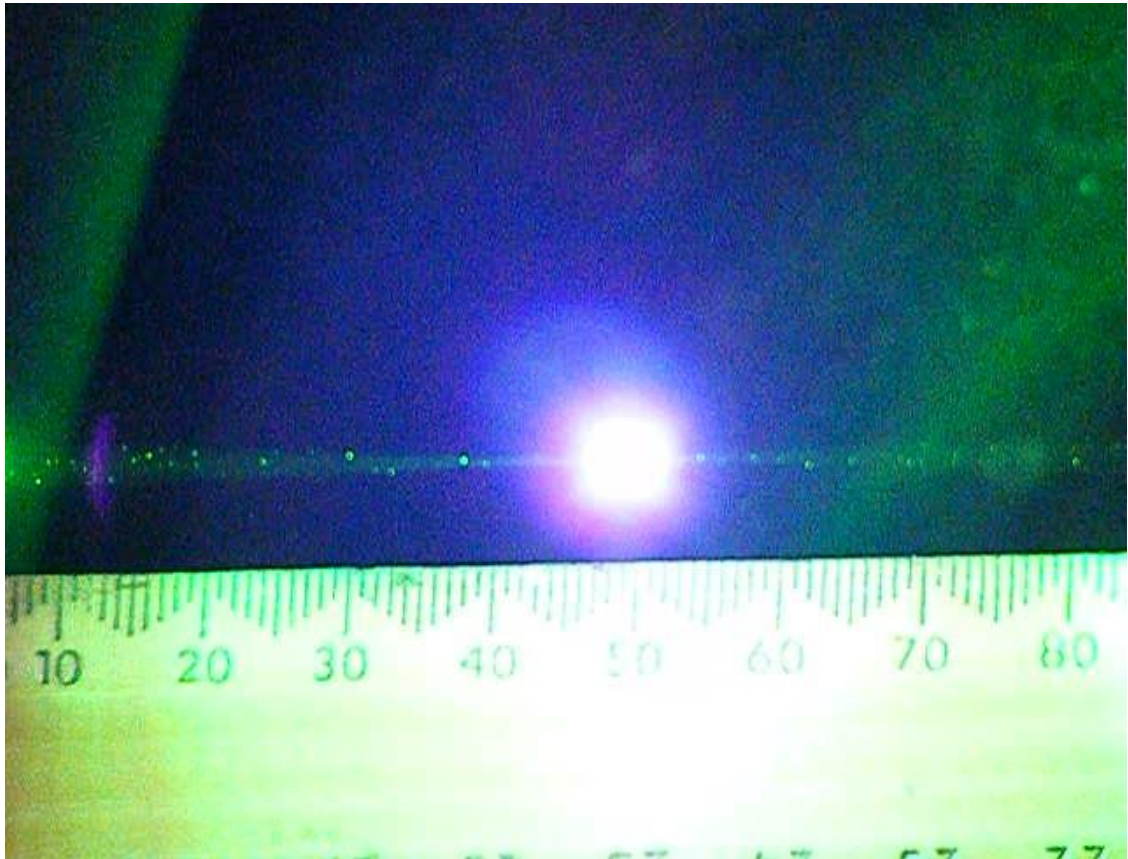


**Figure 83.** Frame 1787 from a 5 min video capture, showing the laser induced plasma obtained using 5 cm focal length lens. The laser is frequency doubled to 532 nm as can be seen by the green reflections from dust in the air.

Many of the frames from the videos allowed the size and position of the plasmas to be examined, but it was obvious that the camera had problems capturing a complete set of good quality images for analysis. Many of the frames (see Figure 84) show a cross like object/image often above the focal point of the beam. During the recording of these videos, it became apparent that the presence of these cross like objects meant that the camera had been unable to capture a good image of a plasma that had formed. The objects appear in the same horizontal position but their position in the vertical direction changes cyclically. Their position in the vertical direction gradually decreases before starting again at a high position (Figure 85). These objects may be residual images caused by the CCD imaging chip being incompletely reset between imaging cycles but the reason for the cyclic movement of these images in the video is unknown.



**Figure 84.** Frame 5342 from a 5 minute video capture showing the cross image phenomenon. A plasma has formed, but the camera was unable to capture an image of the plasma. This frame was taken from a video recorded for a 5 cm focal length lens without frequency doubling.

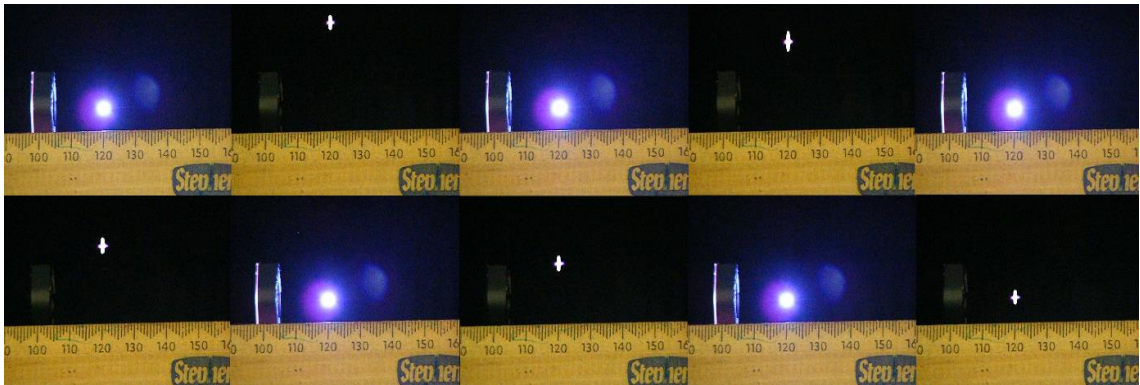


**Figure 85.** A sequence of images showing how the position of the cross-like objects changes over time. The frames shown are numbers 517, 545, 574, 602, 631, 659, 688, 716, 745 and 773. The blank frames in between are all blank frames. These frames are taken from the video recorded with a 2 cm focal length lens with no frequency doubling at a repetition rate of 1 Hz.

The presence of these cross like objects could be due to differences in the timing of the plasma and the imaging interval of the CCD chip in the camera. Frames featuring these crosses occur at regular intervals during the video, indicating that

a timing issue may be the cause. The lifetime of the spectral intensity of similar plasmas is typically in the order of 1  $\mu\text{s}$  (Harilal, 2004), so it is quite possible that the camera could not image such a short lifetime object correctly especially if the plasmas occurs between frames. A potential solution is most likely to use a camera that has a manually adjustable exposure time and frame rate. These images were recorded in the data as the presence of a plasma of unknown size. For import into the R statistical package, an unknown is represented by "N/A" in the data table. R can then be instructed to ignore unknown quantities in the statistical analysis.

A summary of the results for each lens setup tested is shown in Table 13. From a cursory examination of the results of lens testing it was obvious that the focal length of the lens is an important factor effecting the reliability of pulse to pulse plasma generation. The probability of a laser pulse inducing a plasma decreased dramatically as the focal length increased.

Lens Setup	Focal Length (mm)	Reciprocal of Square of Focal Length (mm <sup>-2</sup> )	Laser Repetition Rate Hz	Frequency Doubled	Number of Laser pulses	No of Plasmas Induced	Number of Corrupted Plasma Frames	Probability of Plasma Occurrence per Pulse (P)	Logit (P)	Mean Plasma Size (mm)	Variance Plasma Size (mm)	Mean Plasma Location (mm)	Variance Plasma Location (mm)
Chinese Lens	100	0.0001	1	0	317	4	1	0.0126	-4.3599	4.00	2.00	93.67	1.06
Chinese Lens	100	0.0001	3	0	965	1	0	0.0010	-6.8711	1.00	0.00	106.00	0.00
Chinese Lens	100	0.0001	5	0	1612	4	0	0.0025	-5.9965	2.25	0.19	85.50	42.75
Chinese Lens	100	0.0001	1	1	315	0	0	0.0000	NA	NA	NA	NA	NA
Chinese Lens	100	0.0001	3	1	964	3	0	0.0031	-5.7694	2.17	1.72	82.00	56.00
Chinese Lens	100	0.0001	5	1	1610	3	0	0.0019	-6.2835	1.67	0.22	99.00	44.67
Thorlabs 10cm Plano-Convex	100	0.0001	1	0	314	1	0	0.0032	-5.7462	1.00	0.00	68.50	0.00

Thorlabs 10cm Plano- Convex	100	0.0001	3	0	966	14	1	0.0145	-4.2195	1.38	0.58	73.65	123.59
Thorlabs 10cm Plano- Convex	100	0.0001	5	0	1612	9	0	0.0056	-5.1824	1.56	0.30	72.11	105.88
Thorlabs 10cm Plano- Convex	100	0.0001	1	1	316	3	0	0.0095	-4.6476	1.33	1.39	94.67	54.89
Thorlabs 10cm Plano- Convex	100	0.0001	3	1	963	3	0	0.0031	-5.7683	0.83	0.06	95.67	32.89
Thorlabs 10cm Plano- Convex	100	0.0001	5	1	1614	4	0	0.0025	-5.9977	1.00	0.00	92.50	144.63
Thorlabs 5cm Plano- Convex	50	0.0004	1	0	317	295	114	0.9306	2.5959	5.86	0.95	41.65	0.35

Thorlabs 5cm Plano- Convex	50	0.0004	3	0	961	19	1	0.0198	-3.9036	2.17	1.39	43.75	12.78
Thorlabs 5cm Plano- Convex	50	0.0004	5	0	1615	10	3	0.0062	-5.0783	2.64	1.19	43.86	5.91
Thorlabs 5cm Plano- Convex	50	0.0004	1	1	317	317	140	1.0000	NA	4.84	0.42	50.00	0.00
Thorlabs 5cm Plano- Convex	50	0.0004	3	1	962	13	5	0.0135	-4.2905	3.56	2.46	48.50	11.50
Thorlabs 5cm Plano- Convex	50	0.0004	5	1	1613	5	1	0.0031	-5.7733	2.63	0.92	50.00	21.38
Thorlabs 2cm Plano- Convex	20	0.0025	1	0	313	288	119	0.9201	2.4441	4.41	0.17	20.00	0.00

Thorlabs 2cm Plano- Convex	20	0.0025	3	0	961	961	367	1.0000	NA	5.36	0.15	20.00	0.00
Thorlabs 2cm Plano- Convex	20	0.0025	5	0	1609	1609	646	1.0000	NA	4.56	0.07	20.00	0.00
Thorlabs 2cm Plano- Convex	20	0.0025	1	1	315	248	104	0.7873	1.3087	4.44	0.46	20.00	0.00
Thorlabs 2cm Plano- Convex	20	0.0025	3	1	965	965	384	1.0000	NA	4.62	0.03	20.00	0.00
Thorlabs 2cm Plano- Convex	20	0.0025	5	1	1612	1470	586	0.9119	2.3372	4.03	0.09	20.00	0.00

**Table 13.** A summary of the results of the lens testing experiments.

Following import into R, a useful way to look for interrelationships between variables is to plot a correlation matrix, or for a more visual summary of correlation, a scatterplot matrix, can be plotted. The correlation matrix is, plotted in Table 14 using the 'Pearson' method with complete observations only (variables with a value of N/A are excluded).



	Focal	Reciprocal	Square	Doubled	Rate	Frame	Plasma	Size	Location	Temp
Focal	1	-0.949075304	-0.929846921	-0.008589024	-0.365080921	-0.01676064	-0.100769151	-0.11623971	0.98833389	0.23712866
Reciprocal	-0.949075304	1	0.998416073	0.001678308	0.444115742	0.02236289	0.059157506	-0.02094755	-0.96904087	-0.2503195
Square	-0.92984692	0.998416073	1	0.000426273	0.453487468	0.02312455	0.051094826	-0.04522273	-0.95524806	-0.2500022
Doubled	-0.008589024	0.001678308	0.000426273	1	0.061758111	0.01163772	0.01465599	-0.32669864	-0.00323229	0.85519552
Rate	-0.365080921	0.444115742	0.453487468	0.061758111	1	0.02343258	0.005234258	-0.31359691	-0.39032919	0.2099904
Frame	-0.016760642	0.022362891	0.023124547	0.011637725	0.023432584	1	0.014064016	-0.08142314	-0.01795697	0.19418208
Plasma	-0.100769151	0.059157506	0.051094826	0.01465599	0.005234258	0.01406402	1	0.07403905	-0.11683694	0.01155565
Size	-0.116239709	-0.020947549	-0.045222727	-0.326698636	-0.313596907	-0.08142314	0.074039051	1	-0.0883324	-0.33323145
Location	0.988333893	-0.969040867	-0.955248064	-0.00323229	-0.39032919	-0.01795697	-0.116836939	-0.0883324	1	0.23990648
Temp	0.237128664	-0.250319503	-0.250002197	0.855195517	0.209990402	0.19418208	0.011555653	-0.33323145	0.23990648	1

**Table 14.** The correlation matrix of the dependant and independent variables in the lens testing experiments. The variables are 'Focal' – Focal length in metres, 'Reciprocal' – Reciprocal of the focal length in  $m^{-1}$ , 'Square' – The reciprocal of the square of focal length, 'Doubled' – Whether the laser is frequency doubled or not (Boolean Value), 'Rate' – Rate of laser pulsing in Hz, 'Frame' – Frame number, 'Plasma' – Whether the plasma is formed from the pulse, Size – Diameter of observed plasma in mm, 'Location' – Distance of plasma from lens in mm, 'Temp' – Temperature of coolant water in °K.

In the correlation matrix in Table 14, zero represents no correlation. A value of 1 represents a perfectly proportional or a positive correlation and value of -1 represents a perfectly inverse relationship or negative correlation. The matrix shows, as expected, a strong positive correlation between the focal length and plasma location. A strong positive correlation between frequency doubling and temperature can be explained by the fact that the frequency doubling experiments were often conducted after the experiments without frequency doubling. As a result of this, the temperature of the laser coolant was often higher with the frequency doubled tests as the laser had already been in use for some time. Small negative correlations ( $\sim -0.3$ ) are seen between frequency doubling, the pulse rate of the laser, the laser temperature and the plasma size. There is also a small negative correlation of -0.39 between the plasma location and the laser pulse rate.

To further analyse the data, multiple regression analysis was performed for each of the dependent variables in the R statistical software package. For each dependent variable, an analysis was performed with the focal point or the reciprocal of the square of focal point as one of the variables. Multiple regression analysis assumes that the independent variables are linearly related to the dependent variable. If this is not the case, the variables may need to be transformed before a multiple regression fit can be applied. Plotting each dependent variable against each independent variable may show the nature of the relationship between variables and whether any of them need to be transformed. From the scatter plot matrices in Figure 86 it was not obvious that a transformation needed to be made for any of the variables.

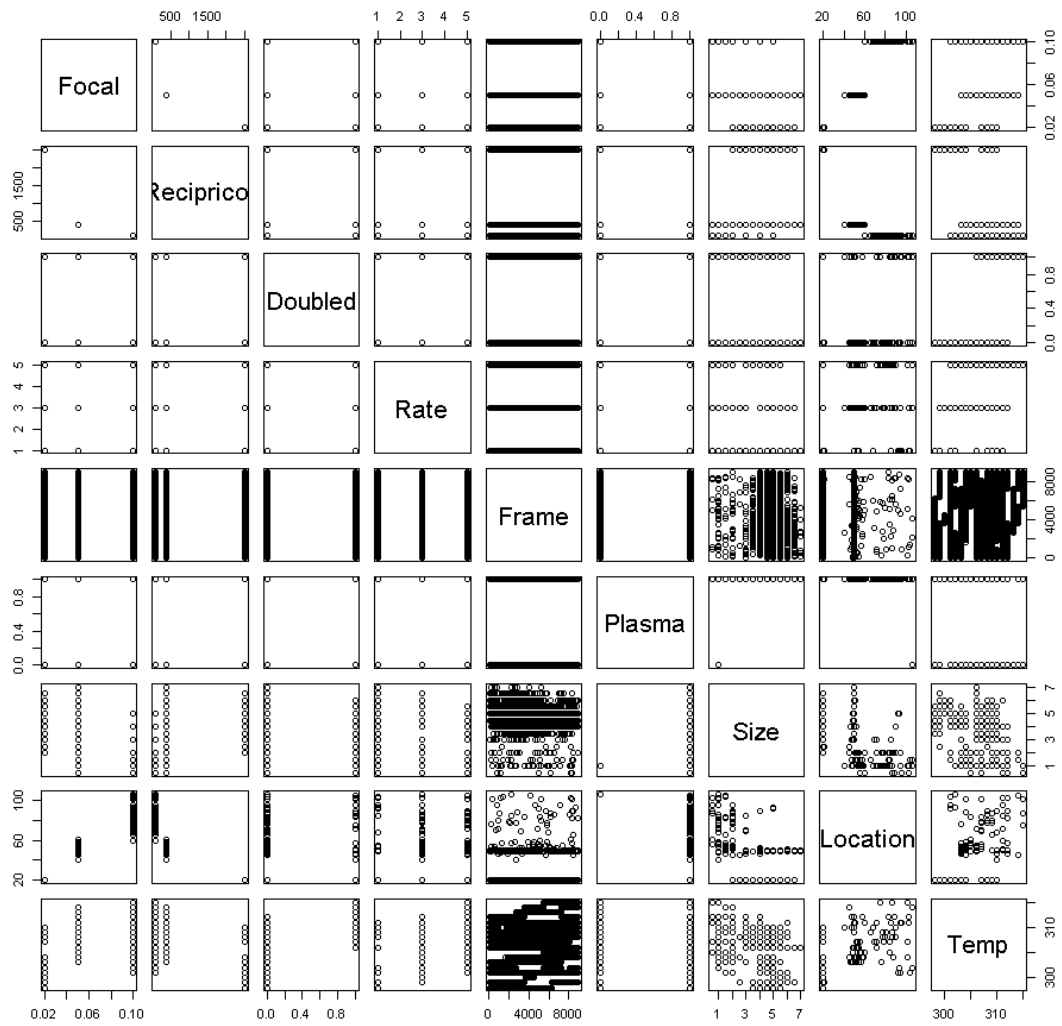


**Figure 86.** Scatter plot of the dependant and independent variables in the lens testing experiments.

The occurrence of a plasma seemed to be uncorrelated with any other independent variable but the needs to be transformed in order to see possible dependencies. The variables denoting whether there was a plasma in the frame (0 or 1), is a nominal dependant variable and its dependencies must be examined using logarithmic regression. This is done by modelling the variable as a probability and then converting the probabilities to logits using:

$$\text{logit}(p) = \ln\left(\frac{p}{1-p}\right)$$

The predictive logistic regression model for plasma occurrence is therefore:

$$\text{logit}(p) = \ln\left(\frac{p}{1-p}\right) = \varepsilon_1 + \varepsilon_2 F + \varepsilon_3 R + \varepsilon_4 D + \varepsilon_5 N + \varepsilon_6 T$$

$F$  is the reciprocal of focal length or the reciprocal of the square of the focal length,  $R$  is the laser repetition rate,  $D$  is whether the laser is frequency doubled,  $N$  is the frame number and  $T$  is the laser temperature. In this model, it was assumed that each of the independent variables has a linear relationship to  $\text{logit}(p)$ . Rearranging for the probability  $p$ :

$$\text{Plasma Probability Per Laser Pulse, } p = \frac{e^x}{1 + e^x}$$

Where  $x = \varepsilon_1 + \varepsilon_2 F + \varepsilon_3 R + \varepsilon_4 D + \varepsilon_5 N + \varepsilon_6 T$

A graph of  $p$  against  $x$  is shown in Figure 87. The domain of  $p$  is 0 to 1,  $p=0.5$  at  $x=0$ , increases as  $x$  increases and decreases as  $x$  decreases. Therefore, the larger the terms in the equation for  $x$ , the greater the probability of a plasma occurrence per pulse.

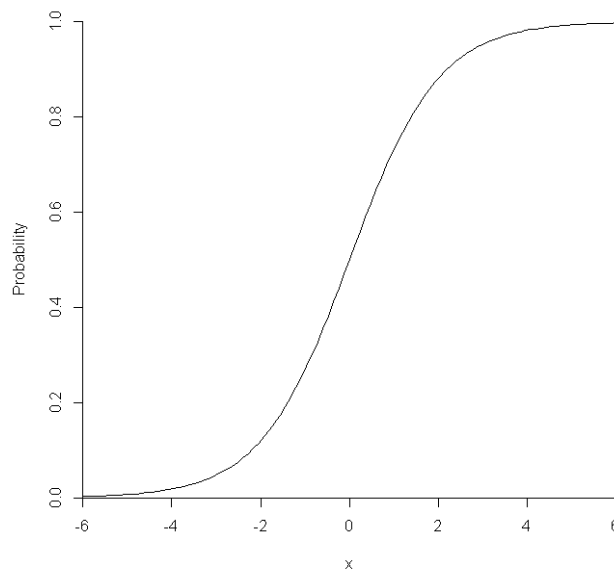


**Figure 87.** A graph of the plasma probability against  $x$ .

Logarithmic regression in R of with the reciprocal of focal length as one of the independent variables, gave an output of:

*Deviance Residuals:*

<i>Min</i>	<i>1Q</i>	<i>Median</i>	<i>3Q</i>	<i>Max</i>
-3.8524	-0.1578	-0.0563	0.0434	3.9712

*Coefficients:*

	<i>Estimate</i>	<i>Std. Error</i>	<i>z value</i>	<i>Pr(&gt; z )</i>
<i>(Intercept)</i>	-4.950e+01	5.993e+00	-8.260	< 2e-16 ***
<i>Reciprocal</i>	2.568e-01	4.207e-03	61.033	< 2e-16 ***
<i>Doubled</i>	-1.155e+00	1.146e-01	-10.079	< 2e-16 ***
<i>Rate</i>	-1.216e+00	3.469e-02	-35.063	< 2e-16 ***
<i>Frame</i>	-2.701e-05	1.528e-05	-1.768	0.077 .
<i>Temp</i>	1.508e-01	1.958e-02	7.705	1.3e-14 ***

---

*Signif. codes:* 0 '\*\*\*' 0.001 '\*\*' 0.01 '\*' 0.05 '.' 0.1 ' ' 1

*(Dispersion parameter for binomial family taken to be 1)*

*Null deviance: 27811.0 on 23515 degrees of freedom*  
*Residual deviance: 5282.2 on 23510 degrees of freedom*  
*(1 observation deleted due to missingness)*  
*AIC: 5294.2*

*Number of Fisher Scoring iterations: 8*

This output showed that the focal length, repetition rate, frequency doubling and temperature all significantly ( $p < 0.001$ ) affected the pulse to pulse plasma probability or logit ( $p$ ). The frame number was not significant at the level of  $p < 0.05$ . An ANOVA test showed the change in deviance obtained when each of the terms was added to the model in the order specified in the model formula. The ANOVA output was:

	<i>Df</i>	<i>Deviance</i>	<i>Resid. Df</i>	<i>Resid. Dev</i>	<i>Pr(&gt;Chi)</i>
<i>NULL</i>			23515	27811.0	
<i>Reciprocal</i>	1	20705.6	23514	7105.3	< 2.2e-16 ***

<i>Doubled</i>	1	38.6	23513	7066.8	5.247e-10	***
<i>Rate</i>	1	1725.0	23512	5341.8	< 2.2e-16	***
<i>Frame</i>	1	0.0	23511	5341.8	0.8952	
<i>Temp</i>	1	59.5	23510	5282.2	1.201e-14	***

---

*Signif. codes:* 0 '\*\*\*' 0.001 '\*\*' 0.01 '\*' 0.05 '.' 0.1 ' ' 1

The output shows that all the terms apart from frame number were highly significant when they were added into the model. Removing the frame number as an independent variable from the model gave an output of:

*Deviance Residuals:*

<i>Min</i>	<i>1Q</i>	<i>Median</i>	<i>3Q</i>	<i>Max</i>
-3.8217	-0.1551	-0.0535	0.0428	3.9883

*Coefficients:*

	<i>Estimate</i>	<i>Std. Error</i>	<i>z value</i>	<i>Pr(&gt; z )</i>
<i>(Intercept)</i>	-47.10005	5.84507	-8.058	7.75e-16 ***
<i>Reciprocal</i>	0.25627	0.00421	60.874	< 2e-16 ***
<i>Doubled</i>	-1.11891	0.11295	-9.906	< 2e-16 ***
<i>Rate</i>	-1.21533	0.03476	-34.966	< 2e-16 ***
<i>Temp</i>	0.14261	0.01904	7.489	6.95e-14 ***

---

*Signif. codes:* 0 '\*\*\*' 0.001 '\*\*' 0.01 '\*' 0.05 '.' 0.1 ' ' 1

*(Dispersion parameter for binomial family taken to be 1)*

*Null deviance:* 27811.0 on 23515 degrees of freedom  
*Residual deviance:* 5285.4 on 23511 degrees of freedom  
 (1 observation deleted due to missingness)  
*AIC:* 5295.4

*Number of Fisher Scoring iterations:* 8

The AIC value gives an indication of which model is the better fit. Better fitting models have lower AIC values. The AIC values of both models were very similar but the model that includes the frame number had a slightly lower AIC value indicating a slightly better fit. An ANOVA comparison of these two models in R gave an output of:

*Model 1: Plasma ~ Reciprocal + Doubled + Rate + Frame + Temp*

*Model 2: Plasma ~ Reciprocal + Doubled + Rate + Temp*

	<i>Resid. Df</i>	<i>Resid. Dev</i>	<i>Df</i>	<i>Deviance</i>	<i>Pr(&gt;Chi)</i>
1	23510	5282.2			
2	23511	5285.4	-1	-3.1278	0.07697 .

---

*Signif. codes: 0 '\*\*\*' 0.001 '\*\*' 0.01 '\*' 0.05 '.' 0.1 ' ' 1*

The ANOVA model comparison showed that the two models were not significantly different from each other. Even though the inclusion of the frame number variable in the model gave a slightly better fit, adding the frame number did not significantly alter the model. For these reasons, for simplicity and to obtain the minimum adequate model, the frame number was dropped as an independent variable.

Another model was constructed using the reciprocal of the square of focal length in  $m^{-2}$  as a predictor variable (instead of the reciprocal of focal length) and compared to the first model. The summary of the output from R for this new logistic regression model was:

*Deviance Residuals:*

<i>Min</i>	<i>1Q</i>	<i>Median</i>	<i>3Q</i>	<i>Max</i>
-3.7574	-0.1926	-0.0885	0.0453	3.6239

*Coefficients:*

	<i>Estimate</i>	<i>Std. Error</i>	<i>z value</i>	<i>Pr(&gt; z )</i>
<i>(Intercept)</i>	-3.006e+01	4.798e+00	-6.265	3.72e-10 ***
<i>Square</i>	3.755e-03	5.823e-05	64.494	< 2e-16 ***

<i>Doubled</i>	-8.427e-01	9.722e-02	-8.668	< 2e-16	***
<i>Rate</i>	-1.126e+00	3.261e-02	-34.525	< 2e-16	***
<i>Frame</i>	-1.535e-05	1.446e-05	-1.061	0.289	
<i>Temp</i>	9.644e-02	1.573e-02	6.130	8.80e-10	***

---

*Signif. codes:* 0 '\*\*\*' 0.001 '\*\*' 0.01 '\*' 0.05 '.' 0.1 ' ' 1

(Dispersion parameter for binomial family taken to be 1)

*Null deviance:* 27811.0 on 23515 degrees of freedom

*Residual deviance:* 5799.4 on 23510 degrees of freedom

(1 observation deleted due to missingness)

*AIC:* 5811.4

*Number of Fisher Scoring iterations:* 7

As with the previous model, the independent variable, Frame Number was not significant. It was reassuring to know that the probability of the plasma occurring in a laser pulse was not significantly affected by the frame number as the frame number is the transformed time dimension. That the plasma probability per pulse was time invariant indicates good reliability of the plasma as a spectroscopic light source and indicates that the intensity at the focal point is not significantly varying over time. Dropping this variable from the model resulted in an output of:

*Deviance Residuals:*

<i>Min</i>	<i>1Q</i>	<i>Median</i>	<i>3Q</i>	<i>Max</i>
-3.7398	-0.1917	-0.0861	0.0451	3.6369

*Coefficients:*

*Estimate Std. Error z value Pr(>|z|)*

(Intercept) -2.919e+01 4.729e+00 -6.173 6.69e-10 \*\*\*

Square 3.753e-03 5.832e-05 64.360 < 2e-16 \*\*\*

Doubled -8.302e-01 9.651e-02 -8.602 < 2e-16 \*\*\*



Rate      -1.126e+00 3.264e-02 -34.487 < 2e-16 \*\*\*  
Temp      9.336e-02 1.547e-02 6.036 1.58e-09 \*\*\*  
---  
Signif. codes: 0 '\*\*\*' 0.001 '\*\*' 0.01 '\*' 0.05 '.' 0.1 ' ' 1

(Dispersion parameter for binomial family taken to be 1)

Null deviance: 27811.0 on 23515 degrees of freedom  
Residual deviance: 5800.5 on 23511 degrees of freedom  
(1 observation deleted due to missingness)  
AIC: 5810.5

Number of Fisher Scoring iterations: 7

This was the minimal adequate model as all the terms were significant. The higher AIC value indicated that this was a worse fit than the previous minimal adequate model for the logarithmic regression of the dependant variable 'Plasma in Frame'. An ANOVA comparison of these two minimal adequate models gave an output of:

Model 1: Plasma ~ Reciprocal + Doubled + Rate + Temp  
Model 2: Plasma ~ Square + Doubled + Rate + Temp

	Resid. Df	Resid. Dev	Df	Deviance	Pr(>Chi)
1	23511	5285.4			
2	23511	5800.5	0	-515.16	

The reduction in the residual deviation of 515.16 showed that the first minimal adequate model, using the reciprocal of focal length as a predictor, was a better model. The regression diagnostic plots for this minimum adequate model are shown in Figure 88.

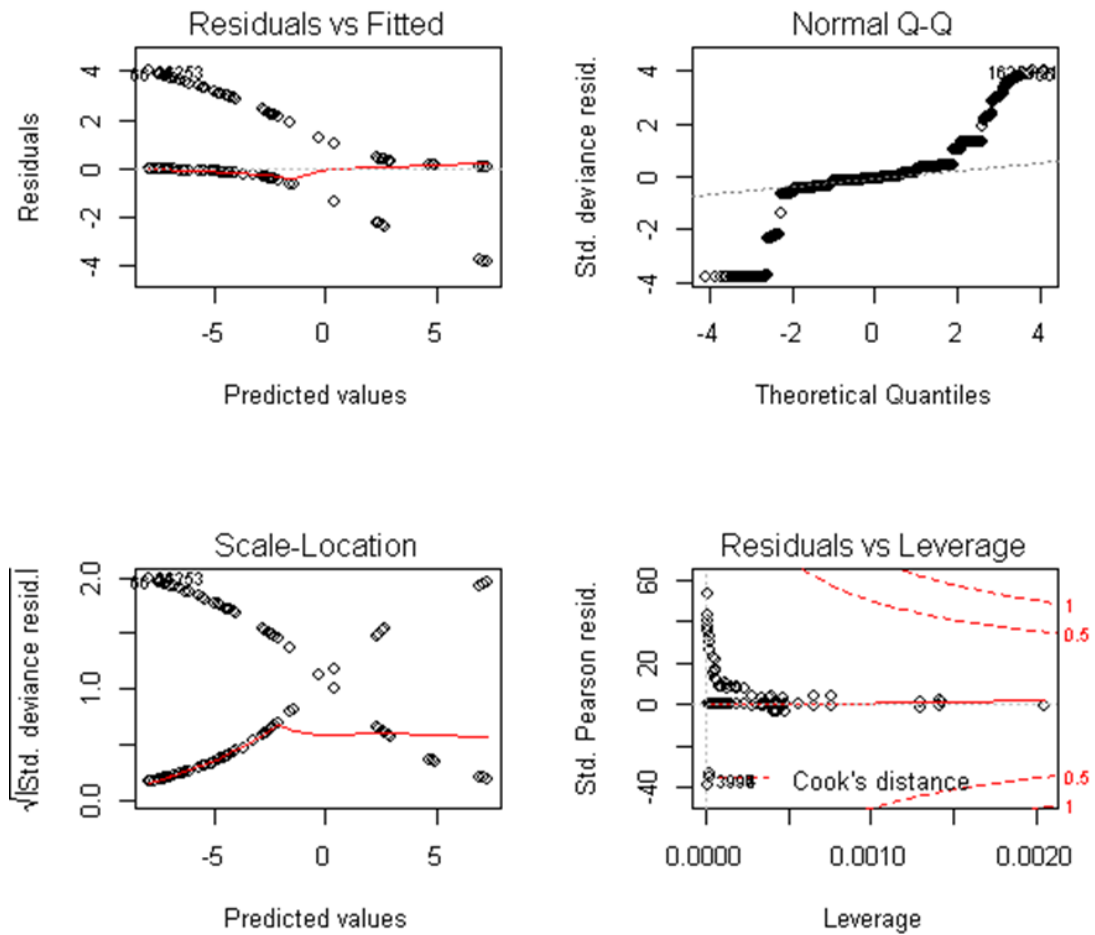


**Figure 88.** The diagnostic plots for the logarithmic regression of the dependent binary variable 'Plasma in frame Y/N'. The independent variables are Reciprocal of Focal Length, Frequency Doubled Y/N, Repetition Rate and Laser Temperature.

The diagnostic plots in Figure 88 showed that the model was a reasonably good one. The graphs on the left side showed that the variance in the residuals did not change as the predicted values changed (no heteroscedasticity). This indicated that the linear fit was a good fit to the data. The top left graph indicated that the errors in the fit were normally distributed. For most of the data points this was true but for some outlying data points the errors deviated from a normal distribution. The bottom right graph showed whether any of the data points were outliers and were excessively influencing the data and needed to be removed from the analysis (data points for which Cook's Distance is greater than 0.5). The graph showed that the data had no outliers.

The minimal adequate model was therefore:

$$\ln\left(\frac{p}{1-p}\right) = -47.1 + 0.256F - 1.22R - 1.12D + 0.14T$$

Rearranging for the probability  $p$ :

$$\text{Plasma Probability Per Laser Pulse, } p = \frac{e^x}{1 + e^x}$$

$$\text{where } x = -47.1 + 0.256F - 1.22R - 1.12D + 0.14T$$

$F$  is the reciprocal of focal length in  $\text{m}^{-1}$ ,  $R$  is the laser pulse rate in Hz,  $D$  is the frequency doubling Boolean variable, and  $T$  is the laser temperature in Kelvin. Interesting points to note from this model are:

- The probability of a plasma occurring decreases as the focal length increases. A plot of the probability against focal length is shown in Figure 89.

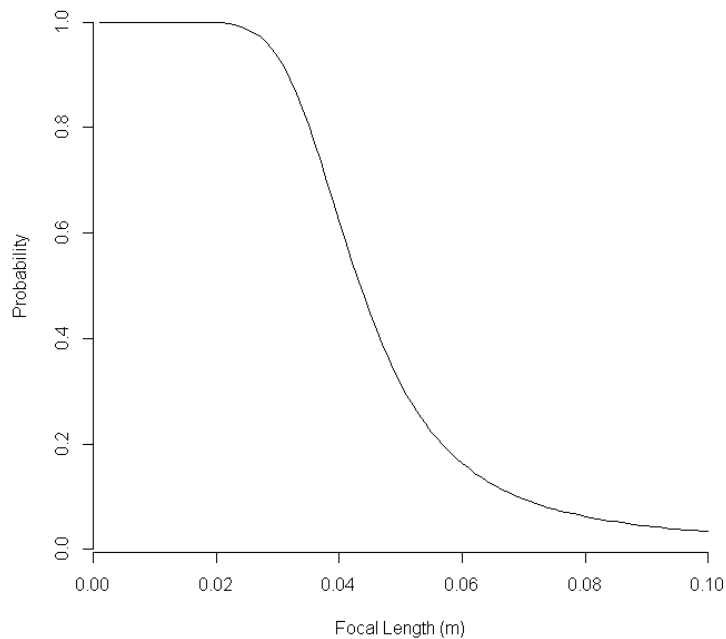


**Figure 89.** A graph of the plasma probability per pulse against the focal length from the logarithmic regression modelling. The other parameters held constant with a laser repetition rate of 1Hz, no frequency doubling and a constant temperature of 303°K (30°C).

- Increasing the laser pulse rate and frequency doubling the laser to 532 nm both decrease the plasma probability.
- As the laser temperature increases the probability of a plasma increases.

The dependant numerical variable, 'Size' was examined using standard multiple regression modelling. The first step was to plot 'Size' against the independent variables 'Focal', 'Reciprocal' and 'Square' to determine which independent variable gave the best linear fit. These box plots are shown in Figure 90-92. In these plots, the variable 'Size' is approximately inversely proportional to 'Focal', with 'Size' appearing to be the closest to a linear relationship with 'Reciprocal'.

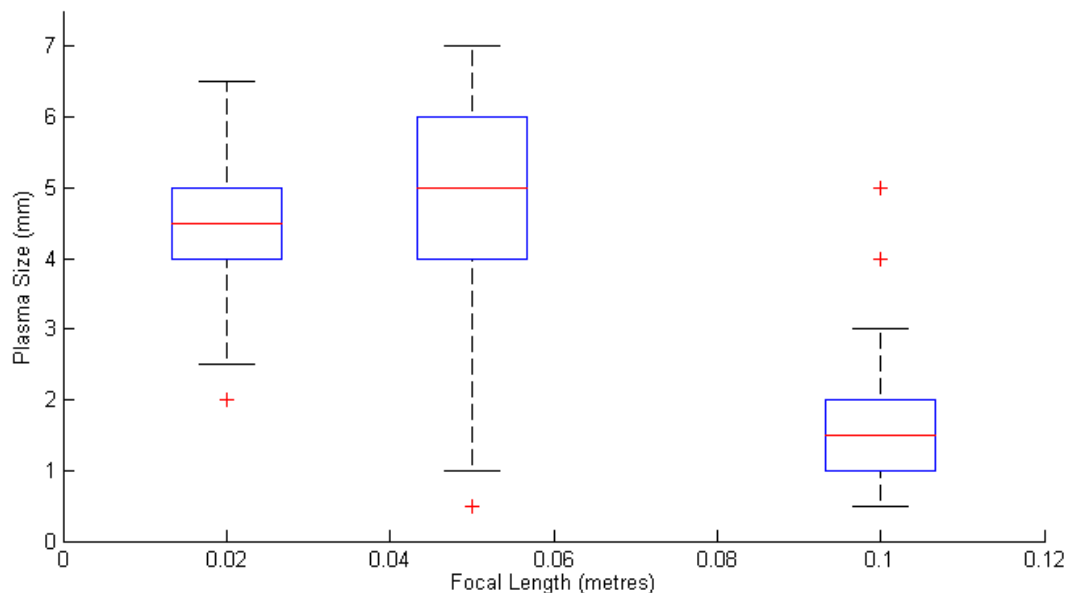


**Figure 90.** A box plot of the plasma size ('Size') against the focal length ('Focal').

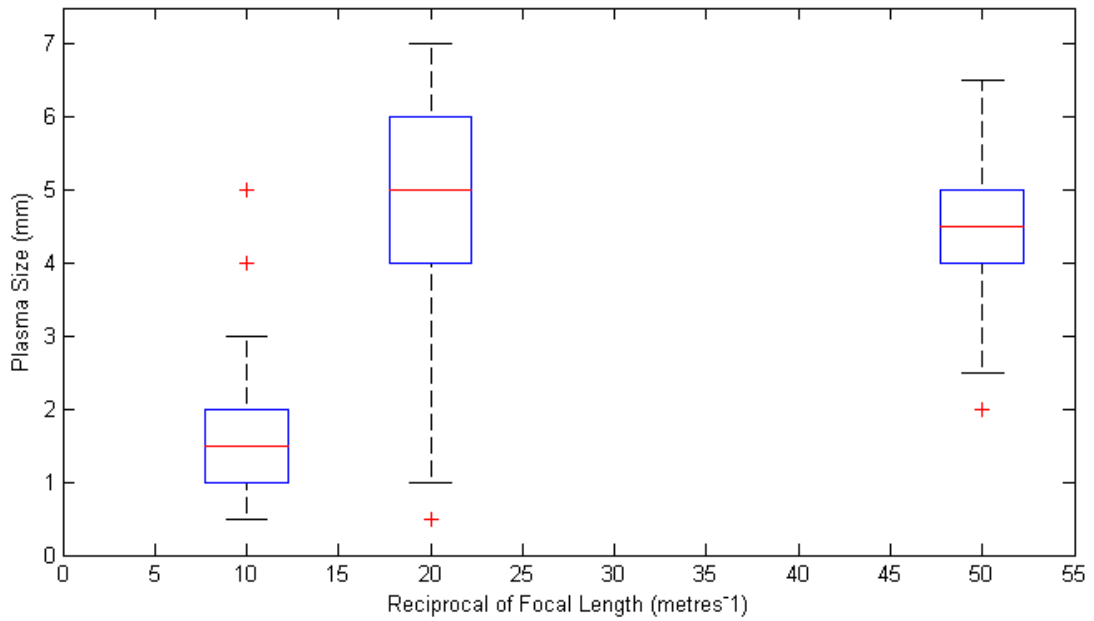


**Figure 91.** A box plot of the plasma size ('Size') against the reciprocal of focal length ('Reciprocal').

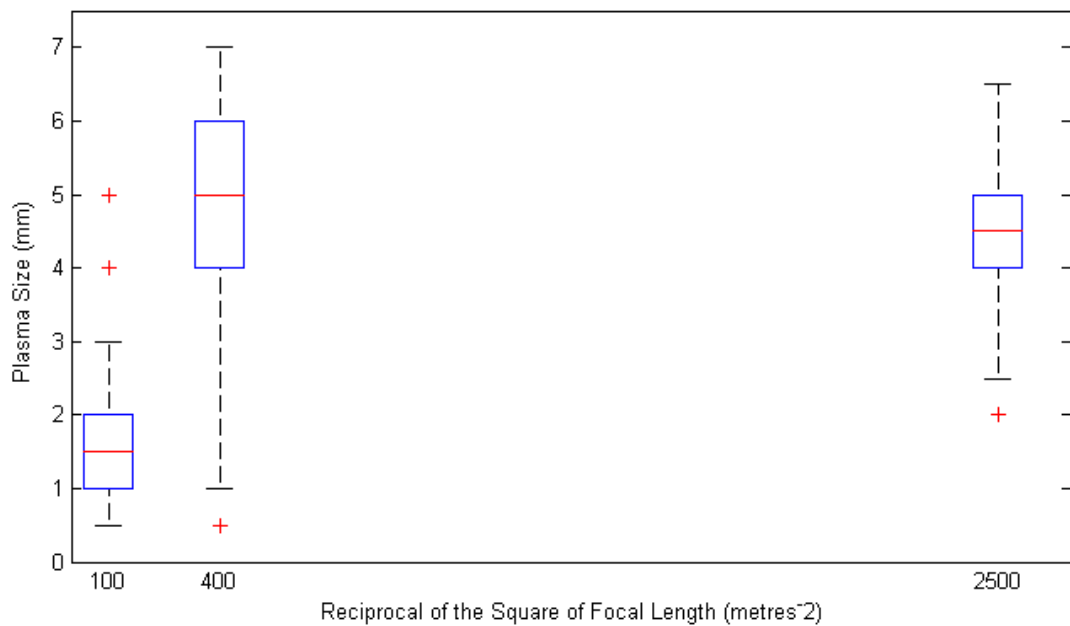


**Figure 92.** A box plot of the plasma size ('Size') against the reciprocal of the square of focal length ('Square').

Two models were constructed and tested with 'Reciprocal' or 'Square' as an independent variable in the models. The predictive multiple linear regression model for plasma size was therefore:

$$\text{Plasma Size} = \varepsilon_1 + \varepsilon_2 F + \varepsilon_3 R + \varepsilon_4 D + \varepsilon_5 N + \varepsilon_6 T$$

Where  $F$  is the reciprocal of focal length or the reciprocal of the square of the focal length,  $R$  is the laser repetition rate,  $D$  is whether the laser is frequency doubled,  $N$  is the frame number and  $T$  is the laser temperature.

The multiple regression output with reciprocal of focal length as an independent variable was:

*Residuals:*

<i>Min</i>	<i>1Q</i>	<i>Median</i>	<i>3Q</i>	<i>Max</i>
-4.2999	-0.1650	-0.0448	0.3581	2.2284

*Coefficients:*

	<i>Estimate</i>	<i>Std. Error</i>	<i>t value</i>	<i>Pr(&gt; t )</i>
<i>(Intercept)</i>	-3.345e+01	3.002e+00	-11.14	<2e-16 ***
<i>Reciprocal</i>	3.057e-02	1.957e-03	15.62	<2e-16 ***
<i>Doubled</i>	-1.271e+00	6.622e-02	-19.20	<2e-16 ***
<i>Rate</i>	-2.741e-01	1.094e-02	-25.06	<2e-16 ***
<i>Frame</i>	-5.659e-05	4.960e-06	-11.41	<2e-16 ***
<i>Temp</i>	1.260e-01	9.838e-03	12.81	<2e-16 ***

---

*Signif. codes:* 0 '\*\*\*' 0.001 '\*\*' 0.01 '\*' 0.05 '.' 0.1 ' ' 1

*Residual standard error: 0.6672 on 3940 degrees of freedom*

*(19571 observations deleted due to missingness)*

*Multiple R-squared: 0.2451, Adjusted R-squared: 0.2441*

*F-statistic: 255.8 on 5 and 3940 DF, p-value: < 2.2e-16*

The output showed that all the independent variables were significant in the model. This model did not require removal of a variable to improve it and was therefore a minimal adequate model. The multiple regression output with reciprocal of the square of focal length as an independent variable was:

Residuals:

Min	1Q	Median	3Q	Max
-4.4092	-0.1499	-0.0455	0.3715	2.1587

Coefficients:

	Estimate	Std. Error	t value	Pr(> t )
(Intercept)	-2.723e+01	3.039e+00	-8.958	<2e-16 ***
Square	3.758e-04	2.929e-05	12.829	<2e-16 ***
Doubled	-1.150e+00	6.739e-02	-17.063	<2e-16 ***
Rate	-2.552e-01	1.123e-02	-22.715	<2e-16 ***
Frame	-5.130e-05	5.026e-06	-10.208	<2e-16 ***
Temp	1.070e-01	1.003e-02	10.663	<2e-16 ***

---

Signif. codes: 0 '\*\*\*' 0.001 '\*\*' 0.01 '\*' 0.05 '.' 0.1 ' ' 1

Residual standard error: 0.6736 on 3940 degrees of freedom

(19571 observations deleted due to missingness)

Multiple R-squared: 0.2305, Adjusted R-squared: 0.2295

F-statistic: 236 on 5 and 3940 DF, p-value: < 2.2e-16

This model was also a minimal adequate model as all of the independent variables were significant. The two models had very similar adjusted R-squared and F-statistic values. The adjusted R-squared value is the percentage, between 0 and 1, of the variance explained by the model. An adjusted R squared value of 1 is a perfect fit. The adjusted R squared value was slightly larger in the first model (0.2441 compared to 0.2295) indicating a better fit. The residual sum of the squares was also slightly less in the first model. The first model with the reciprocal of focal length as an independent variable was the better model. The predictive linear regression model for plasma size was therefore:

$$\text{Plasma Size in mm} = -33.45 + 0.03057F - 0.02741R - 1.271D \\ - (5.659 \times 10^{-5})N + 0.126T$$

Where  $F$  is the reciprocal of focal length or the reciprocal of the square of the focal length,  $R$  is the laser repetition rate,  $D$  is whether the laser is frequency doubled,  $N$  is the frame number and  $T$  is the laser temperature. Points to note about this model are:

- The plasma size increased inversely with focal length. A plot of the plasma size against focal length is shown in Figure 93. The plasma size tended to infinity as the focal length decreased. This was physically impossible, showing that the model was too simple to predict plasma sizes at very short focal lengths. In practice, there was minimum focal length that could be used as the plasma would come into contact with the surface of the lens for very short focal lengths.

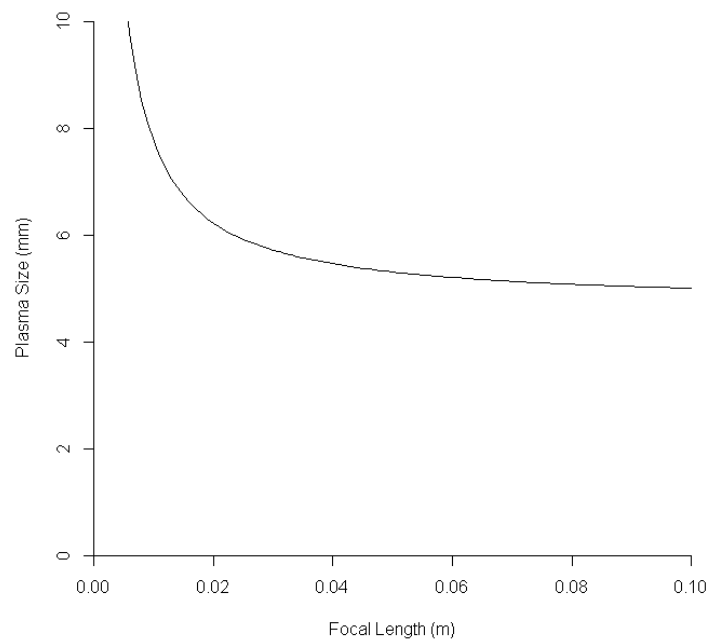


**Figure 93.** A graph of Plasma Size against Focal Length from the best fit multiple regression model. The other parameters in the model were held constant. The parameters were the laser repetition rate at 1Hz, no frequency doubling, a frame number of zero and a constant temperature of 30°C (303°K).



- Increasing the laser pulse rate decreased the plasma size. However, the effect is very small, with an average size difference of 0.11mm between 1 and 5 Hz.
- Frequency doubling the laser to 532 nm decreased the plasma size by an average of 1.27 mm.
- As the frame number increased the plasma size decreased. Over 9000 frames (5 mins) the plasma size decreased by an average of 0.51 mm. This relationship was most likely asymptotic as time goes to infinity, meaning that the plasma size approached a minimum value over time.
- As the laser temperature increased the plasma size increased proportionally. An increase of 10°C increased the size of the plasma by an average of 1.26 mm.
- Laser temperature and Frame Number should be related because as the Frame Number increases the laser should get hotter. The relationship of plasma size to Frame Number and Temperature that was seen in the model is expected in that both variables have a positive effect on plasma size. This is a slightly unexpected result as the power of the laser is negatively related to temperature (See Figure 41).

The regression diagnostic plots for the 'Size' minimum adequate model are shown in Figure 94. The plots showed that the assumptions of the multiple regression model were reasonably upheld. The top and bottom right plots showed that the model exhibited a small amount of heteroscedasticity, with the residuals increasing in magnitude as the fitted values increased. However, it was difficult to see most of the data points in the plot. The vast majority of the 3940 residuals appeared to be equally distributed. The plots did not show any non-linearity indicating that a linear model was a good one. The top left plot showed that the residuals were not normally distributed, the negative residuals deviating from a normal distribution. However, because most of the residuals appeared to be normally distributed and the fact that the effects of non-normality are mitigated by large datasets, there was little reason to abandon the model as not being representative of the data. The bottom left plot showed that no data points had undue leverage on the model.

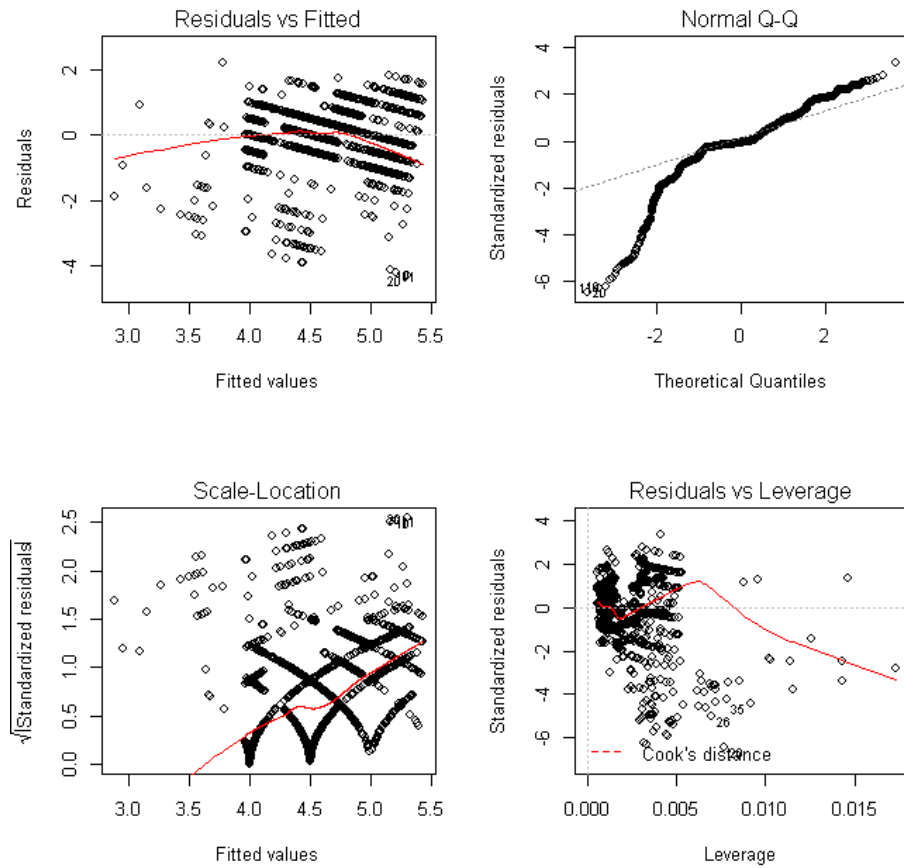


**Figure 94.** The diagnostic plots for the multiple linear regression of the dependent binary variable 'Plasma Size'. The independent variables are the Reciprocal of Focal Length, Frequency Doubled Y/N, Repetition Rate, Frame Number and Laser Temperature.

The dependant numerical variable, 'Location' was also examined using standard multiple regression modelling. The location of the plasma was obviously directly proportional to the focal length of the lens. The independent variable  $F$  in the predictive regression equation was therefore the focal length in mm. The full predictive equation was:

$$\text{Plasma Distance from Lens in mm} = \varepsilon_1 + \varepsilon_2 F + \varepsilon_3 R + \varepsilon_4 D + \varepsilon_5 N + \varepsilon_6 T$$

Where  $F$  is the focal length in mm,  $R$  is the laser repetition rate,  $D$  is whether the laser is frequency doubled,  $N$  is the frame number and  $T$  is the laser temperature. The multiple linear regression output from R was:

Residuals:

Min	1Q	Median	3Q	Max
-32.412	-0.265	0.023	0.176	14.954

Coefficients:

	Estimate	Std. Error	t value	Pr(> t )
(Intercept)	-7.762e+01	6.233e+00	-12.454	< 2e-16 ***
Focal	8.794e+02	3.299e+00	266.520	< 2e-16 ***
Doubled	-1.582e+00	1.450e-01	-10.907	< 2e-16 ***
Rate	-4.306e-01	2.284e-02	-18.856	< 2e-16 ***
Frame	-7.823e-05	1.168e-05	-6.696	2.45e-11 ***
Temp	2.722e-01	2.109e-02	12.908	< 2e-16 ***

---

Signif. codes: 0 '\*\*\*' 0.001 '\*\*' 0.01 '\*' 0.05 '.' 0.1 ' ' 1

Residual standard error: 1.634 on 3940 degrees of freedom  
(19571 observations deleted due to missingness)

Multiple R-squared: 0.9788, Adjusted R-squared: 0.9787

F-statistic: 3.631e+04 on 5 and 3940 DF, p-value: < 2.2e-16

All the independent variables were significant in the model and the adjusted R-squared value was 0.9787, indicating a very good fit. The predictive equation was therefore:

$$\text{Plasma Distance from Lens in mm} = -77.62 + 879.4F - 0.43R - 1.582D \\ - (7.823 \times 10^{-5})N + 0.27T$$

Points of note from this predictive model are:

- The relationship between focal Length and location was a positive linear relationship as expected. The plasma was most likely to occur very near to the focal point.

- Increasing the laser pulse rate and frequency doubling the laser decreased the plasma distance from the lens. If the plasma distance from the focal lens decreases, it implies that the breakdown intensity has been obtained at a distance closer to the lens than the focal point (Bindhu et al., 2004, Bindhu et al., 2003). This could have been because the laser had more peak pulse power or, in the case of frequency doubling, because some of the photons in the pulse had double the energy. The effect of frequency doubling upon the plasma location was to generate plasmas at an average of 1.6 mm closer to the focusing lens. The photons generated by the doubler have a wavelength of 532 nm and twice the energy of 1064 nm photons but overall the pulses will have less energy due to absorption and scattering in the doubling crystal. The breakdown thresholds at this wavelength may also be altered due to the (unknown) wavelength dependency of absorption.

The effect of frequency doubling the laser and increasing the repetition rate upon plasma location was a surprising result in view of the fact that, according to the predictive models, both of these parameters decrease both the likelihood of a plasma occurring and the mean plasma size.

- The plasma location was closer to the lens as the frame number increased. Over the 5 minute period, the plasma moved closer to the lens by an average of 0.7mm. Over a longer period of time, the plasma location looks like it approaches an asymptotic value, but was approximately a linear relationship over this 5 minute period.
- The temperature of the laser was proportional to plasma location. This is possibly due to a drop in the peak laser power as the temperature increased (due to a drop in the stimulated emission cross section of Neodymium, see Figure 41). A drop in laser power reduces the peak intensity along the optical axis causing the breakdown intensity to occur closer to the focal point of the lens.

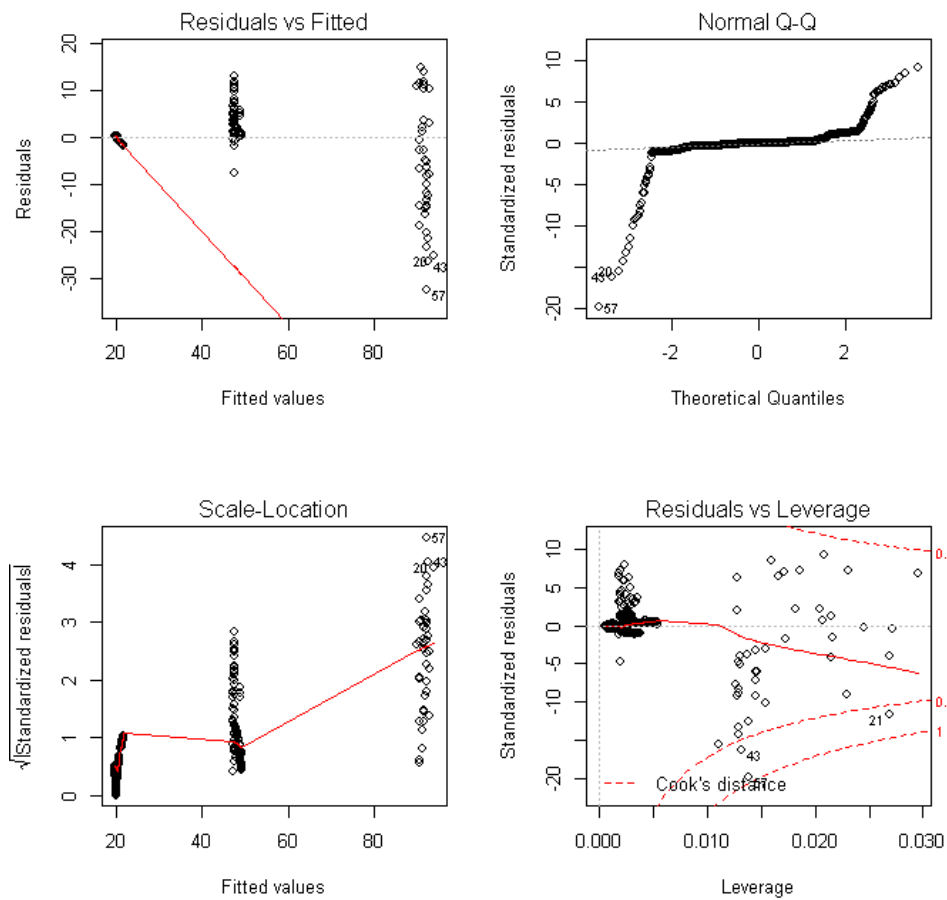


**Figure 95.** The diagnostic plots for the linear model that predicts the distance of the plasma from the focal lens.

From the diagnostic plots in Figure 95, it was observed that the model suffered from heteroscedasticity, with the residuals increasing in size as the focal length increased. This meant that it became more difficult to accurately predict the plasma location at increasing focal lengths due to increasing variances. The model was not rejected because of heteroscedasticity, as the zero residual line lay approximately through the centre of the distribution of the data points. In the Q-Q plot there were outlying data points, the errors of which were not normally distributed but it must be remembered that there were 3940 data points included in the analysis. Only a few of these data points did not meet the requirement of normally distributed errors so the model was not rejected due to a few data points having non-normally distributed errors. The residuals vs leverage plot showed that a few data points have undue leverage upon the model. Owing to the large number of data points in the dataset, any change in

the model caused by outliers is going to be very small. For this reason and the fact that the zero residual line passed approximately through the data points, outliers were not removed in an effort to improve the model.

Following from the statistical analysis above it was be concluded that:

- The best lens for plasma generation had the shortest possible focal length. Short focal length lenses were much more likely to produce a plasma due to the smaller diameter of the beam produced at the focal point and the consequent high intensities. The size of the plasma also increased as a function of focal length, indicating that the plasma may be hotter and therefore have a higher spectral power output. The position of the plasma had the least variance at shorter focal lengths with a very small variance at 20 mm. This was very important for the design of a spectrometer as the plasma must be generated with little positional variance if light was to be captured and collimated into a beam. A 20 mm focal length lens was also the shortest focal length lens that could possibly be used without risking damage to the lens from the plasma itself.
- Using a frequency doubler decreased both the likelihood of a plasma occurring and the overall plasma size. This indicated that frequency doubling decreased the pulse peak power and/or increased the breakdown threshold. Even if a frequency doubler had no effect on the breakdown threshold, its use decreases the power of the beam because of losses due to imperfections in the doubling crystal. The spectrometer did not therefore use a frequency doubler for plasma generation.
- Increasing the repetition rate of the laser reduced both the likelihood of plasma occurrence and the size of a plasma. This effect was very small and will not make much difference to the reliability of plasma production and plasma spectral power output at higher repetition rates.

- Changes in the temperature of the laser affected the probability, size and location of a laser induced plasma, most likely due to changes in laser pulse power output. In order to reduce temperature related fluctuations, the laser temperature needed to be controlled through effective cooling. The laser cuts off when the water temperature reaches 50°C and effective cooling also extends the life of the pumping flashlamp. During extended periods of high repetition pulsing the cooling water can attain 50°C. If this occurs the laser automatically shuts down, possibly ruining ongoing experiments. For these reasons, the cooling system was improved by extending the tubing through which cooling water was pumped. The extended tubing was then placed in a bath of water at room temperature into which heat is exchanged (Figure 96). The water in the cooling bath can be changed regularly or cooled itself if more effective cooling is required.

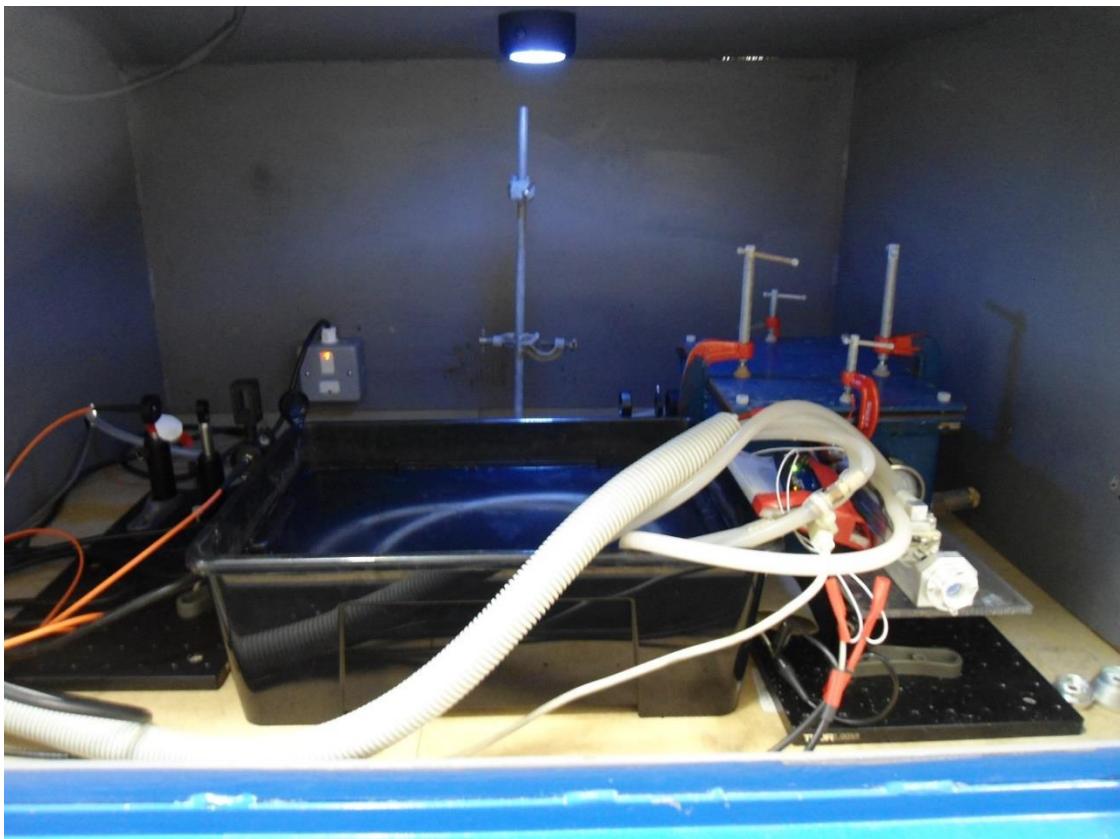


**Figure 96.** The plasma spectrometer cooling system. The thin white tubes exchange heat with the large water bath. The water in the bath can be easily changed should it become too hot.

In conclusion, the best lens for plasma generation was the 20 mm focal length lens. This lens was the most reliable for pulse to pulse plasma generation and generated plasmas with the least positional variance. Any plano-convex 20 mm lens with a diameter larger than the diameter of the beam (6 mm) can be used. A plano-convex lens is normally used to focus a parallel beam to a point. The Thorlabs LA4647, UV Fused silica plano-convex lens, diameter 12.5 mm, focal length 2 cm was the lens selected for laser focusing in the spectrometer.

### 3.3 Noble Gases as the Plasma Medium

Disappointingly, a laser spark in air at atmospheric pressure did not produce any light below  $\lambda=380$  nm (Figure 52). For the purposes of biological spectroscopy, this was a problem as many important biological chromophores are absorbent in the range 200-300 nm. The plasma spark was also unreliably generated in air which would result in missing/erroneous readings. One potential method of improving the reliability of plasma generation and increasing the plasma's electron density and temperature, thereby increasing spectral power output and photon energy, would be to change the gaseous medium in which the plasma was formed.

Ionising a molecular gas requires an input of energy to overcome covalent bonding. The main constituent of air, molecular nitrogen has one of the strongest covalent bonds with a bond dissociation energy of 945 kJ (2004). The bond dissociation energy is a measure of the energy stored in the potential energy of the bond. If this energy is input in the form of laser photons, a molecule can lose enough covalently bonded electrons for the repulsive forces between positively charged ions to become larger than the attractive forces provided by the bonds. The result is a Coulomb explosion in which the atoms of a molecule fly apart, rapidly accelerated by the repulsive forces (Légaré et al., 2005, Wu et al., 2011). A Coulomb explosion is an endothermic process overall because energy is required to overcome the electrostatic forces in covalent bonds. This energy is absorbed from the external EM field (laser) to ionise covalent electrons and generate high kinetic energy positive ions. The



breakdown thresholds of molecular gases should therefore be greater than atomic gases because less of the energy of the laser pulse is available for electron ionisation and heating.

Plasmas formed in molecular gases form a variety of reactive/unstable species during the cooling process. Plasmas generated in air produce ozone which is a powerful oxidising agent that can damage a variety of materials and can be harmful for health. A noble gas plasma produces no such compounds and upon cooling forms back into an inert atomic gas. In LIBS, the target material being identified is often a solid or liquid in an argon atmosphere. Argon is most often used owing to its relative cheapness and its high atomic mass. Surrounding the target sample with a gas with a high atomic mass increases the temperature and lifetime of the plasma, due to the reduced energy transfer and diffusion of the plasma particles into the relatively high mass argon medium. In a plasma spectrometer, instead of a solid or liquid target, the gas itself is used as the plasma medium. The effect on electron density and temperature, due to reduced energy transfer and diffusion, of using a high atomic mass gaseous medium will be negated because the plasma will be surrounded by atoms and ions of identical mass.

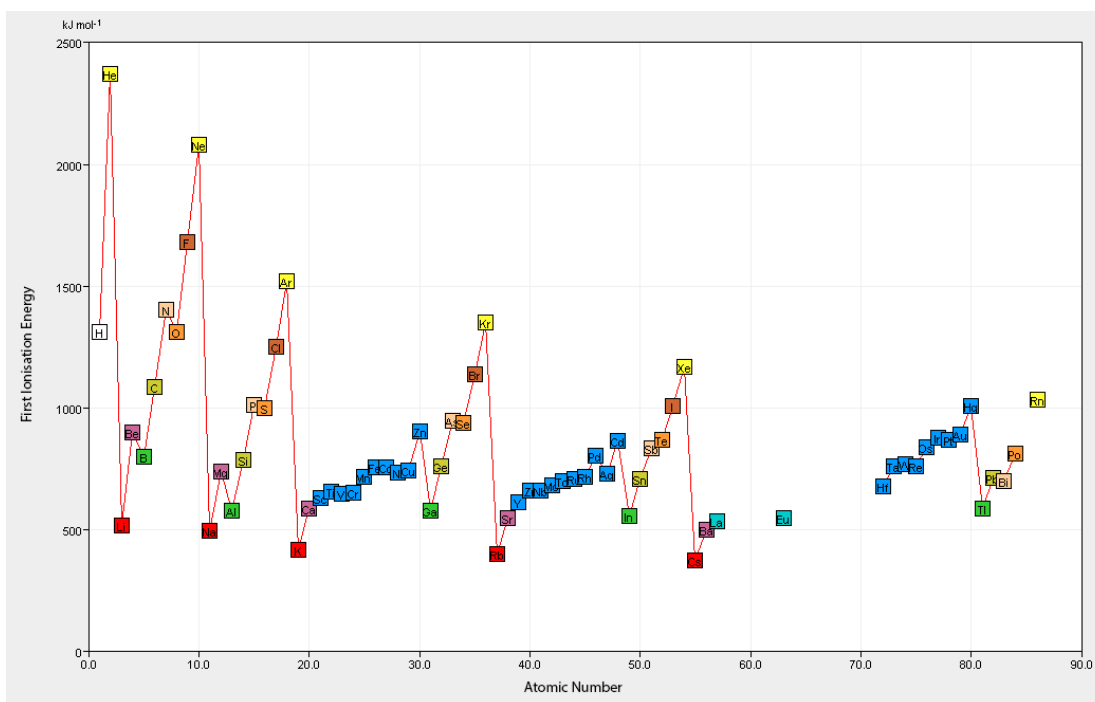


**Figure 97.** A graph of first ionisation energy against atomic number for the first six periods of elements in the periodic table. The noble gases in Group 8 appear as yellow data points. The first ionisation energy (in kJ/mol) of the Group 8 elements is: He 2372.57, Ne 2080.22, Ar 1520.61, Kr 1350, Xe 1170.37, Rn 1037.22. Reproduced from (Moore, 1970).

The first ionisation energy of a noble gas gives a good indication of the relative breakdown thresholds under focused laser light. Figure 97 shows the first ionisation energies of the first six periods of elements. The noble gases have the highest ionisation energies of any group in the periodic table because their atoms have the most energetically stable electronic configurations. The other groups of elements have lower ionisation energies but are unstable in a single unbonded atomic state. These elements must form covalent, ionic, metallic and other bonds to obtain stable electron states. In order to generate a plasma via laser heating, extra energy must be input to overcome these bonds. This is the latent heat of the phase transition from gas into plasma. If the same amount of energy is input to both a molecular gas and a noble gas so that they both form plasmas, the noble gas plasma will be hotter (as long as the gases start at the same temperature and pressure) because none of the input energy has been used to overcome bonding.

Figure 97 shows that as atomic number increases in a periodic group, the first ionisation energy also falls. This is caused by the inner electrons in an atom shielding the nuclear charge from the outer electrons. This shielding reduces the effective nuclear charge 'felt' by the outer electrons, giving them more potential energy (the potential energy of bound electrons is negative) and reducing the ionisation energy. As the atomic number increases, the shielding effect increases due to larger numbers of electrons in atomic orbitals. This decrease in ionisation energy as atomic number increases means that heavy noble gases should have low breakdown thresholds. The effect of this is threefold:

1. Lower breakdown thresholds mean that plasmas should be more reliably formed in a heavy noble gas. Ideally, each laser pulse should generate a plasma.
2. The plasma temperature should be higher. Any energy in the laser pulse that is not used to dissociate molecules or ionise electrons is available to increase the kinetic energy of the free electrons.
3. The electron density in a heavy noble gas plasma should be higher. Reducing the ionisation energy increases the likelihood of (multi)photon ionisation, resulting in the production of greater numbers of free electrons. The increased kinetic energy (temperature) of free electrons (by Point 2.) increases the rate of collisional ionisation due to free electrons impacting bound electrons at higher energies.

It should therefore be easier to form plasmas in high atomic number noble gases and these plasmas should have higher intensity and shorter wavelength emission. Experimental data from numerous authors shows that this is indeed the case. Agostini et al showed, in low pressure conditions where cascade ionisation is very unlikely, that the number of ions created by multiphoton ionisation in a LIP increases as atomic number increases due to the lower ionisation energies (Figure 98) (Agostini et al., 1970a).

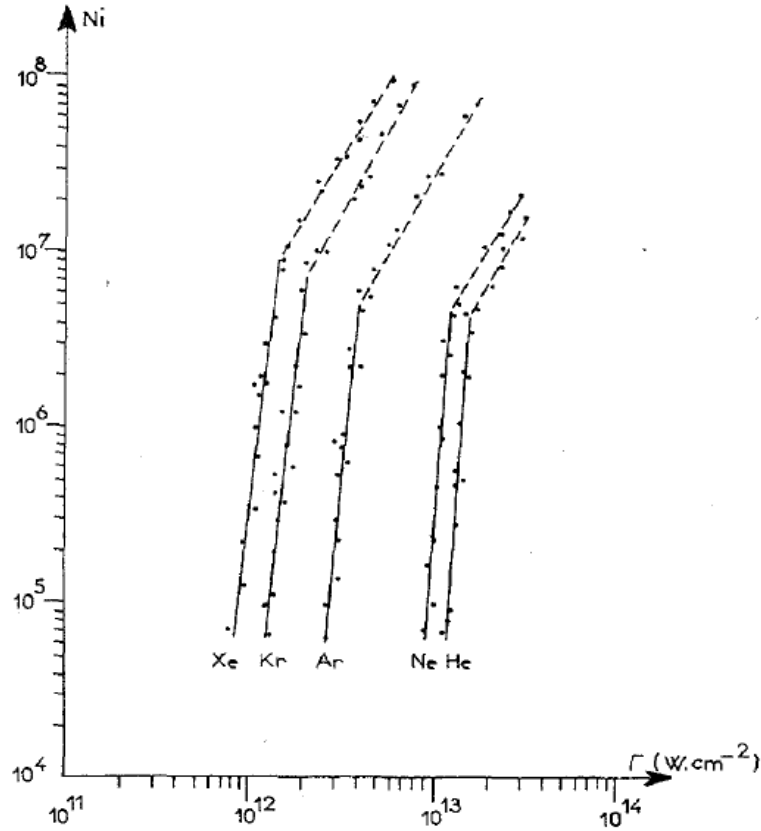


**Figure 98.** The number of multiphoton ions created as a function of laser intensity at the focal point. The gas pressure is  $2.6 \times 10^{-7}$  atm and the laser used is an Nd:YAG at  $1.06 \mu\text{m}$ . The pressure used is very low so that ions present are only produced by multiphoton absorption. Reproduced from Aghostini et al, *Multiphoton ionization of rare gases at  $1.06 \mu\text{m}$  and  $0.53 \mu\text{m}$* , 1970.

Data from *Bruscher et Al* (Buscher et al., 1965), presented in Table 15 show that the breakdown threshold intensity is inversely proportional to ionisation energy except for He and Ne. This is attributed to the fact that the electron-atom collision cross section for cascade ionisation is higher for He than for Ne at low electron energies.

Threshold Intensities at a Pressure of 2000 Torr ( $10^{10}$ W/cm <sup>2</sup> )					Ionisation Energy (eV)
Gas	$\lambda=10600\text{\AA}$	$\lambda=6943\text{\AA}$	$\lambda=5300\text{\AA}$	$\lambda=3471\text{\AA}$	
He	1.4	7.6			24.58
Ne	2	10			21.56
Ar	0.51	5.1	4.7	0.91	15.76
Kr	0.39	3.3			13.99
Xe	0.2	1.9	1.06	0.4	12.13
<b>Pulse Width (ns)</b>	40	40	28	20	
<b>Spot Area (<math>\mu\text{m}^2</math>)</b>	3480	1050	827	185	

**Table 15.** Results of threshold breakdown intensity measurements for LIPs formed in noble gases at different Nd:YAG laser harmonics. Reproduced from Buscher et Al, *Phys Rev Lett*, 1965 (Buscher et al., 1965).

Based on the ionisation energies of the noble gases and previously published data, the best gas to use would be Xenon. Radon has a smaller first ionisation energy but is radioactive. The choice of which noble gas to use in a plasma spectrometer also depends upon several other factors:

- What is the probability of each pulse generating a plasma in each gas? This is a function of the breakdown intensities of each gas.
- Which gas produces plasmas that produce the most intense, shortest wavelength brehmsstrahlung emission (highest electron temperatures and densities)?
- The price per unit volume of each gas. The prices of each gas as quoted by/purchased from BOC LTD were:

N4.6 Helium 99.996% Material Number 101720-L	£0.82 per litre
N5.0 Neon 99.999% Material Number 112008-BC	£1.10 per litre
N5.0 Grade A Argon	£0.02 per litre
N5.0 Krypton Material Number 112034-BC	£3.15 per litre
N5.0 Xenon Material Number 112005-BC	£29.50 per litre

Xenon is prohibitively expensive for testing with a prototype instrument. All of the other gases were purchased for testing.

### 3.4 The Pressure Dependency of Laser Induced Breakdown

As well as investigating the effect of different noble gases, it is known that breakdown thresholds, electron temperatures and densities in laser induced plasmas depend on gas pressure. The isothermal pressure dependency of laser induced breakdown in gases has been investigated by several authors with the discovery that different electron generation processes (multiphoton ionisation and cascade ionisation) dominate at different pressures (Krasnyuk et al., 1969, Morgan et al., 1971, Young and Hercher, 1967, Buscher et al., 1965). The pressure dependence of breakdown intensity threshold generally behaves as:

$$I_{Br} \propto p^\alpha \quad \text{Equation 20}$$

$\alpha$  is a number between minus one and zero that depends upon the particular noble gas and the laser wavelength (Chylek et al., 1990a).

The effect of varying the gas pressure affects the number of free electrons generated via the cascade ionisation processes. The mean free path of electrons in an ideal gas is inversely proportional to pressure. In the low pressures regime (<0.1 atm), the mean free path of electrons in the plasma approximates the dimensions of the focal volume. At these pressures, multiphoton ionisation is the only mechanism of free electron production. Several authors have used this to investigate multiphoton ionisation processes

(G.S. Voronov., 1965, Agostini et al., 1979, Lompre et al., 1977, Martin and Mandel, 1976, Hollis, 1978). For multiphoton ionisation, the pressure dependency was found to be:

$$I_{Br} \propto p^{-1/k}$$

Where  $k$  is the number of photons that are absorbed during ionisation.

At pressures greater than about 0.1 atm, the dominant mechanism of free electron production is cascade ionisation (Agostini et al., 1970a), occurring after the initial production of seed electrons from multiphoton absorption processes. An increase in the pressure of the gaseous medium decreases the mean free path of electrons in the plasma. This has a two-fold effect: to decrease the average kinetic energy (temperature) of free electrons and to increase the electron density.

The first effect of decreasing the electron temperatures is somewhat counterintuitive, but decreasing the mean path of a free electron decreases the average length of time before a collision occurs. During this length of time an electron gains kinetic energy (accelerates) from the electric field of the pulse. Isothermally increasing the pressure of a gas therefore reduces the average kinetic energy, and therefore the temperature, of free electrons in the focal volume. This is partly compensated for by a decrease in the rate of electron diffusion out of the focal volume during the length of the pulse.

The second effect is caused by an increase in the rate of collisional ionisation events, also due to a decrease in the mean free path of electrons in the gas. An increase in the rate of collisional ionisation means increased free electron production and an increase in electron density. Increasing the pressure should therefore result in an overall increase in spectral brightness. The breakdown threshold also decreases as the rate of collisional ionisation increases. For cascade ionisation, if only free electron gain processes are considered, the experimentally derived relation of breakdown intensity to pressure is:

$$I_{Br} \propto p^{-1}$$

Note that the pressure dependence of cascade ionisation is much stronger than the pressure dependence of multiphoton ionisation.

The value of  $\alpha$  in Equation 20 is determined experimentally. One of the earliest papers to investigate this pressure dependence is Buscher et al (Buscher et al., 1965). The authors measured the breakdown intensities of argon and xenon using the first and second harmonics of Nd:YAG and ruby lasers across a range of pressures. The results are shown in Figure 99. At all wavelengths, the breakdown threshold exhibited the type of pressure dependency associated with cascade breakdown.

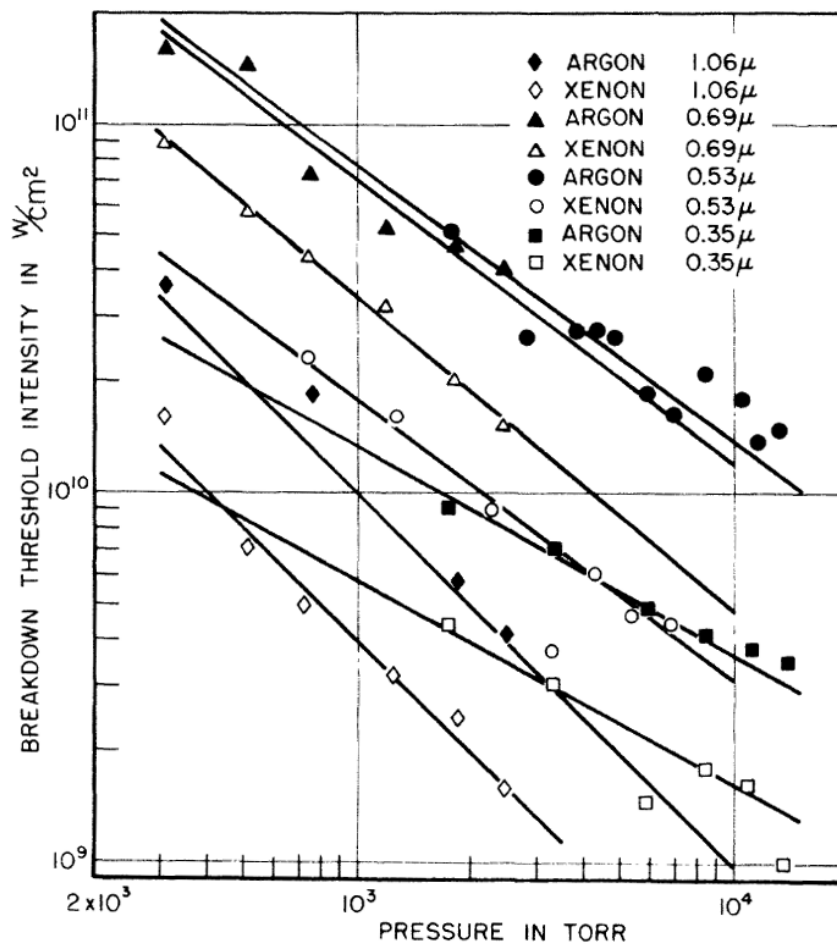


**Figure 99.** Breakdown threshold intensities against pressure for Argon and Xenon at 4 different wavelengths. Reproduced from Buscher et al, *Phys Rev Lett*, 1965 (Buscher et al., 1965).



Another early publication by Alcock *et al* investigated the pressure dependence at first (694 nm) and second (347 nm) harmonics of a ruby laser in a number of different gases (Alcock *et al.*, 1972). The results for second harmonic breakdown are shown in Figure 100. The results reveal that the effect of varying the pressure on breakdown intensities is very similar for each gas with a value for  $\alpha$  of approximately -0.4. These results were in good agreement with Buscher *et al* (Buscher *et al.*, 1965).

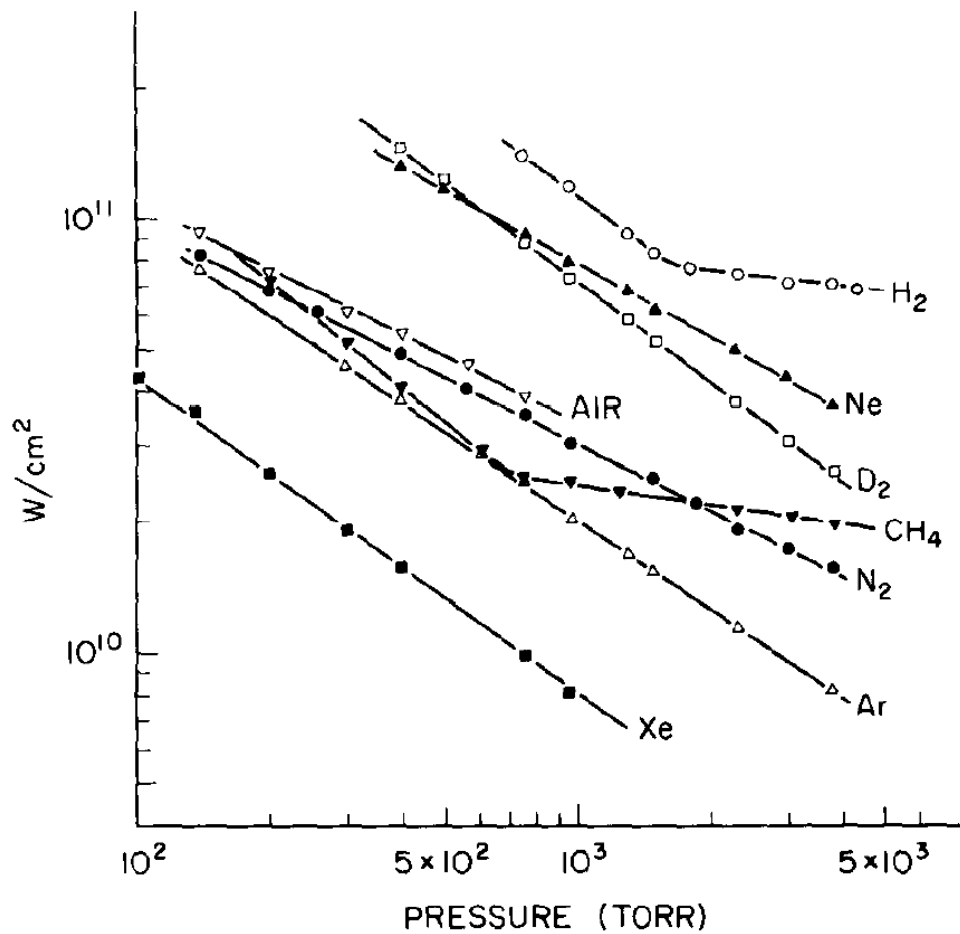


**Figure 100.** The relationship of breakdown intensity against pressure for several gases at the second harmonic of a ruby laser ( $\lambda=3472\text{\AA}$ ) with 7cm focal length lens. From Alcock *et al*, *New features of laser-induced gas breakdown in the ultraviolet*. *Optics Communications*, 1972 (Alcock *et al.*, 1972).

Rosen and Weyl conducted an experimental and theoretical investigation into the breakdown of nitrogen and the noble gases argon, neon and xenon at different pressures (Weyl *et al.*, 1982). They used a frequency doubled (532

nm) or triple (355 nm) Nd:YAG laser with a pulse duration of 15 ns. For argon, the authors found that the breakdown threshold intensity varied as  $p^{-0.85}$  for both wavelengths. A graph of the results for argon at different pressures is shown in Figure 101. For the noble gases neon and xenon, the authors found that the breakdown threshold varied as  $p^{-1}$  for both wavelengths (data not shown). These results, in agreement with Alcock *et al* and Buscher *et al*, show a dominance of cascade ionisation at these pressures. The breakdown thresholds for xenon were also the lowest of any of the gases, in agreement with fact that xenon has the lowest ionisation energy (12.13 eV).

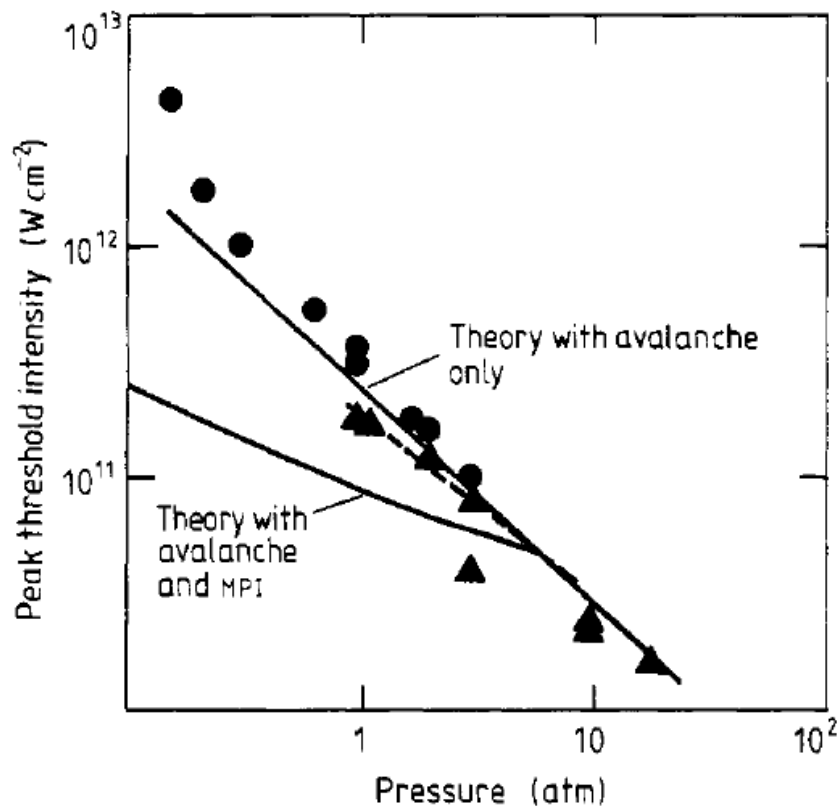


**Figure 101.** Experimental and theoretical laser-induced breakdown thresholds for argon at  $\lambda=532$  nm. Circles represent experiments with  $f/10$  optics, Triangles are  $f/30$  optics. The lines show the theoretical predicted values calculated by the authors. The data are in good agreement with cascade ionisation dominated breakdown. The spaced line shows the data from (Buscher *et al.*, 1965). Reproduced from Weyl and Rosen, *Laser-induced breakdown of argon at 0.35  $\mu\text{m}$* , 1982 (Weyl *et al.*, 1982).

At very high pressures, a reduction in the rate of cascade ionisation should be observed in a manner analogous to Paschen's law (Equation 19), where the

breakdown voltage between two parallel plates increases at high pressures. This increase in the breakdown voltage is due to a decrease in the mean free path of electrons with the result that electrons have less time to be accelerated and gain energy from the external electric field. If the mean free path is too short, electrons do not gain enough energy for collisions to ionise bound electrons. The voltage between the plates must be increased for breakdown to occur. Similar behaviour should be observed in laser induced plasmas at very high pressures. Recent work by Yashiro *et al* (Yashiro *et al.*, 2011) shows that at pressure of up to 2 MPa (20 atm) breakdown thresholds still obey the type of inverse relationship in Equation 20 associated with cascade breakdown. It is possible that pressures higher than 2 MPa are needed to see a reduction in the rate of cascade ionisation due to small mean free paths.

Nearly all investigators have found that there was a pressure dependence on the breakdown intensity of noble gases of the form  $I_{BR} \propto P^\alpha$  with varying values of  $\alpha$  depending upon which gas was being tested. This behaviour is exactly what would be expected if the intensity threshold were dependent upon electron mean free path. Table 16 summarises the experimental values of  $\alpha$  in several papers that examine the pressure dependence upon breakdown intensity at different harmonics of an Nd:YAG laser for the gases Ar and Xe. There is however wide variation in the value of  $\alpha$  which is difficult to attribute to any one particular factor. It is possible that an as yet unidentified variable is affecting the results. It should be noted however that some variables, particularly lens aberration, are difficult to control and have a large effect on plasma formation.

Experiment [Reference]	Gas (Wavelength $\mu\text{m}$ )					
	Xe (1.064)	Xe (0.532)	Xe (0.355)	Ar (1.064)	Ar (0.532)	Ar (0.355)
(Chylek et al., 1990b)	-0.8	-0.7	-0.8	-0.4	-0.5	-0.6
(Rosen and Weyl, 1987)		-0.6			-0.6	
(Armstrong et al., 1983b)		-1	-0.9		-1	-1.1
(Dewhurst, 1978)				-0.5		
(Dewhurst et al., 1974)	-0.5					
(Ireland and Morgan, 1974)				-0.6	-0.5	
(Ireland et al., 1974)			-0.7			
(Morgan et al., 1971)			-0.7			
(Alcock and Richardson, 1968)			-0.8			
(Buscher et al., 1965)	-0.7				-0.8	
(Yashiro et al., 2011)				-0.58	-0.65	

**Table 16.** A summary of the experimentally derived pressure dependence of laser induced breakdown in argon and xenon from several literature sources.

The strong pressure dependence of breakdown intensity means that it would be advantageous to construct the light source so that the highest possible gas pressure can safely be used. Increasing the gas pressure should increase the

reliability of the plasma (plasma occurrence per pulse) and increase the electron density in the plasma, resulting in greater spectral emission.

### 3.5 Gas Testing and Results

Having devised a method for reliably recording the intensity of single plasmas, the instrument could now be tested with noble gases at different pressures. Each of the noble gases (helium, neon, argon and krypton) were tested at pressures up to 2.2 bar in intervals of 0.2 bar. When changing the gas, the chamber was flushed a number of times with each new gas to remove as much air/other gases as possible. For each test, the laser was set to maximum power at 2 pulse/sec. To determine the effect of frequency doubling the laser, each test was performed with frequency doubling. The tests were performed for a period of 5 minutes, producing 600 spectra for each run of different gases and pressures. These 600 spectra were averaged to obtain average intensity against wavelength graphs. These graphs are shown in Figures 102-109.

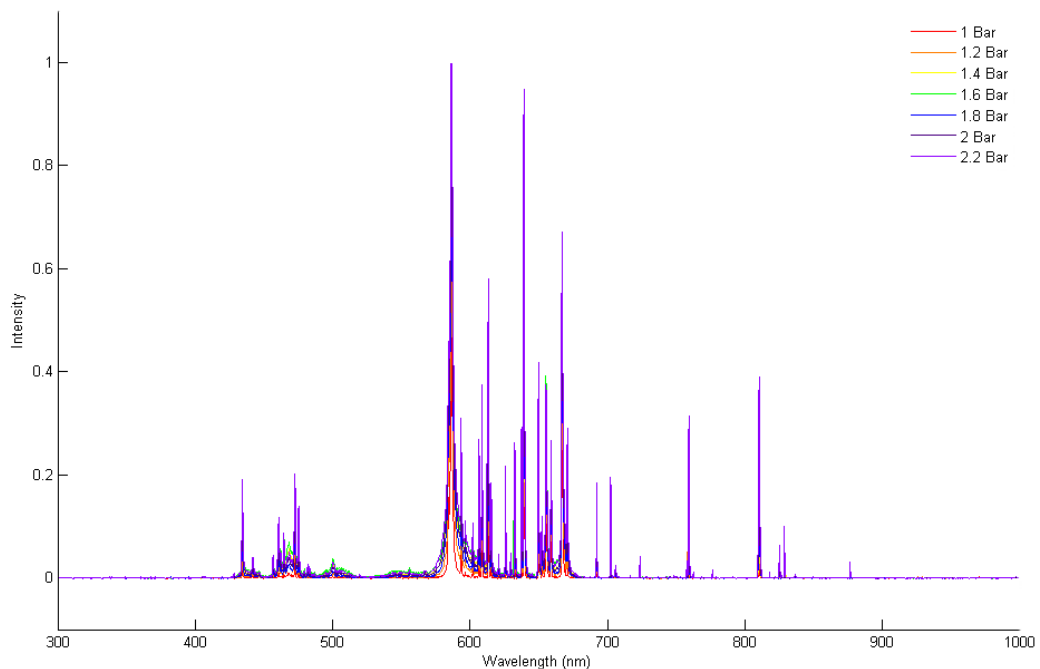


**Figure 102.** The mean spectra of light emitted from a laser induced plasma in helium at pressures of up to 2.2 bar.

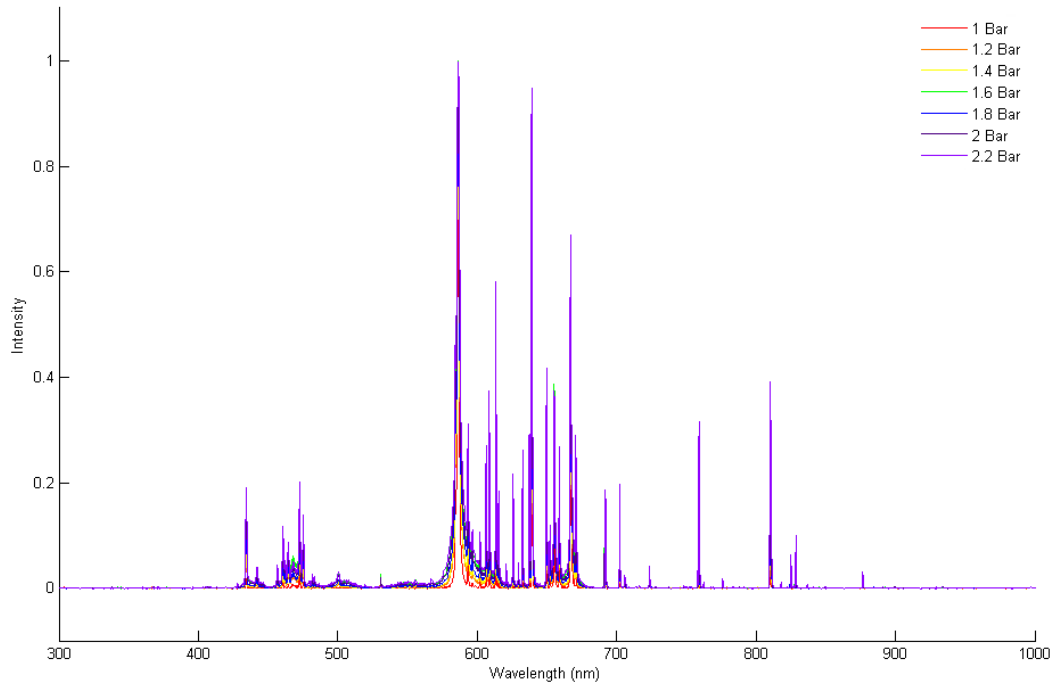


**Figure 103.** The mean spectra of light emitted from a laser induced plasma in helium at pressures of up to 2.2 bar. The laser is frequency doubled to 532 nm.

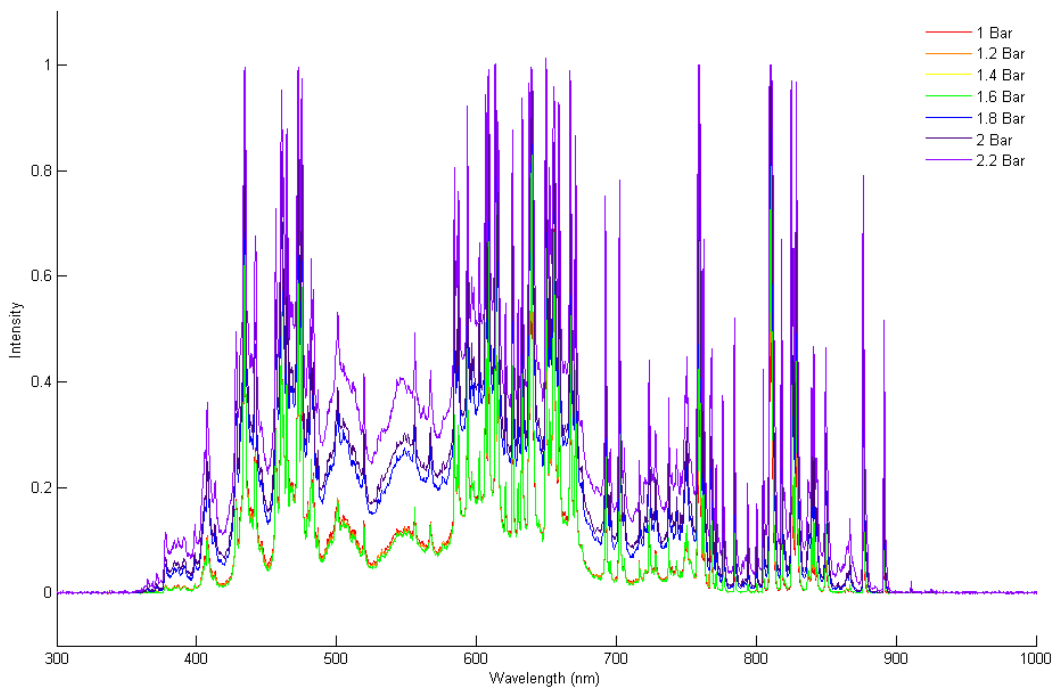


**Figure 104.** The mean spectra of light emitted from a laser induced plasma in neon at pressures of up to 2.2 bar.

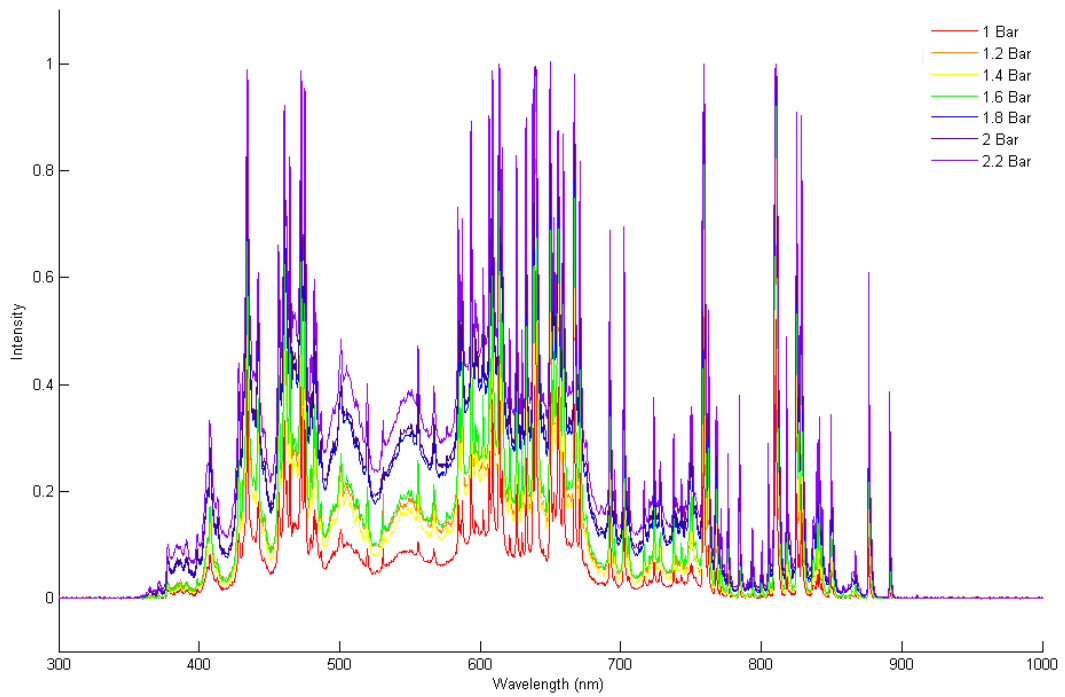


**Figure 105.** The mean spectra of light emitted from a laser induced plasma in neon at pressures of up to 2.2 bar. The laser is frequency doubled to 532 nm.

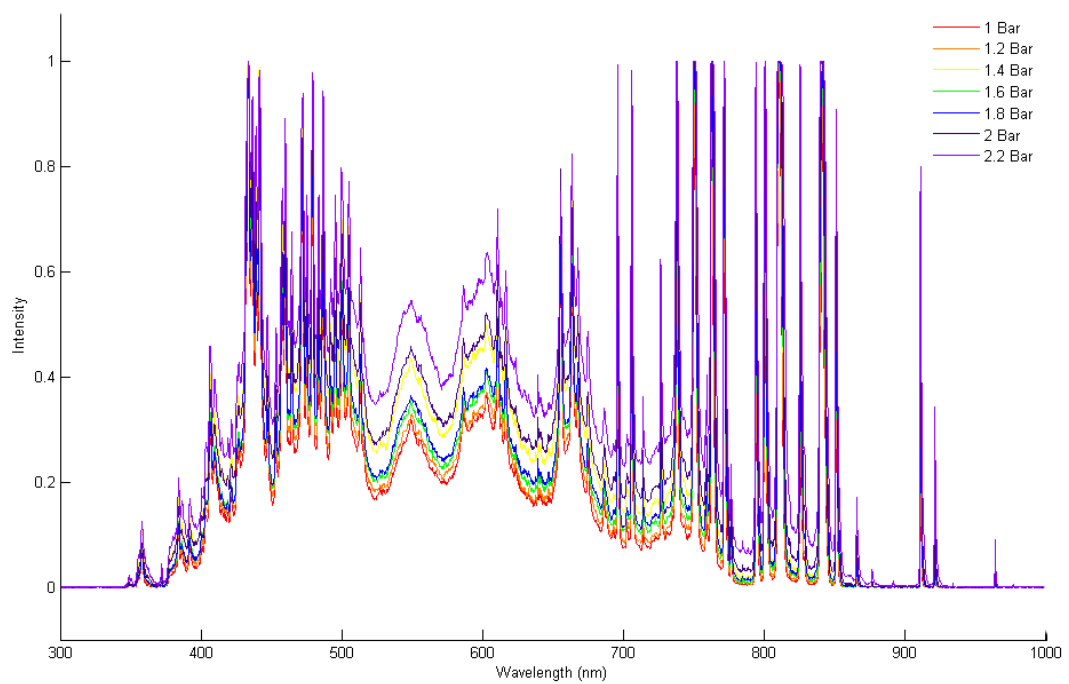


**Figure 106.** The mean spectra of light emitted from a laser induced plasma in argon at pressures of up to 2.2 bar.

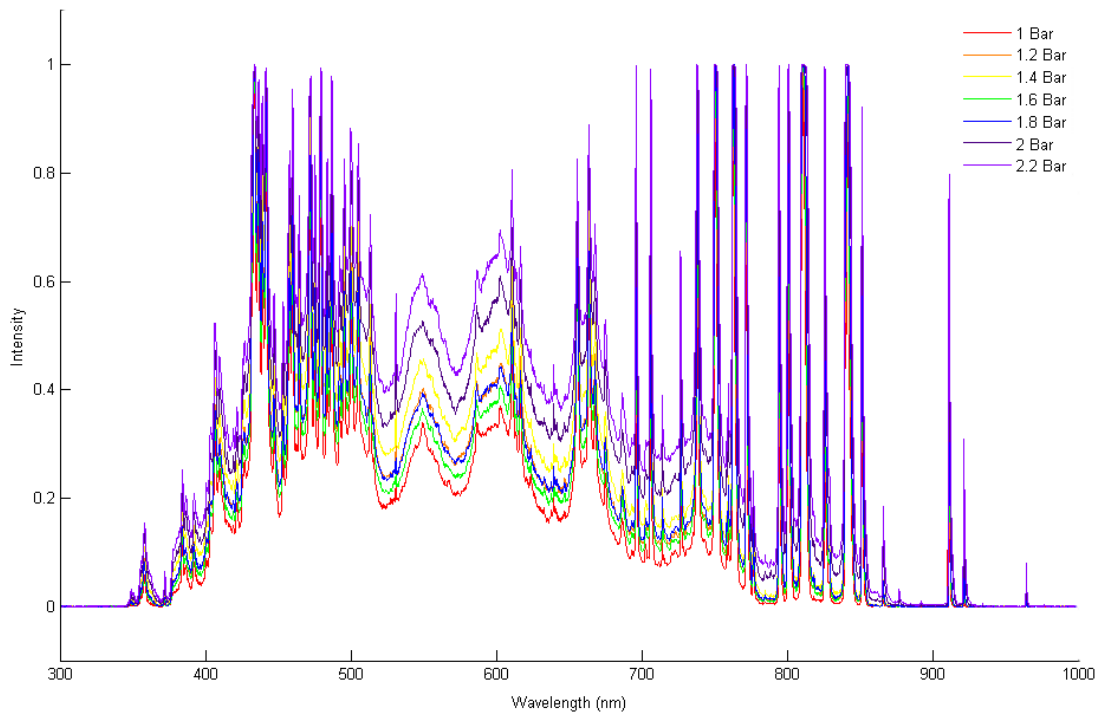


**Figure 107.** The mean spectra of light emitted from a laser induced plasma in argon at pressures of up to 2.2 bar. The laser is frequency doubled to 532 nm.

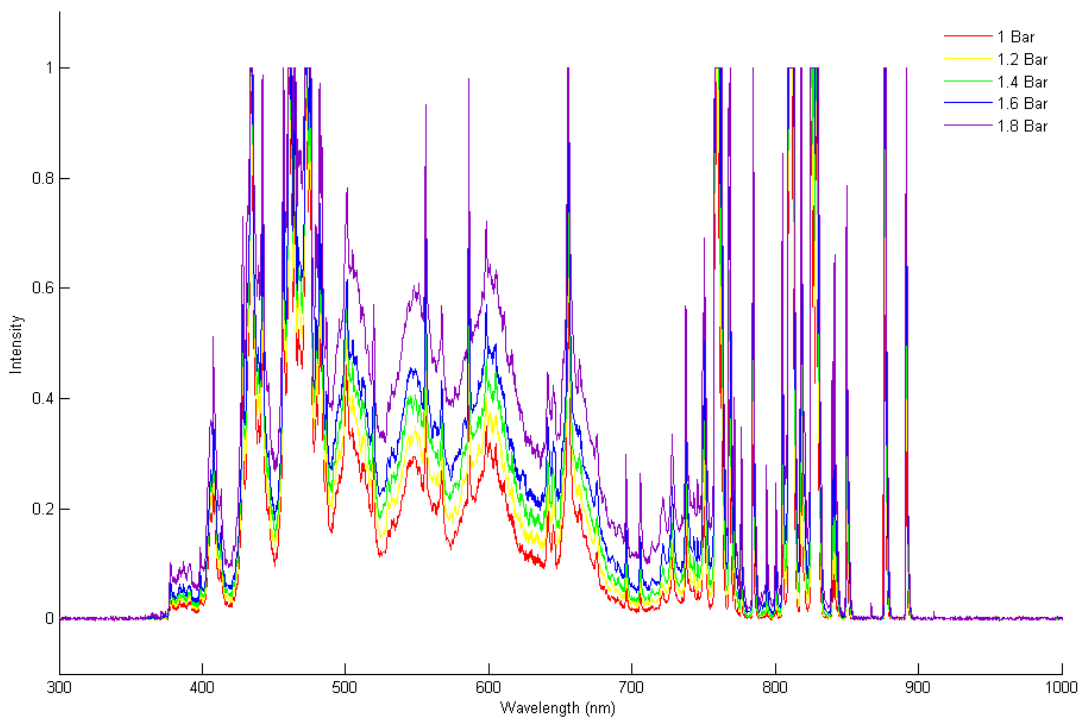


**Figure 108.** The mean spectra of light emitted from a laser induced plasma in krypton at pressures of up to 1.8 bar.



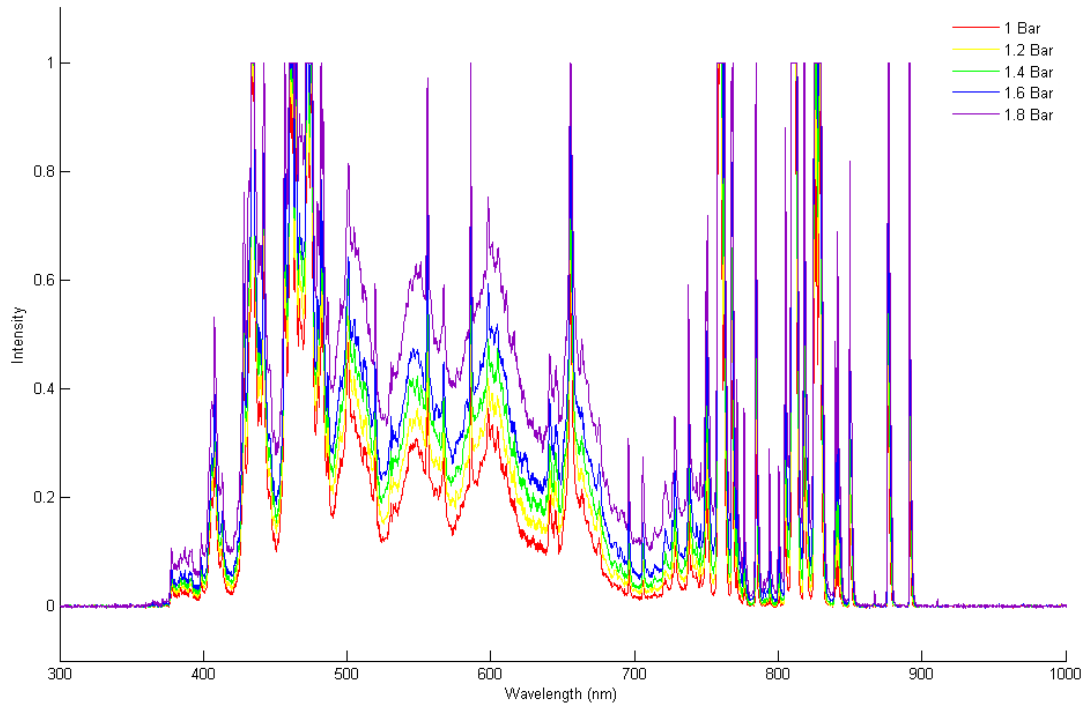


**Figure 109.** The mean spectra of light emitted from a laser induced plasma in krypton at pressures of up to 1.8 bar. The laser is frequency doubled to 532 nm.

The spectrometer records a spectrum as a list of values of relative intensity against a value of wavelength. The intensity has units of power/wavelength. The relative power emitted across all wavelengths is the integral of the intensity over the wavelength or the area under the spectrum. The spectrometer outputs the wavelength as a single value but this can be approximated to a wavelength range  $d\lambda$ , by deleting the wavelength of the previous value. The power at any wavelength is obtained by multiplying  $d\lambda$  by the intensity at that wavelength. The power across all wavelengths is found by summing the contributions to the power for each wavelength range.

This method of determining the total, spectral power works best for small  $d\lambda$ . In these spectra  $d\lambda$  is very small, ranging from 0.2 at 200 nm to 0.24 at 1100 nm. This gives a total of 3648 wavelength regions that contribute to the total spectral power. This is the number of pixels across the width of the CCD in the spectrometer. The spectral contributions from noise are removed by recording a 5 minute blank spectrum to determine the maximum value obtained by the dark noise. This was found to reach a maximum value of 0.008. It was decided

that any contribution to the spectral power below an intensity of 0.01 would not be included. The total spectral power for each of the gases tested at different pressures, with or without frequency doubling is shown in Figure 110 & Table 17.

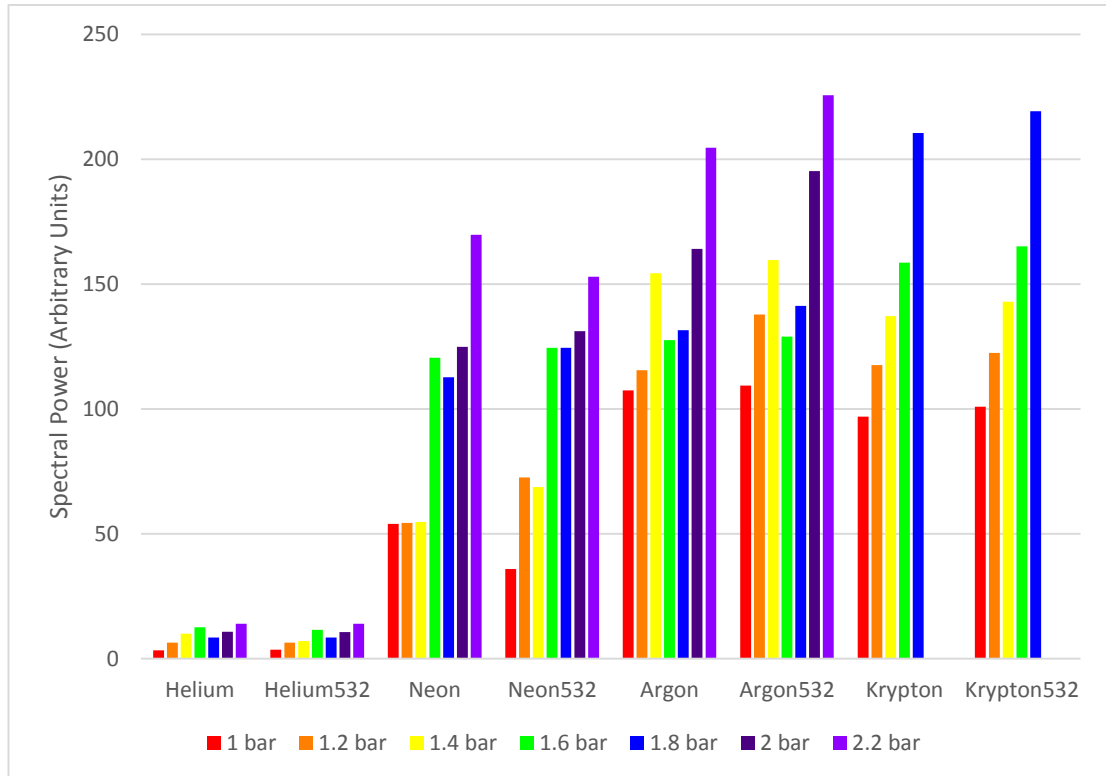


**Figure 110.** The total spectral power for each of the gases tested, showing the effect of pressure and frequency doubling. The frequency doubled tests are shown as 532(nm). The colour scheme used to show pressure is the same as in Figures 102-109.

	Helium	Helium532	Neon	Neon532	Argon	Argon532	Krypton	Krypton532
1 bar	1.00	1.10	16.19	10.79	32.25	32.82	29.07	30.29
1.2 bar	1.91	1.94	16.30	21.77	34.65	41.36	35.27	36.75
1.4 bar	2.99	2.13	16.43	20.63	46.33	47.90	41.15	42.88
1.6 bar	3.79	3.49	36.17	37.37	38.26	38.68	47.57	49.56
1.8 bar	2.54	2.55	33.82	37.37	39.45	42.38	63.15	65.79
2 bar	3.23	3.21	37.45	39.36	49.23	58.57		
2.2 bar	4.19	4.19	50.94	45.88	61.38	67.68		

**Table 17.** A summary of the total spectral power (arbitrary units) for each noble gas at different pressures, with or without frequency doubling (532nm). The values are normalised to the smallest value for ease of comparison.

From the results of gas testing it was concluded that:

- None of the gases or pressure changes significantly shifted the emission of the plasma to shorter wavelengths. This was an indication that changing the gas and altering the pressure had little effect upon electron temperature. It was difficult to obtain a plasma temperature for each of the gases using Wien's law as the blackbody spectrum of the emission is obscured by line emission features. The shortest wavelength emitted was from argon which had a small peak just above 350 nm. For the spectroscopy of biological chromophores, many of which absorb between 200 and 300 nm, this posed a problem as the prototype instrument would not be able to conduct experiments that observe changes in native biological chromophores.
- Helium was a very poor gas in which to induce a plasma. The overall intensity was very low compared to other gases, indicating that the electron density in the plasma was low. The spectra of the emission from a helium plasma displayed very well defined spectral lines but very little brehmsstrahlung radiation. This indicated that the helium atoms were undergoing bound-bound transitions with very little production of free electrons. This was also an indication that helium has a high breakdown threshold.
- Frequency doubling made very little difference to the intensity of light given off by the plasma.
- The noble gases showed an increase in the total spectral intensity of light inversely proportional to the first ionisation energies of these elements. The ionisation energies in kJ/mol are: He 2372.57, Ne 2080.22, Ar 1520.61 and Kr 1350.
- The higher the atomic number of the noble gas, the greater the change in intensity with pressure. Krypton showed the greatest difference in the intensities at 1 and 1.8 bar.
- Argon exhibited the least amount of line emission with little line emission emitted between 520 and 660 nm. Krypton, although the best gas for total spectral power overall, showed intense narrow line emission peaks at 556, 586 and 657 nm. As was discussed previously, these line emission peaks can be too intense for the spectrometer to measure correctly.

All of the gases apart from helium, drastically improve the reliability of plasma formation. This can be seen from the average intensity at a single wavelength, for each plasma generated in the test, for each of the gases at a specific pressure. The wavelength chosen should be one at which strong brehmsstrahlung emission can be observed. The number of laser pulses that had less than the dark noise value of intensity (less than 0.01) at this wavelength is the number of pulses (out of 600) that failed to generate a plasma. The average plasma emission recorded by the spectrometer at 600 nm, as well as the standard deviation of the emission is shown in Table 18. If the average intensity was less than 0.01 it was recorded as zero. The data is taken from the experiments that did not use frequency doubling.

Gas	Pressure (bar)	Average Plasma Intensity	Standard Deviation of Intensity	Number of Pulses of Intensity < 0.01
<b>He</b>	1	0	Null	558
	1.2	0.01511	0.019	331
	1.4	0.039	0.031	112
	1.6	0.054	0.037	61
	1.8	0.023	0.022	208
	2	0.036	0.03	103
	2.2	0.053	0.038	71
<b>Ne</b>	1	0.182	0.111	40
	1.2	0.178	0.116	31
	1.4	0.177	0.109	18
	1.6	0.376	0.127	0
	1.8	0.348	0.115	0
	2	0.392	0.148	0
	2.2	0.516	0.153	0
<b>Ar</b>	1	0.326	0.096	0
	1.2	0.346	0.106	0
	1.4	0.452	0.099	0
	1.6	0.376	0.105	0
	1.8	0.382	0.114	0
	2	0.474	0.139	0
	2.2	0.574	0.169	0
<b>Kr</b>	1	0.13	0.067	0
	1.2	0.153	0.077	0
	1.4	0.180	0.078	0
	1.6	0.206	0.098	0
	1.8	0.265	0.098	0

**Table 18.** The mean and standard deviation intensity of the plasma at 600 nm for each gas over a range of pressures from 0 to 2,2 bar. The number of laser pulses that failed to produce an intensity of greater than 0.01 is also shown. These are the tests are conducted with no frequency doubling of the laser.

Both Argon and Krypton showed no data points that were below an intensity of 0.01 indicating that a plasma was produced with each laser pulse. A data point of zero intensity meant that the laser had failed to produce a plasma during the pulse. These results demonstrated that argon was the best gas to use in the prototype instrument. Plasmas were reliably generated in argon, argon was by far the cheapest of the gases, and had the least line emission with good brehmsstrahlung emission. From this point onwards, all testing and experimentation was conducted with an argon plasma as the light source.

It is likely that a much more expensive, high pulse rate, mode-locked laser will need to be employed to generate short wavelength (higher temperature) radiation. Should a more expensive laser be purchased in future, it is recommended that these gases be retested for the emission wavelength distribution and intensity. Xenon may also be a better gas to use in the future as it has a lower ionisation energy than any of the gases tested, but is too expensive to be used currently in a prototype instrument.

# Four

---

## Instrument Measurements

---

### 4.1 The Effect of Heparin on Protein Aggregation

The lack of native biological chromophores within the working range of the spectrometer (380 – 700 nm) limits the experimental options for the testing of time resolved absorbance spectroscopy. As an alternative to absorbance spectroscopy, the plasma instrument can be used for broadband turbidimetry, the attenuation of the broadband light as it passes through a turbid sample. The turbidity of a solution is the cloudiness or haziness due to the Rayleigh scattering of light from large numbers of particles. Turbidity is similar to absorption in that both cause a loss in the intensity of light as it is transmitted through a sample, although the physical mechanisms of turbidity and absorption are very different. Generally, the same apparatus that is used to measure absorbance can be used to measure turbidity, as long as the turbidity measurements are made at wavelengths that are far from any absorption

maxima. Turbidimetry experiments are identical to a Raleigh scattering experiments measured at  $\theta=0$  but Raleigh scattering experiments are not conducted at  $\theta=0$  due to the impossibility of correcting for non-scattered light. In the same way, it is difficult to correct for forward scattered light in turbidimetry experiments.

Turbidity can be expressed mathematically in a manner that is analogous to the Beer-Lambert law:

$$\text{Turbidity} = \ln \frac{I_T}{I_A} = \tau cl \quad \text{Equation 22}$$

$I_T$  is the intensity impinging upon the sample,  $I_A$  is the intensity of the transmitted light,  $\tau$  is the turbidity coefficient,  $c$  is the molar concentration of the scattering particles and  $l$  is the path length. SNRs in turbidimetry therefore increase as the square root of the incident light intensity in an identical manner to SNRs in absorbance spectroscopy. The Raleigh ratio can be determined from the turbidity using the equation:

$$\tau = \frac{16\pi}{3} R_{90}$$

where  $R_{90}$  is the Raleigh ratio when  $\theta = 90^\circ$ .

The scattering of light by particles in solution is highly dependent upon the particle size. If the size of the particles is much smaller than the wavelength of the impinging light, the scattering is modelled using Raleigh scattering but if the wavelength of light is approximately equal to or larger than the particle size, Mie scattering must be used. With Raleigh scattering, the magnitude and direction of the electric field of the light is unchanged across the extent of the particle. As the particle becomes larger, the electric field of the light may no longer be unchanged across the extent of the particle. Interference may also occur due to light waves scattering from different parts of the particle. Scattering by particles of comparable size to the wavelength of the impinging



light is modelled by Mie theory. The size of a scattering particle is often parameterised by:

$$x = \frac{2\pi r}{\lambda}$$

For  $x$  less than 1, the scattering is Rayleigh scattering. For  $x$  equal to or greater than 1, the scattering is Mie scattering. The results of scattering experiments therefore contain information regarding the size of the particles in the fluid.

The time dependent growth of particles is of particular biological interest in the area of protein aggregation. In their biologically active, native state, proteins are typically soluble in water due to hydrophilic amino acids on the protein surface. The regions of the protein containing hydrophobic amino acids are normally folded away inside the core of the protein, away from the polar water molecules. However, if a protein is misfolded, these hydrophobic regions can become exposed. Protein misfolding can occur for a number of reasons including point mutation(s), impaired chaperone proteins, impaired post translational modification such as phosphorylation or glycosylation, exposure to toxins and oxidative damage. Misfolded proteins can interact with the exposed hydrophobic regions of other misfolded proteins, causing proteins to aggregate or clump together. Aggregates precipitate as they become large and insoluble and may become toxic and eventually pathogenic, if the body is unable to degrade and breakdown them down.

Protein aggregation is of particular importance in a variety of diseases known as amyloidoses. These diseases include Alzheimer's (Karran et al., 2011), Parkinson's (Irwin et al., 2013), Huntington's (McGowan et al., 2000), prion disease (Budka, 2003) and Rheumatoid arthritis (Cunnane and Whitehead, 1999). In these diseases, the body is unable to degrade and remove misfolded proteins known as amyloids, through the normal mechanisms of proteolysis and the ubiquitination-proteasome pathway. The build-up of amyloids causes them to aggregate and form fibrils that deposit in organs and tissues. These fibrils display common properties including a highly hydrophobic cross  $\beta$ -sheet structure that forms between the misfolded proteins in an axis perpendicular

to the fibril axis (Eanes and Glenner, 1968, Nelson et al., 2005, Merlini and Bellotti, 2003). These cross beta sheets appear to form regardless of the secondary structural characteristics of the original protein/polypeptide (Uversky and Fink, 2004). Amyloidogenic proteins are often structurally unstable and have the ability to adopt the  $\beta$  sheet structures found in amyloid fibrils.

The term amyloid means “starch-like” and is derived from the Greek word “amylon” for starch. The word amyloid was originally coined by Virchow in 1854 after the presence of an unknown carbohydrate was detected in amyloid (Virchow, 1854). Later investigations determined that these carbohydrates were glycosaminoglycans (GAGs), more specifically heparan sulphate proteoglycans (HSPGs) (Snow and Kisilevsky, 1985, Snow et al., 1988a, Snow et al., 1991). HSPGs have been found in nearly all amyloid plaques investigated to date (Snow et al., 1989, Stenstad et al., 1991, Magnus et al., 1992, Brandt et al., 1974, Snow et al., 1988b, Snow et al., 1987). These HSPGs are known to be deposited during amyloid fibrillogenesis (Snow and Kisilevsky, 1985) and for this reason are thought to play a key role in fibril formation (Snow and Wight, 1989). To date however, the exact mechanism of fibril formation and the involvement of HS has not been discerned.

HSPGs are a group of complex macromolecules that are found extensively in the extracellular matrix (ECM) of all mammalian cells. They consist of a core protein that is covalently bound to one or more highly anionic HS chains. These molecules fall into three groups according to their locality (Sarrazin et al., 2011). These groups are: membrane bound HSPGs such as glycosylphosphatidylinositol (GPI) anchored proteoglycans (glypican core protein) and syndecans, the secreted ECM HSPGs agrin, perlecan and type XVIII collagen and the secretory vesicle proteoglycan (PG) serglycin, onto which mast cell heparin is biosynthesised.

Protein aggregation is also an undesirable phenomenon in many areas of protein production (Fuh, 2011, den Engelsman et al., 2011, Joubert et al., 2011, Hamrang et al., 2013, Cromwell et al., 2006) and analysis (Pullara et al.,

Ferrolino et al., 2013). The problems presented by protein aggregation have led to efforts to identify anti-aggregation agents. Heparin is unique amongst aggregation agents as it is known to both promote and inhibit protein aggregation in different cases. Heparin suppresses and even reverses the aggregation of Zn-insulin (Giger et al., 2008), blocks acetylcholine-receptor (AChR) aggregation at developing neuromuscular junctions (Hirano and Kidokoro, 1989, Wallace, 1990), stabilises prion protein (PrP) and impairs its aggregation (Vieira et al., 2014), prevents the aggregation of creatine kinase by acting as a folding aid (Meng et al., 2001), decreases the rate of recombinant human keratinocyte growth factor (rhKGF) at elevated temperatures (Chen et al., 1994), heparin and HS both reduced the assembly of fibrillin-1 into microfibrils in cultures of skin fibroblasts (Tiedemann et al., 2001) and inhibits the aggregation of porcine and bovine somatotrophin (pST and bST) (Joshi et al., 2008). As well as suppressing aggregation, heparin also induces aggregation with many different proteins. Heparin is often used to promote amyloid fibril formation of Tau protein *in vitro* (Ramachandran and Udgaonkar, 2011), causes mild potentiation of platelet aggregation in plasma (Saba et al., 1984), induces fibril formation in both mutant and wild type apomyoglobin (Vilasi et al.) and aggregates lactoferricin. The low molecular weight heparins (LMWH) enoxaparin and dalteparin inhibited amyloidogenesis and were capable of reversing amyloidogenesis and fibril formation by blocking the formation of pleated  $\beta$ -sheet secondary structures (Zhu et al., 2001).

The presence of heparin causes the almost instantaneous aggregation of lysozyme protein (Takase, 1998). Lysozyme is a 130 amino acid enzyme that hydrolyses the the  $\beta$  1-4 glycosidic linkage of N-acetylmuramic acid and N-acetylglucosamine that occurs in the cell wall of certain bacteria, particularly Gram-positive bacteria. Lysozyme is present in high concentrations in the human body particularly in the liver, articular cartilage, saliva, tears and human milk. Defects in human lysozyme are responsible for its aggregation in amyloidosis type 8 (AMYL8), also known as systematic non-neuropathic amyloidosis (Pepys et al., 1993). Human lysozyme is an inexpensive protein which has been proposed as a model protein to use for investigating the

causes of fibrillogenesis occurring in amyloidogenesis (Merlini and Bellotti, 2005). Fourier transform infrared spectroscopy (FTIR) of lysozyme under conditions in which fibrils form demonstrated an transformation of native  $\alpha$ -helical structures into the amyloid fibril cross  $\beta$ -sheet (Booth et al., 1997). It has been previously reported that a zinc complex of heparin destabilised lysozyme (used here as a model protein) and increased the proportion of  $\beta$ -sheet by 25% (Hughes et al., 2012). The interaction of zinc-heparin with lysozyme destabilised the protein more than heparin alone (as measured by thermal stability fluorescence shift assay (Uniewicz et al., 2010)) and resulted in different secondary structure.

It is known that the bioactivity of heparin both *in vivo* and *in vitro* is altered by the presence of metal cations (Grant et al., 1973). Heparin in the presence of  $\text{Cu}^{2+}$  promotes angiogenesis in endothelial cell tissue culture and is a chemoattractant for capillary endothelium *in vivo* (Grant et al., 1973). Copper ions also promote and stabilise the binding of prion protein (PrP) to heparin/HS (González-Iglesias et al., 2002). Several publications have shown the regulatory effect on FGF signalling of metal cations bound to heparin. The divalent cations  $\text{Ca}^{2+}$  or  $\text{Mg}^{2+}$  bound to heparin restrict autophosphorylation of the FGFR1 receptor in the absence of the FGF1 ligand (Kan et al., 1996). Changing the cation bound to heparin from  $\text{Na}^+$  to  $\text{Cu}^{2+}$  converts the polysaccharide/FGF1/FGFR1c signalling complex from active to inactive. Metal cations bound to heparin also show reduced FGF2 stimulated cell proliferation in BaF3 cells transfected with the FGFR1c receptor compared to a heparin only positive control, indicating that cation binding to heparin alters the conformation required for stability of the ligand/receptor/polysaccharide signalling complex (Rudd et al., 2008b).

Heparin binds to metal cations due to its polyanionic nature. A single heparin chain can bind multiple cations, increasing the already very complex and diverse structural properties of heparin. The binding of heparin to metal cations has been investigated using a variety of techniques including NMR (Chevalier et al., 2004, Rabenstein et al., 1995, Liu and Perlin, 1992, Rej et al., 1990, Rudd et al., 2008b, Hughes et al., 2012), infrared spectroscopy (Grant et al.,

1987, Rudd et al., 2008b), absorbance spectroscopy (Stevic et al., 2011) (Mukherjee et al., 1978), circular dichroism (Rudd et al., 2008b, Mukherjee et al., 1978, Hughes et al., 2012), ion mobility mass spectroscopy (Seo et al., 2011), molecular modelling (Chevalier et al., 2002, Chevalier et al., 2004), electron paramagnetic resonance (EPR)(Rudd et al., 2008b), crystallography (Shao et al., 2006), polarimetry (Grant et al., 1992a) and potentiometry (Grant et al., 1992b, Grant et al., 1992a). These studies focus on the structural properties of cation–heparin complexes and the conformational changes that occur in heparin upon cation binding. A recent study has determined the binding affinities of heparin with various cations (Stevic et al., 2011) as well as the average numbers of cations bound to a heparin molecule. The data revealed significant variation in the binding affinities of cations in the decreasing order  $Mn^{2+} > Cu^{2+} > Ca^{2+} > Zn^{2+} > Co^{2+} > Na^+ > Mg^{2+} > Fe^{3+} > Ni^{2+} > Al^{3+} > Sr^{2+}$ . The trend for the average number of cation binding sites on a heparin molecule was  $Sr^{2+} > Mn^{2+} > Zn^{2+} > Co^{2+} > Ca^{2+} > Na^+ > Mg^{2+} > Ni^{2+} > Fe^{3+} > Cu^{2+} > Al^{3+}$ . The result for Strontium was surprising as it has the lowest binding affinity but the largest mean number of cations per molecule.

As a test system, about which some details are already known, it was of interest to employ the plasma spectrometer to monitor the rate of aggregation of lysozyme in the presence of different heparin salts by turbidimetry. The stoichiometry of the lysozyme-heparin interaction requires an excess of lysozyme so that fibril formation proceeds after the initial binding of lysozyme to heparin. A one to one hundred molar ratio of heparin to lysozyme was chosen for testing. Human lysozyme has a molecular weight of 14.7 kDa (Huang et al., 2002) and the sodium salt (9.5-12.5 %) porcine mucosal heparin (PMH) that was used had a molecular weight of 8-25 kDa, as stated by the manufacturer (A3004 Applichem Heparin sodium salt 208 IU/mg). Heparin and lysozyme can therefore be assumed to have approximately the same molecular weight when determining experimental quantities.

## 4.2 Monitoring Lysozyme and Fibrinogen Aggregation using the Plasma Spectrometer

As noted by previous investigators, heparin almost instantly induces aggregation in lysozyme but the rate of aggregation can be slowed by reducing the concentration of lysozyme and heparin so that aggregation is measurable over a time period that is observable by a spectrometer. In order to determine the lowest possible concentration of lysozyme that could be used in the spectrometer, a range of concentrations of lysozyme were tested from 0.5 – 3 mg/ml. The concentration of heparin tested in each case was held at 20 µg/ml. To ensure that the correct amount of lysozyme was used in each experiment and that aggregation did not occur until the buffer was added, the lysozyme was made up to a known concentration of 5 mg/mL in HPLC grade water. The desired amount of lysozyme for each experiment was then aliquoted and lyophilized.

The aggregation of proteins is known to be dependent upon the pH of the solution (Sahin et al., 2010, Kadima et al., 2004, Chan and Chen, 2001). This is because if the pH of a solution is higher than the pI of a protein, the protein is predominantly negatively charged and if the pH of a solution is lower than the pI of a protein, the protein is predominantly positively charged. This causes electrostatic repulsion between proteins, preventing their aggregation. If the pH of a solution is at the pI of protein, the protein has no overall charge and so it is the attractive forces that tend to dominate and cause the proteins to interact and aggregate. Recombinant human lysozyme expressed in rice has a pI of 10.2 (Huang et al., 2002). The heparin-lysozyme complex that is formed following the addition of heparin, will have a much lower pI than 10.2 due to the highly negatively charged (polyanionic) nature of heparin so the pH at which optimal aggregation occurs may change from pH 10.2. Initial testing revealed that heparin induced aggregation of lysozyme occurred at pH 10 and so this pH was chosen for testing to determine the optimal concentration of lysozyme to use in the spectrometer. The experiments were all carried out in x1 PBS, with the pH of the PBS adjusted to pH 10 with 1M NaOH.

It was important to mix the solutions of heparin and lysozyme correctly so that aggregation occurs evenly throughout the solution. If the heparin is pipetted into a cuvette containing 2 mL of lysozyme solution, the concentration of heparin in certain places will initially be very high, causing aggregation to occur almost instantly and unevenly in the cuvette. The best way to ensure adequate mixing of the lysozyme and heparin is to add the heparin to the cuvette first as follows:

1. The heparin was made up to 5 mg/mL with pH 10 PBS.
2. 8  $\mu$ L of the 5 mg/mL heparin solution was pipetted into the cuvette (gives a final concentration of 20  $\mu$ g/mL after addition of 2 mL lysozyme solution).
3. 2 mL of pH 10 PBS is added to the aliquoted, lyophilized lysozyme and solubilised.
4. The lysozyme solution is then pipetted into the cuvette
5. The sample is then run in the plasma spectrometer at 1 pulse per second for 15 minutes (900 pulses).

Before the experiments to determine the minimum concentration of lysozyme were carried out, the turbidity of the PBS pH 10 solution was determined by the plasma spectrometer over a 5 minute time period using Script 2 as outlined previously. The turbidity of the buffer was then subtracted from the time resolved turbidity of the heparin-lysozyme solution. The .csv files generated by VBA script were then imported into graphing software for visualisation. The results are plotted in Figures 111-116.

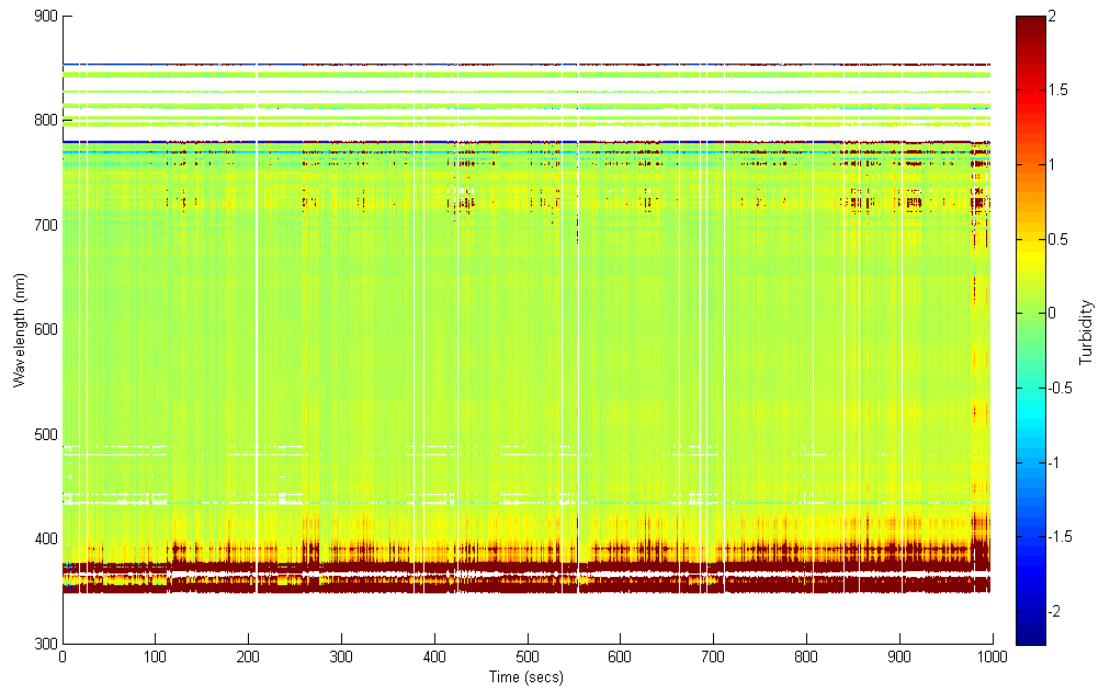


**Figure 111.** The time resolved turbidity spectrum of the pH 10 solution of 0.5 mg/ml lysozyme with 20 µg heparin.

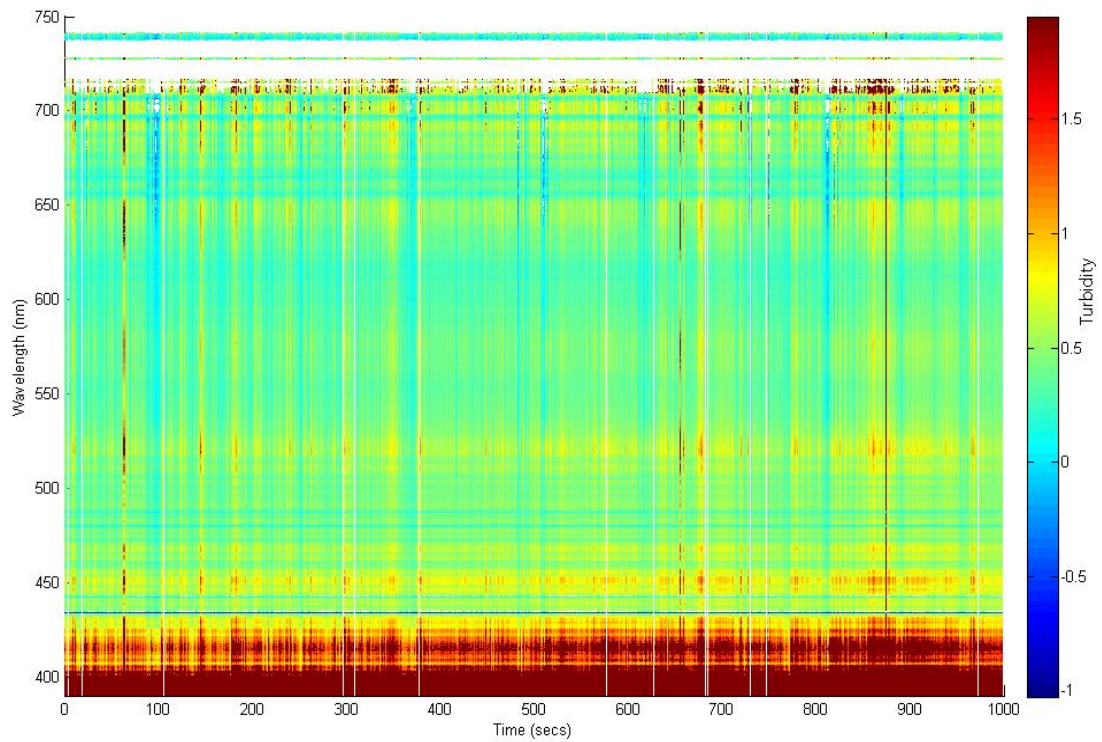


**Figure 112.** The time resolved turbidity spectrum of the pH 10 solution of 1 mg/ml lysozyme with 20 µg heparin.



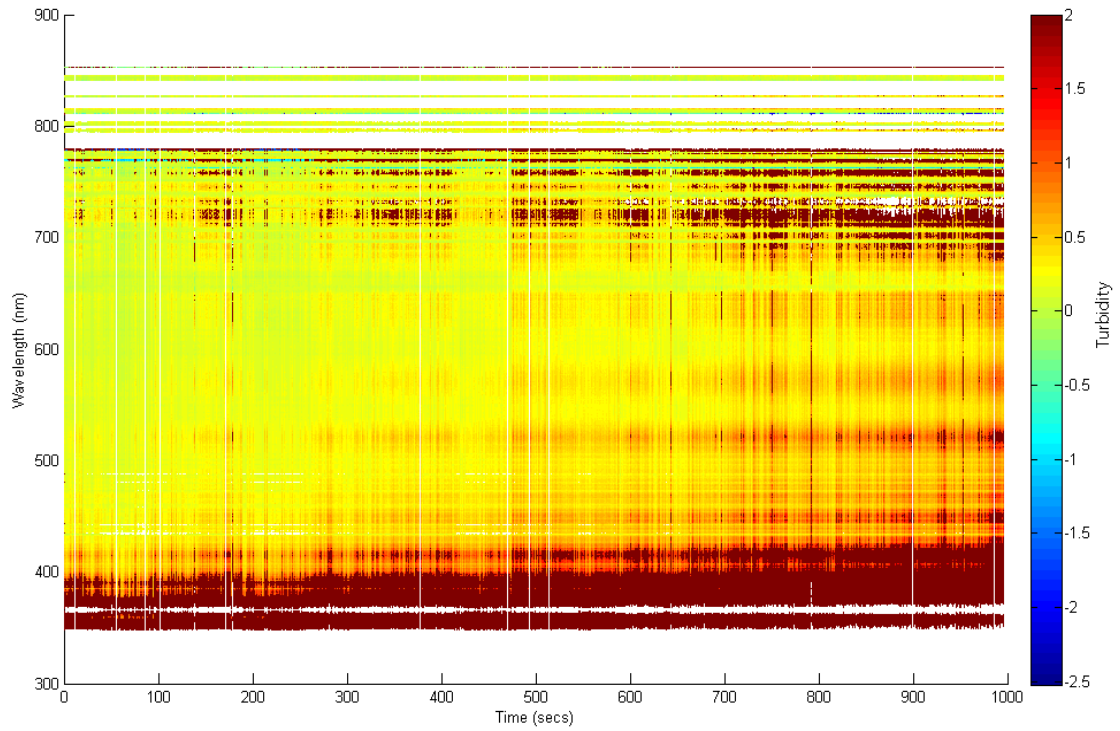


**Figure 113.** The time resolved turbidity spectrum of the pH 10 solution of 1.5 mg/mL lysozyme with 20 µg heparin.

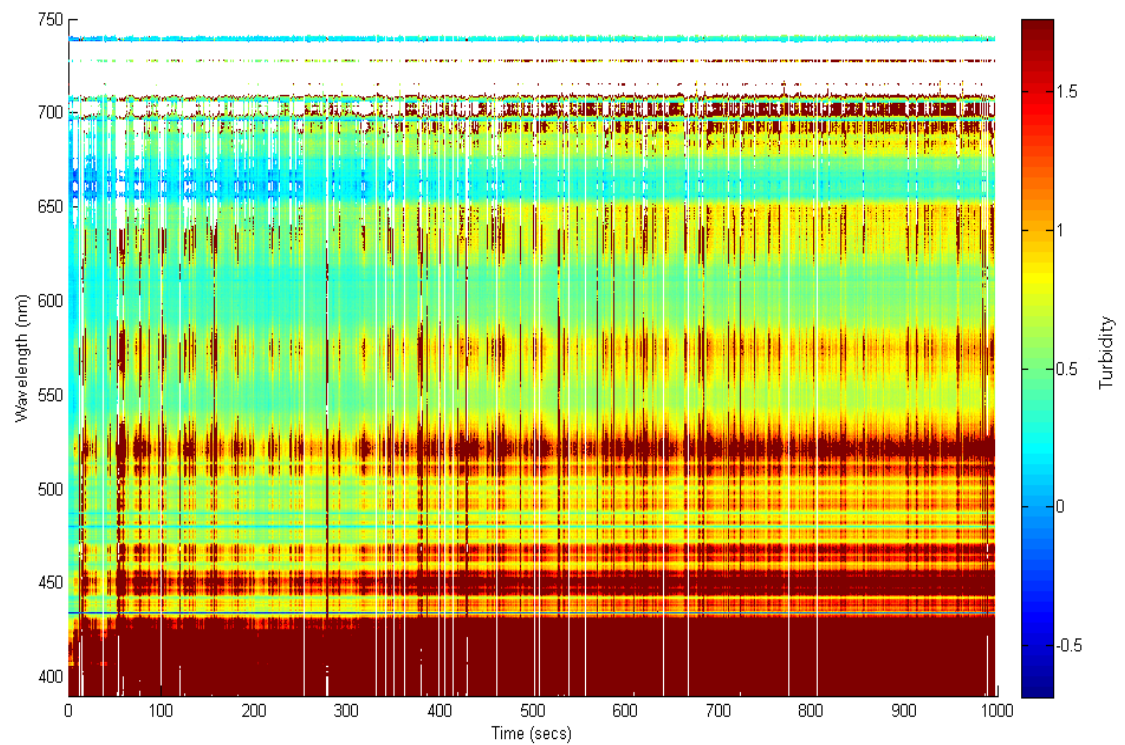


**Figure 114.** The time resolved turbidity spectrum of the pH 10 solution of 2 mg/mL lysozyme with 20 µg heparin.

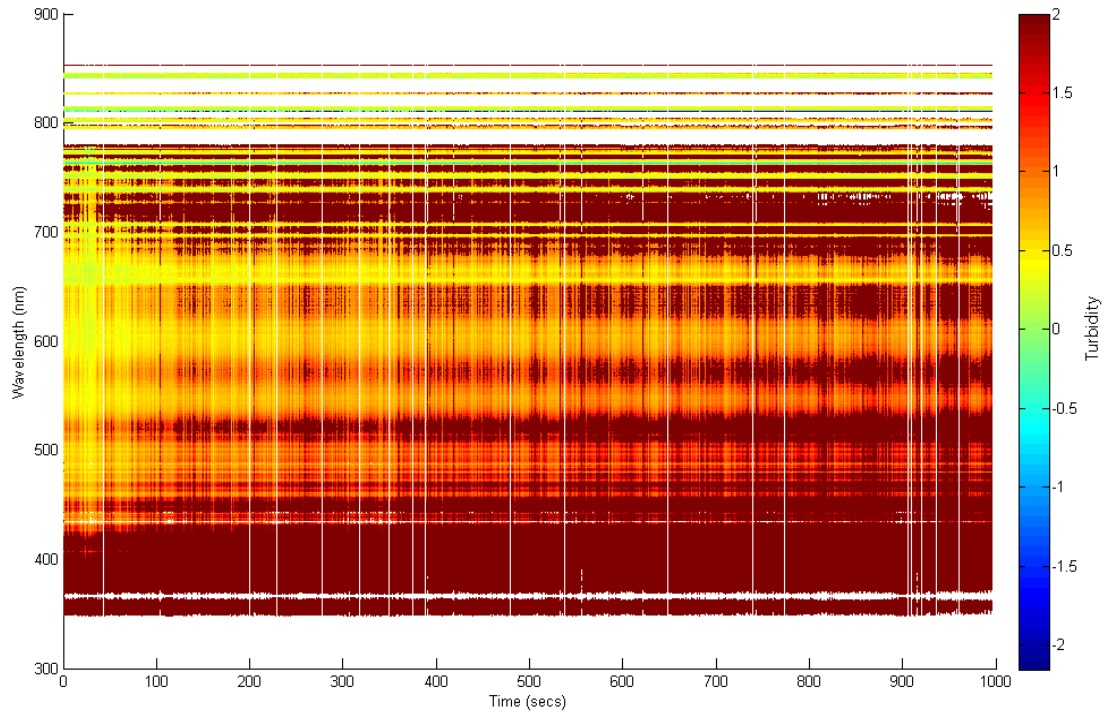


**Figure 115.** The time resolved turbidity spectrum of the pH 10 solution of 2.5 mg/mL lysozyme with 20 µg heparin.

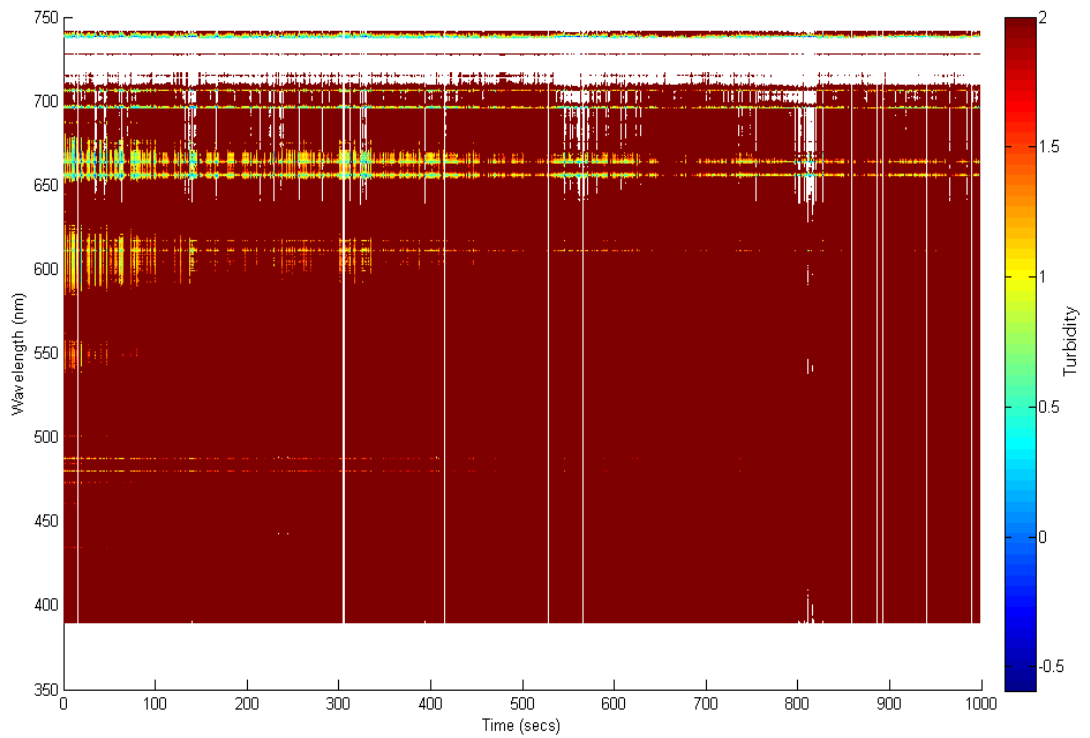


**Figure 116.** The time resolved turbidity spectrum of the pH 10 solution of 3 mg/mL lysozyme with 20 µg heparin.

Figures 111-116 show that the optimal concentration of lysozyme was 2 mg/ml. At this concentration the turbidity of the sample allows enough light to pass through so that the intensity of light entering the CCS200 spectrometer is greater than 0.01 at most wavelengths. At higher concentrations, the intensity of light after passing through the sample is too low for the CCS200 spectrometer to detect and so many data points are assigned the maximum turbidity of 2 (dark red). At concentrations less than 2 mg/ml, the turbidity of the sample is too low and too little light is scattered/absorbed.

Once the optimal concentration of lysozyme to use in the plasma spectrometer was established, experiments were run to determine the effect of pH upon the aggregation rate. A range of pHs were tested from pH 3.5 to 11.5 in increments of pH 0.5. These experiments were carried out in PBS buffer as before, with the pH adjusted with 1M HCl or NaOH. The turbidity, as a function of wavelength, of each of these buffers was determined in the plasma spectrometer using the previous method. These background turbidities were recorded so that they could be subtracted from the time resolved lysozyme-heparin spectra during each analysis. As well as samples containing lysozyme and heparin, a lysozyme only control at each of the pHs was carried out.

The knowledge that cations can exert a strong influence on the bioactivity of heparin prompted an investigation into the effect of heparins in different cationic forms upon protein aggregation. As well as the sodium heparin and the lysozyme only control, the heparin salts  $\text{Fe}^{2+}$ ,  $\text{Cu}^{2+}$  and  $\text{Zn}^{2+}$  were chosen for investigation. These heparins were prepared as follows:

1. The porcine mucosal heparin was exchanged into the acid form using Dowex Marathon cation exchange resin.
2. Each heparin was added to a 10 mM solution of the relevant cation chloride salt.
3. The heparin/cation solution was extensively dialysed against HPLC grade water in 7.5 kDa cellulose acetate dialysis membrane.
4. The retained solution was further desalted by size exchange chromatography using a PD10 column.

5. The cation heparin solution was lyophilised.

All of the experiments were run at the previously determined optimal lysozyme concentration of 2 mg/mL. 2 mL was needed to fill each cuvette and so 4 mg of lyophilised lysozyme was used in each experiment. As before, 40 µg of heparin was used in each experiment and pipetted into to the cuvette first. The lysozyme was then dissolved in the correct pH buffer solution and then pipetted into the cuvette. The cuvette was placed in the beam and the experiment was run for 15 minutes at a pulse rate of 1 pulse per second. It was important to start the experiment quickly after the heparin and lysozyme are mixed because the aggregation process starts straight away. The experiments that were run were as follows:

Lysozyme without heparin.

Lysozyme with commercial sodium heparin.

Lysozyme with zinc heparin

Lysozyme with iron (II) heparin

Lysozyme with copper heparin

Each of these experiments was conducted in PBS buffer in the pH range 3.5-11.5, in increments of 0.5. The time resolved VBA script was then run on the raw data. The script subtracted the background turbidity of the buffer. The .csv file that was output from the script was then imported into graphing software. The final plots for these aggregation experiments are shown in Tables 19-23. The plots are sorted by pH value.

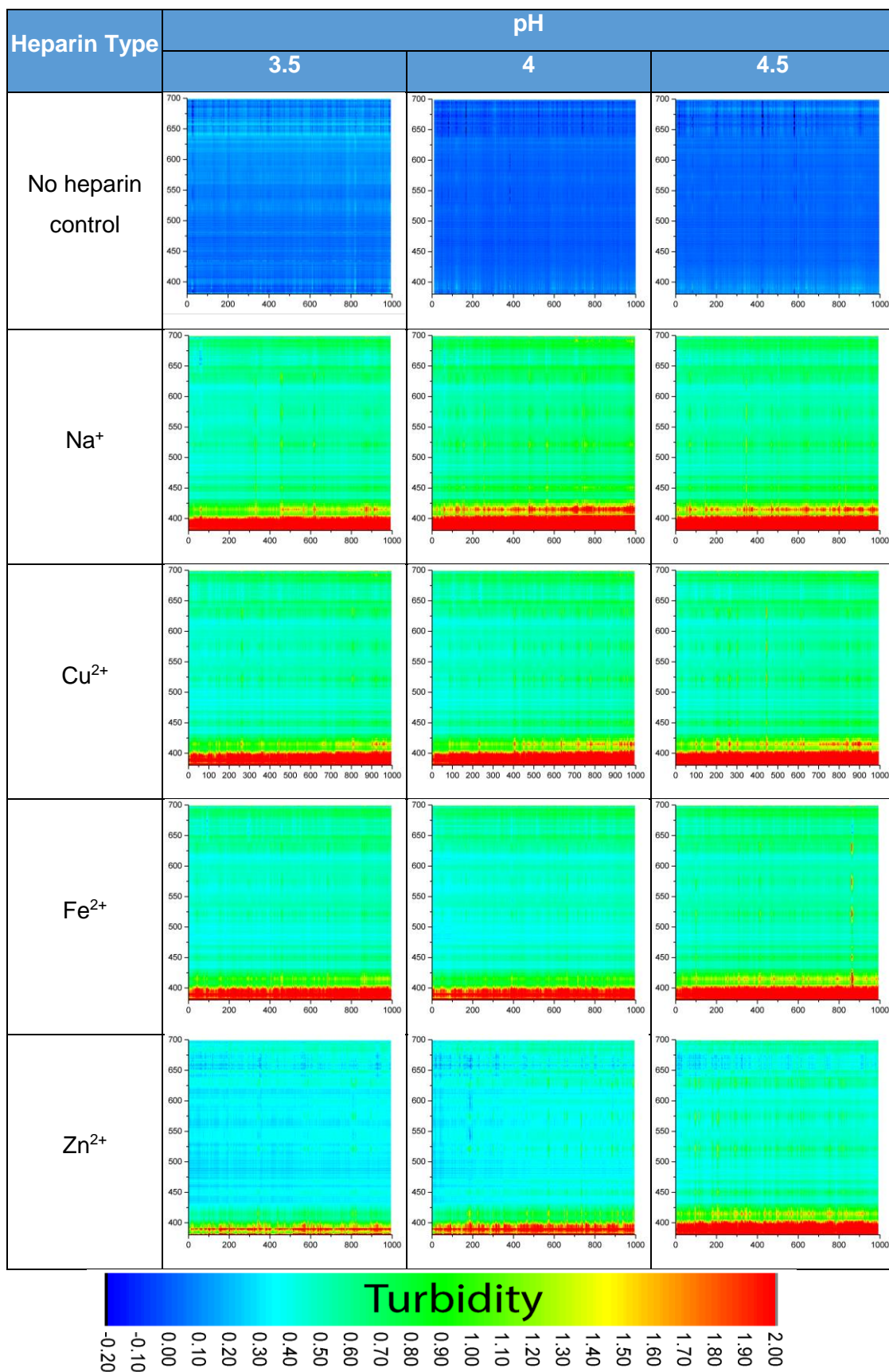


**Table 19.** Plots of the turbidity of lysozyme in the presence of different heparins at pH 3.5-4.5 monitored using the plasma spectrometer. The y axis is wavelength from 380–700 nm and the x axis is time from 0-1000 seconds.

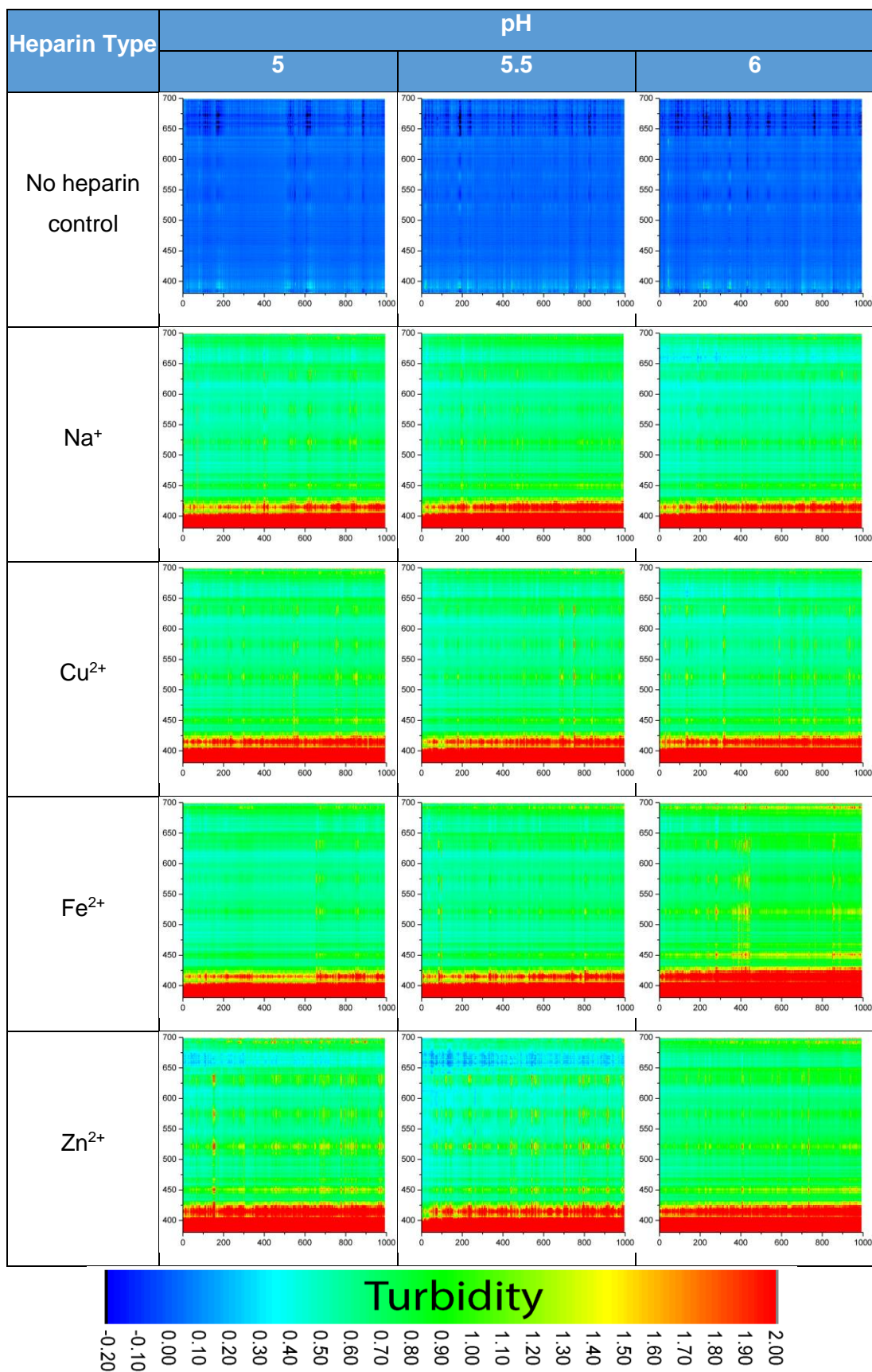


**Table 20.** Plots of the turbidity of lysozyme in the presence of different heparins at pH 5-6 monitored using the plasma spectrometer. The y axis is wavelength from 380–700 nm and the x axis is time from 0-1000 seconds.

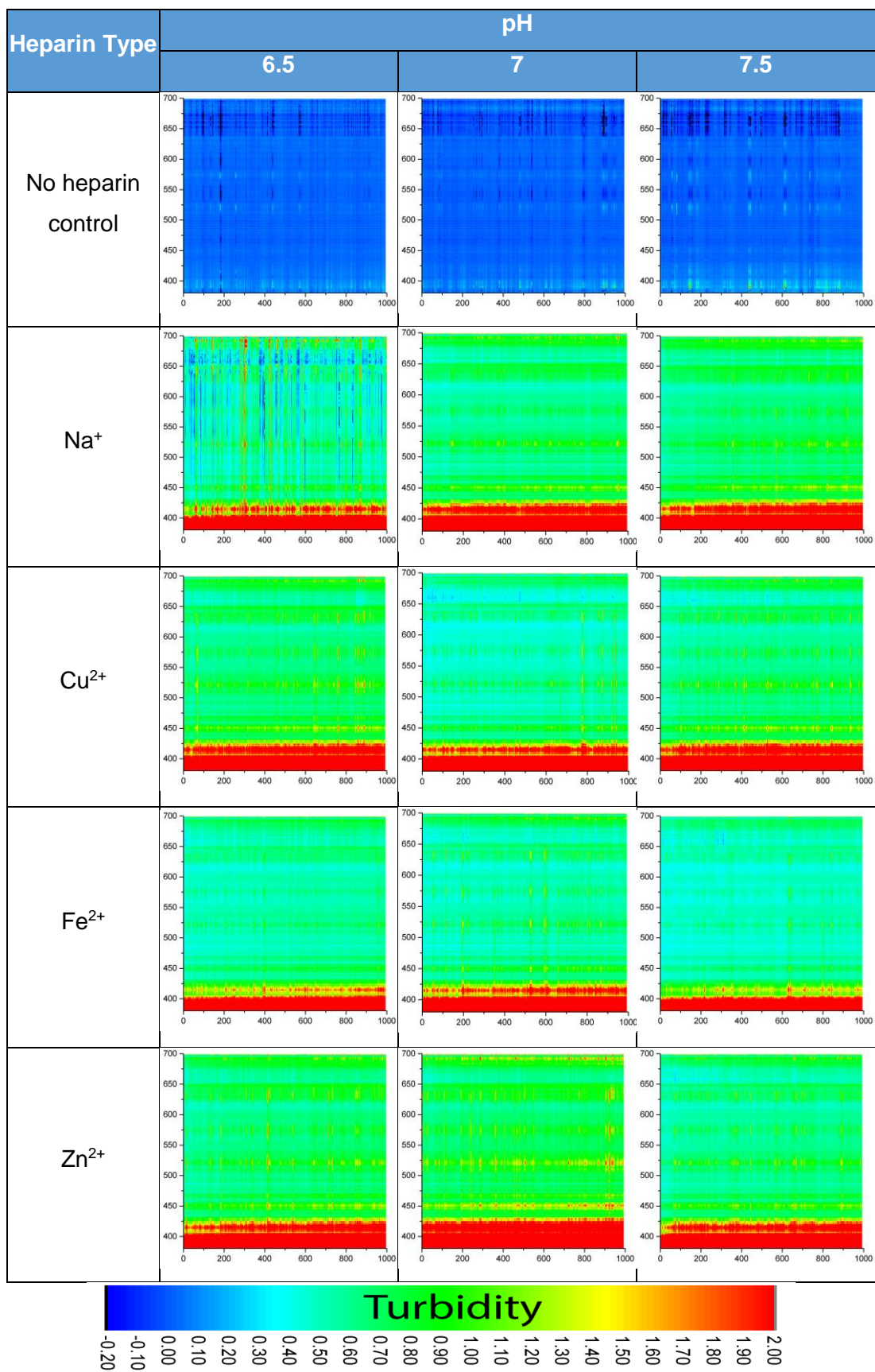


**Table 21.** Plots of the turbidity of lysozyme in the presence of different heparins at pH 6.5-7.5 monitored using the plasma spectrometer. The y axis is wavelength from 380–700 nm and the x axis is time from 0-1000 seconds.

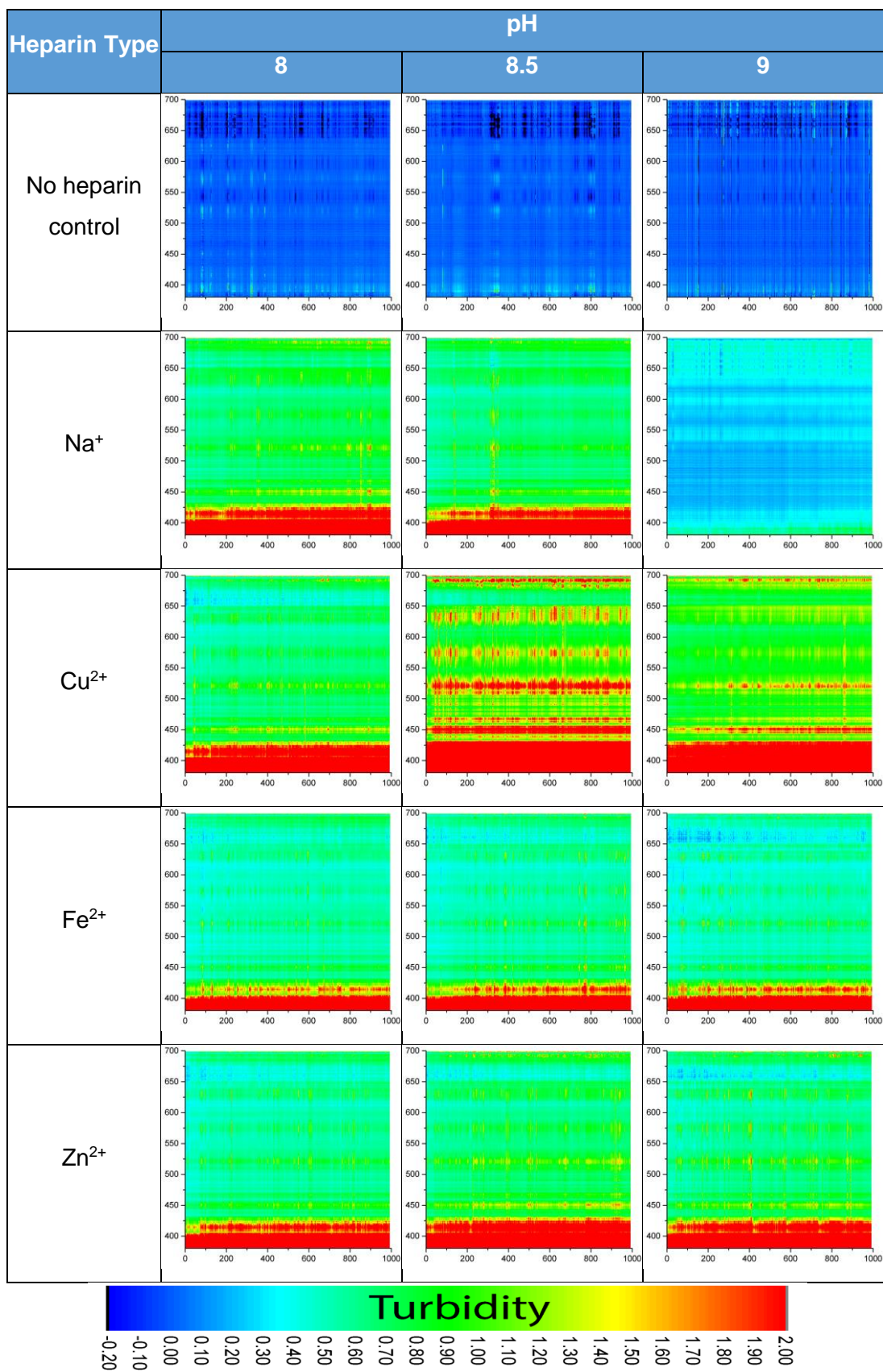


**Table 22.** Plots of the turbidity of lysozyme in the presence of different heparins at pH 8-9 monitored using the plasma spectrometer. The y axis is wavelength from 380–700 nm and the x axis is time from 0-1000 seconds.



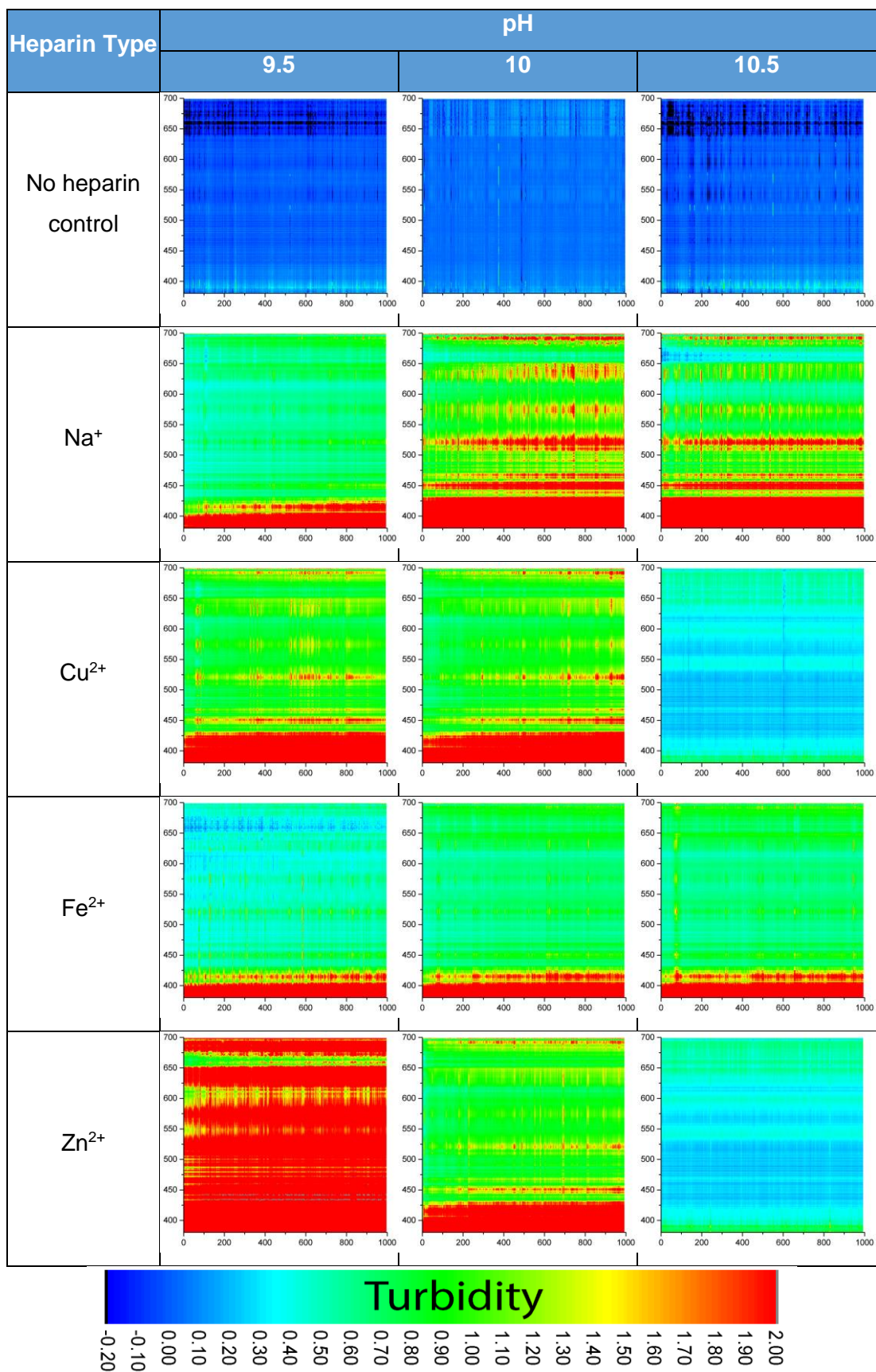


**Table 23.** Plots of the turbidity of lysozyme in the presence of different heparins at pH 9.5-10.5 monitored using the plasma spectrometer. The y axis is wavelength from 380–700 nm and the x axis is time from 0-1000 seconds.

The above spectra obtained using the plasma spectrometer show some interesting features. As expected, very little turbidity is observed when heparin is not present and lysozyme in the presence of sodium heparin appears to aggregate most rapidly around its natural pI of 10. Some spectra showed no aggregation at all at certain pHs, such as sodium heparin at pH 9 and zinc and copper heparin at pH 10.5. These may be anomalies and these experiments need to be repeated to determine whether these results are accurate.

Each of the lysozyme-heparin spectra showed scattering of wavelengths around 400 nm apart from with copper and zinc heparin at pHs 10.5. At this high pH, approximately half of the side chains of the lysines will be deprotonated ( $pK_a \sim 10.4$  (Pace et al., 2009)), changing the protein from its physiological charge and conformation and possibly preventing it aggregating by inhibiting the formation of the anti-parallel  $\beta$  sheet. The other amino acids process side chains that are still in their in their physiological charge states at pH 10.5. Alkaline conditions can also degrade disulphide bonds, of which human lysozyme has four, which are important components that stabilise protein structure and conformation (Andrews, 1928, Florence, 1980). It is also known that the action of alkaline solutions on proteins causes the formation of cross-linked amino acid side chains such as lysinoalanine and lanthionine and causes racemization of L-amino acids to D analogues, although these reactions generally require several hours and the application of heat (Bohak, 1964, Horn et al., 1941, Ziegler et al., 1967). The destabilising effect of alkaline conditions on protein structure may be responsible for the lack of aggregation with zinc and copper heparin, but it should be noted that these pHs do not occur *in vivo* and so these effects are of little biological relevance.

In addition it can be seen that the identity of the cation bound to the heparin influenced the formation of aggregates in the sample. A comparison of the cations showed that:

- Copper heparin showed strong aggregation in the pH range 8.5 to 10 with the strongest aggregation observed at pH 8.5. This indicated a strong interaction between copper heparin and lysozyme at these pHs. The

strong aggregation effect seen at these pHs may be related to the fact that copper has a very strong binding affinity to heparin, compared to the other cations.

- Sodium heparin showed the most aggregation at pH 10, close to the pI of lysozyme.
- Iron (II) heparin showed little turbidity above 400 nm at any of the pHs. This indicated that iron heparin is not as effective at aggregating lysozyme as sodium heparin. The iron heparin showed most aggregation at pH 6.5, although the aggregation is only slight at this pH, possibly indicating that the pI of the lysozyme-heparin complex has been shifted to pH 6.
- Zinc heparin showed a very similar pH dependence to sodium heparin with the most aggregation occurring around pH 9.5. The zinc heparin also showed some aggregation at lower pHs.

Although some aggregation occurs with all of the heparins at all pHs, but aggregation occurs most rapidly when the pH is close to the pI of lysozyme. This indicates that the pI of the heparin:lysozyme complex has not changed from that of lysozyme alone. Heparin binding does not alter the overall charge as heparin in its cationic form has no charge but may act to change the distribution of charge within and on the surface of the lysozyme molecule. It is anticipated that heparin binds in the active site of lysozyme. This catalytic site contains two acid side chains that are involved in hydrolysis: Glu35 and Asp52. It is possible that the heparin binds through the formation of a cationic bridge between the negatively charged Glu35 and Asp52 and heparin. Heparin binding in this way would prevent proton exchange, locking in the negative charge. This would alter the charge of the protein at varying pHs, but would not necessarily change the pI of the complex from that of the protein alone.

It is also possible that the heparin:lysozyme complex provides a nucleation site for further binding by lysozyme molecules and aggregate. The initial binding of heparin causes the lysozyme molecule to adopt a conformation (possibly antiparallel  $\beta$  sheet) that triggers fibril formation through the sequential binding of further lysozyme molecules. If heparin is not present,

fibril formation does not occur due to the lack of an initial lysozyme molecule in the required conformation to initiate aggregation.

Most of the lysozyme with heparin spectra showed high absorbance at short wavelengths just above 400 nm. This may be due to Raleigh scattering, as Raleigh scattering shows a very strong wavelength dependence of approximately  $\lambda^{-4}$ . As the turbidity of the sample increases, the spectra showed increased scattering at longer wavelengths with what looks like a very similar banding pattern occurring above 400 nm. This banding can be seen more clearly by plotting spectra from identical times that show aggregation. Figure 117 shows the turbidity spectra of lysozyme with copper heparin at pH 8.5 and sodium heparin at pH 10 at a time of 702 seconds.

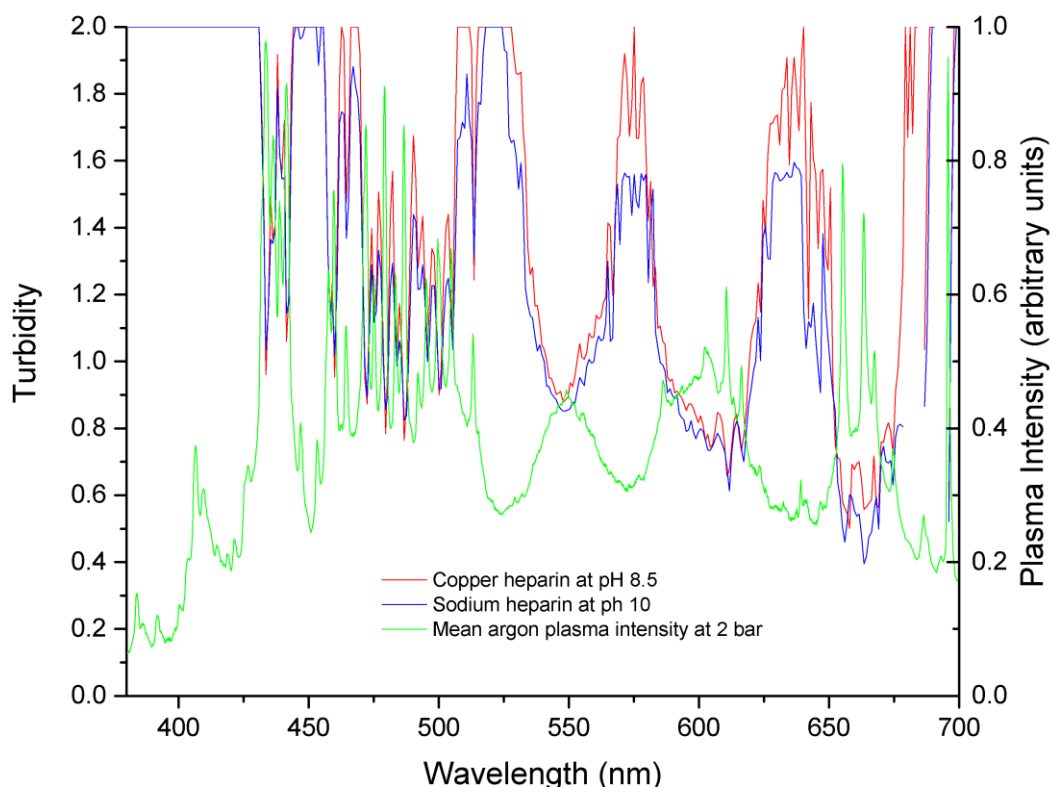


**Figure 117.** The turbidity spectra of lysozyme, aggregating in the presence of copper heparin at pH 8.5 and sodium heparin at pH 10, recorded at 702 seconds. For comparison against the argon plasma source intensity, the average intensity at 2 bar is also shown.

The copper and sodium spectra show turbidity bands occurring in the same wavelengths: at approximately 450, 525, 575 and 630 nm. An overlay of the

light source intensity, the average emission of argon at 2 bar taken from the previous gas testing results, shows that the emission troughs of the argon plasma align with the highest turbidity readings. The banding pattern is therefore very likely due to low light source intensity at these wavelengths. The lysozyme:heparin solution is turbid throughout the 380-700 nm range but as the aggregation proceeds, banding is observed at wavelengths where the emission intensity of plasma is low because the light intensity reaching the detector is falling to zero.

To confirm the origin of the banding patterns, identical experiments were run but using fibrinogen as the aggregating protein. Fibrinogen is relatively inexpensive, large 340 kDa heparin binding glycoprotein consisting of two identical disulphide linked  $\alpha$ ,  $\beta$  and  $\gamma$  chains (Marx, 1988, Mohri and Ohkubo, 1993, Mosesson, 2005). The binding of fibrinogen to GAGs are of interest for several reasons. A mutation in the  $\alpha$  chain of fibrinogen is known to cause the autosomal dominant disease fibrinogen amyloidosis (AFib). In AFib, variant fibrinogen, produced mainly in the liver, is deposited predominantly in the kidneys (Benson et al., 1993, Tennent et al., 2007). AFib is associated with atherosclerotic cardiovascular disease (Gillmore et al., 2009) and it has been suggested that this is caused by the deposition of fibrinogen in vascular walls (Gillmore et al., 2009). Fibrinogen is converted by thrombin into insoluble fibrin during blood clotting. Heparin prevents this conversion by binding to and activating antithrombin (ATIII), which inhibits thrombin. The binding of heparin to fibrinogen has been studied due to its effect upon the coagulation cascade. The binding of heparin to fibrinogen reduces the concentration of heparin available for binding to ATIII. In addition, because both thrombin and fibrinogen both bind heparin, a ternary complex is formed that restricts the inhibition of thrombin by ATIII (Hogg and Jackson, 1989) and results in thrombin retaining its catalytic activity (Becker et al., 1997). It has been demonstrated that metal ions, in particular zinc, augments this heparin-thrombin-fibrin complex and increases the protection of thrombin from inhibition by ATIII. Zinc increased the affinity of heparin for fibrin fourfold (Chan et al., 2012). Fibrinogen has been reported to have zinc dependent heparin binding site localised to its  $\alpha$ C domain (Fredenburgh et al., 2013) and

additional heparin binding sites have been found in the  $\beta$  and  $\gamma$  chains (Mohri et al.) . In addition, some metal ions including  $\text{Ca}^{2+}$ ,  $\text{Fe}^{2+}$ ,  $\text{Cu}^{2+}$ ,  $\text{Ni}^{2+}$ ,  $\text{Hg}^{2+}$ ,  $\text{Zn}^{2+}$ ,  $\text{Cr}^{3+}$  and  $\text{La}^{3+}$  are known to cause immediate aggregation of fibrinogen (Steven et al., 1982). This may be through the binding of the metal ions to carboxyl groups in the fibrinogen, possibly in the heparin binding domains. These carboxyl groups are responsible for repulsion of fibrinogen monomers at neutral pH, as the isoelectric point of fibrinogen is 5.1-6.2 so these groups would be negatively charged.

The concentration of fibrinogen that was used in the experiments was the same as the lysozyme experiments at 2mg/ml. This is approximately the same concentration as is found in blood (2-4 mg/ml (Tennent et al., 2007)). These experiments were identical to the lysozyme experiments. The results of the fibrinogen experiments are shown in Tables 24-28. The plots are sorted by pH value.

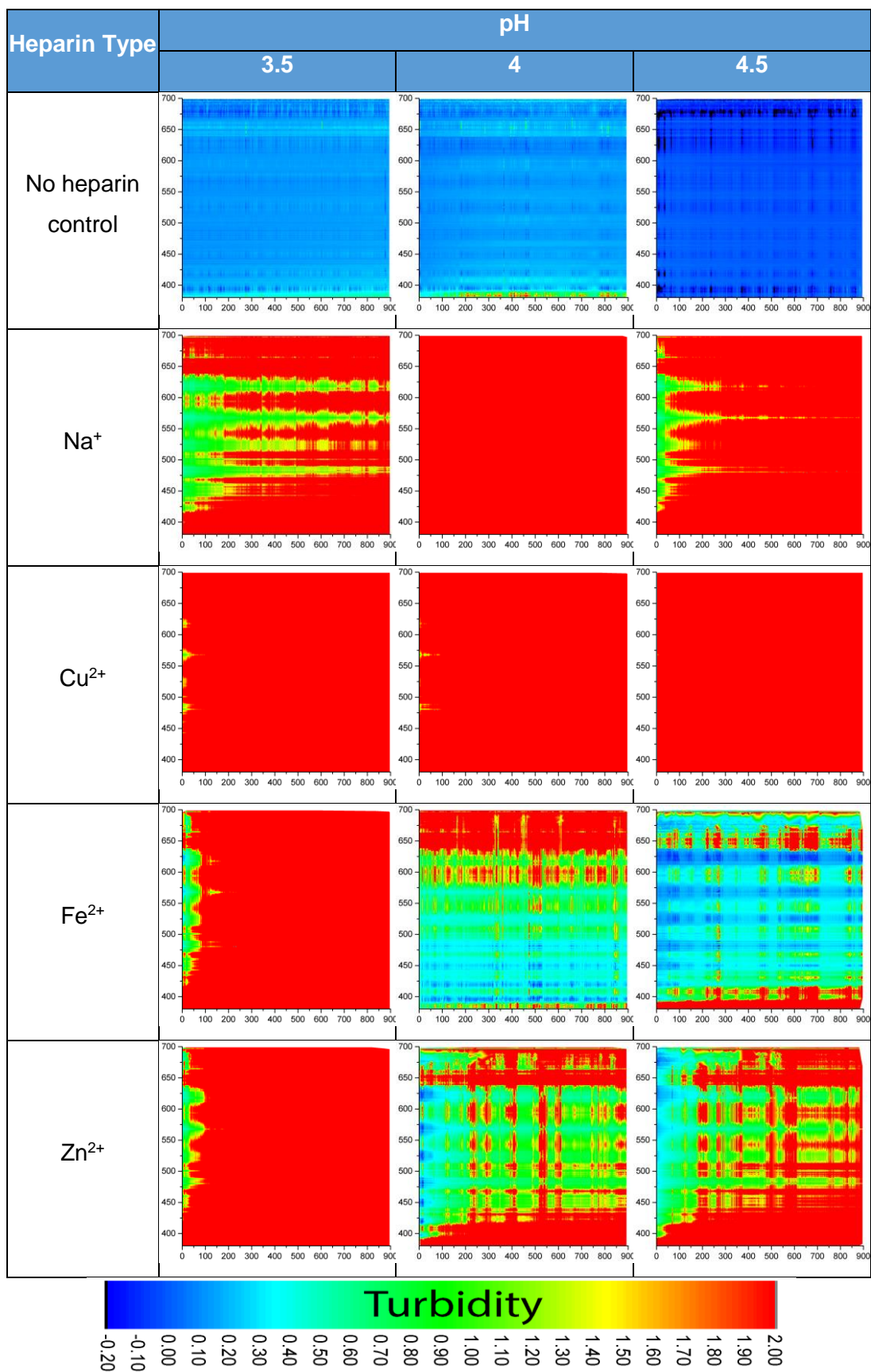


**Table 24.** Plots of the turbidity of fibrinogen in the presence of different heparins at pH 3.5-4.5 monitored using the plasma spectrometer. The y axis is wavelength from 380–700 nm and the x axis is time from 0-1000 seconds.

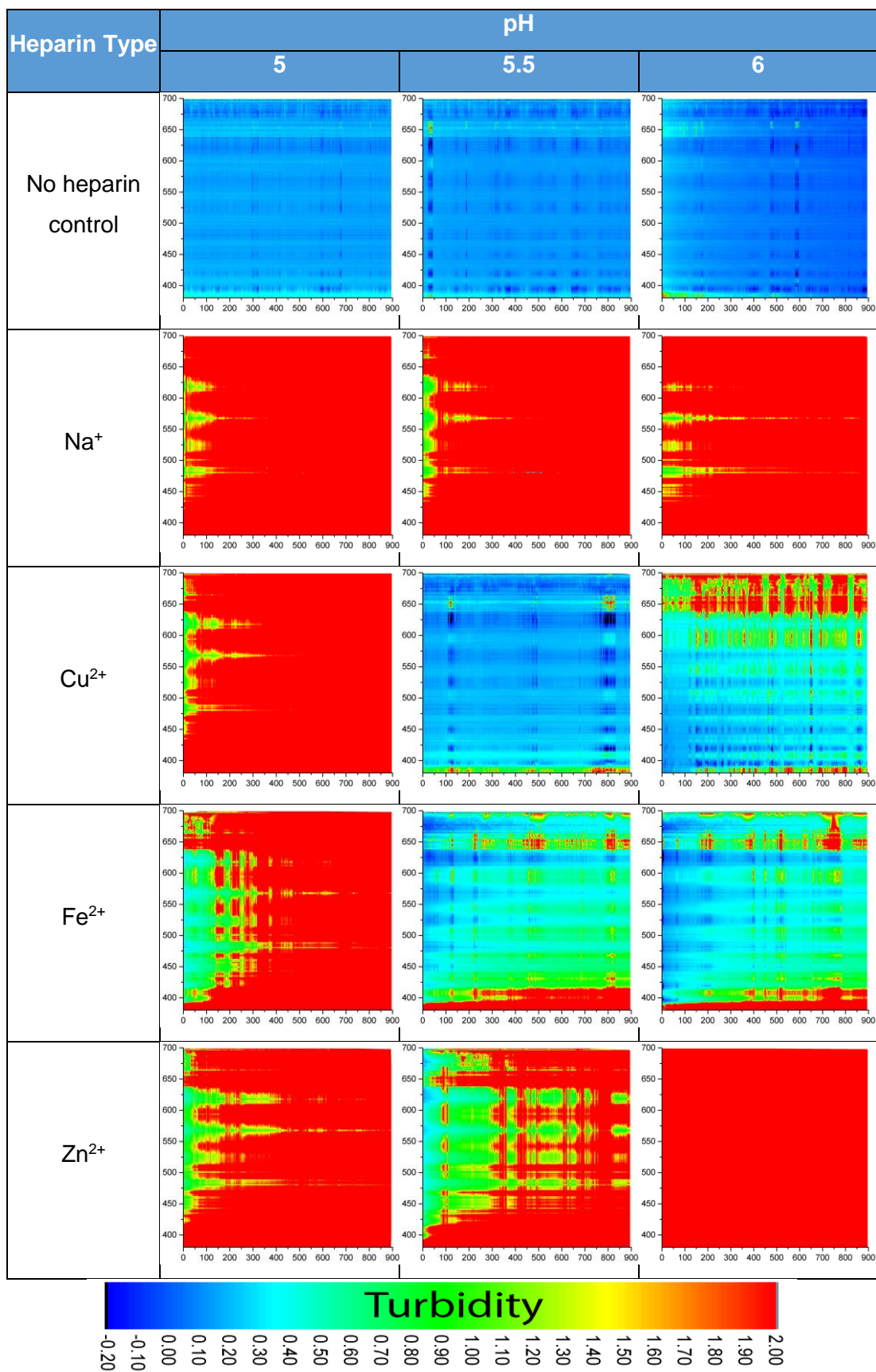


**Table 25.** Plots of the turbidity of fibrinogen in the presence of different heparins at pH 5-6 monitored using the plasma spectrometer. The y axis is wavelength from 380–700 nm and the x axis is time from 0-1000 seconds.



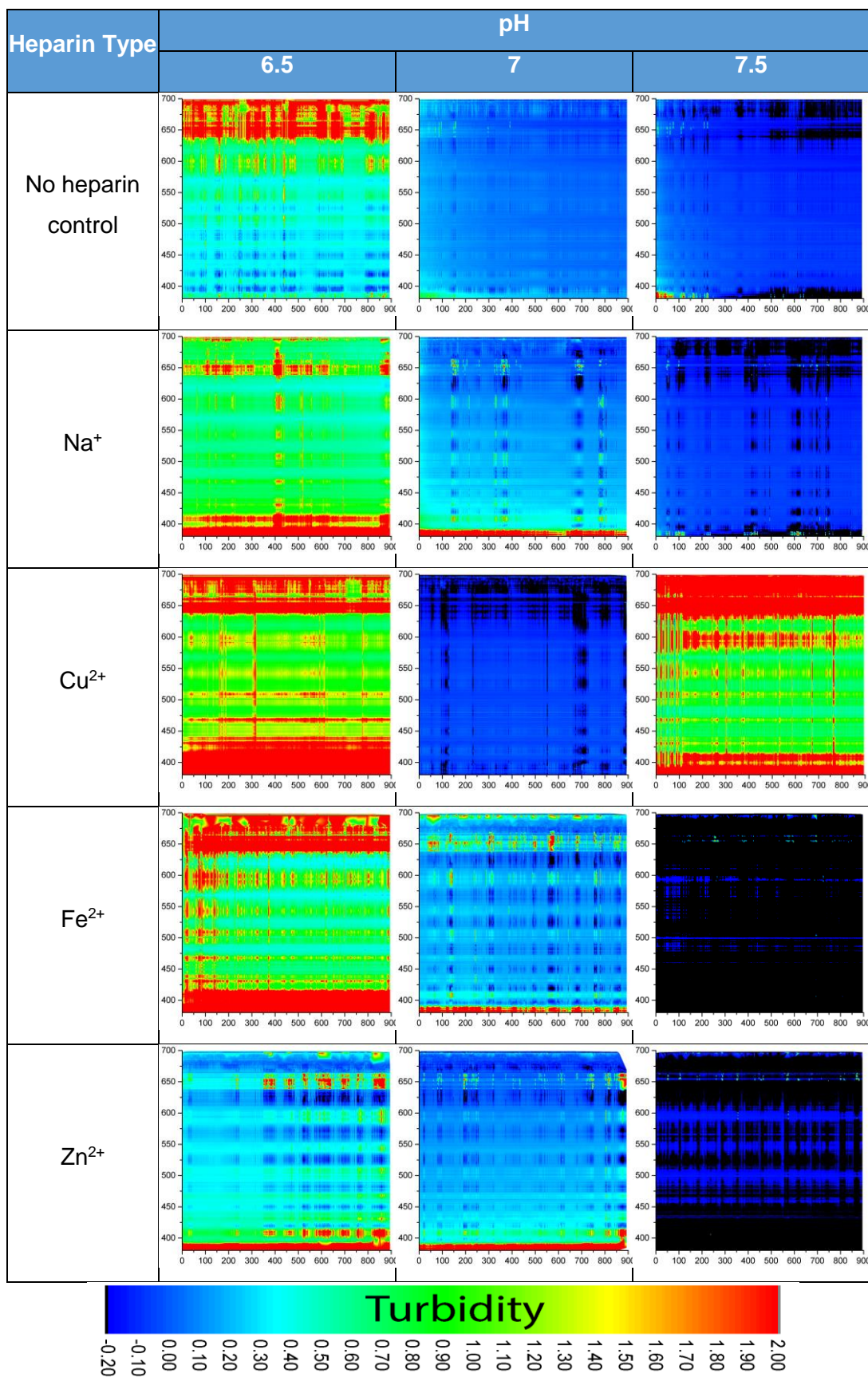


**Table 26.** Plots of the turbidity of fibrinogen in the presence of different heparins at pH 6.5-7.5 monitored using the plasma spectrometer. The y axis is wavelength from 380–700 nm and the x axis is time from 0-1000 seconds.

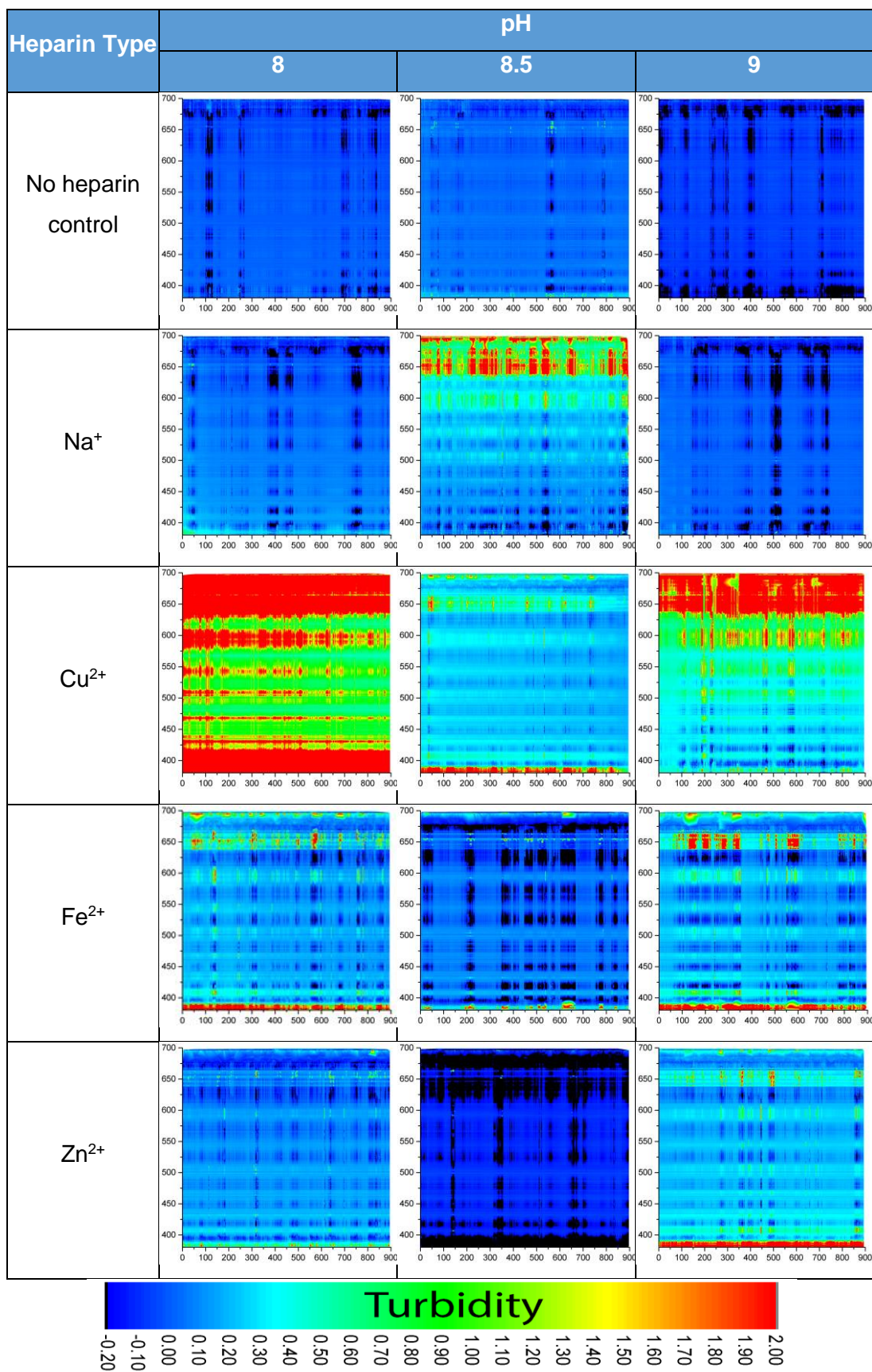


**Table 27.** Plots of the turbidity of fibrinogen in the presence of different heparins at pH 8-9 monitored using the plasma spectrometer. The y axis is wavelength from 380–700 nm and the x axis is time from 0-1000 seconds.

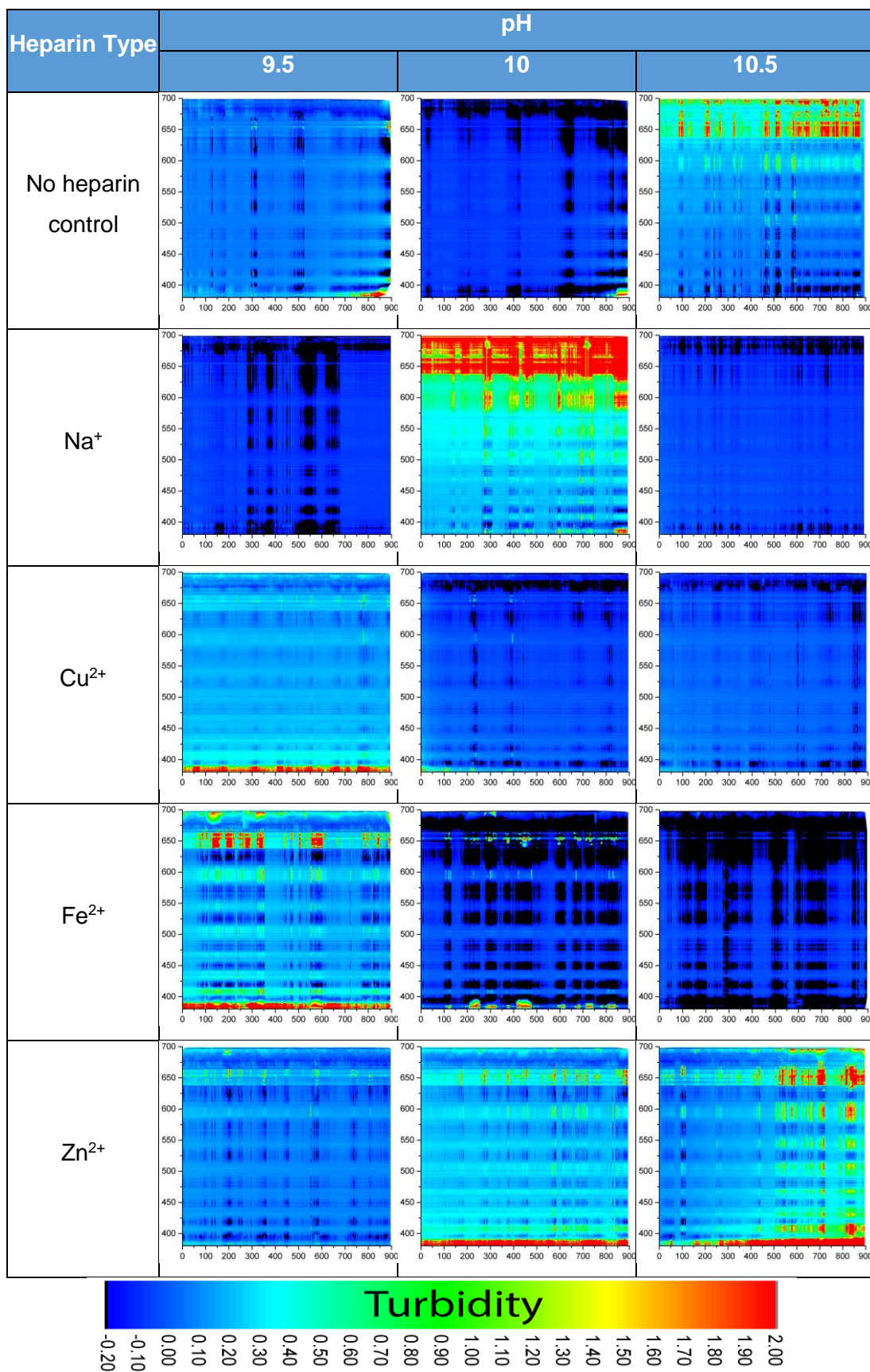


**Table 28.** Plots of the turbidity of fibrinogen in the presence of different heparins at pH 9.5-10.5 monitored using the plasma spectrometer. The y axis is wavelength from 380–700 nm and the x axis is time from 0-1000 seconds.

A comparison of the fibrinogen with the lysozyme experiments shows some obvious differences. Most notable is the shift in the aggregation pH of fibrinogen to the low pH range. This is due to the low isoelectric point of fibrinogen (5.1-6.2). The no heparin control at pH 6.5 shows some aggregation, demonstrating that the isoelectric of fibrinogen is in this range. All of the heparins showed aggregation in the range pH 3.5-5 with sodium and zinc heparin aggregating throughout the pH range 3.5-6. At pH 3.5 it is expected for the Asp and Glu side groups of fibrinogen to be uncharged ( $pK_a \sim 3.9$  and  $4.3$  respectively) but this does not seem to reduce the aggregation or disrupt heparin binding.

It is also clear that aggregated fibrinogen is more turbid than aggregated lysozyme, with some of the fibrinogen spectra, in particular copper in the pH range 3.5-4.5, too turbid for the spectrometer to measure. High turbidities over 640 nm appear in many of the spectra that show aggregation. This may be due to the more rapid aggregation of fibrinogen compared to lysozyme, with large fibrils forming quickly and scattering light. Some investigators record that the aggregation of fibrinogen reaches a steady state in 5 minutes (Steven et al., 1982). Also of note is the fact that fibrinogen shows little turbidity at pHs greater than 6.5. At these pHs, fibrinogen will have an overall negative charge, promoting solubility through electrostatic repulsion. This is contrast to lysozyme that has a turbidity of approximately one for all heparin experiments less than pH 8.5.

Copper aggregates weakly at pHs 7.5, 8 and 9 and is the only cation to show significant aggregation above the isoelectric point of fibrinogen. Copper heparin at pH 7.5 and 8 also appears to be reducing in turbidity over time. This may be due large aggregates precipitating out of solution. Further experiments may confirm the cause of this reduction in turbidity.

Each of the fibrinogen spectra show a similar banding pattern to the lysozyme results. To confirm the previous conclusion that this is due to the low intensity of the argon plasma light source, the banding can be seen more clearly by plotting spectra from identical times that show aggregation. Figure 118 shows

the turbidity spectra of fibrinogen with copper heparin at pH 8.5 and sodium heparin at pH 10, at a time of 202 seconds.

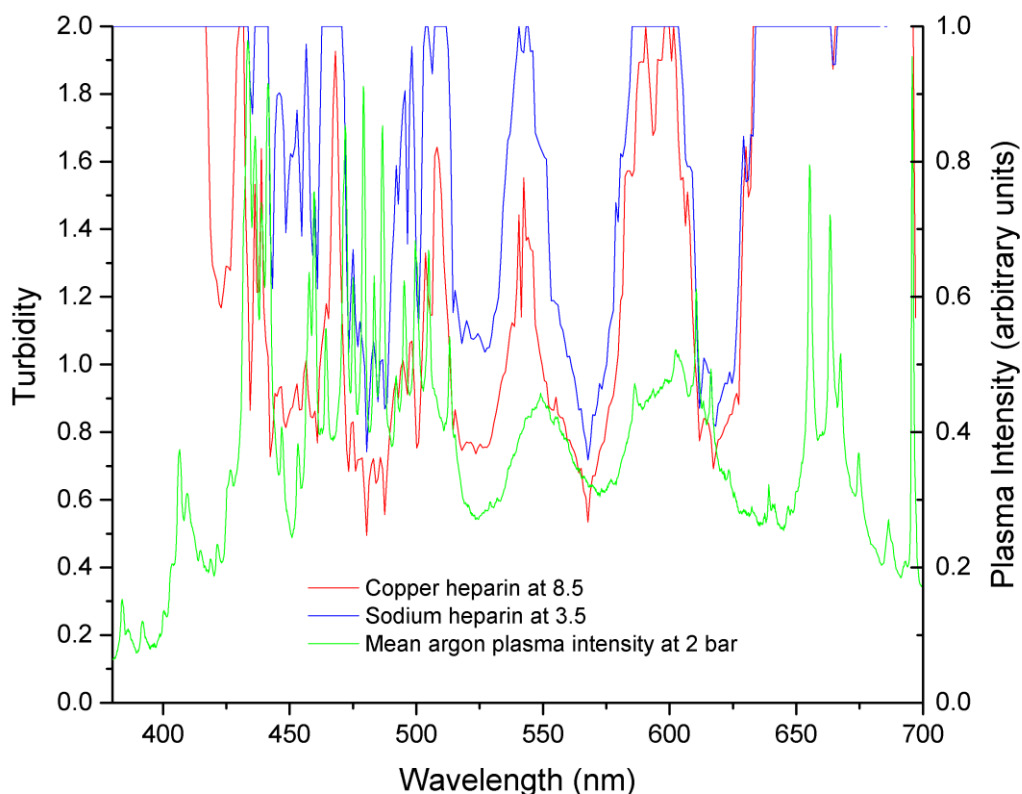


**Figure 118.** The turbidity spectra of fibrinogen, aggregating in the presence of copper heparin at pH 8.5 and sodium heparin at pH 3.5, recorded at 202 seconds. For comparison against the argon plasma source intensity, the average intensity at 2 bar is also shown.

Figure 118 shows that the turbidity bands in copper and sodium spectra occur at the same wavelengths. An overlay of the light source intensity as before, the average emission of argon at 2 bar taken from the previous gas testing results, shows that the emission troughs of the argon plasma do not align with the highest turbidity readings. In fact, the banding is approximately aligned with wavelengths of high source intensities. This can be seen from the intensity peaks at 550 and 600 nm roughly aligning with turbidity peaks at the same wavelengths. This is an unexpected result that does not confirm the previous conclusion that the banding pattern is due to the low light source intensity at these wavelengths and adds credence to the possibility that the observed turbidity of the heparin:fibrinogen solution is wavelength dependant. The cause of the turbidity banding is undetermined but the location of the bands appears to depend upon the protein that is used in the experiment. This

banding cannot be caused by wave interference of the scattered light as the light source is incoherent. Further testing with different aggregating proteins, such as  $\beta$ -lactoglobulin, may confirm that the banding depends upon the protein used and does not originate from an instrumental source .

#### 4.3. Commercial UV/Vis Scanning Spectrophotometer Comparison

For comparison of the plasma spectrometer against a commercially available spectrometer, absorbance assays were carried out using a Tecan Infinite® M200 PRO series plate reader. The assay was carried out in 96 well plate. The following samples were tested at a range of pHs from 3.5 to 11.5, in increments of 0.5:

Lysozyme/fibrinogen only control

Lysozyme/fibrinogen with commercial sodium heparin

Lysozyme/fibrinogen with Fe (II) Heparin

Lysozyme/fibrinogen with Cu(II) Heparin

Lysozyme/fibrinogen with Zn(II) Heparin

To each well of the 96 well plate was added:

1. 4  $\mu$ L of heparin (5 mg/mL) or HPLC water.
2. 156  $\mu$ L of the previously prepared PBS buffer at the required pH.
3. Just before the plate was inserted into the plate reader, 40  $\mu$ L of lysozyme/fibrinogen at 5 mg/ml.

Again, the protein is added last in order to ensure good mixing with heparin and so that aggregation does not start until the plate is ready to be read. Each of the samples were run in triplicate. The plates were scanned in the wavelength interval 400–700 nm in intervals of 10nm. The absorbance of each well was read once every 10 minutes for 1 hour 10 minutes. This is as fast as the plate reader can measure the turbidity at this wavelength resolution. The results of each well were averaged. The contour plots of the results are shown

in Tables 29-37. Tables 29-33 are the lysozyme plots and Tables 34-38 are the fibrinogen plots.

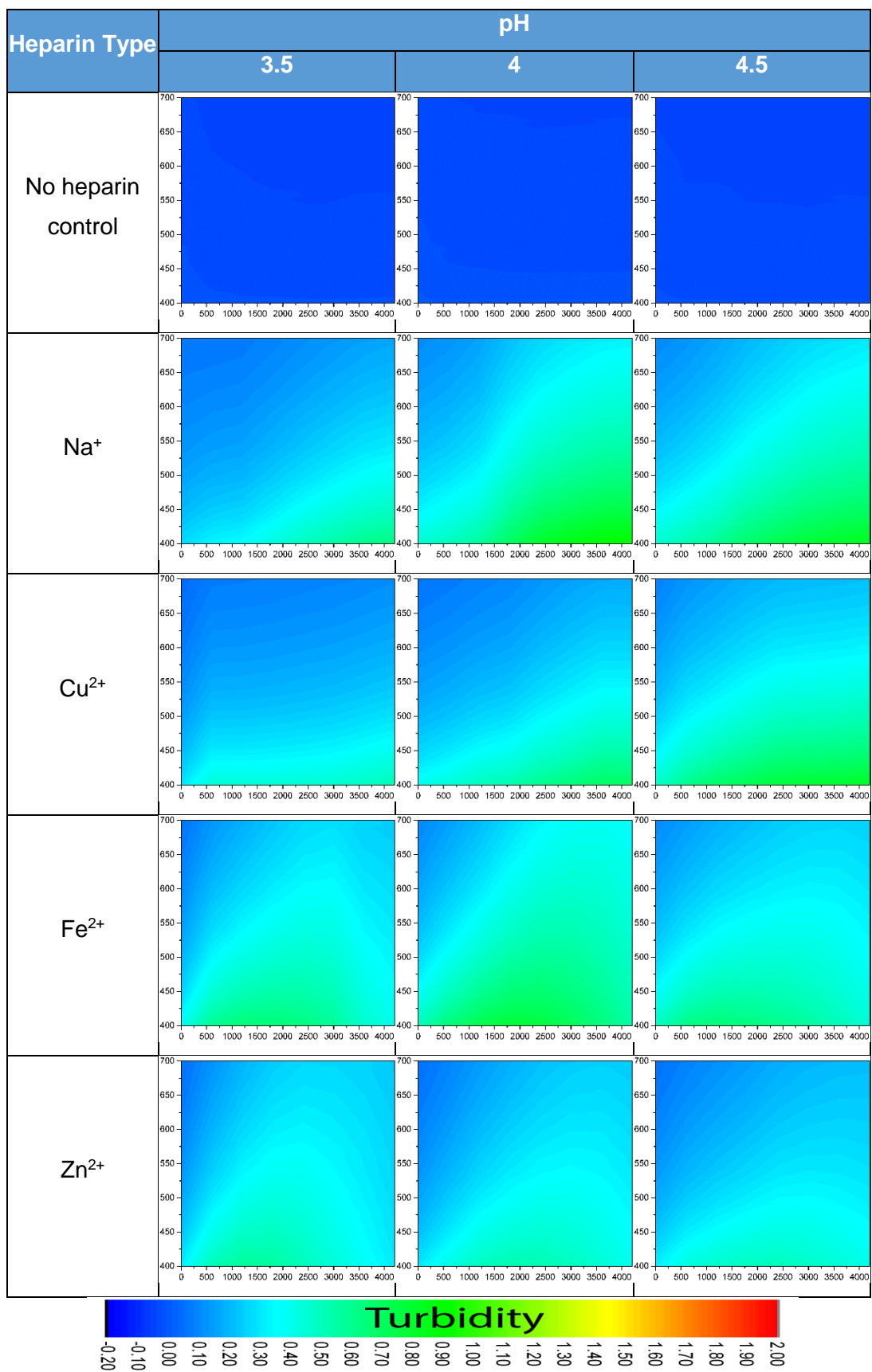


**Table 29.** Plots of the turbidity of lysozyme in the presence of different heparins at pH 3.5-4.5 monitored using the Tecan Infinite plate reader. The y axis is wavelength from 400–700 nm and the x axis is time from 0-4200 seconds.



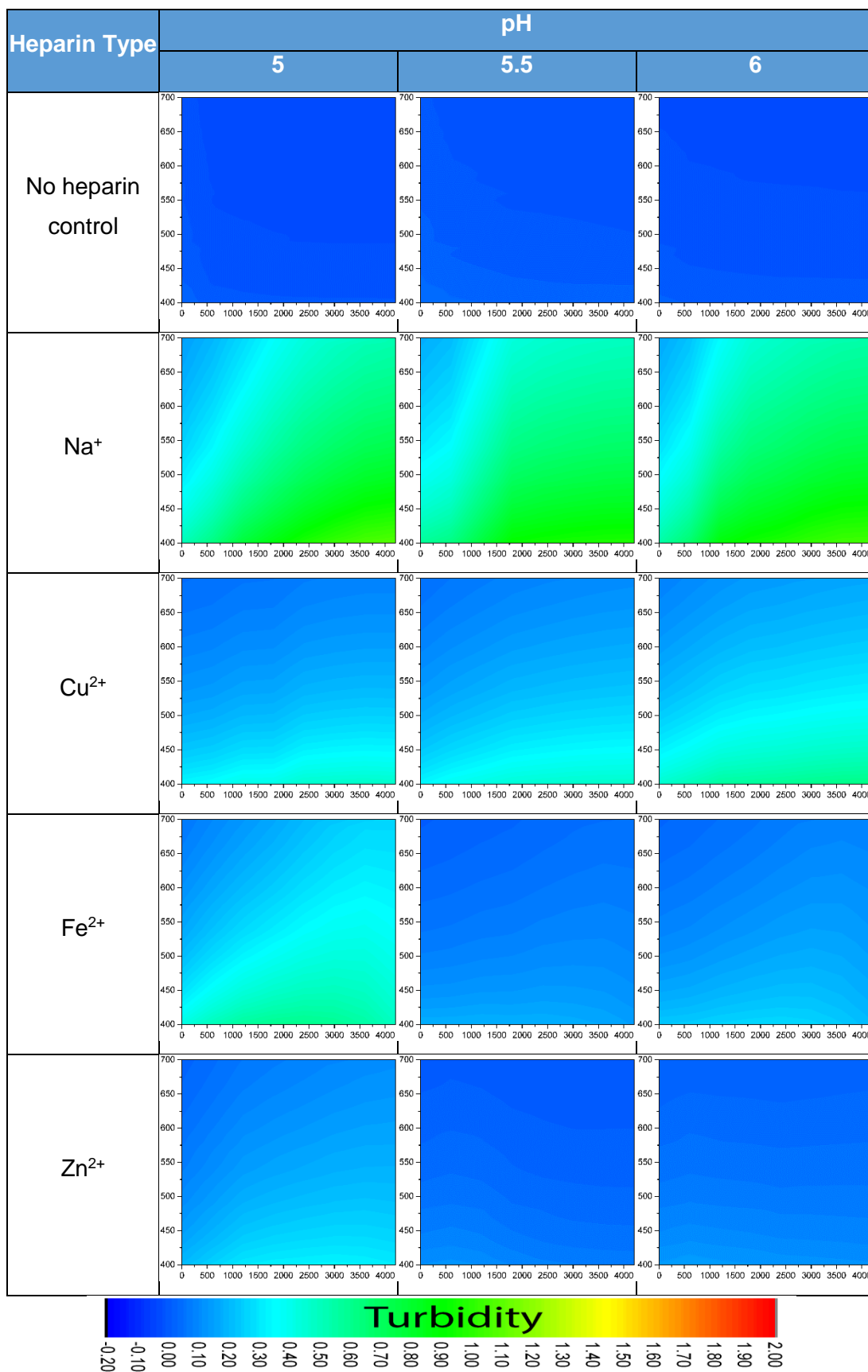


**Table 30.** Plots of the turbidity of lysozyme in the presence of different heparins at pH 5-6 monitored using the Tecan Infinite plate reader. The y axis is wavelength from 400–700 nm and the x axis is time from 0-4200 seconds.

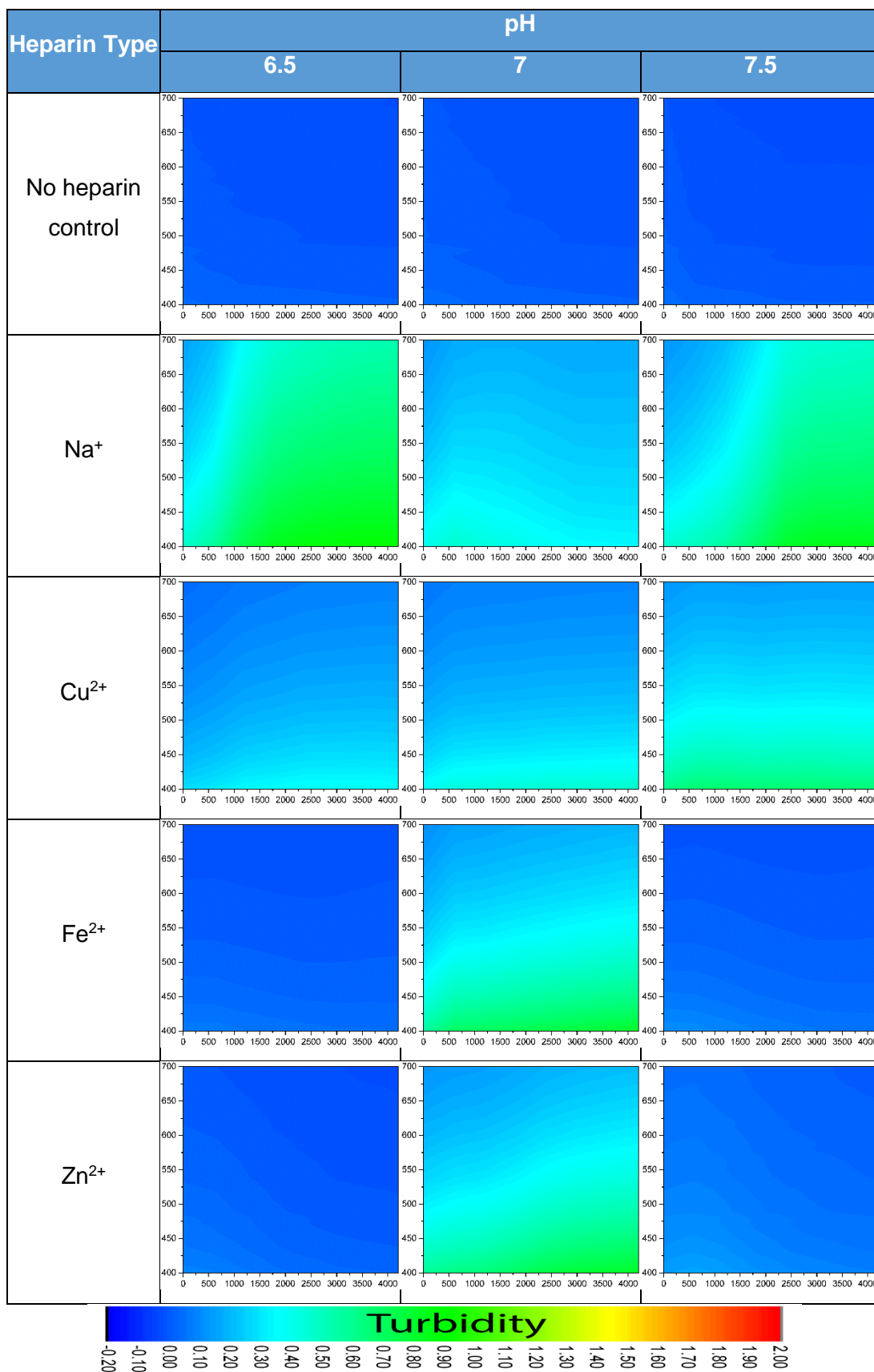


**Table 31.** Plots of the turbidity of lysozyme in the presence of different heparins at pH 6.5-7.5 monitored using the Tecan Infinite plate reader. The y axis is wavelength from 400–700 nm and the x axis is time from 0-4200 seconds.

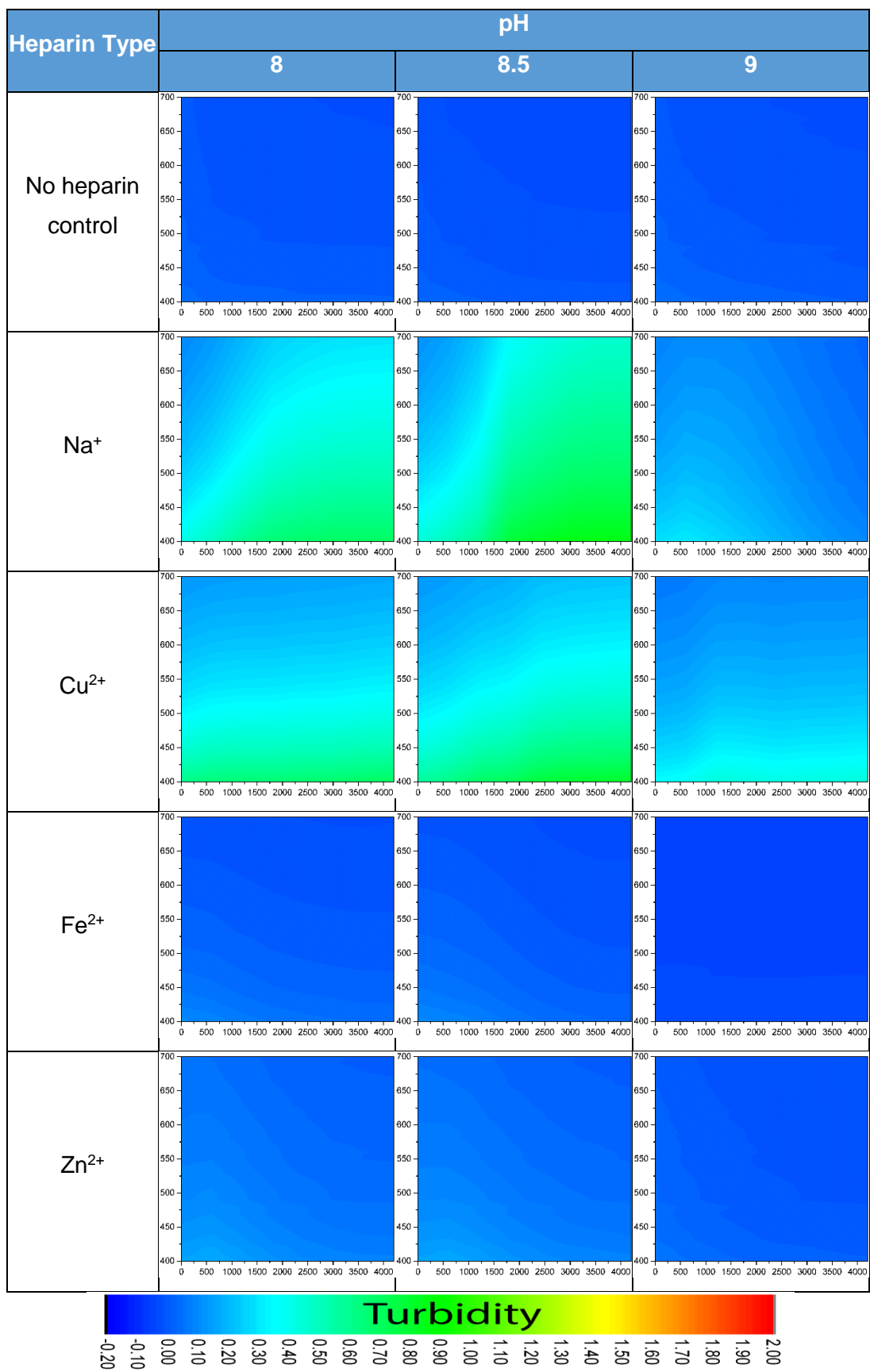


**Table 32.** Plots of the turbidity of lysozyme in the presence of different heparins at pH 8-9 monitored using the Tecan Infinite plate reader. The y axis is wavelength from 400–700 nm and the x axis is time from 0-4200 seconds.

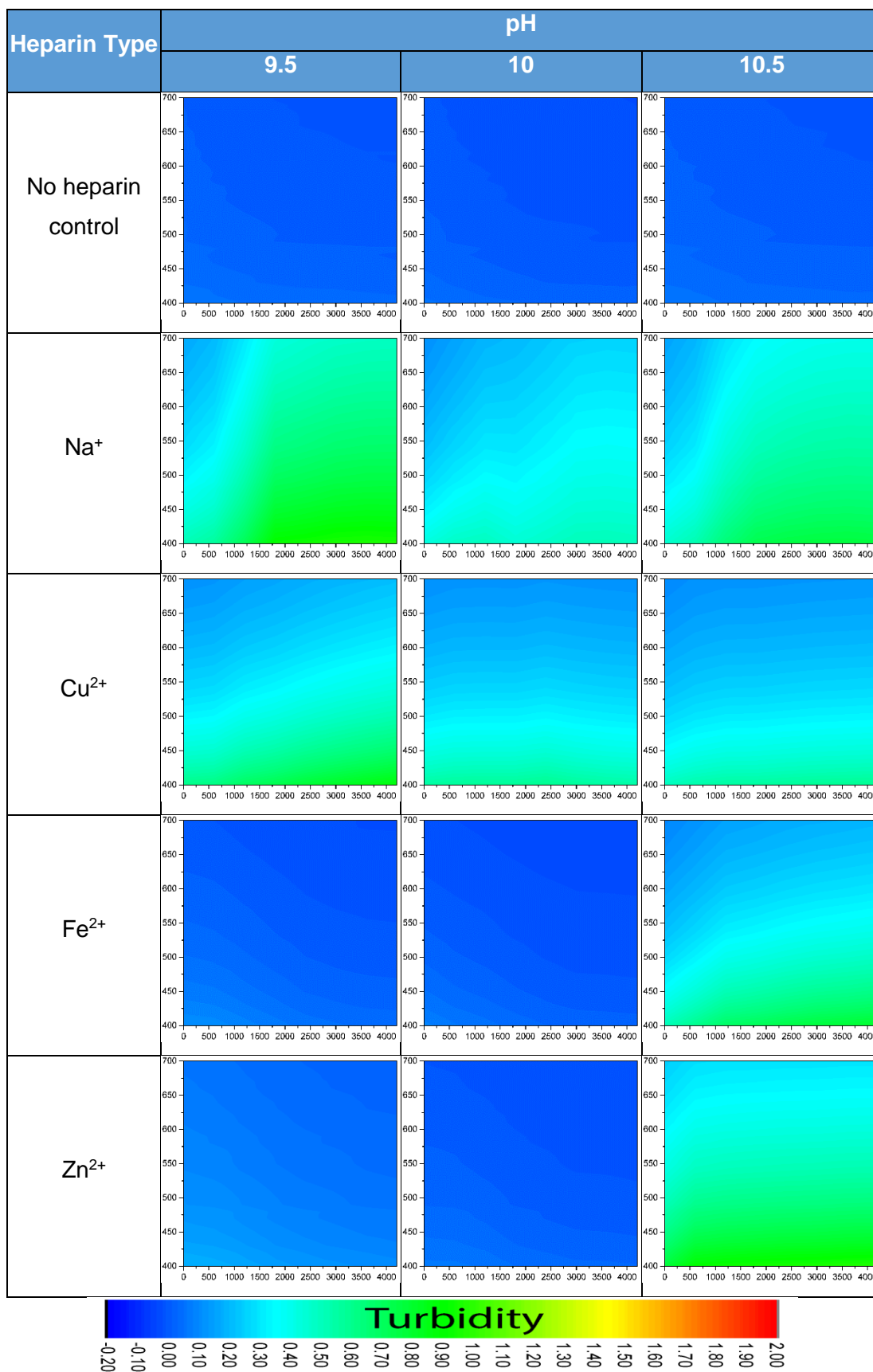


**Table 33.** Plots of the turbidity of lysozyme in the presence of different heparins at pH 5-6 monitored using the Tecan Infinite plate reader. The y axis is wavelength from 400–700 nm and the x axis is time from 0-4200 seconds.

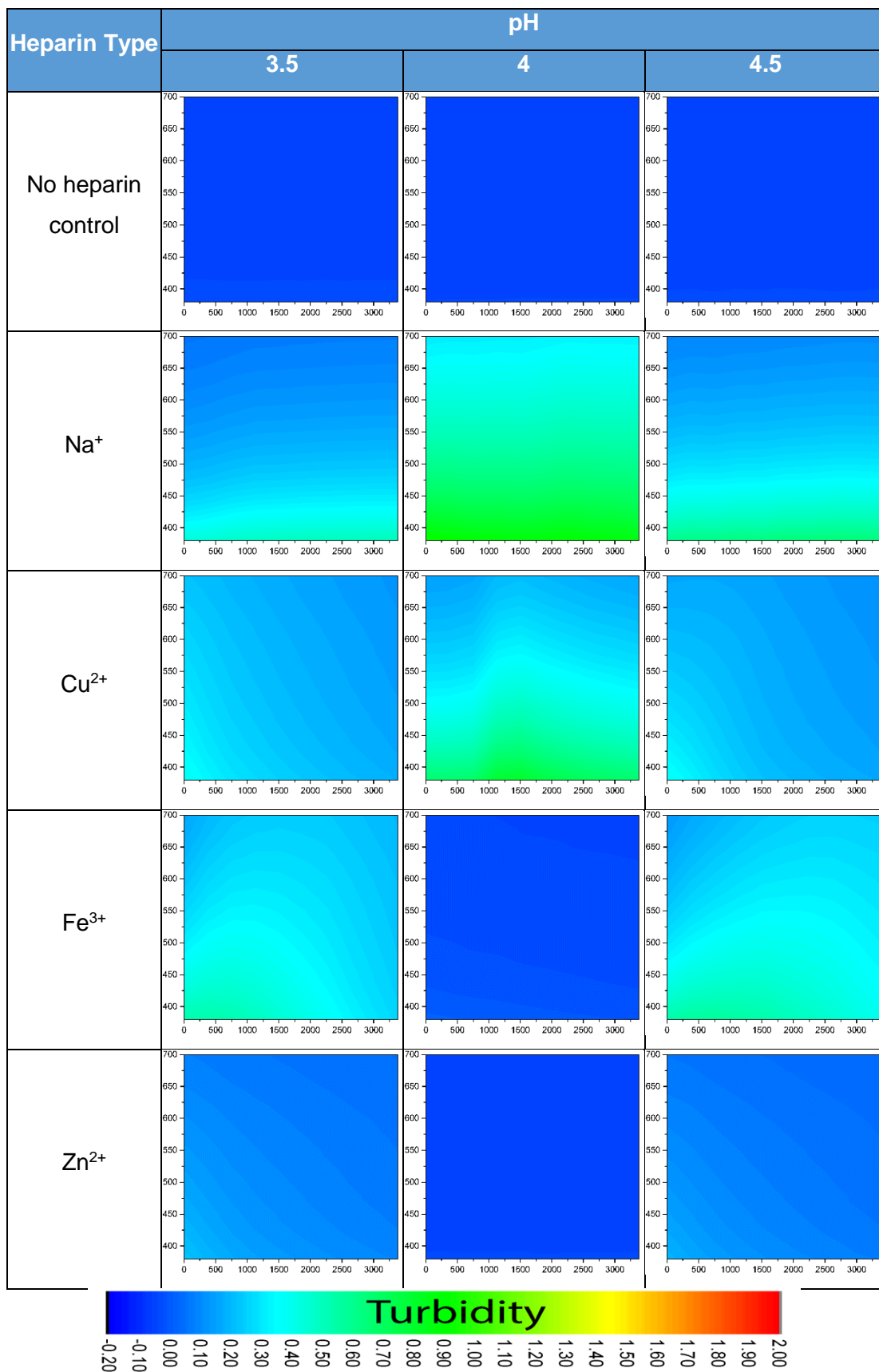


**Table 34.** Plots of the turbidity of fibrinogen in the presence of different heparins at pH 3.5-4.5 monitored using the Tecan Infinite plate reader. The y axis is wavelength from 400–700 nm and the x axis is time from 0-4200 seconds.

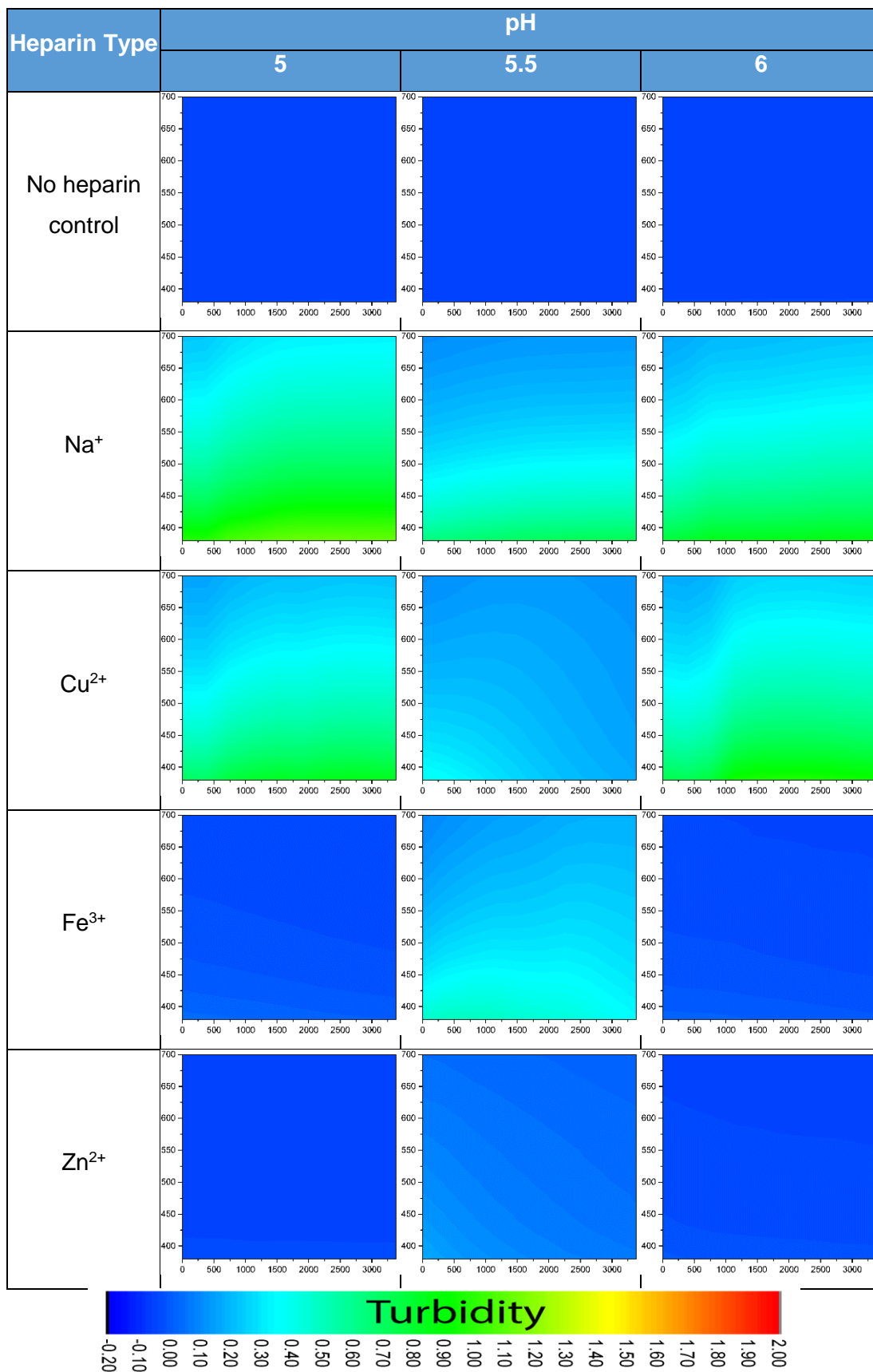


**Table 35.** Plots of the turbidity of fibrinogen in the presence of different heparins at pH 5-6 monitored using the Tecan Infinite plate reader. The y axis is wavelength from 400–700 nm and the x axis is time from 0-4200 seconds.

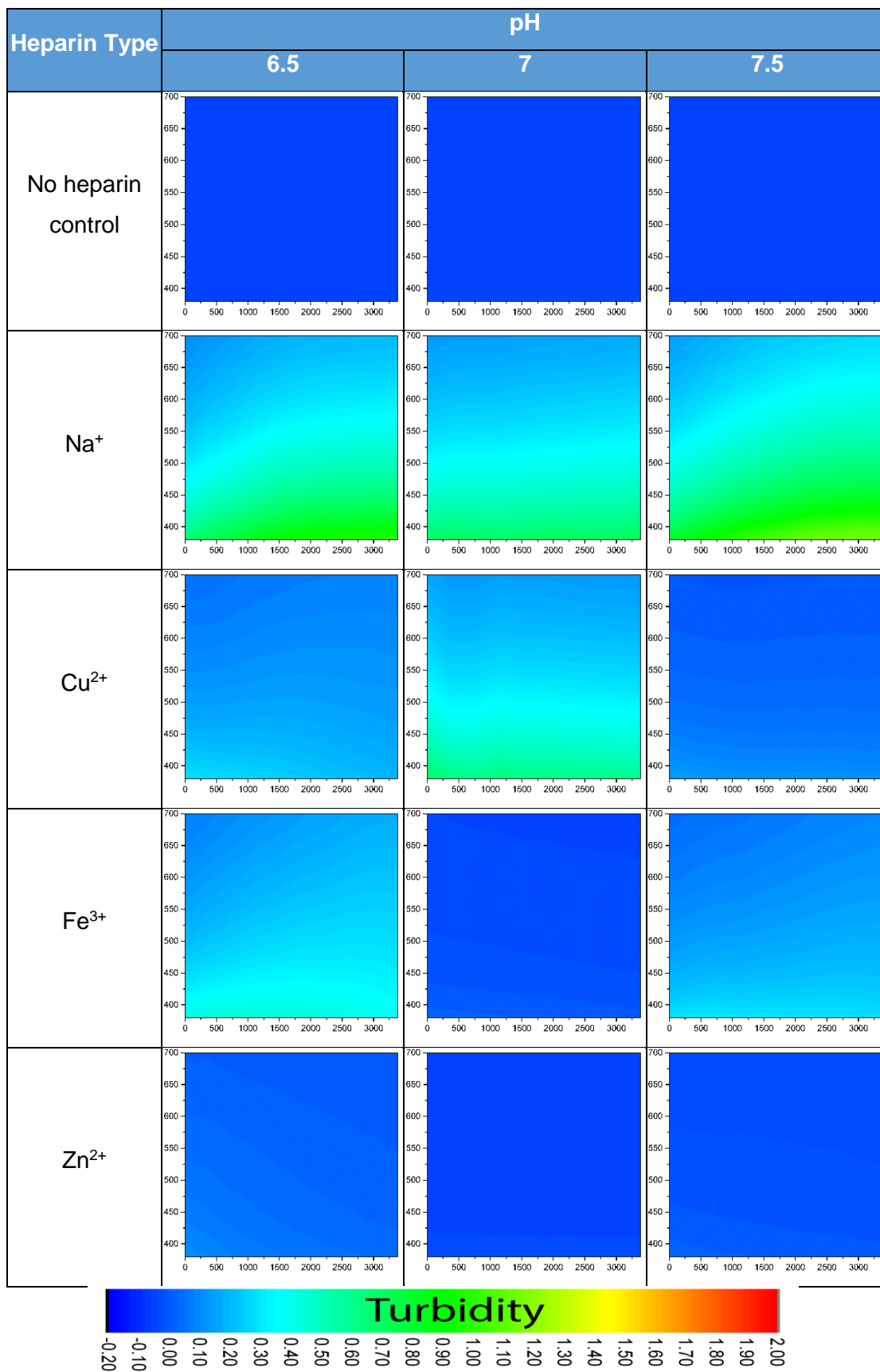


**Table 36.** Plots of the turbidity of fibrinogen in the presence of different heparins at pH 6.5-7.5 monitored using the Tecan Infinite plate reader. The y axis is wavelength from 400–700 nm and the x axis is time from 0-4200 seconds.

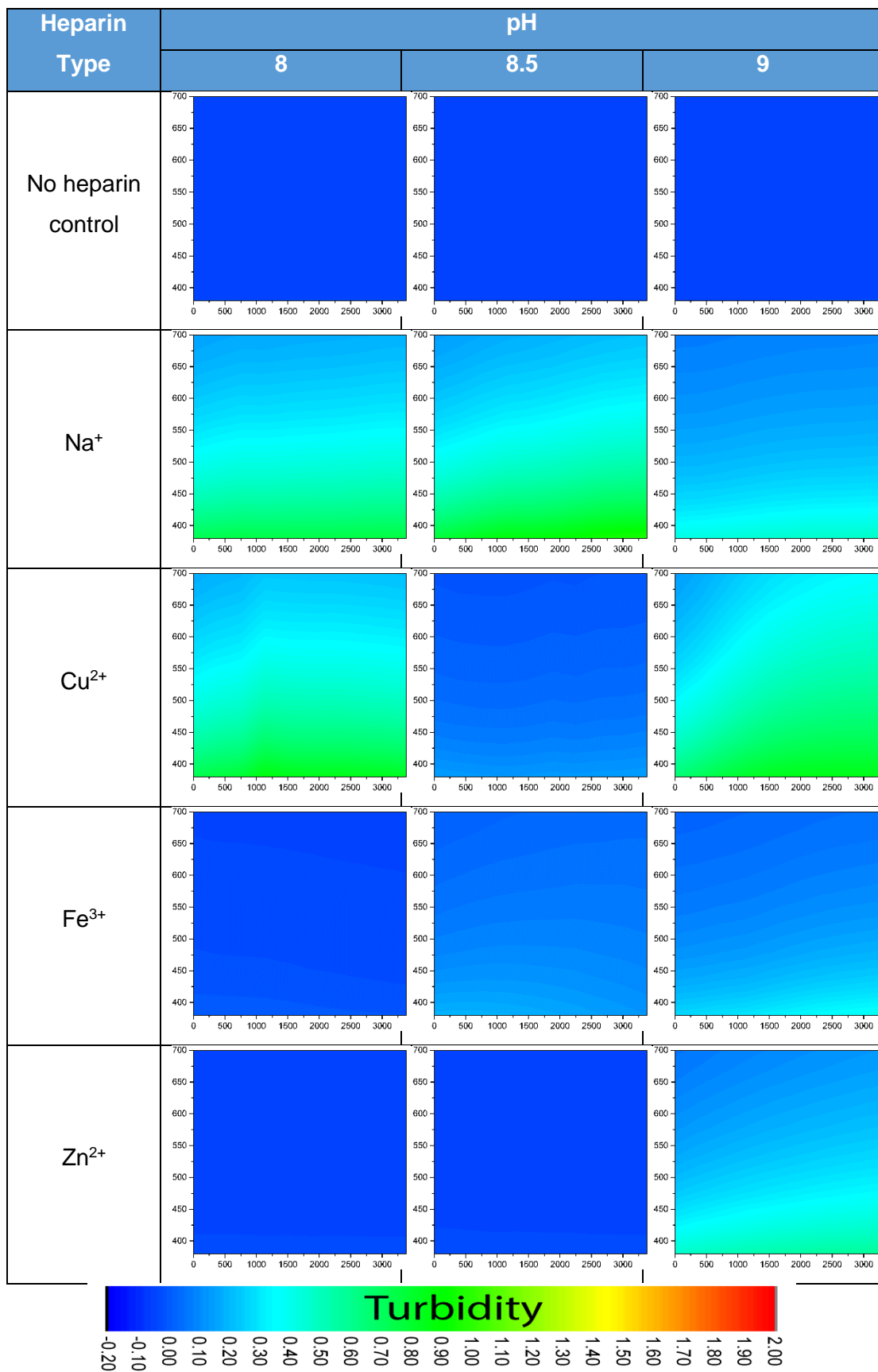


**Table 37.** Plots of the turbidity of fibrinogen in the presence of different heparins at pH 8-9 monitored using the Tecan Infinite plate reader. The y axis is wavelength from 400–700 nm and the x axis is time from 0-4200 seconds.



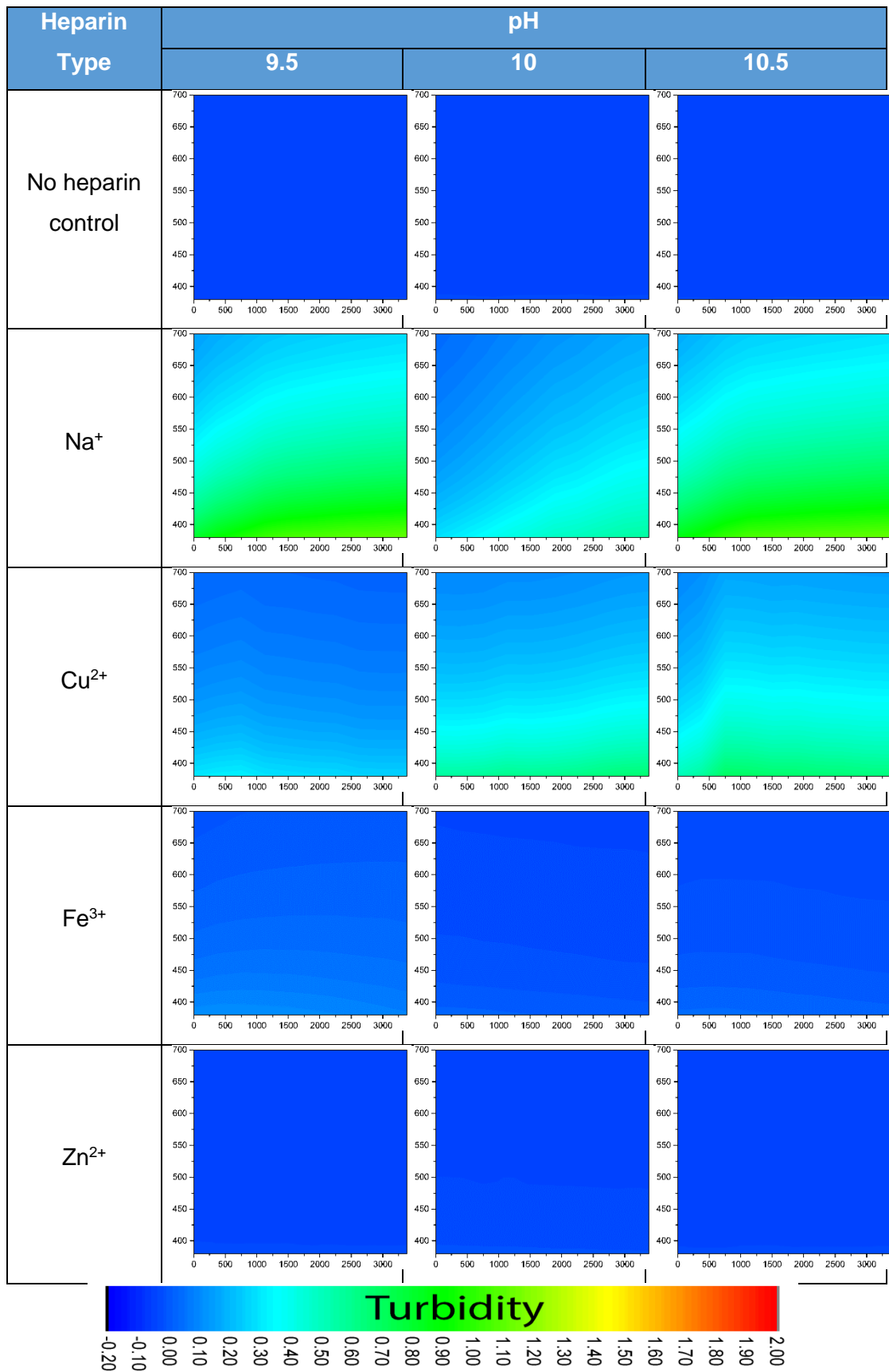


**Table 38.** Plots of the turbidity of fibrinogen in the presence of different heparins at pH 9.5-10.5 monitored using the Tecan Infinite plate reader. The y axis is wavelength from 400–700 nm and the x axis is time from 0-4200 seconds.

The overall turbidities of the plate reader assays are lower due to the shorter path length through the samples. The plate reader is much higher throughput, able to read 96 samples in one run but a comparison of the data obtained from the two spectrometers shows that the plasma spectrometer has some advantages over a conventional spectrometer. Important points to note are:

- The results from both of the spectrometers are approximately the same. Both results show a strong wavelength dependence of absorbance, with the absorbance being strongest at short wavelengths. The results show the kind of wavelength dependence expected from Rayleigh scattering ( $\sim\lambda^{-4}$ ).
- The plasma spectrometer is much higher resolution than the plate reader. The plate reader is only able to scan in increments of 10 nm wavelengths and only once every ten minutes. This was the highest scan rate and wavelength interval that the plate reader was able to run at. An increase in the scan rate requires a reduction in the wavelength interval and *vice versa*. In contrast, the plasma spectrometer is able to scan up to once every 4 seconds (if the experiment was run for one hour) at a wavelength resolution of 0.2 nm. The resolution of the plasma spectrometer is so high that graphing software has difficulty manipulating such large datasets and consequently data reduction methods and averaging must be employed. Data reduction methods are not necessary to manipulate and graph the plate reader data. Owing to the low resolution of the plate reader, no turbidity banding is observed in the experiments.
- The plasma spectrometer is only able to scan one sample at a time whereas the plate reader is able to scan 96 wells during one run. The plate reader is therefore much more effective for high throughput measurement of samples.

### Analysis of Lysozyme/Fibrinogen Turbidity Data

The standard analysis of turbidity data employs the equations of Rayleigh scattering or Mie scattering to determine radii of gyration, molecular weights

and molecular shapes using procedures such as Zimm and Guinier plots. These methods cannot be used in this situation for several reasons:

- The light source is not monochromatic and coherent. Normally scattering spectroscopy uses a laser as the exciting light source. This enables wave mechanics to be employed to determine molecular parameters from the interference patterns generated by the scattering. Because plasma emission is broadband and incoherent, the scattered waves cannot be summed in a simple vectorial manner.
- The unknown size of the aggregates. For particles whose dimensions are small compared with the wavelength of the scattered light, the equations of Raleigh scattering can be used. For particles whose dimensions are larger than the wavelength of light, Mie scattering must be used. The unknown size of the aggregates makes the choice of analytical equations problematic, especially when some particles may be smaller and others larger than the wavelength of light.
- The polydispersity of the aggregating molecular complexes. The molecular masses of the particles in the solution are likely to be of a broad size distribution. In scattering techniques the polydispersity is quantified by a polydispersity index. Samples with a high polydispersity index are unsuitable for analysis using the equations of scattering.
- Scattering analysis requires that the particles in the solution are not interacting with each other. This is obviously not the case in aggregating solutions.
- The molecular shape of the particles in the solution are unknown. Determination of the radius of gyration and molecular mass require some knowledge of the shape of the particles in the solution. The function  $P(\theta)$  is the ratio of the scattered light from a finite particle at an angle  $\theta$  to the scattering of an infinite particle of the same mass.  $P(\theta)$  is a function of the shape of the molecules and is used to derive the radius of gyration and molecular mass.

Although the determination of aggregate parameters and how they change over time is very difficult (if not impossible) from the data, it is easy to compare

how the aggregation rate is affected by the identity of the heparin cation and the pH of the solution by plotting the turbidity of the solution at chosen wavelengths against time. The best wavelengths to choose are ones that have strong plasma emission, as at these wavelengths exact values of high turbidities will still be recorded (recall that if the spectrometer records a value of less than 0.01 then the turbidity is set as the maximum possible value of 2. This will not occur if the intensity of the light is high unless the turbidity is very high). It is also best to choose wavelengths that do not show strong line emission as the intensity at these wavelengths may be higher than spectrometer is able to measure. For this analysis the wavelengths 550 and 600 nm were chosen. It can be seen from Figure 106 that the plasma emission intensity at these wavelengths is high but shows little line emission.

To see how the rate of aggregation varies as pH and heparin type are varied, the turbidities of each sample, determined by both the plasma spectrometer and the plate reader at 550 and 600 nm, were plotted against time and best fit lines determined using least squares linear regression. The gradient of the line of best fit gives an accurate representation of the rate of aggregation for each sample. Turbidities with the maximum possible value of 2 were deleted from the data, as these data points skew the line of best fit. From linear regression, the formula for calculating the gradient is:

$$\textit{Gradient} = \frac{n \sum xy - \sum x \sum y}{n \sum x^2 - (\sum x)^2}$$

where  $x$  is time in seconds and  $y$  is the measured turbidity and  $n$  the number of data points. For each protein, the gradient or the rate of aggregation was plotted against pH for each heparin and wavelength (550 or 600nm) in Figures 119-126. For ease of comparison, results obtained using the plasma spectrometer are shown next to results obtained with the plate reader. Missing data points in the fibrinogen plots are due to the high initial turbidity, resulting in a lack of data with which to calculate a gradient.

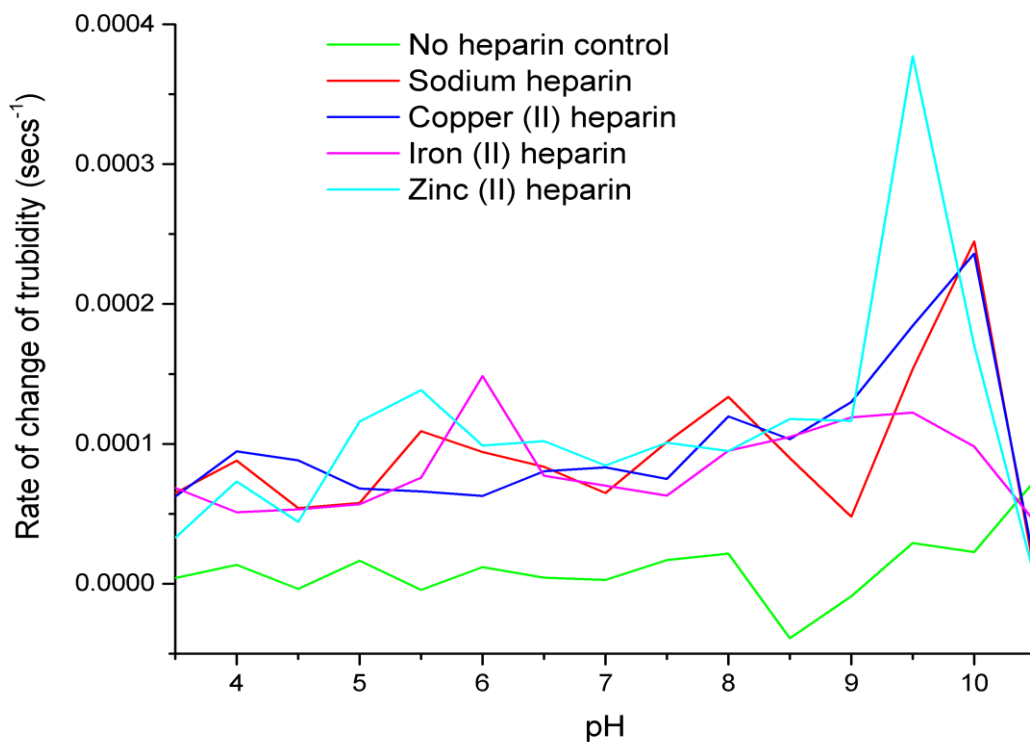


**Figure 119.** The calculated rate of change of turbidity of 2mg/ml lysozyme against pH for each heparin. Each data point represents a single experiment using the plasma spectrometer at 550 nm.

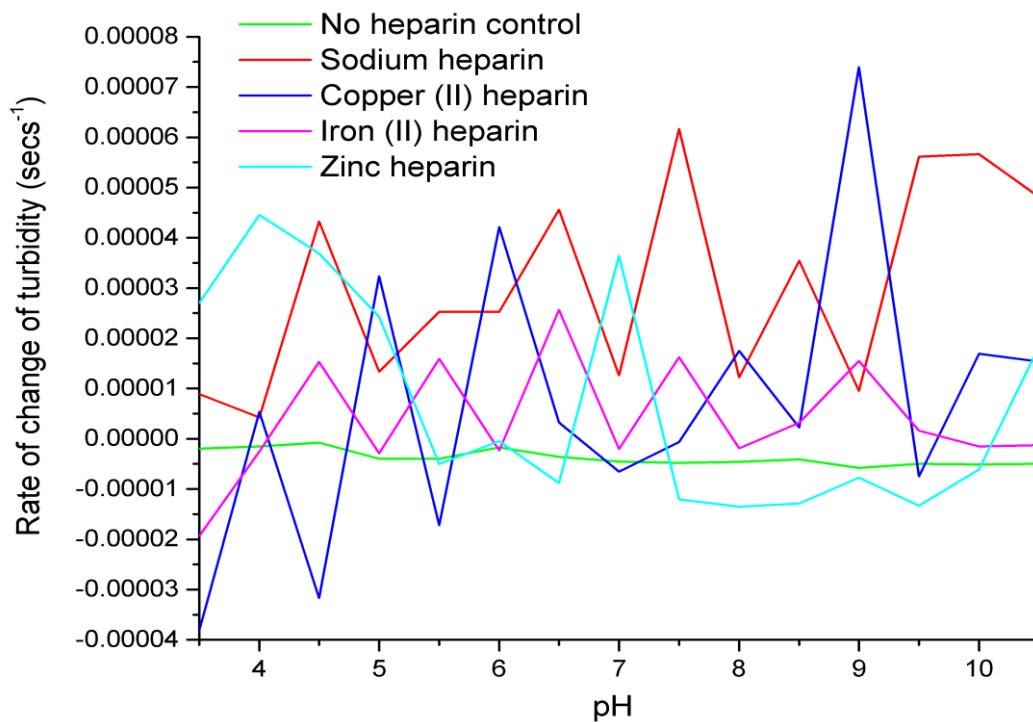


**Figure 120.** The calculated rate of change of turbidity of 2mg/ml lysozyme against pH for each heparin. Each data point represents a single experiment using the plate reader at 550 nm.

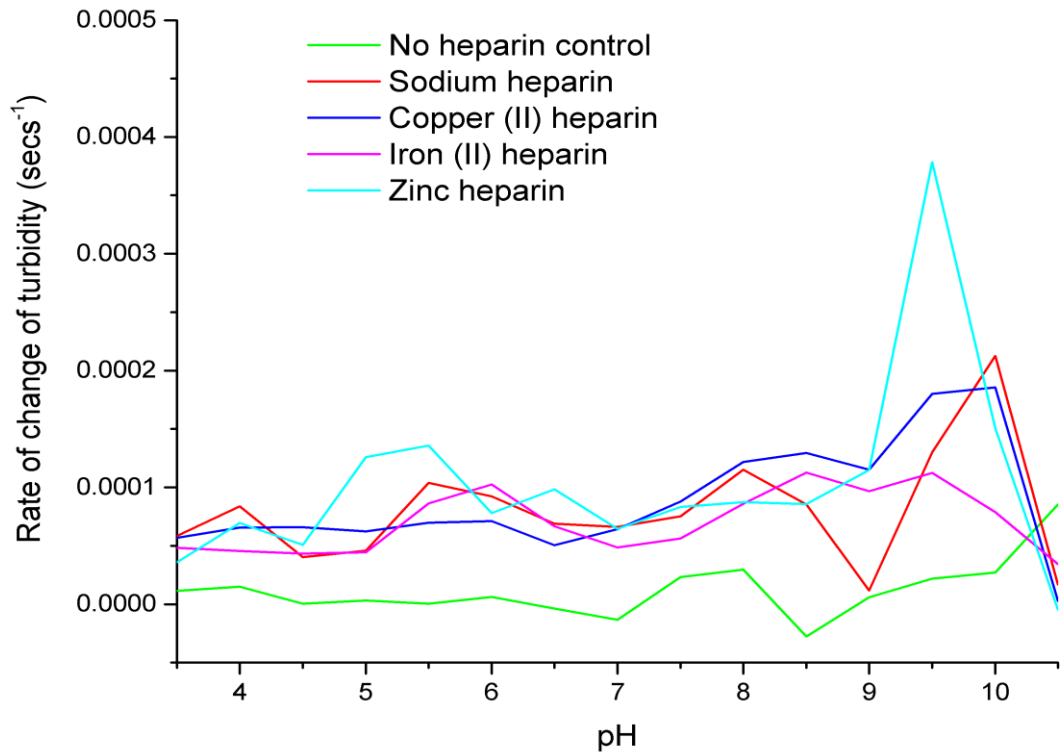


**Figure 121.** The calculated rate of change of turbidity of 2mg/ml lysozyme against pH for each heparin. Each data point represents a single experiment using the plasma spectrometer at 600 nm.

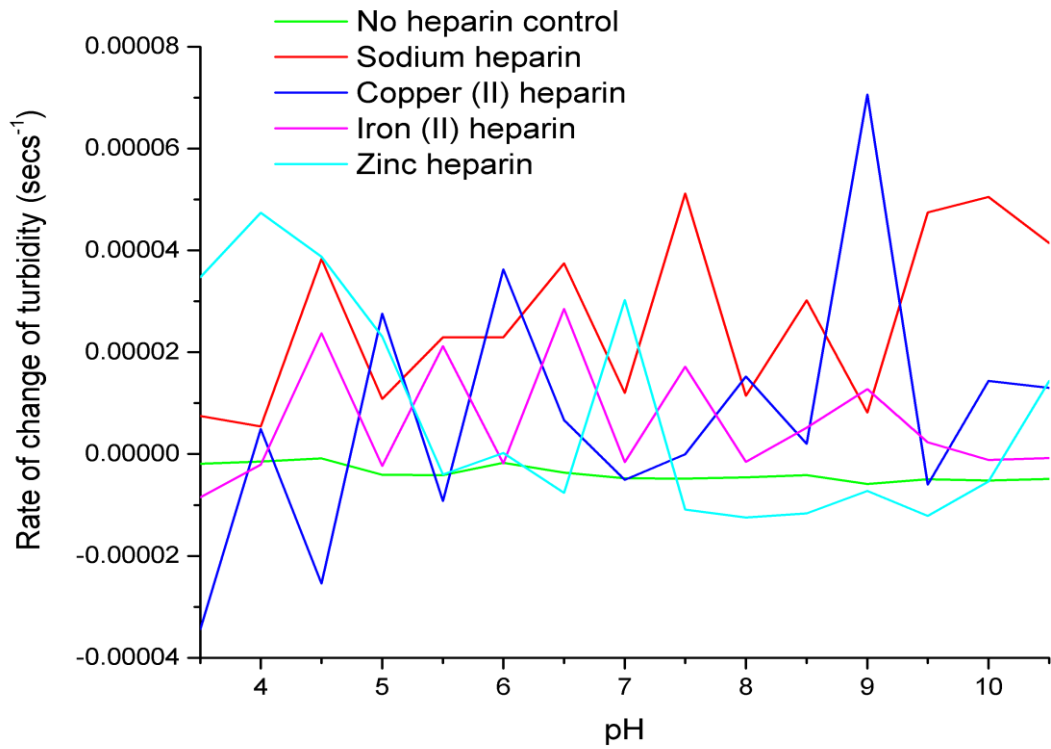


**Figure 122.** The calculated rate of change of turbidity of 2mg/ml lysozyme against pH for each heparin. Each data point represents a single experiment using the plate reader at 600 nm.

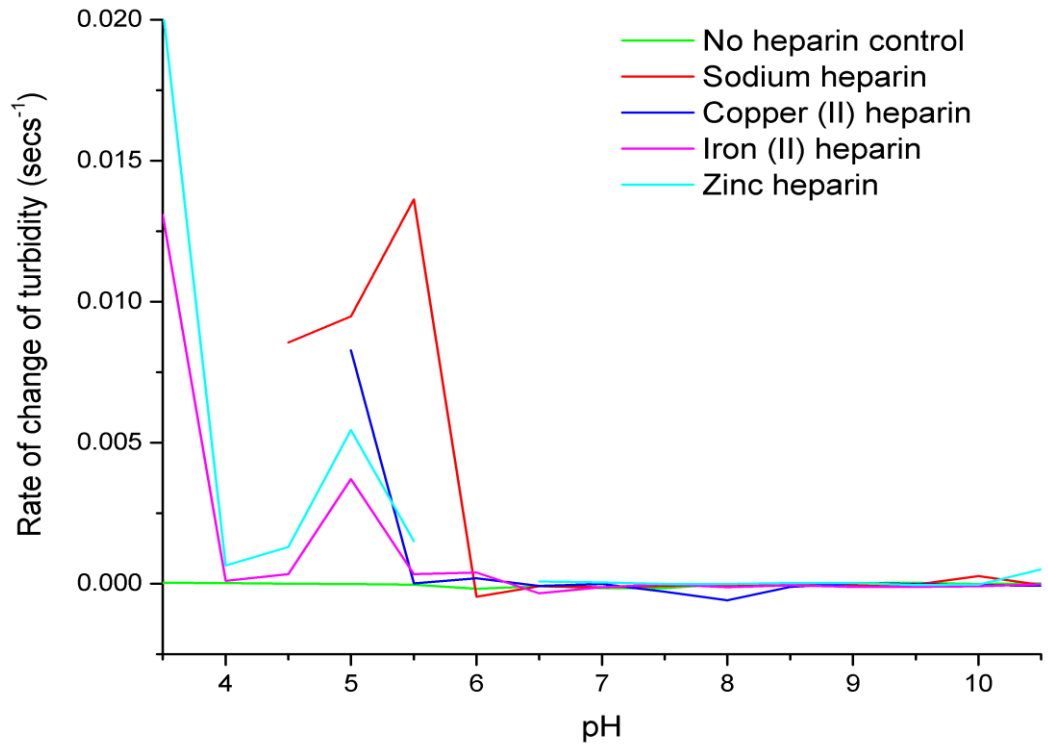


**Figure 123.** The calculated rate of change of turbidity of 2mg/ml fibrinogen against pH for each heparin. Each data point represents a single experiment using the plasma spectrometer at 550 nm. Missing data points are due to the high levels of aggregation (turbidity >2) at those pHs.

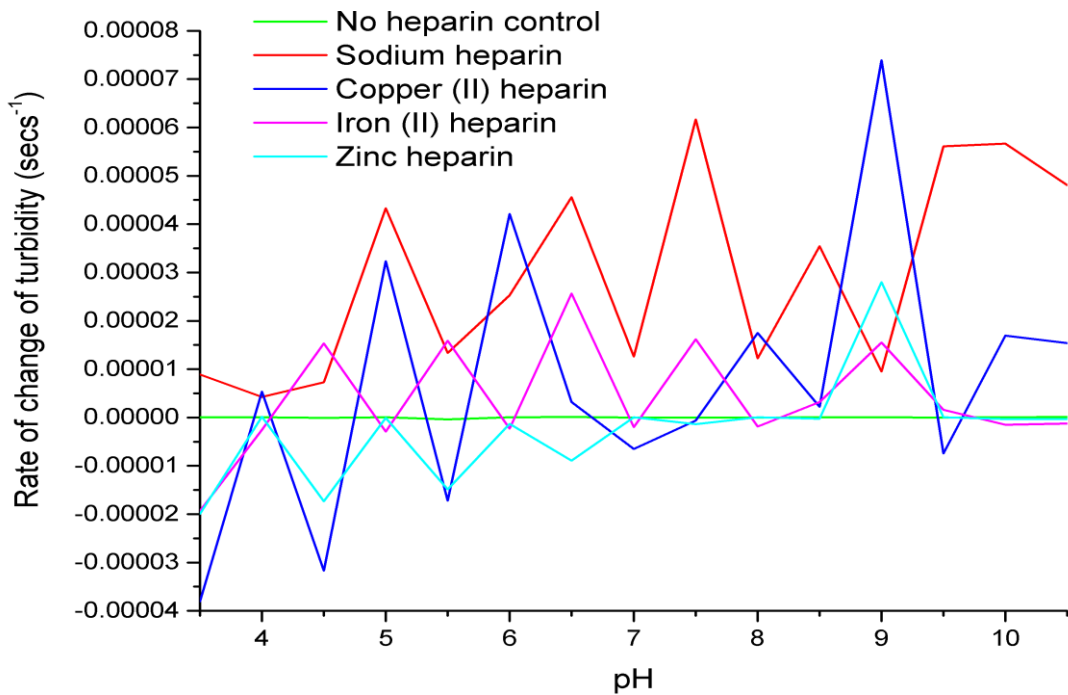


**Figure 124.** The calculated rate of change of turbidity of 2mg/ml fibrinogen against pH for each heparin. Each data point represents a single experiment using the plate reader at 550 nm.

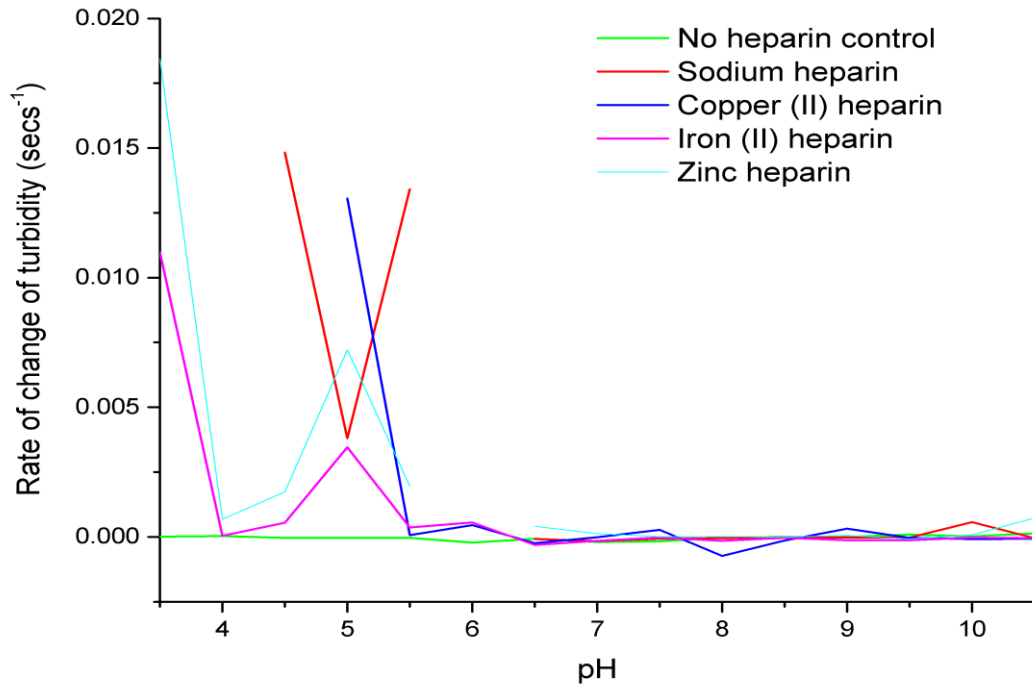


**Figure 125.** The calculated rate of change of turbidity of 2mg/ml fibrinogen against pH for each heparin. Each data point represents a single experiment using the plasma spectrometer at 600 nm. Missing data points are due to the high levels of aggregation (turbidity >2) at those pHs.

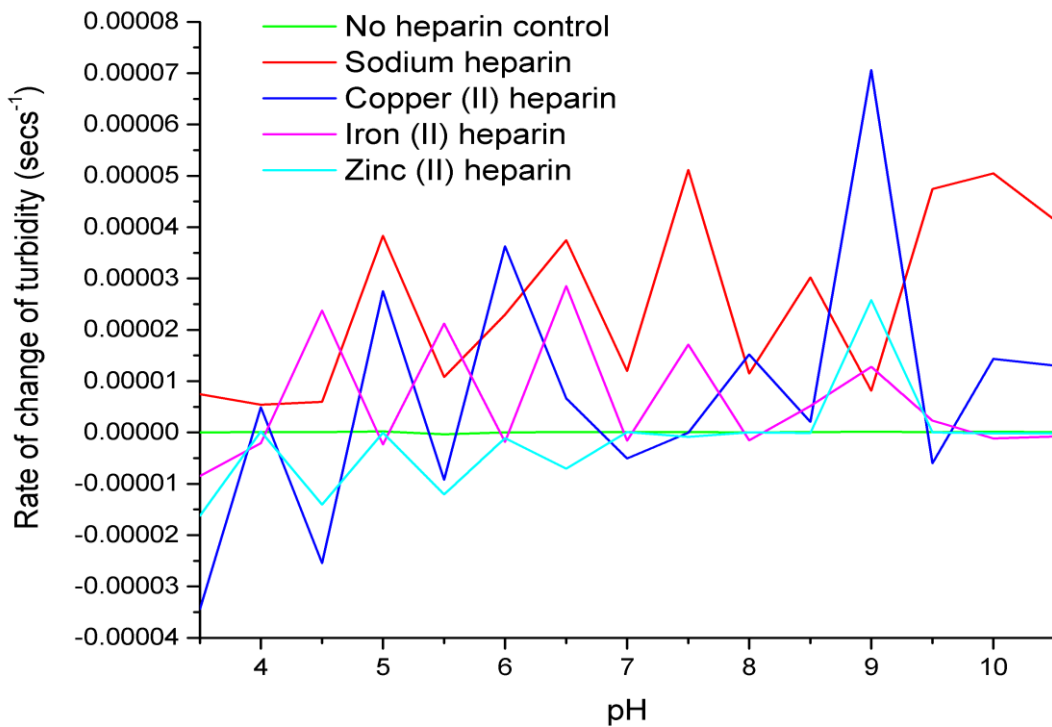


**Figure 126.** The calculated rate of change of turbidity of 2mg/ml fibrinogen against pH for each heparin. Each data point represents a single experiment using the plate reader at 600 nm.



An examination of the plotted graphs shows substantial differences between the plasma spectrometer and the plate reader. Points of interest are:

- The plate reader plots are very erratic compared to the plasma spectrometer. The reason for this is unclear.
- The no heparin control confirms that aggregation does not occur for either protein without the presence of heparin.
- Aggregation is very much pI dependent for both proteins and that aggregation rates are low away from the pI.
- The plate reader shows a slight general positive correlation between rate of aggregation and pH.
- In the plasma spectrometer plots for fibrinogen, the turbidity is approximately zero for all of the heparins at pHs higher than the pI of the protein, indicating that electrostatic repulsion, due to the proteins being negatively charged at these pHs, is preventing aggregation.
- All of the heparins demonstrate the ability to aggregate lysozyme to approximately the same extent. Zinc heparin shows the greatest aggregation rate for lysozyme near its pI. Zinc heparin has been shown to destabilise lysozyme, significantly altering its melting temperature and increasing the proportion of  $\beta$  sheet structures more than the addition of zinc cations alone to lysozyme (Hughes et al., 2012), indicating an important role for cations in the heparin binding and subsequent aggregation of lysozyme and other proteins. It is known that high concentrations of zinc (~10 mM) can cause lysozyme aggregation without the need for heparin (Olma et al., 1996).  $\text{Cu}^{2+}$   $\text{Zn}^{2+}$  and  $\text{Fe}^{2+}$  ions can all inhibit heparin binding at pH 6 (Zou et al., 1992). The reason why zinc shows the highest rate of lysozyme aggregation is not clear but may be related to the fact that heparin has the highest mean number of binding sites per molecule for zinc. Cation binding affinity to acidic side chains and ionic size may also be important factors that affect aggregation rates.
- The plate reader plots show negative rate of change of turbidity for some of the heparins, particularly at low pHs. Fibrinogen in the presence of zinc and copper heparins and lysozyme in the presence of copper heparin both

show decreasing turbidity over time. In both cases, the turbidity is initially low and decreases further, indicating that small aggregates are initially forming but fail to grow in size and fragment with time rather than turbidity decreasing due to large aggregates precipitating out of solution. It is unlikely due to acid hydrolysis of the protein as the pH is not low enough for this to occur.

One of the advantages of the plasma spectrometer over the plate reader is that the assays can be started on the plasma spectrometer much more quickly than the plate reader. The reason for this is that bubbles are easily formed when pipetting protein solutions. This is not a problem for the plasma spectrometer as bubbles float to the top of the cuvette and assays can be started seconds after the protein is pipetted in the cuvette but with a 96 well plate these bubbles must first be burst to allow for clean passage of light through the samples. This can take several minutes, resulting in delayed readings and variation in the starting times of the plate reader assays. This limits the utility of the plate reader to study aggregating proteins in the early stages of aggregation, in particular exactly how heparin/HS is able to initiate aggregation.

# Five

---

## Discussion

---

### 5.1 Cost of Prototype Instrument

The breakdown of costs for the build of the plasma spectrometer can be found in the Materials section above. The total cost of constructing the prototype instrument was £6480.49. Some of the costs of constructing the spectrometer were one time purchases. In particular the Thorlabs taps for cutting the bespoke threads can be reused. The main cost of the prototype are the two Thorlabs spectrometers (£2000 each). Each of these spectrometers could be replaced with a diffraction grating to spit the light into its wavelength components followed by a CCD array detector. This should not be too difficult to do, the most difficult part would be to calibrate the CCD detector for wavelength. The replacement of the Thorlabs spectrometers with a bespoke detector system would substantially reduce the cost of the prototype. As well as the initial costs for the construction of the plasma spectrometer, the operating costs of the instrument were:

- The argon gas used to fill the plasma chamber. This was inexpensive as the chamber only needed to be topped up with argon every few weeks.
- Owing to electrode erosion, the laser pumping flashlamp fails to trigger after approximately 250 thousand flashes and needs to be replaced. New flashlamps were purchased from the manufacturer for \$50.

The overall cost of the prototype is inexpensive compared to cost of commercially available spectrometers, the cost of which can easily run into the tens of thousands of pounds. However, in its current guise, the prototype is only a visible light spectrometer. To achieve the production of shorter wavelength light a much more expensive laser would be required (See Improvements section below). This would substantially increase costs.

## 5.2 Instrument Performance

In its current guise, the plasma spectrometer actually generated much higher intensity light than the CCS200 spectrometer was able to measure. The lenses that focused the broadband light onto the optic fibre ports were positioned to attenuate the intensity. However, the lack of high intensity UV light is disappointing. The use of noble gases as the plasma medium substantially increased the reliability of a laser pulse generating a plasma (100% reliability was easily achieved), but did not shift the emission to shorter wavelengths. To do this, a more expensive, high repetition rate laser would be required.

The data generated with the plasma spectrometer was noisy and subject to substantial intensity fluctuations. The sources of such errors are thought to be due to the fact that the two spectrometers do not measure the light emitted from exactly the same location of the plasma. This is because an image of the pinhole is formed at each of the fibre optic ports but slightly different areas of this image are sampled by the fibre (See Figure 127). The intensity and wavelength of the plasma emission varies across the pinhole because an image of the plasma is projected onto the pinhole. This image is small (a few millimetres across) but is approximately equal to the diameter of the pinhole.

Because the plasma moves around the focal point of the laser focusing lens, different parts of the plasma are projected onto the pinhole between pulses. The pinhole can therefore have substantial differences across it in intensity and wavelength distribution. This problem is aggravated by the fact that the ports are positioned to attenuate the emission, otherwise the detectors would be saturated by too high an intensity. The fibre optic therefore samples slightly different areas of the plasma which can have substantial differences in electron density and temperature.

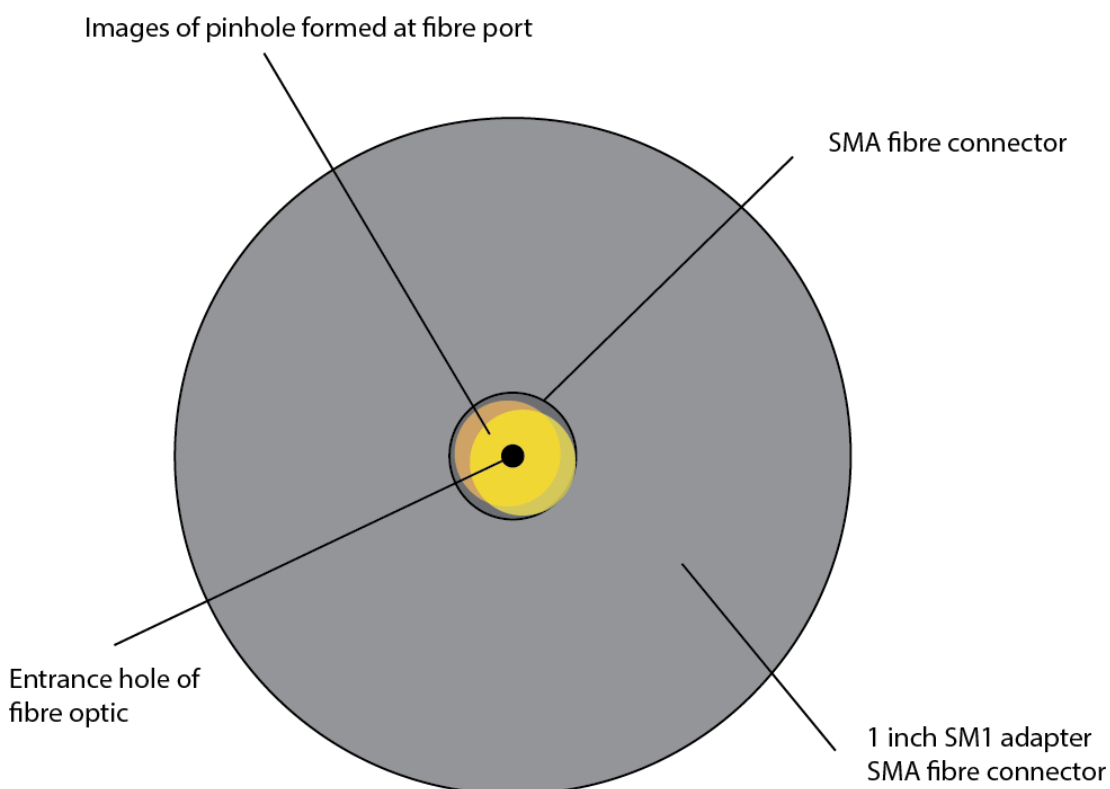


**Figure 127.** The focused images of the pinhole formed at each of the fibre optic ports. The images, in yellow and orange are overlaid to show differences in the areas sampled by the fibre but are actually focused onto two separate ports in the plasma spectrometer.

The problem of the fibre optic port sampling slightly different areas of the plasma is compounded by the fact that the transmission of the beam splitter must be measured prior to measurement of the absorbance/turbidity of a sample. This compounds the errors in further measurements of absorbance or turbidity because the transmission is needed to calculate absorbance/turbidity values. This compounded error is calculated from using Equation 19. These

errors affect the precision but do not affect the accuracy of the spectrometer because they do not change the mean calculated absorbance/turbidity.

A continuous, stable and stationary light source would solve this problem and substantially reduce errors as the image projected onto the pinhole would be stationary and of continuous intensity over time. Even though the fibre optic may sample slightly different parts of the pinhole, the intensity of light entering each fibre would be proportional by a constant factor. Measurement of the transmission of the beam splitter with a constant light source would substantially reduce the error in the transmission and therefore increase the precision of subsequent absorbance/turbidity measurements. A high repetition rate laser in the kHz or MHz range is effectively a continuous and stable source as the plasma would be stationary and of constant intensity, leading to much more precise results for both the transmission of the beam splitter and further measurements of absorbance or turbidity.

### 5.3 Conclusions Relating to the Protein Aggregation of Experiments

Although the aggregation experiments using the plasma spectrometer were noisy and subject to random errors Figures 119-126 that graph the rate of change of turbidity against pH showed promising results. In particular, that the aggregation pH was highly dependent upon the pI of the protein tested. It is worthwhile to note that the pH of aggregation does not change due to the binding to heparin. This indicates that the metal cations do not dissociate from the heparin while in the solution and are central to the aggregation process. If the heparin was in the acid form due to the dissociation of the cation, it is likely that the aggregation pH would change due to the heparin:protein complex having a different pI from the protein alone. The cations are therefore masking the negative charges of the O-sulphate and carboxylic acid groups of the heparin, forming a heparin:cation:protein complex. One further assay that may show interesting results would be to test heparin in its acid form, but this solution would have a very low pH. The binding of acid heparin should result in the shifting of the aggregation to lower pHs due to a lowering of the pI of the

heparin:protein complex from the pI of the protein. The pI change occurs because of the increase in the number of acidic (sulphate) groups.

Initially, it was thought that the banding pattern observed using the plasma spectrometer was due to the spectrum of light emitted from the plasma. Low emission intensities were thought to lead to high turbidities and high emission would lead to low turbidities. The banding patterns should therefore correlate inversely to the plasma emission. This inverse correlation is seen with the aggregation of lysozyme in Figure 117 but further testing with fibrinogen showed that this banding pattern did not follow an inverse correlation with plasma intensity. To confirm that the banding pattern is actually due to the wavelength dependence of turbidity and not a result of emission intensities, the plate reader could be used to scan a single well containing aggregating protein in the presence of heparin. If only a single well is scanned, the plate reader is able to record measurements at a much higher resolution of 0.5 nm. This assay may reveal the source of the banding pattern.

It is difficult to discern the exact role of the heparin salt in the aggregation process from the plasma spectrometer and plate reader results. It may be that the heparin provides a nucleation centre for the proteins to bind to, changing the conformation and secondary structure of the protein into the anti-parallel  $\beta$  sheet found in amyloid plaques. Another possible model is that the heparin binds to a protein and induces an appropriate conformation for binding to other heparin:protein complexes, each protein needing to be bound to heparin first before aggregation and fibril formation can occur. The development of an assay that can record the levels of unbound protein and heparin in the aggregating solution over time would provide great insight into the stoichiometry of the aggregation process and reveal much concerning the role of heparin/HS in the initiation and growth of aggregates.

Following the testing and analysis of the aggregation data, it was realised that several changes could be made to improve the quality of the results. In particular, although PBS is of biological relevance, it lacks buffering capacity away from the pKas of phosphoric acid. Phosphoric acid has three pKas at

2.15, 7.2 and 12.3 which provide buffering capacity around these pHs but it may be better to add other acids with pKas outside of these ranges to provide additional buffering capacity away from these pHs. PBS contains the cations sodium and potassium which do not displace the cations used in these assays because sodium and potassium have lower binding affinities for heparin (see previous chapter). It is always best to use sodium hydroxide to pH the buffers for this reason.

It may be better to ensure adequate mixing and homogenisation of the initial solution to introduce the heparin and lysozyme to each other in identical volumes, e.g. 1 ml of heparin solution to 1 ml of lysozyme. This would greatly reduce the initial concentration of the heparin and slow down the start of the aggregation process. An interesting assay to do would be to lower the concentration of heparin and increase length of time over which the measurements are conducted. Low concentrations of heparin should slow the rate of aggregation down and may reveal the aggregation process in greater detail. For example, the aggregation process may proceed in stages which would be revealed if the rate was much slower. There may also be a minimum concentration of heparin required to enable protein aggregation to initialise and proceed, which could be determined by lowering the heparin concentration in these assays.

## 5.4 Improvements to Plasma Spectrometer

The reason why the plasma emitted very little UV light is because the electron temperature of the plasma was too low. To increase electron temperatures, the plasma needs to be excited multiple times with focused laser light before it has a chance to expand, cool and dissipate. To do this, a laser with a much higher repetition rate of at least kHz would be required. This is the main financial obstacle to the production of UV light down to 180 nm. The lifetime of a laser induced argon plasma is in the order of 1 $\mu$ s (Hohreiter et al., 2004, Harilal, 2004) implying that a laser with a repetition rate of MHz would be required. However, it is known that residual free electrons reside in the focal



volume for several milliseconds, reducing the breakdown threshold at kHz repetition rates. These residual electrons would be further heated by KHz laser pulses maybe enough to generate the high temperatures needed for substantial emission in the mid-UV region. It is obvious though that high electron temperatures can be obtained by high pulse power, high repetition rate lasers. However, the combination of a high enough pulse power to initiate a laser spark and high repetition rate makes these lasers expensive (in the tens of thousands of pounds), which was beyond the scope of this project. By using a high repetition rate laser, the plasma effectively becomes a continuous, constant intensity light source. This would overcome the problems inherent with using a pulsed light source such as timing of the light capture interval by the detector and the pulse to pulse intensity variation.

In many spectrometers, the absorbance of a sample minus the absorbance of the buffer is determined by simultaneously scanning two cuvettes contain the sample in buffer and the buffer on its own. The cuvettes are placed in the beams that are created by the beam splitter, one in each beam. For a light source of varying intensity, such as a low repetition rate LIP, the pulse to pulse intensity of the beams before passing through the cuvette is impossible to determine without sampling the beam. In the plasma instrument, the intensity of the reflected beam is recorded to determine the wavelength dependent intensity of the transmitted beam before it passes through the sample. If a cuvette containing the buffer is placed in the reflected beam, the pulse to pulse intensity of the source can no longer be determined. However, it should be possible using an arrangement of two beam splitters and three detectors to modify the plasma spectrometer for this kind of simultaneous buffer absorbance subtraction, but this adds expense to the instrument. The loss of intensity of light due to the use of two beam splitters should not be a problem as the intensity of the light is too high for the detectors to measure without attenuation by plano-convex lenses before entering the optical fibres. This schematic of this arrangement is shown in Figure 128.

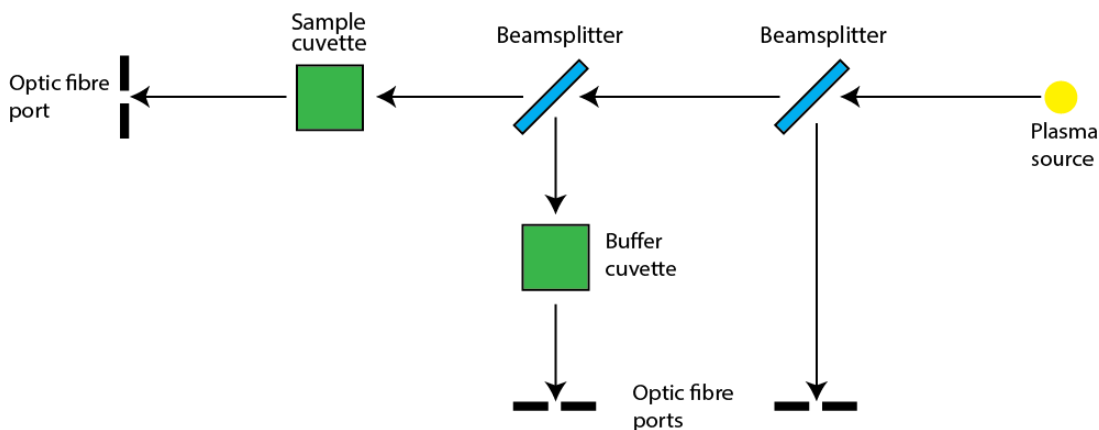


**Figure 128.** A schematic of the optical arrangement for the simultaneous determination of sample absorbance minus the background absorbance due to buffer absorbance.

If the source is of constant intensity, or has a constant average intensity over the required measurement time interval, the intensities of both beams before passing through the sample can easily be determined if the transmission of the beam splitter is known. With a light source of constant intensity, there is no longer a need to measure the intensity of the beam by beam sampling with a beam splitter. Instead, a reference sample containing the buffer/solvent can be placed in one of the beams and the intensity measurements after passing through the cuvettes used to calculate the sample minus the absorbance/turbidity of the buffer/solvent. This avoids the need to carry out a separate measurement the absorbance/turbidity of the solvent/buffer. This could be done if a high repetition rate laser was used to generate the plasma.

The plasma spectrometer could be greatly improved by using detectors that are able to measure a greater intensity (dynamic) range. The CCS200 detectors limited the absorbance range of the plasma spectrometer to a range of 0 to 2, because the minimum intensity value that could be measured is 0.01 and the maximum intensity value is 1. In practice, an absorbance of 2 is not obtainable as this value was only obtained when the beam passing through the sample has the minimum intensity of 0.01 and the reference beam has the maximum intensity of 1. The actual working absorbance range is more like 0 – 1.5. The absorbance range of the plasma spectrometer could be improved by using a detector with a greater measureable intensity range. A detector that possessed a logarithmic intensity response would be ideal. Using a more

sensitive detector would remove the need for so many of the data points in the results being assigned the maximum value of 2 (dark red in Figures 111-116) because the intensity of the transmitted beam was too low to be measured.

Although the focusing of pulsed laser light is a simple and effective way to concentrate very quickly concentrate energy into a small area, suddenly raising the temperature of the medium, energetically it is extremely inefficient. The laser is pumped by discharging a large capacitor through the flashlamp inside the laser housing. This creates a very high current density in the flashlamp which ionises the xenon gas. The capacitor used to pump the laser in this project has a capacitance of 100 $\mu$ F and is charged to 1000V. The energy that is discharged through the flashlamp is therefore:

$$\text{Energy stored in capacitor} = \frac{1}{2} QV^2 = \frac{1}{2} \times 10^{-4} \times 1000^2 = 50J$$

The pulse intensity of the laser as measured previously was 280 mJ. This is therefore an efficiency of 0.56%. Further to this, only a fraction of the energy in the laser pulse is actually re-emitted as broadband light. Some of the pulse energy is transmitted straight through before the plasma is formed (See Figure 77) and other losses occur from a variety of causes such as electron diffusion, imperfect capture and collimation of the emitted light, imperfect optics etc.

Following the calculation of the laser efficiency it was quickly realised that a broadband, plasma light source, the flashlamp, was being used to create another plasma light source, the laser induced plasma. This prompted a measurement of the spectral output of the flashlamp inside the laser using the CCS200. This spectrum is shown in Figure 129. The shape of the spectrum is roughly blackbody with the peak looking to around 540nm. From Wien's Law this is a temperature of 5364.8K. This is slightly cooler than the laser induced plasma in air. There is however, very little line emission in the flashlamp spectra. This indicates that the plasma is actually much hotter than is evident from the spectrum as the ratio of line emission to continuum emission decreases as temperature increases.

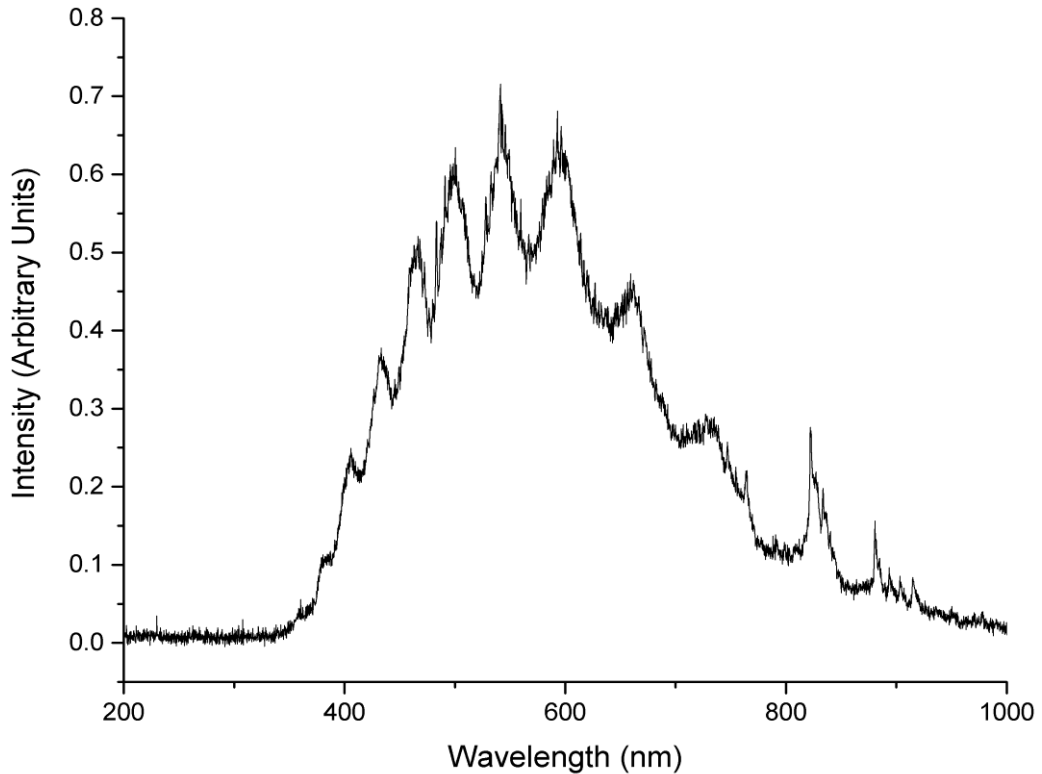


**Figure 129.** *The spectrum of the flashlamp inside the ML-LASER-YB5 Nd:YAG laser, captured with CCS200 spectrometer.*

The broad humps seen in the above spectrum are an indication that the flashlamp envelope is absorbing some of the emitted light. Flashlamps are often doped to prevent emission of short UV radiation which causes solarisation of the envelope material. Figure 130 shows the transmission properties of different flashlamp envelope materials. Solarisation is the discolouration of the flashlamp due to ion impurities, causing broadband reduction of the transmittance of the lamp. The absorbance bands seen in the flashlamp spectra may therefore be due to solarisation and or doping agents in the envelope materials. It is likely that the envelope material of the lamp is doped, resulting in a lack of radiation below 350 nm. It would be interesting to obtain the spectrum of light emitted from a flashlamp that has synthetic quartz as an envelope material. As can be seen from Figure 130, this envelope material is transmissive down to around 150 nm. It may therefore be possible to obtain short wavelength light below 300 nm using a synthetic quartz flashlamp.

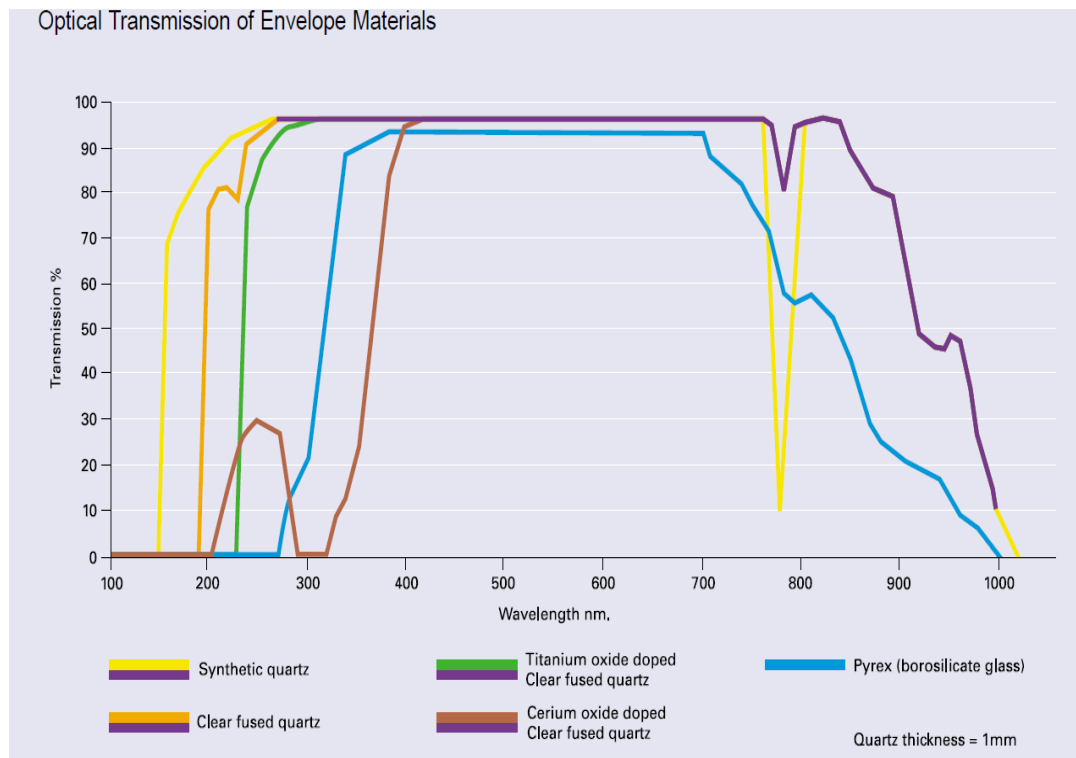


**Figure 130.** The transmission properties of various flashlamp envelope materials. Source: Perkin Elmer flashlamp catalogue. Source:

<http://www.dmlittle.eclipse.co.uk/lasers/documentation/Perkin%20Elmer%20Flashlamp%20Catalog.pdf>

One way to improve the intensity of the plasma, increasing the efficiency of conversion of laser pulse energy into broadband light and increasing the emission at short wavelengths, is to pregenerate a low temperature plasma at the focal point of the laser focusing lens. Plasma is highly absorbing of impinging EM radiation due to inverse brehmsstrahlung absorption and so should absorb a much greater proportion of the energy of the laser pulse. Preionising the gaseous medium should also allow for the generation of higher electron temperatures and subsequently shorter wavelength emission because less of the energy of the laser pulse is required for photoionisation. This is possible to do by focusing the laser pulse onto the plasma generated between the electrodes of a xenon arc lamp. Light sources that are able to generate very short wavelength light, such as the Energetiq EQ-1500, by focusing a continuous wave or pulsed laser onto a xenon arc, have recently become available during the course of this project. These light sources, retailing for around £10000, are known as Laser Driven Light Sources (LDLS)

and are able to generate light down to 170 nm, (the cut off of the synthetic fused silica bulb). The practical cut off for the emission from these sources is the absorbance of oxygen in air, generating ozone below 200 nm. Ozone is itself absorbent of UV radiation, mainly in the range 220-280 nm. This effect can be mitigated by flushing the source and the light path with nitrogen, but even then the limit is around 180 nm.

## Six

---

### Conclusions

---

Although it is unlikely that LIP technologies will compete with deuterium and tungsten halogen bulbs as light sources in benchtop spectrometers, due to the reliability, stability and inexpensive nature of these bulbs, it is quite possible that LIP sources may well be able to compete with very expensive, high tech sources such as synchrotrons due the cost of building, managing and maintaining such devices, the expense of which can easily run into the hundreds of millions of pounds. The main expense in building a viable LIP source for biological spectroscopy is a high repetition rate, high power rate laser. Lasers capable of generating plasmas with emission in the mid-UV are available at a fraction of the cost of synchrotron sources. The running costs of a LIP source are also much cheaper even using expensive xenon gas as the plasma medium. Laser induced plasma technologies offer a promising future for the generation of short wavelength broadband light. From the use of focused laser light in such cutting edge applications as the production of EUV light for CPU lithography and the generation of the extremely high temperatures needed for nuclear fusion to occur (hundreds of millions of

degrees Kelvin), it is obvious that laser induction methods show great promise for the future of high temperature plasma generation.

Apart from laser induced plasmas, other methods of plasma generation and manipulation show great promise as sources of short wavelength, broadband light. Very shorter wavelength light production, down to soft x-rays, is now available using z-pinch plasma confinement technologies. Plasmas by their ionised nature are highly conductive. Passing a current through a plasma results in its compression of the plasma due to the Lorentz force. The Lorentz force is a magnetic force that is generated by the movement of charge in the plasma. An example of Lorentz force is that two wires carrying a current in the same direction will attract each other. In a plasma, this force results in the compression and subsequent heating of the plasma. This compression is limited by the outward diffusion of the plasma, which increases in magnitude as the temperature increases. The term z-pinch refers to the direction of the current in the plasma which is modelled in the z direction. This technology enables very high plasma temperatures and the generation of short wavelength radiation. In most z-pinch instruments, the current is generated by magnetic induction coils which allow for electrodeless operation. This is important as one of the main problems with plasma production, in flashlamps for example, is the erosion of the electrodes due to bombardment by high energy electrons. However, as magnetic induction requires a changing magnetic field and the current is supposed to flow in one direction of the plasma, the current in the induction coil must be increased over time. This places a limit on the lifetime of a z-pinch plasma.

The advent of high intensity, short wavelength, relatively inexpensive light sources allows for some interesting spectroscopic applications. In particular, in relation to the measurement of aggregating particles, broadband cavity spectroscopy can be attempted using a broadband source. Cavity resonance spectroscopy is a highly sensitive technique that is able to measure the optical extinction coefficients of an absorbing or scattering sample. This technique is able to measure samples that have very low absorbance/scattering and/or at very low concentrations. In cavity resonance spectroscopy, the light (usually



from a laser) is guided into an optical cavity. Optical cavities, such as those found in lasers, are made of two highly reflective mirrors facing each other so that a light beam bounces from one to the other. If the light is coherent, a standing wave is set up inside the cavity due to interference. Owing to constructive interference, this standing wave can be very intense. If a sample is then placed inside the cavity, the path length through the sample can be very large, often several hundred metres. The technique of cavity ring down spectroscopy involves turning off the cavity pumping light source resulting in the exponential decay of the intensity of light in the cavity. This decay occurs faster if an absorbing sample is present. By measuring the decay time of the light in the cavity, an absorbance coefficient can be determined. If a scattering sample is placed in the cavity and the cavity is allowed to achieve dynamic equilibrium, the scattering of a sample can be measured at 90° to the axis of the cavity. This should allow the measurement of the scattered light intensity from samples that have very low concentrations and/or very low scattering cross sections, because of the very large path lengths achievable using an optical cavity. If a broadband source is used to pump the cavity, broadband scattering should be measurable using this technique.

It is envisaged that the advent of high intensity broadband bench top light sources will provide interesting opportunities for short wavelength spectroscopy that has up till now only been available from synchrotron light sources. These plasma based technologies will provide researchers with opportunities to develop spectroscopic techniques that are able to better discern the structure-function relations of biomolecules.

Finally, it is for me to reflect on the collaboration process and offer a few words of advice to future students, academics and industrialists. Two things are extremely important for any collaboration: the maintenance of communication throughout the project between the collaborators and a mutual understanding of the motivations behind each of the parties involved. Communication is key to any project and must be maintained on a regular basis throughout. In an academic-industrial collaboration, it can be too easy to allow communication to lapse, with each party often assuming that the student is taking direction

from the other collaborator. This may result in wasted time, especially in the early stages of the project, and can leave the student can feel isolated and lacking direction. This is a situation that all parties should strive to prevent. In addition, each collaborating party has different motivations behind their involvement in the project and it is important to understand that these may not always be commensurate. The motivation of the student is to study the academic subject area, learn and to obtain a qualification; the motivation of the academic is to investigate and research new areas of science and to develop the necessary new tools and instruments to do this, as well as guide the student through to obtaining a qualification; the motivation of the industrialist is to determine whether a profitable commercial product, which they have the ability to manufacture, is viable. It is of utmost importance that each collaborator bear in mind each other's motivations if everyone is to gain the most from the project. In closing, I would like to say that it has been a privilege to be at the forefront of such an interesting and unusual academic-industrial collaboration.

## References

2004. *CRC handbook of chemistry and physics*, London, CRC Press.
2005. Polysaccharides *In: DUMITRIU, S. (ed.) Structural Diversity and Functional Versatility*. 2nd Revised edition ed. Baton Rouge/US: Taylor and Fransis Inc.
2015. Heparin Market - Global Industry Analysis, Size, Share, Growth, Trends and Forecast 2015 - 2023 Transparency Market Research.
- ABDELHALIM, M. A. K., ALHADLAQ, H. A. & MOUSSA, S. A. 2010. Elucidation of the effects of a high fat diet on trace elements in rabbit tissues using atomic absorption spectroscopy. *Lipids in Health and Disease*, 9, 2-2.
- ADAMSON, A. W. & CIMOLINO, M. C. 1984a. A laser-produced plasma as a pulsed source of continuum infrared radiation for time-resolved absorption spectroscopy. *The Journal of Physical Chemistry*, 88, 488-490.
- ADAMSON, A. W. & CIMOLINO, M. C. 1984b. A laser-produced plasma as a pulsed source of continuum infrared radiation for time-resolved absorption spectroscopy. *J Phys Chem*, 88, 488-490.
- AGOSTINI, P., BARJOT, G., MAINFRAY, G., MANUS, C. & THEBAULT, J. 1970a. Multiphoton ionization of rare gases at 1.06 $\mu$ m and 0.53 $\mu$ m. *Quantum Electronics, IEEE Journal of*, 6, 782-788.
- AGOSTINI, P., BARJOT, G., MAINFRAY, G., MANUS, C. & THEBAULT, J. 1970b. Multiphoton ionization of rare gases at 1.06 $\mu$ m and 0.53 $\mu$ m. *Quantum Electronics, IEEE Journal of*, 6, 782-788.
- AGOSTINI, P., FABRE, F., MAINFRAY, G., PETITE, G. & RAHMAN, N. K. 1979. Free-Free Transitions Following Six-Photon Ionization of Xenon Atoms. *Physical Review Letters*, 42, 1127-1130.
- AKHMANOV, S. A., KOVRIGIN, A. I., STRUKOV, M. M. & KHOKHLOV, R. V. 1965. Frequency dependence of the threshold breakdown of optical breakdown in air *JETP Letters*, 1.
- ALCOCK, A. J., DEMICHELIS, C. & RICHARDSON, M. C. 1968. Production of a spark by a train of mode - locked laser pulses. *Physics Letters A*, 28, 356-357.
- ALCOCK, A. J., KATO, K. & RICHARDSON, M. C. 1972. New features of laser-induced gas breakdown in the ultraviolet. *Optics Communications*, 6, 342-344.
- ALCOCK, A. J. & RICHARDSON, M. C. 1968. Creation of a Spark by a Single Subnanosecond Laser Pulse. *Physical Review Letters*, 21, 667-670.
- ALLEN, K. R. & PHILLIPS, K. 1959. Effect of Humidity on the Spark Breakdown Voltage. *Nature*, 183, 174-175.
- ANDERSSON, J. & BARTH, A. 2006. FTIR studies on the bond properties of the aspartyl phosphate moiety of the Ca<sup>2+</sup>-ATPase. *Biopolymers*, 82, 353-357.
- ANDREINI, C., BANCI, L., BERTINI, I. & ROSATO, A. 2006. Counting the Zinc-Proteins Encoded in the Human Genome. *Journal of Proteome Research*, 5, 196-201.
- ANDREWS, J. C. 1928. THE ALKALINE DECOMPOSITION OF CYSTINE. *Journal of Biological Chemistry*, 80, 191-210.
- ARMSTRONG, R. A., LUCHT, R. A. & RAWLINS, W. T. 1983a. Spectroscopic investigation of laser-initiated low-pressure plasmas in atmospheric gases. *Applied Optics*, 22, 1573-1577.

- ARMSTRONG, R. A., LUCHT, R. A. & RAWLINS, W. T. 1983b. Spectroscopic investigation of laser-initiated low-pressure plasmas in atmospheric gases. *Appl. Opt.*, 22, 1573-1577.
- ASHIKARI, S., HABUCHI, H. & KIMATA, K. 1995. Characterization of Heparan Sulfate Oligosaccharides That Bind to Hepatocyte Growth Factor. *Journal of Biological Chemistry*, 270, 29586-29593.
- AVIEZER, D., HECHT, D., SAFRAN, M., EISINGER, M., DAVID, G. & YAYON, A. 1994. Perlecan, basal lamina proteoglycan, promotes basic fibroblast growth factor-receptor binding, mitogenesis, and angiogenesis. *Cell*, 79, 1005-1013.
- BADGER, R. M. 1940. The Relation Between the Energy of a Hydrogen Bond and the Frequencies of the O–H Bands. *The Journal of Chemical Physics*, 8, 288-289.
- BAKSHI, V. 2006. EUV Source Technology: Challenges and Status *EUV Sources for Lithography* [Online], SPIE Press, Bellingham, Washington USA. Available: <http://spie.org/samples/PM149.pdf>.
- BANDEKAR, J. 1992. Amide modes and protein conformation. *Biochimica et Biophysica Acta (BBA) - Protein Structure and Molecular Enzymology*, 1120, 123-143.
- BAO, X., MOSEMAN, E. A., SAITO, H., PETRYANIK, B., THIRIOT, A., HATAKEYAMA, S., ITO, Y., KAWASHIMA, H., YAMAGUCHI, Y., LOWE, J. B., VON ANDRIAN, U. H. & FUKUDA, M. 2010. Endothelial Heparan Sulfate Controls Chemokine Presentation in Recruitment of Lymphocytes and Dendritic Cells to Lymph Nodes. *Immunity*, 33, 817-829.
- BARAVIAN, G., GODART, J. & SULTAN, G. 1976. Resonant multiphoton ionization of neon. Experimental determination of the polarizability of the 3p level. *Physical Review A*, 14, 761-767.
- BARTH, A. & MÄNTELE, W. 1998. ATP-Induced Phosphorylation of the Sarcoplasmic Reticulum Ca<sup>2+</sup> ATPase: Molecular Interpretation of Infrared Difference Spectra. *Biophysical Journal*, 75, 538-544.
- BARTH, A., MÄNTELE, W. & KREUTZ, W. 1991. Infrared spectroscopic signals arising from ligand binding and conformational changes in the catalytic cycle of sarcoplasmic reticulum calcium ATPase. *Biochimica et Biophysica Acta (BBA) - Bioenergetics*, 1057, 115-123.
- BARTNIK, A., FEDOSEJEVS, R., WACHULAK, P., FIEDOROWICZ, H., SERBANESCU, C., SAIZ, E. G., RILEY, D., TOLEIKIS, S. & NEELY, D. 2013. Photo-ionized neon plasmas induced by radiation pulses of a laser-plasma EUV source and a free electron laser FLASH. *Laser and Particle Beams*, 31, 195-201.
- BASTIAANS, G. J. & MANGOLD, R. A. 1985. The calculation of electron density and temperature in Ar spectroscopic plasmas from continuum and line spectra. *Spectrochimica Acta Part B: Atomic Spectroscopy*, 40, 885-892.
- BAZIN, H. G., MARQUES, M. A., OWENS, A. P., LINHARDT, R. J. & CRUTCHER, K. A. 2002. Inhibition of Apolipoprotein E-Related Neurotoxicity by Glycosaminoglycans and Their Oligosaccharides†. *Biochemistry*, 41, 8203-8211.
- BECKER, D. L., FREDENBURGH, J. C., STAFFORD, A. R. & WEITZ, J. I. 1997. Molecular Basis for the Resistance of Fibrin-Bound Thrombin to Inactivation by Heparin/Serpin Complexes. *In: CHURCH, F. C., CUNNINGHAM, D. D.,*

- GINSBURG, D., HOFFMAN, M., STONE, S. R. & TOLLEFSEN, D. M. (eds.) *Chemistry and Biology of Serpins*. Boston, MA: Springer US.
- BEILBY, J. P., PRINS, A. W. & SWANSON, N. R. 1999. Determination of Hepatic Iron Concentration in Fresh and Paraffin-embedded Tissue. *Clinical Chemistry*, 45, 573.
- BEKEFI, G. 1966. *Radiation Processes in Plasmas*, New York, John Wiley.
- BENITZ, W. E., LESSLER, D. S., COULSON, J. D. & BERNFIELD, M. 1986. Heparin inhibits proliferation of fetal vascular smooth muscle cells in the absence of platelet-derived growth factor. *Journal of Cellular Physiology*, 127, 1-7.
- BENSON, M. D., LIEPNIKS, J., UEMICHI, T., WHEELER, G. & CORREA, R. 1993. Hereditary renal amyloidosis associated with a mutant fibrinogen [alpha]-chain. *Nat Genet*, 3, 252-255.
- BETHE, H. & HEITLER, W. 1934. On the Stopping of Fast Particles and on the Creation of Positive Electrons. *Proceedings of the Royal Society of London. Series A*, 146, 83-112.
- BIELESCH, U., BUDDE, M., FREISINGER, B., SCHÄFER, J. H., UHLENBUSCH, J. & VIÖL, W. 1998. High repetition rate laser-induced plasma as a VUV radiation source. *Journal of Physics D: Applied Physics*, 31, 2286.
- BINDHU, C. V., HARILAL, S. S., TILLACK, M. S., NAJMABADI, F. & GAERIS, A. C. 2004. Energy Absorption and Propagation in Laser-Created Sparks. *Applied Spectroscopy*, 58, 719-726.
- BINDHU, C. V. H., S. S., TILLACK, M. S., NAJMABADI, F. & GAERIS, A. C. 2003. Laser propagation and energy absorption by an argon spark. *Journal of Applied Physics*, 94, 7402-7407.
- BLEACKLEY, M. & MACGILLIVRAY, R. A. 2011. Transition metal homeostasis: from yeast to human disease. *BioMetals*, 24, 785-809.
- BOCK, R. M., LING, N.-S., MORELL, S. A. & LIPTON, S. H. 1956. Ultraviolet absorption spectra of adenosine-5'-triphosphate and related 5'-ribonucleotides. *Archives of Biochemistry and Biophysics*, 62, 253-264.
- BOHAK, Z. 1964. Nε-(dl-2-Amino-2-carboxyethyl)-l-lysine, a New Amino Acid Formed on Alkaline Treatment of Proteins. *Journal of Biological Chemistry*, 239, 2878-2887.
- BOOTH, D. R., SUNDE, M., BELLOTTI, V., ROBINSON, C. V., HUTCHINSON, W. L., FRASER, P. E., HAWKINS, P. N., DOBSON, C. M., RADFORD, S. E., BLAKE, C. C. F. & PEPYS, M. B. 1997. Instability, unfolding and aggregation of human lysozyme variants underlying amyloid fibrillogenesis. *Nature*, 385, 787-793.
- BORGHESE, A. & DI PALMA, T. M. 2007. Laser-plasma-based vacuum-ultraviolet light source for tunable single-photon ionization. *Appl. Opt.*, 46, 4948-4953.
- BOUR, P., KUBELKA, J. & KEIDERLING, T. A. 2000. Simulations of oligopeptide vibrational CD: Effects of isotopic labeling. *Biopolymers*, 53, 380-395.
- BOYLE, M. J., RICHARDS, J. S., GILSON, P. R., CHAI, W. & BEESON, J. G. 2010. Interactions with heparin-like molecules during erythrocyte invasion by *Plasmodium falciparum* merozoites.
- BRANDT, K. D., SKINNER, M. & COHEN, A. S. 1974. Characterization of the mucopolysaccharides associated with fractions of guanidine-denatured amyloid fibrils. *Clinica Chimica Acta*, 55, 295-305.

- BRUSSAARD, P. J. & VAN DE HULST, H. C. 1962. Approximation Formulas for Nonrelativistic Bremsstrahlung and Average Gaunt Factors for a Maxwellian Electron Gas. *Reviews of Modern Physics*, 34, 507-520.
- BUCKINGHAM, A. D. 1994. Introductory lecture. The theoretical background to vibrational optical activity. *Faraday Discussions*, 99, 1-12.
- BUDKA, H. 2003. Neuropathology of prion diseases. *British Medical Bulletin*, 66, 121-130.
- BÜLOW, H. E., TJOE, N., TOWNLEY, R. A., DIDIANO, D., VAN KUPPEVELT, T. H. & HOBERT, O. Extracellular Sugar Modifications Provide Instructive and Cell-Specific Information for Axon-Guidance Choices. *Current Biology*, 18, 1978-1985.
- BUNKIN, F. V., KRASYUK, I. K., MARCHENKO, V. M., PASHININ, P. P. & PROKHOROV, A. M. 1971. Structure of a Spark Produced by a Picosecond Laser Pulse Focused in a Gas. *Soviet Physics JETP*, 33, 717.
- BUSCHER, H. T., TOMLINSON, R. G. & DAMON, E. K. 1965. Frequency Dependence of Optically Induced GAS Breakdown. *Physical Review Letters*, 15, 847-849.
- BUTLER, G. S., APTE, S. S., WILLENBROCK, F. & MURPHY, G. 1999. Human Tissue Inhibitor of Metalloproteinases 3 Interacts with Both the N- and C-terminal Domains of Gelatinases A and B: REGULATION BY POLYANIONS. *Journal of Biological Chemistry*, 274, 10846-10851.
- CAPILA, I., HERNÁIZ, M. A. J., MO, Y. D., MEALY, T. R., CAMPOS, B., DEDMAN, J. R., LINHARDT, R. J. & SEATON, B. A. 2001. Annexin V–Heparin Oligosaccharide Complex Suggests Heparan Sulfate–Mediated Assembly on Cell Surfaces. *Structure*, 9, 57-64.
- CAPILA, I., VANDERNOOT, V. A., MEALY, T. R., SEATON, B. A. & LINHARDT, R. J. 1999. Interaction of heparin with annexin V. *FEBS Letters*, 446, 327-330.
- CARLSSON, P., PRESTO, J., SPILLMANN, D., LINDAHL, U. & KJELLÉN, L. 2008. Heparin/Heparan Sulfate Biosynthesis: PROCESSIVE FORMATION OF N-SULFATED DOMAINS. *Journal of Biological Chemistry*, 283, 20008-20014.
- CASTELLOT, J. J., HOOVER, R. L., HARPER, P. A. & KARNOVSKY, M. J. 1985. Heparin and glomerular epithelial cell-secreted heparin-like species inhibit mesangial-cell proliferation. *The American Journal of Pathology*, 120, 427-435.
- CHAN, C. H., MOODY, C. D. & MCKNIGHT, W. B. 1973. Significant loss mechanisms in gas breakdown at 10.6  $\mu$ m. *Journal of Applied Physics*, 44, 1179-1188.
- CHAN, H. H., LESLIE, B. A., STAFFORD, A. R., ROBERTS, R. S., AL-ASWAD, N. N., FREDENBURGH, J. C. & WEITZ, J. I. 2012. By Increasing the Affinity of Heparin for Fibrin, Zn<sup>2+</sup> Promotes the Formation of a Ternary Heparin–Thrombin–Fibrin Complex That Protects Thrombin from Inhibition by Antithrombin. *Biochemistry*, 51, 7964-7973.
- CHAN, R. & CHEN, V. 2001. The effects of electrolyte concentration and pH on protein aggregation and deposition: critical flux and constant flux membrane filtration. *Journal of Membrane Science*, 185, 177-192.
- CHEN, B.-L., ARAKAWA, T., MORRIS, C., KENNEY, W., WELLS, C. & PITT, C. 1994. Aggregation Pathway of Recombinant Human Keratinocyte Growth Factor and Its Stabilization. *Pharmaceutical Research*, 11, 1581-1587.

- CHEN, Y., MAGUIRE, T., HILEMAN, R. E., FROMM, J. R., ESKO, J. D., LINHARDT, R. J. & MARKS, R. M. 1997. Dengue virus infectivity depends on envelope protein binding to target cell heparan sulfate. *Nat Med*, 3, 866-871.
- CHEN, Y. L., LEWIS, J. W. L. & PARIGGER, C. 2000. Spatial and temporal profiles of pulsed laser-induced air plasma emissions. *Journal of Quantitative Spectroscopy and Radiative Transfer*, 67, 91-103.
- CHENG, H., SUKAL, S., DENG, H., LEYH, T. S. & CALLENDER, R. 2001. Vibrational Structure of GDP and GTP Bound to RAS: An Isotope-Edited FTIR Study†. *Biochemistry*, 40, 4035-4043.
- CHEVALIER, F., ANGULO, J., LUCAS, R., NIETO, PEDRO M. & MARTÍN-LOMAS, M. 2002. The Heparin–Ca<sup>2+</sup> Interaction: Structure of the Ca<sup>2+</sup> Binding Site. *European Journal of Organic Chemistry*, 2002, 2367-2376.
- CHEVALIER, F., LUCAS, R., ANGULO, J., MARTIN-LOMAS, M. & NIETO, P. M. 2004. The heparin–Ca<sup>2+</sup> interaction: the influence of the O-sulfation pattern on binding. *Carbohydrate Research*, 339, 975-983.
- CHUNG, S. W., BAE, S. M., LEE, M., AL-HILAL, T. A., LEE, C. K., KIM, J. K., KIM, I.-S., KIM, S. Y. & BYUN, Y. 2015. LHT7, a chemically modified heparin, inhibits multiple stages of angiogenesis by blocking VEGF, FGF2 and PDGF-B signaling pathways. *Biomaterials*, 37, 271-278.
- CHYLEK, P., JARZEMBSKI, M. A., SRIVASTAVA, V. & PINNICK, R. G. 1990a. Pressure dependence of the laser-induced breakdown thresholds of gases and droplets. *Applied Optics*, 29, 2303-2306.
- CHYLEK, P., JARZEMBSKI, M. A., SRIVASTAVA, V. & PINNICK, R. G. 1990b. Pressure dependence of the laser-induced breakdown thresholds of gases and droplets. *Appl. Opt.*, 29, 2303-2306.
- COHLBERG, J. A., LI, J., UVERSKY, V. N. & FINK, A. L. 2002. Heparin and Other Glycosaminoglycans Stimulate the Formation of Amyloid Fibrils from  $\alpha$ -Synuclein in Vitro†. *Biochemistry*, 41, 1502-1511.
- COLOMBRES, M., HENRÍQUEZ, J. P., REIG, G. F., SCHEU, J., CALDERÓN, R., ALVAREZ, A., BRANDAN, E. & INESTROSA, N. C. 2008. Heparin activates Wnt signaling for neuronal morphogenesis. *Journal of Cellular Physiology*, 216, 805-815.
- COPELAND, R., BALASUBRAMANIAM, A., TIWARI, V., ZHANG, F., BRIDGES, A., LINHARDT, R. J., SHUKLA, D. & LIU, J. 2008. Using a 3-O-Sulfated Heparin Octasaccharide To Inhibit the Entry of Herpes Simplex Virus Type 1†. *Biochemistry*, 47, 5774-5783.
- CRAXTON, R. S., ANDERSON, K. S., BOEHLY, T. R., GONCHAROV, V. N., HARDING, D. R., KNAUER, J. P., MCCRORY, R. L., MCKENTY, P. W., MEYERHOFER, D. D., MYATT, J. F., SCHMITT, A. J., SETHIAN, J. D., SHORT, R. W., SKUPSKY, S., THEOBALD, W., KRUER, W. L., TANAKA, K., BETTI, R., COLLINS, T. J. B., DELETTREZ, J. A., HU, S. X., MAROZAS, J. A., MAXIMOV, A. V., MICHEL, D. T., RADHA, P. B., REGAN, S. P., SANGSTER, T. C., SEKA, W., SOLODOV, A. A., SOURES, J. M., STOECKL, C. & ZUEGEL, J. D. 2015. Direct-drive inertial confinement fusion: A review. *Physics of Plasmas*, 22, 110501.
- CROMWELL, M. E. M., HILARIO, E. & JACOBSON, F. 2006. Protein aggregation and bioprocessing. *The AAPS Journal*, 8, E572-E579.

- CUNNANE, G. & WHITEHEAD, A. S. 1999. Amyloid precursors and amyloidosis in rheumatoid arthritis. *Best Practice & Research Clinical Rheumatology*, 13, 615-628.
- D'YACHKOV, L. G., KURILENKOV, Y. K. & VITEL, Y. Radiative continua of noble gas plasmas. *Journal of Quantitative Spectroscopy and Radiative Transfer*, 59, 53-64.
- DAIBER, J. W. & WINANS, J. G. 1968. Radiation from Laser-Heated Plasmas in Nitrogen and Argon. *Journal of the Optical Society of America*, 58, 76-79.
- DAMON, E. K. & TOMLINSON, R. G. 1963. Observation of Ionization of Gases by a Ruby Laser. *Applied Optics*, 2, 546-546.
- DAVIS, J. P., SMITH, A. L., GIRANDA, C. & SQUICCIARINI, M. 1991. Laser-induced plasma formation in Xe, Ar, N<sub>2</sub>, and O<sub>2</sub> at the first four Nd:YAG harmonics. *Appl. Opt.*, 30, 4358-4364.
- DE MICHELIS, C. 1970. Gas breakdown produced by a train of mode-locked laser pulses. *Optics Communications*, 2, 255-256.
- DEN ENGELSMAN, J., GARIDEL, P., SMULDERS, R., KOLL, H., SMITH, B., BASSARAB, S., SEIDL, A., HAINZL, O. & JISKOOT, W. 2011. Strategies for the Assessment of Protein Aggregates in Pharmaceutical Biotech Product Development. *Pharmaceutical Research*, 28, 920-933.
- DENG, H. & CALLENDER, R. 1999. [8] Raman spectroscopic studies of the structures, energetics and bond distortions of substrates bound to enzymes. *Methods in Enzymology*. Academic Press.
- DESAI, U. R., PETITOU, M., BJÖRK, I. & OLSON, S. T. 1998. Mechanism of Heparin Activation of Antithrombin: ROLE OF INDIVIDUAL RESIDUES OF THE PENTASACCHARIDE ACTIVATING SEQUENCE IN THE RECOGNITION OF NATIVE AND ACTIVATED STATES OF ANTITHROMBIN. *Journal of Biological Chemistry*, 273, 7478-7487.
- DEWHURST, R. J. 1978. Comparative data on molecular gas breakdown thresholds in high laser-radiation fields. *Journal of Physics D: Applied Physics*, 11, L191.
- DEWHURST, R. J., PERT, G. J. & RAMSDEN, S. A. 1974. Laser-induced breakdown in the rare gases using picosecond Nd:glass laser pulses. *Journal of Physics B: Atomic and Molecular Physics*, 7, 2281.
- DIETZ, A. A. & RUBINSTEIN, H. M. 1973. Serum gold. I. Estimation by atomic absorption spectroscopy. *Annals of the Rheumatic Diseases*, 32, 124-127.
- DIOUMAEV, A. K. 2001. Infrared Methods for Monitoring the Protonation State of Carboxylic Amino Acids in the Photocycle of Bacteriorhodopsin. *Biochemistry (Moscow)*, 66, 1269-1276.
- DOMBROWSKI, C., SONG, S. J., CHUAN, P., LIM, X., SUSANTO, E., SAWYER, A. A., WOODRUFF, M. A., HUTMACHER, D. W., NURCOMBE, V. & COOL, S. M. 2008. Heparan Sulfate Mediates the Proliferation and Differentiation of Rat Mesenchymal Stem Cells. *Stem Cells and Development*, 18, 661-670.
- DYER, R. B., GAI, F., WOODRUFF, W. H., GILMANSHIN, R. & CALLENDER, R. H. 1998. Infrared Studies of Fast Events in Protein Folding. *Accounts of Chemical Research*, 31, 709-716.
- EANES, E. D. & GLENNER, G. G. 1968. X-RAY DIFFRACTION STUDIES ON AMYLOID FILAMENTS. *Journal of Histochemistry & Cytochemistry*, 16, 673-677.



- ELLIOTT, A. & AMBROSE, E. J. 1950. Structure of Synthetic Polypeptides. *Nature*, 165, 921-922.
- ENGELHARDT, H., KRÄMER, M. & WALDHOFF, H. 1990. Enhancement of protein detection by microwave-induced hydrolysis and OPA derivatization. *Chromatographia*, 30, 523-526.
- EVANS, L. R. & MORGAN, C. G. 1968. Multiple Collinear Laser-produced Sparks in Gases. *Nature*, 219, 712-713.
- EVANS, L. R. & MORGAN, C. G. 1969. Intensity distribution of focussed laser beams in bio-medical studies. *Physics in Medicine and Biology*, 14, 205.
- FABIAN, H., MANTSCH, H. H. & SCHULTZ, C. P. 1999. Two-dimensional IR correlation spectroscopy: Sequential events in the unfolding process of the  $\lambda$  Cro-V55C repressor protein. *Proceedings of the National Academy of Sciences*, 96, 13153-13158.
- FERRO, D. R., PROVASOLI, A., RAGAZZI, M., CASU, B., TORRI, G., BOSSENNEC, V., PERLY, B., SINAÏ, P., PETITOU, M. & CHOAY, J. 1990. Conformer populations of I-iduronic acid residues in glycosaminoglycan sequences. *Carbohydrate Research*, 195, 157-167.
- FERROLINO, M. C., ZHURAVLEVA, A., BUDYAK, I. L., KRISHNAN, B. & GIERASCH, L. M. 2013. A delicate balance between functionally required flexibility and aggregation risk in a  $\beta$ -rich protein. *Biochemistry*, 52, 8843-8854.
- FEYZI, E., LUSTIG, F., FAGER, G., SPILLMANN, D., LINDAHL, U. & SALMIVIRTA, M. 1997. Characterization of Heparin and Heparan Sulfate Domains Binding to the Long Splice Variant of Platelet-derived Growth Factor A Chain. *Journal of Biological Chemistry*, 272, 5518-5524.
- FEYZI, E., SALDEEN, T., LARSSON, E., LINDAHL, U. & SALMIVIRTA, M. 1998. Age-dependent Modulation of Heparan Sulfate Structure and Function. *Journal of Biological Chemistry*, 273, 13395-13398.
- FIGADERE, B., DEVLIN, F. J., MILLAR, J. G. & STEPHENS, P. J. 2008. Determination of the absolute configuration of the sex pheromone of the obscure mealybug by vibrational circular dichroism analysis. *Chemical Communications*, 1106-1108.
- FINNEY, L. A. & O'HALLORAN, T. V. 2003. Transition Metal Speciation in the Cell: Insights from the Chemistry of Metal Ion Receptors. *Science*, 300, 931-936.
- FLINT, N., COVE, F. L. & EVANS, G. S. 1994. Heparin stimulates the proliferation of intestinal epithelial cells in primary culture. *Journal of Cell Science*, 107, 401-411.
- FLORENCE, T. M. 1980. Degradation of protein disulphide bonds in dilute alkali. *Biochemical Journal*, 189, 507-520.
- FOMENKOV, I. V., BÖWERING, N., RETTIG, C. L., MELNYCHUK, S. T., OLIVER, I. R., HOFFMAN, J. R., KHODYKIN, O. V., NESS, R. M. & PARTLO, W. N. 2004. EUV discharge light source based on a dense plasma focus operated with positive and negative polarity. *Journal of Physics D: Applied Physics*, 37, 3266.
- FORSTEN-WILLIAMS, K., CHU, C. L., FANNON, M., BUCZEK-THOMAS, J. A. & NUGENT, M. A. 2008. Control of Growth Factor Networks by Heparan Sulfate Proteoglycans. *Annals of biomedical engineering*, 36, 2134-2148.
- FREDENBURGH, J. C., LESLIE, B. A., STAFFORD, A. R., LIM, T., CHAN, H. H. & WEITZ, J. I. 2013. Zn<sup>2+</sup> Mediates High Affinity Binding of Heparin to the  $\alpha$ C Domain of Fibrinogen. *Journal of Biological Chemistry*, 288, 29394-29402.

- FREDERICKSON, C. J., SUH, S. W., SILVA, D., FREDERICKSON, C. J. & THOMPSON, R. B. 2000. Importance of Zinc in the Central Nervous System: The Zinc-Containing Neuron. *The Journal of Nutrition*, 130, 1471S-1483S.
- FREEDMAN, T. B., CAO, X., YOUNG, D. A. & NAFIE, L. A. 2002. Density Functional Theory Calculations of Vibrational Circular Dichroism in Transition Metal Complexes: Identification of Solution Conformations and Mode of Chloride Ion Association for (+)-Tris(ethylenediaminato)cobalt(III)<sup>†</sup>. *The Journal of Physical Chemistry A*, 106, 3560-3565.
- FREEDMAN, T. B., NAFIE, L. A. & KEIDERLING, T. A. 1995. Vibrational optical activity of oligopeptides. *Biopolymers*, 37, 265-279.
- FRIEDLAND, L. 1975. Quantum aspects of laser-induced breakdown in argon. *Physical Review A*, 12, 2024.
- FUH, K. 2011. Modern-day challenges in therapeutic protein production. *Expert Review of Proteomics*, 8, 563-564.
- G.S. VORONOV., N. B. D. 1965. Ionisation of the Xenon Atom by the Electric Field of Ruby Laser Emission. *JETP Letters*, 1, 66.
- GAMAL, Y. E. & HARITH, M. A. 1983. Secondary ionisation processes in laser-induced cascade ionisation. *Journal of Physics D: Applied Physics*, 16, 1901.
- GAUNT, J. A. 1930. Continuous Absorption. *Philosophical Transactions of the Royal Society of London. Series A, Containing Papers of a Mathematical or Physical Character*, 229, 163-204.
- GIBBS, J. W. 1882. *American Journal of Science*, 23.
- GIGER, K., VANAM, R. P., SEYREK, E. & DUBIN, P. L. 2008. Suppression of Insulin Aggregation by Heparin. *Biomacromolecules*, 9, 2338-2344.
- GILLMORE, J. D., LACHMANN, H. J., ROWCZENIO, D., GILBERTSON, J. A., ZENG, C.-H., LIU, Z.-H., LI, L.-S., WECHALEKAR, A. & HAWKINS, P. N. 2009. Diagnosis, Pathogenesis, Treatment, and Prognosis of Hereditary Fibrinogen A $\alpha$ -Chain Amyloidosis. *Journal of the American Society of Nephrology*, 20, 444-451.
- GONZÁLEZ-IGLESIAS, R., PAJARES, M. A. A., OCAL, C., CARLOS ESPINOSA, J., OESCH, B. & GASSET, M. A. 2002. Prion Protein Interaction with Glycosaminoglycan Occurs with the Formation of Oligomeric Complexes Stabilized by Cu(II) Bridges. *Journal of Molecular Biology*, 319, 527-540.
- GÖPPERT-MAYER, M. 1931. Über Elementarakte mit zwei Quantensprüngen. *Annalen der Physik*, 401, 273-294.
- GRANT, D., LONG, W. F., MOFFAT, C. F. & WILLIAMSON, F. B. 1992a. Cu(2+)-heparin interaction studied by polarimetry. *Biochem J*, 283, 243-246.
- GRANT, D., LONG, W. F. & WILLIAMSON, F. B. 1987. Infrared spectroscopy of heparin-cation complexes. *Biochemical Journal*, 244, 143-149.
- GRANT, D., LONG, W. F. & WILLIAMSON, F. B. 1992b. A potentiometric titration study of the interaction of heparin with metal cations. *Biochem J*, 285, 477-280.
- GRANT, G. T., MORRIS, E. R., REES, D. A., SMITH, P. J. C. & THOM, D. 1973. Biological interactions between polysaccharides and divalent cations: The egg-box model. *FEBS Letters*, 32, 195-198.
- GREENFIELD, N. J. 2006. Using circular dichroism collected as a function of temperature to determine the thermodynamics of protein unfolding and binding interactions. *Nature protocols*, 1, 2527-2535.
- GRIEM, H. R. 1964. *Principals of Plasma Spectroscopy*, New York, McGraw-Hill.

- GRIFFITH, M. J. 1983. Heparin-catalyzed inhibitor/protease reactions: kinetic evidence for a common mechanism of action of heparin. *Proceedings of the National Academy of Sciences of the United States of America*, 80, 5460-5464.
- GUIMOND, S., MACCARANA, M., OLWIN, B. B., LINDAHL, U. & RAPRAEGER, A. C. 1993. Activating and inhibitory heparin sequences for FGF-2 (basic FGF). Distinct requirements for FGF-1, FGF-2, and FGF-4. *Journal of Biological Chemistry*, 268, 23906-23914.
- GUPTA, V. P. & KEIDERLING, T. A. 1992. Vibrational CD of the amide II band in some model polypeptides and proteins. *Biopolymers*, 32, 239-248.
- HABUCHI, H., SUZUKI, S., SAITO, T., TAMURA, T., HARADA, T., YOSHIDA, K. & KIMATA, K. 1992. Structure of a heparan sulphate oligosaccharide that binds to basic fibroblast growth factor. *Biochemical Journal*, 285, 805-813.
- HAHN, D. W. & OMENETTO, N. 2010. Laser-Induced Breakdown Spectroscopy (LIBS), Part I: Review of Basic Diagnostics and Plasma—Particle Interactions: Still-Challenging Issues within the Analytical Plasma Community. *Applied Spectroscopy*, 64, 335A-336A.
- HAMRANG, Z., RATTRAY, N. J. W. & PLUEN, A. 2013. Proteins behaving badly: emerging technologies in profiling biopharmaceutical aggregation. *Trends in Biotechnology*, 31, 448-458.
- HAN, W.-G., ELSTNER, M., JALKANEN, K. J., FRAUENHEIM, T. & SUHAI, S. 2000. Hybrid SCC-DFTB/molecular mechanical studies of H-bonded systems and of N-acetyl-(L-Ala)<sub>n</sub>N'-methylamide helices in water solution. *International Journal of Quantum Chemistry*, 78, 459-479.
- HANAFI, M., OMAR, M. M. & GAMAL, Y. E. E. D. 2000. Study of laser-induced breakdown spectroscopy of gases. *Radiation Physics and Chemistry*, 57, 11-20.
- HANSSON, B. A. M., RYMELL, L., BERGLUND, M., HEMBERG, O. E., JANIN, E., THORESEN, J. & HERTZ, H. M. Liquid-xenon-jet laser-plasma source for EUV lithography. 2001. 1-8.
- HANSSON, B. A. M., RYMELL, L., BERGLUND, M., HEMBERG, O. E., JANIN, E., THORESEN, J., MOESSON, S., WALLIN, J. & HERTZ, H. M. Status of the liquid-xenon-jet laser-plasma source for EUV lithography. 2002. 102-109.
- HARILAL, S. S. 2004. Spatial and Temporal Evolution of Argon Sparks. *Appl. Opt.*, 43, 3931-3937.
- HARILAL, S. S., O'SHAY, B. & TILLACK, M. S. 2005a. Debris mitigation in a laser-produced tin plume using a magnetic field. *Journal of Applied Physics*, 98, 036102.
- HARILAL, S. S., O'SHAY, B., TILLACK, M. S. & MATHEW, M. V. 2005b. Spectroscopic characterization of laser-induced tin plasma. *Journal of Applied Physics*, 98, 013306.
- HASSANEIN, A., BURTSEVA, T., ALLAIN, J. P., RICE, B. J., BAKSHI, V. & SAFRONOV, V. Experimental investigation of materials damage induced by hot Xe plasma in EUV lithography devices. 2004. 122-132.
- HASSANEIN, A., SIZYUK, V., SIZYUK, T. & MOROZOV, V. Optimization of EUV laser and discharge devices for high volume manufacturing. Available: <https://engineering.purdue.edu/CMUXE/Publications/Valeryi/SPIE07AH.pdf>.

- HELLWIG, P., MOGI, T., TOMSON, F. L., GENNIS, R. B., IWATA, J., MIYOSHI, H. & MÄNTELE, W. 1999. Vibrational Modes of Ubiquinone in Cytochrome bo<sub>3</sub> from *Escherichia coli* Identified by Fourier Transform Infrared Difference Spectroscopy and Specific <sup>13</sup>C Labeling. *Biochemistry*, 38, 14683-14689.
- HIENERWADEL, R., BOUSSAC, A., BRETON, J., DINER, B. A. & BERTHOMIEU, C. 1997. Fourier Transform Infrared Difference Spectroscopy of Photosystem II Tyrosine D Using Site-Directed Mutagenesis and Specific Isotope Labeling. *Biochemistry*, 36, 14712-14723.
- HIGASHIYAMA, S., ABRAHAM, J. A. & KLAGSBRUN, M. 1993. Heparin-binding EGF-like growth factor stimulation of smooth muscle cell migration: dependence on interactions with cell surface heparan sulfate. *The Journal of Cell Biology*, 122, 933-940.
- HIRANO, Y. & KIDOKORO, Y. 1989. Heparin and heparan sulfate partially inhibit induction of acetylcholine receptor accumulation by nerve in *Xenopus* culture. *The Journal of Neuroscience*, 9, 1555-1561.
- HODGSON, E. R. & MOROÑO, A. 2001. Radiation enhanced dielectric breakdown in insulating gases for NBI systems. *Fusion Engineering and Design*, 56–57, 545-549.
- HOF, M. & MACHAN, R. 2014. *Handbook of Spectroscopy*, Wiley.
- HOGG, P. J. & JACKSON, C. M. 1989. Fibrin monomer protects thrombin from inactivation by heparin-antithrombin III: implications for heparin efficacy. *Proceedings of the National Academy of Sciences of the United States of America*, 86, 3619-3623.
- HOHREITER, V., CARRANZA, J. E. & HAHN, D. W. 2004. Temporal analysis of laser-induced plasma properties as related to laser-induced breakdown spectroscopy. *Spectrochimica Acta Part B: Atomic Spectroscopy*, 59, 327-333.
- HOLLEY, R. J., PICKFORD, C. E., RUSHTON, G., LACAUD, G., GALLAGHER, J. T., KOUSKOFF, V. & MERRY, C. L. R. 2011. Influencing Hematopoietic Differentiation of Mouse Embryonic Stem Cells using Soluble Heparin and Heparan Sulfate Saccharides. *Journal of Biological Chemistry*, 286, 6241-6252.
- HOLLIS, M. J. 1978. Multiphoton ionization and EM field gradient forces. *Optics Communications*, 25, 395-398.
- HORN, M. J., JONES, D. B. & RINGEL, S. J. 1941. ISOLATION OF A NEW SULFUR-CONTAINING AMINO ACID (LANTHIONINE) FROM SODIUM CARBONATE-TREATED WOOL. *Journal of Biological Chemistry*, 138, 141-149.
- HOWELL, A. L., TAYLOR, T. H., MILLER, J. D., GROVEMAN, D. S., ECCLES, E. H. & ZACHARSKI, L. R. 1996. Inhibition of HIV-1 infectivity by low molecular weight heparin. *International Journal of Clinical and Laboratory Research*, 26, 124-131.
- HRICOVÍNI, M. 2015. Solution Structure of Heparin Pentasaccharide: NMR and DFT Analysis. *The Journal of Physical Chemistry B*, 119, 12397-12409.
- HUANG, J., WU, L., YALDA, D., ADKINS, Y., KELLEHER, S., CRANE, M., LONNERDAL, B., RODRIGUEZ, R. & HUANG, N. 2002. Expression of functional recombinant human lysozyme in transgenic rice cell culture. *Transgenic Research*, 11, 229-239.
- HUGHES, A. J., HUSSAIN, R., COSENTINO, C., GUERRINI, M., SILIGARDI, G., YATES, E. A. & RUDD, T. R. 2012. A zinc complex of heparan sulfate destabilises lysozyme

- and alters its conformation. *Biochemical and Biophysical Research Communications*, 425, 794-799.
- HUGHES, T. P. 1975. Plasmas and Laser Light.
- HULETT, M. D., FREEMAN, C., HAMDORF, B. J., BAKER, R. T., HARRIS, M. J. & PARISH, C. R. 1999. Cloning of mammalian heparanase, an important enzyme in tumor invasion and metastasis. *Nat Med*, 5, 803-809.
- IGOR V. FOMENKOV, D. C. B., ALEXANDER N., BYKANOV, A. I. E., WILLIAM N. PARTLO,, DAVID W. MYERS, N. R. B., GEORGIY O. VASCHENKO, OLEH V. KHODYKIN,, JERZY R. HOFFMAN, E. V., L., R. D. S., JUAN A. & CHAVEZ, C. P. C. 2007. Laser-Produced Plasma Source System Development *Emerging Lithographic Technologies XI* [Online]. Available: [http://www.cymer.com/files/pdfs/Technology/2007/Laser\\_Produced\\_Plasma\\_Source\\_System\\_Development.PDF](http://www.cymer.com/files/pdfs/Technology/2007/Laser_Produced_Plasma_Source_System_Development.PDF).
- IKEHATA, A., HIGASHI, N. & OZAKI, Y. 2008. Direct observation of the absorption bands of the first electronic transition in liquid H<sub>2</sub>O and D<sub>2</sub>O by attenuated total reflectance far-UV spectroscopy. *The Journal of Chemical Physics*, 129, 234510.
- INTERNATIONAL QUANTUM ELECTRONICS, C. 1964. *Quantum electronics; proceedings of the third international congress. Electronique quantique; comptes-rendus de la 3e conference internationale, Paris. [By] P. Grivet [and] N. Bloembergen*, Paris, New York, Dunod; Columbia University Press.
- IRELAND, C. L. M. & MORGAN, C. G. 1974. Gas breakdown by single similar 20 ps, 1.06  $\mu$ m and 0.53  $\mu$ m laser pulses. *Journal of Physics D: Applied Physics*, 7, L87.
- IRELAND, C. L. M., YI, A., AARON, J. M. & MORGAN, C. G. 1974. Focal-length dependence of air breakdown by a 20-psec laser pulse. *Applied Physics Letters*, 24, 175-177.
- IRIE, A., YATES, E. A., TURNBULL, J. E. & HOLT, C. E. 2002. Specific heparan sulfate structures involved in retinal axon targeting. *Development*, 129, 61-70.
- IRWIN, D. J., LEE, V. M. Y. & TROJANOWSKI, J. Q. 2013. Parkinson's disease dementia: convergence of  $\alpha$ -synuclein, tau and amyloid- $\beta$  pathologies. *Nature reviews. Neuroscience*, 14, 626-636.
- ISHITSUKA, R., KOJIMA, K., UTSUMI, H., OGAWA, H. & MATSUMOTO, I. 1998. Glycosaminoglycan Binding Properties of Annexin IV, V, and VI. *Journal of Biological Chemistry*, 273, 9935-9941.
- JACKSON, R. L., BUSCH, S. J. & CARDIN, A. D. 1991. Glycosaminoglycans: molecular properties, protein interactions, and role in physiological processes. *Physiological Reviews*, 71, 481-539.
- JOSHI, S. B., KAMERZELL, T. J., MCNOWN, C. & MIDDAUGH, C. R. 2008. The interaction of heparin/polyanions with bovine, porcine, and human growth hormone. *Journal of Pharmaceutical Sciences*, 97, 1368-1385.
- JOUBERT, M. K., LUO, Q., NASHED-SAMUEL, Y., WYPYCH, J. & NARHI, L. O. 2011. Classification and Characterization of Therapeutic Antibody Aggregates. *Journal of Biological Chemistry*, 286, 25118-25133.
- KADIMA, W., ØGENDAL, L., BAUER, R., KAARSHOLM, N., BRODERSEN, K., HANSEN, J. F. & PORTING, P. 2004. The influence of ionic strength and pH on the aggregation properties of zinc-free insulin studied by static and dynamic laser light scattering. *Biopolymers*, 33, 1643-1657.

- KALLAPUR, S. G. & AKESON, R. A. 1992. The neural cell adhesion molecule (NCAM) heparin binding domain binds to cell surface heparan sulfate proteoglycans. *Journal of Neuroscience Research*, 33, 538-548.
- KAN, M., WANG, F., KAN, M., TO, B., GABRIEL, J. L. & MCKEEHAN, W. L. 1996. Divalent Cations and Heparin/Heparan Sulfate Cooperate to Control Assembly and Activity of the Fibroblast Growth Factor Receptor Complex. *Journal of Biological Chemistry*, 271, 26143-26148.
- KARIYA, Y., YOSHIDA, K., MORIKAWA, K., TAWADA, A., MIYAZONO, H., KIKUCHI, H. & TOKUYASU, K. 1992. Preparation of unsaturated disaccharides by eliminative cleavage of heparin and heparan sulfate with heparitinases. *Comparative Biochemistry and Physiology Part B: Comparative Biochemistry*, 103, 473-479.
- KARRAN, E., MERCKEN, M. & STROOPER, B. D. 2011. The amyloid cascade hypothesis for Alzheimer's disease: an appraisal for the development of therapeutics. *Nat Rev Drug Discov*, 10, 698-712.
- KARZAS, W. J. & LATTER, R. 1961. Electron Radiative Transitions in a Coulomb Field. *Astrophysical Journal Supplement*, 6.
- KEIDERLING, T. A. 1986. Vibrational CD of biopolymers. *Nature*, 322, 851-852.
- KEIDERLING, T. A. 2002. Protein and peptide secondary structure and conformational determination with vibrational circular dichroism. *Current Opinion in Chemical Biology*, 6, 682-688.
- KEIDERLING, T. A. & XU, Q. 2002. Unfolded peptides and proteins studied with infrared absorption and vibrational circular dichroism spectra. *Advances in Protein Chemistry*. Academic Press.
- KLÄHN, M., SCHLITTER, J. & GERWERT, K. 2005. Theoretical IR spectroscopy based on QM/MM calculations provides changes in charge distribution, bond lengths, and bond angles of the GTP ligand induced by the Ras-protein. *Biophysical Journal*, 88, 3829-3844.
- KNAPP-MOHAMMADY, M., JALKANEN, K. J., NARDI, F., WADE, R. C. & SUHAI, S. 1999. L-Alanyl-L-alanine in the zwitterionic state: structures determined in the presence of explicit water molecules and with continuum models using density functional theory. *Chemical Physics*, 240, 63-77.
- KOECHNER, W. 1970. Thermal Lensing in a Nd:YAG Laser Rod. *Appl. Opt.*, 9, 2548-2553.
- KONG, J. & YU, S. 2007. Fourier Transform Infrared Spectroscopic Analysis of Protein Secondary Structures. *Acta Biochimica et Biophysica Sinica*, 39, 549-559.
- KOTT, L., PETROVIC, J., PHELPS, D., ROGINSKI, R. & SCHUBERT, J. 2014. Determination of a Low-Level Percent Enantiomer of a Compound with No Ultraviolet Chromophore Using Vibrational Circular Dichroism (VCD): Enantiomeric Purity by VCD of a Compound with Three Chiral Centers. *Applied Spectroscopy*, 68, 1108-1115.
- KRASUYUK, I. K., PASHININ, P. P. & PROKHOROV, A. M. 1969. Investigation of Breakdown in N<sub>2</sub> Under the Influence of a picosecond Ruby Laser. *JETP Letters*, 9, 354.
- KRIMM, S. & BANDEKAR, J. 1986. Vibrational Spectroscopy and Conformation of Peptides, Polypeptides, and Proteins. In: C.B. ANFINSEN, J. T. E. & FREDERIC, M. R. (eds.) *Advances in Protein Chemistry*. Academic Press.

- KROESEN, G. M. W., DEN BOER, J. H. W. G., BOUFENDI, L., VIVET, F., KHOULI, M., BOUCHOULE, A. & DE HOOG, F. J. 1996. In situ infrared absorption spectroscopy of dusty plasmas. *Journal of Vacuum Science & Technology A: Vacuum, Surfaces, and Films*, 14, 546-549.
- KUBELKA, J. & KEIDERLING, T. A. 2001a. Ab Initio Calculation of Amide Carbonyl Stretch Vibrational Frequencies in Solution with Modified Basis Sets. 1. N-Methyl Acetamide. *The Journal of Physical Chemistry A*, 105, 10922-10928.
- KUBELKA, J. & KEIDERLING, T. A. 2001b. Differentiation of  $\beta$ -Sheet-Forming Structures: Ab Initio-Based Simulations of IR Absorption and Vibrational CD for Model Peptide and Protein  $\beta$ -Sheets. *Journal of the American Chemical Society*, 123, 12048-12058.
- KUBELKA, J., SILVA, R. A. G. D. & KEIDERLING, T. A. 2002. Discrimination between Peptide 310- and  $\alpha$ -Helices. Theoretical Analysis of the Impact of  $\alpha$ -Methyl Substitution on Experimental Spectra. *Journal of the American Chemical Society*, 124, 5325-5332.
- KUHN, W. 1930. The physical significance of optical rotatory power. *Transactions of the Faraday Society*, 26, 293-308.
- LAPIERRE, F., HOLME, K., LAM, L., TRESSLER, R. J., STORM, N., WEE, J., STACK, R. J., CASTELLOT, J. & TYRRELL, D. J. 1996. Chemical modifications of heparin that diminish its anticoagulant but preserve its heparanase-inhibitory, angiostatic, anti-tumor and anti-metastatic properties. *Glycobiology*, 6, 355-366.
- LÉGARÉ, F., LEE, K. F., LITVINYUK, I. V., DOOLEY, P. W., WESOŁOWSKI, S. S., BUNKER, P. R., DOMBI, P., KRAUSZ, F., BANDRAUK, A. D., VILLENEUVE, D. M. & CORKUM, P. B. 2005. Laser Coulomb-explosion imaging of small molecules. *Physical Review A*, 71, 013415.
- LENCIONI, D. E. 1973. The effect of dust on 10.6- $\mu$  m laser-induced air breakdown. *Applied Physics Letters*, 23, 12-14.
- LENCIONI, D. E. 1974. Laser-induced air breakdown for 1.06- $\mu$  m radiation. *Applied Physics Letters*, 25, 15-17.
- LEWIS, A. B. 1939. The Effects of Irradiation, Humidity and Sphere Material on the Sparkover Voltage of the Two-Centimeter Sphere Gap. *Journal of Applied Physics*, 10, 573-577.
- LI, Y. & YU, F. T. S. 1989. Intensity distribution near the focus of an apertured focused gaussian beam. *Optics Communications*, 70, 1-7.
- LI, Z., HOU, W.-S. & BRÖMME, D. 2000. Collagenolytic Activity of Cathepsin K Is Specifically Modulated by Cartilage-Resident Chondroitin Sulfate $\dagger$ . *Biochemistry*, 39, 529-536.
- LIN, X., BUFF, E. M., PERRIMON, N. & MICHELSON, A. M. 1999. Heparan sulfate proteoglycans are essential for FGF receptor signaling during *Drosophila* embryonic development. *Development*, 126, 3715-3723.
- LINDAHL, U., BÄCKSTRÖM, G., THUNBERG, L. & LEDER, I. G. 1980. Evidence for a 3-O-sulfated D-glucosamine residue in the antithrombin-binding sequence of heparin. *Proceedings of the National Academy of Sciences of the United States of America*, 77, 6551-6555.
- LINDAHL, U., THUNBERG, L., BÄCKSTRÖM, G., RIESENFELD, J., NORDLING, K. & BJÖRK, I. 1984. Extension and structural variability of the antithrombin-binding sequence in heparin. *Journal of Biological Chemistry*, 259, 12368-12376.

- LIU, Z. & PERLIN, A. S. 1992. Regioselectivity in the sulfation of some chemically-modified heparins, and observations on their cation-binding characteristics. *Carbohydrate Research*, 236, 121-133.
- LOMPRE, L. A., MAINFRAY, G., MANUS, C. & THEBAULT, J. 1977. Multiphoton ionization of rare gases by a tunable-wavelength 30-psec laser pulse at 1.06  $\mu\text{m}$ . *Physical Review A*, 15, 1604-1612.
- LOO, B.-M., KREUGER, J., JALKANEN, M., LINDAHL, U. & SALMIVIRTA, M. 2001. Binding of Heparin/Heparan Sulfate to Fibroblast Growth Factor Receptor 4. *Journal of Biological Chemistry*, 276, 16868-16876.
- LORTAT-JACOB, H., GROSDIDIER, A. & IMBERTY, A. 2002. Structural diversity of heparan sulfate binding domains in chemokines. *Proceedings of the National Academy of Sciences of the United States of America*, 99, 1229-1234.
- LOWISCH, M., KUERZ, P., MANN, H.-J., NATT, O. & THUERING, B. Optics for EUV production. 2010. 763603-763603-11.
- LYON, M., DEAKIN, J. A., MIZUNO, K., NAKAMURA, T. & GALLAGHER, J. T. 1994. Interaction of hepatocyte growth factor with heparan sulfate. Elucidation of the major heparan sulfate structural determinants. *Journal of Biological Chemistry*, 269, 11216-23.
- LYON, M. & GALLAGHER, J. T. 1998. Bio-specific sequences and domains in heparan sulphate and the regulation of cell growth and adhesion. *Matrix Biology*, 17, 485-493.
- MACCARANA, M., CASU, B. & LINDAHL, U. 1993. Minimal sequence in heparin/heparan sulfate required for binding of basic fibroblast growth factor. *Journal of Biological Chemistry*, 268, 23898-23905.
- MAGNUS, J. H., STENSTAD, T., HUSBY, G. & KOLSET, S. O. 1992. Isolation and partial characterization of heparan sulphate proteoglycans from human hepatic amyloid. *Biochem J*, 288 ( Pt 1), 225-31.
- MAKER, P. D., TERHUNE, R. W. & SAVAGE, C. M. Optical Third Harmonic Generation. *In: GRIVET, P. & BLOEMBERGEN, N., eds. Quantum Electronics*, 1964. Dunod Éditeur, Paris, and Columbia University Press, New York, 1559.
- MARCHETTI, M., TRYBALA, E., SUPERTI, F., JOHANSSON, M. & BERGSTRÖM, T. 2004. Inhibition of herpes simplex virus infection by lactoferrin is dependent on interference with the virus binding to glycosaminoglycans. *Virology*, 318, 405-413.
- MARCUM, J. A., MCKENNEY, J. B., GALLI, S. J., JACKMAN, R. W. & ROSENBERG, R. D. 1986. *Anticoagulant active heparin-like molecules from mast cell-deficient mice*.
- MARTIN, E. A. & MANDEL, L. 1976. Electron energy spectrum in laser-induced multiphoton ionization of atoms. *Applied Optics*, 15, 2378-2380.
- MARX, G. 1988. Zinc binding to fibrinogen and fibrin. *Archives of Biochemistry and Biophysics*, 266, 285-288.
- MCGOWAN, D. P., VAN ROON-MOM, W., HOLLOWAY, H., BATES, G. P., MANGIARINI, L., COOPER, G. J. S., FAULL, R. L. M. & SNELL, R. G. 2000. Amyloid-like inclusions in Huntington's disease. *Neuroscience*, 100, 677-680.
- MENEGHETTI, M. C. Z., HUGHES, A. J., RUDD, T. R., NADER, H. B., POWELL, A. K., YATES, E. A. & LIMA, M. A. 2015. Heparan sulfate and heparin interactions with proteins. *Journal of the Royal Society Interface*, 12, 20150589.



- MENG, F.-G., PARK, Y.-D. & ZHOU, H.-M. 2001. Role of proline, glycerol, and heparin as protein folding aids during refolding of rabbit muscle creatine kinase. *The International Journal of Biochemistry & Cell Biology*, 33, 701-709.
- MERLINI, G. & BELLOTTI, V. 2003. Molecular Mechanisms of Amyloidosis. *New England Journal of Medicine*, 349, 583-596.
- MERLINI, G. & BELLOTTI, V. 2005. Lysozyme: A paradigmatic molecule for the investigation of protein structure, function and misfolding. *Clinica Chimica Acta*, 357, 168-172.
- MEYER, I. & TIMM, U. 1972. *Optics Communications*, 6, 339-341.
- MEYERAND, R. G., JR. & HAUGHT, A. F. 1963. Gas Breakdown at Optical Frequencies. *Physical Review Letters*, 11, 401-403.
- MIHALYI, E. 1968. Numerical values of the absorbances of the aromatic amino acids in acid, neutral, and alkaline solutions. *Journal of Chemical & Engineering Data*, 13, 179-182.
- MIYAZAWA, T., SHIMANOUCI, T. & MIZUSHIMA, S. I. 1956. Characteristic Infrared Bands of Monosubstituted Amides. *The Journal of Chemical Physics*, 24, 408-418.
- MOHRI, H., IWAMATSU, A. & OHKUBO, T. Heparin binding sites are located in a 40-kD  $\gamma$ -chain and a 36-kD  $\beta$ -chain fragment isolated from human fibrinogen. *Journal of Thrombosis and Thrombolysis*, 1, 49-54.
- MOHRI, H. & OHKUBO, T. 1993. Fibrinogen Binds to Heparin: The Relationship of the Binding of Other Adhesive Proteins to Heparin. *Archives of Biochemistry and Biophysics*, 303, 27-31.
- MOLINARI, V. G., MOSTACCI, D., ROCCHI, F. & SUMINI, M. 2004. Approximate averaged Gaunt factors for free-free Bremsstrahlung emission from a weakly degenerate plasma. *Journal of Analytical Atomic Spectrometry*, 19, 457-461.
- MOORE, C. E. 1970. Ionisation Potentials and Ionisation Limits Derived From the Analysis of Optical Spectra. In: COMMERCE, U. D. O. (ed.). Washington: Secretary of Commerce.
- MORGAN, C. G. 1975. Laser-induced breakdown of gases. *Reports on Progress in Physics*, 38, 621.
- MORGAN, F., EVANS, L. R. & MORGAN, C. G. 1971. Laser beam induced breakdown in helium and argon. *Journal of Physics D: Applied Physics*, 4, 225.
- MORIO, H., HONDA, Y., TOYODA, H., NAKAJIMA, M., KUROSAWA, H. & SHIRASAWA, T. 2003. EXT gene family member rib-2 is essential for embryonic development and heparan sulfate biosynthesis in *Caenorhabditis elegans*. *Biochemical and Biophysical Research Communications*, 301, 317-323.
- MORRIS, E. R., REES, D. A., SANDERSON, G. R. & THOM, D. 1975. Conformation and circular dichroism of uronic acid residues in glycosides and polysaccharides. *Journal of the Chemical Society, Perkin Transactions 2*, 1418-1425.
- MOSESSON, M. W. 2005. Fibrinogen and fibrin structure and functions. *Journal of Thrombosis and Haemostasis*, 3, 1894-1904.
- MOTA, R., PARAFITA, R., GIULIANI, A., HUBIN-FRANSKIN, M. J., LOURENÇO, J. M. C., GARCIA, G., HOFFMANN, S. V., MASON, N. J., RIBEIRO, P. A., RAPOSO, M. & LIMÃO-VIEIRA, P. 2005. Water VUV electronic state spectroscopy by synchrotron radiation. *Chemical Physics Letters*, 416, 152-159.

- MUHARREM, B., WERNER, A. W., CHRIS, J. L., FRED, A. V. G., GERTJAN, K., GUUS, R. & FRED, B. 2012. Active multilayer mirrors for reflectance tuning at extreme ultraviolet (EUV) wavelengths. *Journal of Physics D: Applied Physics*, 45, 494001.
- MUKHERJEE, D. C., PARK, J. W. & CHAKRABARTI, B. 1978. Optical properties of Cu(II) complexes with heparin and related glycosaminoglycans. *Archives of Biochemistry and Biophysics*, 191, 393-399.
- MULLOY, B. & FORSTER, M. J. 2000. Conformation and dynamics of heparin and heparan sulfate. *Glycobiology*, 10, 1147-1156.
- MULLOY, B., FORSTER, M. J., JONES, C. & DAVIES, D. B. 1993. N.m.r. and molecular-modelling studies of the solution conformation of heparin. *Biochemical Journal*, 293, 849-858.
- MURPHY, J. W., CHO, Y., SACHPATZIDIS, A., FAN, C., HODSDON, M. E. & LOLIS, E. 2007. Structural and Functional Basis of CXCL12 (Stromal Cell-derived Factor-1 $\alpha$ ) Binding to Heparin. *The Journal of biological chemistry*, 282, 10018-10027.
- MUSSELMAN, R. L. 1987. High-efficiency infrared lamp housing. *Journal of Physics E: Scientific Instruments*, 20, 928.
- NAGARAJAN, U., PAKKIRISWAMI, S. & PILLAI, A. B. 2015. Sugar tags and tumorigenesis. *Frontiers in Cell and Developmental Biology*, 3, 69.
- NAHMIA, A. J. & KIBRICK, S. 1964. INHIBITORY EFFECT OF HEPARIN ON HERPES SIMPLEX VIRUS. *Journal of Bacteriology*, 87, 1060-1066.
- NAIDU, M. S. & KAMARAJU, V. 1996. *High Voltage Engineering*, McGraw-Hill.
- NELSON, R., SAWAYA, M. R., BALBIRNIE, M., MADSEN, A. Ø., RIEKEL, C., GROTHE, R. & EISENBERG, D. 2005. Structure of the cross- $\beta$  spine of amyloid-like fibrils. *Nature*, 435, 773-778.
- NEVSKAYA, N. A. & CHIRGADZE, Y. N. 1976. Infrared spectra and resonance interactions of amide-I and II vibrations of  $\alpha$ -helix. *Biopolymers*, 15, 637-648.
- NOGUCHI, T., INOUE, Y. & TANG, X.-S. 1999. Structure of a Histidine Ligand in the Photosynthetic Oxygen-Evolving Complex As Studied by Light-Induced Fourier Transform Infrared Difference Spectroscopy. *Biochemistry*, 38, 10187-10195.
- OLMA, R., MARTIN, J. A., DEL SOCORRO, J. M., GARCIA, O. & TEIJON, J. M. 1996. *Metal Ions in Biology and Medicine*, Paris, John Libbey Eurotxt.
- ORI, A., WILKINSON, M. C. & FERNIG, D. G. 2011. A Systems Biology Approach for the Investigation of the Heparin/Heparan Sulfate Interactome. *Journal of Biological Chemistry*, 286, 19892-19904.
- ORIEL. 2012. Spectral Irradiance. Available: [http://assets.newport.com/webDocuments-EN/images/Light\\_Sources.pdf](http://assets.newport.com/webDocuments-EN/images/Light_Sources.pdf).
- ORLOV, R. Y., SKINDAN, I. B. & TELEGIN, L. S. 1972. Investigation of Breakdown Produced in Dielectrics by Ultrashort Laser Pulses. *Soviet Physics JETP*, 34, 418.
- PACE, C. N., GRIMSLEY, G. R. & SCHOLTZ, J. M. 2009. Protein Ionizable Groups: pK Values and Their Contribution to Protein Stability and Solubility. *Journal of Biological Chemistry*, 284, 13285-13289.
- PACHECO, R., SERRALHEIRO, M. L. M., KARMALI, A. & HARIS, P. I. 2003. Measuring enzymatic activity of a recombinant amidase using Fourier transform infrared spectroscopy. *Analytical Biochemistry*, 322, 208-214.

- PANCOSKA, P., BITTO, E., JANOTA, V., URBANOVA, M., GUPTA, V. P. & KEIDERLING, T. A. 1995. Comparison of and limits of accuracy for statistical analyses of vibrational and electronic circular dichroism spectra in terms of correlations to and predictions of protein secondary structure. *Protein Science*, 4, 1384-1401.
- PARISH, C. R. 2006. The role of heparan sulphate in inflammation. *Nat Rev Immunol*, 6, 633-643.
- PARTHASARATHY, N., GOLDBERG, I. J., SIVARAM, P., MULLOY, B., FLORY, D. M. & WAGNER, W. D. 1994. Oligosaccharide sequences of endothelial cell surface heparan sulfate proteoglycan with affinity for lipoprotein lipase. *Journal of Biological Chemistry*, 269, 22391-22396.
- PATERLINI, M. G., FREEDMAN, T. B. & NAFIE, L. A. 1986. Vibrational circular dichroism spectra of three conformationally distinct states and an unordered state of poly(L-lysine) in deuterated aqueous solution. *Biopolymers*, 25, 1751-1765.
- PATEY, S. J., EDWARDS, E. A., YATES, E. A. & TURNBULL, J. E. 2006. Heparin Derivatives as Inhibitors of BACE-1, the Alzheimer's  $\beta$ -Secretase, with Reduced Activity against Factor Xa and Other Proteases. *Journal of Medicinal Chemistry*, 49, 6129-6132.
- PAULINI, J. & SIMON, G. 1993. A theoretical lower limit for laser power in laser-enhanced arc welding. *Journal of Physics D: Applied Physics*, 26, 1523.
- PEPYS, M. B., HAWKINS, P. N., BOOTH, D. R., VIGUSHIN, D. M., TENNENT, G. A., SOUTAR, A. K., TOTTY, N., NGUYEN, O., BLAKE, C. C. F., TERRY, C. J., FEEST, T. G., ZALIN, A. M. & HSUAN, J. J. 1993. Human lysozyme gene mutations cause hereditary systemic amyloidosis. *Nature*, 362, 553-557.
- PETER, K., SCHWARZ, M., CONRADT, C., NORDT, T., MOSER, M., KÜBLER, W. & BODE, C. 1999. Heparin Inhibits Ligand Binding to the Leukocyte Integrin Mac-1 (CD11b/CD18). *Circulation*, 100, 1533-1539.
- PHUOC, T. X. 2000. Laser spark ignition: experimental determination of laser-induced breakdown thresholds of combustion gases. *Optics Communications*, 175, 419-423.
- PINNICK, R. G., CHYLEK, P., JARZEMBSKI, M., CREEGAN, E., SRIVASTAVA, V., FERNANDEZ, G., PENDLETON, J. D. & BISWAS, A. 1988. Aerosol-induced laser breakdown thresholds: wavelength dependence. *Applied Optics*, 27, 987-996.
- POLAVARAPU, L. P. & ZHAO, C. Vibrational circular dichroism: a new spectroscopic tool for biomolecular structural determination. *Fresenius' Journal of Analytical Chemistry*, 366, 727-734.
- PULLARA, F., EMANUELE, A., PALMA-VITTORELLI, M. B. & PALMA, M. U. Protein Aggregation/Crystallization and Minor Structural Changes: Universal versus Specific Aspects. *Biophysical Journal*, 93, 3271-3278.
- RABENSTEIN, D. L. 2002a. Heparin and heparan sulfate: structure and function. *Natural Product Reports*, 19, 312-331.
- RABENSTEIN, D. L. 2002b. Heparin and heparan sulfate: structure and function. *Nat Prod Rep*, 19, 312-31.
- RABENSTEIN, D. L., ROBERT, J. M. & PENG, J. 1995. Multinuclear magnetic resonance studies of the interaction of inorganic cations with heparin. *Carbohydrate Research*, 278, 239-256.

- RAFFAELE, M. & PETER, F. 2013. The self-assembly, aggregation and phase transitions of food protein systems in one, two and three dimensions. *Reports on Progress in Physics*, 76, 046601.
- RAGAZZI, M., FERRO, D. R., PERLY, B., SINAI, P., PETITOU, M. & CHOAY, J. 1990. Conformation of the pentasaccharide corresponding to the binding site of heparin for antithrombin III. *Carbohydrate Research*, 195, 169-185.
- RAMACHANDRAN, G. & UDGAONKAR, J. B. 2011. Understanding the Kinetic Roles of the Inducer Heparin and of Rod-like Protofibrils during Amyloid Fibril Formation by Tau Protein. *Journal of Biological Chemistry*, 286, 38948-38959.
- RAPAPORT, A., ZHAO, S., XIAO, G., HOWARD, A. & BASS, M. 2002. Temperature Dependence of the 1.06-  $\mu\text{m}$  Stimulated Emission Cross Section of Neodymium in YAG and in GSGG. *Appl. Opt.*, 41, 7052-7057.
- REGT, J. M. D., DIJK, J. V., MULLEN, J. A. M. V. D. & SCHRAM, D. C. 1995. Components of continuum radiation in an inductively coupled plasma. *Journal of Physics D: Applied Physics*, 28, 40.
- REHMAN, I. U., MOVASAGHI, Z. & REHMAN, S. 2012. *Vibrational Spectroscopy for Tissue Analysis*, Taylor & Francis.
- REJ, R. N., HOLME, K. R. & PERLIN, A. S. 1990. Marked stereoselectivity in the binding of copper ions by heparin. Contrasts with the binding of gadolinium and calcium ions. *Carbohydrate Research*, 207, 143-152.
- RICE, K. G. & LINHARDT, R. J. 1989. Study of structurally defined oligosaccharide substrates of heparin and heparan monosulfate lyases. *Carbohydrate Research*, 190, 219-233.
- ROSEN, D. I. & WEYL, G. 1987. Laser-induced breakdown in nitrogen and the rare gases at 0.53 and 0.357  $\mu\text{m}$ . *Journal of Physics D: Applied Physics*, 20, 1264.
- ROSENBERG, R. D. & LAM, L. 1979. Correlation between structure and function of heparin. *Proceedings of the National Academy of Sciences*, 76, 1218-1222.
- ROSENHECK, K. & DOTY, P. 1961. THE FAR ULTRAVIOLET ABSORPTION SPECTRA OF POLYPEPTIDE AND PROTEIN SOLUTIONS AND THEIR DEPENDENCE ON CONFORMATION. *Proceedings of the National Academy of Sciences*, 47, 1775-1785.
- RUDD, T. R., GUIMOND, S. E., SKIDMORE, M. A., DUCHESNE, L., GUERRINI, M., TORRI, G., COSENTINO, C., BROWN, A., CLARKE, D. T., TURNBULL, J. E., FERNIG, D. G. & YATES, E. A. 2007. Influence of substitution pattern and cation binding on conformation and activity in heparin derivatives. *Glycobiology*, 17, 983-993.
- RUDD, T. R., NICHOLS, R. J. & YATES, E. A. 2008a. Selective Detection of Protein Secondary Structural Changes in Solution Protein–Polysaccharide Complexes Using Vibrational Circular Dichroism (VCD). *Journal of the American Chemical Society*, 130, 2138-2139.
- RUDD, T. R., SKIDMORE, M. A., GUIMOND, S. E., GUERRINI, M., COSENTINO, C., EDGE, R., BROWN, A., CLARKE, D. T., TORRI, G., TURNBULL, J. E., NICHOLS, R. J., FERNIG, D. G. & YATES, E. A. 2008b. Site-specific interactions of copper(II) ions with heparin revealed with complementary (SRCD, NMR, FTIR and EPR) spectroscopic techniques. *Carbohydrate Research*, 343, 2184-2193.
- RUSNATI, M., COLTRINI, D., ORESTE, P., ZOPPETTI, G., ALBINI, A., NOONAN, D., DI FAGAGNA, F. D. A., GIACCA, M. & PRESTA, M. 1997. Interaction of HIV-1 Tat

- Protein with Heparin: ROLE OF THE BACKBONE STRUCTURE, SULFATION, AND SIZE. *Journal of Biological Chemistry*, 272, 11313-11320.
- RUSNATI, M., TULIPANO, G., SPILLMANN, D., TANGHETTI, E., ORESTE, P., ZOPPETTI, G., GIACCA, M. & PRESTA, M. 1999. Multiple Interactions of HIV-1 Tat Protein with Size-defined Heparin Oligosaccharides. *Journal of Biological Chemistry*, 274, 28198-28205.
- RUSNATI, M., TULIPANO, G., URBINATI, C., TANGHETTI, E., GIULIANI, R., GIACCA, M., CIOMEI, M., CORALLINI, A. & PRESTA, M. 1998. The Basic Domain in HIV-1 Tat Protein as a Target for Polysulfonated Heparin-mimicking Extracellular Tat Antagonists. *Journal of Biological Chemistry*, 273, 16027-16037.
- RYBICKI, G. B. & LIGHTMAN, A. P. 2004. *Radiative Processes in Astrophysics*, John Wiley and Sons, Inc.
- SABA, H. I., SABA, S. R. & MORELLI, G. A. 1984. Effect of heparin on platelet aggregation. *American Journal of Hematology*, 17, 295-306.
- SAHIN, E., GRILLO, A. O., PERKINS, M. D. & ROBERTS, C. J. 2010. Comparative effects of pH and ionic strength on protein–protein interactions, unfolding, and aggregation for IgG1 antibodies. *J. Pharm. Sci.*, 99, 4830-4848.
- SANDERSON, P. N., HUCKERBY, T. N. & NIEDUSZYNSKI, I. A. 1987. Conformational equilibria of  $\alpha$ -L-iduronate residues in disaccharides derived from heparin. *Biochemical Journal*, 243, 175-181.
- SANDERSON, R. D. 2001. Heparan sulfate proteoglycans in invasion and metastasis. *Seminars in Cell & Developmental Biology*, 12, 89-98.
- SANDERSON, R. D., YANG, Y., SUVA, L. J. & KELLY, T. 2004. Heparan sulfate proteoglycans and heparanase—partners in osteolytic tumor growth and metastasis. *Matrix Biology*, 23, 341-352.
- SARRAZIN, S., LAMANNA, W. C. & ESKO, J. D. 2011. Heparan Sulfate Proteoglycans. *Cold Spring Harbor Perspectives in Biology*, 3.
- SCOPES, R. K. 1974. Measurement of protein by spectrophotometry at 205 nm. *Analytical Biochemistry*, 59, 277-282.
- SEO, Y., SCHENAUER, M. R. & LEARY, J. A. 2011. Biologically relevant metal-cation binding induces conformational changes in heparin oligosaccharides as measured by ion mobility mass spectrometry. *International Journal of Mass Spectrometry*, 303, 191-198.
- SHAO, C., ZHANG, F., KEMP, M. M., LINHARDT, R. J., WAISMAN, D. M., HEAD, J. F. & SEATON, B. A. 2006. Crystallographic Analysis of Calcium-dependent Heparin Binding to Annexin A2. *The Journal of biological chemistry*, 281, 31689-31695.
- SHUGAR, D. & FOX, J. J. 1952. Spectrophotometric studies of nucleic acid derivatives and related compounds as a function of pH: I. Pyrimidines. *Biochimica et Biophysica Acta*, 9, 199-218.
- SILBER, L. E., WALENGA, J. M., FAREED, J. & KOVACS, E. J. 1993. Heparan sulphate inhibition of cell proliferation induced by TGF $\beta$  and PDGF. *Mediators of Inflammation*, 2, 299-302.
- SILVA, R. A. G. D., KUBELKA, J., BOUR, P., DECATUR, S. M. & KEIDERLING, T. A. 2000. Site-specific conformational determination in thermal unfolding studies of helical peptides using vibrational circular dichroism with isotopic substitution. *Proceedings of the National Academy of Sciences*, 97, 8318-8323.

- SIMEONSSON, J. B. & MIZIOLEK, A. W. 1994. Spectroscopic studies of laser-produced plasmas formed in CO and CO<sub>2</sub> using 193, 266, 355, 532 and 1064 nm laser radiation. *Applied Physics B*, 59, 1-9.
- SINGH, J. & KHAKUR, S. 2007. *Laser Induced breakdown Spectroscopy*, Elsevier.
- SINGH, R. D. & KEIDERLING, T. A. 1981. Vibrational circular dichroism of poly( $\gamma$ -benzyl-L-glutamate). *Biopolymers*, 20, 237-240.
- SIRCAR, A., DWIVEDI, R. & THAREJA, R. K. 1996. Laser induced breakdown of Ar, N<sub>2</sub> and O<sub>2</sub> gases using 1.064, 0.532, 0.355 and 0.266  $\mu$ m radiation. *Applied Physics B*, 63, 623-627.
- SKIDMORE, M. A., DUMAX-VORZET, A. F., GUIMOND, S. E., RUDD, T. R., EDWARDS, E. A., TURNBULL, J. E., CRAIG, A. G. & YATES, E. A. 2008. Disruption of Rosetting in Plasmodium falciparum Malaria with Chemically Modified Heparin and Low Molecular Weight Derivatives Possessing Reduced Anticoagulant and Other Serine Protease Inhibition Activities. *Journal of Medicinal Chemistry*, 51, 1453-1458.
- SKIDMORE, M. A., KAJASTE-RUDNITSKI, A., WELLS, N. M., GUIMOND, S. E., RUDD, T. R., YATES, E. A. & VICENZI, E. 2015. Inhibition of influenza H5N1 invasion by modified heparin derivatives. *MedChemComm*, 6, 640-646.
- SMITH, D. C. & TOMLINSON, R. G. 1967. EFFECT OF MODE BEATING IN LASER-PRODUCED GAS BREAKDOWN. *Applied Physics Letters*, 11, 73-75.
- SNOW, A., KISILEVSKY, R. & WIGHT, T. 1988a. Immunolocalization of Heparan Sulfate Proteoglycans to AA Amyloid Deposition Sites in Spleen and Liver During Experimental Amyloidosis. In: ISOBE, T., ARAKI, S., UCHINO, F., KITO, S. & TSUBURA, E. (eds.) *Amyloid and Amyloidosis*. Springer US.
- SNOW, A. D., BRAMSON, R., MAR, H., WIGHT, T. N. & KISILEVSKY, R. 1991. A temporal and ultrastructural relationship between heparan sulfate proteoglycans and AA amyloid in experimental amyloidosis. *Journal of Histochemistry & Cytochemistry*, 39, 1321-1330.
- SNOW, A. D. & KISILEVSKY, R. 1985. Temporal relationship between glycosaminoglycan accumulation and amyloid deposition during experimental amyloidosis. A histochemical study. *Lab Invest*, 53, 37-44.
- SNOW, A. D., KISILEVSKY, R., WILLMER, J., PRUSINER, S. B. & DEARMOND, S. J. 1989. Sulfated glycosaminoglycans in amyloid plaques of prion diseases. *Acta Neuropathologica*, 77, 337-342.
- SNOW, A. D., MAR, H., NOCHLIN, D., KIMATA, K., KATO, M., SUZUKI, S., HASSELL, J. & WIGHT, T. N. 1988b. The presence of heparan sulfate proteoglycans in the neuritic plaques and congophilic angiopathy in Alzheimer's disease. *The American Journal of Pathology*, 133, 456-463.
- SNOW, A. D. & WIGHT, T. N. 1989. Proteoglycans in the pathogenesis of Alzheimer's disease and other amyloidoses. *Neurobiology of Aging*, 10, 481-497.
- SNOW, A. D., WILLMER, J. P. & KISILEVSKY, R. 1987. Sulfated glycosaminoglycans in Alzheimer's disease. *Human Pathology*, 18, 506-510.
- ŠOLTÉS, L. & KOGAN, G. 2009. Catabolism of hyaluronan: involvement of transition metals. *Interdisciplinary Toxicology*, 2, 229-238.
- SOMLYO, A. P., BOND, M. & SOMLYO, A. V. 1985. Calcium content of mitochondria and endoplasmic reticulum in liver frozen rapidly in vivo. *Nature*, 314, 622-625.

- SOMMERFELD, A. J. F. 1953. *Atombau und Spektrallinien*, New York, Frederick Ungar.
- SRIVASTAVA, S. N., THOMPSON, K. C., ANTONSEN, E. L., QIU, H., SPENCER, J. B., PAPKE, D. & RUZIC, D. N. 2007. Lifetime measurements on collector optics from Xe and Sn extreme ultraviolet sources. *Journal of Applied Physics*, 102, 023301.
- STALLCOP, J. R. & BILLMAN, K. W. 1974. Analytical formulae for the inverse bremsstrahlung absorption coefficient. *Plasma Physics*, 16, 1187.
- STENSTAD, T., MAGNUS, J. H., KOLSET, S. O., CORNWELL, G. G. & HUSBY, G. 1991. Macromolecular Properties of Glycosaminoglycans in Primary AL Amyloid Fibril Extracts of Lymphoid Tissue Origin. *Scandinavian Journal of Immunology*, 34, 611-617.
- STEPHENS, P. J., DEVLIN, F. J., SCHÜRCH, S. & HULLIGER, J. 2008. Determination of the absolute configuration of chiral molecules via density functional theory calculations of vibrational circular dichroism and optical rotation: The chiral alkane D3-anti-trans-anti-trans-anti-trans-perhydrotriphenylene. *Theoretical Chemistry Accounts*, 119, 19-28.
- STEVEN, F. S., GRIFFIN, M. M., BROWN, B. S. & HULLEY, T. P. 1982. Aggregation of fibrinogen molecules by metal ions. *International Journal of Biological Macromolecules*, 4, 367-369.
- STEVIC, I., PARMAR, N., PAREDES, N., BERRY, L. & CHAN, A. C. 2011. Binding of Heparin to Metals. *Cell Biochemistry and Biophysics*, 59, 171-178.
- STRICKER, J. & PARKER, J. G. 1982. Experimental investigation of electrical breakdown in nitrogen and oxygen induced by focused laser radiation at 1.064  $\mu$ m. *Journal of Applied Physics*, 53, 851-855.
- SUMMERFORD, C. & SAMULSKI, R. J. 1998. Membrane-Associated Heparan Sulfate Proteoglycan Is a Receptor for Adeno-Associated Virus Type 2 Virions. *Journal of Virology*, 72, 1438-1445.
- SWEENEY, M. D., YU, Y. & LEARY, J. A. 2006. Effects of Sulfate Position on Heparin Octasaccharide Binding to CCL2 Examined by Tandem Mass Spectrometry. *Journal of the American Society for Mass Spectrometry*, 17, 1114-1119.
- T.L, E. 1985. Electron temperature determination in LTE and non-LTE plasmas. *Journal of Quantitative Spectroscopy and Radiative Transfer*, 33, 197-211.
- TAKASE, K. 1998. Reactions of denatured proteins with other cellular components to form insoluble aggregates and protection by lactoferrin. *FEBS Letters*, 441, 271-274.
- TAMBAY, R. & THAREJA, R. K. 1991. Laser-induced breakdown studies of laboratory air at 0.266, 0.355, 0.532, and 1.06  $\mu$ m. *Journal of Applied Physics*, 70, 2890-2892.
- TANAKA, T., INOUE, K., KODAMA, T., KYOGOKU, Y., HAYAKAWA, T. & SUGETA, H. 2001. Conformational study on poly[ $\gamma$ -( $\alpha$ -phenethyl)-L-glutamate] using vibrational circular dichroism spectroscopy. *Biopolymers*, 62, 228-234.
- TANAKA, T., KODAMA, T. S., MORITA, H. E. & OHNO, T. 2006. Electronic and vibrational circular dichroism of aromatic amino acids by density functional theory. *Chirality*, 18, 652-661.
- TENNENT, G. A., BRENNAN, S. O., STANGOU, A. J., O'GRADY, J., HAWKINS, P. N. & PEPYS, M. B. 2007. Human plasma fibrinogen is synthesized in the liver. *Blood*, 109, 1971-1974.

- THOENGES, D. & BARTH, A. 2002. Direct Measurement of Enzyme Activity with Infrared Spectroscopy. *Journal of Biomolecular Screening*, 7, 353-357.
- TIEDEMANN, K., BÄTGE, B., MÜLLER, P. K. & REINHARDT, D. P. 2001. Interactions of Fibrillin-1 with Heparin/Heparan Sulfate, Implications for Microfibrillar Assembly. *Journal of Biological Chemistry*, 276, 36035-36042.
- TOMLINSON, R. C., DAMON, E. K. & BRUSCHER. Proceedings of the Physics of Quantum Electronics. In: KELLY, R. P., LAX, B. & TANNENWALD, P. E., eds. *Physics of Quantum Electronics*, 1966. McGraw-Hill, New York, 527-537.
- TONGE, P. J. & CAREY, P. R. 1990. Length of the acyl carbonyl bond in acyl-serine proteases correlates with reactivity. *Biochemistry*, 29, 10723-10727.
- TONGE, P. J., FAUSTO, R. & CAREY, P. R. 1996. FTIR studies of hydrogen bonding between  $\alpha,\beta$ -unsaturated esters and alcohols. *Journal of Molecular Structure*, 379, 135-142.
- TORRES, J., KUKOL, A., GOODMAN, J. M. & ARKIN, I. T. 2001. Site-specific examination of secondary structure and orientation determination in membrane proteins: The peptidic  $^{13}\text{C}\alpha\text{-}^{18}\text{O}$  group as a novel infrared probe. *Biopolymers*, 59, 396-401.
- TRINDADE, E. S., OLIVER, C., JAMUR, M. C., ROCHA, H. A. O., FRANCO, C. R. C., BOUÇAS, R. I., JARROUGE, T. R., PINHAL, M. A. S., TERSARIOL, I. L. S., GOUVÊA, T. C., DIETRICH, C. P. & NADER, H. B. 2008. The binding of heparin to the extracellular matrix of endothelial cells up-regulates the synthesis of an antithrombotic heparan sulfate proteoglycan. *Journal of Cellular Physiology*, 217, 328-337.
- TSAI, C. S. 2006. Studies of Biomacromolecular Structures: Spectroscopic Analysis of Conformation. *Biomacromolecules*. John Wiley & Sons, Inc.
- TURNBULL, J. E., FERNIG, D. G., KE, Y., WILKINSON, M. C. & GALLAGHER, J. T. 1992. Identification of the basic fibroblast growth factor binding sequence in fibroblast heparan sulfate. *Journal of Biological Chemistry*, 267, 10337-10341.
- UNIEWICZ, K. A., ORI, A., XU, R., AHMED, Y., WILKINSON, M. C., FERNIG, D. G. & YATES, E. A. 2010. Differential scanning fluorimetry measurement of protein stability changes upon binding to glycosaminoglycans: a screening test for binding specificity. *Anal Chem*, 82, 3796-802.
- UVERSKY, V. N. & FINK, A. L. 2004. Conformational constraints for amyloid fibrillation: the importance of being unfolded. *Biochimica et Biophysica Acta (BBA) - Proteins and Proteomics*, 1698, 131-153.
- VAN STRYLAND, E. W., SOILEAU, M. J., SMIRL, A. L. & WILLIAMS, W. E. 1981. Pulse-width and focal-volume dependence of laser-induced breakdown. *Physical Review B*, 23, 2144-2151.
- VAN WIJK, X. R. & VAN KUPPEVELT, T. 2014. Heparan sulfate in angiogenesis: a target for therapy. *Angiogenesis*, 17, 443-462.
- VIEIRA, T. C. R. G., CORDEIRO, Y., CAUGHEY, B. & SILVA, J. L. 2014. Heparin binding confers prion stability and impairs its aggregation. *The FASEB Journal*.
- VILASI, S., SARCINA, R., MARITATO, R., DE SIMONE, A., IRACE, G., SIRANGELO, I., VILASI, S., SARCINA, R., MARITATO, R., DE SIMONE, A., IRACE, G., SIRANGELO, I., VILASI, S., SARCINA, R., MARITATO, R., DE SIMONE, A., IRACE, G., SIRANGELO, I. & ORGEL, J. P. R. O. Heparin Induces Harmless Fibril Formation



- in Amyloidogenic W7FW14F Apomyoglobin and Amyloid Aggregation in Wild-Type Protein In Vitro. *PLoS One*, 6, e22076.
- VIRCHOW, R. 1854. *Virchows Arch. Pathol. Anat. Physiol.*
- VLODAVSKY, I., FRIEDMANN, Y., ELKIN, M., AINGORN, H., ATZMON, R., ISHAI-MICHAELI, R., BITAN, M., PAPPO, O., PERETZ, T., MICHAL, I., SPECTOR, L. & PECKER, I. 1999. Mammalian heparanase: Gene cloning, expression and function in tumor progression and metastasis. *Nat Med*, 5, 793-802.
- WALKER, A., TURNBULL, J. E. & GALLAGHER, J. T. 1994. Specific heparan sulfate saccharides mediate the activity of basic fibroblast growth factor. *Journal of Biological Chemistry*, 269, 931-5.
- WALLACE, B. 1990. Inhibition of agrin-induced acetylcholine-receptor aggregation by heparin, heparan sulfate, and other polyanions. *The Journal of Neuroscience*, 10, 3576-3582.
- WEBB, L. M., EHRENGRUBER, M. U., CLARK-LEWIS, I., BAGGIOLINI, M. & ROT, A. 1993. Binding to heparan sulfate or heparin enhances neutrophil responses to interleukin 8. *Proceedings of the National Academy of Sciences of the United States of America*, 90, 7158-7162.
- WEYL, G. M., ROSEN, D. I., WILSON, J. & SEKA, W. 1982. Laser-induced breakdown of argon at 0.35  $\mu\text{m}$ . *Physical Review A*, 26, 1164-1167.
- WHARTON, C. W. 2000. Infrared spectroscopy of enzyme reaction intermediates. *Natural Product Reports*, 17, 447-453.
- WILLIAMS, W., SOILEAU, M. J. & VAN STRYLAND, E. W. 1983. Picosecond air breakdown studies at 0.53  $\mu\text{m}$ . *Applied Physics Letters*, 43, 352-354.
- WOODS, A. H. & O'BAR, P. R. 1970. Absorption of Proteins and Peptides in the Far Ultraviolet. *Science*, 167, 179-181.
- WU, C., YANG, Y., WU, Z., CHEN, B., DONG, H., LIU, X., DENG, Y., LIU, H., LIU, Y. & GONG, Q. 2011. Coulomb explosion of nitrogen and oxygen molecules through non-Coulombic states. *Physical Chemistry Chemical Physics*, 13, 18398-18408.
- YALÇIN, Ş., CROSLLEY, D. R., SMITH, G. P. & FARIS, G. W. 1999. Influence of ambient conditions on the laser air spark. *Applied Physics B*, 68, 121-130.
- YARWOOD, J., SHUTTLEWORTH, T., HASTED, J. B. & NANBA, T. 1984. A new radiation source for the infrared region. *Nature*, 312, 742-744.
- YASHIRO, H., SASAKI, F. & FURUTANI, H. 2011. Measurement of laser-induced breakdown threshold intensities of high-pressure gasses and water droplets to determine the number density of an aerosol. *Optics Communications*, 284, 3004-3007.
- YASUI, S. C. & KEIDERLING, T. A. 1986. Vibrational circular dichroism of polypeptides. VI. polytyrosine  $\alpha$ -helical and random-coil results. *Biopolymers*, 25, 5-15.
- YIN, X., TRUTY, J., LAWRENCE, R., JOHNS, S. C., SRINIVASAN, R. S., HANDEL, T. M. & FUSTER, M. M. 2010. A critical role for lymphatic endothelial heparan sulfate in lymph node metastasis. *Molecular Cancer*, 9, 316-316.
- YOUNG, M. & HERCHER, M. 1967. Dynamics of Laser-Induced Breakdown in Gases. *Journal of Applied Physics*, 38, 4393-4400.
- ZERNIKE, F. & NIJBOER, B. R. A. 1946. *La Théorie des Images Optiques*, Revue d'Optique.

- ZHANG, X., WANG, B. & LI, J.-P. 2014. Implications of heparan sulfate and heparanase in neuroinflammation. *Matrix Biology*, 35, 174-181.
- ZHU, H., YU, J. & KINDY, M. S. 2001. Inhibition of amyloidosis using low-molecular-weight heparins. *Molecular Medicine*, 7, 517-522.
- ZIEGLER, K. L., MELCHERT, I. & LURKEN, C. 1967. N[delta]-(2d-amino-2-carboxyethyl)-ornithine, a New Amino-acid from Alkali-treated Proteins. *Nature*, 214, 404-405.
- ZIMM, B. H. 1948. Apparatus and Methods for Measurement and Interpretation of the Angular Variation of Light Scattering; Preliminary Results on Polystyrene Solutions. *The Journal of Chemical Physics*, 16, 1099-1116.
- ZOU, S., MAGURA, C. E. & HURLEY, W. L. 1992. Heparin-binding properties of lactoferrin and lysozyme. *Comparative Biochemistry and Physiology Part B: Comparative Biochemistry*, 103, 889-895.

## Appendix A: Derivation of the Thermal Brehmsstrahlung Emission from Plasma

In this derivation, the plasma is assumed to be a linear, isotropic and homogeneous or an LIH plasma. A plasma is linear if propagating EM waves can be superposed at all times and localities, isotropic if its physical properties are the same in all directions and homogeneous if its physical properties are the same at all positions. These assumptions may not hold true in a laser induced plasma, in particular the assumptions of homogeneity and linearity, as electron temperatures and densities often vary as a function of position and direction.

The derivation consists of several stages:

- Determination of the transverse electric field  $E_t$  radiated by an electron accelerated in the coulomb field of a positive ion.
- Fourier transform  $E_t$  to obtain as a function of frequency.
- Determine the Poynting vector of the radiated EM wave.
- Integrate the Poynting vector over all directions to obtain the power radiated at frequency  $\nu$ , by a single electron.
- Determination of the power spectrum for a volume of electron number density  $N_e$  and positive ion number density  $N_p$ .
- Determination of the power spectrum for a volume with a thermal distribution of electron velocities.
- Construction and solution of the radiative transfer equation.
- Determination of the absorption coefficient.

This analysis also ignores the contribution to the continuous emission due to free-bound state transitions. This emission will also be of a continuous nature due to the initial electron states being a continuum. The effect of nuclear charge shielding from bound electrons is also ignored.

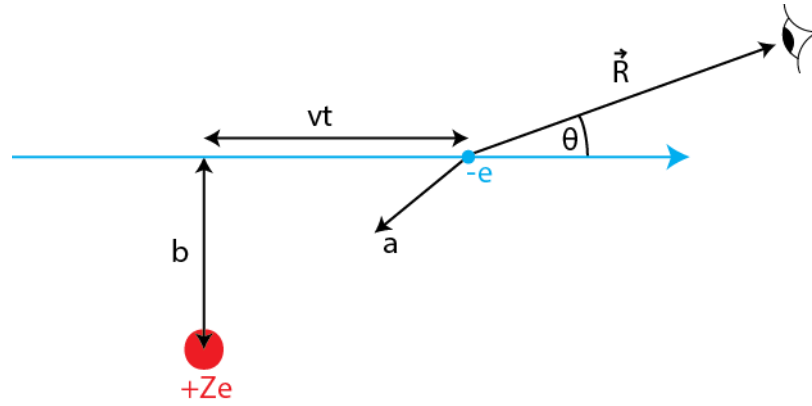


**Figure 131.** An electron moving past a positive ion of charge  $+Ze$  at time  $t$ . The trajectory of the electron is assumed to be linear with its closest approach at a distance  $b$  from the nucleus of an ion.

Consider the non-relativistic interaction between a free electron and a singly charged nucleus in Figure 131. From electromagnetics, it is known that the trajectory of the electron is that of a hyperbola but for simplicity all collisions are treated as if they result in only small angle deviations from a linear path. The closest approach of the electron is the distance  $b$  at  $t=0$ . The electron moving in the static electric field of a positive ion experiences a Coulomb force towards the ion. In the limit as  $v \gg c$ , the position of the electron at  $t$  is very close to  $vt$ . In this limit, the magnitude of the acceleration  $a$  due to the Coulomb force is:

$$|a| = \frac{Ze^2}{4\pi\epsilon_0(b^2 + v^2t^2)m_e}$$

The radiated electric field  $E$  at a distance  $|R| = r$  and angle  $\theta$  from the path of an accelerating electron is:

$$E = \frac{e|a| \sin \theta}{4\pi\epsilon_0 c^2 r} = \frac{Ze^3 \sin \theta}{16\pi^2 \epsilon_0^2 c^2 r (b^2 + v^2 t^2) m_e}$$

The Fourier transform of  $E$  determines the field as a function of frequency  $f$ .

$$\begin{aligned}
E(f) &= \int_{-\infty}^{\infty} E(t) e^{-2\pi i f t} dt = \frac{Z e^3 \sin \theta}{16\pi^2 \varepsilon_0^2 c^2 r m_e} \int_{-\infty}^{\infty} \frac{e^{-2\pi i f t}}{b^2 + v^2 t^2} dt \\
&= \frac{Z e^3 \sin \theta}{16\pi^2 \varepsilon_0^2 c^2 r m_e v^2} \int_{-\infty}^{\infty} \frac{e^{-2\pi i f t}}{\frac{b^2}{v^2} + t^2} dt
\end{aligned}$$

This integral resists the usual substitution techniques of elementary calculus, but can be solved by using the residue theorem and the Jordan lemma from complex analysis:

$$\begin{aligned}
\int_{-\infty}^{\infty} \frac{e^{-iBx}}{A^2 + x^2} dx &= \frac{\pi}{A} e^{-A|B|} \\
\therefore E(f) &= \frac{Z e^3 \sin \theta}{16\pi \varepsilon_0^2 c^2 r m_e v b} e^{-2\pi b|f|/v}
\end{aligned}$$

The time averaged Poynting vector describes the energy flux density or irradiance (rate of energy transfer per unit area) of an EM field. In the limit as  $\vec{R}$  becomes very large, the Poynting vector is that of a plane wave:

$$\begin{aligned}
\text{Poynting vector } \vec{S} &= \frac{\varepsilon_0 c}{2} E^2 \vec{r} = \frac{\varepsilon_0 c}{2} \left( \frac{Z e^3 \sin \theta}{16\pi \varepsilon_0^2 c^2 r m_e v b} e^{-2\pi b|f|/v} \right)^2 \vec{r} \\
&= \frac{Z^2 e^6 \sin^2 \theta}{512\pi^2 \varepsilon_0^3 c^3 r^2 m_e^2 v^2 b^2} e^{-4\pi b|f|/v} \vec{r}
\end{aligned}$$

The total power emitted by the electron per unit frequency is now obtained by integrating over all possible directions of  $\vec{R}$  using polar coordinates:

$$\begin{aligned}
\frac{dW}{df} &= \frac{Z^2 e^6}{512\pi^2 \varepsilon_0^3 c^3 m_e^2 v^2 b^2} e^{-4\pi b f / v} \int_0^{2\pi} \int_0^\pi \frac{\sin^2 \theta}{r^2} r^2 \sin \theta d\theta d\phi \\
&= \frac{Z^2 e^6}{512\pi^2 \varepsilon_0^3 c^3 m_e^2 v^2 b^2} e^{-4\pi b f / v} \int_0^{2\pi} \int_0^\pi \sin^3 \theta d\theta d\phi \\
&= \frac{Z^2 e^6}{512\pi^2 \varepsilon_0^3 c^3 m_e^2 v^2 b^2} e^{-4\pi b f / v} 2\pi \int_0^\pi \sin^3 \theta d\theta
\end{aligned}$$

This integral is solved using the identity  $\sin^2 \theta = 1 - \cos^2 \theta$  and the substitution  $u = \cos \theta$ .

$$\int_0^\pi \sin^3 \theta \, d\theta = \frac{4}{3}$$

$$\frac{dW}{df} = \frac{Z^2 e^6}{192\pi \epsilon_0^3 c^3 m_e^2 v^2 b^2} e^{-4\pi b f / v}$$

In the high and low frequency regimes, the emission becomes:

$$\frac{dW}{df} = \begin{cases} \frac{Z^2 e^6}{192\pi \epsilon_0^3 c^3 m_e^2 v^2 b^2}, & b \ll v/f \\ 0, & b \gg v/f \end{cases}$$

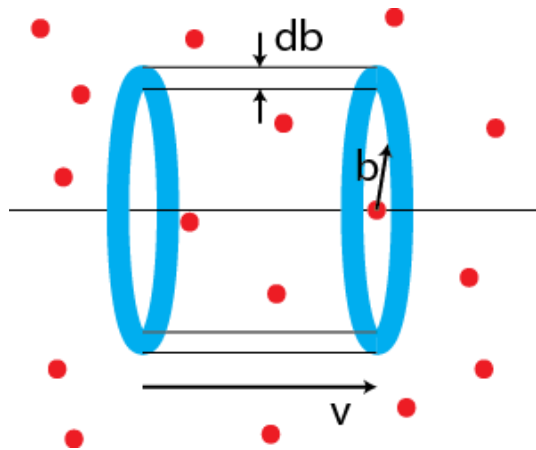


**Figure 132.** A cloud of plasma with ion density  $N_i$  and electron density  $N_e$ . The cylindrical ring of radius  $b$  and width  $db$  is the volume through which electrons at a velocity  $v$  will pass at a distance  $b$  to an ion in time  $t$ .

If the electrons in a plasma of electron number density  $N_e$  have a velocity  $v$ , the number of electrons per unit time passing through a cylindrical ring of width  $db$  and radius  $b$  around an ion is:

$$2\pi N_e v b \, db$$

For a plasma with electron density  $N_e$ , the total number of collisions is:

$$2\pi N_i N_e v b \, db$$

The **power radiated per unit frequency per unit volume** is obtained by multiplying the energy radiated per collision by the number of collisions in unit time and then integrating over all  $b$ :

$$\frac{dW}{dfdt dV} = 2\pi N_i N_e \frac{Z^2 e^6}{192\pi \epsilon_0^3 c^3 m_e^2 v} \int_0^\infty \frac{e^{-4\pi b f/v}}{b} db$$

Substituting  $b = vx/4\pi f$  this becomes:

$$\frac{dW}{dfdt dV} = \frac{Z^2 e^6 i N_e}{96\epsilon_0^3 c^3 m_e^2 v} \int_0^\infty \frac{e^{-x}}{x} dx$$

This integral is solved using the power series expansion of  $e^x$  substituting  $-x$  for  $x$ :

$$e^x = \sum_{n=0}^{\infty} \frac{x^n}{n!} \qquad e^{-x} = \sum_{n=0}^{\infty} \frac{-1^n x^n}{n!}$$

Simply dividing through by  $x$  to obtain the expansion of  $e^{-x}/x$  results in a function that has an undefined integral at  $n=0$ . Instead, the first term of the series is extracted before dividing through and integrating:

$$e^{-x} = 1 + \sum_{n=1}^{\infty} \frac{-1^n x^n}{n!}$$

$$\frac{e^{-x}}{x} = \frac{1}{x} + \sum_{n=1}^{\infty} \frac{-1^n x^{n-1}}{n!}$$

$$\int \frac{e^{-x}}{x} = \ln|x| + \sum_{n=1}^{\infty} \frac{-1^n x^n}{n \cdot n!}$$

Using this result gives the **power radiated per unit frequency per unit volume** as:

$$\frac{dW}{dfdt dV} = \frac{Z^2 e^6 N_i N_e}{96\epsilon_0^3 c^3 m_e^2 v} \left[ \ln \left| \frac{4\pi b f}{v} \right| + \sum_{n=1}^{\infty} \frac{-1^n \left( \frac{4\pi b f}{v} \right)^n}{n \cdot n!} \right]_0^\infty$$

The series in this equation converges under a ratio test but its convergence value is unknown. The series cannot therefore be replaced by a simpler function of  $f$  and  $v$ . The integral is also impossible to evaluate using these limits due to  $\ln(\infty) = \infty$ ,  $\infty^n$  and the fact that  $\ln 0$  is undefined. To get around these problems, limits of  $b$  ( $b_{max}$  and  $b_{min}$ ) are set. The equation now becomes:

$$\begin{aligned} \frac{dW}{dfdt dV} &= \frac{Z^2 e^6 N_i N_e}{96 \epsilon_0^3 c^3 m_e^2 v} \left[ \ln \left| \frac{4\pi b f}{v} \right| + \sum_{n=1}^{\infty} \frac{-1^n \left( \frac{4\pi b f}{v} \right)^n}{n \cdot n!} \right]_{b_{min}}^{b_{max}} \\ &= \frac{Z^2 e^6 N_i N_e}{96 \epsilon_0^3 c^3 m_e^2 v} \left( \ln \left( \frac{b_{max}}{b_{min}} \right) + \sum_{n=1}^{\infty} \frac{1}{n \cdot n!} \left( \frac{4\pi f (b_{min} - b_{max})}{v} \right)^n \right) \end{aligned}$$

In order to choose a value for  $b_{max}$ , we look at a graph of the function  $F(x) = e^{-x}/x$ . Figure 133 shows that the function goes to zero very fast as  $x$  increases. Above  $x=4$  the function is almost zero. I therefore choose the upper integration limit to be  $X_{max} = 4$ . This is equivalent to setting  $b_{max} = v/\pi f$ .

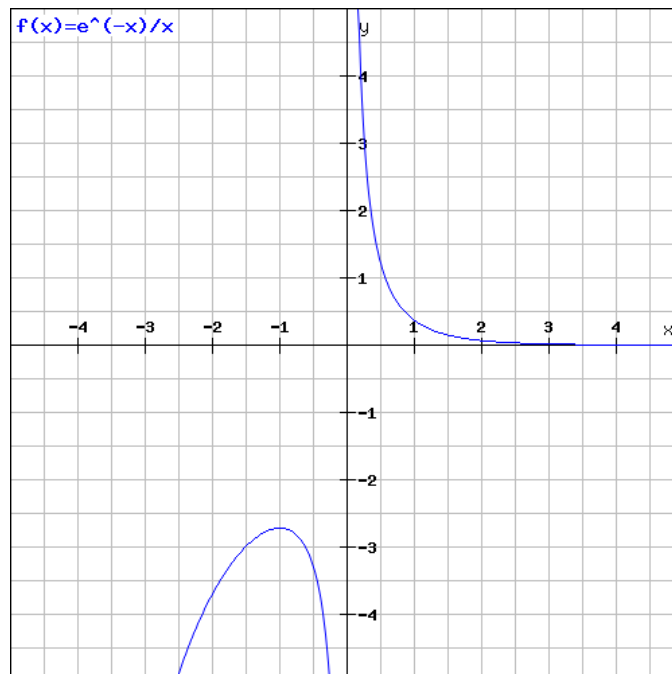


**Figure 133.** A plot of the function  $f(x) = e^{-x}/x$ .

The lower integration limit  $b_{min}$  is set by one of the following considerations:



1. The straight line approximation will begin to breakdown as  $\Delta v$  normal to the path  $\rightarrow v$ .  $\Delta v$  normal to the path can be calculated by integrating the component of the acceleration normal to the path.

$$\Delta v = \frac{Ze^2}{4\pi\epsilon_0 m_e} \int_{-\infty}^{\infty} \frac{b}{(b^2 + v^2 t^2)^{3/2}} dt = \frac{Ze^2}{4\pi\epsilon_0 m_e b^2} \int_{-\infty}^{\infty} \left(1 + \frac{v^2}{b^2} t^2\right)^{-3/2} dt$$

This integral is solved by making the substitution  $t = \frac{b}{v} \tan \theta$  and  $dt = \frac{b}{v} \sec^2 \theta d\theta$ . The substitution  $1 + \tan^2 \theta = \sec^2 \theta$  is also used. The limits of this integral become  $\theta_{Max} = \frac{\pi}{2}$  and  $\theta_{Min} = \frac{-\pi}{2}$ .

$$\Delta v = \frac{Ze^2}{2\pi\epsilon_0 m_e b v}$$

$B_{min1}$  is now taken as  $\Delta v \rightarrow v$ :

$$b_{min1} = \frac{Ze^2}{2\pi\epsilon_0 m_e v^2}$$

2. The uncertainty principal prohibits the electron from becoming too close to the ion. By the uncertainty principal we have  $\Delta x \Delta p \geq \hbar$ . Taking  $\Delta x = b$  and  $\Delta p = m_e v$  it follows that:

$$b_{min2} = \frac{\hbar}{m_e v}$$

We use as  $b_{min}$  whichever lower integration limit is the largest. Therefore  $b_{min1}$  is used if:

$$\frac{b_{min1}}{b_{min2}} > 1$$

For a plasma in thermal equilibrium  $v = \sqrt{3kT/m_e}$ .

$$\frac{b_{min1}}{b_{min2}} = \frac{Ze^2}{2\pi\epsilon_0 m_e v^2} \frac{m_e v}{\hbar} = \frac{Ze^2}{\epsilon_0 v \hbar} = \frac{Ze^2}{\epsilon_0 \hbar} \sqrt{\frac{m_e}{3k}} T^{-1/2}$$

Therefore  $b_{min1}$  prevails if:

$$\frac{Ze^2}{\varepsilon_0 h} \sqrt{\frac{m_e}{3k}} T^{-\frac{1}{2}} > 1$$

$$T < \left(\frac{Ze^2}{\varepsilon_0 h}\right)^2 \frac{m_e}{3k}$$

For singly charged ion plasmas ( $Z=1$ ),  $T < 6.32 \times 10^5 K$

For most laboratory plasmas at low temperatures  $\sim 10000K$ , it is therefore the classical limit  $b_{min1}$  that plays the most important role. Putting the relevant  $b_{max}$  and  $b_{min}$  and rearranging gives:

$$\frac{dW}{df dt dV} = \frac{Z^2 e^6 N_i N_e}{96 \varepsilon_0^3 c^3 m_e^2 v} \left( \ln \left( \frac{2 \varepsilon_0 m_e v^3}{Z e^2 f} \right) + \sum_{n=1}^{\infty} \frac{1}{n \cdot n!} \left( \frac{2 Z e^2 f}{\varepsilon_0 m_e v^3} - 4 \right)^n \right)$$

This is the approximate formula in SI units for the spectral intensity or the **emission from a low temperature plasma in Joules per unit time per unit frequency per unit volume.**

For any regime, quantum and frequency effects are conveniently included by introducing a multiplicative factor or *Gaunt factor*  $g(v, f)$  and  $n_r$ , the real part of the refractive index of the plasma such that:

$$\frac{dW}{df dt dV} = \frac{Z^2 e^6 N_i N_e}{96 \pi^4 \varepsilon_0^3 c^3 m_e^2} \frac{n_r}{v} \frac{\pi}{\sqrt{3}} g(v, f) \quad \textbf{Equation 23}$$

The factors of  $\pi/\sqrt{3}$  and  $1/\pi^4$  are inserted to conform to the conventional definition of the Gaunt factor (Gaunt, 1930). The Gaunt factor obtained here for a low temperature plasma is therefore:

$$g(v, f) = \sqrt{3} \pi^3 \left( \ln \left( \frac{2 \varepsilon_0 m_e v^3}{Z e^2 f} \right) + \sum_{n=1}^{\infty} \frac{1}{n \cdot n!} \left( \frac{2 Z e^2 f}{\varepsilon_0 m_e v^3} - 4 \right)^n \right)$$

The emission from a plasma can be determined from Equation 23 if the distribution of electron velocities is known. This can often be very difficult to determine and often the assumption of thermal equilibrium is assumed. If thermal is assumed, the electrons follow a Maxwell-Boltzmann distribution and the emission from the plasma can be found by integrating Equation 23 over the Maxwell-Boltzmann distribution.

## Appendix B: The C++ Control Code for the Plasma Spectrometer

The C++ code for the PC command line program uses a standard Microsoft Windows API: windows.h for serial port communication. The full C++ code for the command line program is:

```
// Controller Software for PC:Arduino Communication

// include libraries
#include "stdafx.h"
#include <iostream>
#include <windows.h>
#include <string>
#include <fstream>
#include <time.h>
#include <sstream>
using namespace std;

// Declare globals
ofstream csvfile;
HANDLE hSerial;
char readbuffer;
char writebuffer[1];
DWORD bytesSent;
char replate;
int lengthtime;
char letter;
char repeat='y';
char photodiode;
char answer;
DWORD mask;
DWORD errors;
COMSTAT status;
char buffer[1];
int toRead;
DWORD bytesRead;
time_t tstarttime1;
int starttime1;
int endtime1;
time_t trealtime1;
int realtime1;
time_t tstarttime2;
int starttime2;
int endtime2;
time_t trealtime2;
int realtime2;
int count=1;
int bytes=0;

int openport();
//Prototype functions

int openport()
{
    //Tell user that port-opening has been initiated
    printf("Opening Serial Port\n");

    //Announce current task
    printf("Attaching handle\n");
}
```

```

//Attempt to attach a handle to serial port
hSerial = CreateFile(L"COM4",
    GENERIC_READ | GENERIC_WRITE,
    0,
    0,
    OPEN_EXISTING,
    FILE_ATTRIBUTE_NORMAL,
    0);

if(hSerial==INVALID_HANDLE_VALUE)
{
    if(GetLastError()==ERROR_FILE_NOT_FOUND)
    {
        //Print Error if necessary
        printf("ERROR: Handle was not attached. Reason: COM4 not available.\n");
        return 0;
    }

    //Error if necessary
    printf("Mmm, something went wrong.\n");
    return 0;
}
else printf("Done!\n"); //Successfully Attached handle to serial port

//Announce current task
printf("Setting Parameters\n");

//Set serial port parameters

DCB dcbSerialParams = {0};

if (!GetCommState(hSerial, &dcbSerialParams))
{
    printf("Failed!\n"); // Return error
    return 0;
}
else // sets coms parametes
{
    dcbSerialParams.BaudRate=CBR_57600; // sets Baud rate
    dcbSerialParams.ByteSize=8;
    dcbSerialParams.StopBits=ONESTOPBIT;
    dcbSerialParams.Parity=NOPARITY;
}

if(!SetCommState(hSerial, &dcbSerialParams)) // Return error if needed
{
    printf("ALERT: Serial port failed!\n");
    return 0;
}
else printf("Done!\n\n");
//Serial port has been successfully configured

Sleep(1000);
return 0;
}

int main()
{
    openport(); // runs the function openport to initialise serial comms

    PurgeComm(hSerial,PURGE_RXCLEAR); //clear incoming and outgoing buffers
    PurgeComm(hSerial,PURGE_TXCLEAR);
}

```

```

do
{
    int option;

    // Print a list of options to the screen
    printf("\nPlasma Spectrometer Control Software\n\n");
    printf("Choose from the following options.\n\n");
    printf("1. Read output from photodiode.\n");
    printf("2. Run sample.\n");
    printf("3. Run sample at 1 scan every 4 seconds.\n");
    printf("4. Purge buffer.\n\n");
    printf("Please enter 1,2,3 or 4.\n");

    cin>>option; //get the users choice
    ofstream csvfile("C:\\Photodiode.csv"); // open a csv file
    count=0;
    switch(option)
    {
        case 1: // This checks the output of the photodiode and prints to a csv
            printf("Would like to record the output from the photodiode to a
.csv file? Please enter y or n.\n");
            cin>>photodiode;

            if (photodiode=='y')
            {
                printf("File will be created called C:/Photodiode.csv\n");
            }

            printf("Enter recording time in seconds.\n");
            cin>>lengthtime;

            //
            printf("Enter 'y' to start recording.\n");

            cin>>answer;

            printf("Recording data.\n");

            tstarttime1=time(NULL); // sets the length of time the output is
read
            starttime1=tstarttime1;
            endtime1=lengthtime+starttime1;

            trealtime1=time(NULL);
            realtime1=realtime1;

            writebuffer[0]='a'; // writes an a to the output buffer when
finished
            WriteFile(hSerial,writebuffer,1,&bytesSent,NULL);

            do
            {
                ClearCommError(hSerial,&errors,&status); // check
comm status

                if(status.cbInQue=0) // if byte is waiting in input buffer
                {
                    Sleep(1);
                }
                else
                {
                    //Read a char
                    ReadFile(hSerial,buffer,1,&bytesRead,NULL);

```

```

// print char to screen
printf("%c",buffer[0]);

if (photodiode=='y') //prints char to csv
{
    if(buffer[0]!='\r')
    {
        csvfile<<buffer[0];
    }
}

trealtime1=time(NULL);
realtime1=realtime1;
}
while (endtime1>realtime1);

ClearCommError(hSerial,&errors,&status); //get comm status
if(status.cbInQue>0) //run if anything in input buffer
{
    ReadFile(hSerial,buffer,1,&bytesRead,NULL);

//read char from buffer

do
{
    printf("%c",buffer[0]); //print char to
screen

    if (photodiode=='y') //print to csv if
required
    {
        csvfile<<buffer[0];
    }

    ReadFile(hSerial,buffer,1,&bytesRead,NULL); //read char from input buffer
//letter=buffer[0];
}
while(buffer[0]!='\r'); // do while char not equal
to carriage return

writebuffer[0]='d'; // write a d to output buffer
WriteFile(hSerial,writebuffer,1,&bytesSent,NULL);

break;

case 2: // runs a sample at 1 to 6 HZ
printf("Enter recording time in seconds.\n");
cin>>lengthtime;

printf("Enter repetition rate of laser from 1-6.\n");
cin>>reprate;

printf("Enter 'y' to start recording.\n");
PurgeComm(hSerial,PURGE_RXCLEAR); //purge input and
output buffers

PurgeComm(hSerial,PURGE_TXCLEAR);

cin>>answer;

writebuffer[0]='b'; //write a b to output buffer

```

```

WriteFile(hSerial,writebuffer,1,&bytesSent,NULL);

writebuffer[0]=reprate; // write variable reprate to output buffer
WriteFile(hSerial,writebuffer,1,&bytesSent,NULL);

printf("Recording data.\n");

tstarttime2=time(NULL); // Sets the length of time to run
starttime2=tstarttime2;
endtime2=lengthtime+starttime2;

trealtime2=time(NULL);
realttime2=realttime2;

do
{
    ClearCommError(hSerial,&errors,&status); //
get comm status

    if(status.cbInQue>0) // if anything in buffer
    {
        printf("%i ",count); // print number
of pulses to screen
        count++;

        ReadFile(hSerial,buffer,1,&bytesRead,NULL); //read input buffer

        do
        {
            printf("%c",buffer[0]); // print char in
input buffer to screen

            ReadFile(hSerial,buffer,1,&bytesRead,NULL); //read input buffer
        }
        while(buffer[0]!='\n');

        printf("%c",buffer[0]);

//print buffer to screen
    }
    else
    {
        Sleep(5);
    }

    trealttime2=time(NULL);
    realttime2=realttime2;
}
while (endtime2>realttime2);

Sleep(10);
ClearCommError(hSerial,&errors,&status); // get
comm status

if(status.cbInQue>0) // run if anything in buffer
{
    printf("%i ",count); //print number of pulses
to screen
    count++;
    ReadFile(hSerial,buffer,1,&bytesRead,NULL);
//read input buffer

    do
    {

```



```

screen
printf("%c",buffer[0]); // print input buffer to

// read input buffer
ReadFile(hSerial,buffer,1,&bytesRead,NULL);
}
while(buffer[0]!='\n');
}
else
{
Sleep(5);
}

writebuffer[0]='d'; //write a d to output buffer
WriteFile(hSerial,writebuffer,1,&bytesSent,NULL);

break;

case 3: //records once every 4 seconds. For doing 1 hour scans
printf("Enter recording time in seconds.\n");
cin>> lengthtime;
printf("Enter 'y' to start recording.\n");
cin>>answer;

output buffer
PurgeComm(hSerial,PURGE_RXCLEAR); //purge input and
PurgeComm(hSerial,PURGE_TXCLEAR);

writebuffer[0]='c'; //write a c to output buffer
WriteFile(hSerial,writebuffer,1,&bytesSent,NULL);

tstarttime2=time(NULL); // sets length of time to run for
starttime2=tstarttime2;
endtime2=lengthtime+starttime2;

trealtime2=time(NULL);
realttime2=trealtime2;

printf("Recording data.\n");

do
{
ClearCommError(hSerial,&errors,&status);

//get comm status
buffer
if(status.cbInQue>0) // if anything in input
number to screen
{
printf("%i ",count); //print pulse
count++;

ReadFile(hSerial,buffer,1,&bytesRead,NULL); //read input buffer

do
{
buffer to screen
printf("%c",buffer[0]); //print char in

ReadFile(hSerial,buffer,1,&bytesRead,NULL); //read next char
}
while(buffer[0]!='\n'); //do while buffer
is not a new line char

```

```

                                                                    printf("%c",buffer[0]); // print char
in buffer to screen
                                                                    }
                                                                    else
                                                                    {
                                                                    Sleep(5);
                                                                    }

                                                                    trealtime2=time(NULL);
                                                                    realtime2=trealttime2;
                                                                    }
                                                                    while (endtime2>realtime2);

                                                                    Sleep(10);
                                                                    ClearCommError(hSerial,&errors,&status); //get comm
staus

                                                                    if(status.cbInQue>0) // if anything in input buffer
                                                                    {
                                                                    printf("%i ",count); // print pulse number to
screen
                                                                    count++;
                                                                    ReadFile(hSerial,buffer,1,&bytesRead,NULL);

                                                                    // read input buffer

                                                                    do
                                                                    {
                                                                    printf("%c",buffer[0]); //print char in buffer to
screen

                                                                    ReadFile(hSerial,buffer,1,&bytesRead,NULL);

                                                                    // read next char in buffer

                                                                    }
                                                                    while(buffer[0]!='\n');
                                                                    }
                                                                    else
                                                                    {
                                                                    Sleep(5);
                                                                    }

                                                                    writebuffer[0]='d';
                                                                    WriteFile(hSerial,writebuffer,1,&bytesSent,NULL);

                                                                    break;

case 4: // clears input and output buffers
                                                                    ClearCommError(hSerial,&errors,&status); //check if anything
in buffer
                                                                    bytes=status.cbInQue; // write number of bytes in buffer to
screen
                                                                    printf("%i bytes in buffer cleared.\n",bytes);

                                                                    PurgeComm(hSerial,PURGE_RXCLEAR); //purge buffers
                                                                    PurgeComm(hSerial,PURGE_TXCLEAR);

                                                                    Sleep(10);

                                                                    break;
                                                                    }

                                                                    PurgeComm(hSerial,PURGE_RXCLEAR); // purge buffers
                                                                    PurgeComm(hSerial,PURGE_TXCLEAR);

```

```

        printf("\nRecording has finished.\n");
        printf("Would you like to choose another option? Please enter 'y' or
'n'.\n");
        cin>>repeat;
    }
    while (repeat=='y');

    printf("Program will close in 5 seconds.\n");
    Sleep(5000);
    return 0;
}

```

The Arduino script that runs continuously on the Arduino Uno microcontroller is:

```

// Arduino Uno Photodiode and Spectrometer Control Script//
// Joe Holman

char incoming;
int sensor;
char rebrate;
int delaytime;
//Declare Variables

// The next part runs when the Arduino is Initiated
void setup()
{
    Serial.begin(57600);
    //Sets the Baud Rate
    pinMode(11, OUTPUT);
    pinMode(10, OUTPUT);
    //Sets pin 11 and 10 to output
}

// The next part runs in a continuous loop
void loop()
{
    if(Serial.available(>0); // Checks the Serial Buffer
    {
        incoming = Serial.read();
        // read the incoming byte:

        switch(incoming)
        {
            case 'a': // do if byte is a
                do
                {
                    sensor=analogRead(A0); // read photodiode voltage
                    Serial.println(sensor); // print voltage to screen
                }
                while(Serial.available(<1);

                break;

            case 'b': // if byte is b
                delay(10);
                rebrate=Serial.read();//read bytes of laser repetition rate

```

depending on rebrate

```
switch(rebrate) //sets delay time between pulse and triggering
{
    case '1':
        delaytime=950;
        break;
    case '2':
        delaytime=450;
        break;
    case '3':
        delaytime=293;
        break;
    case '4':
        delaytime=210;
        break;
    case '5':
        delaytime=160;
        break;
    case '6':
        delaytime=126;
        break;
    default: delaytime=960;
}

do
{
    sensor=analogRead(A0); // read photodiode voltage
    if(sensor>400) // run if voltage>400
    {
        Serial.println(sensor); // voltage to screen
        delay(delaytime);
        digitalWrite(11,HIGH); // set pin 11 to +5V
        digitalWrite(10,HIGH); // set pin 10 to +5
        delay(10);
        digitalWrite(11,LOW); // set pin 11 to +0V
        digitalWrite(10,LOW); // set pin 11 to +0V
    }
    else
    {
        digitalWrite(11,LOW); // set pin 11 to +0V
        digitalWrite(10,LOW); // set pin 10 to +0V
    }
}
while(Serial.available(<1);
break;

case 'c': // do if byte is c
delay(5);

do
{
    sensor=analogRead(A0); //read photodiode voltage
    if(sensor>400); // do if voltage > 400
    {
        Serial.println(sensor);//print voltage to screen
        delay(3950); // delay for 3950ms
        digitalWrite(11,HIGH); // set pin 11 to +5V
        digitalWrite(10,HIGH); // set pin 10 to +5V
        delay(10);
        digitalWrite(11,LOW); // set pin 11 to 0V
        digitalWrite(10,LOW); // set pin 10 to 0V
    }
    else
    {
```

```
digitalWrite(11,LOW); // set pin 11 to 0V
digitalWrite(10,LOW); // set pin 10 to 0V
    }
}
while(Serial.available()<1);
break;
case 'd': // do if byte is d
break;
}
}
}
```

## Appendix C: Visual Basic for Applications Code for Analysis of Plasma Spectrometer Data

### Script 1: VBA Code for determination of beam splitter transmission

```
' Non-Time Resolved Plasma Spectrometer Absorbance Script
```

```
' Joe Holman
```

```
Sub AbsorbanceOfSample()
```

```
' Substantially speeds up script execution
```

```
Application.Calculation = xlCalculationManual
```

```
'Declare Variables
```

```
Dim DataColumns As Long
```

```
Dim DataRows As Long
```

```
Dim u As Long
```

```
Dim v As Long
```

```
Dim ColumnNumber As Integer
```

```
Dim TransTime As Long
```

```
Dim ReflTime As Long
```

```
Let ColumnNumber = 2
```

```
' This loop checks for missing data and adds columns if necessary
```

```
Do While Not (IsEmpty(Worksheets("Trans").Cells(1, ColumnNumber).Value) And  
(IsEmpty(Worksheets("Refl").Cells(1, ColumnNumber).Value)))
```

```
    If (IsEmpty(Worksheets("Trans").Cells(1, ColumnNumber).Value) Or  
(IsEmpty(Worksheets("Refl").Cells(1, ColumnNumber).Value))) Then
```

```
Worksheets("Trans").Cells(1, ColumnNumber).EntireColumn.Delete  
Worksheets("Refl").Cells(1, ColumnNumber).EntireColumn.Delete
```

Else

```
TransTime = Val(Worksheets("Trans").Cells(1, ColumnNumber).Value)  
ReflTime = Val(Worksheets("Refl").Cells(1, ColumnNumber).Value)
```

Dim Difference As Integer

```
Difference = TransTime - ReflTime
```

If Difference > 100 Then

```
Worksheets("Trans").Cells(1, ColumnNumber).EntireColumn.Insert
```

End If

If Difference < -100 Then

```
Worksheets("Refl").Cells(1, ColumnNumber).EntireColumn.Insert
```

End If

```
ColumnNumber = ColumnNumber + 1
```

End If

Loop

'Get size of trans worksheet

```
Let DataColumns = Worksheets("Trans").UsedRange.SpecialCells(xlCellTypeLastCell).Column
```

```
Let DataRows = Sheets("Trans").UsedRange.SpecialCells(xlCellTypeLastCell).Row
```

' Create new worksheet called "Working"

```
Worksheets.Add(After:=Worksheets(Worksheets.Count)).Name = "Working"
```

```
'Turn on calculations
```

```
Application.Calculation = xlCalculationAutomatic
```

```
'Copy wavelengths to new worksheet
```

```
Worksheets("Working").Range("A2").FormulaR1C1 = "=(Trans!RC+Ref!RC)/2"
```

```
Range("A2").Copy Destination:=Range("A3:A3649")
```

```
'Calculate absorbances for each laser pulse
```

```
Worksheets("Working").Range("B2").Formula =
```

```
"=IF(OR(Ref!B2=1,Trans!B2=1,Ref!B2<0.01,Splitter!$B2=""),"",IF(Trans!B2<0.01  
,2,LOG((Splitter!$B2*Ref!B2)/Trans!B2)))"
```

```
Range("B2").Copy Destination:=Range(Cells(2, 2), Cells(3649, DataColumnns))
```

```
' Create new worksheet called "Output"
```

```
Worksheets.Add(After:=Worksheets(Worksheets.Count)).Name = "Output"
```

```
'Copy "Working" to "Output"
```

```
Worksheets("Working").Cells.Copy
```

```
Worksheets("Output").Range("A1").PasteSpecial Paste:=xlPasteValues,
```

```
Operation:=xlNone, SkipBlanks _
```

```
:=False, Transpose:=False
```

```
' Create new worksheet called "Mean"
```

```
Worksheets.Add(After:=Worksheets(Worksheets.Count)).Name = "Mean"
```

```
' Create worksheet header
```

```
Worksheets("Mean").Range("A1").Value = "Wavelength"
```

```
Worksheets("Mean").Range("B1").Value = "Mean"
```

```
Worksheets("Mean").Range("C1").Value = "StandardDeviation"
```

```
Worksheets("Mean").Range("D1").Value = "NumDataPoints"
```



' Copy wavelength column

Worksheets("Mean").Range("A2").Formula = "=Output!A2"

Range("A2").Copy Destination:=Range("A3:A" & DataRows)

' Calculate mean of absorbance data

Worksheets("Mean").Range("B2").FormulaR1C1 = "=If(Count(Output!RC2:RC" &  
DataColumns & ")=0, """, AVERAGE(Output!RC2:RC" & DataColumns & "))"

Worksheets("Mean").Range("B2").AutoFill Destination:=Range("B2:B" & DataRows)

' Close and save workbook

Application.DisplayAlerts = False

ActiveWorkbook.Save

Application.DisplayAlerts = True

ActiveWorkbook.Close SaveChanges:=False

End Sub

Sub Main()

With Application

.ScreenUpdating = False

'List files for processing here

Workbooks.Open ("C:\Conc\Azure0\_5.xlsm")

AbsorbanceOfSample

.ScreenUpdating = True

End With

End Sub

**Script 2:** VBA Code for determination of the absorbance/turbidity of non-time varying samples.

' Non-Time Resolved Plasma Spectrometer Absorbance Script

' Joe Holman

Sub AbsorbanceOfSolvent()

' Speed up script execution

Application.Calculation = xlCalculationManual

'Declare Variables

Dim DataColumns As Long

Dim DataRows As Long

Dim u As Long

Dim v As Long

Dim ColumnNumber As Integer

Dim TransTime As Long

Dim ReflTime As Long

Let ColumnNumber = 2

' This loop checks for missing data and adds columns if necessary

Do While Not (IsEmpty(Worksheets("Trans").Cells(1, ColumnNumber).Value) And  
(IsEmpty(Worksheets("Refl").Cells(1, ColumnNumber).Value)))

    If (IsEmpty(Worksheets("Trans").Cells(1, ColumnNumber).Value) Or  
(IsEmpty(Worksheets("Refl").Cells(1, ColumnNumber).Value))) Then

        Worksheets("Trans").Cells(1, ColumnNumber).EntireColumn.Delete

        Worksheets("Refl").Cells(1, ColumnNumber).EntireColumn.Delete

Else

```
TransTime = Val(Worksheets("Trans").Cells(1, ColumnNumber).Value)
```

```
ReflTime = Val(Worksheets("Refl").Cells(1, ColumnNumber).Value)
```

Dim Difference As Integer

```
Difference = TransTime - ReflTime
```

If Difference > 100 Then

```
Worksheets("Trans").Cells(1, ColumnNumber).EntireColumn.Insert
```

End If

If Difference < -100 Then

```
Worksheets("Refl").Cells(1, ColumnNumber).EntireColumn.Insert
```

End If

```
ColumnNumber = ColumnNumber + 1
```

End If

Loop

'Get size of trans worksheet

```
Let DataColumns =
```

```
Worksheets("Trans").UsedRange.SpecialCells(xlCellTypeLastCell).Column
```

```
Let DataRows = Sheets("Trans").UsedRange.SpecialCells(xlCellTypeLastCell).Row
```

' Create new worksheet called "Working"

```
Worksheets.Add(After:=Worksheets(Worksheets.Count)).Name = "Working"
```

'Turn on calculations

```
Application.Calculation = xlCalculationAutomatic
```

'Create wavelengths on new worksheet

```
Worksheets("Working").Range("A2").FormulaR1C1 = "=(Trans!RC+Ref!RC)/2"  
Range("A2").Copy Destination:=Range("A3:A3649")
```

'Calculate absorbances for each laser pulse

```
Worksheets("Working").Range("B2").Formula =  
"=IF(OR(Ref!B2=1,Trans!B2=1,Ref!B2<0.01,Splitter!$B2=""),"",IF(Trans!B2<0.01  
,2,LOG((Splitter!$B2*Ref!B2)/Trans!B2)))"  
Range("B2").Copy Destination:=Range(Cells(2, 2), Cells(3649, DataColumns))
```

' Create new worksheet called "Output"

```
Worksheets.Add(After:=Worksheets(Worksheets.Count)).Name = "Output"
```

'Copy "Working" to "Output"

```
Worksheets("Working").Cells.Copy  
Worksheets("Output").Range("A1").PasteSpecial Paste:=xlPasteValues,  
Operation:=xlNone, SkipBlanks _  
:=False, Transpose:=False
```

' Create new worksheet called "Mean"

```
Worksheets.Add(After:=Worksheets(Worksheets.Count)).Name = "Mean"
```

' Create worksheet header

```
Worksheets("Mean").Range("A1").Value = "Wavelength"  
Worksheets("Mean").Range("B1").Value = "Mean"  
Worksheets("Mean").Range("C1").Value = "StandardDeviation"  
Worksheets("Mean").Range("D1").Value = "NumDataPoints"
```

'Copy wavelength column

```
Worksheets("Mean").Range("A2").Formula = "=Output!A2"  
Range("A2").Copy Destination:=Range("A3:A" & DataRows)
```

' Calculate mean of absorbance data

```
Worksheets("Mean").Range("B2").FormulaR1C1 = "=If(Count(Output!RC2:RC" &  
DataColumns & ")=0,""",AVERAGE(Output!RC2:RC" & DataColumns & "))"
```

```
Worksheets("Mean").Range("B2").AutoFill Destination:=Range("B2:B" & DataRows)
```

End Sub

Sub Main()

With Application

```
.ScreenUpdating = False
```

' List of files for script execution

```
Workbooks.Open ("C:\Conc\Working.xlsm")
```

```
AbsorbanceOfSolvent
```

```
.ScreenUpdating = True
```

End With

End Sub

**Script 3:** VBA Code for determination of the absorbance/turbidity of time varying samples.

' Time resolved absorbance calculation and dataset creation script

' Joe Holman

' Function to convert column letter to number

Function ConvertToLetter(iCol As Long) As String

Dim iAlpha As Long

Dim iRemainder As Long

iAlpha = Int(iCol / 27)

iRemainder = iCol - (iAlpha \* 26)

If iAlpha > 0 Then

ConvertToLetter = Chr(iAlpha + 64)

End If

If iRemainder > 0 Then

ConvertToLetter = ConvertToLetter & Chr(iRemainder + 64)

End If

End Function

Sub TimeResolved()

' Turn of calculation to speed up code execution

Application.Calculation = xlCalculationManual

'Declare variables

Dim MyNamefull As String

Let MyNamefull = ActiveWorkbook.Name

Dim MyName As Variant

Dim Mytest As String

Dim DataColumns As Long

Dim DataRows As Long

Dim u As Long

Dim v As Long

Dim ColumnNumber As Integer

Dim TransTime As Long

Dim ReflTime As Long

Dim FileSaveName As Variant

Dim Maximum As Double

Let ColumnNumber = 2

MyName = Split(MyNamefull, ".")

Mytest = MyName(0)

' Set path for output csv file

Application.DefaultFilePath = "C:\Users\Joe\Desktop\"

FileSaveName = Application.DefaultFilePath & Mytest & ".csv"

' Delete all wavelengths between 380 and 700nm

Worksheets("Trans").Range(Worksheets("Trans").Cells(2285,1),

Worksheets("Trans").Cells(3649, 1)).EntireRow.Delete

Worksheets("Refl").Range(Worksheets("Refl").Cells(2285, 1),

Worksheets("Refl").Cells(3649, 1)).EntireRow.Delete

Worksheets("Buffer").Range(Worksheets("Buffer").Cells(2285,1),

Worksheets("Buffer").Cells(3649, 1)).EntireRow.Delete

Worksheets("Splitter").Range(Worksheets("Splitter").Cells(2285,1),

Worksheets("Splitter").Cells(3649, 1)).EntireRow.Delete

Worksheets("Trans").Range(Worksheets("Trans").Cells(2, 1),

Worksheets("Trans").Cells(865, 1)).EntireRow.Delete

Worksheets("Refl").Range(Worksheets("Refl").Cells(2, 1),

Worksheets("Refl").Cells(865, 1)).EntireRow.Delete

Worksheets("Buffer").Range(Worksheets("Buffer").Cells(2,1),

Worksheets("Buffer").Cells(865, 1)).EntireRow.Delete

```
Worksheets("Splitter").Range(Worksheets("Splitter").Cells(2,1),  
Worksheets("Splitter").Cells(865, 1)).EntireRow.Delete
```

```
' Get dataset sizes
```

```
Let DataColumns =
```

```
Worksheets("Trans").UsedRange.SpecialCells(xlCellTypeLastCell).Column
```

```
Let DataRows = Sheets("Trans").UsedRange.SpecialCells(xlCellTypeLastCell).Row
```

```
' Remove the ms unit from the measurement times
```

```
Dim cell1 As Range
```

```
For Each cell1 In Worksheets("Trans").Range(Worksheets("Trans").Cells(1,2),  
Worksheets("Trans").Cells(1, DataColumns))
```

```
cell1 = Val(cell1)
```

```
Next cell1
```

```
Dim cell2 As Range
```

```
For Each cell2 In Worksheets("Refl").Range(Worksheets("Refl").Cells(1,2),  
Worksheets("Refl").Cells(1, DataColumns))
```

```
cell2 = Val(cell2)
```

```
Next cell2
```

```
' Inserts empty columns in missing measurements
```

```
Do While Not (IsEmpty(Worksheets("Trans").Cells(1, ColumnNumber).Value) And  
(IsEmpty(Worksheets("Refl").Cells(1, ColumnNumber).Value)))
```

```
if (IsEmpty(Worksheets("Trans").Cells(1, ColumnNumber).Value) Or  
(IsEmpty(Worksheets("Refl").Cells(1, ColumnNumber).Value))) Then
```

```
Worksheets("Trans").Cells(1, ColumnNumber).EntireColumn.Delete
```

```
Worksheets("Refl").Cells(1, ColumnNumber).EntireColumn.Delete
```

```
Else
```



```
TransTime = Val(Worksheets("Trans").Cells(1, ColumnNumber).Value)
```

```
ReflTime = Val(Worksheets("Refl").Cells(1, ColumnNumber).Value)
```

```
Dim Difference As Integer
```

```
Difference = TransTime - ReflTime
```

```
If Difference > 100 Then
```

```
    Worksheets("Trans").Cells(1, ColumnNumber).EntireColumn.Insert
```

```
End If
```

```
If Difference < -100 Then
```

```
    Worksheets("Refl").Cells(1, ColumnNumber).EntireColumn.Insert
```

```
End If
```

```
ColumnNumber = ColumnNumber + 1
```

```
End If
```

```
Loop
```

```
' Get number of row and columns in "Trans"
```

```
Let DataColumns =
```

```
Worksheets("Trans").UsedRange.SpecialCells(xlCellTypeLastCell).Column
```

```
Let DataRows = Sheets("Trans").UsedRange.SpecialCells(xlCellTypeLastCell).Row
```

```
' Create a new worksheet called "Working"
```

```
Worksheets.Add(After:=Worksheets(Worksheets.Count)).Name = "Working"
```

```
Worksheets("Working").Activate
```

### ' Turn on calculation

```
Application.Calculation = xlCalculationAutomatic
```

### ' Create times in seconds

```
Worksheets("Working").Range("B1").FormulaR1C1 =  
"=IF(OR(Trans!RC="",Refl!RC=""),"",Trans!RC/1000)"  
Worksheets("Working").Range("B1").Copy  
Destination:=Worksheets("Working").Range(Worksheets("Working").Cells(1,3),  
Worksheets("Working").Cells(1, DataColumns))
```

### ' Create wavelength column

```
Worksheets("Working").Range("A2").FormulaR1C1 = "=(Trans!RC+Refl!RC)/2"  
Range("A2").Copy Destination:=Range("A3:A1420")
```

### ' Calculate absorbance column

```
Worksheets("Working").Range("B2").Formula =  
"=IF(OR(Refl!B2=1,Trans!B2=1,Refl!B2="",Trans!B2=""),Refl!B2<0.01,Splitter!$B2  
="",Buffer!$B2=""),"",IF(Trans!B2<0.01,2,(LOG((Splitter!$B2*Refl!B2)/Trans!B  
2))-Buffer!$B2))"  
Range("B2").CopyDestination:=Range(Worksheets("Working").Cells(2,2),  
Worksheets("Working").Cells(1420, DataColumns))
```

### ' Turn off calculation

```
Application.Calculation = xlCalculationManual
```

### ' Create a new worksheet and copy data from "Working"

```
Worksheets.Add(After:=Worksheets(Worksheets.Count)).Name = "Average"  
Worksheets("Working").Cells.Copy  
Worksheets("Average").Range("A1").PasteSpecial Paste:=xlPasteValues,  
Operation:=xlNone, SkipBlanks _  
:=False, Transpose:=False
```

```
' Declare variables
```

```
Dim Row As Integer
```

```
Dim FirstRow As Integer
```

```
Dim LastRow As Integer
```

```
' Turn on calculation
```

```
Application.Calculation = xlCalculationAutomatic
```

```
' Average every three rows
```

```
For Row = 2 To 1420 Step 1
```

```
    FirstRow = ((4 * Row) - 6)
```

```
    LastRow = ((4 * Row) - 3)
```

```
    Worksheets("Average").Range(Cells(Row, 1), Cells(Row,  
DataColumns)).FormulaR1C1 = "=IF(SUM(Working!R" & FirstRow & "C:R" & LastRow  
& "C)=0,"""",AVERAGE(Working!R" & FirstRow & "C:R" & LastRow & "C))"
```

```
Next
```

```
' Turn off calculation
```

```
Application.Calculation = xlCalculationManual
```

```
' Delete excess rows
```

```
Worksheets("Average").Range("A356:A1420").EntireRow.Delete
```

```
' Create a copy of worksheet "Average" called "Copy"
```

```
Worksheets.Add(After:=Worksheets(Worksheets.Count)).Name = "Copy"
```

```
Worksheets("Average").Cells.Copy
```

```
Worksheets("Copy").Range("A1").PasteSpecial Paste:=xlPasteValues,
```

```
Operation:=xlNone, SkipBlanks _
```

```
:=False, Transpose:=False
```

```
' Turn on automatic calculation
```

```
Application.Calculation = xlCalculationAutomatic
```

```

' Declare integers
Dim Column As Integer
Let Column = 2
Dim FirstColumn As Integer
Dim LastColumn As Integer
Let DataColumns =
Worksheets("Copy").UsedRange.SpecialCells(xlCellTypeLastCell).Column
Dim FinalColumn As Integer
Let FinalColumn = (DataColumns / 2)

' Average and merge every two columns
For Column = 2 To FinalColumn Step 1
    FirstColumn = ((2 * Column) - 2)
    LastColumn = ((2 * Column) - 1)
    Worksheets("Copy").Range(Cells(1, Column), Cells(355, Column)).FormulaR1C1 =
    "=IF(SUM(Average!RC" & FirstColumn & ":RC" & LastColumn &
    ")=0,"""",AVERAGE(Average!RC" & FirstColumn & ":RC" & LastColumn & "))"
Next

' Turn on manual calculation
Application.Calculation = xlCalculationManual

' Delete excess columns
Worksheets("Copy").Range(Cells(1, (FinalColumn + 1)), Cells(1,
DataColumns)).EntireColumn.Delete

' Get number of rows and columns in "Copy"
Let DataColumns =
Worksheets("Copy").UsedRange.SpecialCells(xlCellTypeLastCell).Column
Let DataRows = Sheets("Copy").UsedRange.SpecialCells(xlCellTypeLastCell).Row

```

' Delete blank rows and columns

For u = DataRows To 2 Step -1

    If WorksheetFunction.Count(Sheets("Copy").Range(Sheets("Copy").Cells(u, 2),  
Sheets("Copy").Cells(u, DataColumns))) = 0 Then Rows(u).EntireRow.Delete

Next

For v = DataColumns To 2 Step -1

    If WorksheetFunction.Count(Sheets("Copy").Range(Cells(2, v), Cells(DataRows,  
v))) = 0 Then Columns(v).EntireColumn.Delete

Next

' Get number of rows and columns in "Copy"

DataColumns = Sheets("Copy").UsedRange.SpecialCells(xlCellTypeLastCell).Column

DataRows = Sheets("Copy").UsedRange.SpecialCells(xlCellTypeLastCell).Row

' Create a new worksheet called "Output"

Worksheets.Add(After:=Worksheets(Worksheets.Count)).Name = "Output"

' Create header and send to csv output

Open FileSaveName For Output As #1

Print #1, "Wavelength(nm),Time(s),Intensity"

' The following For loop creates the data points

For i = 1 To DataRows - 1

    ' Copy wavelength, time, and absorbance information to "Output"

    Worksheets("Copy").Range("A" & (i + 1)).Copy

    Sheets("Output").Range("A1:A" & DataColumns - 1).PasteSpecial

Paste:=xlPasteValues, Operation:=xlNone, SkipBlanks \_

    :=False, Transpose:=False

```

Worksheets("Copy").Range(Worksheets("Copy").Cells(1, 2),
Worksheets("Copy").Cells(1, DataColumns)).Copy
    Sheets("Output").Range("B1:B" & DataColumns - 1).PasteSpecial
Paste:=xlPasteValues, Operation:=xlNone, SkipBlanks _
:=False, Transpose:=True

```

```

Worksheets("Copy").Range(Worksheets("Copy").Cells((i + 1), 2),
Worksheets("Copy").Cells((i + 1), DataColumns)).Copy
    Sheets("Output").Range("C1:C" & DataColumns - 1).PasteSpecial
Paste:=xlPasteValues, Operation:=xlNone, SkipBlanks _
:=False, Transpose:=True

```

```
Worksheets("Output").Activate
```

```
' Get number of datapoints (rows) in "Ouput"
```

```
DataRows = Sheets("Output").UsedRange.SpecialCells(xlCellTypeLastCell).Row
```

```
Dim w As Integer
```

```
' Delete data point row if any value is blank
```

```
For w = DataRows To 1 Step -1
```

```
    If Worksheets("Output").Cells(w, 3).Value = "" Then
```

```
Rows(w).EntireRow.Delete
```

```
Next w
```

```
' Get number of datapoints (rows) in "Ouput"
```

```
DataRows = Sheets("Output").UsedRange.SpecialCells(xlCellTypeLastCell).Row
```

```
' Declare variables
```

```
Dim j As Long
```

```
Dim k As Long
```

```
Dim celldata As Variant
```

```

Dim cellref As String

' Convert to csv format and write to variable "celldata"
For j = 1 To DataRows
    For k = 1 To 3
        If k = 3 Then
            cellref = "C" & j
            celldata = celldata + Range(cellref).Text
        Else
            cellref = ConvertToLetter(k) & j
            celldata = celldata + Range(cellref).Text + ","
        End If
    Next k

    ' Print celldata to csv file
    Print #1, celldata
    celldata = ""

Next j

Next i

'close csv file
Close #1

' Save and close workbook
Application.DisplayAlerts = False
ActiveWorkbook.Save
Application.DisplayAlerts = True
ActiveWorkbook.Close SaveChanges:=True

End Sub

```

```
Sub Main()
```

```
With Application
```

```
' Turn off screen application
```

```
.ScreenUpdating = False
```

```
' List workbooks here for batch processing
```

```
Workbooks.Open ("C:\Conc\Lys2mgmlZnHep20ug10_5Working.xlsm")
```

```
TimeResolved
```

```
' Turn on screen updating
```

```
.ScreenUpdating = True
```

```
End With
```

```
End Sub
```